AEROELASTIC BEHAVIOUR OF COMPOSITE WINGS

by

George A. Georghiades

Thesis submitted for the Degree of Doctor of Philosophy

CITY UNIVERSITY

Department of Mechanical Engineering and Aeronautics

January, 1997

To my fiancée Maria

CONTENTS

LIST OF TABLES

LIST OF FIGURES

D.1 Coordinate system for Davies Lifting Surface theory.

D.2 Flutter speed prediction for Loring wing using the Determinant method (i.e., Δ=0). I : locus of the roots of the imaginary part (i.e., Δ_I=0), R : locus of the roots of the real part (i.e., Δ_R =0).

D.3 V-g plot for Loring wing.

D.4 V-ω plot for Loring wing.

ACKNOWLEDGEMENTS

The author wishes to acknowledge the support of the Overseas Research Students Awards Scheme (ORS) and the Department of Mechanical Engineering and Aeronautics of City University. Dr. Peter Lush the then Head of Centre for Aeronautics provided help in securing the departmental contribution.

The author would like to thank his supervisor Dr. J. Ranjan Banerjee for his invaluable help throughout the course of this research. He made substantial contribution to this thesis, both as an active participant and as a sounding board for new ideas.

He also wishes to express sincere appreciation for helpful suggestions from reviewers and colleagues during the course of this research effort. He is indebted to Dr. Shigun J. Guo for many useful comments and suggestions. He is also extremely indebted to Mr. Adam Sobey for his continued guidance and supervision.

DECLARATION

I hereby grant powers of discretion to the University Librarian to allow this thesis to be copied in whole or in part without further reference to me. This permission covers only single copies made for study purposes, subject to normal conditions of acknowledgement.

George A. Georghiades

ABSTRACT

This research work presents series of investigations into the structural, dynamic and aeroelastic behaviour of composite wings. The study begins with a literature review where the development of aeroelastic tailoring and specific applications of the technology are discussed in detail. A critique of methods for the determination of cross-sectional rigidity properties follows for beams constructed of laminated and thin-walled materials. Chordwise stiffness is shown to be an important parameter that must be considered as it has a significant effect on the amount of bending-torsion coupling present in a beam and, as a consequence, on the value of torsional rigidity. The free vibration characteristics of such beams are then examined using the dynamic stiffness matrix method. Natural frequencies and mode shapes of various beams are studied using the fibre angle, β, and the bending-torsion coupling which is measured (in this study) by the non-dimensional parameter ψ, as design variables. The results show that ψ has only a marginal effect on the natural frequencies of composite beams (wings) but can significantly modify the mode shapes of such beams. It can be used to decouple modes which are geometrically (inertially) coupled in the same way as mass balancing but without a weight penalty. It can also be used to abate the unfavourable coupling introduced by sweep angle.

Classical flutter and divergence of swept and unswept uniform cantilever wings are investigated using laminated flat beams (plates) and thin-walled beams of rectangular and biconvex cross-sections. Various parameters, such as, the fibre angle, β, the coupling parameter, ψ, the angle of sweep, Λ, the static unbalance, x_α, and the non-dimensional ratio of the fundamental (uncoupled) bending to fundamental torsional frequency, ω_h/ω_α, are varied and their subsequent effects on aeroelastic stability are investigated. The importance of torsional rigidity GJ on the flutter of composite wings is shown to be substantial in contrast with ψ, which is generally the most important parameter to be considered when the objective is that of increasing the divergence speed. Modal interchanges in the free vibration and flutter of laminated composite wings are shown to be primarily responsible for behaviour not experienced with metallic wings, in particular the effect of wash-in and wash-out on flutter. The most intriguing features of these investigations, however, are those which show that models adequate for the analysis of composite wings may be based on two parameters, the frequency ratio ω_h/ω_α and the coupling parameter ψ. Some results are confirmed by independent optimisation studies. Finally, a preliminary investigation is carried out into the flutter suppression and gust alleviation of a laminated composite wing by the use of active controls. The results show that by using an active control in an optimum trailing edge position the gust response of a wing can be significantly alleviated without compromising the already optimised flutter speed by the use of aeroelastic tailoring.

NOTATION

A	(i) Cross-sectional Area
	(ii) Axial stiffness in terms of the extensional stiffness terms A_{ij}
A_e	Enclosed area of the cross-section for thin-walled beams
A_{ij}	Extensional stiffness terms
a	Distance between elastic axis and mid-chord of the cross-section
B	Coupling stiffness in terms of the extensional stiffness terms A_{ij}
B_{ij}	Coupling stiffness terms
b	Semi-chord length
C	In-plane stiffness in terms of the extensional stiffness terms A_{ij}
C_1 , C_2	Control law parameters
C(k)	Theodorsen's function
c	(i) Chord length (width)
	(ii) Circumference
D_{ij}	Bending stiffness terms
d	Beam depth
E	Young's modulus
E_1 , E_2	Young's modulus in the fibre and transverse directions
E_x , E_y ,G_{xy}	Equivalent elastic constants
EI	Bending rigidity
EI_0	Bending rigidity when all the fibres in the laminate are set to zero degrees
EA	Extensional rigidity
F	Axial force
G	Shear modulus
G_1, G_2	Control law parameters
G_v , G_h	Effective in-plane shear stiffness of the vertical and horizontal walls of a beam respectively
G_{12}	Shear modulus in the 1-2 plane
g(s,x)	Warping function
GJ	Torsional rigidity
GJ_0	Torsional rigidity when all the fibres in the laminate are set to zero degrees
H	Net bending displacement
H_{ij}	Combinations of element compliances

$H_g(\omega)$	Frequency response function of a wing
h	(i) Bending displacement
	(ii) Beam horizontal walls
h_p	Bending displacement at a specific point on a wing
I	Inertial forces
I_α	Mass moment of inertia per unit length
K	Bending-torsion coupling rigidity
K_{ij}	Stiffness elements of dynamic stiffness matrix of a bending-torsion coupled composite beam
K^*_{ij}	Stiffness elements of dynamic stiffness matrix of an extension-torsion coupled composite beam
K_{BT}	Bending-torsion coupling rigidity
K_{ET}	Extension-torsion coupling rigidity
k_x , k_y ,k_{xy}	Curvatures corresponding to moments M_x , M_y , and M_{xy}
L	(i) Lift force
	(ii) Spanwise length
L_g	Scale length of a turbulence
M	(i) Pitching moment
	(ii) Number of layers in the vertical walls (laminates)
M_x , M_y	Bending moments per unit length
M_{xy}	Twisting moment per unit length
M_z	Chordwise bending moment
m	Mass per unit length
N	Number of layers in the horizontal walls (laminates)
N_x , N_y ,	Normal forces per unit length in x and y directions
N_{xy}	Shear force per unit length in x-y plane
P	Axial force
P_{ij}	Stiffness elements relating forces and displacements
Q_i	Generalised forces corresponding to externally applied forces
Q_y ,Q_z	Shear forces
Q_w	Generalised warping related force
q_i	Generalised coordinates
q(C)	Objective function
R	GJ/EI
r_α	Radius of gyration
r_n	Projection of the position vector r in the normal direction

S	Shear force
T	(i) Axial force or Tension
	(ii) Torque
t	(i) Time
	(ii) Thickness
U	Axial displacement
υ	Beam vertical walls
V	(i) Speed of the flow
	(ii) Flight speed
V_D	Divergence speed
V_{D0}	Divergence speed when all the fibres in the laminate are at $\beta = 0^0$
V_F	Flutter speed
V_{F0}	Flutter speed when all the fibres in the laminate are at $\beta = 0^0$
u, v, w	Displacement components in x, y, and z directions
W	Downwash of a sinusoidal vertical gust
$\widetilde{W}_g$	Amplitude of the gust velocity
x_α	Distance between shear centre and centroid of the cross-section

Greek Symbols

β	(i) Fibre angle
	(ii) Non-dimensional warping function
γ_{xy} , γ_{yz} ,γ_{xz}	Shear strains in x-y, y-z, and x-z planes
Γ	Cross-section shape
δ	Control rotation
ε_x , ε_y ,ε_z	Normal strains in x, y, and z directions
Θ	Bending rotation
Λ	Sweep angle
λ	Torsional warping function
ν	Poisson's ratio
ρ	Density (air, material, etc.)
σ	Stress
$\sigma_{n\alpha}$	Root mean square value of the normal acceleration

σ_g^2	Mean square value of the gust (wing) response
$\sigma_{\omega g}^2$	Mean square value of gust velocity
ϕ	Normal mode shape
φ	Torsional rotation
φ_p	Torsional rotation at a specific point on a wing
Φ	Net torsional rotation
Φ_i	Mode shape at note i
$\Phi_\alpha(\omega)$	Wing response power spectrum
$\Phi_g(\omega)$	Atmospheric turbulence power spectrum
ψ	Bending-torsion coupling (cross-coupling) parameter
ω	(i) Natural (circular) frequency
	(ii) Gust frequency
ω^*	Trial frequency
ω_h	Uncoupled fundamental bending frequency
ω_α	Uncoupled fundamental torsional frequency

Matrices

[C]	Damping type control law in complex matrix form
[D]	Generalised damping matrix
[F]	Force matrix
[K]	Stiffness matrix
$[K_G]$	Generalised stiffness matrix
$[K_D]$	Generalised Dynamic stiffness matrix
{k}	Bending and twisting curvatures
[M]	Mass matrix
$[M_G]$	Generalised mass matrix
{M}	Bending and twisting moments
{N}	In-plane forces
{q}	Modal coordinates (column matrix)
$\{q_m\}$	Generalised coordinates of main lifting surface
$\{q_\delta\}$	Generalised coordinates of the control surface
$[AC_\delta]$	$[QA_\delta][C\}$

$[QA]$	Flutter matrix
$[QA_m]$	Generalised unsteady aerodynamic matrix of the wing
$[QA_\delta]$	Generalised unsteady aerodynamic matrix of the control surface
$[QA]_I$	Imaginary part of generalised unsteady aerodynamic matrix
$[QA]_R$	Real part of generalised unsteady aerodynamic matrix
$\{QF\}_E$	Generalised aerodynamic force matrix resulting from external excitation
$[QF]$	Generalised aerodynamic matrix
$[QG]$	Generalised aerodynamic force due to the gust loading
$[\Phi_P]$	Modal matrix

Abbreviations

ADCA	Advanced Design Composite Aircraft
ADOP	Aeroelastic Design Optimisation Program
ADS	Automated Design Synthesis
AFFDL	Air Force Flight Dynamics Laboratory
ASTROS	Automated STRuctural Optimisation System
CALFUN	CALculation of Flutter speed Using Normal modes
CAS	Circumferentially Asymmetric Stiffness
COMBO	COMposite Box Optimisation program
CRLP	Chordwise Rigid Laminated Plate
CUS	Circumferentially Uniform Stiffness
DARPA	Defence Advanced Research Projects Agency
DFP	Davidon-Fletcher-Powell variable metric method
FASTOP	Flutter And STrength Optimisation Program
FW	Free Warping
HARP	High Aspect Ratio Plate model
HiMAT	Highly Manoeuvrable Advanced Technology
L-S	Lifting Surface theory
MMC	Metal Matrix Composite
NABSA	Nonhomogeneous Anisotropic Beam Section Analysis
PSD	Power Spectral Density
RMS	Root Mean Square
S-T	Strip Theory
SWEEP	Structural WEight Estimation Program

TACT	Transonic AirCraft Technology program
TSO	Tailoring and Structural Optimisation
WICAD	Wing/Inlet Composite Advanced Development
WRE	Warping Restraint Effect

CHAPTER 1

GENERAL INTRODUCTION

1. GENERAL INTRODUCTION

1.1 Background

The optimal utilisation of structural material in aircraft design has always been an objective of designers. The minimum weight aspect of aircraft design is well known. Shanley [1.1] writes,

> *"primary function of the aircraft structure is to transmit forces through space ...the objective is to do this with the minimum possible weight and at minimum cost...the optimum structure is the one that does the best overall job of minimising the undesirable quantities (weight, air resistance, cost, service troubles, production time, etc.)."*

While weight is undeniably a measure of utmost importance to the structural designer, the real objective is performance, which may involve weight as a constraint, but also includes, among others, range, payload, and turn rate.

Flexibility is generally associated with light weight so that aeroelastic problems were encountered and known from the earliest days of flight. We may recall that the Wright Brothers in 1903 made favourable use of flexibility in the lateral control of their aircraft by wing warping, and that they were aware of the adverse effect of torsional deformations on the thrust of a propeller. Wing divergence, a static aeroelastic problem, has been surmised as the probable cause of S. P. Langley's failure to control his machine in its flight over Potomac in the same year. During World War I, in 1916, elevator flutter of a British bomber was investigated by the renowned pioneer F. W. Lanchester and was remedied by raising the torsional rigidity of the elevators.

Although numerous other aeroelastic incidents followed in the pre-World War II period, problems in aeroelasticity did not attain the prominent role that they now play until the early stages of the war. This is partly because by that time the problem had been understood and the foundations of the basic theory had been laid with sources of contributions in many countries, such as, UK, USA and the Netherlands, and partly because aircraft speeds were relatively low and their

thickness to chord ratio was relatively high, thus giving the structural engineer the required design flexibility to obtain the required bending and torsional rigidities and thus producing structures sufficiently rigid to preclude most aeroelastic phenomena.

Although many isolated aeroelastic incidences still occurred in that period, they could generally be explained away and given an ad-hoc solution. In particular, problems relating to flutter were prevented by isolating the motions in several freedoms, such as, by mass balancing of the lifting surfaces at the expense of an additional weight, and/or by raising the lowest critical flutter speed safely beyond possible speeds of flight by increase of the relevant natural frequencies. The latter was usually effected by designing for increased stiffness with a less than proportional increase of weight or, preferably, without any increase of weight. Problems with classical torsional divergence were overcome by increasing wing torsional rigidity which also led to an unwelcome increase in weight.

Thus the two basic remedies for aeroelastic problems, increased stiffness and mass balance, were already well established, and together with damping mechanisms, are still the basic elements that must be properly incorporated into the vehicle structure to avoid aeroelastic instabilities.

For most designs developed between the two World Wars, flutter, which usually involved coupling between an almost pure bending and a pure torsional mode due to the unswept and more or less constant chord wing planforms, would most often occur at a lower airspeed than divergence and was therefore given more attention. This situation changed in the late 40's with the first approaches towards transonic flight as a result of the advent of jet engine and the introduction of improved light alloy structures. It was found that the best way to reduce the high transonic drag build-up was to sweep the wing relative to the airflow either forward or backward. However, the divergence speed drops dramatically for even slight forward sweep angles because of what is known as "wash-in". The spanwise bending of a swept-forward wing induces an increase in the local streamwise angle of attack, resulting in an increase in aerodynamic loads. A swept-back wing experiences an opposite, or "wash-out", effect. The only known cure for the wash-in of metallic wings is to increase the bending stiffness by adding extra quantity of material, resulting in an unacceptable increase in structural weight. As a result, high performance aircraft have had their wings swept back for the last 40 years. Only a

handful of swept-forward designs have flown, most of them adopting this configuration for nonaerodynamic reasons.

The objective of ever improved performance has led to thinner, lighter and more flexible wings which, coupled with moderately high aspect ratio and sweep, induced unintentional couplings between the various modes of structural deformation. Therefore, the classical flutter problem, where almost pure bending mode couples with almost pure torsional one, has been transformed into a more complex one. These unintentional couplings, which proved to have adverse effects in design, have overlapped stability, response, and flutter. Correspondingly this has narrowed the aeroelastic margins of required stiffness, so that aeroelastic problems have become more complex.

In the ten year period from 1947-57 a survey indicated that more than 100 different aeroelastic incidents occurred in the United States alone, for civil and military aircraft. These occurred mostly of control surfaces and tabs, but also included all-movable surfaces, wings carrying external stores, and one case of a T-tail aeroplane.

As a result, structural engineers were confronted with requirements for stiffness which were now very severe (especially for the transonic speed range) so that their ability to meet such stiffness levels became increasingly marginal. This necessitated thinner and lighter wings, so designers turned to more complicated designs in order to control aeroelastic instabilities. Hill's isoclinic wing is an excellent example of such practice. Hill sought to improve the aeroelastic performance of the wing, being primarily concerned with aeroplane longitudinal and lateral stability as well as aileron reversal. This wing was designed so that its incidence, or inclination to the airflow, remained constant along the span when the wing flexed. This was achieved, in part, by placing the torsion box well back in the wing. This showed that with careful design, bending-torsion coupling on a scale which had not previously been experienced could be successfully accommodated.

Almost 20 years elapsed before the idea to control passively the wing incidence due to flexural distortion was again proposed as a result of the more or less simultaneous invention, around 1960, of graphite fibres in the UK and boron fibres in the USA. The introduction of composite materials into the realm of aircraft

design in the early 70s, has led to new airframe design concepts as well as the re-evaluation of older concepts. The main attraction in using composite materials is the substantial weight saving that could be achieved because of their superior strength-to-weight and stiffness-to-weight ratios, compared with conventional materials of aircraft construction such as aluminium alloy. Weight savings of the order of 25% can generally be achieved using current composites in place of metals. Other attractions of composite materials are their enhanced fatigue and damage tolerance and the benefits afforded by the ability to incorporate more refined aerodynamic design into planform and aerofoil section geometries when compared with conventional aircraft materials.

Today almost every aerospace company is developing products made with fibre-reinforced composite materials. The most common application of composites in fixed wing aircraft structures is in the skin of wings, tails, and control surfaces as shown in Table 1.1.

Table 1.1

Aircraft applications of composite materials

Aircraft	**Applications**
F-14	Boron/epoxy horizontal tail skins
F-15	Boron/epoxy horizontal and vertical tail skins
F-16	Graphite/epoxy horizontal and vertical tail skins and control surfaces
F/A-18	Graphite/epoxy wing skins, horizontal and vertical tail skins, speed brake, and control surfaces
AV-8B	Graphite/epoxy wing (skin plus substructure), horizontal tail skin, forward fuselage, and control surfaces
X-29†	Graphite/epoxy wing skins
Boeings 757 and 767	Graphite/epoxy control surfaces, graphite-aramid/epoxy fairings, cowlings, etc.
Lear Fan 2100	"Almost all" graphite/epoxy structure

Due to their outstanding properties, fibre-reinforced laminated composite thin-walled beams are likely to play a crucial role in the construction of aeronautical and aerospace vehicles. While the main driving force behind their increasing use

† the only fixed wing aircraft application where the anisotropic nature of fibre composites is utilised to minimise an aeroelastic problem, namely that of torsional divergence.

has been their high specific stiffness and strength, fibre reinforced materials have another property, anisotropy. This anisotropic property can be used to induce elastic coupling between various modes of structural deformation of fibre composite structures to a far greater degree than is possible, if at all, in their metallic counterparts. However, these elastic couplings are typically not exploited in composite designs. In particular, this inherent tailorability of composite structures has not been taken advantage of in aeroelasticity, partly because the mechanisms of inducing favourable effects by control deformation are insufficiently understood. As with the introduction of any new technology, a large amount of basic research is needed in order to obtain a better understanding of new problems created by the use of composite materials.

As a consequence, the successful employment of laminated composite materials in aircraft structures, coupled with their anisotropic property, has generated a renewed interest in the field of aeroelasticity. By exploiting the directional properties of composite materials, and thereby creating aerodynamic loads through controlled deformation, aeroelastic instabilities such as flutter and divergence, could be controlled without weight penalties (i.e., mass balancing, increase in bending and torsional rigidities by adding material, etc.). The technology to design for a predetermined aeroelastic response of a lifting surface using composite materials has been named aeroelastic tailoring. Shirk et al. [1.2] defines aeroelastic tailoring as,

> *"...the embodiment of directional stiffness into an aircraft structural design to control aeroelastic deformation, static or dynamic, in such a fashion as to affect the aerodynamic and structural performance of that aircraft in a beneficial way."*

As a result, a great deal of research activity has been devoted to the improvement of aeroelastic stability of wings by use of composites. The application of this new technology has resulted in the possibility of practically eliminating (without any weight penalty) the occurrence of aeroelastic divergence of a swept-forward wing aircraft. Both the tremendous research activity in this field (see literature review in chapter 2), and the successful construction of the Grumman X-29 swept-forward wing experimental aircraft (here the anisotropic nature of fibre composites is utilised to minimise the torsional divergence problem) reveal the

exceptional interest expended to this problem. Along with many, known advantages conferred by the use of structural composites, a series of challenges arise in consequence.

Some of these challenges derived from the complexities arising from the anisotropic nature of composite materials themselves, and the multiplicity of structural couplings, which do not exist in the case of isotropic structures such as light alloy ones. If one looks closer at the problem of divergence, only a reduction in wash-in is required, without increasing the bending rigidity. On the other hand, it has been shown that an increase in wash-in can raise the flutter speed significantly. Thus, the directional properties of laminated composite materials can be oriented to alter the static and dynamic characteristics of beams (wings) made of such materials, leading to aeroelastic tailoring and thus to possible optimisation of design.

The introduction of composite materials can be regarded as a landmark in the history of aircraft design and the unusual static and dynamic characteristics of these materials are expected to have far reaching consequences on aeroelasticity.

It is in this area of aeronautical research that the work reported in this thesis falls, and the particular tasks which are undertaken are discussed in section 1.3. The next section reviews contributions by others in the field.

1.2 Research Efforts in the Field

In varying degrees of complexity, several theoretical and experimental studies have examined the various aspects and benefits of aeroelastic tailoring. There have been mainly two major levels of research effort. The first one, typically used in industry, makes use of practically oriented numerical methods to perform the design work. The Wing Aeroelastic Synthesis Procedure (TSO) [1.3] and the Flutter And STrength Optimisation Program (FASTOP) [1.4] are excellent examples of this type of activity.

The second level of research effort is less of practical nature but is more academic in content and thereby enabling one to understand the complications and

consequences of the new technology as well as to assess the limits and problems associated with its application. This latter level of research concentrates upon the mathematical modelling of structures. Many references in the literature proposed a beam-like model for the structural deformation of the wing, since the tailoring was focused on bending-torsion deformation coupling, while in others, more complicated models were used to observe the various aspects of aeroelastic tailoring. In general, they all concentrated on stability of the aircraft in divergence and flutter, lateral control effectiveness, and load redistribution.

Krone [1.5] appears to be the first author to show that divergence instabilities could be eliminated by use of composites for certain classes of swept-forward wings without any weight penalty when compared with an equivalent swept-back design. Encouraged by Krone's work [1.5], many studies of the aeroelastic stability of laminated wings have appeared over the past fifteen years. Many of these studies have used ply orientation as a design variable with and/or without the presence of bending-torsion coupling [1.6-1.9]. The most intriguing features of these works, however, are those which show the required trade-off, or compromise, between flutter speed and divergence speed. The objective of increased flutter speed invariably leads to a wash-in (bend-up/twist-up) condition which is undesirable for divergence. Conversely, any increase in the divergence speed due to wash-out (bend-up/twist-down) condition is likely to be accompanied by a decrease in flutter speed.

Several other investigators have studied the aeroelastic stability of laminated wings in recent years using rigidity properties as design variables [1.10-1.12] instead of ply orientation. One of the most important of these studies was carried out by Weisshaar [1.12] who theoretically showed that both flutter and divergence can be eliminated.

A significant number of theoretical observations were later validated experimentally [1.13-1.15]. One interesting experimental work was that of Landsberger and Dugundji [1.15] who showed that by designing a wing to exhibit wash-out behaviour (bend-up/twist-down) by the use of positive ply angle lay-up, the adverse geometric divergence effect of swept-forward wings can be overcome. There are also a few more researchers who investigated experimentally the aeroelastic behaviour of composite wings utilising the whole aircraft configuration

[1.16-1.17], in which the importance of including the rigid-body modes in any aeroelastic analysis of composite wings was emphasised.

A number of other researchers have investigated the design latitude available for desired aeroelastic effects [1.18-1.20]. An excellent example is the work of Shirk and Griffin [1.20] who used an aeroelastic optimisation program to design three wing structures for minimum weight, maximum wash-in, and maximum wash-out. The authors demonstrated the ability to tailor a wing aeroelastically for centre-of-pressure control either from a load relief standpoint or for an increased flexible lift.

It is clear from such studies that the unique features of laminated composite materials make them prime candidates for aeroelastic tailoring efforts. On the other hand, the wide range of possible material geometry and manufacture makes it difficult to conduct general studies of the type commonly done for metallic construction. For this reason the present research focuses only on one class of composite wings, namely that of uniform wings of constant chord.

It is important to note that despite the extensive research that has already been carried out in this field, it is not yet clear precisely how bending-torsion can be used in beneficial way leading to an enhanced flutter and/or divergence speed. For example, although the wash-in effect has been shown to be useful for flutter but undesirable for divergence, it was only shown for a limited number of ply lay-ups. In addition, no researchers appear to have provided a pattern for the understanding and prediction of flutter behaviour for composite wings. Furthermore, there are a number of uncharacteristic features in the aeroelastic behaviour of composite wings which no one appears to have given any details or any convincing reasons as to the cause of their unusual occurrence. It is therefore quite apparent that the effect of tailoring upon flutter and divergence of the “clean” wing configuration is not yet well fully understood (or well documented) and thus the subject matter needs further investigation.

1.3 Research Aims and Objectives

The main aim of the present research is to study the potential of composite materials to enhance aeroelastic stability. The study will restrict its discussion to the effects of aeroelastic tailoring upon wing flutter and divergence of uniform constant chord cantilever composite wings without added mass in the subsonic region. Such a wing is often referred to as a "clean" wing.

Aeroelastic tailoring will be discussed extensively in terms of laminated composite construction. Despite the wealth of information available in the literature today, formal strategies and design goals for efficient utilisation of advanced composite materials have yet to be fully developed. Such design strategies require consideration of issues such as durability and damage tolerance, automatic controls and their interaction with structural response, and overall aircraft performance. It is important to note that, rather than attempting to present results which are acceptable to the structural engineer, this study concentrates on discussing aeroelastic tailoring as a way of maximising measures of performance. In the course of this discussion, two essential prerequisites of any aeroelastic analysis will be examined, namely the static and dynamic behaviour of composite wings. In addition, the possibility of alleviating the gust response of a wing by the use of active controls without reducing its already optimised flutter speed is studied.

Firstly, analytical stiffness modelling of laminated composite beams is examined, since conventional simplifying assumptions which are generally satisfactory for metallic structure have sometimes been found to be inaccurate for composite structures [1.21-1.24]. In particular, equivalent beam stiffness models for laminated composite flat beams (plates) and thin-walled beams are examined, as well as finite element models for such idealisations. Previous studies [1.21, 1.24] have disclosed the importance of properly modelling or estimating the rigidity and coupling properties. This research discusses an extension of these studies in a more unified and comprehensive manner than previously presented.

In addition to the discussion of stiffness models for laminated composite beams, this research also examines the second essential prerequisite of any aeroelastic analysis, the free vibration behaviour of composite beams. An extensive amount of literature related to the dynamic effects of bending-torsion deformation is

in existence. References [1.21-1.31] are significant examples of such literature. The present research focuses upon a number of the same phenomena presented by the references cited previously. One important contribution made in this study, however, is the use of dynamic stiffness matrix method in the free vibration analysis (and later in the aeroelastic analysis) of composite wings. Some advantages of the dynamic stiffness method in free vibration analysis are well known [1.32], particularly when higher frequencies and better accuracies are required. Furthermore, the emphasis of the present study is upon the dynamic behaviour oriented towards aeroelastic tailoring analysis. The effects of bending-torsion and inertia couplings on free vibration natural frequencies and mode shapes and their impact upon aeroelastic characteristics of wings are presented in detail.

The study then continues with its main objective which is the understanding of the mechanism and potential of composites for passive structural control of flutter and divergence. The approach to this investigation is similar to the one used by Weisshaar in a number of investigations into the flutter and divergence behaviour of laminated composite wings [1.6, 1.8, 1.12]. The present study can be regarded as a continuation of those investigations. In addition to showing the effect of fibre orientation and other rigidity and structural parameters on flutter and divergence (using mostly unidirectional laminates), this study takes a step further and takes the view that in some cases it might be more advantageous to stick to classical aeroelasticity, and thus maximising the torsional rigidity (GJ) or the ratio of the fundamental (uncoupled) torsional and bending frequency (ω_α/ω_h) using uncoupled laminates (i.e., without controlled deformation).

The study then approximates, by the use of suitable non-dimensional parameters, the flutter behaviour of realistic composite wings exhibiting wash-in and wash-out behaviour. This enables the understanding and prediction of such behaviour which can be regarded as an important contribution to the field of aeroelasticity. Furthermore, a number of other uncharacteristic features of composite wings are also investigated and explained.

In the course of the above discussions, parameters are identified which have significant effects on many aeroelastic features. Trend information together with potential exceptions will also be discussed. A discussion of laminate tailoring both in terms of laminate geometry and overall characteristics is also included. Finally,

potential trade-offs and conflicts are discussed. Some of the principal results of the above investigations are confirmed by carrying out independent optimisation studies.

Having established an ability to optimise the flutter speed of a composite wing design, attention turns to gust alleviation of such wings by the use of trailing edge active controls. This is achieved without compromising the already optimised flutter speed. An extensive amount of literature related to flutter suppression and gust alleviation by the use of active controls is in existence. References [1.33-1.36] are significant examples of such literature. In contrast to the references cited previously, in the present study control laws are optimised taking into consideration both flutter suppression and gust alleviation.

1.4 Method of Analysis

The study is wholly theoretical (and computational) and as a consequence many well established ideas and computer implementations are used.

To formulate the stiffness model the well established lamination theory is used and is shown to be satisfactory. The free vibration characteristics of composite wings are examined using an exact dynamic stiffness matrix formulation [1.37] which can be superior to conventional methods when predicting natural frequencies. It is important to note that this study appears to be one of the first to use an exact dynamic stiffness formulation in the flutter analysis of composite wings. As will be shown later (in contrast to the metallic wings), accuracies in the free vibration characteristics of composite wings are of vital importance in any aeroelastic analysis since these have a profound effect upon the aeroelastic characteristics of such wings.

The aeroelastic analysis is carried out using the method of generalised coordinates using normal modes. In the structural idealisation of the wing, beam elements are used without undue simplification to obtain the dynamic stiffness matrix of the wing. The natural frequencies and the normal mode shapes are then calculated using the Wittrick-Williams algorithm [1.38]. The unsteady aerodynamic

idealisation uses a Strip theory of Theodorsen type, which is based on two-dimensional (2D) incompressible flow, and/or a Lifting Surface theory of Multhopp type [1.39] which takes into account the effect of three-dimensional (3D) compressible flow.

Finally, the results for all optimisation studies are obtained using the well established computer program ADS (Automatic Design Synthesis) [1.40].

1.5 The Importance and Limitations of the Study

In addition to the formal engineering mission of research, there is an educational mission. The ability of large scale computer codes to provide detailed numerical answers to properly posed questions has, in some cases, outstripped the ability to interpret these answers and to display creative thinking. Much remains to be accomplished in this area of emerging technology. By providing the information presented in this study and the reasons why the wings behave as they do, it is hoped that a further interest and understanding of aeroelastic tailoring will follow, with improved design in prospect. This will enable structural engineers to be in vanguard to those seeking truly integrated designs.

In the course of this research a number of difficulties have been encountered. The most important one being the unusual static, dynamic and aeroelastic features of composite wings when compared to those of their metallic counterparts. Weisshaar [1.41] writes,

> *"Note also that,..., no stable airspeed for flutter could be found using six or more modes. While it is unlikely that this theoretical situation could occur in reality, this data is presented to illustrate the complex nature of tailoring".*

Many other researchers faced similar difficulties. Among them, Cesnik et al. [1.7] investigated the flutter behaviour of a thin-walled box-beam by the use of fibre orientation. The authors write,

> *"The plot is not smooth due to the changes of the lowest flutter mode shape. Future work will include examining these flutter mode shapes and its variation with ply angle, which should provide a better understanding about the phenomenon"*

Another important difficulty was the lack of vigorous analytical and experimental data. Much of what has been published is analytical and in non-dimensional form making a direct comparison difficult for validation purposes.

These difficulties, however, have not undermined the quality and outcome of this research as the author has compensated this by conduct of extensive original theoretical research. During the course of this research effort, a significant number of the above unexplained phenomena have been explained.

1.6 Outline of the Study

In this chapter the main objectives and importance of the study are defined. The specific objectives of the study and the particular method of analysis are outlined. The procedure that is followed during each stage of the research process and the difficulties that are encountered are detailed. The results and discussions of this research effort are organised as follows.

In **Chapter 2** a detailed review of available literature is undertaken in order to establish the development of aeroelastic tailoring, and identify the key areas of research. The potential and associated problems of aeroelastic tailoring to enhance aeroelastic performance and the theory underlying the technology are discussed. A summary of trend studies that have been performed and discussion of more specific applications are presented. Emphasis is given to the academic level of research where the problems are analysed with various degrees of complexities and their merits are observed in detail.

Chapter 3 deals with the stiffness modelling of composite beams. Firstly, a summary of relevant literature is provided. Then the most popular stiffness models

associated with published work are discussed. These cover both flat beams (plates) and thin-walled box-beams. Explicit expressions for the bending, torsional and bending-torsion coupling rigidities are provided for all the models discussed. In order to understand the differences between the various models, expressions for the displacement field, associated strain field and rigidity parameters are provided using the same notation. These expressions are then compared for various box-beam models and the significance of any differences are discussed. Finally, in order to examine the effect of ply orientation on the rigidity and coupling parameters, a parametric study is carried out using stiffness models selected from the literature.

Chapter 4 discusses the free vibration characteristics of composite beams. Natural frequencies of composite beams exhibiting bending-torsion or extension-torsion coupling are calculated using an exact dynamic stiffness matrix method. Numerical results are compared with experiment and also with those given by other methods, e.g., Rayleigh-Ritz, partial Ritz and finite elements, and cover a representative cross-section of the literature. These results are presented for five types of cantilever composite beams of which three are flat beams of solid rectangular cross-section and two are thin-walled rectangular box-beams. Emphasis is placed on how the fibre orientation, the bending-torsion coupling, and the static unbalance (inertia coupling) affect the natural frequencies and mode shapes of composite beams.

Chapter 5 presents the results of three different but related studies of aeroelastic tailoring. The first study surveys aeroelastic stability trends for selected configurations as a function of significant design parameters, such as, the stiffness ratio of torsional and bending rigidity, wing sweep, static unbalance (inertia placement) and the bending-torsion coupling parameter. Significant trends, features, and limitations of tailoring are then identified.

In the second study an analytical investigation is carried out into the flutter and divergence behaviour of swept and unswept composite wings. In particular, the effect of stiffness and coupling parameters on flutter and divergence speeds of graphite/epoxy cantilevered wings is investigated using the fibre and sweep angles as design variables. Emphasis is given on how the fibre orientation affects the stiffness

and coupling parameters of a composite wing, and in turn, how these parameters affect the flutter and divergence speeds.

The third study, which is partly motivated by the second, is focused on the aeroelastic stability improvements that can be achieved through the use of the elastic coupling between bending and torsional deformations and the torsional rigidity. Results obtained by laminates possessing various degrees of bending-torsion coupling are presented alongside those obtained by two uncoupled wings. One is the uncoupled laminate wing offering the maximum possible torsional rigidity and the other is a metallic wing made of aluminium. The aim is to show under what circumstances bending-torsion coupling can be used beneficially to raise and/or eliminate flutter and divergence and those where a conventional design is used, so that maximising the torsional rigidity might be a better choice.

In **Chapter 6** further studies into the flutter behaviour of composite wings are carried out. In the first study the flutter behaviour of swept and unswept composite wings exhibiting wash-in behaviour is examined using suitable non-dimensional parameters. In this way, the flutter behaviour of realistic composite wings is approximated making the understanding and prediction of such behaviour possible. The conclusions drawn from this study are also confirmed by independent optimisation studies.

The second study is focused on the aeroelastic characteristics of wings exhibiting wash-out behaviour. The method of analysis is essentially that of the first study. In the third study two uncharacteristic features of composite wings are investigated by identifying the contribution from each normal mode to the flutter mode. These are (i) the unexpected blips or abrupt changes in the flutter behaviour of composite wings occurring at certain fibre angles of the laminate, and (ii) the wash-in behaviour being more beneficial for the flutter of composite wings than wash-out.

In **Chapter 7** attention is focused on achieving a maximum flutter speed of a cantilever composite wing, and at the same time alleviating its gust response by applying both aeroelastic tailoring as well as active control technology. This problem is essentially described as a constrained optimisation one where the objective is to alleviate the gust response of a wing subject to a certain specified flutter speed. Control law parameters are optimised for four different spanwise control positions.

In **Chapter 8** the principal conclusions are developed. Also included are **Appendices** detailing : **(A)** the macromechanical properties of composite materials; **(B)** stiffness models for thin-walled composite beams; **(C)** the development of dynamic stiffness matrix of a bending-torsion coupled composite beam; **(D)** the use of generalised coordinates and normal modes in the flutter analysis; and finally **(E)** the program options available for the optimisation program ADS (Automated Design Synthesis).

CHAPTER 2

LITERATURE REVIEW

2. LITERATURE REVIEW

2.1 Introduction

The purpose of this chapter is to outline the development of aeroelastic tailoring and identify the key areas of research and the potential and associated problems of composite materials to enhance aeroelastic performance. This helps the reader to become familiar with the mysteries and consequences of the new technology as well as to assess the limitations and problems associated with its use.

As with the introduction of any new technology, activity proceeds at two levels. The first involves practical application of numerical methods to support the design mission while the second is more academic in nature so that principles may be examined without a large number of unnecessary details. This latter level of research is related to earlier attempts to understand the new technology and assess the limits and problems associated with its application.

In section 2.2 the development of aeroelastic tailoring and a significant number of specific applications are presented while in section 2.3 emphasis is given to the more academic level of research where the problems are analysed with various degrees of complexities and their merits are observed in detail. In section 2.4 the potential areas for future aeroelastic tailoring efforts are discussed and finally in section 2.5 some conclusions are drawn.

2.2 The Development of Aeroelastic Tailoring and Specific Applications

Earlier investigations by Voigt [2.1], Brown [2.2], and Hearmon [2.3] indicated the existence of an elastic coupling between bending and torsional degrees of freedom in materials such as crystalline substances and plywood. However, inspired by the above studies, the first to apply the design concepts of aeroelastic tailoring was Munk [2.4] in a wooden propeller design invented in 1949. The purpose of Munk's investigation was to provide a fixed pitch propeller the blades of which twist

elastically and favourably as the thrust changes. This was achieved by orienting the fibres (the grains of the wood) in such a way as to cause the blades of the propeller to deform favourably as the load increases.

In 1953, a novel wing design, known as the AERO-ISOCLINIC wing, was incorporated into the design of the Short S.B.4 or SHERPA prototype invented by Hill [2.5]. A special design feature of this wing was that it was designed so that its incidence, or inclination to the airflow, remained constant along the span despite flexural distortions due to aerodynamic pressure distribution. These aeroelastic characteristics of the aero-isoclinic wing were achieved, in part, by placing the torsion-box further back in the wing [2.6]. This wing is an excellent demonstration of aeroelastic tailoring. It satisfies the definition of aeroelastic tailoring presented in chapter 1, wherein aircraft performance is the driving goal.

The idea to control the wing incidence passively due to flexural distortion had been forgotten for about two decades, until 1969, when, as part of a program to improve transonic performance, General Dynamics submitted a proposal to the Air Force Flight Dynamics Laboratory (AFFDL) to apply advanced filamentary composite materials to the design of a supercritical wing [2.7]. The objective of the program was to provide the best wing shape (primarily twist distribution) at both cruise and design manoeuvre condition. At General Dynamics, Waddoups, McCullers, and Naberhaus [2.8] had been pursuing the application of advanced composites for design improvements other than the obvious weight savings. Motivated by Maske's work, they showed [2.8] that the directional properties of composites could be used to provide a significant level of anisotropy to create coupling between bending and torsional deformations to produce the desired shape control for the supercritical wing.

In the same year (1969), General Dynamics was selected by AFFDL for the development of a pilot computer program for the aeroelastic and strength optimisation of aircraft lifting surfaces using the unique properties of advanced filamentary composite materials [2.9]. The most significant product of this work was the Wing Aeroelastic Synthesis Procedure, later simply called TSO (aeroelastic Tailoring and Structural Optimisation) developed by Waddoups, McCullers, Ashton, and Naberhaus [1.3]. It was a mathematical programming based on penalty method approach using the Davidon-Fletcher-Powell algorithm [2.10] for unconstrained minimisation.

This program was developed for the preliminary design of lifting surfaces, with the structure idealised as a plate. However, despite the limitations associated with a plate model, TSO is a powerful design tool with good aerodynamic representation, and comprises various aeroelastic analysis procedures. The project was completed in 1972 with the theoretical background provided by Dong [2.11], Young [2.12], Barton [2.13], Waddoups [2.14, 2.15], and Ashton [2.16, 2.17].

Rockwell was selected in 1975, to design and fabricate a 0.5-scale remotely piloted research vehicle of a Highly Manoeuvrable Advanced Technology (HiMAT) aircraft under contract to NASA. In February 1978, the first aeroelastically tailored HiMAT test aircraft was ready for flight tests [2.18]. The design objective was to satisfy the cruise goal by designing the wing with jig shape and aeroelastically tailoring the canard and wing skins to deform and satisfy the desired 8-g manoeuvre goal. The flight-test program, begun in 1979, successfully demonstrated the benefits of aeroelastic shape control.

The contributions made by AFFDL and General Dynamics were mainly due to exploration of the high specific strength (ultimate tensile strength/density of the material) and specific stiffness (modulus/density) properties of composite materials.

The X-29, a swept-forward wing demonstrator aircraft, is one of the most recent applications of aeroelastic tailoring. The application of aeroelastic tailoring (advanced composites) in this case took advantage of an old idea, sweeping the wings forward. The benefits of wing sweep were known as early as 1935 [2.19], but it was not until the 1940s that sweeping the wing either forward or aft to reduce transonic drag was seriously considered. Despite the higher aerodynamic superiority of the swept-forward wings, their vulnerability to aeroelastic divergence made the designers abandon this idea, the cure of which was to stiffen the wing with a weight penalty. As a result, aft-swept wings dominated virtually all high-performance aircraft.

The reintroduction of the swept-forward concept was due mainly to the doctoral dissertation of Krone [2.20, 2.21] who showed that, with little or no weight penalty, tailored composites could be used to avoid divergence of a swept-forward wing. Grumman further investigated forward sweep for improved transonic

manoeuvring performance using Krone's data on aeroelastic characteristics [2.21]. The Defence Advanced Research Projects Agency (DARPA) in 1977, initiated studies to verify divergence avoidance with aeroelastically tailored composites along with performance evaluations of swept-forward wing designs [2.22]. These studies were performed by General Dynamics, Grumman, and Rockwell under the technical directions of AFFDL. Grumman was selected by DARPA to design and build the X-29 [2.22], a swept-forward wing flight demonstrator whose first flight occurred in December 1984.

During the period 1971-1986 aeronautical journals were flooded by numerous research studies in the aeroelastic tailoring area. These mainly focused on two different directions:

1. General studies of composite mechanics, in order to comprehend the phenomenon, evaluate the theory and carry out parametric studies.

2. Specific application of the technology to particular designs.

Aeroelastic tailoring has reached this stage through developments in fibrous composite materials and mathematical programming methods. The former increased aircraft structural design options, while the later allowed the designer to use efficiently the numerous design variables.

Tsai and Hahn [2.23] were the first to provide a theory of the mechanics that helped to predict and design structures making use of the directional stiffness and strength characteristics of composites and the better stiffness-to-weight ratio. They demonstrated various methods of coupling the in-plane and out-of-plane deformations of laminated beams and plates. Similar work was later provided by Jones [2.24] and Datoo [2.25]. In addition, Shirk and Griffin [2.26] demonstrated deformation control with laminate design.

Although fibrous composites offer new opportunities for structural design, the increased number of variables, such as the fibre orientation, the number of plies and the thickness of each ply in the laminate, increases the complexity of the design problem. In McCullers' [2.27] words:

> *"Advantageous utilisation of the anisotropic properties of composites requires consideration of additional designs variables and use of complex behaviour and failure mode analysis techniques. Many metal design problems can be reduced to the determination of a single thickness for each member. A composite laminate, however, requires the determination of the number of plies and the orientation of each ply for the material(s) selected, which increases the magnitude and complexity of the design problem. Therefore, although optimisation techniques are very useful in metal design problems, they are almost essential for the efficient design of composite structures".*

Therefore an aspect of aeroelastic tailoring which has rapidly attracted the attention of many researchers in the field, is the development of optimisation techniques. Aeroelastic tailoring is considered to be a particular application of the general field of structural optimisation under aeroelastic constraints such as flutter and divergence. Some excellent survey papers on the subject are Refs [2.28-2.30].

The first attempt to develop an optimisation program with special reference to aeroelastic tailoring was TSO [1.3] of which scope and limitations were mentioned earlier. Several optimisation and other computer programs have followed TSO.

The Transonic Aircraft Technology (TACT) program demonstrated the application of aeroelastic tailoring with advanced composites by designing an aerodynamically efficient wing with jig shape for the cruise condition and to wash-out at the 7.33-g condition [2.31]. In addition, the design had constraints on pivot loads, wing loads, flutter speed, and panel buckling. A parametric study [2.31] showed that material bending-torsion coupling variations had greater effect than variations in box chord dimension. The twist of composite was found to be double that of aluminium and a reduction of 4% in pivot load, along with fulfilment of flutter speed requirements without any weight penalty. These studies were subsequently confirmed on a 1/24 - scale model in a wing tunnel [2.32].

In 1975 Grumman was contracted by the Airforce Flight Dynamics Laboratory AFFDL to define the benefits and results of the application of composite materials to an Advanced Design Composite Aircraft (ADCA) [2.33, 2.34]. It was

intended that the aircraft would be smaller, lighter, and less costly but capable of performing a supersonic penetration interdiction fighter mission at lower life cycle costs than its metallic counterpart. As a result of using the ADCA program, an aeroelastic tailoring technology of the wing and vertical stabiliser was developed [2.33].

The important characteristics of the wing were mission performance, take-off gross weight, transonic manoeuvre condition, and wing shape at supersonic cruise. A comparison of tailored and untailored aeroelastic wing for twist characteristics subject to minimum structural weight and strength at ultimate load constraints showed that the tailored design fulfilled supersonic cruise requirements with negligible improvements in transonic manoeuvrability.

The plies were rotated through fifteen degrees aft of the main load-carrying axis in case of the vertical tail which improved flutter speed and increased effectiveness in generating yawing moments. Tail effectiveness can be utilised in two ways. Firstly, keeping the size of the tail surface constant, the lateral directional stability and rolling performance can be improved which will decrease the lateral manoeuvre loads and ease the response requirements of the control system. Secondly, without making any change in the lateral stability performance of the aircraft the tail size may be reduced, thus decreasing the drag and weight associated with the tail.

General Dynamics also conducted further studies through several contracts with AFFDL. The first study [2.34] resulted in the TSO program and a 3/8 scale demonstrative component of a conceptual fighter wing with an ultimate objective of increasing aerodynamic effectiveness by elastic camber and twist. A parametric study was conducted on ten minimum weight graphite/epoxy skin designs with two different objectives, namely maximum static aeroelastic lift and maximum load relief. The design objective was to achieve maximum flexible-to-rigid lift ratio through camber and twist control while maintaining an uninterrupted tip-to-tip spanwise ply orientation. Graphite/epoxy was used for the skin, with full-depth aluminium honeycomb, and fibre glass spars. The structure was analysed by both TSO and a finite element package with influence coefficient and vibration tests. The disagreement in static deflections and frequencies between tests and predictions

were within 5%. The eventual output of this study was a build up of confidence in the analytical procedures adopted in the design [2.33].

In a second study [2.35], the TSO computer program code was extended to study performance benefits through shape control. The investigation concentrated on a low aspect ratio fighter wing and a high aspect ratio bomber wing. The findings were as follows:

1. A composite wing should be tailored aeroelastically to provide acceptable aerodynamic characteristics with minimum weight, otherwise a low drag polar break lift coefficient or an undesirable aerodynamic centre shift could completely negate the benefit of reduced weight.

2. Maximising camber while obtaining high negative twist (i.e., wash-out) should be utilised to obtain the best drag polar.

3. The planform geometry can be improved by the weight saving feature of the composites. It was shown, for example, that an extension in the span of the fighter wing gives 5.8% greater sustained turn rate than a wing with a usual leading-edge flap at Mach number 0.9 and 2.3% increase at Mach number 1.2.

4. In the case of the extended-span bomber wing, a 13.6% increase in ferrying range and 15.6% increase in refuel altitude were predicted.

In a third contract [2.36-2.38], wind tunnel data for tailored wing design were obtained demonstrating the range of beneficial aeroelastic response attainable. The wing planform was the product of another research and development program on a similar planform of an extended-span fighter wing, which provided good transonic manoeuvrability without losing supersonic performance.

The design study considered three aeroelastically tailored wings and a rigid steel one [2.38]. These are discussed briefly as below.

1. The first wing was designed to reduce drag at transonic manoeuvre conditions by aeroelastic camber and negative twist, i.e., wash-out. The analysis indicated that the flutter speed of the wash-out wing was higher than that of the F-16

metal wing. This was not expected since the aeroelastically tailored wings had larger areas and aspect ratios and thinner airfoil sections than the F-16 metal wing.

2. The second wing was designed to increase the lift-curve slope through camber and positive twist, i.e., wash-in. Such a design is applicable to vertical tail surfaces, where in the case of conventional designs, the effectiveness of the surface is lost due to aeroelastic effects. Hence the wash-in and wash-out capabilities of composite wings gave the concept of deformation control using fibrous materials.

3. The third wing was an untailored design, having balanced composite wing laminate with equal amounts of cross plies.

4. The steel wing provided a conventional model data base.

The datum was provided by the untailored design and was compared with the tailored wings to establish the benefits of aeroelastic tailoring.

A unique feature of this test was the simultaneous acquisition of all data (force, pressure, aeroelastic shape, and steady-state and dynamic bending moment), which provided an excellent data base for evaluation of design methods. This program demonstrated that aeroelastic tailoring of a wing can produce a significant reduction in transonic drag due to lift, or for different design approach, a significant increase in lift-curve slope compared to the rigid wing. The program also demonstrated the effectiveness of the analysis/design procedures in preliminary design.

General Dynamics also worked on the preliminary design of the Wing/Inlet Composite Advanced Development (WICAD) program [2.39] to :

1. Provide a flight worthy wing and inlet for the F-16.

2. Develop and demonstrate advanced composite conceptual design technology to manufacture low-cost, lightweight, and durable fighter wing and inlet structures.

The study using TSO revealed a laminate skin weighing 67.5% of an aluminium skin, a flexible-to-rigid lift ratio of 1.116, and a flutter speed 12.7% higher than the aluminium skin design. However, this program of investigation was terminated after a period of only seven months before any validation of the aeroelastically tailored design through ground or flight testing was conducted.

HiMAT was the first modern, aeroelastically tailored remotely piloted research vehicle, designed and constructed by Rockwell for the NASA Dryden Flight Research Centre [2.40-2.43]. The outboard and the canard were aeroelastically tailored in such a way that the aircraft was capable of sustaining a 8-g turn at Mach 0.9 at an altitude of 25,000 feet. There was an additional transonic manoeuvre requirement while maintaining the aircraft's subsonic cruise performance. The flight tests were carried out in 1979.

The wing and canard were aeroelastically tailored by a two phase iterative process. Firstly, a preliminary sizing was obtained by using the computer codes AC87 and AC89, which were developed by Rockwell [2.41] and based on advanced composite beam theory, followed by a detailed design verification with NASTRAN [2.41]. The process was iterated until twist and strength requirements were satisfied. HiMAT programme demonstrated the feasibility of unbalanced, graphite/epoxy laminates in controlling aeroelastic twist. However, the results obtained at 110% limit load at 8-g manoeuvre test conducted on wing and canard did not agree well with the analytical predictions. This was due to the non-linear behaviour of composite properties in the transverse direction to the fibres.

DARPA funded General Dynamics, Grumman, and Rockwell to prepare a feasibility study on a swept-forward wing, small fighter class aircraft flight demonstrator, the X-29 [2.44]. These studies followed experimental investigations by Grumman [2.45] and Rockwell [2.46] to assess the accuracy of predicting wing divergence speed. Other aspects of these experiments were focused on the understanding of divergence of a fixed-root swept-forward wing, model design and fabrication process for simulation of aeroelastic properties and the sub-critical divergence test techniques. Despite the different approaches adopted by the two companies the ultimate results were similar.

Grumman [2.45] used FASTOP (Flutter And STrength Optimisation Program) and found that rotating the laminate sequence of [0, ±45, 90] until the primary bending plies are 9 degrees forward of the reference structural axis and the required bending-torsion coupling is achieved to minimise the undesired wash-in tendencies. On the other hand, Rockwell [2.46] used TSO to design a laminate with the cross plies oriented 30 degrees forward of and 51 degrees aft of the reference axis along with the primary bending plies oriented at 9 degrees forward of the reference axis. The models were tested in the NASA Langley Research Centre's 16 feet transonic dynamics tunnel. Experimental results showed that wing divergence could be avoided by the application of aeroelastic shape control, possible due to tailoring of the advanced composites.

A high aspect ratio wing with an aft sweep of 35 degrees of a cargo transport aeroplane was studied by Gimmestad [2.47] for aeroelastic effects, such as effects of flexibility and jig twisting. Results were compared with those of an aluminium wing and the following general conclusions were drawn [2.47]:

1. It was felt that aeroelastic effects and jig twist must be taken into account in preliminary design to achieve performance enhancement.

2. Anisotropic effects can have several consequences, particularly on stability and control.

3. Anisotropic effects witnessed in composites can also be seen in conventional materials but to a much lesser extent.

In yet another study, Gimmestad [2.48] using TSO showed that a composite winglet of KC-135 can be designed for substantially larger aeroelastic wash-out losses in order to reduce wing bending moments.

In another study TSO was used by Triplett [2.49] to design a wing for the fighter aircraft F-15 which saved 55 lbs weight and gave a reduction in drag, thus improving the roll effectiveness. Other parts of the study covered the preliminary design of a horizontal tail, a prototype aircraft movable outer wing panel, and a conceptual aircraft wing. In the case of the conceptual aircraft wing, a 3% weight

saving was achieved but with 4.6 degrees wash-out twist the weight penalty was 2.5%.

Triplett also pointed out in another study [2.50] that there can be no weight penalty while dealing with the problem of divergence of swept-forward wings. However, it was shown that the induced drag increases with the swept-forward configuration.

Whilst the bulk of analytical and experimental research into aeroelastic tailoring has taken place in the USA, a significant contribution has come from Europe. The work of Sensburg et al. [2.51] is an excellent example of European activity. In this work, the application of aeroelastic tailoring for passive load alleviation on an extended wing version of the Airbus A300 was studied. It was shown that a rigid extended wing resulted in 1.7% increase in root bending moment with aeroelastic tailoring as compared to 7% on a conventional material.

Schweiger et al. [2.52] studied the potentials of laminate orientation on a high aspect ratio glider to control wing/body flutter due to the interaction between swept wing bending and the short period mode.

Lavi fighter developed by Grumman for Israel Aircraft Industries, has utilised FASTOP to optimise the advanced composite structures for improved control effectiveness of the wing elevons and the overall performance of the fin [2.53].

Similar approaches to FASTOP appeared in the field of optimisation. COMBO (COMposite Box Optimisation program) [2.54] and SWEEP (Structural WEight Estimation Program) [2.55] are excellent examples of such approaches. A very recent addition to the aeroelastic optimisation programmes is the development of the computer program ADOP (Aeroelastic Design Optimisation Program) [2.56] by McDonnell Douglas Corporation. This programme results from considerable improvement and modification of an existing aeroelastic analysis program called ASTROS (Automated STRuctural Optimisation System) [2.57]. Although ADOP is now capable of handling a complete aircraft configuration with up to 250,000 degrees of freedom, it seemingly appears to be a very expensive tool to perform design optimisation. Such a programming tool inevitably makes an extensive use of computer time, and therefore it is beyond the scope of most designers. Thus the

development of an aeroelastic computer program which is short, compact and completely self-contained is of great value. CALFUNOPT (CALFUN with OPTimisation) [2.58-2.60] is such a program in FORTRAN which has been developed jointly by City University and the University of Bath in recent years.

By implementing the optimisation capability through the use of ADS (Automated Design Synthesis) [1.40], CALFUNOPT has been developed from an earlier analysis version of the program CALFUN (CALculation of Flutter speed Using Normal modes) [2.58] which computes flutter speed, flutter frequency and aeroelastic modes of metallic or composite wings using normal modes and generalised coordinates. CALFUN and CALFUNOPT which are currently under further development have been extensively used to obtain results reported in this thesis.

2.3 Analytical Approaches

In varying degrees of complexity, several theoretical studies have examined the various aspects and benefits of aeroelastic tailoring. A number of references propose structural idealisations for use in aeroelastic analyses. In others, more complex models which include the effects of camber, have been used to examine aspects of aeroelastic tailoring. In these studies a number of ply parameters, such as the fibre orientation or some form of non-dimensional stiffness or flexibility parameters, have been used as design variables. In general they all concentrate on the stability in flutter and divergence, lateral control effectiveness, and load redistribution for both swept and unswept wings. It is to this second level of research that the literature review that follows will be confined.

In the area of stability that the work reported in this thesis falls, Krone [2.20, 2.21] was one of the pioneers who investigated the ability of composite materials to enhance divergence of swept-forward wings. In his studies he concludes that swept-forward wings without divergence or weight penalties may be possible through the use of selective laminated advanced composites. In particular, he concludes that the detrimental effect of divergence on swept-forward aerofoils can be successfully controlled by the use of advanced composite materials. In his view, the key to accomplishing this is the ability to tailor the composite layer thickness

distributions and orientations so as to obtain a design that produces optimum stiffness and strength characteristics.

Prompted by Krone's work, many studies of the aeroelastic stability of laminated wings have appeared over the last two decades. Many of these studies have used ply orientation as a design variable with and/or without the presence of bending-torsion coupling. References [1.6, 1.19, 2.61-2.65] are significant examples of such literature.

Housner and Stein [1.9], Weisshaar [1.6, 2.61-2.62], Lerner and Markowitz [2.63], Sherrer et al. [2.64] and Schneider et al. [2.65] all followed Krone's work [2.20-2.22]. Lerner and Markowitz [2.63] applied a modified version of FASTOP to perform initial design studies for the X-29. In a series of simple wind tunnel tests, AFFDL demonstrated the effect of laminate rotation on divergence speed. Sherrer et al. [2.64] showed that a simple rotation of a 0/±45 family of orthotropic graphite/epoxy laminates would increase the divergence speed of a wing at various leading-edge sweeps. Schneider et al. [2.65] developed a routine, in which the FASTOP was incorporated, to examine the variation of divergence speed with ply angle and the variation of optimised wing weight and divergence speed with wing-box sweep.

Housner and Stein [1.9] examined the effect of ply orientation for a symmetrically balanced (i.e., uncoupled), cross-ply laminate upon flutter of a beam-like wing. Because the study was limited to symmetrical and balanced cross-ply laminates, bending-torsion coupling was not present. Changes in flutter speed were shown to be dependent solely on changes in bending and torsional stiffnesses as plies were reoriented. In addition, their studies showed that the highest critical flutter speed for swept and unswept wings occurred when the fibre orientation was near $\pm 45^0$.

Weisshaar and Foist [1.6] later examined the potential effects of material laminate tailoring on the flutter of moderate-to-high aspect ratio wings. In contrast to Ref. [1.9], the authors included the bending-torsion stiffness coupling in their investigation. The most intriguing features of Ref. [1.6] are those which show that negative (positive in their notation) bending-torsion coupling which results into a wash-in behaviour (bend-up/twist-up) is more effective for flutter of a fixed root wing

than is positive bending-torsion coupling (wash-out). In particular, by investigating a unidirectional laminate they showed that the flutter speed can be raised significantly at a range of negative fibre angles in the region of very high bending-torsion coupling.

Several other investigators have studied the aeroelastic stability of laminated wings in recent years using rigidity properties as design variables instead of ply orientation. References [1.8, 1.11, 1.24, 2.47, 2.54, 2.66, 2.68-2.71] are significant examples of such literature.

Austin et al. [2.54] and Gimmestad [2.47] have investigated the effects of tailoring upon aircraft designs subject to a combination of realistic constraints. Austin et al. [2.54] discussed, in detail, a stiffness model that may be used to describe a laminated box-beam with spars. The authors recognised the presence of a non-dimensional parameter in the tailoring process. They used a parameter combination that is essentially equal to the non-dimensional ratio of the bending-torsion coupling stiffness to bending stiffness (K/EI). (One drawback of using this parameter is that it does not have fixed limits.) An additional interesting feature of this study is that it is possible to prevent flutter (at the expense of a low divergence speed) for certain ranges of the above non-dimensional parameter.

Influenced by the work of Housner and Stein [1.9], Weisshaar [2.66] went a step forward and, unlike Austin et al. [2.54], defined a bounded bending-torsion coupling parameter as a measure of the bending-torsion coupling in a structure. This bending-torsion coupling parameter is a function of the orientation and stacking sequence of symmetrical laminate plies with respect to a reference axis along the wing.

Weisshaar [1.8] developed algebraic expressions to predict the static aeroelastic divergence characteristics of swept-forward wings constructed of composite materials using a laminated box-beam model to describe the wing structure. The box-beam model used was similar to that employed by Housner and Stein [1.9] but valid for both balanced and unbalanced laminates. The author showed that the elastic coupling between bending and torsion, introduced by composite materials, can successfully negate the undesirable effect of swept-forward wings on divergence. In particular, it was concluded that the ratio of

the bending-torsion coupling rigidity to torsional rigidity (K/GJ) should be tailored such that it has a relatively large positive value (negative in their notation), i.e., an upward bending moment should result in nose-down twist of the wing. In other words the wing should exhibit wash-out behaviour when loaded vertically.

Niblett [1.11], used the analysis of Mansfield and Sobey [2.67], applicable for wings of moderate-to-high aspect ratio, to relate asymmetry of lay-up and cross-flexibility. The author introduced the concept of bend-twist "cross-flexibility" and defined a bounded non-dimensional cross-flexibility parameter so that aeroelastic tailoring could be investigated without the problem of varying fibre orientation. The author found that the effect of cross-flexibility on divergence speed is reduced as the flexibility in bending is increased, the torsional flexibility being maintained constant.

Following the lead of Austin et al. [2.54] and Niblett [1.11], Weisshaar and Foist [1.24] developed a bending-torsion coupling parameter ψ in terms of the bending, torsional and bending-torsion coupling stiffness developed in Ref. [2.66] (i.e., EI, GJ, and K, respectively). This bending-torsion coupling parameter, which has received wide attention over the last decade, was defined as $\psi = K/\sqrt{EIGJ}$ [1.24] with limits $-1<\psi<1$. These limits enable one to categorise a beam-like structure as highly coupled or lightly coupled, with values near zero categorised as lightly coupled, while absolute values of ψ near unity are associated with highly coupled structures.

Using the bending-torsion coupling parameter ψ developed in Ref. [1.24], Weisshaar [2.68] showed that both flutter and divergence can be eliminated at a relatively small values of this parameter for both swept and unswept wings. Similar work was carried out by Lottati [2.69] who also showed that flutter and divergence can be eliminated at certain combinations of bending-torsion coupling stiffness (K) and wing sweep (Λ).

A significant number of theoretical observations were later validated experimentally [1.13-1.15]. Weisshaar [1.13] illustrated by experimentation the potential effects of laminate design on wing divergence speed using flexible swept and unswept composite wing models. He showed that maximum divergence speeds

are found in wings with ply fibres swept between 0 and 30 degrees forward of a structural reference axis. Landsberger and Dugundji [1.15] continued the work of Hollowell and Dugundji [1.14], who explored the flutter and divergence behaviour of a series of stiffness-coupled, graphite/epoxy, unswept cantilever plate wings. Using that work [1.14] as a foundation, Landsberger and Dugundji [1.15] extended the range by analytically and experimentally investigating the flutter and divergence behaviour of some new ply lay-up patterns with various amounts of bending-torsion coupling. The investigation was carried out for unswept and 30 degree swept-forward cantilever plate wings. The flutter and divergence investigations showed the large variation in aeroelastic properties possible by changes in ply lay-ups. A positive ply angle lay-up $[+15_2 /0]_s$ was shown to have efficient bending-torsion coupling to overcome the adverse geometric divergence effect of a 30 degree swept-forward wing.

Several researchers carried out theoretical and experimental studies by utilising the whole aircraft configuration [2.72-2.76], rather than a cantilever wing. Bakthavatsalam [2.72], for example, examined ways to suppress the interference flutter caused by the interaction of wing and tail lifting surfaces of a closely coupled wing-tail flutter model. The author showed that, apart from the pronounced effect on increasing the flutter speed by orienting the fibres of the main wing to wash-in, by tailoring the closely coupled tail to wash-out and reducing its stiffness could also produce an increase in flutter speed, although at a lesser extent. This passive technique of controlling flutter speed by tail deformation is directly comparable to results of active flutter suppression obtained by testing of the model using a rotating tail surface [2.73]. The wash-out tail surface design results in a wing deflection and tail rotation that have the same phasing as the active system. Although higher flutter speeds were obtained using the active system, applying the passive technique may allow a cost and weight reduction.

Other investigators illustrated the importance of the rigid-body modes on the aeroelastic behaviour of laminated composite wings. Foist [2.74] and Weisshaar and Foist [2.75] examined the potential effects of wing root boundary conditions on the flutter and divergence of laminated composite lifting surfaces. One interesting effect observed in Refs [2.74] and [2.75] was that laminate designs that yield high flutter speeds when the wing is cantilevered at the root may suffer from body-freedom flutter when the wing root is allowed freedom to move with the

fuselage. In Ref. [2.74] the model used was a 30 degree swept-back laminated composite wing. The results obtained revealed that during structural optimisation studies where flutter and divergence are design constraints for a wash-in-type wing (such as would be desirable for control effectiveness or lift effectiveness), the designer should include rigid-body modes in the flutter analysis during the design iterations. At the very least, in the final design the flutter speed of the cantilever wing should be compared with the flutter speed of the whole aircraft.

Similar work to that of Foist [2.74] and Weisshaar and Foist [2.75] was carried out by Chen and Dugundji [2.76]. In particular, an analytical and experimental investigation was made of the aeroelastic flutter and divergence behaviour of graphite/epoxy 30 degree swept-forward wings with rigid-body pitch and plunge freedoms present. The tests revealed large variations in aeroelastic behaviour of four different ply orientation wings. The tests also showed that the swept-forward wings developed body-freedom flutter rather than divergence when rigid-body modes were present. For the model free in pitch only, body-freedom flutter was again encountered, but at a lower airspeed. The presence of the plunge freedom apparently raised the flutter speed.

A number of other researchers have investigated the design latitude available for desired aeroelastic effects [1.14, 1.19, 1.21-1.24, 2.26, 2.35, 2.77-2.80]. Shirk and Griffin [2.26] used TSO to design three wing structures with the same planform to meet minimum weight, maximum wash-in, and maximum wash-out with flutter and control reversal constraints. The authors demonstrated the ability to tailor aeroelastically a wing to control the centre-of-pressure position either from a load relief standpoint or for increased flexible lift.

Weisshaar [1.19] also discussed the potential effects of bending-torsion coupling upon spanwise centre-of-pressure position and lateral control effectiveness of swept-back and swept-forward wings. The author illustrated that the proper orientation of a significant fraction of laminate structure fibres can markedly affect important static aeroelastic characteristics of a wing, such as divergence speed, spanwise centre of pressure, and aileron effectiveness. Results indicate that laminate design can be used effectively to increase the aileron reversal dynamic pressures.

Since aeroelastic twist and camber affect performance, Lynch et al. [2.35], undertook an analytical study to determine the amount of camber and twist achievable by aeroelastic tailoring. Using an improved version of TSO, a 0/±45 family was examined in which the laminate contained varying percentages of plies in each of the three orientations. The authors produced graphs showing the twist and camber available on a lightweight fighter wing at a given design condition. They also showed that rotating the laminate by $\pm 10^0$ also resulted in significant variations in camber and tip twist angles. Furthermore, the effect of these orientations on roll effectiveness, flutter speed, and tip deflection were studied. The ability to achieve performance benefits by increasing span or decreasing wing depth due to the strength and stiffness characteristics of composites was also demonstrated.

Studies by Weisshaar [1.21] and Weisshaar and Foist [1.24], and similar studies by Hollowell and Dugundji [1.14], Crawley and Dugundji [1.22], and Jensen et al. [1.23], concluded that the inclusion of chordwise bending is of vital importance even for high aspect ratio configurations. Otherwise, the torsional frequencies predicted may not be reliable for plates with high bending-torsion stiffness coupling. Flutter results obtained using theories with infinite chordwise rigidity as an assumption, may be poor when compared to experimental results. Weisshaar and Foist [1.24] compared the algebraic expressions developed by Weisshaar [1.21] (resulting from the assumption of chordwise rigidity of the beam model), to those obtained from the Mansfield and Sobey tube model [2.67] and from a plate model [2.23]. This revealed some rather outstanding differences in stiffness predictions [1.24]. These differences can be significant for advanced composite plate-like structures with a substantial proportion of off-axis plies.

McCullers et al. [2.78] performed an extensive series of experiments on anisotropic plates to obtain static and dynamic response of a wing structure by varying anisotropy, planform shape, (i.e., leading-edge angle, taper ratio, and aspect ratio), curvature, boundary conditions, thickness distribution, skin thickness, shear modulus, and tapered cores. Stiffnesses and free vibration characteristics were predicted, measured, and compared in detail.

Other researchers investigated the extension-torsion coupling of composite laminates though outside the scope of the present work. For example, Dwyer and

Rogers [2.79] and Rogers [2.80] applied the extension-torsion coupling, present in a symmetrical but balanced laminate to tailor aeroelastically a propeller design. Since the efficiency of propellers depends upon the angle between the blade mean chord line and the plane of rotation, Dwyer and Rogers [2.79] used composites to provide coupling between the centrifugal force applied to the blades and the shearing strain in the plane of the blade cross-section to control passively the angle of attack. An idealised thin-walled tube model was used to examine the variation of stress-strain coupling and allowable stress with property axis and composite fibre orientation.

As in the case of Hill's aero-isoclinic wing [2.5], some researchers have shown that aeroelastic tailoring can be achieved by other means other than composite materials. Gimmestad [2.47], Williams [2.81] and Gratke and Williams [2.82] have shown that an arrangement of stiffeners (spars and ribs) can be used to control directional stiffness and bending-torsion coupling. In addition, Gimmestad [2.47] showed that because in a standard wing design the stringers are oriented parallel to the wing rear spar, the direction of maximum stiffness is actually swept forward of the assumed elastic axis and as a result the adverse effect, from the flutter standpoint, of wash-out already present on swept-back wings is augmented. This may lead to smaller flutter margins than predicted by isotropic theory.

More powerful and sophisticated analytical structural models were developed in the late 80s and early 90s in order to investigate the aeroelastic behaviour of composite wings. In particular, a number of box-beam models, such as, Rehfield et al. [2.83], Smith and Chopra [2.84], Berdichevsky et al. [2.85] and Song and Librescu [2.86], have been developed which more closely represent real aircraft wing/helicopter blade structures and more accurately account for elastic couplings when compared to plate models.

Librescu and Simovich [2.87] formulated a simple algorithm that allows for the determination, in a closed form, of the divergence instability of advanced composite swept wing structures. The analysis includes warping restraint effects and their influence on divergence. Although in the case of metallic wings warping restraint has a stabilising effect (more pronounced with small aspect ratio and diminishing effect with moderate aspect ratio wing), its effect is more complex in the case of composite wings.

It should be stressed that with one exemption [2.69], the free-warping (FW) model for wing twist has been unanimously adopted in the treatment of the divergence instability. Librescu and Khdeir [2.88] and Librescu and Thangjitham [2.89] analysed the divergence instability of a swept-forward composite wing by also incorporating the Warping Restraint Effect (WRE). Towards this goal, the authors developed a powerful method based on the state space concept and used in conjunction with the Jordan canonical form. The results obtained from this study emphasised the complex role played by the warping restraint effect in the divergence instability of swept-forward composite wings. In particular, the results obtained on the basis of this approach showed that the WRE gives a reduction in the divergence speed, with respect to its free-warping counterpart. The study also showed that WRE could be significant in the case of large aspect ratio wings.

Song and Librescu [2.86, 2.90] analysed the free vibration and aeroelastic divergence of aircraft wings modelled as thin-walled anisotropic beams (box-beams). A number of non-classical effects featuring the behaviour of composite thin-walled beams of closed contour were incorporated and their implications were emphasised. In particular, the results illustrated the effects played by transverse shear deformability and warping inhibition on the divergence instability of swept wings and on their sub-critical static aeroelastic response, which could be useful towards a better understanding of the roles played by these effects and, consequently, towards a more rational aeroelastic design of wing, helicopter blades and tilt-rotor aircraft structures made of advanced composite materials.

Cesnik et al. [2.91] carried out an aeroelastic stability analysis for high aspect ratio composite wings. The structural model used in this analysis was based on an asymptotically correct cross-sectional formulation and a non-linear geometric exact beam analysis. Like Song and Librescu [2.86, 2.90], the authors emphasised the importance of using the right stiffness formulation in order to model material couplings. They showed the variations of divergence and flutter speeds with the changes in the lamination angle of a box-beam model of a wing cross-section, and some of the effects of a non-linear structural model on the aeroelastic stability of a slender wing.

Finally, Chattopadhyay et al. [2.92] developed a higher order theory for structural and aeroelastic analysis of composite wing box sections with moderately

thick walls. The structural model was validated through correlation with other existing theories and available experimental data. The procedure is then used to perform aeroelastic analysis of composite wings with various ply arrangements. Numerical results are presented to demonstrate the effect of ply orientation on aeroelastic behaviour, such as flutter and divergence speeds.

2.4 Future of Aeroelastic Tailoring

As has been pointed out above, the concept of aeroelastic tailoring existed well before the introduction of composite materials, hence it will be very unfair to limit our attention to Glass, Carbon, Kevlar reinforced fibre plastics, etc. A new category of materials has already been introduced known as MMC, i.e., Metal Matrix Composite. A typical MMC may constitute Boron fibres in Aluminium matrix. The macromechanics of a generally orthotropic lamina is equally applicable to structures made of MMC. The high temperature metal constituents and minimum degradation of properties due to environmental changes, are distinguishing features of MMC which make it very popular in the aircraft industry.

Aeroelastic tailoring has been concerned with the advanced filamentary composites and mathematical programming techniques though procedures for the efficient utilisation of advanced composite materials in aircraft design have not yet been fully developed. The performance and durability of a particular design depends on the structural dynamic behaviour and flexibility of an aircraft. Hence these characteristics are expected to be taken into account in the development of aeroelastic tailoring strategies. It has been mentioned that directional stiffness and the resulting aerodynamic coupling influence a number of areas of aircraft performance. Thus a comprehensive approach in the design procedure is required to fulfil all the requirements simultaneously.

Large space structures are another potential area of aeroelastic tailoring research. The repetitive lattice arrangement of a number of space structures form an anisotropic design. Active control of these space structures can be enhanced by achieving passive modal control through tailoring the orientations of the structural members.

Aeroelastic tailoring is also playing an important role in the design procedures of aerospace structures and is becoming a component of such a procedure.

2.5 Conclusions

The review of the literature has shown that as with the introduction of any new technology, research activity on the use of composite materials for aeroelastic tailoring purposes has proceeded at two levels. The first involves practical application of numerical methods to perform design work while the second is more academic and is related to earlier attempts to understand the new technology and assess the limits and problems associated with its application.

It is clear from the above studies that the unique features of laminated composite materials make them prime candidates for aeroelastic tailoring efforts. However, despite the extensive research that has already been carried out in this field, the effect of tailoring upon flutter and divergence of clean wing configuration in the subsonic region, which is the intent of this research to investigate, has not yet been well documented and understood.

The next chapter deals with stiffness modelling of composite beams which is an essential prerequisite of any aeroelastic investigation. In particular, the various methods associated with published work that have been developed for the modelling of flat beams (plates) and thin-walled beams (box-beams) are examined and comparisons where possible made.

CHAPTER 3

STIFFNESS MODELLING OF COMPOSITE BEAMS

3. STIFFNESS MODELLING OF COMPOSITE BEAMS

3.1 Introduction

The successful prediction of the dynamic characteristics of a beam-like structure, such as, an aircraft wing or a helicopter blade, depends on the accurate evaluation of the rigidity (stiffness) properties. For isotropic materials, accurate theoretical models and experimental procedures for the prediction of these rigidity properties have already been established. The material properties of isotropic materials, such as, Young's modulus and Shear modulus, are independent of the cross-section of the structure and the loading conditions and thus the rigidity properties depend on the geometrical properties of the cross-section.

In anisotropic materials, such as, graphite/epoxy and boron/epoxy, the material and, in consequence the rigidity properties vary with the fibre orientation (see, for example, Figs A.4 - A.9 in Appendix 'A'), the stacking sequence of the plies, the geometrical properties of the cross-section, and the loading conditions. Thus, an alternative and, as it turns out, more complicated theoretical analysis is required to predict the rigidity properties of a composite structure.

In the past two decades, considerable efforts have been made to obtain estimates of structural properties of composite structures complicated mainly by the coupling between the various modes of structural deformation occurring in composite materials but non-existing in metallic ones. Despite the increased appearance of the finite element [3.1-3.8] and direct analytical methods [1.8, 1.9, 1.21, 2.67, 2.84-2.85, 3.9-3.17] during the past two decades, the structural behaviour of composite beams does not appear to be thoroughly understood. Some of the methods have not been fully developed and most of them have not been thoroughly validated experimentally for general composite designs.

The objective of this chapter is to discuss and compare the most popular stiffness models that have been developed for the modelling of laminated composite beams, such as, flat beams (plates) and thin-walled beams (box-beams). Each investigator uses his own notation and in order to compare directly one method with

another all of the analyses have been recreated in common notation. This rephrasing has involved a considerable amount of original work.

From the aeroelastic viewpoint, a bending-torsion coupled composite fixed root aircraft wing is characterised by its rigidity parameters EI (bending rigidity), GJ (torsional rigidity), and K (bending-torsion coupling rigidity). These rigidity parameters can be computed is several ways, as it is discussed in this chapter. The effect of fibre orientation on the above three rigidity parameters is examined using several stiffness models. The assumption that the beam is effectively rigid in the chordwise sense which is accounted for conventional metallics (i.e., the bending deformation perpendicular to the spanwise axis is considered negligible), is examined for the case of composites.

For conventional metallics, the effects of warping upon torsional behaviour is also very often excluded. The effect of this warping constraint upon composite beams has been investigated in a number of cases [2.84-2.85, 3.14-3.17]. While this effect is not examined in this study, the way that this has been accounted for in the literature is discussed.

The material in this chapter is presented as follows. Section 3.2 is concerned with reviewing the literature related to stiffness modelling of composite beams and covers both finite element based approaches (section 3.2.1) and analytical approaches (section 3.2.2). Section 3.3 discusses the most popular stiffness models associated with published work and cover both flat beams (plates) and thin-walled beams (box-beams). In order to enable the reader to understand the differences between the various stiffness models, expressions for the displacement field, warping terms and stiffness properties (EI, GJ and K) are provided using the same notation. Then section 3.4 compares the above expressions for various box-beam models and the significance of any difference is discussed. A parametric investigation into the effect of fibre orientation on the rigidity and coupling parameters follows in section 3.5, with the results for flat beams (plates) given first, followed by the results for thin-walled beams (box-beams). Finally, some conclusions are drawn in section 3.6

3.2 Review of the Literature

Two separate approaches associated with published work have been developed for the modelling of composite beams. One is the well known finite-element-based approach and the other is usually termed as the analytical approach. The former is not the subject of this research effort and it will only be briefly summarised. Work based on the latter is the main concern of this study which focuses on the determination of the cross-sectional properties of mainly flat beams (plates) and thin-walled box-beams. These cross-sectional properties will be used in chapter 4 to investigate the dynamic characteristics of composite beams (wings). Surprisingly, most of the existing stiffness models have been developed by researchers from the helicopter community.

3.2.1 Finite-Element-Based Approaches

The advantage that the finite element method offers is the modelling flexibility and versatility which no analytical method can provide so that almost any structural analysis can be reduced to an automatic process. However, its disadvantage is the loss of physical insight. With this method one can determine the warp functions, shear centre, and elastic properties for any cross-sectional geometry that can be modelled with two-dimensional finite elements.

Worndle [3.1] developed a method for the determination of the position of shear centre and warping functions based on a two-dimensional finite-element analysis. However, his analysis is restricted to composite materials with the fibres at an angle of zero degrees (i.e., in a direction along the span of the beam (helicopter blade)) which results in zero coupling. A finite element model of the cross-section yields the out-of-plane warping function and the shear centre location. Although the out-of-plane warping is determined for both torsion and shear strain only the torsional warping is used in the global deformation analysis. It is further assumed that the material and geometrical properties of the blade are slowly varying and that the stress field is uniaxial. It was shown that this analysis is twice as fast as a three-dimensional finite element analysis of a uniform beam.

Bauchau [3.2] developed an anisotropic beam theory in which out-of-plane cross-section warping is expanded in terms of so-called eigenwarpings. Other types of warping, for example, that due to in-plane deformation, are neglected and the analysis is restricted to multicelled, thin-walled beams and, as in Ref. [3.1], to the transversely isotropic case.

Kosmatka [3.3] used Worndle's [3.1] analysis but included blades made of orthotropic materials with arbitrary fibre orientation instead of transversely isotropic materials. Rather than considering beam cross-sections that are rigid in their own planes or beams with uniaxial stress fields as in previously described work, Kosmatka [3.3] uses the complete strain energy of the beam in determining the in- and out-of-plane warping. As is known for an anisotropic beam, the equations that govern the in- and out-of-plane warping functions are fully coupled. However, only the torsional warping is taken into account in his non-linear analysis and the stress field is restricted to be uniaxial.

A similar two-dimensional finite element based procedure for determining generalised warping functions to those described above was formulated by Giavotto et al. [3.4]. The difference is that this analysis is valid for general anisotropy and includes both in-plane and out-of-plane warping. Furthermore, the complete strain energy is used instead of approximations of uniaxial stress or cross-section in-plane rigidity. Finally the two-dimensional, finite-element, cross-sectional analysis reduces to a linear system of second-order differential equations with constant coefficients, which possesses both general eigensolutions and particular solutions. Thus in terms of cross-sectional analysis, this work is the most general. Borri and Mantegazza [3.5] and Borri and Merlini [3.6] later extended the work of Giavotto et al. [3.4] to include non-linear deformation.

Finally, Lee and Stemple [3.7], and Stemple and Lee [3.8] developed a finite-element based approach in which the warping behaviour is determined through specification of warping nodes over the cross-section. It considers only thin-walled cross-sections, and out-of-plane warping.

3.2.2 Analytical Approaches

The introduction of composite materials into aircraft structures has added the material coupling rigidity term to the complexity of the problem. Housner and Stein [1.9] developed a model suitable only for balanced and symmetrical laminates subjected to bending and torsional loads. Thus the material coupling between the bending and the torsional deformation of the wing was excluded in this study. The bending and the torsional stiffness of the wing are assumed to arise solely from thin, laminated composite cover sheets forming the upper and lower surfaces of the wing. The equivalent bending and torsional stiffnesses of the resulting box-beam are computed by using classical Euler-Bernoulli beam deformation assumptions.

A similar model was used by Weisshaar [1.8, 1.21] in his investigation of the divergence behaviour of swept-forward composite wings and the elastic coupling between wing bending and torsional deformations was included in these studies. Simple expressions are given for all three important rigidities for fixed wings, i.e., bending, torsional, and bending-torsion coupling rigidities.

Mansfield and Sobey [2.67] performed a contour load-displacement analysis and examined a composite thin cylindrical tube (beam) having an arbitrary lay-up of fibre composite plies which was subjected to axial, bending and torsional loads. Expressions were derived for the coupled bending, torsional, and extensional rigidities for linear displacements of a hollow single-cell composite tube. However, the torsion-related warping and the transverse shear deformation were neglected. Libove [3.9], presented more or less the same theory later on and admitted that at the time of his investigations he was not aware of Mansfield and Sobey's contributions to the subject [2.67]. Mansfield [3.10] later extended the theory to two-celled beams.

Rehfield [3.11] pointed out that the above theoretical developments were rather difficult to follow, and a single variationally consistent theory was not clearly emerging. Although transverse shear and warping of the beam cross-section are significant in modelling composite beams, neither is included in the above works [2.67, 3.9-3.10]. Despite this the authors gave new ideas about aeroelastic tailoring which was then begun to be explored. Their intention was to show the various types of couplings that could be present in a structure rather than analysing them.

Rehfield [3.11] performed a similar contour analysis to Mansfield and Sobey [2.67] in which a general rotor-blade cross-section is idealised as a single-celled box-beam subjected to axial, bending, torsional, transverse shear, and warping loads. The torsional warping function and the transverse shear deformation were included. As with Mansfield and Sobey [2.67], Rehfield tried to give the analyst an understanding of the couplings that exist in composite structures and to promote the use of these couplings for desirable effect, such as, aeroelastic tailoring. The potential energy formulation was used in his theory and explicit formulae for all the elements of the stiffness matrix are provided. The main difference between this model and those of Mansfield and Sobey [2.67] and Mansfield [3.10] is the inclusion of restrained torsional warping and transverse shear deformation. Nixon [3.12] compared the theory of Rehfield [3.11] with experimental data and showed that transverse shear is extremely important for the accurate modelling of extension-torsion coupled circular tubes. Hodges et al. [3.13] further demonstrated the accuracy and effectiveness of Rehfield's [3.11] approach by showing favourable correlation between this relatively simple theory and a NASTRAN - finite element model for a single-closed cell beam.

Meanwhile, Hong and Chopra [3.14-3.15], developed a non-linear analysis for thin-walled composite beams, undergoing transverse bending (flap and lag), torsion and axial deflections based on non-linear strain displacement relations of Hodges and Dowell [3.16]. However, their aim was not the development of a model so that the three-dimensional contributions could be recovered from one-dimensional beam formulation but the use of a specialised, simple model for the blade cross-section. The main aim was to assess the stability of rotor blades for various values of ply orientation and other geometric parameters. The beam was treated as a single-cell beam composed of an arbitrary lay-up of composite plies. A simple analytical expression was given for the cross-sectional warping, while the effects of transverse shear were neglected. Stiffness coupling terms caused by bending-torsion and extension-torsion couplings were correlated with different composite ply lay-ups. Their results showed that such couplings can have a significant effect on stability and serve as an impetus for further development of analytical approaches.

Extensive investigations in the behaviour of structural coupling terms due to ply orientations were carried out by Chandra et al. [3.17] and Smith and Chopra [2.84]. In Ref. [3.17], following the coupled non-linear analysis of Hong and Chopra [3.14], the authors developed a simplified linear analysis for extension, bending and

torsion of thin-walled symmetric composite beams. As in the case of Ref. [3.14], the effects of cross-sectional warping due to torsion were included in an approximate manner and the effects of transverse shear were neglected. The authors carried out experiments to validate the theory. The theory correlated reasonably well with experimental data. In Ref. [2.84] a direct analytical method was developed for the prediction of the effective elastic rigidities and corresponding load deformation behaviour of composite symmetric and anti-symmetric box-beam structures subjected to axial, bending, torsional and shear loads. The importance of three non-classical structural phenomena was investigated for coupled composite beams, namely the torsion-related warping, the couplings associated with transverse shear deformation and the two dimensional elasticity of the plies which are very important for accurate composite thin-walled beam analysis.

Finally, Berdichevsky et al. [2.85] developed a variationally and asymptotically consistent theory in order to derive the governing equations of anisotropic thin-walled beams closed sections subjected to axial, bending and torsional loads. This theory is based on an asymptotic analysis of two-dimensional shell theory. Closed-form expressions for the beam stiffness coefficients, stress and displacement fields are provided. It is assumed that the in-plane deformation of the cross-section is zero, but the out-of-plane warping is included. In addition to the classical out-of-plane torsional warping, two new contributions are identified by the authors; these are the axial strain and bending warping. The theory correlated very well with both experimental data and other theories in the literature.

3.3 Stiffness Modelling of Composite Beams of Solid Cross-Section

3.3.1 Composite Beam of Solid Cross-Section

At any cross-section on the beam (see Fig. 3.1), the relationship between the internal bending moment resultant, M, torque, T, and the beam curvature, $\frac{\partial^2 h}{\partial^2 y}$, and twist rate, $\frac{\partial \varphi}{\partial y}$, may be expressed as,

$$\begin{Bmatrix} M \\ T \end{Bmatrix} = \begin{bmatrix} EI & -K \\ -K & GJ \end{bmatrix} \begin{Bmatrix} h'' \\ \varphi' \end{Bmatrix} \tag{3.1}$$

where primes denote differentiation with respect to y, the axial coordinate.

The moment-curvature and in-plane stress-strain relations for the general case of a laminate are given in Eqns (A.15) and (A.16) of Appendix 'A' as follows:

$$\begin{Bmatrix} N \\ M \end{Bmatrix} = \begin{bmatrix} A & B \\ B & D \end{bmatrix} \begin{Bmatrix} \varepsilon \\ k \end{Bmatrix} \tag{3.2}$$

where $N = \begin{Bmatrix} N_x \\ N_y \\ N_{xy} \end{Bmatrix}$ are the in-plane forces

$M = \begin{Bmatrix} M_x \\ M_y \\ M_{xy} \end{Bmatrix}$ are the bending and twisting moments

$k = \begin{Bmatrix} k_x \\ k_y \\ k_{xy} \end{Bmatrix}$ are the bending and twisting curvatures

and A_{ij}, B_{ij}, and D_{ij} are the in-plane, coupling, and flexural moduli respectively.

In the case of a mid-surface symmetric laminate, the B_{ij} terms of Eqn. (3.2) will sum to zero and thus the relationship between bending moments, twisting moments and curvatures may be expressed for a Cartesian axis system as (see Eqn. (A.16)),

$$\begin{Bmatrix} M_x \\ M_y \\ M_{xy} \end{Bmatrix} = \begin{bmatrix} D_{11} & D_{12} & D_{16} \\ D_{12} & D_{22} & D_{26} \\ D_{16} & D_{26} & D_{66} \end{bmatrix} \begin{Bmatrix} k_x \\ k_y \\ k_{xy} \end{Bmatrix} \tag{3.3}$$

The elements D_{ij} are anisotropic flexural moduli of a laminated composite plate and are functions of laminate ply geometry, material properties and stacking sequence, while k_x, k_y and k_{xy} are the plate curvatures.

If the coordinate system shown in Fig. 3.1 is adopted with the y-axis aligned in the spanwise direction and the fibre angle measured from y- to x-axis, then Eqn. (3.3) must be modified as,

$$\begin{Bmatrix} M_x \\ M_y \\ M_{xy} \end{Bmatrix} = \begin{bmatrix} D_{22} & D_{12} & D_{26} \\ D_{12} & D_{11} & D_{16} \\ D_{26} & D_{16} & D_{66} \end{bmatrix} \begin{Bmatrix} k_x \\ k_y \\ k_{xy} \end{Bmatrix} \tag{3.4}$$

Adopting the coordinate system given in Fig. 3.1, with spanwise bending moment M_y and an end torque M_{xy} with no chordwise bending moment M_x, Eqn. (3.4) is modified as follows:

$$\begin{Bmatrix} 0 \\ M_y \\ M_{xy} \end{Bmatrix} = \begin{bmatrix} D_{22} & D_{12} & D_{26} \\ D_{12} & D_{11} & D_{16} \\ D_{26} & D_{16} & D_{66} \end{bmatrix} \begin{Bmatrix} k_x \\ k_y \\ k_{xy} \end{Bmatrix} \tag{3.5}$$

or

$$0 = D_{22}k_x + D_{12}k_y + D_{26}k_{xy} \tag{3.6}$$

$$M_y = D_{12}k_x + D_{11}k_y + D_{16}k_{xy} \tag{3.7}$$

$$M_{xy} = D_{26}k_x + D_{16}k_y + D_{66}k_{xy} \tag{3.8}$$

From Eqn. (3.6)

$$k_x = -\left(D_{12}k_y + D_{26}k_{xy}\right) / D_{22} \ , \tag{3.9}$$

so that,

$$M_y = \left(D_{11} - \frac{D_{12}^2}{D_{22}}\right)k_y + \left(D_{16} - \frac{D_{26}D_{12}}{D_{22}}\right)k_{xy} \tag{3.10}$$

and similarly

$$M_{xy} = \left(D_{16} - \frac{D_{12}D_{26}}{D_{22}}\right)k_y + \left(D_{66} - \frac{D_{26}^2}{D_{22}}\right)k_{xy} \tag{3.11}$$

In matrix form

$$\begin{Bmatrix} M_y \\ M_{xy} \end{Bmatrix} = \begin{bmatrix} \left(D_{11} - \frac{D_{12}^2}{D_{22}}\right) & \left(D_{16} - \frac{D_{26}D_{12}}{D_{22}}\right) \\ \left(D_{16} - \frac{D_{26}D_{12}}{D_{22}}\right) & \left(D_{66} - \frac{D_{26}^2}{D_{22}}\right) \end{bmatrix} \begin{Bmatrix} k_y \\ k_{xy} \end{Bmatrix} \tag{3.12}$$

A term by term comparison between Eqns (3.1) and (3.12) shows that

$$EI = D_{11} - \frac{D_{12}^2}{D_{22}} \tag{3.13}$$

$$GJ = D_{66} - \frac{D_{26}^2}{D_{22}} \tag{3.14}$$

$$K = D_{16} - \frac{D_{12}D_{26}}{D_{22}} \tag{3.15}$$

3.3.2 Flat Beam : A High-Aspect-Ratio Plate (HARP) Model

In the case of a mid-surface symmetric laminated plate, the relationship between plate bending moments, twisting moment and curvatures may be expressed as in Eqn. (3.3) where

$$k_x = -\frac{\partial^2 w}{\partial x^2} \quad ; \quad k_y = -\frac{\partial^2 w}{\partial y^2} \quad ; \quad k_{xy} = -2\frac{\partial^2 w}{\partial x \partial y} \tag{3.16}$$

If the same coordinate system and sign convention is adopted as in Fig. 3.1, the plate deflection $w(x,y)$ and the beam deflection $h(y)$ and rotation $\varphi(y)$ are defined as,

$$h(y) = w(0,y) \tag{3.17}$$

and

$$\left.\frac{\partial w}{\partial x}\right|_{x=0} = -\varphi(y) \tag{3.18}$$

The plate curvatures, in this case, can be approximated as follows:

$$k_y = -h'' \tag{3.19}$$

and

$$k_{xy} = 2\left.\frac{\partial^2 w}{\partial x \partial y}\right|_{x=0} = -2\varphi' \tag{3.20}$$

The relationships between moment resultants on the beam cross-section and those on the plate cross-section are defined in Ref. [2.23] as,

$$M = -M_y c \tag{3.21}$$

$$T = 2cM_{xy} \tag{3.22}$$

where c is the plate chord. Following the same procedure as in Eqns (3.5) - (3.11), then Eqn. (3.5) may reduce to the following form

$$\begin{Bmatrix} M_y \\ M_{xy} \end{Bmatrix} = c \begin{bmatrix} \left(D_{11} - \frac{D_{12}^2}{D_{22}}\right) & -2\left(D_{16} - \frac{D_{26}D_{12}}{D_{22}}\right) \\ -2\left(D_{16} - \frac{D_{26}D_{12}}{D_{22}}\right) & 4\left(D_{66} - \frac{D_{26}^2}{D_{22}}\right) \end{bmatrix} \begin{Bmatrix} h'' \\ \varphi' \end{Bmatrix} \tag{3.23}$$

A term by term comparison between Eqns (3.1) and (3.23) shows that

$$EI = c\left(D_{11} - \frac{D_{12}^2}{D_{22}}\right) \tag{3.24}$$

$$GJ = 4\,c\left(D_{66} - \frac{D_{26}^2}{D_{22}}\right) \tag{3.25}$$

$$K = 2\,c\left(D_{16} - \frac{D_{12}D_{26}}{D_{22}}\right) \tag{3.26}$$

In Ref. [1.24] a stiffness cross-coupling parameter, ψ, was identified as measure of bending-torsion coupling present in a structure. This non-dimensional parameter was defined as,

$$\psi = \frac{K}{\sqrt{EIGJ}} \tag{3.27}$$

or in D-matrix terms

$$\psi = \frac{D_{16}D_{22} - D_{12}D_{26}}{\sqrt{\left(D_{11}D_{22} - D_{12}^2\right)\left(D_{66}D_{22} - D_{26}^2\right)}} \tag{3.28}$$

with limits

$$-1 < \psi < 1 \tag{3.29}$$

The above limits of the bending-torsion coupling parameter enable one to categorise a beam-like structure as highly coupled, with values near zero categorised as lightly coupled, while absolute values of ψ near unity categorised as highly coupled.

Equations (3.18) and (3.19) have been used as approximations to the plate curvatures in order the two-dimensional plate model can be reduced to a one-dimensional beam model. It worth noticing that in the above plate model the chordwise curvature k_x or "camber" bending has not been restrained.

3.3.3 Flat Beam : A Chordwise-Rigid Laminated Plate Model (CRLP)

In realistic wings, high torsional rigidity is usually provided by closely spaced ribs. When this is the case, chordwise rigidity can be assumed in terms of bending displacement and torsional rotation, and a modified flat beam (plate) model can be used to calculate the stiffnesses of a wing (beam). The approach used originally by Housner and Stein [1.9] to symmetrical balanced laminates and later by Weisshaar [2.66] to symmetrical, unbalanced laminates will be adopted to develop this model.

The assumed displacement

$$w(x,y) = h(y) - x\varphi(y) \tag{3.30}$$

is used for plate deflection. The assumption of chordwise rigidity results in the following expressions for plate curvatures:

$$k_x = 0 \quad ; \quad k_y = -h'' \quad ; \quad k_{xy} = -2\varphi' \tag{3.31}$$

Therefore, Eqn. (3.3) may reduce to

$$\begin{Bmatrix} M_x \\ M_y \\ M_{xy} \end{Bmatrix} = \begin{bmatrix} D_{22} & D_{12} & D_{26} \\ D_{12} & D_{11} & D_{16} \\ D_{26} & D_{16} & D_{66} \end{bmatrix} \begin{Bmatrix} 0 \\ -h'' \\ -2\varphi' \end{Bmatrix} \tag{3.32}$$

In this case the chordwise moment, M_x, is not zero, but is given by

$$M_x = -D_{12}h'' - 2D_{26}\varphi' \tag{3.33}$$

Using the same relationships between moment resultants on the beam cross-section and those on the plate cross-section as in Eqns (3.21) and (3.22), the bending, torsional, and coupling stiffnesses for the chordwise rigid laminated plate (CRLP) can then be obtained from Eqn. (3.32). These are as follows:

$$EI = cD_{11} \tag{3.34}$$

$$GJ = 4cD_{66} \tag{3.35}$$

$$K = 2cD_{16} \tag{3.36}$$

and therefore,

$$\psi = \frac{D_{16}}{\sqrt{D_{11}D_{66}}} \tag{3.37}$$

A term by term comparison between Eqns (3.34) - (3.36) and Eqns (3.24) - (3.26) shows that the HARP and CRLP models are identical only when the term D_{22} tends to infinity (i.e., infinite chordwise rigidity).

3.4 Stiffness Modelling of Thin-walled, Single-Cell, Composite Beams

An important deficiency of the laminated flat beam (plate) models previously described is that none of them takes into account the flexible transverse shear webs which are present in thin-walled (single and multi-cell) torque boxes widely used in wing design.

Two special lay-ups, the circumferentially uniform stiffness (CUS) and circumferentially asymmetric stiffness (CAS), have been considered for thin-walled beams in the recent literature [2.83-2.85, 3.17-3.19] (see Fig. 3.2). The CUS configuration produces extension-torsion coupling [2.84]. The axial, coupling and

shear stiffnesses *A*, *B* and *C* given in Eqns (3.38)-(3.40) below are constant throughout the cross-section, and hence the name circumferentially uniform stiffness (CUS) was adopted by Rehfield and Atilgan [3.18], Hodges et al. [3.19] and Rehfield et al. [2.83]. In the CUS configuration, the ply lay-ups on opposite flanges are of reversed orientation and hence the name antisymmetric configuration was adopted by Chandra et al. [3.17] and Smith and Chopra [2.84].

On the other hand the CAS configuration produces bending-torsion coupling [2.84]. The stiffness *A* (Eqn. (3.38)) is constant throughout the cross-section while the coupling stiffness, *B* (Eqn. (3.39)), in opposite members is of opposite sign and hence the name circumferentially asymmetric stiffness (CAS) was adopted in Refs [2.83, 3.18-3.19]. The stiffness *C* (Eqn. (3.40)) in opposite members is equal. The ply lay-ups along the horizontal members are mirror images (see Fig. 3.2), and hence the name symmetric configuration was adopted in Refs [2.84, 3.17].

The stiffnesses *A, B* and *C* are related to the usual laminate in-plane stiffness matrix *A* of classical lamination theory (see Eqn. (A.17) in Appendix 'A') as follows (see, for example Refs [2.23-2.25]):

$$A = A_{11} - \frac{A_{12}^2}{A_{22}} \tag{3.38}$$

$$B = 2\left[A_{16} - \frac{A_{12} A_{26}}{A_{22}} \right] \tag{3.39}$$

$$C = 4\left[A_{66} - \frac{A_{26}^2}{A_{22}} \right] \tag{3.40}$$

Several theories have been developed for the analysis of thin-walled anisotropic beams. A review has been provided in section 3.2. A basic element in the analytical modelling development is the derivation of the effective stiffness coefficients and governing equations which allows three-dimensional (3D) state of stress to be recovered from one-dimensional (1D) beam formulation. For isotropic or orthotropic materials this is a classical problem, which is considered in a number of text books

such as Megson [3.20], Timoshenko and Goodier [3.21], Sokolnikoff [3.22], Washizu [3.23], Crandall et al. [3.24], Wempner [3.25], Gjelsvik [3.26] and Libai and Simmonds [3.27].

For generally anisotropic materials, a number of 1D theories have been developed by Reissner and Tsai [3.28], Mansfield and Sobey [2.67], Rehfield [3.11], Libove [3.9], Rehfield and Atilgan [3.18], Chandra et al. [3.17], Smith and Chopra [2.84] and Berdichevsky et al. [2.85]. The derivation of stiffness coefficients from the displacement field for Refs [2.67, 2.84-2.85, 3.11, 3.17-3.18] is presented in detail in Appendix 'B'. Here only the displacement fields, warping terms and stiffness coefficients are presented. This is because the differences among the various stiffness models mainly lie in the treatment of the above sets of expressions. In order to make a comparison feasible, all the theories examined have been transformed into the notation of Berdichevsky et al. [2.85]. In Table 3.1 a summary is given of the most popular theories for stiffness predictions of thin-walled composite beams; this includes the type of loadings and the non-classical effects considered in each of them.

3.4.1 Mansfield and Sobey Stiffness Model [2.67]

A simple contour analysis for stiffness prediction of thin-walled laminated composite beams has been suggested by Mansfield and Sobey [2.67]. The authors have analysed a cylindrical tube subjected to torsion, bending and longitudinal tension. The thin-walled, single-cell closed cross-section used is shown in Fig. 3.3. The authors adopted the classical assumptions of neglecting shear and hoop stresses and considering the shear flow to be constant. The torsion-related warping and transverse shear deformation were neglected. Their displacement field, in Cartesian coordinates and the notation of Berdichevsky et al. [2.85], is of the form

$$u_1 = U_1(x) - y(s)U_2'(x) - z(s)U_3'(x)$$

$$u_2 = U_2(x) - z(s)\varphi(x) \tag{3.41}$$

$$u_3 = U_3(x) + y(s)\varphi(x)$$

The forces and moments are linearly related to the displacements by a symmetric 4x4 stiffness matrix, P, defined as,

$$F = Pu \tag{3.42}$$

or as,

$$\begin{Bmatrix} T \\ M_x \\ M_y \\ M_z \end{Bmatrix} = \begin{bmatrix} P_{11} & P_{12} & P_{13} & P_{14} \\ P_{12} & P_{22} & P_{23} & P_{24} \\ P_{13} & P_{23} & P_{33} & P_{34} \\ P_{14} & P_{24} & P_{34} & P_{44} \end{bmatrix} \begin{Bmatrix} U_1' \\ \varphi' \\ U_3'' \\ U_2'' \end{Bmatrix} \tag{3.43}$$

where T, M_x, M_y and M_z represent the tension, torsional moment, spanwise and chordwise bending moment, respectively. Correspondingly, U_1', φ', U_3'' and U_2'' are the axial strain, twisting curvature, spanwise and chordwise bending curvature respectively.

The stiffness elements P_{33}, P_{22} and P_{23} in Eqn. (3.43) represent the bending, torsional and bending-torsion coupling rigidity respectively. These are given as [2.67],

$$EI = \oint z^2 H_{11} ds + \frac{\oint z H_{21} ds}{\oint H_{22} ds} \tag{3.44}$$

$$GJ = \frac{4 A_e^{\,2}}{\oint H_{22} ds} \tag{3.45}$$

$$K = \frac{2 A_e}{\oint H_{22} ds} \tag{3.46}$$

where A_e is the enclosed area of the cross-section and the H_{ij} terms are combinations of element compliances and therefore stiffnesses. It would be unnecessarily cumbersome to seek to write these H_{ij} stiffness elements in terms of the in-plane moduli A_{ij}.

3.4.2 Rehfield [3.11] and Rehfield and Atilgan [3.18] Stiffness Models

A similar contour analysis for the prediction of stiffness parameters applicable to any cross-section is given by Rehfield [3.11]. However, in this analysis the restrained torsional warping and transverse shear deformation were included. Rehfield's displacement field, in Cartesian coordinates (see Fig. 3.3) and the notation of Berdichevsky et al. [2.85], is of the form

$$u_1 = U_1(x) - y(s)\left[U_2'(x) - 2\gamma_{xy}(x)\right] - z(s)\left[U_3'(x) - 2\gamma_{xz}(x)\right] + g(s,x)$$

$$u_2 = U_2(x) - z(s)\varphi(x) \tag{3.47}$$

$$u_3 = U_3(x) + y(s)\varphi(x)$$

where γ_{xz} and γ_{xy} are the transverse shear strains, $\varphi(x)$ is an arbitrary function that represents the cross-sectional rotation about the x-axis, and $g(s,x)$ is the warping function given by

$$g(s,x) = \overline{G}(s)\varphi'(x) \tag{3.48}$$

where

$$\overline{G}(s) = 2A_e\frac{s}{l} - \int_0^s r_n(\tau)d\tau \tag{3.49}$$

and r_n is the projection of the position vector r in the normal direction, so that,

$$\oint r_n ds = 2A_e \tag{3.50}$$

The torsional warping function in Eqn. (3.49) was later modified by Rehfield and Atilgan [3.18] as,

$$\overline{G}(s) = \int_o^s \left[\frac{2A_e}{l\overline{c}_1}c_1 - r_n(\tau)\right]d\tau \tag{3.51}$$

where

$$c_1 = \frac{1}{C - \left(\left(B^2\right)/A\right)} \tag{3.52}$$

A, *B* and *C* are the in-plane stiffnesses given in Eqns (3.38) - (3.40).

The forces and moments are linearly related to the displacements by a symmetric 7x7 stiffness matrix, P, defined as,

$$F = Pu \tag{3.53}$$

The generalised internal forces, F, can be expressed in a column matrix form as,

$$F = \begin{bmatrix} T & Q_y & Q_z & M_x & M_y & M_z & Q_w \end{bmatrix} \tag{3.54}$$

where T is the tension, Q_y and Q_z are the shear forces, M_x is the torsional moment, M_y and M_z are the bending moments and Q_w is the generalised warping related force.

Similarly, the deformational variables, u, can be expressed in a column matrix form as,

$$u = \begin{bmatrix} U_1'(x) & \gamma_{xy} & \gamma_{xz} & \varphi'(x) & \left\{U_2''(x) - 2\gamma'_{xy}(x)\right\} & \left\{U_3''(x) - 2\gamma'_{xz}(x)\right\} & \varphi''(x) \end{bmatrix} \tag{3.55}$$

$U_1'(x)$ is the axial strain, while $\varphi'(x)$, $\left\{U_2''(x) - 2\gamma'_{xy}(x)\right\}$ and $\left\{U_3''(x) - 2\gamma'_{xz}(x)\right\}$ are the twisting and bending curvatures, respectively. $\varphi''(x)$ is the additional kinematic variable associated with torsional warping.

All the stiffness terms of matrix, P, are expressed in terms of Eqns (3.38) - (3.40). The bending, torsional and bending-torsion coupling stiffnesses are given as [3.11],

$$EI = \oint_{\Gamma} Az^2 ds \tag{3.56}$$

$$GJ = \left(\frac{A_e}{c}\right)^2 \oint_{\Gamma} C\, ds \tag{3.57}$$

$$K = \frac{A_e}{c} \oint_{\Gamma} Bz\, ds \tag{3.58}$$

where $c = \oint_{\Gamma} ds$ is the circumference, and Γ represents the cross-section shape.

3.4.3 Chandra et al. Stiffness Model [3.17]

Following the coupled non-linear analysis of Hong and Chopra [3.14] for a composite blade undergoing flap bending, lag bending, elastic twist, and axial deflections, a simplified non-contour analysis for the prediction of stiffnesses applicable to thin-walled (box-beam) structures was derived by Chandra et al. [3.17] for extension, bending and torsion of thin-walled symmetric and antisymmetric composite beams. The effects of cross-sectional warping due to torsion are included in an approximate manner [3.14] and the effects of transverse shear are neglected. Unlike the contour analysis of Mansfield and Sobey [2.67] and Rehfield [3.11], in this analysis the four sides of the box-beam are modelled as general composite laminated plates.

The displacement field expressed in Cartesian coordinates (see Fig. 3.4) and using the notation of Berdichevsky et al. [2.85], is of the form

$$\begin{aligned} u_1 &= U_1(x) - yU_2'(x) - zU_3'(x) - \lambda\varphi'(x) \\ u_2 &= U_2(x) - z\varphi(x) \\ u_3 &= U_3(x) + y\varphi(x) \end{aligned} \tag{3.59}$$

where λ is the torsional warping function which is given in an approximate manner as,

$$\lambda = \frac{(c-d)}{(c+d)} yz \tag{3.60}$$

where c and d are the beam width and depth respectively.

The relation between moments and curvatures are given as,

$$\begin{Bmatrix} M_y \\ M_x \end{Bmatrix} = \begin{bmatrix} EI & K \\ K & GJ \end{bmatrix} \begin{Bmatrix} U_2'' \\ \varphi' \end{Bmatrix} \tag{3.61}$$

where

$$EI = \sum_{K=1}^{N} \iint_{h,h} \overline{C}_{11}^{(K)} z^2 dydz + \sum_{l=1}^{M} \iint_{\upsilon,\upsilon} \overline{C}_{11}^{(K)} z^2 dydz \tag{3.62}$$

$$GJ = \sum_{K=1}^{N} \iint_{h,h} \overline{C}_{66}^{(K)} z^2 dydz + \sum_{l=1}^{M} \iint_{\upsilon,\upsilon} \overline{C}_{66}^{(K)} \hat{y}^2 dydz \tag{3.63}$$

$$K = \sum_{K=1}^{N} \iint_{h,h} \overline{C}_{16}^{(K)} \hat{z} z dydz \tag{3.64}$$

The $\overline{C}_{ij}$, $\hat{y}$, $\hat{z}$ terms are given by Eqns (B.34)-(B.36) and (B.42) in Appendix 'B'. Subscript h represents the horizontal (top and bottom) flanges of the laminated box-beam and υ represents the vertical (the left and right). N and M are numbers of layers in the horizontal and vertical laminates respectively.

3.4.4 Smith and Chopra Stiffness Model [2.84]

This analysis is an extension of that of Chandra et al. [3.17]. Each beam wall is considered to be a single laminated plate as shown in Fig. 3.4 and subjected to axial, bending, torsional and shear loads. Only when the warping function is considered are the cross-sections treated using the contour level of thin-walled

beams, and this is then transformed from contour form to two-dimensional cross-sectional form. The warping function is then carried through the entire analysis, from the initial kinematic relations to the effective stiffnesses of the beam cross-section. In addition, the transverse shear deformation is also included.

The displacement field of Smith and Chopra [2.84] is similar to that of Rehfield [3.11] (see Eqn. (3.47)). In Cartesian coordinates (Fig. 3.3) and the notation of Berdichevsky et al. [2.85], it is of the form

$$u_1 = U_1(x) - y\left[U_2'(x) - \gamma_{xy}(x)\right] - z\left[U_3'(x) - \gamma_{xz}(x)\right] - \lambda\varphi'(x)$$

$$u_2 = U_2(x) - z\varphi(x) \tag{3.65}$$

$$u_3 = U_3(x) + y\varphi(x)$$

where $\lambda\varphi'(x)$ represents the warping of the cross-section. In this analysis, the thin-walled beam theory approach described in Megson [3.20] is modified to determine the shape of the warping deflections for a composite box-beam. The warping function is defined along the contour as,

$$\lambda(s) = 2A_e\left(\frac{\delta_{os}}{\delta} - \frac{A_{os}}{A_e}\right) \tag{3.66}$$

For the rectangular box-beam under consideration, the enclosed area of the cross-section is $A_e = cd$. A_{os} is the area swept out by a generator, with origin at the box-beam centre, from $s = 0$ to $s = s$ on the contour. Other contour parameters in Eqn. (3.66) are defined as,

$$\delta = \int_s \frac{ds}{G(s)t(s)} \qquad \text{and} \qquad \delta_{os}(s) = \int_0^s \frac{ds}{G(s)t(s)} \tag{3.67}$$

For relatively thin walled beams, the contour warping function $\lambda(s)$, can be simply transformed into the two-dimensional cross-sectional form

$$\lambda(y,z) = \beta yz \tag{3.68}$$

with β given by

$$\beta = -\frac{(1-\alpha)}{(1+\alpha)} \qquad \text{and} \qquad \alpha = \left(\frac{c}{d}\right)\left(\frac{t_\upsilon}{t_h}\right)\left(\frac{G_\upsilon}{G_h}\right) \tag{3.69}$$

G_υ and G_h are the effective in-plane shear stiffness of the vertical and horizontal walls respectively.

The forces and moments are linearly related to the displacements by a symmetric 6x6 stiffness matrix, P, defined as,

$$F = Pu \tag{3.70}$$

where

$$F = \begin{bmatrix} T & Q_y & Q_z & M_x & M_y & M_z \end{bmatrix} \tag{3.71}$$

and

$$u = \begin{bmatrix} U_1'(x) & \gamma_{xy} & \gamma_{xz} & \varphi'(x) & \left\{U_2''(x) - 2\gamma_{xy}'(x)\right\} & \left\{U_3''(x) - 2\gamma_{xz}'(x)\right\} \end{bmatrix} \tag{3.72}$$

The bending, torsional and bending-torsion coupling stiffnesses are given as,

$$EI = \iint_{h,\upsilon} \overline{Q}_{11} z^2 dA - c_2 \iint_{h,\upsilon} \overline{Q}_{12} z^2 dA \tag{3.73}$$

$$\begin{aligned} GJ = {} & (1+\beta)^2 \iint_h \overline{Q}_{66} z^2 dA + (1-\beta)^2 \iint_\upsilon \overline{Q}_{66} y^2 dA \\ & + d_0\left[(1-\beta)\iint_\upsilon \overline{Q}_{26} y dA - (1+\beta)\iint_h \overline{Q}_{26} z dA\right] \\ & + d_1(1-\beta)\iint_\upsilon \overline{Q}_{26} y^2 dA - d_2(1+\beta)\iint_h \overline{Q}_{26} z^2 dA \end{aligned} \tag{3.74}$$

$$K = (1+\beta)\iint_\upsilon \overline{Q}_{16} z^2 dA - d_2 \iint_{h,\upsilon} \overline{Q}_{12} z^2 dA \tag{3.75}$$

where β is the non-dimensional warping function.

The above stiffness parameters contain a number of constants, such as, c_2, d_0, d_1 and d_2. These constants arise from the refined treatment of the two dimensional in-plane elastic behaviour and are given by Eqn. (B. 60) in Appendix 'B'.

3.4.5 Berdichevsky et al. Stiffness Model [2.85]

One of the most recent and thorough theories for the prediction of stiffness parameters of thin-walled beams subjected to axial, bending and torsional loads has been developed by Berdichevsky et al. [2.85]. It is a variationally and asymptotically consistent theory applicable to any single-cell cross-section and laminate configuration. The theory is based on an asymptotic analysis of two-dimensional shell theory. In addition to the classical out-of-plane torsional warping, two new contributions were included; these are the axial strain and bending warping. However, the transverse shear deformation was neglected.

A displacement field consistent with a hypothesis of in-plane nondeformability of the cross-section, but allowing for out-of-plane warping is derived using an asymptotic variational method.

In Cartesian coordinates the displacement field is given by

$$\begin{aligned} u_1 &= U_1(x) - y(s)U_2'(x) - z(s)U_3'(x) + G(s)\varphi'(x) \\ &+ g_1(s)U_1'(x) + g_2(s)U_2''(x) + g_3(s)U_3''(x) \\ u_2 &= U_2(x) - z(s)\varphi(x) \\ u_3 &= U_3(x) + y(s)\varphi(x) \end{aligned} \tag{3.76}$$

where

$$G(s) = \int_0^s \left[\frac{2A_e}{l\bar{c}} c(\tau) - r_n(\tau) \right] d\tau$$

$$g_1(s) = \int_0^s \left[b(\tau) - \frac{\bar{b}}{\bar{c}} c(\tau) \right] d\tau$$

$$g_2(s) = -\int_0^s \left[b(\tau) y(\tau) - \frac{by}{\bar{c}} c(\tau) \right] d\tau \qquad (3.77)$$

$$g_3(s) = -\int_0^s \left[b(\tau) z(\tau) - \frac{bz}{\bar{c}} c(\tau) \right] d\tau$$

and

$$b(s) = -\frac{2B(s)}{C(s)} \qquad c(s) = \frac{1}{C(s)} \qquad (3.78)$$

The first four terms in the expression for u_1 (Eqn. (3.76)) are analogous to the classical theory of extension, bending and torsion of beams. The additional terms $g_1(s)U_1'$, $g_2(s)U_2''$ and $g_3(s)U_3''$ in u_1 represent warping to axial strain and bending. These new terms emerge naturally in addition to the classical torsion-related warping $G(s)\varphi'$. They are strongly influenced by the material's anisotropy, and vanish for materials that are either orthotropic or whose properties are antisymmetric relative to the shell middle surface.

The relationship between forces, moments and displacements can then be written in matrix form as in Eqn. (3.43) where T, M_x, M_y and M_z represent the tension, torsional moment and bending moments, respectively. The cross-sectional stiffnesses, denoted by P_{ij} in Eqn. (3.43), are formulated in terms of closed form integrals of the material constants and geometry. The bending, torsional and bending-torsion coupling stiffnesses are given as,

$$EI = \oint \left(A - \frac{B^2}{C} \right) z^2 ds + \frac{\left[\oint (B/C) z ds \right]^2}{\oint (1/C) ds} \qquad (3.79)$$

$$GJ = \frac{1}{\oint (1/C)ds} A_e^2 \tag{3.80}$$

$$K = -\frac{\oint (B/C)zds}{\oint (1/C)ds} A_e \tag{3.81}$$

3.5 Comparison of the Various Thin-Walled Beam Theories

A very important element in any analytical modelling development is the inclusion of the cross-sectional warping which allows the three-dimensional (3D) contributions to be recovered from a one-dimensional (1D) beam formulation. One major difference among the various theories lies in the methodology used to derive the warping of the cross-section and to include its contributions into a 1D theory. In Refs [2.83-2.84, 3.11, 3.17-3.18], the displacement field of classical thin-walled beam theory is used with shear deformation as the basis of its analytical development. In Ref. [3.18] a shear correction factor was introduced (see Eqn. (3.51)) in order to reduce the overestimated bending stiffness. In Ref. [2.85], in addition to the classical torsion-related warping, the derived displacement field includes out-of-plane warping due to uniform axial extension and bending as well (see Eqn. (3.76)).

In the pioneering work of Reissner and Tsai [3.28], the derived constitutive relationships are similar to Eqn. (3.43). However, the authors left to the reader the derivation of the explicit expressions for the stiffness coefficients, which may be why their work was overlooked. A number of assumptions were adopted in the Reissner and Tsai [3.28] development regarding material properties, such as, neglecting the coupling between in-plane strains and curvatures which can be significant in anisotropic materials.

Mansfield and Sobey [2.67] and Libove [3.9] obtained the beam flexibilities relating the stretching, twisting and bending deformations to the applied axial load, torsional and bending moments for a special origin and axes orientation. The authors adopted the assumptions of negligible resultant hoop-stress and a membrane state in the thin-walled beam section. Although they did not refer to the work of Reissner and

Tsai [3.28], their stiffnesses coincide for the special case outlined in Ref. [3.28]. This special case refers to that where the classical assumptions of neglecting shear and hoop stresses and considering the shear flow to be constant is adopted.

The displacement field of Mansfield and Sobey [2.67] in Eqn. (3.41) does not take into account the torsion-related warping or any other sort of warping or transverse shear deformation. On the other hand, in Chandra et al. [3.17] the torsional warping is given in an approximate manner (see Eqns (3.59) and (3.60)). In this work, as in Ref. [2.67], the transverse shear deformation is not included.

The displacement field of Smith and Chopra [2.84] in Eqn. (3.65) is identical to that of Rehfield [3.11] in Eqn. (3.47). However, their warping function is identical to the modified expression of Rehfield and Atilgan [3.18] given in Eqn. (3.51). The warping function, is then transformed from contour form to two-dimensional cross-sectional form, and is the only point in their analysis where the cross-section is treated on the contour level of thin-walled beam theory. Their formulation, as in the case of Rehfield [3.11], comprises only the torsion-related warping (Eqn. (3.65)). Apart from the similar displacement field and warping function, the authors' approach is different from that of Rehfield [3.11] and Berdichevsky et al. [2.85]. In this analysis the four sides of the box-beam are modelled as general composite laminated plates (see Fig. 3.4).

The displacement fields of Rehfield [3.11] and Berdichevsky et al. [2.85] in Cartesian coordinates are given in Eqns (3.47) and (3.76) respectively, and their respective warping functions in Eqns (3.48) and (3.77). A comparison of the two displacement fields shows that the warping function in Rehfield's formulation comprises the torsion-related contribution $(G(s)\varphi'(x))$ but does not include explicit terms that express the bending-related warping. As can be seen from Eqns (3.49) and (3.77) the torsional warping function, $G(s)$, of the two theories are not the same. The two warping functions are identical when the shear stiffness C is constant (see Eqn. (3.40)), that is, when the wall stiffness and thickness are uniform along the cross-sectional circumference.

The expressions for the stiffness coefficients given by Chandra et al. [3.17] (Eqns (3.62)-(3.64)) are similar to those given by Smith and Chopra [2.84]

(Eqns (3.73)-(3.75)). The additional parameters in the expressions for the stiffness coefficients in Ref. [2.84] are due to the more sophisticated warping function (Eqn. 3.66) and expression for the strain in the z direction (Eqn. (B. 51) in Appendix 'B'). The expressions for the stiffness coefficients given in the above two analyses are different from the expressions given by the analyses of Mansfield and Sobey [2.67], Rehfield [3.11] and Berdichevsky et al. [2.85].

The differences in the expressions for the stiffness coefficients among the contour analyses [2.67, 2.85, 3.11] are mainly due to the different methodology used to derive the warping of the cross-section. The inclusion of the warping function in the expression for the axial displacement, see for example Eqns (3.65) and (3.76), has a substantial effect on the bending stiffness. A comparison of the expressions for the bending stiffness (EI) given by Rehfield [3.11] and Berdichevsky et al. [2.85] in Eqns (3.56) and (3.79) respectively, shows that in addition to the parameters given in Eqn. (3.56), Eqn. (3.79) contains extra parameters due to the additional terms in the expression for axial displacement (Eqn. (3.76)) representing warping due to axial strain and bending. However, the expressions for the torsional stiffness GJ (Eqns (3.57) and (3.80)) and bending-torsion coupling stiffness K (Eqns (3.58) and (3.81)) of the two theories are quite similar. The expressions for the torsional and bending-torsion coupling stiffnesses of the two theories coincide when the shear stiffness C of Eqn. (3.40) is constant, that is, when the wall stiffness and thickness are uniform along the cross-sectional circumference.

3.6 Case Study - A Thin-Walled Box-Beam

In preliminary aeronautical design, the rigidity and deflection characteristics of a flat beam (plate) or thin-walled beam are useful to the understanding and study of bending-torsion features of actual lifting surfaces with moderate-to-high aspect ratio. Thus, it is important to examine and compare the cross-sectional rigidity predictions of the various beam models, such as those previously described, in order to get an insight into the rigidity characteristics and the resulting coupled deflection behaviour of composite beams. For example, many studies such as those of Refs [1.14, 1.23, 3.29], have shown that there may be substantial differences in predicted natural frequencies depending upon whether or not chordwise bending is included. Therefore,

the stiffness predictions of flat beam (plate) models need to be compared. One of the important weaknesses of flat beam models is that they cannot account for flexible transverse shear webs. However, as in actual wing design torque boxes with flexible vertical webs are widely used, the flat beam models need to be compared with thin-walled box-beam models.

To illustrate some of the characteristics of the various beam models, a thin-walled single-cell cross-sectional shape is considered as shown in Fig. 3.5 (a). The stiffnesses of this singe-cell beam can be predicted using one of the box-beam models described previously. Otherwise, the box-beam shown in Fig. 3.5 (a) can be idealised as two flat beams as shown in Fig. 3.5 (b). The latter approach was adopted in a number of aeroelastic analyses such as those of Refs [1.9, 2.66].

Initially, the ratio of the box width (c), to box depth (d), is considered to be equal to 2 and the ratio of plate thickness (t) to plate width (c) is 0.025. The material used is unidirectional Hercules AS1/3501-6 graphite-epoxy. Both the flat beams and the box-beams have ply symmetry with respect to the middle surface. The coordinate system and sign convention used is shown in Fig. 3.1. Since the stiffnesses are symmetrical about $\beta = 0^0$, the fibre angle is allowed to vary between 0^0 and 90^0.

For this illustration the two previously described flat beam models, that is, the HARP and CRLP (see sections 3.3.2 and 3.3.3), and the box-beam models developed by Rehfield [3.11], Chandra et al. [3.17], and Berdichevsky et al. [2.85] are used.

Figure 3.6 shows the bending stiffness (EI) as a function of fibre angle β for the two flat beam models and the box-beam model given by Berdichevsky et al. [2.85]. The bending stiffness data has been non-dimensionalised with respect to the term (EI_{REF}), the bending stiffness of the box-beam model when the fibre angle of all sides is set to $\beta = 0^0$. In the case of the box-beam model only the fibre angle of the horizontal (top and bottom) flanges is varied while the fibre angle of the vertical (right and left) flanges is set to 0^0. From Fig. 3.6 it can be seen that the bending stiffness predicted by the CRLP is similar to, but somewhat larger than, the HARP model prediction as expected. This is because the second term of Eqn. (3.24) vanishes as the chordwise bending stiffness term D_{22} goes to infinity (i.e., when infinite chordwise

rigidity is assumed). From the same figure it is also seen that the HARP model underestimates the bending stiffness when compared to the box-beam model.

In Fig. 3.7 the bending-torsion coupling parameter ψ is plotted against the fibre angle β for the three models. Significant differences in predicted values of this parameter are apparent. The values of ψ predicted by CRLP are much higher than those predicted by HARP and box-beam model with maximum value of about $\psi = 0.8$ occurring at a fibre angle of 35^0. The maximum value of ψ predicted by the HARP is 0.7 and by the box-beam model 0.48 and occur at a fibre angle of 25^0 and 20^0 respectively. From the aeroelasticity standpoint, this difference in the predicted value of ψ is extremely important as this can have significant impact upon the predicted flutter and divergence speed.

Figure 3.8 compares the torsional rigidity (GJ) of each of the three models. GJ_{REF} is the torsional stiffness given by the box-beam model [2.85] when the fibre angle of all the sides of the beam is set to $\beta = 0^0$. From Fig. 3.8, it can be seen that, although GJ is symmetrical about $\beta=45^0$ for the CRLP, it is not symmetrical about $\beta = 45^0$ for the HARP and box-beam model. This is due to the fact that the torsional rigidity term D_{66} which describes the torsional rigidity of the CRLP (see, for example, Eqn. (3.35)) is symmetrical about $\beta = 45^0$ (see Fig. A.9 in Appendix 'A'). In contrast, the chordwise bending rigidity term D_{26}^2 / D_{22} and chordwise membrane strain term A_{26}^2 / A_{22} included in the HARP and box-beam models in Eqns (3.25) and (3.40) respectively are increasing from their minimum value at $\beta=0^0$ to their maximum at $\beta = 90^0$ (see Figs A.8 and A.9 in Appendix 'A'). The maximum torsional rigidity for both HARP and box-beam model is offered near $\beta = 30^0$ while for the CRLP at $\beta = 45^0$.

The difference in the computed torsional rigidity between the flat beam and box-beam models is attributed to the fact that the latter has flexible vertical shear webs, while the plate models assume transverse shear rigidity. This was first noted in Ref. [1.21]. In the plate models vertical webs infinitely stiff in shear are assumed. Thus, the torsional stiffness predicted by the box-beam model should be less than that predicted by either the HARP or the CRLP for an identical cross-section as shown in Fig. 3.8. According to Bredt-Batho formula [3.20] for an isotropic material the ratio of torsional rigidity of a rectangular cross-section box-beam with flexible shear webs

(GJ_f) to the torsional rigidity of the same beam with rigid vertical webs (GJ_r) is given by

$$\frac{GJ_f}{GJ_r} = \frac{1}{1+d/c}$$

The difference in the predicted value of torsional rigidity between HARP and the box-beam model declines rapidly as the box-beam cross-section changes from a square (c / d = 1) to a thin rectangle ($c / d >> 1$). This is illustrated in Fig. 3.9 where the width-to-depth ratio (c / d) of the box-beam has been increased from 2 to 6. Figure 3.9 shows that the stiffnesses predicted by the two models are similar at this width-to-depth ratio with the HARP still giving higher torsional rigidity. In Fig. 3.10 where the c / d = 10 the box-beam model gives higher torsional rigidity than the HARP. This can be attributed to the fact that the assumptions made in the bending analysis of thin-walled beams that the top and the bottom flanges of the beam are in membrane mode is not valid for high width-to-depth ratios. In other words, the use of axial stiffness terms A_{ij} in Eqns (3.38)-(3.40) instead of the bending stiffness terms D_{ij} in Eqns (3.24)-(3.26) (see also Eqns (A.20) and (A.21) in Appendix 'A') is not valid for high width-to-depth ratios. It is important to note that the axial stiffness terms A_{ij} have usually higher values than the bending stiffness terms D_{ij} and therefore the bending and torsional stiffnesses are overestimated in this case (see Figs A.8 and A.9 in Appendix 'A').

Figures 3.11-3.13 show the non-dimensional rigidity and coupling parameters, as functions of the fibre angle, β, for the box-beam models developed by Rehfield [3.11], Chandra et al. [3.17], and Berdichevsky et al. [2.85]. As in the previous investigation, the fibre angle in the horizontal walls (top/bottom) is allowed to vary between 0^0 and 90^0 while the fibre angle of the vertical walls is fixed at $\beta = 0^0$. The bending and torsional stiffnesses have been non-dimensionalised with respect to the terms EI_B and GJ_B respectively, the bending and torsional stiffnesses obtained by the model of Berdichevsky et al. [2.85] when all the fibres in the laminate are at angle $\beta = 0^0$. From Figs 3.11-3.13, it can be seen that the Rehfield [3.11] and Berdichevsky et al. [2.85] models give the same values for EI and GJ when bending-torsion coupling is not present, i.e., when the fibre angle, β, is at 0^0 and 90^0. When

bending-torsion coupling is present, however, the Rehfield's model gives slightly higher values for EI and GJ and ψ as expected (see section 3.5). The results obtained by Chandra et al. [3.17] model resemble the ones obtained by CRLP model with infinite chordwise rigidity as an assumption.

In Fig. 3.14 the rigidity and coupling parameters are plotted against the fibre angle, β for Rehfield [3.11] and Berdichevsky et al. [2.85] box-beam models. However, in this case the fibre angle of all four sides is varied. The variation of torsional rigidity (Fig. 3.14) and bending-torsion coupling rigidity (not shown here) with fibre angle, coincides for the two models. This is because the expressions for the above two rigidities coincide for the two models when the shear stiffness C (Eqn. 3.40) is constant, that is, when the wall stiffness and thickness are uniform along the cross-sectional circumference. The predicted values of bending rigidity (EI) and as a consequence of the bending-torsion coupling parameter ψ for the two models are also very closed as can be seen from Fig. 3.14.

3.7 Conclusions

A very important element in any analytical modelling development of thin-walled beams (box-beams) is the inclusion of the cross-sectional warping which allows the three-dimensional (3D) contributions to be recovered from a one-dimensional (1D) beam formulation. The major difference between the various theories lies generally in the methodology used to analyse the box-beam and particularly in the methodology used to derive the warping of the cross-section and to include its contributions into a 1D theory.

Three different methods have been mainly used to analyse a thin-walled composite beam. Two of these are the contour analysis [2.67, 3.9, 3.11] and the variational asymptotical analysis [2.85] where the displacements and stresses are integrated around the cross-section and as a consequence the cross-section is analysed as one part whatever its shape. The third is the simplified linear analysis used in Refs [2.84, 3.17] where the four sides of the thin-walled beam are modelled as general composite laminated plates.

An important advantage of the contour and variational-asymptotical analyses is that the cross-sectional warping can be more accurately predicted as it is taken around the cross-section. However, in the simplified theory where each side of the beam is modelled as a plate, the torsion-related warping is expressed in an approximate manner [2.84, 3.17].

Analysis also shows that one must be very careful in choosing a model for the prediction of stiffnesses of a laminated composite beam. The CRLP model can give satisfactory results only when the wing has such a high torsional rigidity for the chordwise rigidity to be assumed. Chordwise rigidity is often assumed in wing design when stiff, closely spaced ribs are present within a wing of moderate-to-high aspect ratio. If this is not the case, the HARP model is definitely a better choice. When a thin-walled beam cross-section is present within a wing, such as, a torque box of small width-to-depth ratio, a box-beam model like the ones given by Berdichevsky et al. [2.85] and Rehfield [3.11] is a better choice. However, if the width-to-depth ratio of the thin-walled beam is large, the HARP model appears to be a better choice since the use of axial stiffness terms A_{ij} (instead of the bending stiffness terms D_{ij}) in box-beam models to estimate the stiffness properties is not valid for high width-to-depth ratios because it results in an overestimation of stiffnesses.

Since the presence of stiffness coupling has a significant effect on the static characteristics of composite beams it must also have similar effect on the dynamic characteristics of such beams. Therefore, the next chapter sets out to investigate the free vibration behaviour of composite beams mainly when stiffness coupling is present.

TABLE 3.1

Loadings and non-classical effects considered in the various analytical theories for stiffness predictions of thin-walled composite beams

		Loadings considered					Non-classical effects included			
Authors and Reference	**Date**	**Axial**	**Torsional**	**Bending**	**Shear**	**Warping**	**Transverse shear**	**Warping due to torsion**	**Warping due to bending**	**Warping due axial strain**
Reissner and Tsai [3.28]	**1972**	**Yes**	**Yes**	**Yes**	**No**	**No**	**No**	**No**	**No**	**No**
Mansfield and Sobey [2.67]	**1979**	**Yes**	**Yes**	**Yes**	**No**	**No**	**No**	**No**	**No**	**No**
Hong and Chopra [3.14]	**1985**	**Yes**	**Yes**	**Yes**	**No**	**No**	**No**	**Yes**	**No**	**No**
Rehfield [3.11]	**1985**	**Yes**	**Yes**	**Yes**	**Yes**	**Yes**	**Yes**	**Yes**	**No**	**No**
Libove [3.9]	**1988**	**Yes**	**Yes**	**Yes**	**No**	**No**	**No**	**No**	**No**	**No**
Rehfield and Atilgan [3.18]	**1989**	**Yes**	**Yes**	**Yes**	**Yes**	**Yes**	**Yes**	**Yes**	**No**	**No**
Chandra et al. [3.17]	**1990**	**Yes**	**Yes**	**Yes**	**No**	**No**	**No**	**Yes**	**No**	**No**
Smith and Chopra [2.84]	**1991**	**Yes**	**Yes**	**Yes**	**Yes**	**No**	**Yes**	**Yes**	**No**	**No**
Berdichevsky et al. [2.85]	**1992**	**Yes**	**Yes**	**Yes**	**No**	**No**	**No**	**Yes**	**Yes**	**Yes**

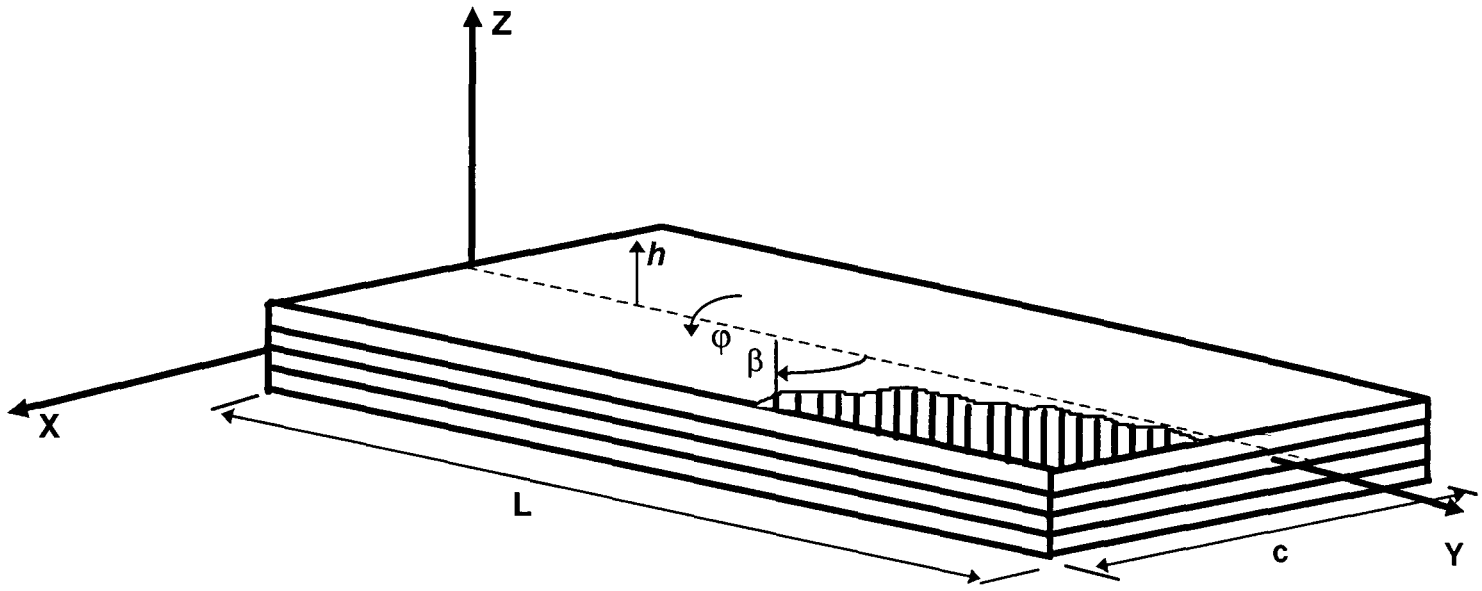

Fig. 3.1. Coordinate system and sign convention for positive ply angle of a laminated composite beam.

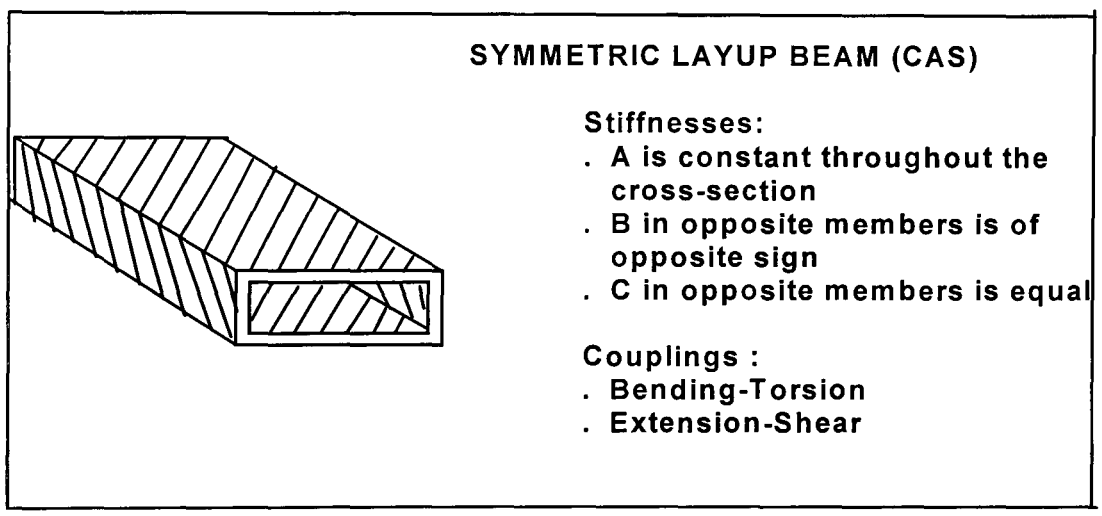

Fig. 3.2. Box-beam lay-up designations.

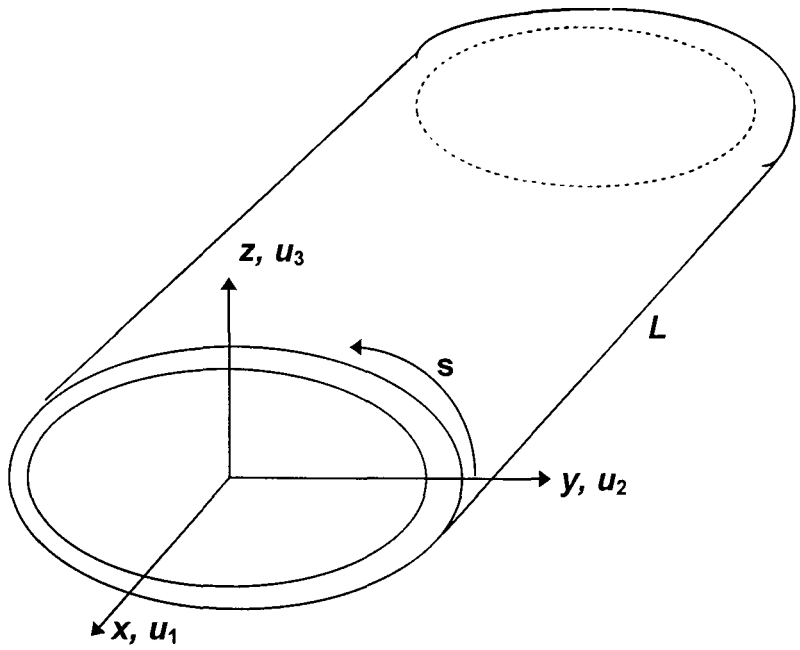

Fig. 3.3. Cartesian coordinate system

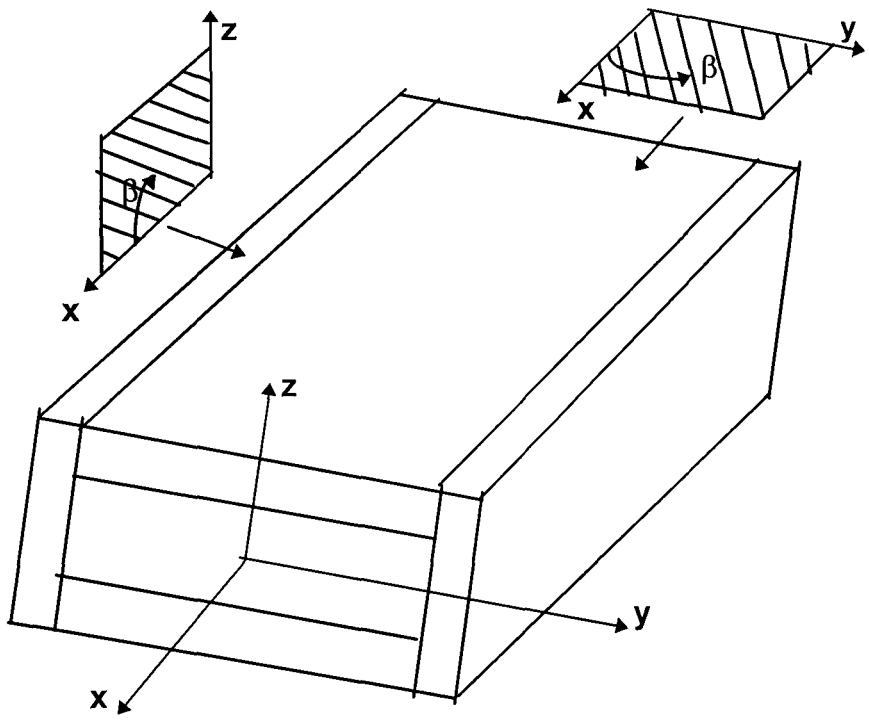

Fig. 3.4. Box-beam configuration and coordinates for Refs [2.84, 3.17].

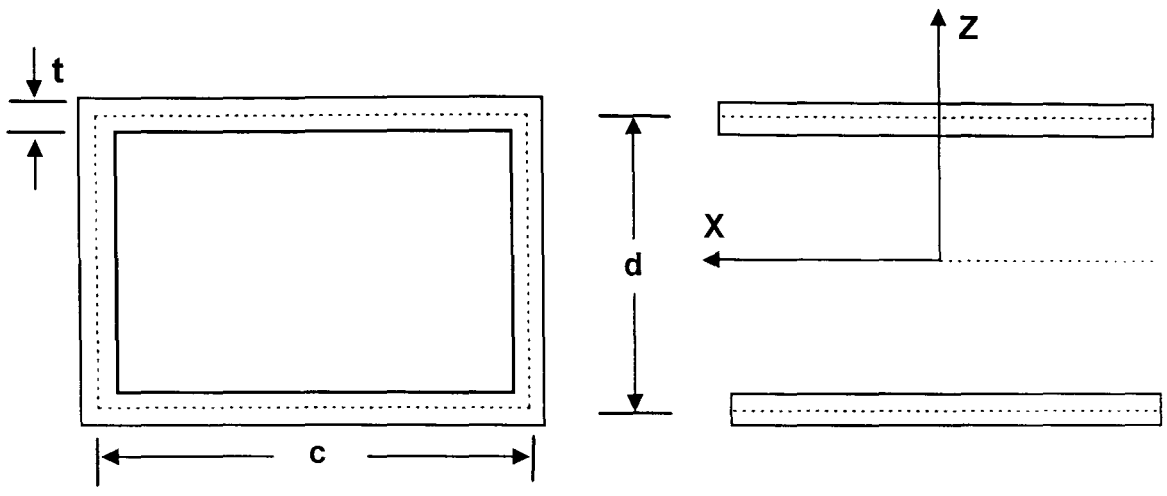

(a) Box-beam cross-section (b) Box-beam idealised as two flat beams

Fig. 3.5. Cross-sectional properties and coordinates for the beams of the case study.

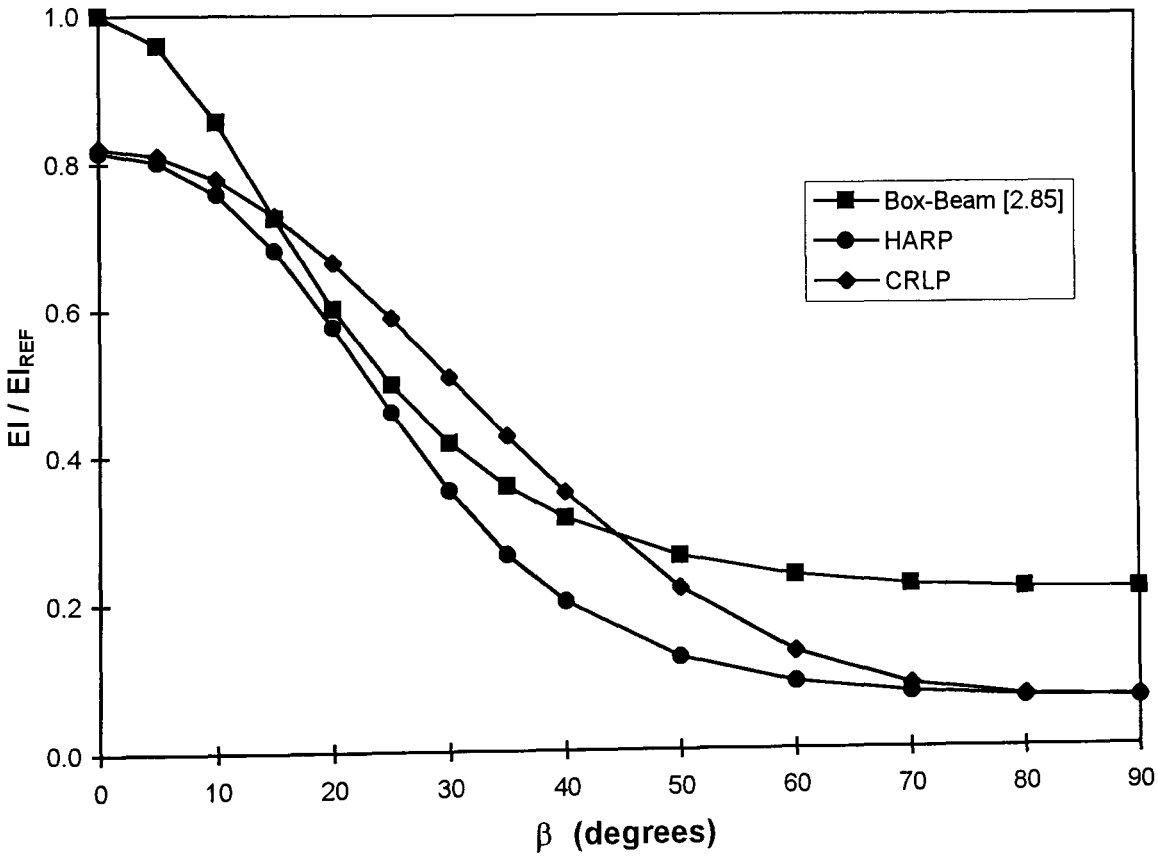

Fig. 3.6. Bending rigidity EI as a function of fibre angle, β, for HARP, CRLP, and a box-beam model [2.85] with unidirectional laminates; c/d = 2, t/d = 0.025.

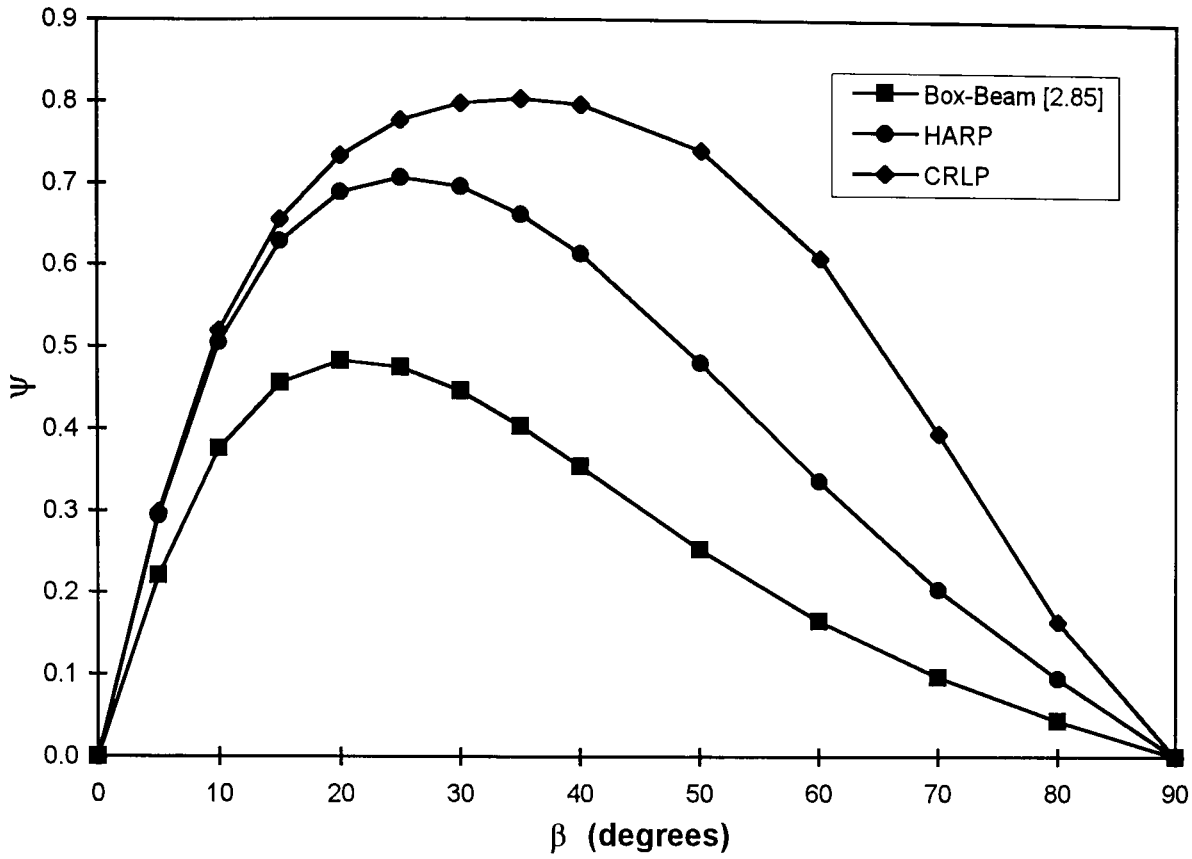

Fig. 3.7. Bending-torsion coupling parameter ψ as a function of fibre angle, β, for HARP, CRLP, and a box-beam model [2.85] with unidirectional laminates; c/d = 2, t/d = 0.025.

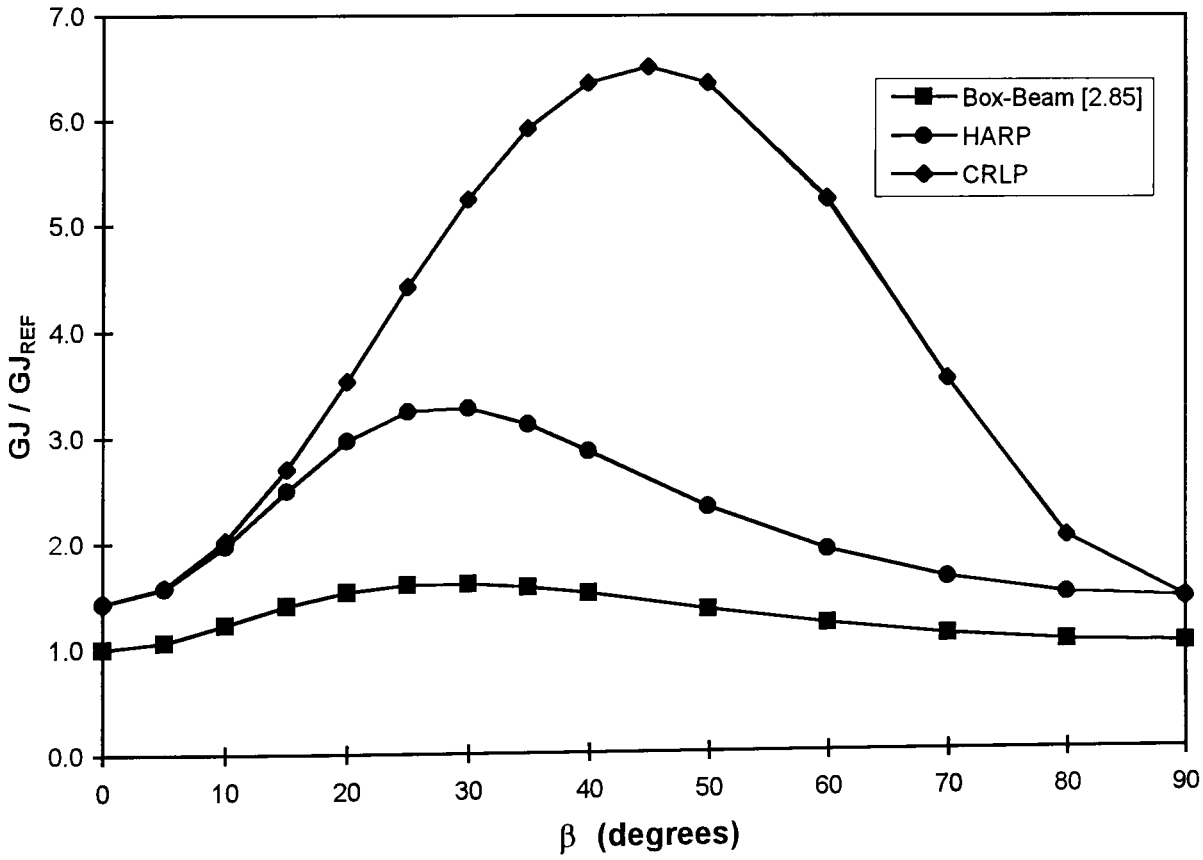

Fig. 3.8. Torsional rigidity GJ as a function of fibre angle, β, for HARP, CRLP, and a box-beam model [2.85] with unidirectional laminates; c/d = 2, t/d = 0.025.

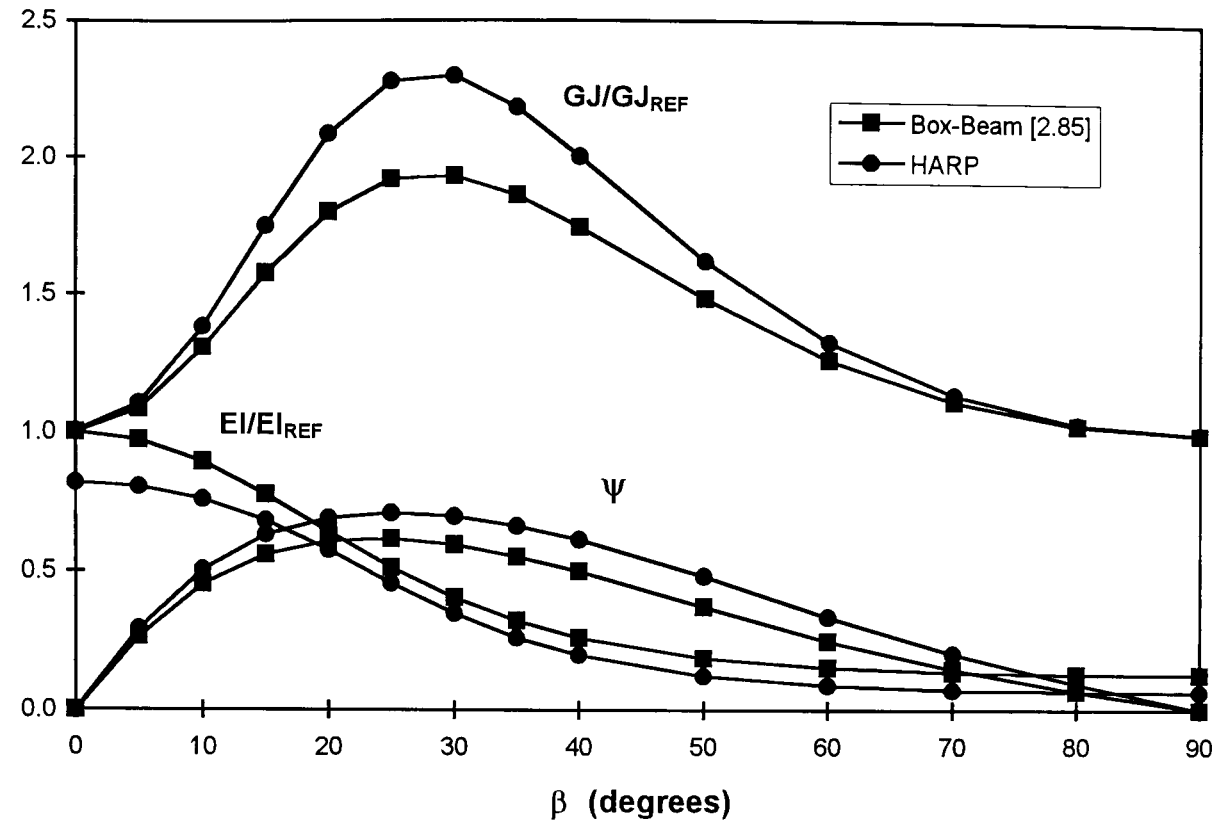

Fig. 3.9. Rigidity and coupling parameters as functions of fibre angle, β, for HARP and a box-beam model [2.85] with unidirectional laminates; c/d = 6, t/d = 0.025.

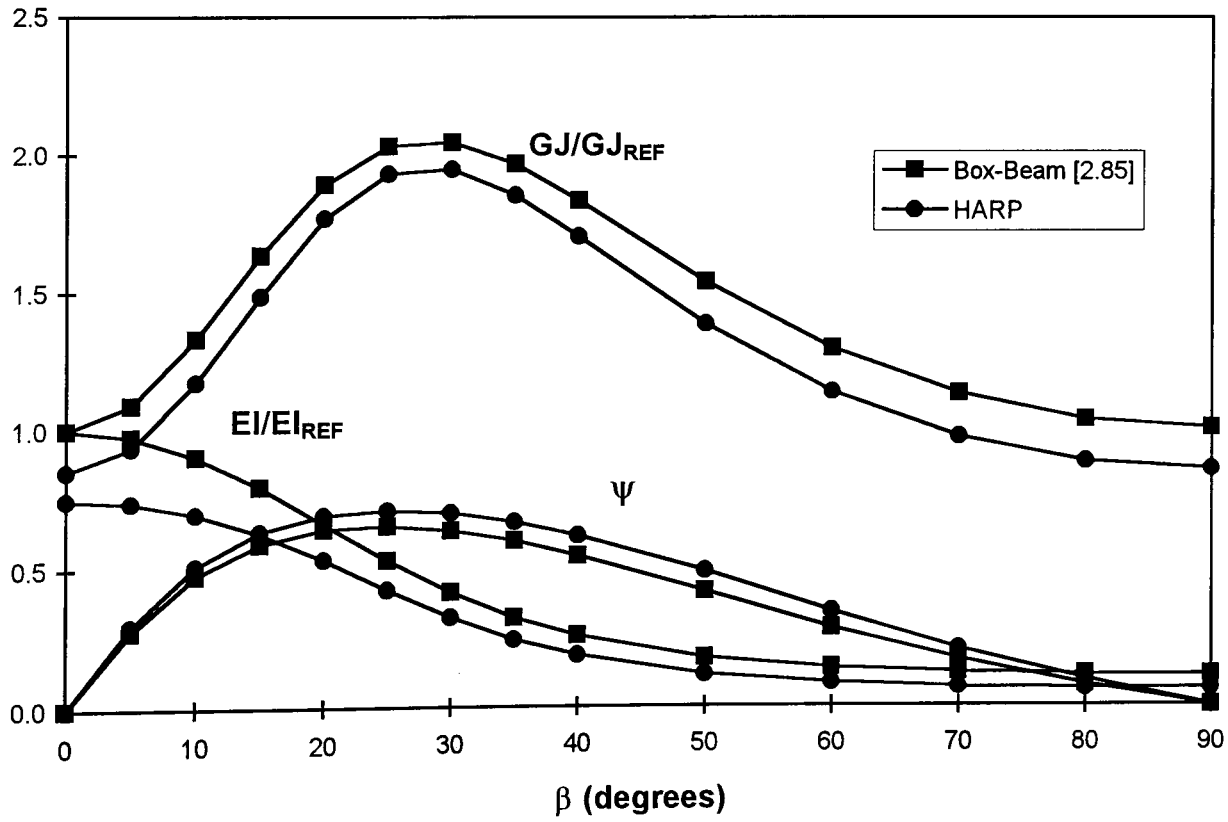

Fig. 3.10. Rigidity and coupling parameters as functions of fibre angle, β, for HARP and a box-beam model [2.85] with unidirectional laminates; c/d = 10, t/d = 0.025.

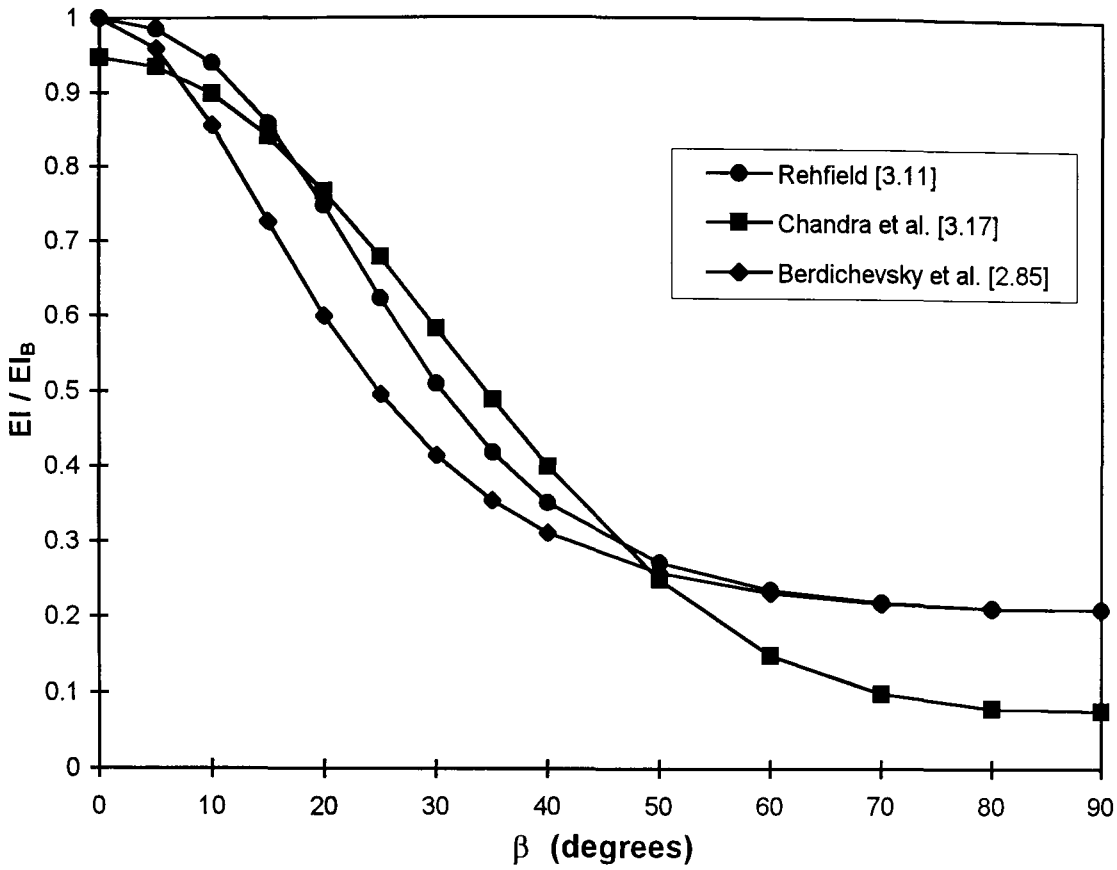

Fig. 3.11. Bending rigidity EI as a function of fibre angle, β, for three box-beam models with unidirectional laminates; c/d = 2, t/d = 0.025.

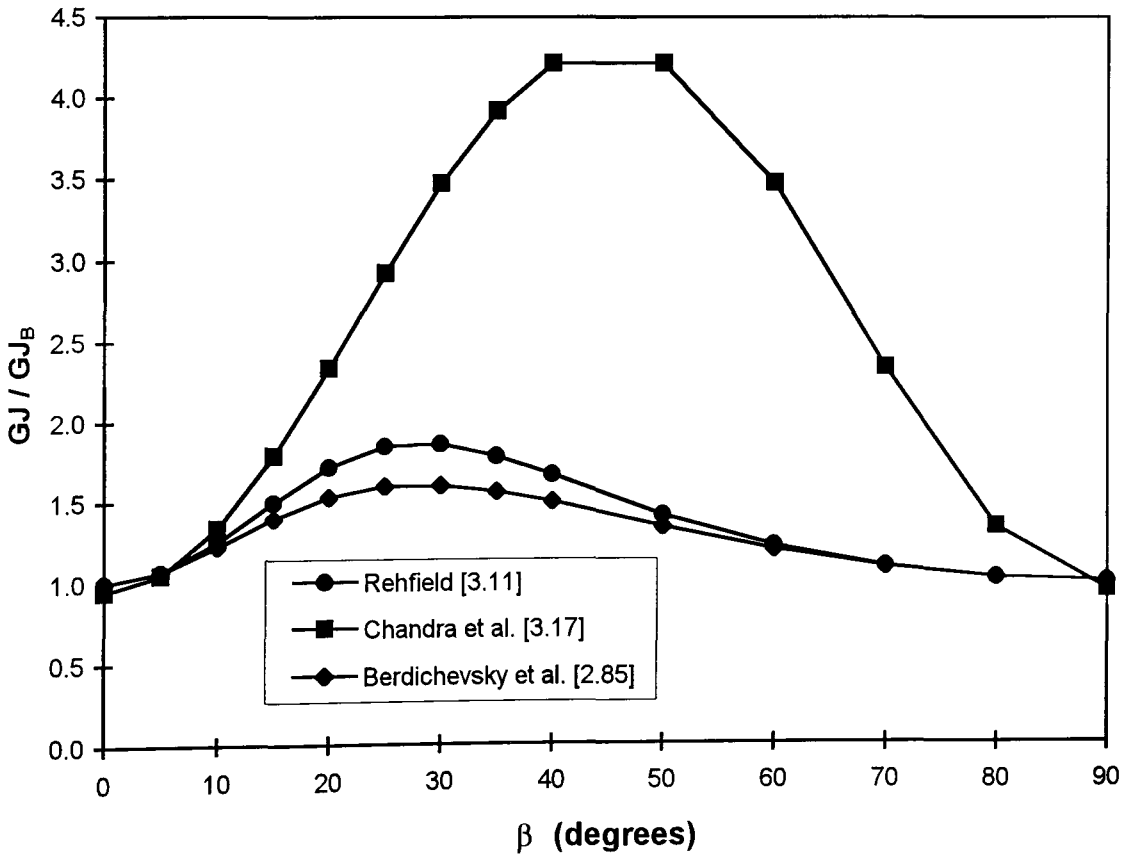

Fig. 3.12. Torsional rigidity GJ as a function of fibre angle, β, for three box-beam models with unidirectional laminates; c/d = 2, t/d = 0.025.

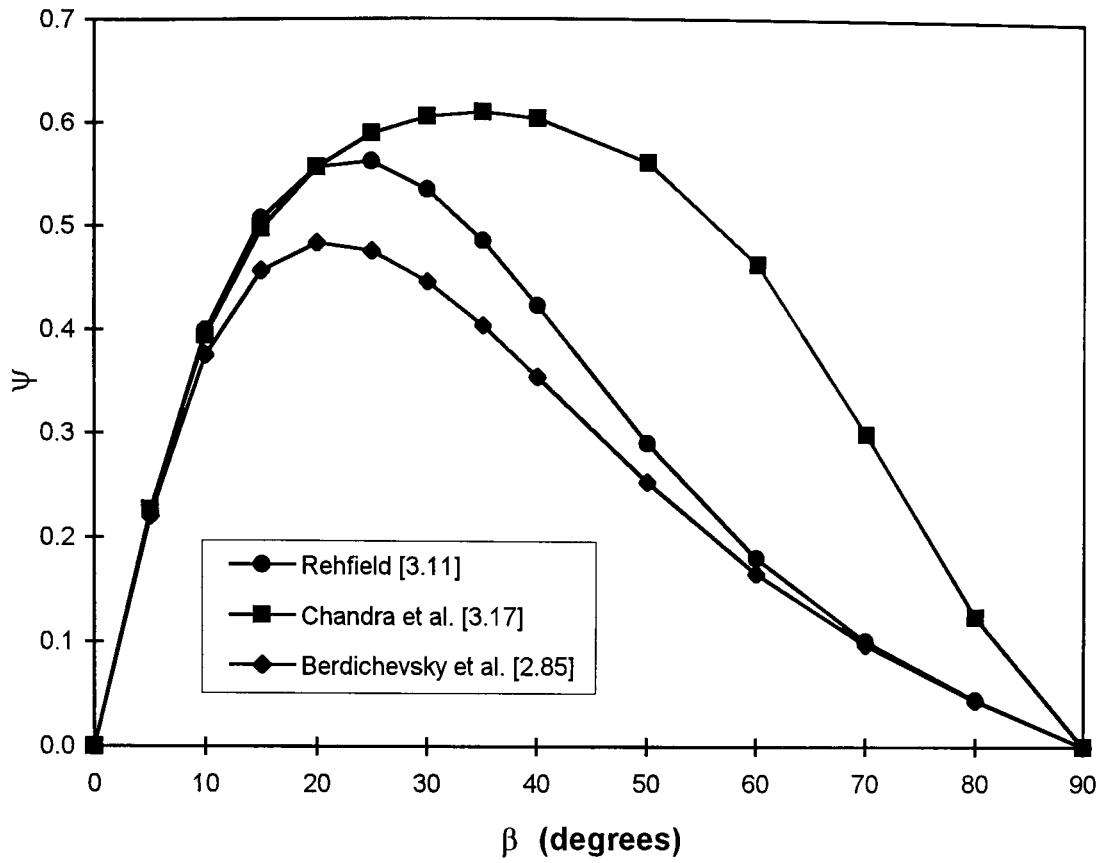

Fig. 3.13. Bending-torsion coupling parameter ψ as a function of fibre angle, β, for three box-beam models with unidirectional laminates; c/d = 2, t/d = 0.025.

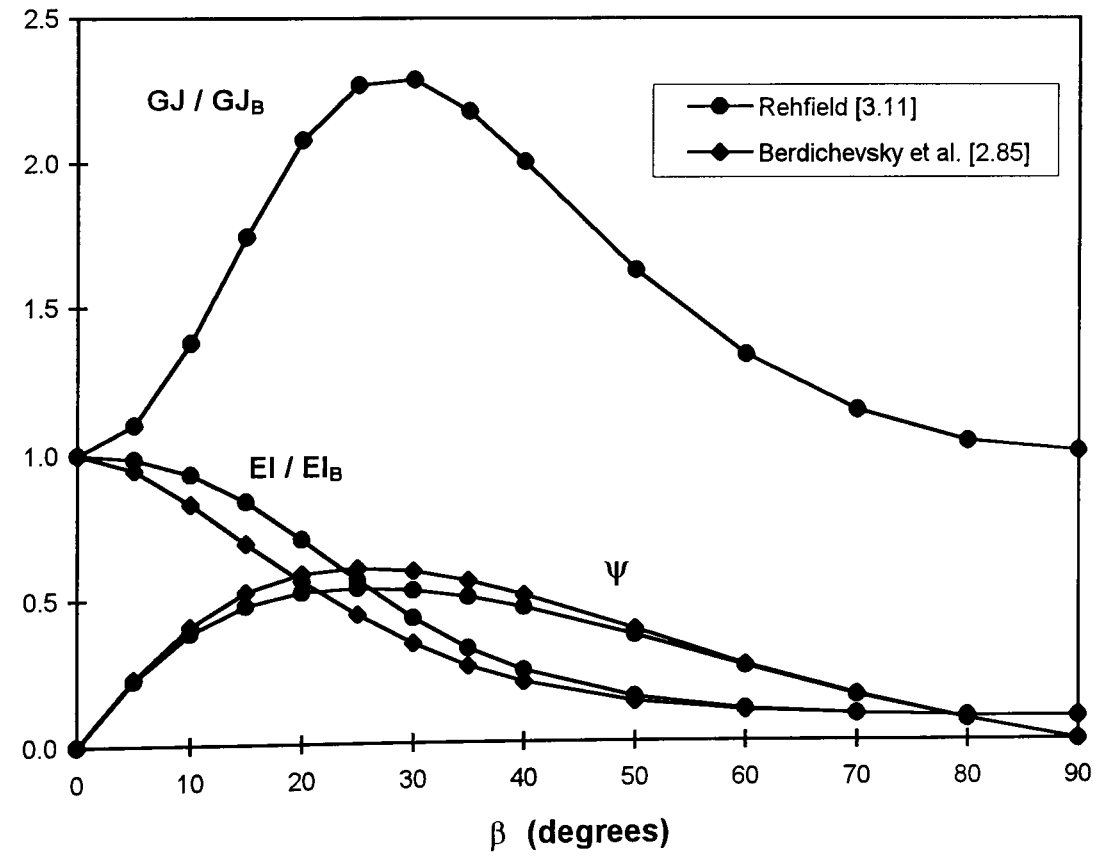

Fig. 3.14. Rigidity and coupling parameters as functions of fibre angle, β, for two box-beam models with unidirectional laminates; c/d = 2, t/d = 0.025. The fibre angle of all four sides of the beam is varied.

CHAPTER 4

FREE VIBRATION ANALYSIS OF COMPOSITE WINGS

4. FREE VIBRATION ANALYSIS OF COMPOSITE WINGS

4.1 Introduction

In the previous chapter the most popular stiffness models that have been developed for the modelling of laminated composite beams were examined. The importance of the need to model plate or beam-like composite structures has been emphasised in the literature [4.1-4.18], particularly in the context of vibration or aeroelastic analysis of aerospace vehicles. For example, a high aspect ratio composite wing has been modelled using beam idealisation to carry out aeroelastic calculations [1.19, 4.5] to reasonable accuracy. Such modelling is still justified because the aircraft industry often uses it, in the so-called *stick* model, for simple, quick and adequate preliminary aeroelastic calculations [4.19] to predict divergence or flutter speed of high aspect ratio wings, e.g., those of transport aircraft. A detailed finite element analysis would obviously take vastly more computer time and so tends to make preliminary optimisation studies, e.g., aeroelastic tailoring, too costly when a large number of design variables are involved. Hence researchers continue to develop refined beam theory giving further impetus to the already stimulated field of composite beam vibration.

The literature also rightly points out that, for composite wings which exhibit coupling between various modes (e.g., bending and torsional) of structural deformation, as usually occurs due to the anisotropic nature of fibrous composites, the traditional finite element analysis based on plate or shell element idealisation "masks the fundamental behaviour" [1.23] of the structure, so that "insight into the coupling mechanism is lost" [3.29]. Using beam theory often overcomes this difficulty by giving better insights into the fundamental vibration characteristics [1.23, 3.29].

This chapter therefore focuses upon the free vibration characteristics of composite beams exhibiting bending-torsion coupling while some results are presented for beams exhibiting extension-torsion coupling.

In most investigations of composite beam vibration the bending-torsion coupling effect [1.37, 4.1-4.3, 4.10, 4.17], which is applicable to aircraft wings and helicopter blades [1.19, 1.24, 4.5] has been examined. In others the extension-torsion

coupling effect [4.9, 4.12, 4.16] which principally relates to helicopter blades is studied. Abarcar and Cunniff [4.1] were among the earliest investigators to study the effects of fibre orientation on the natural frequencies of composite beams and their results indicated the existence of bending-torsion interaction. Later Teoh and Huang [4.2] and Teh and Huang [4.3] further investigated the free vibration characteristics of composite beams, using respectively, an exact differential equation approach from which frequency equations were derived, and a finite element approach. These investigations yielded results for flat composite beams of solid rectangular cross-section, for which the only form of coupling was bending-torsion. The general conclusion drawn in these papers is that the extent of the bending-torsion coupling present, and its subsequent effect on the free vibrational modes of a laminated composite beam, depend both on the fibre orientation of the laminate, and on the wavelength of the vibrational mode.

Jensen, Crawley and Dugundji [1.23] used a Rayleigh-Ritz type analysis to examine the effects of laminate unbalance on the natural frequencies and mode shapes of cantilever graphite/epoxy plates with bending-torsion coupling. Their results were mainly centred on symmetric lay-ups (laminates) and were validated both by comparison with a detailed finite element analysis [4.4] using general anisotropic plate elements and by comparison with experimental results. Their results showed that, for the type of problems they investigated, five assumed modes (two bending, two torsional and one chordwise) were required for their Rayleigh-Ritz formulation to determine the first three natural frequencies and mode shapes of the cantilever plate to adequate accuracy. They emphasised the importance of choosing a mode which involves chordwise deformation in order to calculate the natural frequencies accurately. Two years later, Jensen and Crawley [3.29] used both a partial Ritz (Kantorovich) and a Rayleigh-Ritz method to produce some further results. An important feature of their work was that they utilised the modes given by an earlier detailed finite element analysis [4.4] to guide the choice of which assumed modes to use in their formulation. Their results generally agreed well with both the finite element and experimental results.

Weisshaar and Foist [1.24] used beam theory to understand the basic features of bending-torsion coupling in vibrating composite wings of moderate-to-high aspect ratio. They adopted an aeroelastician's viewpoint and characterised a bending-torsion coupled composite beam (wing) by its rigidity parameters, namely

EI (bending), GJ (torsional) and K_{BT} (bending-torsion coupling). Their beam model used classical laminated plate theory to derive expressions for these parameters [1.24]. They showed the importance of including chordwise bending curvature in these derivations, consistently with the conclusions of Refs [1.23, 3.29] reported above. They confirmed this by comparing the natural frequencies obtained by using the two flat beam (plate) models discussed previously in sections 3.3.2 and 3.3.3, namely a high aspect ratio plate (HARP) model which includes chordwise bending curvature and a chordwise rigid laminated plate (CRLP) model which ignores it [1.24].

It follows that accurate determination of the natural frequencies of a composite beam requires an accurate determination of its rigidities. This is also true for extension-torsion coupled composite beams [4.8-4.9, 4.12, 4.16] for which the extensional, torsional and extension-torsion coupling rigidities, i.e., EA, GJ and K_{ET}, are of principal importance when determining the natural frequencies. The necessity to determine the rigidities EA, EI, GJ, K_{BT} and K_{ET} (of which only the last two can be negative) accurately, using both theoretical and experimental means, has received considerable attention in recent years [2.84-2.85, 3.17, 4.8, 4.9] so that very powerful and accurate analytical methods such as those discussed in section 3.4 are now available to determine them. The cross-sectional finite element [4.9] and variational-asymptotical [2.85, 4.18] methods merit special mention because they give very accurate results, particularly for solid and thin-walled closed cross-section composite beams. Once the rigidity properties of a composite beam of any cross-section are known accurately by either theoretical or experimental means, the dynamic stiffness matrix method [1.37, 4.16] which is often called an *exact* method, is generally superior to conventional methods when predicting natural frequencies. This chapter provides results obtained using this method, firstly for comparison with results from other methods and as a consequence to increase awareness of the method, and secondly for further investigations into the free vibration characteristics of composite beams.

Recent investigators of the problem of free vibration analysis of composite beams include Hodges et al. [4.9], Banerjee and Butler [4.16], Teboub and Hajela [4.17], Armanios and Badir [4.18] and Banerjee and Williams [1.37]. The methods of [4.9, 4.17-4.18] are quite accurate but are principally for a single uniform straight composite beam rather than an assembly of such beams. In contrast, the authors of Refs [1.37, 4.16] have used the dynamic stiffness matrix method, which not only has

all of the essential features of the finite element analysis (e.g., the usual assembly procedure based on coordinate transformation) but also has the great advantage that it converges on *exact* natural frequencies for structures consisting of assemblies of uniform beams, while requiring only one *exact* element to represent each uniform beam. The method can be used to calculate the natural frequencies of a tapered composite beam by modelling it as an assembly of many uniform composite beams, such as, a stepped beam. An incidental benefit of the method [1.37, 4.16] is that it gives the *exact* free vibration characteristics of a single uniform composite beam simply by applying appropriate boundary (end) conditions to its dynamic stiffness matrix.

Because the essential purpose of the present chapter is to present results as concisely as possible, it was necessary to be selective when choosing comparators from the broad cross-section of published results. Therefore a small but carefully selected sample was chosen, representing work at MIT [1.23, 3.29], Purdue University [1.24], Georgia Institute of Technology [4.9, 4.18, 4.20], and Rensselaer Polytechnic Institute [4.17]. This choice was influenced by several factors, such as, the availability of : the basic composite beam data; details of the theory; experimental results and; on occasions, the author's private communications with investigators to seek further detail.

Section 4.2 and 4.3 give brief summaries of published theory used to obtain results presented, as follows. Section 4.2 covers the dynamic stiffness matrices which relate the harmonically varying forces at the nodes of a bending-torsion and an extension-torsion coupled composite beam to the corresponding displacements. Then section 4.3 covers the application of the Wittrick-Williams algorithm [1.38, 4.21] to ensure convergence on exact natural frequencies. The results for natural frequencies follow in section 4.4, with the results for bending-torsion coupled composite beams given first and compared with the results of Refs [1.23-1.24, 4.9, 4.17-4.18, 4.20], after which extension-torsion coupled results are presented and compared with those of Refs [4.9, 4.18]. The results for mode shapes are discussed in section 4.5 and some conclusions are drawn in section 4.6.

Note that the effects of shear deformation, rotary inertia and warping stiffness are considered to be small and are neglected in the theory and results presented.

4.2 Theory of Dynamic Stiffness Matrix

The dynamic stiffness matrix of a structural element, e.g., a composite beam element [1.37, 4.16], is usually derived from the exact analytical solution of the basic governing differential equations of motion of the element undergoing harmonic vibration. In the finite element terminology, this can be interpreted as using the *exact* shape function of the element rather than adopting the usual procedure of using an approximate shape function. An important difference between the two methods is that the dynamic stiffness matrix method uses a single transcendentally frequency dependent matrix of an element, which accounts for both mass and stiffness properties, whereas the finite element method uses separate mass and stiffness matrices which are both generally independent of frequency. Another related and significant difference is that, unlike the finite element method, the dynamic stiffness method accounts for the infinite number of natural frequencies of a vibrating structure and so can be used to find higher natural frequencies exactly, i.e., without the discretisation errors of the finite element method.

4.2.1 Dynamic Stiffness Matrix of a Bending-Torsion Coupled Composite Beam

A simple example of a bending-torsion coupled composite beam is a symmetric but unbalanced laminate, (see Fig. 4.1 which shows the coordinate system and the positive direction of ply orientation). Banerjee and Williams recently derived the dynamic stiffness matrix of a bending-torsion coupled composite beam [1.37] in terms of EI, GJ, K_{BT}, mass per unit length m, the mass moment of inertia per unit length I_α, and the length of the beam L. These physical properties are assumed to be known either theoretically [2.85, 4.8-4.9] or experimentally [3.17, 2.84]. A detailed derivation of the dynamic stiffness matrix of a bending-torsion coupled composite beam is provided in Appendix 'C'. Here a brief summary is presented.

Following the same method (and same notation wherever possible) as Ref. [1.37] the natural frequencies and mode shapes of a composite beam (wing) are calculated as follows.

The coupled bending-torsional beam theory for free natural vibration of a composite beam as shown in Fig. 4.1 with shear deformation, rotary inertia and warping stiffness neglected, is governed by the following differential equations [1.37]:

$$EIh''' + K\varphi'' + m\ddot{h} = 0 \tag{4.1}$$

$$GJ\varphi'' + Kh'' - I_\alpha \ddot{\varphi} = 0 \tag{4.2}$$

where h and φ are respectively, the bending and torsional displacements, m is the mass per unit length, I_α is the polar mass moment of inertia per unit length about the Y-axis, and primes and dots denote differentiation with respect to position y and time t , respectively.

If h and φ, vary sinusoidally with time and circular frequency ω, then

$$\left.\begin{aligned} h(y,t) &= H(y)\sin\omega t \\ \varphi(y,t) &= \Phi(y)\sin\omega t \end{aligned}\right\} \tag{4.3}$$

where $H(y)$ and $\Phi(y)$ are the amplitudes of the sinusoidally varying bending displacement and torsional rotation respectively.

Substituting Eqns (4.3) into Eqns (4.1) and (4.2), the general solution for $H(y)$ and $\Phi(y)$ can be obtained in terms of six arbitrary constants [1.37], A_i (i = 1,2,...6). Then using the end conditions for bending displacement $H(y)$, bending rotation $\theta(y)$ (=$H'(y)$) and twist $\Phi(y)$ for end 1 and end 2 of the beam (see Fig. 4.2), the following matrix relationship can be obtained (see Ref. [1.37]).

$$\{U\} = [B]\{A\} \tag{4.4}$$

where

$$\{U\} = \begin{Bmatrix} \mathrm{H}_1 & \theta_1 & \Phi_1 & \mathrm{H}_2 & \theta_2 & \Phi_2 \end{Bmatrix}^T \tag{4.5}$$

$$\{A\} = \begin{Bmatrix} A_1 & A_2 & A_3 & A_4 & A_5 & A_6 \end{Bmatrix}^T \tag{4.6}$$

are the displacement and constant vectors respectively; $[B]$ is a 6x6 frequency dependent matrix related to the end conditions for displacements, and the upper suffix T denotes a transpose.

Similarly by introducing end conditions for forces (i.e., shear force $S(y)$, bending moment $M(y)$ and torque $T(y)$) into Eqn. (4.4) the nodal forces can be expressed in terms of the constants A_i (i = 1,2,...6) in matrix form as follows

$$\{F\} = [D]\{A\} \tag{4.7}$$

where

$$\{F\} = \begin{Bmatrix} S_1 & M_1 & T_1 & S_2 & M_2 & T_2 \end{Bmatrix}^T \tag{4.8}$$

and $[D]$ is a frequency dependent 6x6 matrix related to the end conditions for forces (see Fig. 4.2).

Equation (4.4) can be arranged in the form

$$\{A\} = [B]^{-1}\{U\} \tag{4.9}$$

By introducing Eqn. (4.9) into Eqn. (4.7), the relationship between the nodal forces and displacements can be obtained as,

$$\{F\} = [B]^{-1}[D]\{U\} = \left[K_D\right]\{U\} \tag{4.10}$$

where

$$\left[K_D\right] = [D][B]^{-1} \tag{4.11}$$

is the required dynamic stiffness matrix relating harmonically varying forces and displacements at the nodes (ends) of the beam element.

The force-displacement relationship (Eqn. (4.10)) for a bending-torsion coupled beam with the end conditions, i.e., end forces and end displacements, shown in Fig. 4.2 is given by

$$\begin{bmatrix} S_1 \\ M_1 \\ T_1 \\ S_2 \\ M_2 \\ T_2 \end{bmatrix} = \begin{bmatrix} K_{1,1} & K_{1,2} & K_{1,3} & K_{1,4} & K_{1,5} & K_{1,6} \\ & K_{2,2} & K_{2,3} & K_{2,4} & K_{2,5} & K_{2,6} \\ & & K_{3,3} & K_{3,4} & K_{3,5} & K_{3,6} \\ & SYM & & K_{4,4} & K_{4,5} & K_{4,6} \\ & & & & K_{5,5} & K_{5,6} \\ & & & & & K_{6,6} \end{bmatrix} \begin{bmatrix} H_1 \\ \theta_1 \\ \Phi_1 \\ H_2 \\ \theta_2 \\ \Phi_2 \end{bmatrix} \quad (4.12)$$

where S, M and T with subscripts 1 and 2 are respectively the amplitudes of the harmonically varying shear force, bending moment and torque at ends 1 and 2 while H, θ and Φ are the corresponding bending displacement, bending rotation and twist amplitudes.

Reference [1.37] presented explicit expressions for each of the dynamic stiffness elements $K_{i,j}$ (i, j = 1,2,....6) of the dynamic stiffness matrix of Eqn. (4.12). These expressions are frequency dependent in addition to their dependence on EI, GJ, K_{BT}, m, I_α and L. Calculation of natural frequencies of entire structures follows from the Wittrick-Williams algorithm [1.38, 4.21] as described in section 4.3.

4.2.2 Dynamic Stiffness Matrix of an Extension-Torsion Coupled Composite Beam[+]

A composite beam may exhibit extension-torsion coupling instead of bending-torsion coupling. For example, when a composite beam is formed by wrapping a laminate of symmetric but unbalanced lay-up and joining its longitudinal edges to form a doubly symmetric cross-section, e.g., a square, rectangle or circle, it exhibits extension-torsion coupling [2.84, 4.16, 4.18, 4.22] without coupling with flexure. The harmonically varying force and displacement amplitudes at the nodes (i.e., ends) of such a composite beam are shown in Fig. 4.3. The corresponding dynamic stiffness matrix was derived by Banerjee and Butler [4.16] in terms of EA, GJ, K_{ET}, m, I_α and L. Hence the stiffness equation is

[+] Pure extension-torsion coupling is not of any major interest to the aeroelasticians of fixed wing aircraft but for the completeness of free vibration results, an extension-torsion coupled composite beam is included in this chapter to demonstrate the predictable accuracy of the dynamic stiffness matrix method.

$$\begin{bmatrix} F_1 \\ T_1 \\ F_2 \\ T_2 \end{bmatrix} = \begin{bmatrix} K^*_{1,1} & K^*_{1,2} & K^*_{1,3} & K^*_{1,4} \\ & K^*_{2,2} & K^*_{2,3} & K^*_{2,4} \\ & & K^*_{3,3} & K^*_{3,4} \\ & & & K^*_{4,4} \end{bmatrix} \begin{bmatrix} U_1 \\ \Phi_1 \\ U_2 \\ \Phi_2 \end{bmatrix} \tag{4.13}$$

where F and T with subscripts 1 and 2 are respectively the amplitudes of the harmonically varying end (axial) force and torque at nodes 1 and 2, while U and Φ are the corresponding displacement and twist amplitudes. (Note that the asterisk has been introduced to avoid confusion with the stiffness elements of Eqn. (4.12).)

Explicit analytical expressions for each of the dynamic stiffness elements K^*_{ij} (i, j = 1, 2, 3, 4) are given in Ref. [4.16]. As in the case of bending-torsion coupled beam, these elements are all transcendentally frequency dependent and so again the calculation of the natural frequencies of structures is based on the use of the Wittrick-Williams algorithm [1.38, 4.21], see below.

4.3 Application of the Wittrick - Williams Algorithm

The above element dynamic stiffness matrices can be used to compute the natural frequencies and mode shapes of bending-torsion or extension-torsion coupled composite beams or of structures constructed from such beams, e.g., a non-uniform composite wing or helicopter blade. The overall dynamic stiffness matrix of the (final) structure can be obtained by assembling the dynamic stiffness matrices of the individual elements, exactly as in the usual finite element method [4.21]. To calculate the natural frequencies of the structure, use is made of the well known algorithm of Wittrick and Williams [1.38, 4.21]. Basically the algorithm (unlike its proof) is very simple to use and it gives the number of natural frequencies of a structure that lie below an arbitrarily chosen trial frequency ω^*. If j is the number of eigenvalues present in a range of frequency from zero to ω^*, then

$$j = j_o + s\left\{K^*_D\right\} \tag{4.14}$$

where

j = number of natural frequencies of the structure exceeded by the trial frequency ω^*

j_o = number of natural frequencies which will still be exceeded if constraints were imposed upon the structure so as to suppress all the nodal displacements

$= \sum j_m$

j_m = number of natural frequencies of a component member with its ends clamped, which have been exceeded by ω^*.

K_D^* = the overall dynamic stiffness matrix evaluated at $\omega = \omega^*$

$s\{K_D^*\}$ = number of negative elements on the leading diagonal of $K_D^{*\Delta}$

$K_D^{*\Delta}$ = upper triangular matrix obtained by the application of Gauss elimination to K_D^*

Hence it is possible to converge on any required natural frequency within a desired accuracy by any one of several rational ways of choosing successive trial frequencies. An important feature of the algorithm is that it guarantees that no natural frequency of the structure is missed, even in the exceptional cases where two modes have the same frequency.

4.4 Free Vibration Analysis of Composite Beams

First, bending-torsion coupled composite beams made of flat graphite (carbon)/epoxy laminates with lay-up $[\beta_2 / 0^0]_s$ are considered, because the free vibration characteristics of such composite beams have been quite extensively investigated [1.23, 3.29, 4.4]. Using the basic material properties given in Refs [1.23, 3.29] which are reproduced in Table 4.1, the rigidity and other cross-sectional details were calculated for a wide range of the values of the ply orientation β, using two different models, namely the High Aspect Ratio Plate (HARP) model, which includes chordwise bending curvature, and the Chordwise Rigid Laminated Plate (CRLP)

model which ignores it. These two models correspond to Eqns (3.24)-(3.26) and Eqns (3.34)-(3.36) of chapter 3, respectively. Table 4.2 gives results for representative values of β.

Note that, as in Refs [1.23, 3.29], $[\beta_2 / 0]_s$ results for $\beta = 0^0$ have not been given but instead almost identical results for $[\beta_2 / 0]_s$ are given. The reason is that in this chapter the experimental results compared with, are for $[0_2 / 90]_s$ instead of $[0_2 / 0]_s$, because of the fragile nature of unidirectional laminates.

The natural frequencies of these beams, with cantilever end conditions, were then calculated by using the dynamic stiffness matrix method. Table 4.3 shows these results, along with those of Refs [1.23, 3.29, 4.4]. The results show that the natural frequencies given by the Rayleigh-Ritz and partial Ritz (beam) methods are consistently higher than those from the dynamic stiffness formulation, as expected, and that the Rayleigh-Ritz solutions with four modes and the partial Ritz solutions with two modes are less accurate when compared with detailed finite element analysis and experimental results. Interestingly, Rayleigh-Ritz with five modes and partial Ritz with three modes gave better accuracy than the dynamic stiffness method. However, this conclusion is specific to the range of problems of Table 4.3 and so cannot be taken as a general rule. Indeed the detailed finite element results of Ref. [4.4] helped the authors of Refs [1.23] and [3.29] in choosing the modes that they used for these particular problems. Therefore the Rayleigh-Ritz and partial Ritz methods are unlikely to be so accurate for real life problems, for which prior knowledge of the deformation pattern through the use of detailed finite element analysis is most unlikely to be available. Another important difference is that the choice of assumed modes is very problem dependent and hence subjective judgement often has to be made in deciding the approximate shapes, whereas the dynamic stiffness matrix method has no such limitation and hence gives consistently good results for any type of composite beam problem.

To gain further insight into the above $[\beta_2/0^0]_s$ lay-up results, the non-dimensional bending and torsional rigidities are plotted in Fig. 4.4 together with the bending-torsion coupling parameter ψ defined in Eqn. (3.27) as $\psi = |K_{BT}|/(EI\ GJ)^{1/2}$ for both the HARP and CRLP models. Note that ψ describes the degree of coupling between the bending and torsional deformations and lies within the range $-1<\psi<1$,

with increasing values of $|\psi|$ giving greater coupling between the deformations. In Fig. 4.4, EI_0 and GJ_0 are respectively the bending and torsional rigidities corresponding to $\beta = 0^0$, so that all of the plies in the laminate are longitudinal.

Figure 4.5 (a) shows the variation of the first three natural frequencies of this composite cantilever beam against the ply orientation. Dynamic stiffness results given by the HARP and CRLP models are shown alongside the experimental and finite element results and the Rayleigh-Ritz (four modes) and partial Ritz (two modes) results of Refs [1.23, 3.29, 4.4]. Similar results but for the improved Rayleigh-Ritz (five modes) and partial Ritz (three modes) results of Refs [1.23, 3.29] are shown in Fig. 4.5 (b).

For small values of β, i.e., approximately for $0^0<\beta<15^0$, the first three natural frequencies of the beam were observed to be, respectively, bending dominated, torsion dominated and bending dominated. Therefore they can be denoted, respectively, as first bending, first torsional and second bending modes, see Table 4.3 and Figs 4.5 (a) and 4.5 (b). However, for $\beta \geq 15^0$, the torsional displacement in all modes became quite pronounced and, more significantly, the third mode changed to a torsional one instead of being the second bending mode, as indicated on Figs 4.5 (a) and 4.5 (b). This is also evident from the representative modes shown in Fig. 4.6.

From Fig. 4.5 (a) the CRLP model, the Rayleigh-Ritz 4 modes and partial Ritz 2 modes are clearly inadequate when predicting the torsion dominated modes for higher values of β. This accords with earlier investigations reported in Refs [1.23-1.24, 3.29]. A significant departure from the experimental results is observed in the regions where the mode frequency is primarily dependent upon the torsional rigidity (GJ) and at the same time the bending-torsion stiffness coupling is high. The maximum torsional frequency is given by the above three models at $\beta = 45^0$. This is the fibre angle where the maximum GJ can be obtained when the chordwise bending is ignored (see, for example, Fig. 4.4). In the case of the Rayleigh-Ritz 4 modes and partial Ritz 2 modes the chordwise mode was omitted [1.23, 3.29].

When Figs 4.5 (a) and 4.5 (b) are interpreted using the rigidity variations of Fig. 4.4 and the representative modes shown in Fig. 4.6, the following trends are

observed. The first natural frequency which is characterised as first bending, varies similarly to the non-dimensional bending rigidity, i.e., the frequency decreases monotonically due to decrease in spanwise bending rigidity. The second natural frequency is first torsional for $0^0 < \beta \leq 15^0$, coupled with bending for $15^0 < \beta \leq 45^0$, and then it becomes the second bending mode for $\beta > 45^0$. Finally the third natural frequency starts as the second bending mode for $\beta = 0^0$, and then for $0^0 < \beta \leq 15^0$ it mixes with first torsion before becoming a pure torsional mode for $\beta > 15^0$. Trends similar to above were also observed by the authors of Refs [1.23, 3.29]. It is interesting to note that due to the declining value of bending rigidity EI and increasing value of torsional rigidity GJ as the fibre angle increases from $\beta = 0^0$, the natural frequencies of modes 2 and 3 approach each other while those of modes 1 and 2 move apart in the vicinity of $\beta = 15^0$ (i.e., around $\psi = 0.55$, see Fig. 4.4). This frequency phenomenon is even more pronounced when inertia coupling is present as can be seen from Fig. 4.7 where two values of static unbalance (x_α) (defined as the non-dimensional distance between the shear centre and the centroid of the cross-section in terms of fractional semi-chord b), are considered. The above frequency phenomenon can have significant effects on aeroelastic stability as it will be shown in the next two chapters.

As a second example, Fig. 4.8 shows the variation with the bending-torsion coupling parameter ψ of the four natural frequencies of a composite cantilever beam for which GJ/EI = 0.5 and $x_\alpha = 0.0$. The results were obtained for a cantilever with EI = 0.24 Nm^2, GJ = 0.12 Nm^2, m = 0.093 kg/m, $I_\alpha = 0.5046 \times 10^{-4}$ kgm and L = 0.23 m. The different values of ψ were obtained by varying K_{BT}. The results of Fig. 4.8 agree to plotting accuracy with Fig. 8 of Ref. [1.24] and so accord with the conclusions drawn in Ref. [1.24] that only the third natural frequency (i.e., second bending at $\psi = 0$) varies significantly for $\psi < 0.4$. However, for $\psi > 0.6$ all four natural frequencies vary significantly. It is important to note that since ψ is shown to have marginal effect on natural frequencies when static unbalance is not present (see Fig. 4.8), the variation of natural frequencies observed in Figs 4.5 (a) and 4.5 (b) can be attributed solely to variations of bending and torsional rigidities as the ply angles were reoriented.

Figures 4.9 and 4.10 show the first four natural frequencies as functions of ψ for the same example beam as above but with two values of static unbalance (x_α) as

$\pm 0.2b$ and $\pm 0.4b$ respectively. The results of these two figures also confirm that around $\psi = \pm 0.55$, the natural frequencies of modes 2 and 3 approach each other whereas those of modes 1 and 2 move apart. When static unbalance is present the effect of bending-torsion stiffness coupling on natural frequencies appears to be more significant. This is in contrast to the case shown in Fig. 4.8 where static unbalance was not present.

Although the frequencies of the modes do not merge when bending-torsion coupling is present, i.e., when the fibre angle β increases from $\beta = 0^0$ (see Fig. 4.7), their original uncoupled modes become coupled and interchange their shapes. This is illustrated using the same beam as above vibrating in each of its normal modes. Figure 4.11 shows a sequence of mode shape changes for the first (fundamental) bending mode as the bending-torsion coupling parameter varies from $0 \leq \psi \leq 1$. This mode starts as pure bending and at $0.30<\psi<0.75$ a strong coupling between bending and torsional deformations is seen to be present. At $\psi \geq 0.75$ this mode is seen to be almost a pure torsional mode.

Figure 4.12 shows a sequence of mode shape changes for the second mode (first torsional mode at $\psi = 0$) as a function of ψ. This mode starts as a pure torsional mode and then transforms at high value of ψ to a highly coupled mode resembling a second torsional mode. Figure 4.13 shows similar mode shape changes but for the third mode. This mode at $\psi = 0$ is identified with the second bending mode. The transformation of this mode from pure bending to almost pure torsional resembling an uncoupled third torsional mode is evident.

The third example is a bending-torsion coupled graphite/epoxy laminated cantilever beam of solid rectangular cross-section and with all its plies at either 15^0 or 30^0, for which Ref. [4.17] recently gave theoretical and experimental results. The beam has L = 0.1905 m, width = 0.0127 m, thickness = 0.003175 m and its material properties are given in Table 4.4. The bending, torsional and bending-torsion coupling rigidities were calculated using the HARP model as EI = 3.568 Nm^2, GJ = 1.553 Nm^2 and K_{BT} = 1.668 Nm^2 for the 15^0 lay-up case, and EI = 1.596 Nm^2, GJ = 2.158 Nm^2 and K_{BT} = 1.369 Nm^2 for the 30^0 lay-up case. For both cases m = 0.0625 kg/m and $I_\alpha = 0.8926 \times 10^{-6}$ kgm were used. Table 4.5 shows the first six natural frequencies calculated by the present dynamic stiffness matrix method alongside the theoretical

and experimental results of Ref. [4.17]. It should be noted that the theoretical model used in Ref. [4.17] to obtain the above results did not predict the torsional modes (see lines 19 and 20 of RESULTS AND DISCUSSION section on page 128 of Ref. [4.17]). The agreement of the results from the dynamic stiffness method with those of experimental and theoretical results of Ref. [4.17] is very good (i.e., the disagreement is within 1.5% only) except for the difference of 14% and 12% in respectively, the 4th natural frequency for the 15^0 lay-up and the 5th natural frequency for the 30^0 lay-up, which are both torsional frequencies.

The fourth example is the cantilever rectangular box-beam of Ref. [4.20] with lay-up: $[\beta]_6$ in the top wall, $[-\beta]_6$ in the bottom wall and $[\beta/-\beta]_3$ in the vertical walls. This CAS box-beam configuration exhibits bending-torsion coupling [2.85]. The cross-section of the above box-beam is shown in Fig. 4.14 with L = 0.84455 m, m = 0.0882 Kg/m and $I_\alpha = 9.61725 \times 10^{-6}$ Kgm. Using the basic material properties given in Table 4.6, the rigidity properties were calculated for a wide range of the values of the ply orientation β, using the structural model of Ref. [2.85]. This stiffness model corresponds to Eqns (3.79)-(3.81) of chapter 3. Table 4.7 gives results for representative values of fibre angle β. By using the dynamic stiffness matrix method, the free vibration natural frequencies of the beam are computed as a function of the fibre angle. Table 4.8 shows the first ten natural frequencies calculated by the present dynamic stiffness matrix method alongside the theoretical results of Ref. [4.20]. The agreement between the two sets of results is very good (i.e., the results are well within 1.5%). The symbols T_1 and T_2 denote torsion-dominated modes, whereas B_1 to B_8 denote bending-dominated modes. It is important to note that the mode shapes of lower modes, such as B_1 and T_1, allow clear identification for the dominant components, i.e., dominant first bending and torsion modes respectively. For higher modes, however, such as B_5, both types of deformation can be recognised as having similar contribution. Some frequencies for the higher modes are not provided in Ref. [4.20] as can be seen from Table 4.8.

The numerical values provided in Table 4.8 are plotted in Figs 4.15 (a) and 4.15 (b). Figure 4.15 (a) shows the first five natural frequencies of this composite cantilever box-beam as a function of ply orientation, whereas Fig. 4.15 (b) shows results for the fifth to tenth natural frequencies of the same beam. In the above figures modal changes similar to those of Figs 4.5 (a) and 4.5 (b) are observed with ply

orientation for $0^0<\beta\leq30^0$. For example, in Fig. 4.15 (a), the first and second natural frequencies which are characterised as first and second bending respectively, decrease monotonically due to decrease in spanwise bending rigidity. The third natural frequency is the first torsional for $\beta=0^0$, heavily coupled with bending for $0^0<\beta<15^0$, and then it becomes the third bending mode for $\beta \geq 15^0$. Similarly, the fourth natural frequency is the third bending at $\beta=0^0$, first torsional for $15^0<\beta<30^0$, and then it becomes the fourth bending at $\beta \geq 30^0$. Similar modal changes are observed for the rest of the modes presented in Figs 4.15 (a) and 4.15 (b).

The fifth example is the cantilever rectangular box-beam of Ref. [4.9], which has the cross-section shown in Fig. 4.16 with L = 2.54 m and a [20^0 / -70^0 / 20^0 / -70^0 / -70^0 / 20^0] lay-up for each of its sides. It is made of T300/5208 graphite/epoxy material system with properties given in Table 4.9. This CUS box-beam configuration exhibits extension-torsion coupling [2.85] and its properties were converted to SI units from NABSA (Nonhomogeneous Anisotropic Beam Section Analysis) results, given in Table 1 of Ref. [4.9], as EA = 5.0597×10^6 N, GJ = 190.78 Nm^2 , K_{ET} = -14154 Nm, m = 0.18929 kg/m, $I_\alpha = 3.3822 \times 10^{-5}$ kgm. NABSA is a finite element model based on an extension of the work of Giavotto et al. [3.4]. In this model all types of cross-sectional warping are accounted for. The first four coupled extension-torsion natural frequencies of this beam were calculated by the present dynamic stiffness method as 187.79 Hz, 527.69 Hz, 563.36 Hz and 939.95 Hz, respectively. The finite element results of Ref. [4.9] (see its Table 7) for the first two of these natural frequencies were 180.32 Hz and 544.47 Hz, respectively, i.e., well within 5% of the present results. Recently the authors of Ref. [4.18] used a variational-asymptotical method to calculate the rigidity properties of this beam and used a Hamiltonian method to derive the differential equations and hence the frequency equation, which gave the first two natural frequencies as 177.05 Hz and 531.15 Hz, see Table 1 of Ref. [4.18]. However, the paper does not quote the rigidity properties used in the analysis and so the author has been unable to compute comparative results from the present method although it is clear from the NABSA rigidity results quoted above that reasonable agreement would be anticipated.

The first three natural frequencies for the example box-beam of Ref. [4.9] are also predicted using the dynamic stiffness method with stiffnesses based on three stiffness models, namely that of Rehfield [3.11] (Eqns (3.56)-(3.58)), Chandra et al.

[3.17] (Eqns (3.62)-(3.64)) and Berdichevsky et al. [2.85] (Eqns (3.79)-(3.81)). These results are presented alongside a finite element simulation (NABSA) results in Table 4.10. The frequencies calculated from NABSA model were provided by Hodges et al. [4.9]. From Table 4.10, it can be seen that the frequencies based on variational-asymptotical analysis of Berdichevsky et al. [2.85] are the closest to NABSA frequencies as expected. The agreement between the two set of results is quite satisfactory.

4.5 The Potential of Stiffness Coupling as a Modal Coupler/Decoupler

In the previous section, it has been shown that the directional stiffness properties of fibre reinforced composites (and as a result the presence of stiffness coupling) in a structure can produce significant differences in the free vibrational behaviour of such structures (Figs 4.5 and 4.6) when compared to similar, but orthotropic, ones. In particular, the influence of this parameter upon the free vibration mode shapes was shown to be substantial. This influence suggests its use as passive modal coupler/decoupler. It is therefore of interest to examine the potential for the use of laminate tailoring in coupling/decoupling structures which are geometrically coupled due to inertia placement or wing sweep. This is illustrated using the beam of the second example of section 4.4 vibrating in its first normal mode identified as fundamental bending at $\psi = 0$ (see Fig. 4.11).

Figure 4.17 shows a sequence of mode shape changes of the first mode as a function of selected values of negative bending-torsion coupling parameter ψ. Negative ψ means a positive (upward) bending will result in nose-up twist, i.e., leading edge up. A negative static unbalance x_α, equal to 20% of the semi-chord (b) (i.e., $x_\alpha = - 0.2b$) is introduced. (Note that x_α is negative when the centroid of the cross-section is behind the shear centre.) Figure 4.17 shows that the inertia coupling introduced by the presence of negative x_α (see mode when $\psi = 0$) can be decoupled at a very low value of negative ψ (i.e., $|\psi| < 0.10$). At higher values of ψ the mode transforms to almost a pure torsional mode. However, the wing is vibrating in the opposite direction, i.e., leading edge up, when compared with the wing with $\psi = 0$. The changes in the second (first torsional) mode shape as a function of ψ is not shown as

the effect of moderate-to-high values of ψ (i.e., $|\psi| \leq 0.60$) on the shape of this mode is minimal (see, for example, Fig. 4.12).

Figure 4.18 shows a similar sequence of mode shape changes for the first mode when x_α is positive. In this case the coupling introduced by positive x_α is enhanced by that introduced by negative ψ. The mode transforms to almost a pure torsional mode at a very low value of negative ψ. Figures 4.19 and 4.20 illustrate similar changes in mode shapes as those of Figs 4.17 and 4.18 but with x_α = -0.4b, 0.4b respectively.

Figure 4.21 shows a sequence of mode shape changes for the first normal mode at selected values of ψ for a 30 degree swept-back wing (beam). The static unbalance is set to zero in this case. As can be seen a much higher negative ψ is needed to decouple the mode when moderate sweep-back angle is present when compared to the unswept case with moderate-to-high negative x_α (Figs 4.17 and 4.19). The mode never becomes a pure torsional mode in this case. Finally Figs 4.22 and 4.23 show similar modal shape changes for a 30 degree swept-forward wing which are relevant to divergence instability. Both the negative and the corresponding positive values of ψ are respectively used in obtaining the results shown in these figures. Figure 4.23 shows that a 30 degree swept-forward wing can be completely decoupled at a moderate value of positive ψ. Even if such a degree of coupling is not possible to be introduced in a realistic wing, a small reduction in the adverse natural coupling introduced by swept-forward wings can have welcome results for divergence.

4.6 Conclusions

The free vibration characteristics of bending-torsion and extension-torsion coupled composite beams have been investigated using the dynamic stiffness matrix method. The accuracy of the method in predicting the natural frequencies has been demonstrated by comparing with results for a range of composite beams with varying lay-ups and cross-sections that are available in the literature.

Several other issues related to preliminary design of high aspect ratio wings, have been identified and illustrated in this chapter. The chordwise bending (curvature)

has been shown to have a significant effect on the torsional vibration of composite plates. It is necessary to include chordwise bending in a vibration analysis as the same bending stiffness (D_{ij}) terms which couple spanwise bending to torsion also couple chordwise bending to torsion (see chapter 3). Otherwise, the torsional frequencies predicted may not be reliable for plates with high bending-torsion stiffness coupling since the torsional rigidity will be overestimated.

The chosen examples illustrate the effect of moderate values of bending-torsion stiffness coupling on natural frequencies, which is generally small, while its effect on mode shapes is substantial. The study has shown that ψ can be used as a modal coupler/decoupler, and can be used to decouple modes which are geometrically (inertially) coupled in the same way as mass balancing but without a weight penalty. It can also be used to abate the unfavourable coupling introduced by sweep angle. Thus, the bending-torsion coupling exhibited by composite wings may have significant effect on the aeroelastic (flutter and divergence) behaviour of composite wings.

Having established the opportunity in laminate design to modify structural dynamic characteristics of composite beams (wings), attention now turns to the aeroelastic stability of such beams. The next chapter presents some effects of aeroelastic tailoring upon flutter and divergence of high aspect ratio lifting surfaces.

TABLE 4.1

Material properties of Hercules ASI/3501-6 graphite/epoxy

Property	Value / Unit
E_1	98.0 GN/m^2
E_2	7.90 GN/m^2
ν_{12}	0.28
G_{12}	5.60 GN/m^2
G_{13}	5.60 GN/m^2
G_{23}	5.60 GN/m^2
Ply thickness	0.134x10^{-3} m
Density	1520 kg/m^3

TABLE 4.2

Rigidity properties for HARP and CRLP models of $[\beta_2 / 0]_s$ *lay-up beam (L= 0.305m, m = 0.0931 Kg/m and* $I_\alpha = 4.506x10^{-5}$ *Kgm).*

Ply angle	HARP model			CRLP model		
β (deg)	EI (Nm^2)	GJ (Nm^2)	K (Nm^2)	EI (Nm^2)	GJ (Nm^2)	K (Nm^2)
0	0.3149	0.0739	0.0000	0.3144	0.0739	0.0000
15	0.2723	0.1273	0.1135	0.2903	0.1372	0.1268
30	0.1467	0.1676	0.1041	0.2060	0.2639	0.1797
45	0.0714	0.1332	0.0489	0.1180	0.3273	0.1441
60	0.0464	0.0983	0.0194	0.0618	0.2639	0.0699
75	0.0389	0.0796	0.0066	0.0408	0.1372	0.0172
90	0.0371	0.0739	0.0000	0.0373	0.0739	0.000

TABLE 4.3

Comparison of natural frequencies (Hz) of [β_2 / 0]$_s$ lay-up beam using various methods with B and T respectively indicating predominantly bending or torsional modes.

Ply angle β **(deg)**	**Mode**	**Finite element (365 dof) [4.4]**	**Rayleigh-Ritz (4 modes) [1.23]**	**Rayleigh-Ritz (5 modes) [1.23]**	**Partial Ritz (2 modes) [3.29]**	**Partial Ritz (3 modes) [3.29]**	**Dynamic stiffness (HARP)**	**Dynamic stiffness (CRLP)**	**Experimental Results [1.23]**
0	B_1	11.1	11.1	11.1	11.1	11.1	11.1	11.1	11.2
	T_1	39.5	39.6	39.6	39.7	39.7	33.2	31.4	42.4
	B_2	69.5	69.4	69.3	72.1	72.0	69.2	69.3	70.5
15	B_1	8.9	8.8	8.7	9.0	9.0	8.1	8.1	9.4
	T_1	42.9	48.8	48.2	44.5	43.5	41.0	40.4	45.8
	B_2	62.7	60.5	59.9	66.9	65.0	52.6	52.5	66.2
30	B_1	6.3	6.2	6.2	6.4	6.3	5.6	5.6	6.6
	B_2	37.3	42.0	42.0	39.4	38.9	33.9	33.9	40.0
	T_1	56.9	69.0	60.7	70.9	58.5	51.4	60.9	59.1
45	B_1	4.9	4.9	4.8	4.9	4.9	4.6	4.6	4.8
	B_2	30.1	32.7	32.6	31.6	31.5	28.2	28.3	29.8
	T_1	49.4	73.9	56.3	74.1	51.2	45.0	66.2	51.3
60	B_1	4.2	4.2	4.2	4.2	4.2	4.1	4.1	4.3
	B_2	26.1	27.0	26.8	27.2	27.2	25.4	25.6	27.1
	T_1	41.7	65.4	47.1	65.4	42.7	38.4	59.4	47.7
75	B_1	3.9	3.9	3.9	3.9	3.9	3.8	3.9	3.8
	B_2	24.3	24.5	24.4	25.3	25.3	24.2	24.3	25.1
	T_1	36.7	47.2	39.2	47.4	37.0	34.5	42.7	38.9
90	B_1	3.8	3.8	3.8	3.8	3.8	3.8	3.8	3.7
	B_2	23.9	23.9	23.9	23.8	23.8	23.8	23.8	24.3
	T_1	35.1	35.1	35.1	35.2	35.2	33.2	31.4	38.2

TABLE 4.4

Material properties of the graphite/epoxy cantilever beam of Ref. [4.17]

Property	Value / Unit
E_1	129.11 GN/m^2
E_2	9.408 GN/m^2
ν_{12}	0.3
G_{12}	5.1568 GN/m^2
G_{13}	4.304 GN/m^2
G_{23}	2.541 GN/m^2
Density	1550.1 kg/m^3

TABLE 4.5

Natural frequencies (Hz) for the unidirectional graphite/epoxy cantilever beam of Ref. [4.17]. (The percentage difference is shown with respect to the experimental results.)

	$\beta = 15^0$				$\beta = 30^0$			
Mode No	theory [4.17]	expt [4.17]	Present	% diff	theory [4.17]	expt [4.17]	Present	% diff
1	85.4	82.5	82.1	0.46	52.7	52.7	52.6	0.19
2	531.5	511.3	511.3	0.00	329.8	331.8	328.8	0.90
3	1472.2	1423.4	1413.8	0.67	921.7	924.7	917.4	0.79
4	_____	1526.9	1741.4	14.05	1801.4	1766.9	1783.9	0.96
5	2839.1	2783.6	2743.6	1.44	_____	1827.5	2050.0	12.17
6	3630.0	4364.6	4403.8	0.90	2967.7	2984.0	2938.2	1.53

TABLE 4.6

Material properties of the CAS box-beam of Ref. [4.20]

Property	Property / Unit
E_1	142.0 GN/m^2
E_2	9.8 GN/m^2
$\nu_{12} = \nu_{13}$	0.42
ν_{23}	0.50
G_{12}	6.0 GN/m^2
G_{13}	6.0 GN/m^2
G_{23}	4.83 GN/m^2
Ply thickness	0.1397x10^{-3} m
Density	1604.1 kg/m^3

TABLE 4.7

Rigidity properties for the (CAS) cantilever box-beam of Ref. [4.20] with lay-up : $[\beta]_6$ in the top wall, $[-\beta]_6$ in the bottom wall and $[\beta/-\beta]_3$ in the vertical walls (L= 0.84455 m, m = 0.0882 Kg/m and I_α = 9.61725x10^{-6} Kgm).

Ply angle	Rigidity Properties		
β (deg)	EI (Nm^2)	GJ (Nm^2)	K (Nm^2)
0	281.28	25.776	0.0000
15	196.83	55.103	57.862
30	92.580	83.951	54.255
45	39.801	69.016	24.298
60	24.232	48.771	8.3012
75	20.200	34.620	2.1987
90	19.412	25.776	0.0000

TABLE 4.8

Natural frequencies (Hz) for the Circumferentially Asymmetric Stiffness (CAS) cantilever box-beam of Ref. [4.20] with lay-up : $[\beta]_6$ in the top wall, $[-\beta]_6$ in the bottom wall and $[\beta/-\beta]_3$ in the vertical walls. T indicates pure torsional mode.

	$\beta = 0^0$		$\beta = 15^0$		$\beta = 30^0$		$\beta = 45^0$		$\beta = 60^0$		$\beta = 75^0$		$\beta = 90^0$	
Mode No	**Ref. [4.20]**	**Present**	**Ref. [4.20]**	**Present**	**Ref. [4.20]**	**Present**	**Ref. [4.20]**	**Present**	**Ref. [4.20]**	**Present**	**Ref. [4.20]**	**Present**	**Ref. [4.20]**	**Present**
1	43.757	44.307	30.568	30.800	19.920	20.031	14.688	14.766	12.516	12.619	11.697	11.832	11.491	11.639
2	274.22	277.67	191.10	192.55	124.74	125.42	92.025	92.512	78.432	79.075	73.304	74.149	72.014	72.938
3	483.17 T_1	484.58 T_1	532.73	536.76	348.74	350.65	257.56	258.92	219.59	221.39	205.25	207.62	201.64	204.23
4	767.83	777.47	701.76 T_1	709.69 T_1	681.56	685.35	504.35	507.03	430.23	433.76	402.20	406.83	395.14	400.21
5	1449.5 T_2	1453.7 T_2	1040.1	1047.9	862.68 T_1	875.48 T_1	782.42 T_1	792.72 T_1	660.07 T_1	666.50 T_1	557.98 T_1	561.55 T_1	483.17 T_1	484.58 T_1
6	1504.6	1523.5	1700.7	1713.4	1124.5	1130.8	833.49	837.99	711.14	716.98	664.85	672.51	653.19	661.57
7	———	2422.9	2113.6 T_2	2137.5 T_2	1673.7	1683.1	1243.3	1250.0	1062.0	1070.7	993.12	1004.6	975.75	988.27
8	2487.3	2518.5	2520.0	2538.7	2323.8	2337.4	1733.9	1743.4	1482.7	1495.0	1387.0	1403.0	———	1380.3
9	———	3392.1	———	3485.8	2593.6 T_2	2631.7 T_2	2302.4	2315.9	1970.9	1987.8	1674.0 T_2	1684.7 T_2	1449.5 T_2	1453.7 T_2
10	———	3762.3	———	3587.5	———	3101.5	2352.0 T_2	2382.2 T_2	1983.0 T_2	2001.7 T_2	1846.5	1867.9	———	1837.7

TABLE 4.9

Material properties of the T300/5208 graphite/epoxy box-beam of Ref. [4.9].

Property	Value / Unit
E_1	146.86 GN/m^2
E_2	11.03 GN/m^2
ν_{12}	0.28
G_{12}	6.21 GN/m^2
G_{13}	6.21 GN/m^2
G_{23}	4.83 GN/m^2
Ply thickness	0.1397x10^{-3} m
Density	1604.1 kg/m^3

TABLE 4.10

Comparison of natural frequencies (Hz) for the cantilever box-beam of Ref. [4.9] using the dynamic stiffness method (D.S) with stiffnesses based on three different models, and finite element (F.E) frequencies (Hz) with stiffnesses based on NABSA [4.9].

Mode	F.E Frequencies with NABSA [4.9] Stiffnesses	D.S Frequencies with Ref. [2.85] stiffnesses	D.S Frequencies with Ref. [3.11] Stiffnesses	D.S Frequencies with Ref. [3.17] Stiffnesses
1	3.00	2.96	3.80	3.93
2	19.04	18.54	23.83	24.63
3	54.65	51.92	66.72	68.99

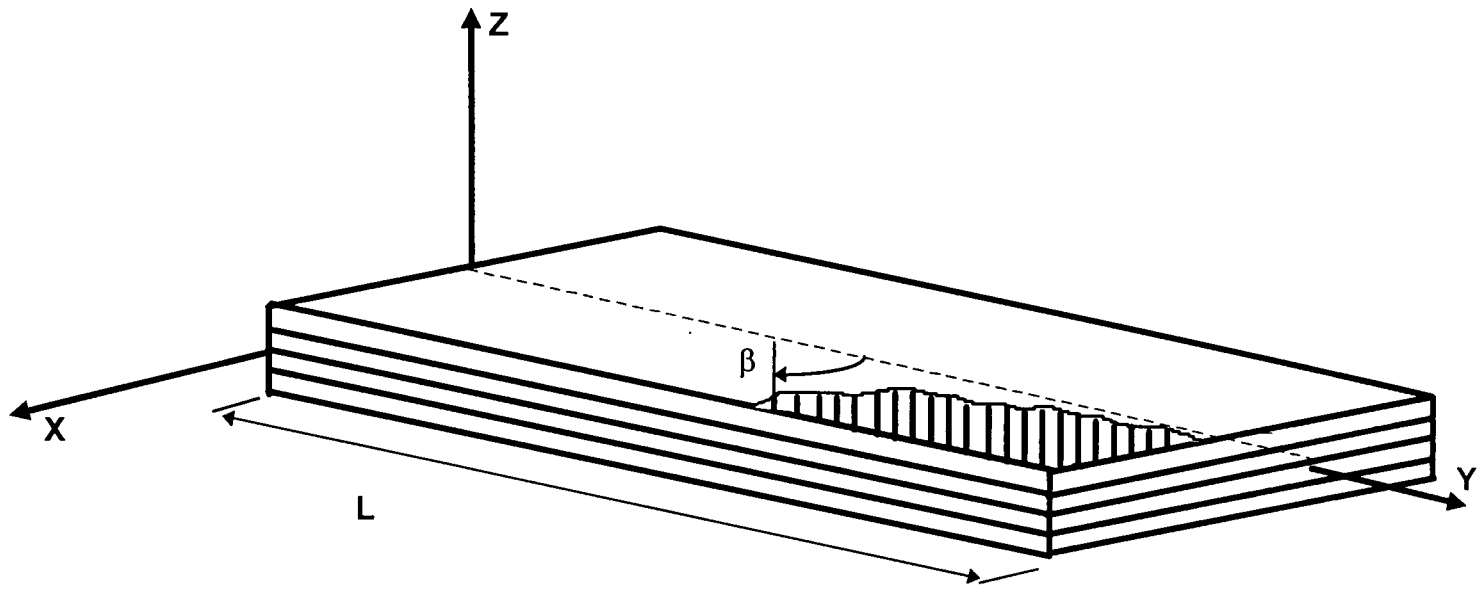

Fig. 4.1. Coordinate system and sign convention for positive ply angle of a laminated composite beam.

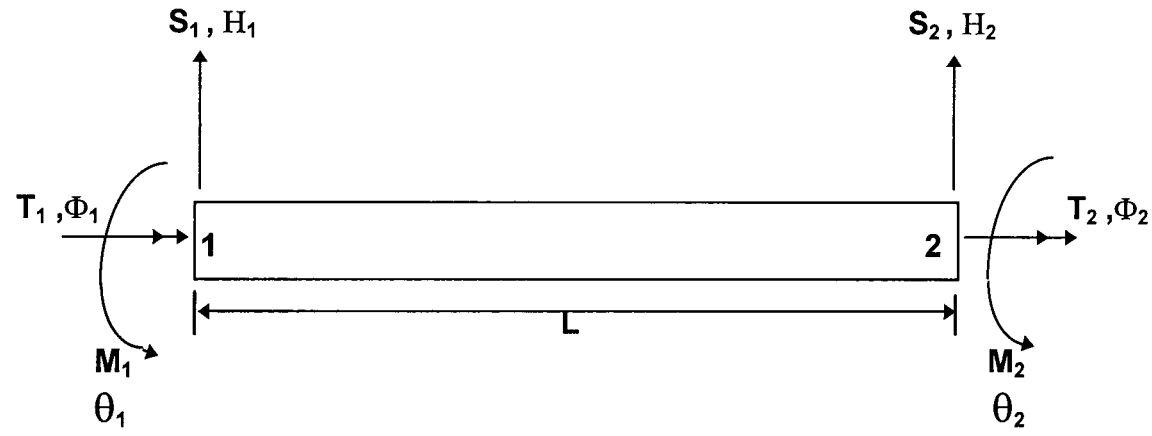

Fig. 4.2. End conditions for forces and displacements of a bending-torsion coupled composite beam.

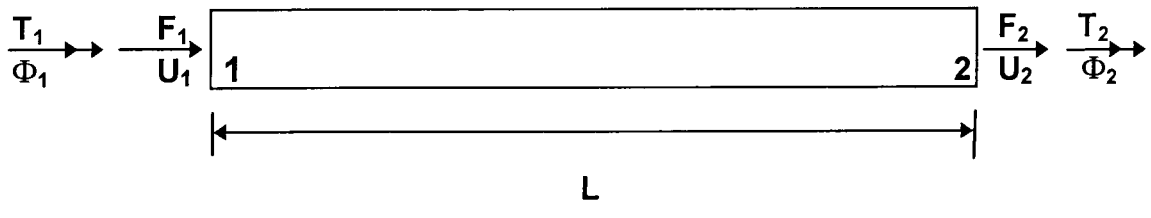

Fig. 4.3. End conditions for forces and displacements of an extension-torsion coupled composite beam.

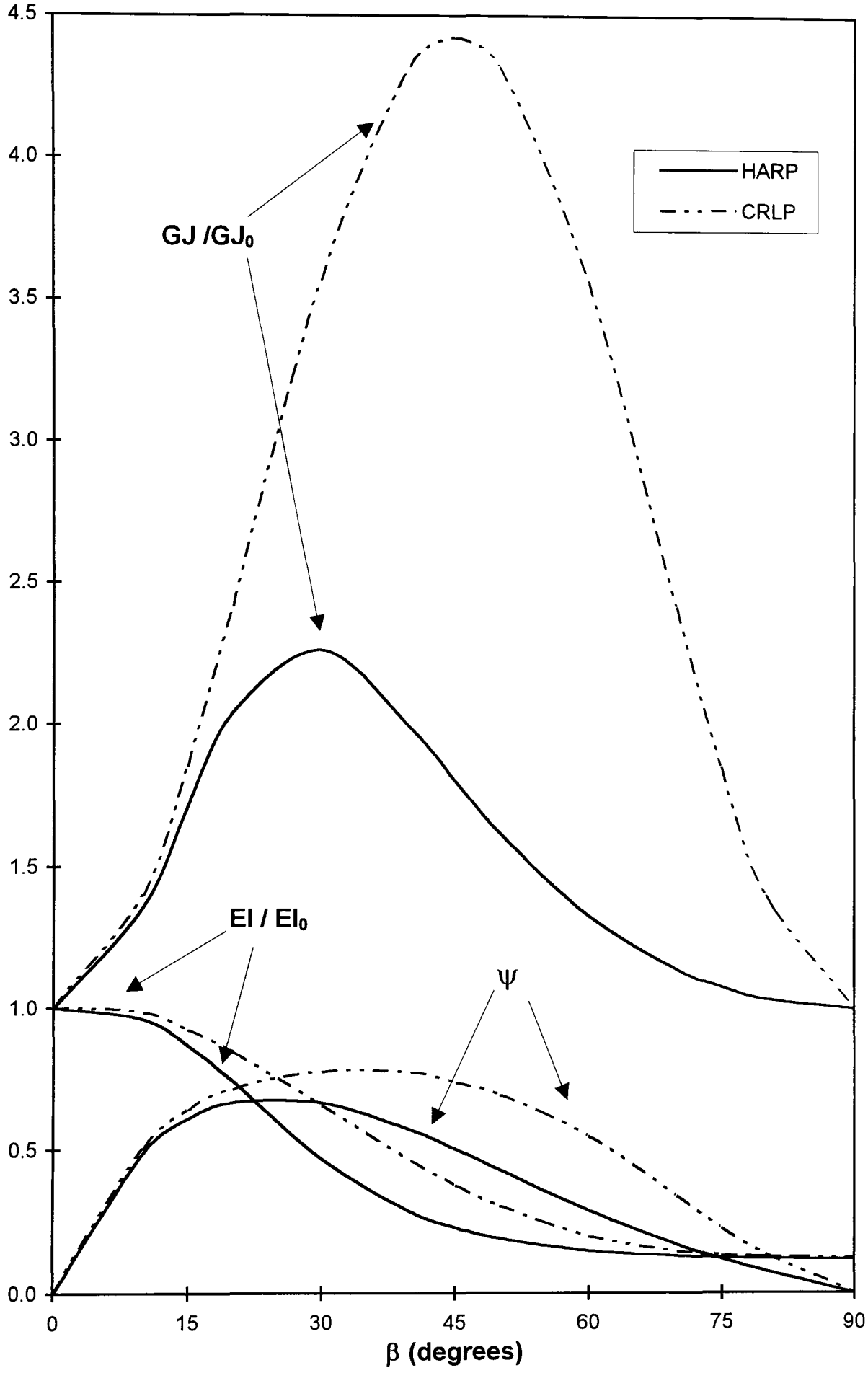

Fig. 4.4. Variation of rigidity properties with fibre orientation, β, for HARP and CRLP models for $[\beta_2 / 0]_s$ lay-up.

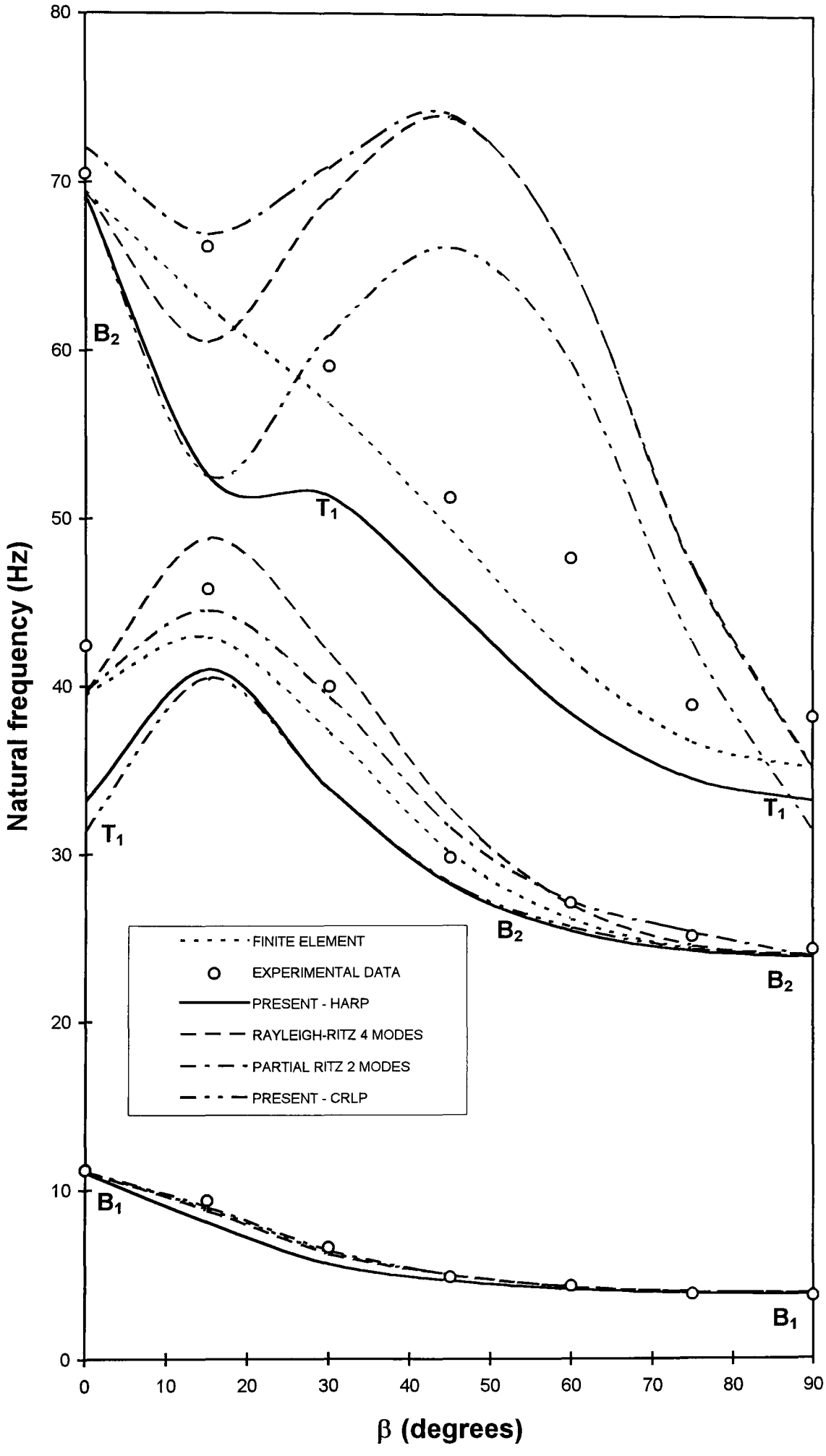

Fig. 4.5 (a). Comparison of natural frequencies given by various methods for $[\beta_2 / 0]_s$ lay-up.

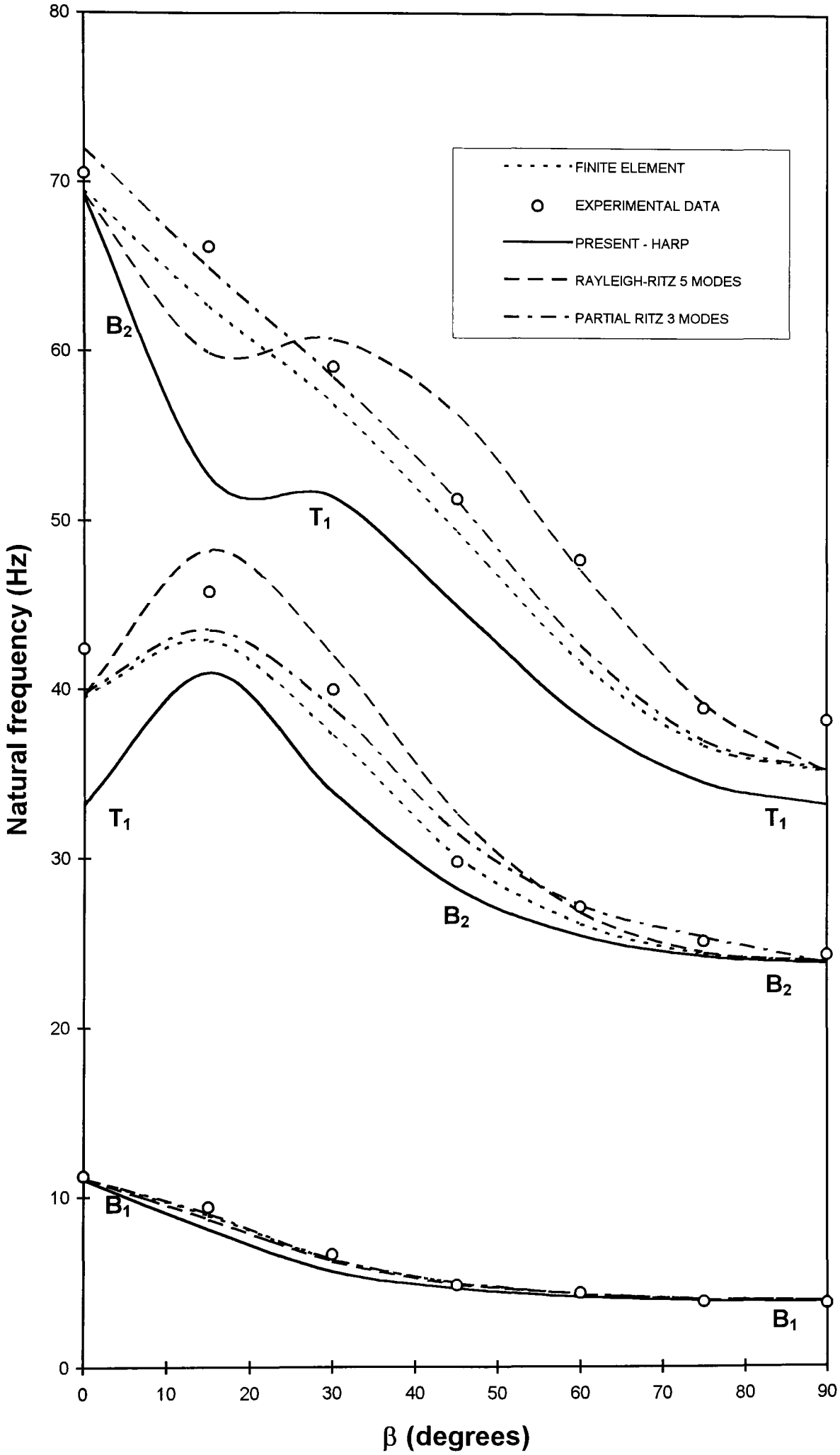

Fig. 4.5 (b). Comparison of natural frequencies given by various methods for $[\beta_2 / 0]_s$ lay-up.

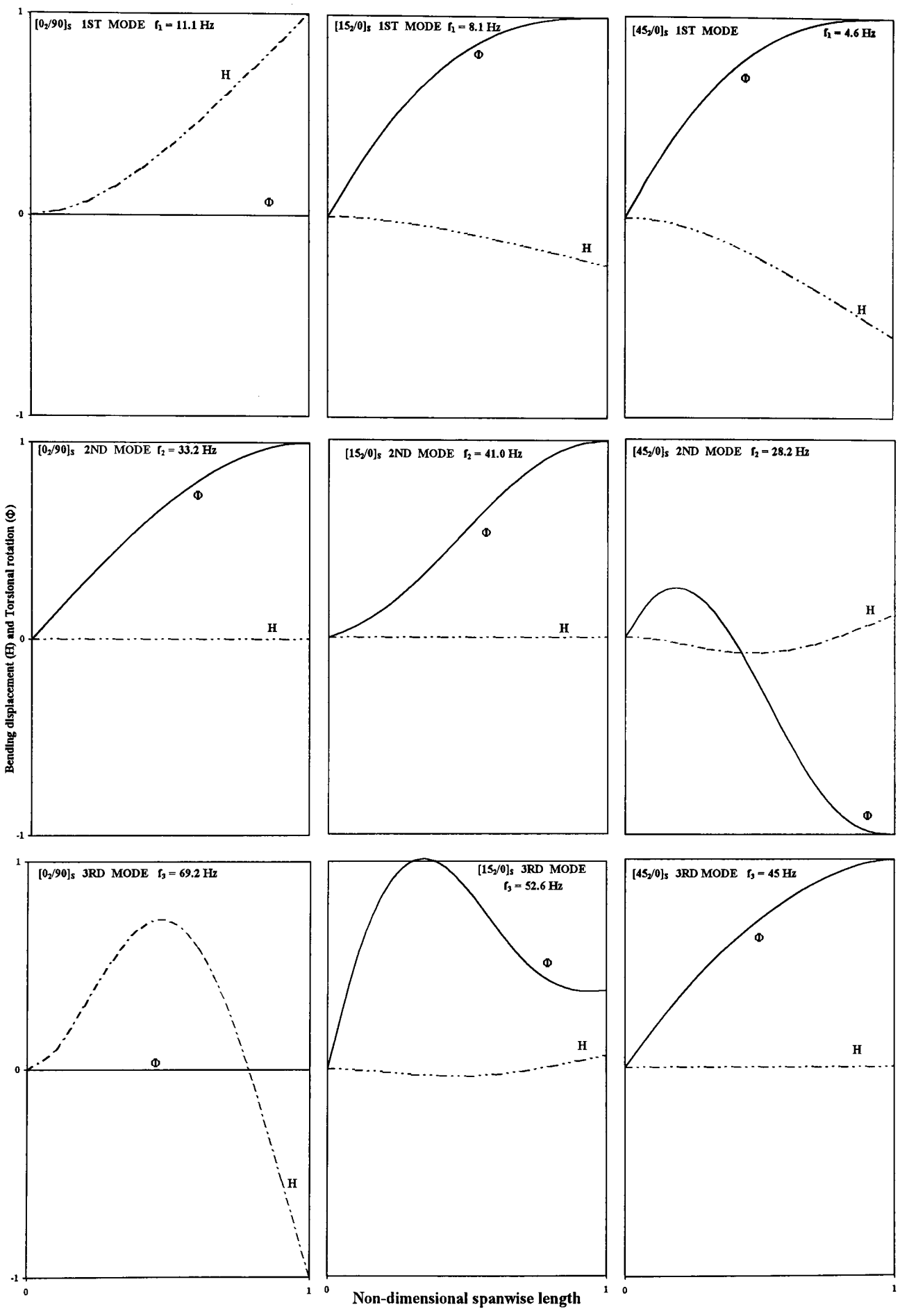

Fig. 4.6. Mode shapes of laminated composite beam for different ply orientation, with H = bending displacement, Φ = torsional rotation and modes normalised so that the largest H or Φ is unity.

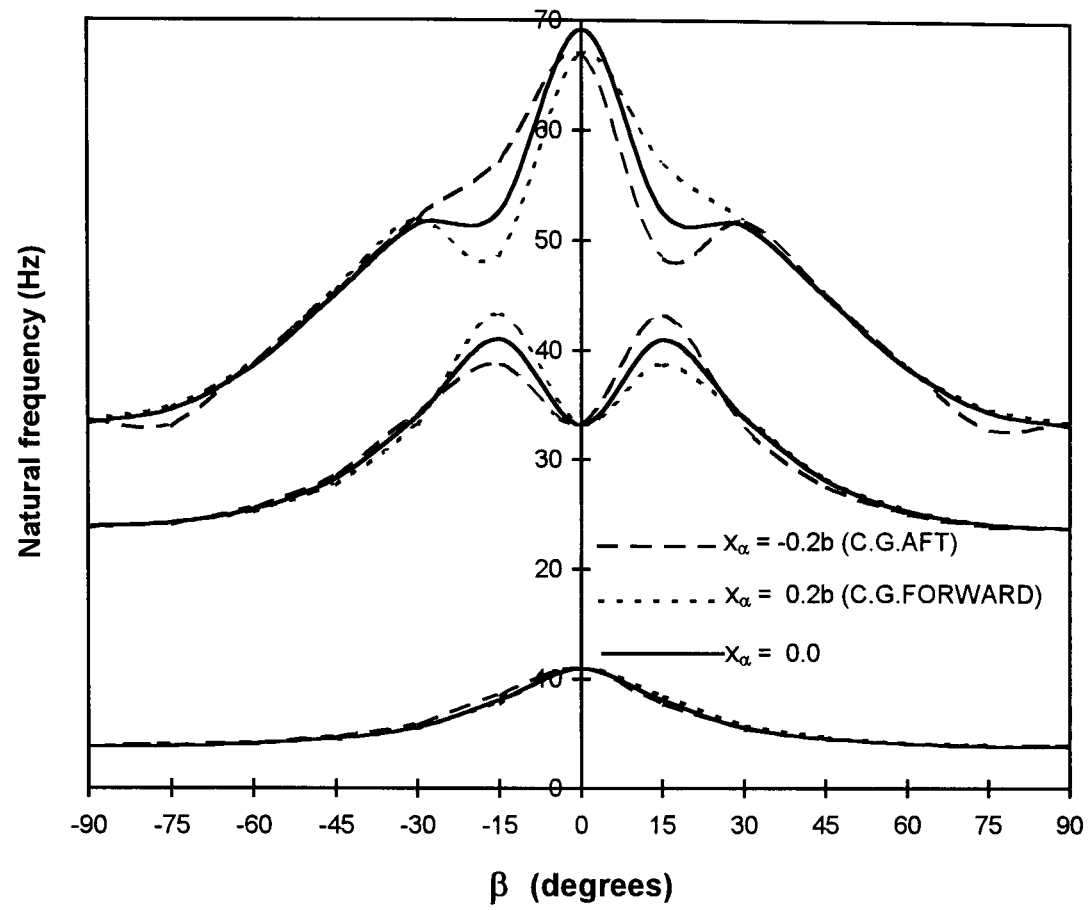

Fig. 4.7. The effect of fibre orientation upon the first three natural frequencies of a beam with laminate configuration $[\beta_2 / 0]_s$, where b is the semi-chord.

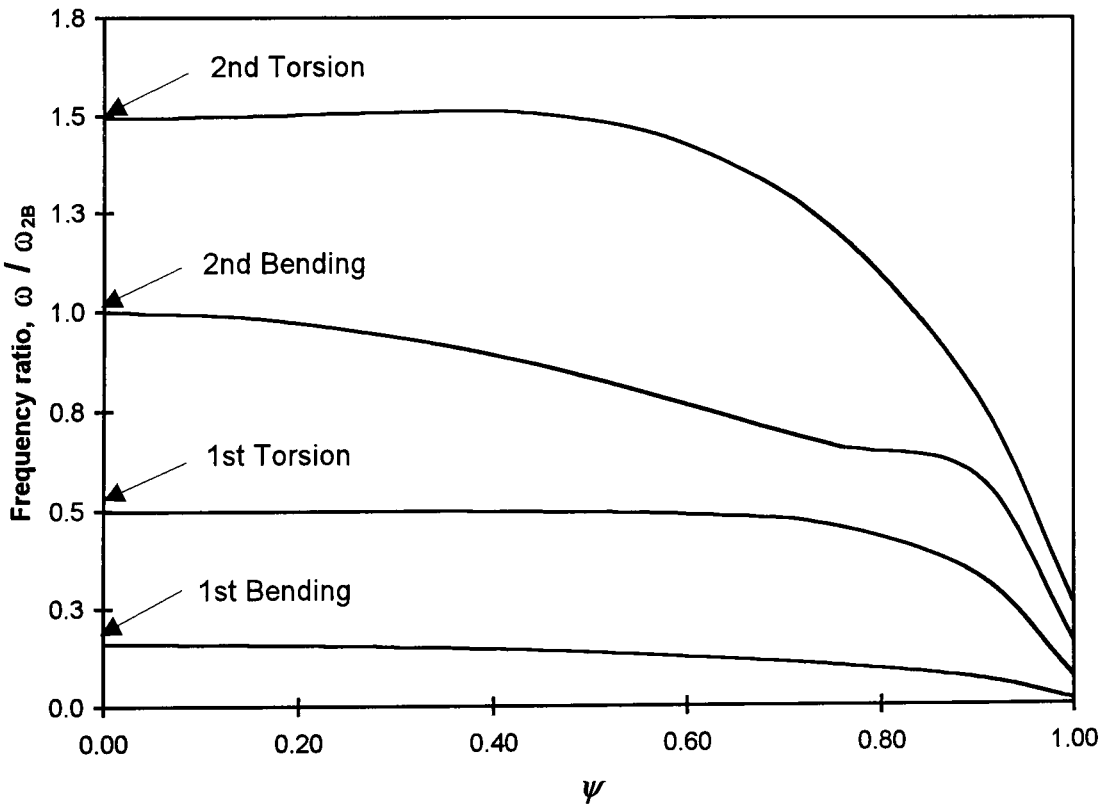

Fig. 4.8. The effect of coupling parameter ψ on the first four dimensionless natural frequencies for a cantilever with GJ/EI = 0.5, where ω_{2B} is the natural frequency of the 3rd mode.

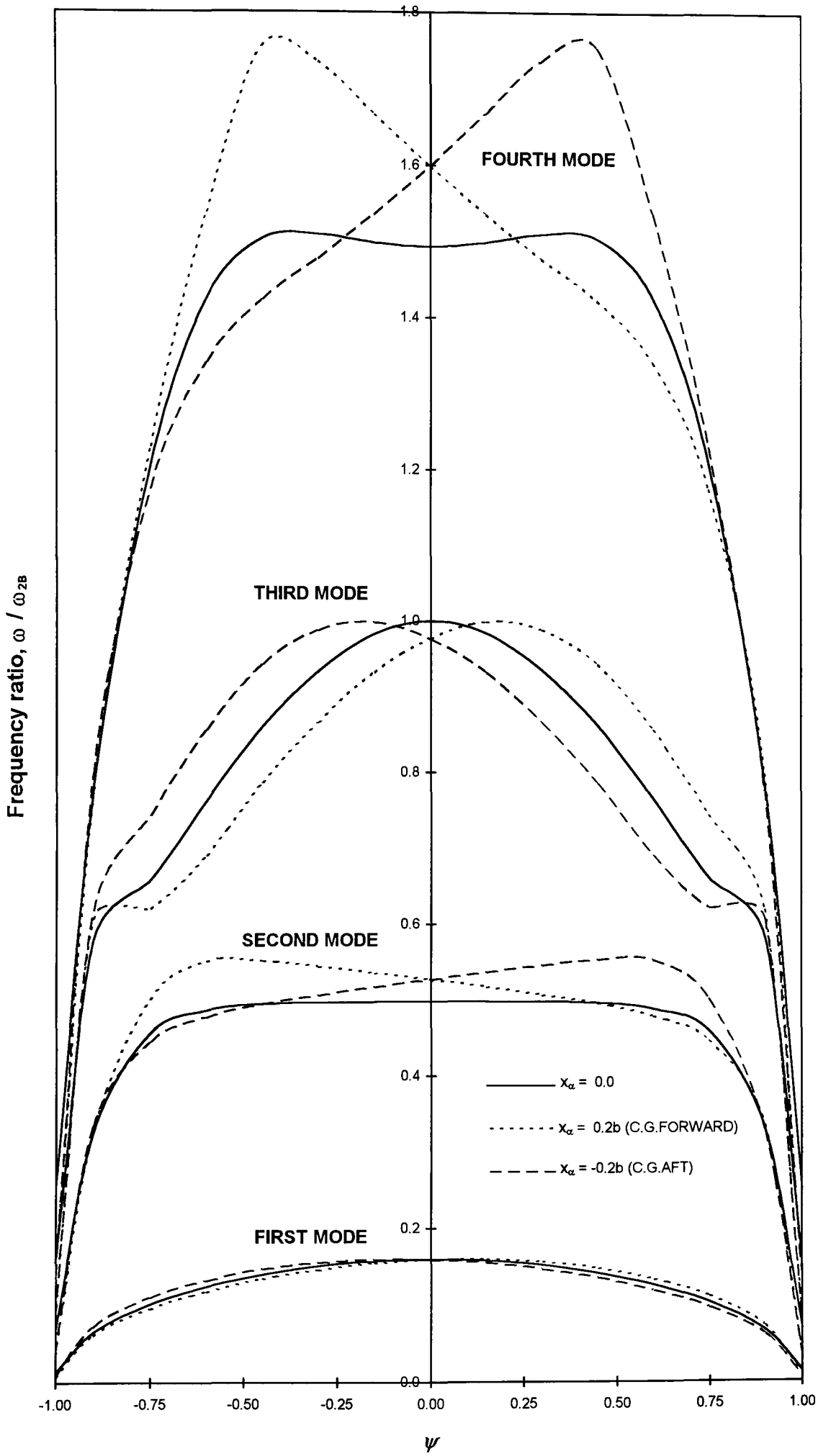

Fig. 4.9. The effect of coupling parameter ψ on the first four dimensionless natural frequencies for a cantilever beam with GJ/EI = 0.5. Three values of x_α are shown, where ω_{2B} is the natural frequency of the 3rd mode.

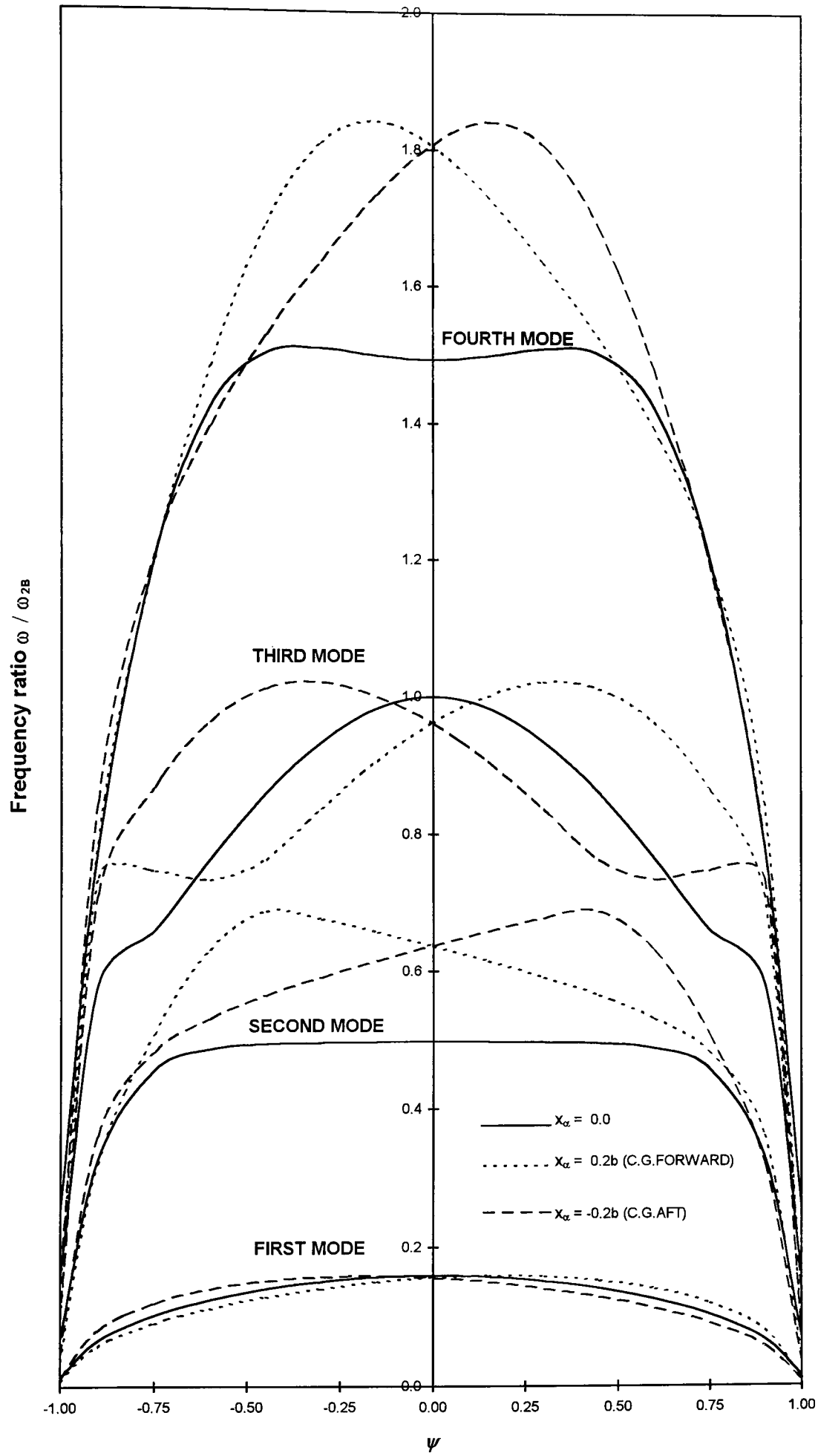

Fig. 4.10. The effect of coupling parameter ψ on the first four dimensionless natural frequencies for a cantilever beam with GJ/EI = 0.5. Three values of x_α are shown, where ω_{2B} is the natural frequency of the 3rd mode.

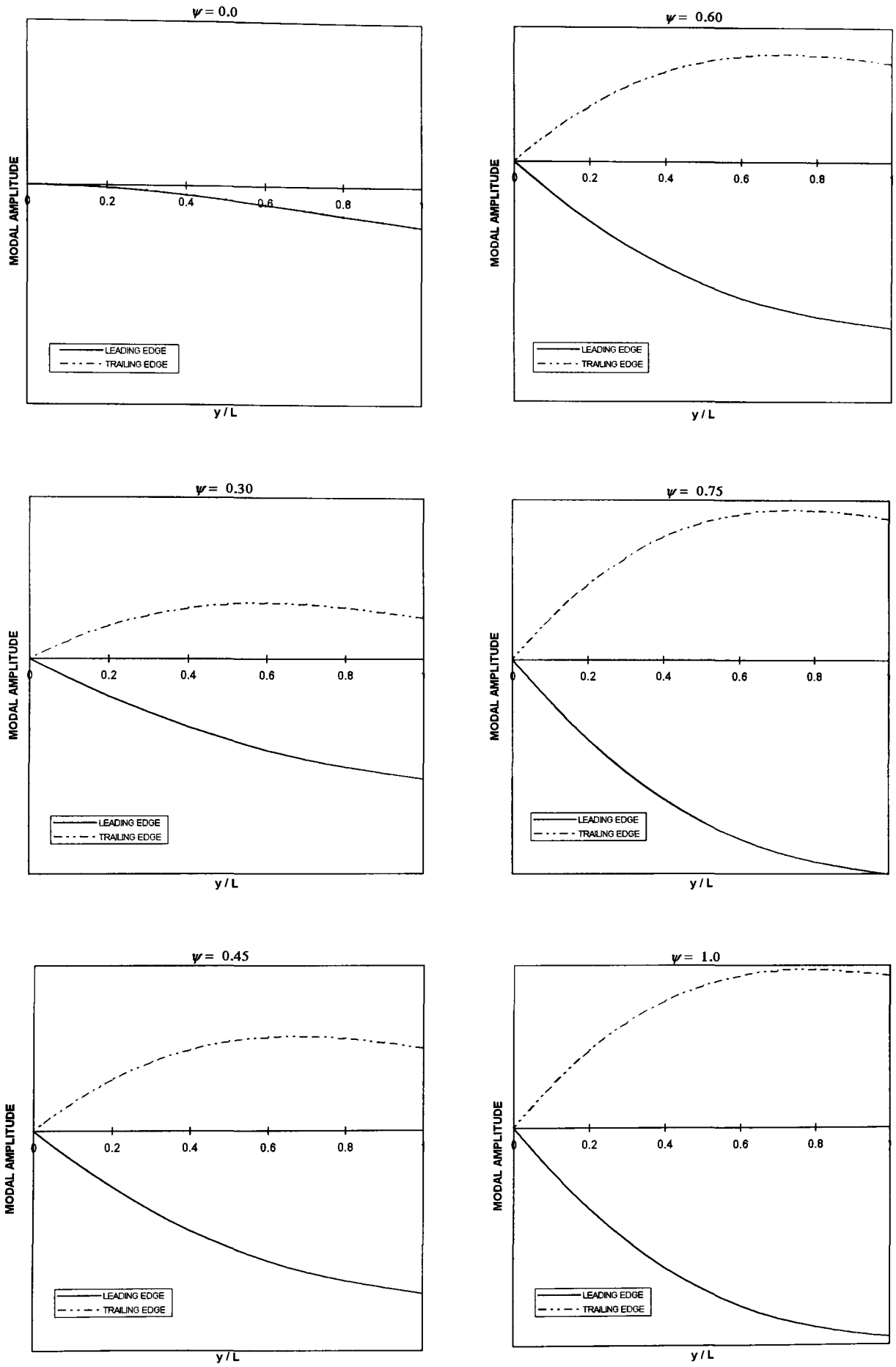

Fig. 4.11. A straight-on view of the first free vibration mode of the example beam for selected values of ψ, R = 0.5.

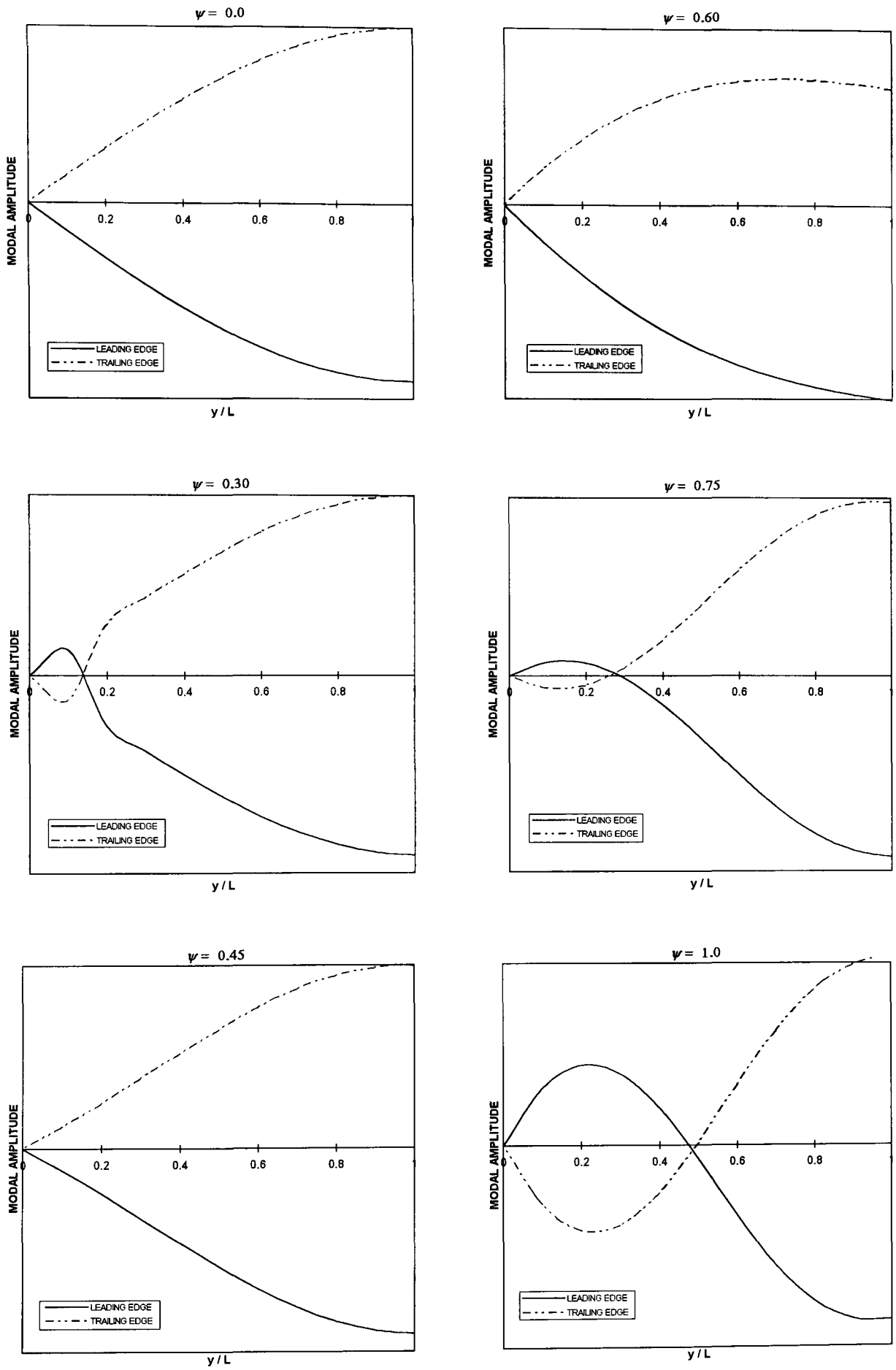

Fig. 4.12. A straight-on view of the second free vibration mode of the example beam for selected values of ψ, R = 0.5.

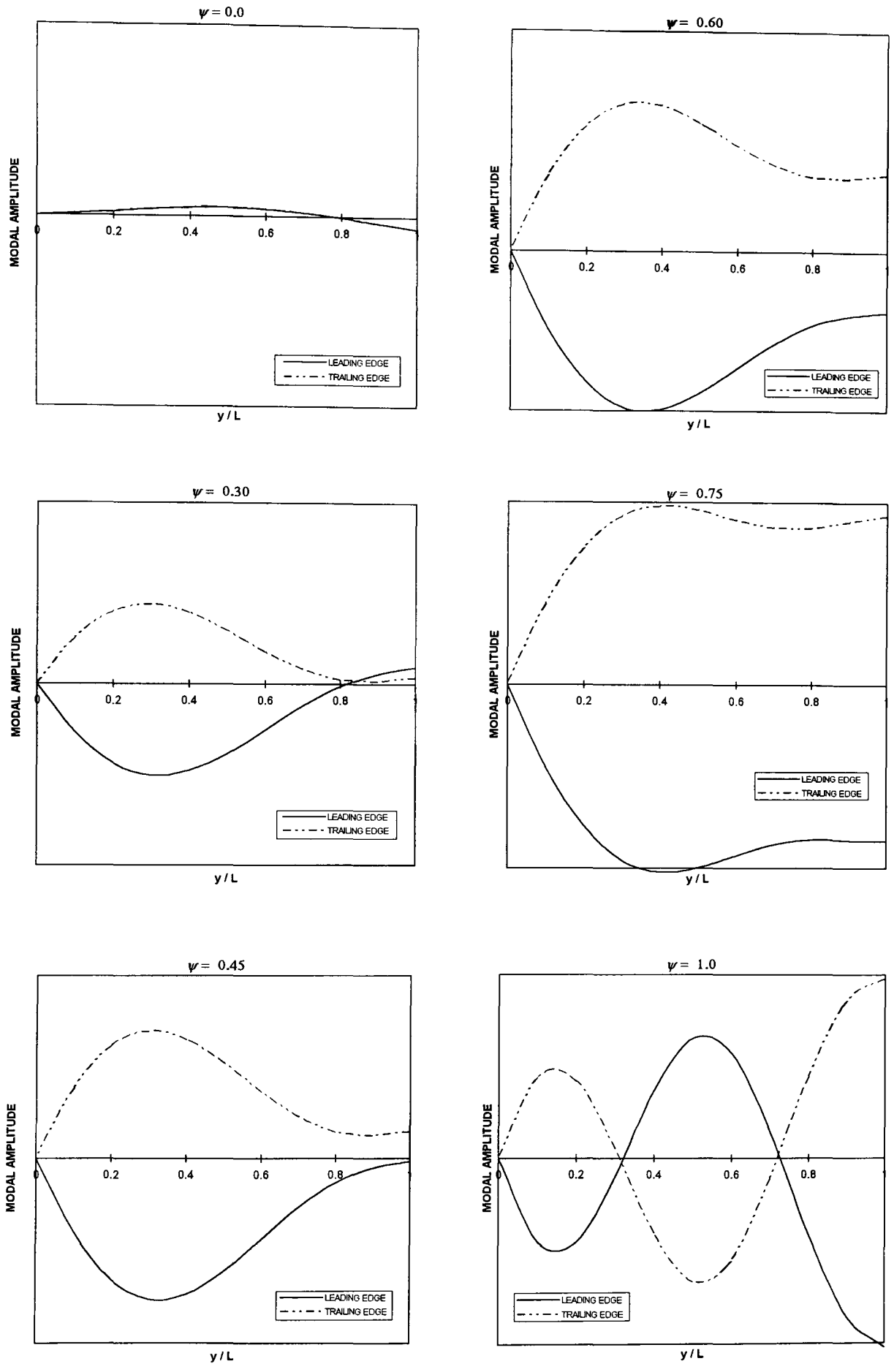

Fig. 4.13. A straight-on view of the third free vibration mode of the example beam for selected values of ψ, R = 0.5.

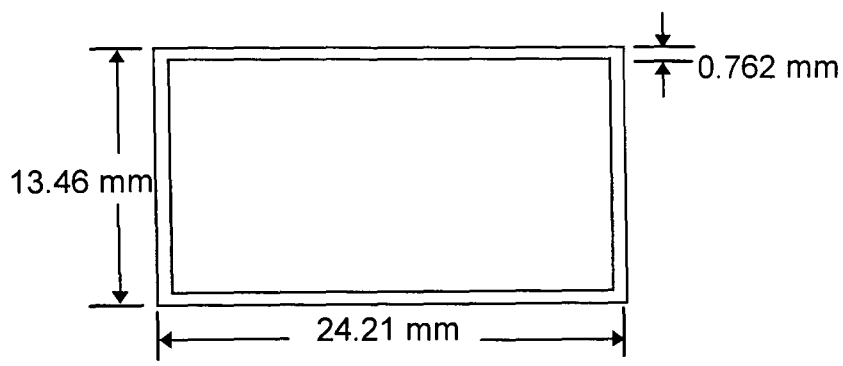

Fig. 4.14. CAS box-beam cross-section of Ref. [4.20]

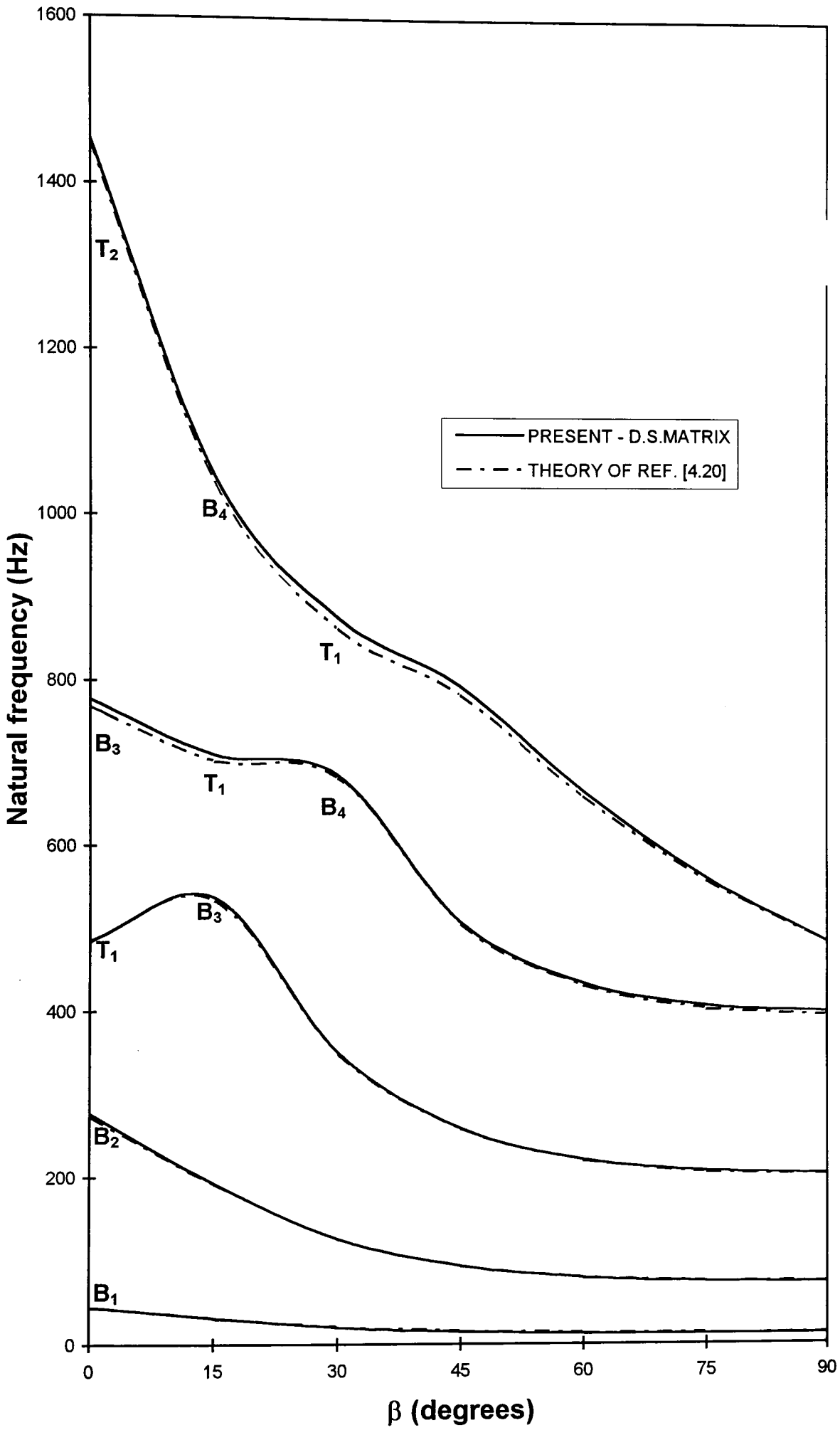

Fig. 4.15 (a). Comparison of the first five natural frequencies given by D.S.Matrix and theory of Ref. [4.20] for the box-beam lay-up : $[\beta]_6$ and $[-\beta]_6$ in the top and bottom walls respectively and $[\beta / -\beta]_3$ in the vertical walls.

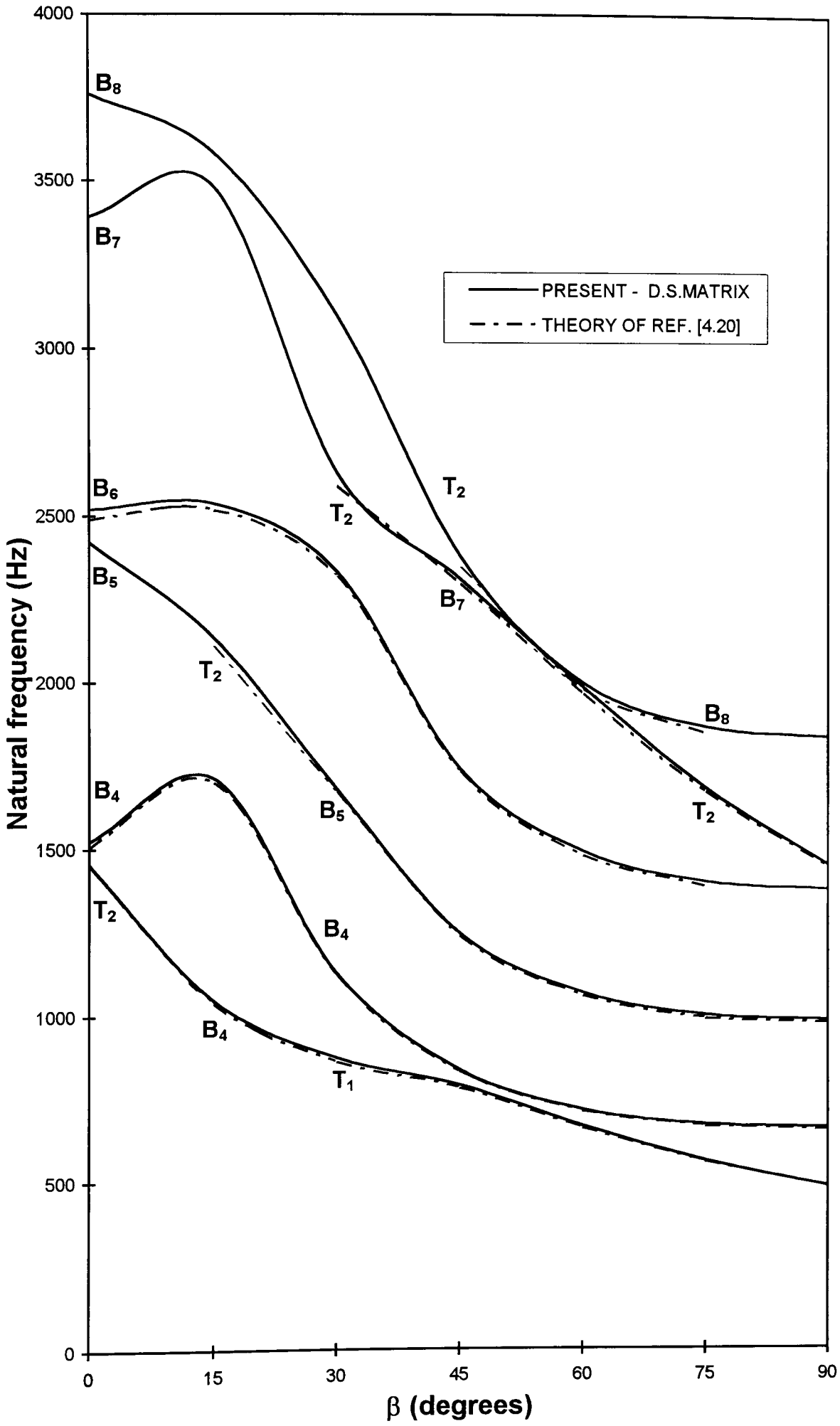

Fig. 4.15 (b). Comparison of the fifth to tenth natural frequencies given by D.S.Matrix and theory of Ref. [4.20] for the box-beam lay-up : $[\beta]_6$ and $[-\beta]_6$ in the top and bottom walls respectively and $[\beta / -\beta]_3$ in the vertical walls.

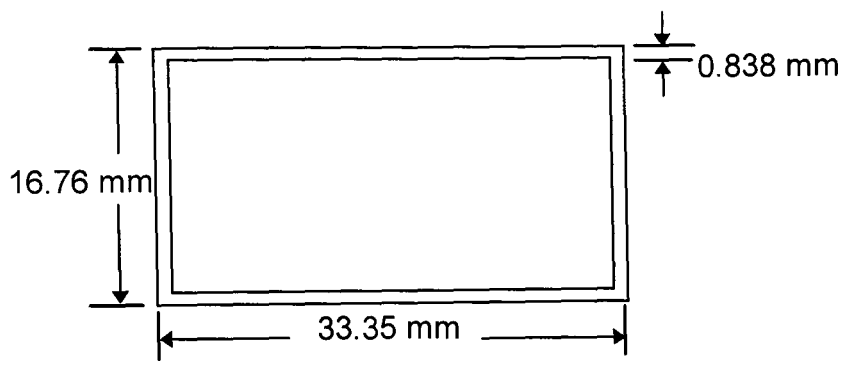

Fig. 4.16. CUS box-beam cross-section of Ref. [4.9]

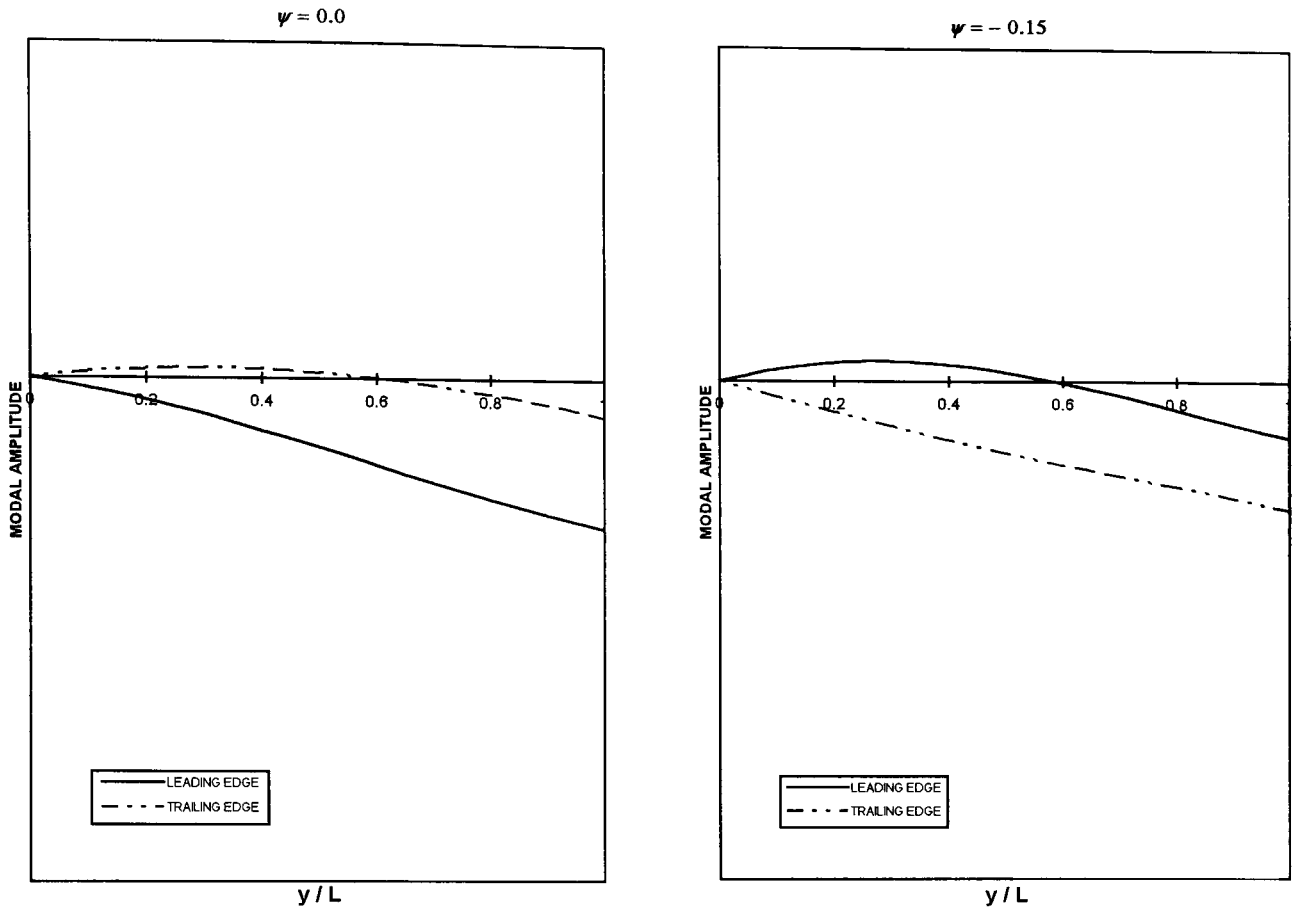

Fig. 4.17. A straight-on view of the first free vibration mode of the example beam for selected negative values of ψ; R = 0.5, x_α = - 0.2b.

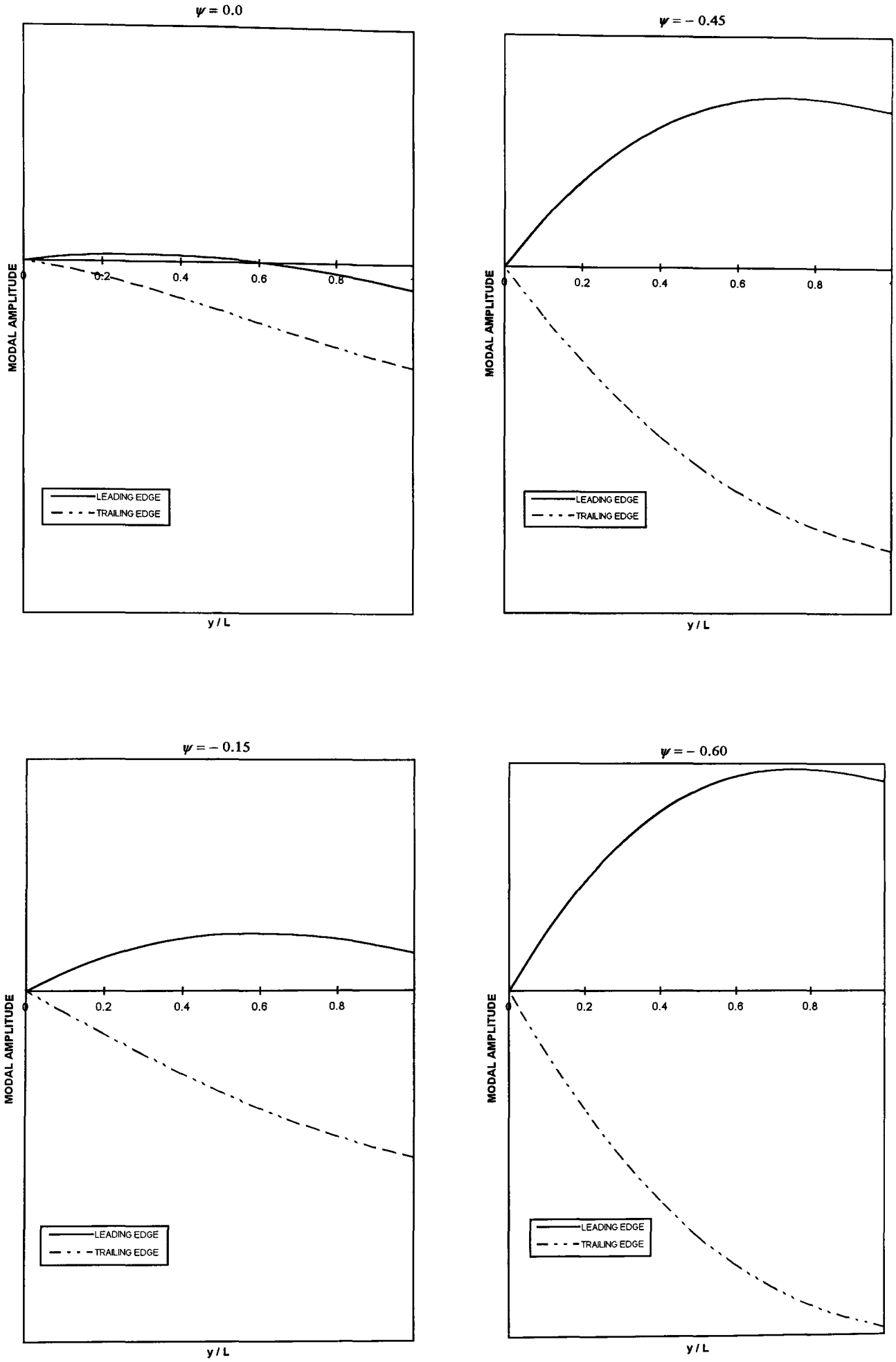

Fig. 4.18. A straight-on view of the first free vibration mode of the example beam for selected negative values of ψ; R = 0.5, x_α = 0.2b.

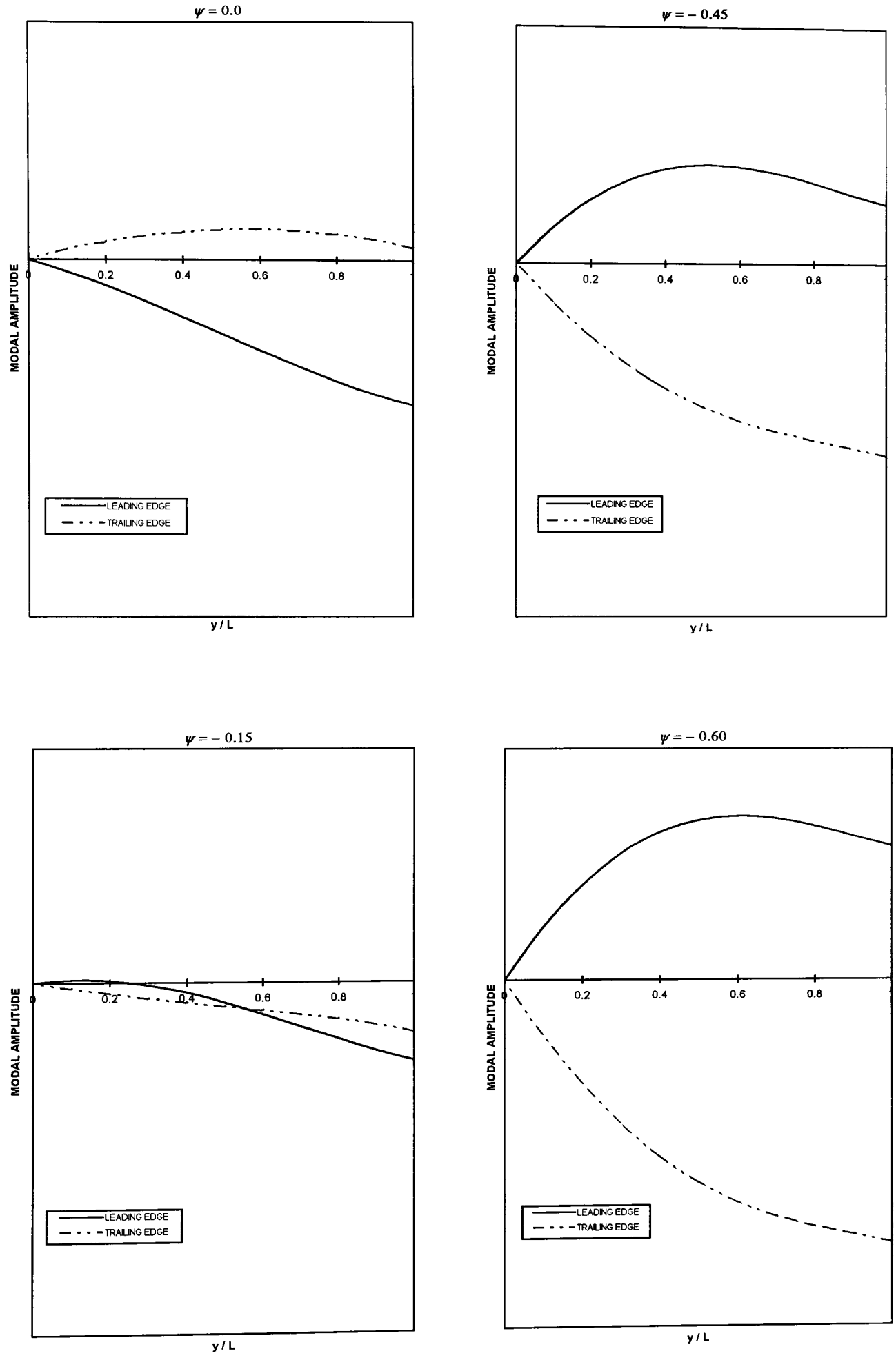

Fig. 4.19. A straight-on view of the first free vibration mode of the example beam for selected negative values of ψ; R = 0.5, x_α = - 0.4b.

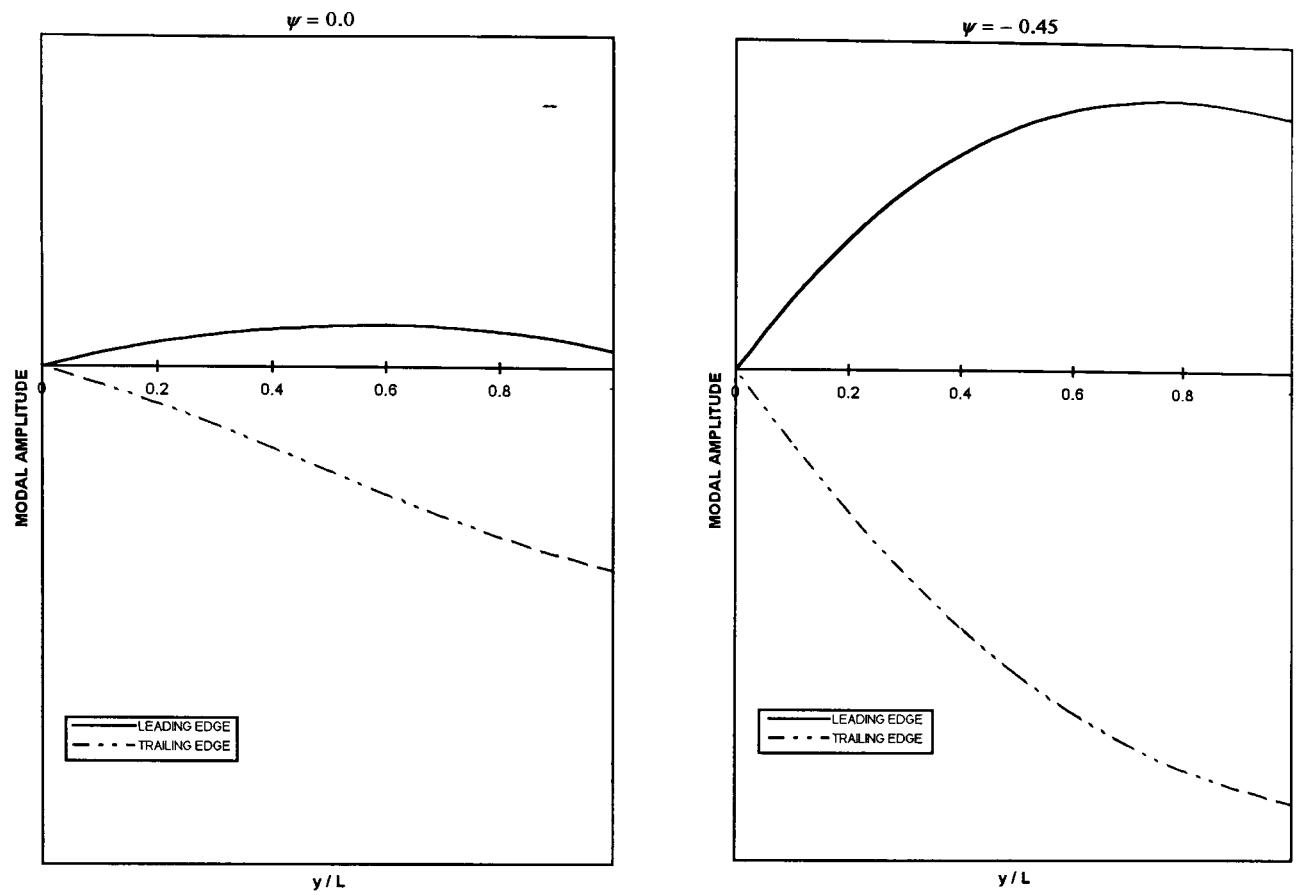

Fig. 4.20. A straight-on view of the first free vibration mode of the example beam for selected negative values of ψ; R = 0.5, x_α = 0.4b.

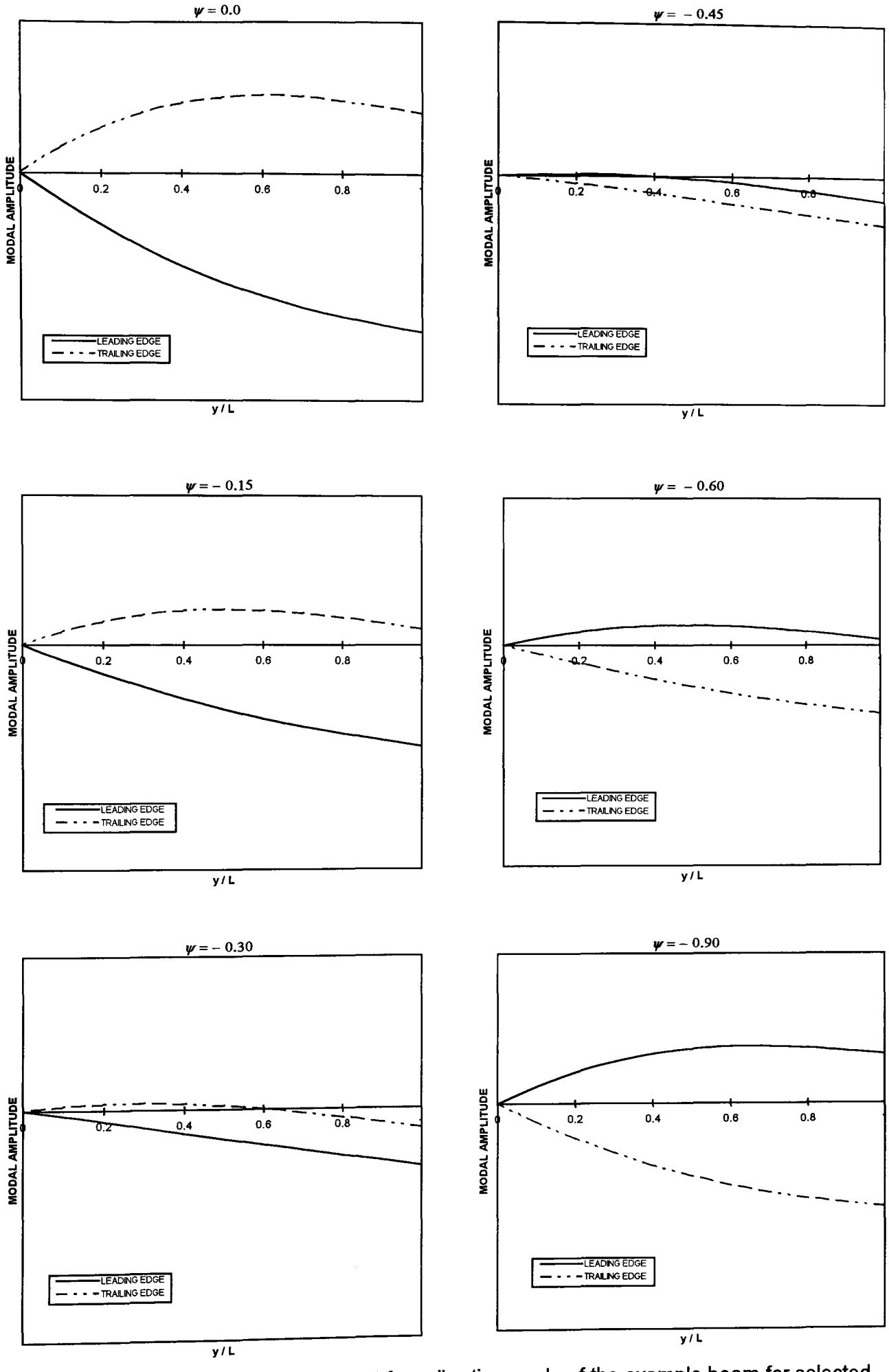

Fig. 4.21. A straight-on view of the first free vibration mode of the example beam for selected negative values of ψ; $\Lambda = 30^0$ backward, R = 0.5, $x_\alpha = 0.0$.

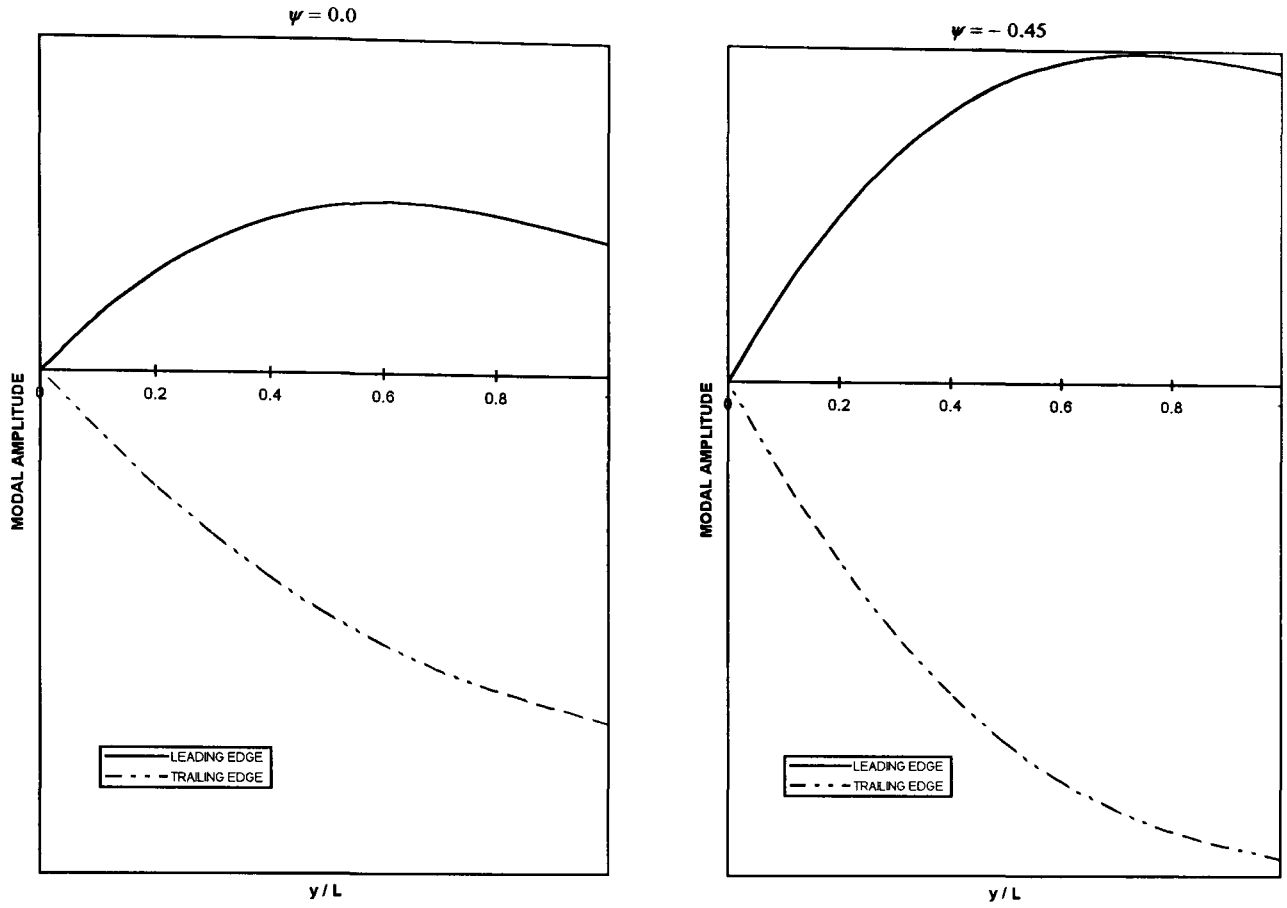

Fig. 4.22. A straight-on view of the first free vibration mode of the example beam for selected negative values of ψ; $\Lambda = 30^0$ forward, R = 0.5, $x_\alpha = 0.0$.

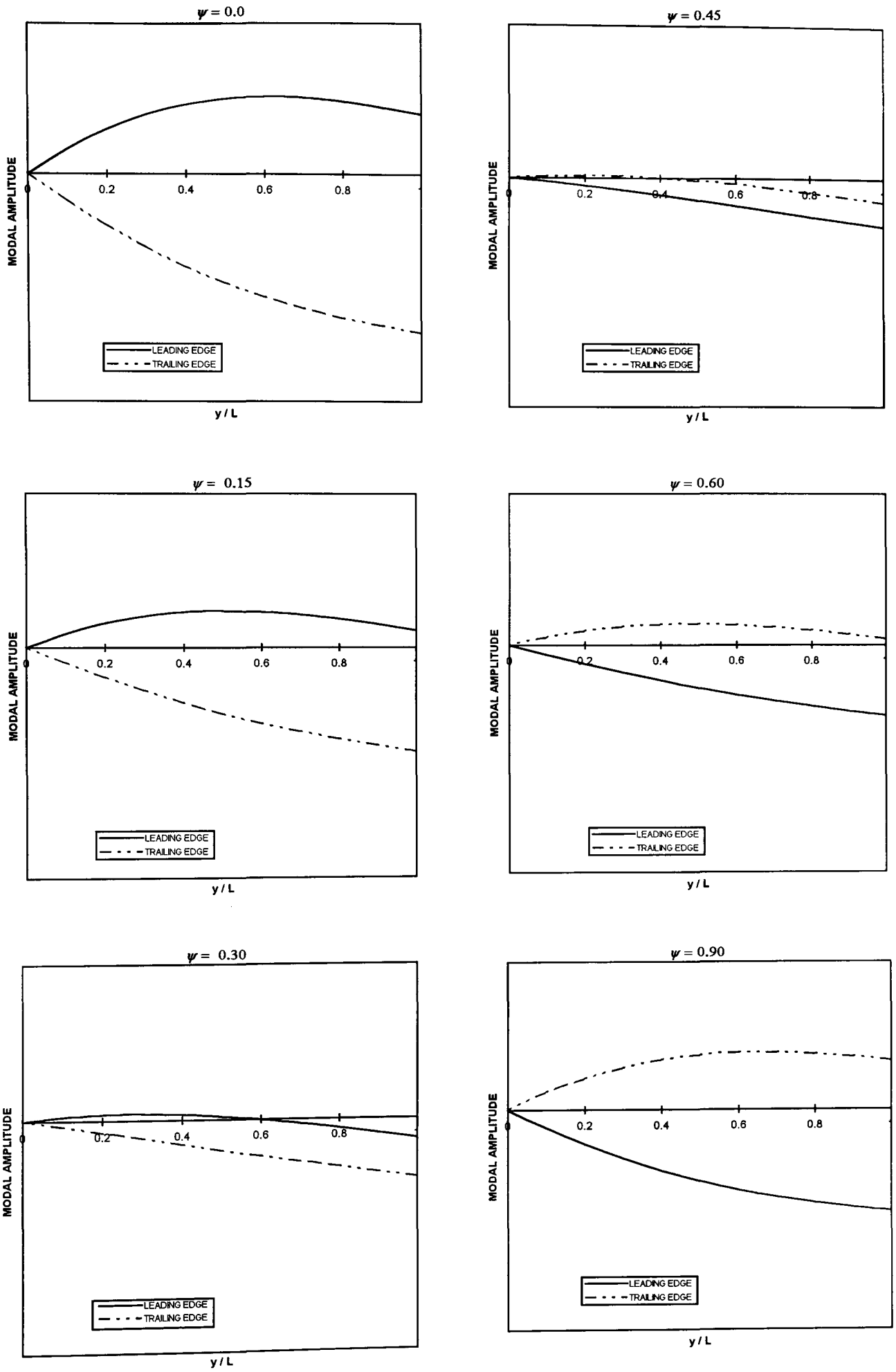

Fig. 4.23. A straight-on view of the first free vibration mode of the example beam for selected positive values of ψ; $\Lambda = 30^0$ forward, R = 0.5, $x_\alpha = 0.0$.

CHAPTER 5

AEROELASTIC TAILORING :

FLUTTER AND DIVERGENCE BEHAVIOUR OF COMPOSITE WINGS

5. AEROELASTIC TAILORING : FLUTTER AND DIVERGENCE BEHAVIOUR OF COMPOSITE WINGS

5.1 Introduction

The ability of stiffness coupling to induce coupling between various modes of structural deformation was illustrated in chapter 4. It is well known that the free vibrational modes of a beam play an important role in the aeroelastic stability of any lifting surface, such as, flutter and divergence which arise from aerodynamic forces introduced by lifting surface deformation [1.6]. As a consequence, the structural response of a composite beam (wing) can be manipulated in a beneficial way leading to aeroelastic tailoring of aircraft wings [2.42, 2.49] and thus to the possibility of optimising design [2.47].

Prior to the advent of composite materials, a common way to raise both the flutter and divergence speeds of a wing was to raise its torsional rigidity at the expense of structural weight. This inevitable extra weight, for instance, made the swept-forward wing (which is accompanied by low divergence speeds) not feasible. It is well known from the classical theory of aeroelasticity [5.1], that a large frequency difference between the fundamental torsional and the fundamental bending modes (i.e., a high non-dimensional frequency ratio ω_α / ω_h, where ω_h and ω_α are respectively the fundamental (uncoupled) bending and torsional natural frequencies) is beneficial to increase the flutter speed for wings whose fundamental bending natural frequency is lower than that of the fundamental torsion. This is because in classical bending-torsion flutter the two frequencies coalesce at a particular airspeed called flutter speed (see, for example, Figs 9.7 and 9.8 on pages 552 and 553 of Ref. [5.1]). Therefore when ω_α is higher than ω_h (which is usually the case), a higher flutter speed can be achieved [5.2] either by raising the torsional rigidity (GJ) or by reducing the bending rigidity (EI). On the other hand, divergence, which is a static phenomenon, is not generally affected by the free vibration characteristics of the wing. It is influenced by the torsional behaviour of the wing instead. For unswept wings, divergence has been shown to be unaffected by changes in bending rigidity but to be sensitive to changes in torsional rigidity [5.1] as expected (naturally, the higher the

torsional rigidity, the higher is the resistance of the wing to sustain torsional moments).

The advent of composite materials, however, led aeroelasticians to exploit the directional strength and stiffness properties of composites to enhance aeroelastic stability through aeroelastic tailoring. The main attraction of composite materials from the aeroelastic standpoint was that by using unbalanced laminates (see, for example, the X-29 experimental swept-forward aircraft [2.44]) which introduce a coupling between the bending and torsional deformations, the vibrational behaviour, and particularly the mode shapes of the wing can be controlled in a beneficial way [1.24]. The wing, for instance, can be designed to exhibit wash-in or wash-out behaviour [1.24].

Although numerous papers have been published in aeronautical and other related journals in the last fifteen years, most of these studies have mainly focused on the potential of bending-torsion material coupling (possible in composite materials but markedly less so in metallic ones) to improve the aeroelastic stability of wings [1.5-1.15] and/or of the whole aircraft configuration [1.16-1.17]. Thus, the benefit that can be derived by raising the torsional rigidity of composite wings at the expense of bending rigidity (i.e., raising the non-dimensional frequency ratio ω_α / ω_h), without in certain cases introducing bending-torsion coupling (e.g., in the cases of symmetric and balanced laminates), has often been overlooked. One notable exception was the investigation of Housner and Stein [1.9] who examined the effect of ply orientation for a symmetrical balanced cross-ply laminate (i.e., uncoupled) upon flutter of a beam-like wing. However, because the study was limited to symmetrical and balanced laminates, bending-torsion coupling was not present. Changes in flutter speed were shown to be dependent solely on changes in bending and torsional stiffnesses as plies were reoriented. Furthermore, their study showed that the highest critical flutter speed for both unswept and swept-back wings occurred when the plies were oriented alternatively near $\pm 45^0$ (Fig. 6 of Ref. [1.9]). Although not explicitly referred to by the authors, this laminate configuration gave the maximum torsional rigidity (see, Fig. 5 on page 100 of Ref. [1.9]).

Weisshaar and Foist [1.6] later examined the potential effects of material tailoring on the flutter of moderate-to-high aspect ratio laminated composite wings. In contrast to Ref. [1.9], the authors included the stiffness coupling in their investigation.

By using a unidirectional laminate, they showed that the flutter speed can be raised significantly at a range of negative (positive in their axis notation) fibre angles in the region of very high negative bending-torsion coupling, i.e., when the wing is designed to exhibit wash-in behaviour (bend-up/twist-up). Although, in the above investigation some significant variation in flutter and divergence speeds was observed when the plies were reoriented, this variation was shown relative to the flutter speed calculated when all the plies in the laminate were set to zero degrees. This laminate configuration, however, offers the maximum bending rigidity and minimum torsional rigidity which is neither favourable for flutter nor for divergence. Thus, the results of the above work are limited in the sense that the investigation was carried out using only a unidirectional laminate and the results were not compared with laminate configurations giving relatively higher torsional rigidity.

Weisshaar [1.8] investigated the divergence behaviour of swept-forward wings using a more realistic laminate configuration to compare the results obtained from a unidirectional laminate. The results of this study showed that a positive value of the ratio of the bending-torsion coupling rigidity to torsional rigidity (K/GJ) (i.e., bend-up/twist-down), can successfully negate the undesirable effect of swept-forward wings on divergence. The same author [1.12] later showed that both flutter and divergence can be eliminated at a relatively small values of the bending-torsion coupling parameter ψ, a measure of bending-torsion coupling in a structure. These results were later confirmed by Lottati [2.69] who also showed that flutter and divergence can be eliminated at certain values of bending-torsion coupling stiffness (K). However, both authors [1.12, 2.69] by maintaining the bending rigidity (EI) and torsional rigidity (GJ) constant and varying only the bending-torsion coupling rigidity (K) to alter the coupling parameter ψ, have not shown whether and how such values can be achieved in a realistic wing.

The shortcomings in the literature which have been briefly discussed above, partly motivated the present work since it does not appear to be clear yet whether by incorporating the stiffness coupling in the analysis, higher aeroelastic stability can be achieved than sticking to the classical theory of aeroelasticity and thus maximising the torsional rigidity (GJ). Therefore, the objective of this chapter is to give an insight into the potential for passive structural control of flutter and divergence that can be achieved through the use of composite materials. Of particular interest in this study is

to investigate the effect of torsional rigidity GJ, and the effect of bending-torsion coupling parameter ψ (defined in Eqn. (3.27)) on flutter and divergence speeds.

In this investigation the rigidity and coupling parameters are established using mainly two independent theories of which one is the High Aspect Ratio Plate (HARP) model (i.e., Eqns (3.24)-(3-26) of chapter 3) and the other is that of thin-walled beam (box-beam) model of Ref. [2.85] (i.e., Eqns (3.79)-(3-81) of chapter 3). The free vibration characteristics are then established using the dynamic stiffness matrix method. This study is one of the first to use an exact dynamic stiffness formulation in the aeroelastic analysis of composite wings of which some advantages in free vibration are well known, particularly when better accuracies are required. As will be shown later in this chapter (in contrast to metallic wings), accuracies in the free vibration characteristics of composite wings are of vital importance in any aeroelastic analysis since these have a profound effect upon the aeroelastic characteristics of such wings.

The dynamic stiffness matrix together with Strip theory two-dimensional, unsteady, incompressible aerodynamics are used by the computer program CALFUN [5.3] (**CAL**culation of **F**lutter speed **U**sing **N**ormal modes [5.4-5.6]) to determine the flutter and divergence speeds. While this approach to modelling the aerodynamic loads may have certain shortcomings when compared to more advanced methods, such as, the Lifting Surface theory, it possesses the advantages of low computational cost and ease of use. The author was well aware of these shortcomings and careful attention has been paid to minimise this factor by validating results obtained using the Strip theory with some selective results obtained using the Lifting Surface theory [1.39].

Ten equal-length elements are used to compute the free vibration frequencies and mode shapes of the wing. Then the first five normal modes were used to compute the flutter speed and were subsequently found to be adequate. (Results were obtained using six and eight normal modes and no significant changes have been observed.) The investigation is carried out on both swept and unswept wings using the coordinate system and sign convention shown in Fig. 5.1.

Sections 5.2 and 5.3 give brief summaries of published theory used to obtain the results presented, as follows. Section 5.2 covers the theory used by the computer program **CALFUN** in the flutter analysis while section 5.3 presents the solution

techniques used to calculate the flutter speed and flutter frequency from the equation of motion for a harmonically oscillating wing. Then section 5.4 covers very briefly the theory for divergence.

The results of three different but related investigations follow in sections 5.5, 5.6 and 5.7. In particular, section 5.5 investigates the flutter and divergence behaviour when important material and geometrical parameters are varied. In section 5.6 an analytical investigation into the flutter characteristics of composite wings is carried out using the fibre angle as design variable. The aim is to show how the fibre orientation affects the rigidity and coupling parameters and in turn how these affect the flutter and divergence behaviour of composite wings. Then section 5.7 is focused on the aeroelastic stability improvements that can be achieved through the use of the elastic coupling between bending and torsional deformations and torsional rigidity. The main aim is to show in which cases the bending-torsion coupling can be used beneficially to raise and/or eliminate flutter and divergence and in which sticking to the classical theory of aeroelasticity, and thus maximising the torsional rigidity, might be a better choice.

In section 5.8 flutter and divergence results obtained using the Strip theory to model the aerodynamic loads are compared with those obtained using the Lifting Surface theory for three different laminate configurations. Finally, brief conclusions are drawn in section 5.9.

5.2 Flutter Analysis Using CALFUN

CALFUN is a computer program in FORTRAN which uses normal modes and generalised coordinates to compute the flutter speed of an aircraft wing from its basic structural and aerodynamic data [5.3]. The basic normal mode method of flutter analysis for a general wing using generalised coordinates was given by Loring [5.6] and application to high aspect ratio wings has been given by, amongst others, Banerjee [5.4-5.5]. In this section an outline of the method is provided while a detailed presentation of the method is provided in Appendix 'D'.

Basically the method relies on the fact that the dynamic stiffness properties (i.e., the frequency dependent combined mass and stiffness properties) and aerodynamic properties of an aircraft wing can be expressed in terms of the generalised coordinates. **CALFUN** calculates the natural frequencies and normal modes of an aircraft wing and then obtains its generalised dynamic stiffness and aerodynamic matrices, respectively. Then it forms the flutter matrix by algebraically summing the generalised dynamic stiffness and aerodynamic matrices.

In the structural idealisation of the wing, beam elements are used in **CALFUN** to obtain the dynamic stiffness matrix of the wing. The natural frequencies ω_i and the normal mode shapes ϕ_i (where i is the order of the natural frequency/normal mode) are then calculated using the Wittrick-Williams algorithm [1.38, 5.7] (see section 4.3).

The generalised dynamic stiffness matrix $[K_D]$ is obtained by diagonalising the dynamic stiffness matrix with the help of the above mode shapes and making use of the orthogonality condition of the normal mode shapes. In the aerodynamic idealisation CALFUN utilises Strip theory (S-T) based on Theodorsen type unsteady incompressible aerodynamics [5.1, 5.8] (as applied to a high aspect ratio wing), or Lifting Surface (L-S) theory, based on Davies' method [1.39] which takes three-dimensional flow and compressibility into account (see Appendix 'D'). The generalised aerodynamic matrix $[QF]$ is calculated by using one of the above two unsteady aerodynamic theories and the principle of virtual work [5.1, 5.6].

The flutter matrix is formed by summing algebraically the generalised dynamic stiffness and aerodynamic matrices. The flutter determinant, which is formed from the flutter matrix, is a complex double eigenvalue problem which is solved using either the Determinant or the alternative V-g method described in the next section (see Appendix 'D' for illustrative examples).

CALFUN also computes the divergence speed of an aircraft wing using the method described in section 5.4.

5.3 Solution Techniques Using the Determinant and V-g Methods

The equation of motion for an oscillating wing in an airflow can be expressed, using the dynamic stiffness matrix method, as follows,

$$\left(\left[K_D(\omega)\right]-\left[QF\right]\right)\{q\}=\{0\} \tag{5.1}$$

i.e.,
$$\left[F(V,\omega)\right]\{q\}=\{0\} \tag{5.2}$$

where $\left[K_D(\omega)\right]$ represents the generalised dynamic stiffness matrix of the wing and $\left[QF\right]$ is the generalised unsteady aerodynamic force in complex matrix form.

The flutter speed V_F and flutter frequency ω_F are obtained when Eqn. (5.1) is satisfied for the non-trivial case, i.e., when the determinant of the coefficient matrix of Eqn. (5.2) is zero. Two independent methods have been used to find V_F and ω_F. The first is the Determinant method where V_F and ω_F can be obtained in an iterative manner by stepping through a range of airspeeds and frequencies until the determinant of the coefficient matrix is zero. Though accurate, this method is computationally expensive when the search ranges for both airspeed and frequency are large.

The second method is the widely used V-g method [5.9] which converts Eqn. (5.1) into a complex eigenequation problem. To use the V-g method, the generalised mass and stiffness matrices have to be extracted from the generalised dynamic stiffness matrix, $\left[K_D(\omega)\right]$, as follows [2.58] :

$$\left[M_G\right]=\left(\left[K_D(\omega_2)\right]-\left[K_D(\omega_1)\right]\right)/\left(\omega_1^2-\omega_2^2\right) \tag{5.3}$$

$$\left[K_G\right]=\left[K_D(\omega_1)\right]+\omega_1^2\left[M\right] \tag{5.4}$$

where ω_1 and ω_2 are two small, arbitrary values of frequency.

5.4 Divergence

Unlike flutter, divergence is a static aeroelastic problem which can be solved directly without the use of normal modes. The problem becomes a single eigenvalue problem to determine the airspeed (the eigenvalue) and the distribution of torsional rotation (the eigenvector). The divergence analysis is treated as a simplified case of flutter analysis using a similar approach to the Determinant method. The divergence speed V_D can be found when the determinant of Eqn. (5.2) is zero, assuming ω is zero. The theory for divergence analysis is relatively simple and readers are referred to Ref. [5.1].

5.5 Flutter and Divergence Behaviour Through Laminate Design

This study investigates the potential for beneficial interaction among bending-torsion coupling, stiffness ratio, wing sweep and mass balancing. The respective parameters chosen for this investigation are the bending-torsion coupling parameter ψ, defined as $\psi = K/\sqrt{EIGJ}$, the stiffness ratio R = GJ/EI, the sweep angle Λ, and the static unbalance, x_α, defined as the non-dimensional distance (as a fraction of semi-chord) between the shear centre and the centroid of the cross-section. As mentioned earlier, x_α is negative when the mass axis is behind the elastic axis which is usually the case (see Fig. 5.1).

The structural and geometrical properties of the example wing are given in Table 5.1. Three different values of the stiffness ratio R are used, namely 0.05, 0.1 and 0.2 respectively. The stiffness ratio is varied by altering only the bending rigidity (EI) while fixing the torsional rigidity (GJ) to the value given in Table 5.1. The bending-torsion coupling parameter ψ is varied by altering only the bending-torsion coupling rigidity (K).

In Fig. 5.2 the non-dimensional flutter and divergence speeds are plotted against the bending-torsion coupling parameter ψ for an unswept wing. V_{F0} represents the flutter speed of the above wing when R = 0.1 and both ψ and Λ are zero. With no bending-torsion coupling, i.e., when ψ = 0, the flutter and divergence speeds for the

type of wing investigated are about equal. It is interesting to note that the negative ψ, which results in wash-in (bend-up/twist-up) behaviour of the wing when it is loaded vertically, increases the flutter speed and decreases the divergence speed while the opposite occurs when a positive ψ is present. This is in accord with the results of earlier investigations [1.12, 2.69]. The flutter and divergence boundaries intersect near $\psi = 0$ which is an optimum value for this case. This optimum value of ψ varies for different cases depending upon the combination of aerodynamic, geometric and inertia characteristics of the wing. For example, when the divergence speed of a wing is considerably greater than its flutter speed (which is usually the case for unswept and swept-back wings), the intersection point shown in Fig. 5.2 will be shifted to the left and as a result the optimum value of ψ will be negative. Similarly, a positive ψ will be needed when the flutter speed of a wing is higher than its divergence speed.

When the stiffness ratio R increases from 0.1 to 0.2 by reducing EI by a factor of 2, both the flutter and the divergence boundaries are raised on the right hand side of the optimum value of ψ, while on the left hand side of the optimum value the converse is true. A reduction of the stiffness ratio to R = 0.05 has similar but opposite effect on flutter and divergence boundaries as can be seen from Fig. 5.2. Similar observations were made by the author of Ref. [1.12] who did not provide any explanation for their occurrence. The shifts in the divergence boundaries when R is altered occur because when bending-torsion coupling is present (i.e., $\psi \neq 0$), the bending rigidity EI, which is the only factor altered to change R, has significant influence on the degree of wash-in or wash-out present in a structure. For example, when negative ψ is present which causes a wash-in behaviour, a reduction in EI (i.e., increase in R) will contribute to more effective wash-in and thus to a lower divergence speed (see Fig. 5.2). On the other hand when positive ψ is present which causes a wash-out behaviour, lower EI is desirable from the divergence standpoint since it will contribute to more effective wash-out which is beneficial for divergence. In contrast, the same concluding remarks do not apply to flutter where a reduction in EI (i.e., increase in R) which contributes to more effective wash-in when ψ is negative appears not to be beneficial for flutter. This is because flutter, which is a dynamic instability (unlike divergence which is a static instability and thus dependent mainly on wash-in and wash-out effects), is affected by changes in free vibration characteristics of the wing which in turn are affected by changes in rigidity parameters. The way the

free vibration characteristics of a wing influence flutter behaviour will be shown later in this chapter and also in chapter 6.

However, the variation of the stiffness ratio has not significantly shifted the optimum value of ψ in this case. This is due to the fact that for the type of wing investigated, the optimum value of ψ occurs near $\psi = 0$, a region where both flutter and divergence speeds appear to be unaffected by changes in the stiffness ratio, R. However, in cases where the optimum value occurs at a relatively high positive or negative value of ψ, the shift will be much more pronounced.

In Fig. 5.2, the group of divergence boundaries intersect at $\psi = 0$ and thus the divergence speed of an unswept uncoupled wing is unaffected by changes in bending rigidity (EI) as expected. The family of flutter boundaries also intersect but not at a common point. It is important to note that flutter can be theoretically eliminated at ψ values of less than -0.5 whereas divergence can be eliminated for ψ values greater than 0.5. This accords with the earlier investigation reported in Ref. [1.12].

Figure 5.3 presents results for a 30 degree swept-back wing, where the effect of wash-out exhibited by swept-back wings is quite apparent. The family of both flutter and divergence boundaries are shifted to the left when compared to those of the unswept wing. When the wing is swept backwards, a higher negative value of ψ is needed to eliminate flutter and a lower (even negative at high values of stiffness ratio) to eliminate divergence, when compared to those of the unswept wing. Note that at moderate sweep back angles, any value of the bending-torsion coupling parameter will not eliminate flutter when the value of the stiffness ratio is large, R = 0.2 in this case. Even at low stiffness ratio, a high value of elastic coupling between the bending and torsional deformations is needed to eliminate flutter. On the other hand, a high stiffness ratio appears to be advantageous for divergence enhancement of swept-back wings as expected.

By contrast, Fig. 5.4 shows the effect of ψ on flutter and divergence speeds for a 30 degree swept-forward wing. Unlike the swept-back wing, the swept-forward wing shifts the family of flutter and divergence boundaries to the right due to the wash-in exhibited by swept-forward wings. In this case a relatively high positive value of ψ is needed to eliminate divergence and a low value of negative ψ to eliminate flutter.

Figure 5.5 shows the variation of the flutter and divergence speeds with sweep angle Λ for various values of ψ. In this case, the stiffness ratio is kept constant at R = 0.1. The results shown in Fig. 5.5 support the previous findings of Figs 5.2-5.4 that the bending-torsion stiffness coupling affects the flutter speed in an opposite trend to that of the divergence speed. The results also show the beneficial effect of forward and backward sweep on the flutter and divergence speeds respectively.

In Fig. 5.6 the flutter speed for an unswept wing is plotted against ψ for different values of the static unbalance x_α. The stiffness ratio is kept constant at R = 0.1. From Fig. 5.6 it can be seen that the adverse effect of negative x_α (i.e., the centroid situated behind the shear centre) can be negated by use of negative ψ. The value of ψ needed to eliminate flutter follows the value of x_α as this goes from high positive to high negative. Another significant observation that can be made from Fig. 5.6, is that at high negative x_α, a positive ψ is more advantageous than a low-to-moderate negative ψ. It is interesting to note the flutter speed plateau which is reached around $V_F / V_{F0} = 0.7$. This was further investigated and it was found that at certain combinations of x_α and ψ, the flutter speed is unaffected by changes in other geometrical and stiffness parameters. The results of this investigation are presented in chapter 6 along with other important investigations into the flutter characteristics of composite wings.

While the results given in this section are based on simplified studies, some tentative concluding remarks can be made. In general, the results have shown the difficulty that exists to tailor aeroelastically a composite wing. This is due to the required design compromise between flutter and divergence. For instance, an attempt to eliminate divergence of a swept-forward wing by introducing a wash-out (bend-up/twist-down), will significantly lower the flutter speed of the wing. On the other hand, if the object is to increase the flutter speed of the wing, it will inevitably lead to a wash-in (bend-up/twist-up) which is generally undesirable from a divergence point of view. The results show that by trading off between wing sweep, material coupling and geometrical coupling, flutter and divergence can both be eliminated. Furthermore, the study shows the importance of the stiffness ratio R and the different strategies required in choosing this ratio for aeroelastic stability enhancement.

5.6 Flutter and Divergence Behaviour by Use of Fibre Orientation

In section 5.5 the potential for beneficial interaction among bending-torsion coupling, stiffness ratio, mass balancing and wing sweep was demonstrated. The most interesting feature of that investigation was the theoretical finding that both flutter and divergence might be eliminated at relatively low value of the coupling parameter ψ under certain combinations with the other three parameters. The advantage of such a choice of parameters is that one is clearly able to attribute or assign responsibility for any behavioural changes in the structure. However, one important disadvantage of the above method is that the results may not apply to a realistic laminate. As shown in chapter 4, the stiffnesses, EI, GJ and K and as result ψ, change simultaneously when the fibre orientation is changed. Therefore, the potential of the stiffness coupling to eliminate flutter and divergence as illustrated in section 5.5 may not be achievable for a realistic laminated composite wing.

In this study, however, emphasis is given on how the fibre orientation affects the stiffness and coupling parameters of a composite wing, and in turn, how these parameters affect flutter and divergence speeds. The analysis is carried out on five types of cantilever composite wings. The first three are flat laminated composite wings of solid rectangular cross-section with the first and second examples exhibiting bending-torsion coupling. In the third flat laminated wing, there is no coupling between the bending and torsional deformations, i.e., $\psi = 0$. The fourth and fifth types of cantilever wings considered are thin-walled beams where the fourth is of rectangular cross-section (i.e., box-beam) and the fifth is of biconvex cross-section. Both these wings exhibit bending-torsion coupling when they are loaded transversely.

First, uniform composite wings made of flat laminates are considered. Prior to the flutter analysis, the rigidity (stiffness) parameters are obtained by classical lamination theory as applied to thin-walled composite beams and plates (see Eqns (3.24)-(3.26) in Chapter 3). The wings are constructed from Hercules ASI/3501-6 graphite/epoxy and are represented by laminated beams (plates) as shown in Fig. 5.1. Their material and other properties are given in Table 5.2. An aeroelastic analysis is then carried out for three different, but related wing configurations. Each wing was modelled using a total of 14 plies.

In one wing, all the fibres of the laminate are assumed to be oriented along a common direction, denoted by the angle β in degrees so that β is same for each ply. In this case the wing has a very high coupling rigidity K and relatively low GJ which results into a relatively large value of ψ.

A second wing has 14% of the plies assumed to be unidirectional, i.e., $\beta = 0^0$, 28% are oriented symmetrically at $\beta=\pm45^0$ (of which 14% at $\beta=+45^0$ and 14% at $\beta=-45^0$), while the remaining 58% of the plies have an orientation β which may be varied. The stacking sequence of a laminate with 14 plies in this case will be encoded as $(0/\pm45/\beta/\beta/\beta/\beta)_s$. For this wing there is a higher GJ but a lower K, whilst the EI is very little altered giving an average value of ψ.

In the third wing, the lay-up is symmetric and balanced. The plies are oriented successively at $\pm\beta$ giving the uncoupled case with $\psi = 0$.

The variations of the non-dimensional bending stiffness (EI/EI_0), torsional stiffness (GJ/GJ_0), the (dimensional) coupling stiffness (K) and the non-dimensional bending-torsion coupling parameter (ψ) against the ply orientation β, for the three wings are shown in Figs 5.7, 5.8 and 5.9 respectively. In these figures, EI_0 and GJ_0 are the bending and torsional stiffnesses corresponding to the fibre orientation of 0^0 for each of the plies in the laminate. (Note that the coupling stiffness K has not been non-dimensionalised because K = 0 when the fibre orientation of all plies in the laminate is zero (i.e., $K_0 = 0$)). Clearly for wing 3, $K = \psi = 0$. Note that K can be negative, and also in Figs 5.7-5.9, the unit of K used is $N\text{-}m^2$.

Based on the rigidity variations shown in Figs 5.7-5.9, the flutter and divergence speeds are computed for the three wings. Results are expressed in terms of the non-dimensional flutter and divergence speed ratios V_F/V_{F0} and V_D/V_{D0} respectively where V_F and V_D are the flutter and divergence speeds for a given stacking sequence (i.e., one of the above three wings) and V_{F0} and V_{D0} are the corresponding flutter and divergence speeds when the angle of sweep, and the fibre orientation in each of the plies in the laminate representing the wing, are set to zero. The investigation is carried out for both swept and unswept wings. The ply angle is allowed to vary from -90^0 to 90^0 whereas the sweep angle from -40^0 to 40^0. (Note that

the wing is rotated about an axis at the root, perpendicular to the wing planform, to provide the required sweep angle.)

The flutter speed results for wing 1 shown in Fig. 5.10 show that for all sweep angles the maximum flutter speed occurs when the fibre angle is in the range $-10^0>\beta>-30^0$. In this region GJ reaches its maximum value whereas K reaches its minimum, see Fig. 5.7. The variation of flutter speed is quite pronounced in this case, particularly for negative fibre angles (i.e., negative coupling) giving much higher flutter speed than positive fibre angles. It is worth noting in Fig. 5.10 that much higher flutter speeds can be obtained for swept-forward wings when compared to those of swept-back wings.

It is interesting to note that some small blips/abrupt changes in the flutter behaviour are noticeable around $\beta= -5^0$ in Fig. 5.10. These uncharacteristic features of composite wings were further investigated and it will be found later that these occur due to modal interchanges (flip-over) which took place around these ply angles. The results of this investigation are provided in the next chapter along with other important investigations into the flutter behaviour of composite wings.

Figure 5.11 shows the variation of divergence speed with fibre angle for wing 1. The effect of bending-torsion coupling is quite pronounced in this case as well. In the case of swept-forward wing, the results show that the elastic coupling between bending and torsional deformations can successfully overcome the undesirable effect (wash-in) of swept-forward wings on divergence when the wing is designed to exhibit wash-out (i.e., when β is positive). In particular, for the type of swept-forward wing investigated, divergence is eliminated in the region of around $10^0<\beta<45^0$. This range corresponds to high positive bending-torsion coupling as evident in Fig. 5.7. However, when the wing is swept backwards, divergence is eliminated at any positive fibre angle.

The results for wing 2 (see Fig. 5.12) show a relatively small variation in flutter speed when compared to those of wing 1. The maximum is found to be occurring at a fibre angle of around -35^0 at which GJ is maximum and K is more or less minimal, see Fig. 5.8. In this case, the effect of coupling is not so pronounced. It may thus be concluded that, in general, when coupling is present, the maximum

flutter speed occurs in the region of maximum GJ and minimum K. The fibre angles in the region $-35^0<\beta<-15^0$ appear to be most effective in giving the maximum flutter speed for wings of the type investigated.

Figure 5.13 illustrates the effect of fibre angle on divergence speed for the wing 2. In the case of swept-forward wing the divergence speed is not eliminated for the specific example investigated. However, it can be significantly raised in the region of high positive ψ. In contrast, divergence is not a problem for the swept-back wing as can be seen from Fig. 5.13. This is due to the lower value of negative bending-torsion coupling (wash-in) present in wing 2 when compared to that of wing 1 (see Figs 5.7 and 5.8).

The results shown in Fig. 5.14 are for the flutter of wing 3 in which K and ψ are both zero (i.e., the uncoupled case). The results clearly indicate that the maximum flutter speed for the unswept and swept-forward wings can be obtained when the plies are alternatively at angles $\pm45^0$ which gives the maximum possible GJ. Interestingly, the maximum achievable flutter speed for the unswept wing 3, shown in Fig. 5.14, is much higher than the corresponding (unswept) flutter speeds (obtained when ψ had maximum negative value) shown in Figs 5.10 and 5.12.

Figure 5.15 shows the variation of divergence speed with fibre angle for wing 3. As in the case of flutter speed, the maximum divergence speed for the unswept wing 3 can be obtained when the plies are alternatively at angles $\pm45^0$ which gives the maximum GJ. This is because the wing is uncoupled and its resistance to torsional rotation is a maximum when its torsional rigidity is a maximum. When the wing is swept backwards no divergence is apparent due to the wash-out behaviour exhibited by swept-back wings. When the wing is swept forward, however, the divergence speed reduces rapidly with fibre angle due to the wash-in effect (which is detrimental to divergence) introduced by the wing sweep. The wash-in effect becomes more effective as the bending rigidity of the wing reduces as explained earlier in section 5.5. In other words, when forward sweep is present for a materially uncoupled wing, the behaviour of divergence speed as a function of fibre angle is similar to that of bending rigidity (see Fig. 5.9). It is interesting to note the sensitivity of divergence speed to bending-torsion coupling (wash-in or wash-out) as opposed to GJ which can be useful when the wing is uncoupled.

The effect of sweep angle is quite pronounced for all the three wings as can be seen from Figs 5.10-5.15. The divergence speed increases as the sweep angle changes from a high negative to a high positive value. This was found in all three cases investigated. The flutter speed increases with the angle of sweep (back and forward) for wings 1 and 2 in which the coupling parameters K and ψ have significant values. Although the flutter behaviour of the swept-forward wing 3 is similar to that of wings 1 and 2 (i.e., the flutter speed increases with angle of sweep) no predictable pattern seems to be apparent in the case of wing 3 when it is swept back. It is worth noting that for the swept-back wing 3, the maximum flutter speed does not occur at the maximum GJ (i.e., when the plies are alternatively at angles $\pm 45^0$) which was the case for the unswept and swept-forward wings. Furthermore as the angle of sweep increases backwards, the maximum flutter speed occurs at a reduced fibre orientation (i.e., at less than 45^0). Although not explicitly referred to by the authors, this phenomenon was also shown in Fig. 6 of Ref. [1.9].

The fourth wing used as an example in this investigation is the cantilever box-beam of Ref. [1.7] with lay-up: [β] in the top wall, [-β] in the bottom wall and [β/-β] in the vertical walls. The cross-section of the box-beam is shown in Fig. 5.16 while its material and other properties are given in Table 5.3. This Circumferentially Asymmetric Stiffness (CAS) configuration exhibits bending-torsion coupling when it is loaded vertically (see chapter 3 and also Ref. [1.7]). Using the basic material properties given in Table 5.3, the rigidity properties were calculated using the theory developed in Ref. [2.85]. This stiffness model corresponds to Eqns (3.79)-(3.81) of chapter 3.

Figure 5.17 shows the variation of the non-dimensional flutter and divergence speeds with ply orientation for the above composite cantilever box-beam. Both flutter and divergence speeds are non-dimensionalised with respect to the divergence speed for $\beta = 0^0$. The results of the present study are shown alongside the finite element results of Ref. [1.7]. Apart from some small discrepancies in the flutter speed in the region of positive ply orientation, the agreement between the two set of results is quite good.

Figure 5.17 shows trends similar to those of the unswept laminated wing 1 of Figs 5.10 and 5.11. Very high flutter speeds are evident in the region of maximum GJ

and minimum ψ. As for divergence, positive ply orientations produce a favourable bending-torsion coupling, leading to very high divergence speeds as expected.

The fifth wing used in this investigation is the thin-walled biconvex cross-section of Refs [5.10-5.11]. The geometrical and other properties of the wing are shown in Fig. 5.18, see Table 5.3 for material properties. The variation of non-dimensional flutter and divergence speeds against the fibre angle is shown in Fig. 5.19. For divergence speeds, the results of the present investigation are shown alongside the results of Ref. [5.10]. (Comparison of flutter speeds has not been possible because Ref. [5.10] does not give such results.) Although the present theory underestimates the divergence speeds of the biconvex wing, the agreement between the two set of results is quite satisfactory. The difference in results can be attributed to the following reason. In the present investigation, the rigidity properties of the wing were obtained using the stiffness model of Ref. [2.85] where the cross-section is represented by twenty-four uniform straight elements. This idealisation underestimates the stiffness properties as opposed to the idealisation of Ref. [5.10] where an exact theory based on variational method was used.

Therefore, the results given in this section also confirm the difficulty that exists to tailor aeroelastically a composite wing. In particular, passive stability enhancement involves a compromise on the magnitude and sense (sign) of the bending-torsion coupling parameter ψ. An attempt to eliminate the divergence of a wing by the use of positive ψ might appreciably lower the flutter speed of the wing undesirably, and vice-versa. One interesting aspect of this study is that, in contrast to the study of section 5.5 where the flutter speed was shown to be eliminated at negative values of ψ of less than -0.5, when a laminated wing is used the flutter speed is not eliminated even when the maximum possible negative ψ is used, i.e., ψ = - 0.707 (see, for example, Figs 5.2 and 5.10). On the other hand, this study confirms the ability of positive ψ to negate the undesirable effect of sweeping a wing forward, so making its design and production possible.

In can be generally concluded from this investigation that a combination of high GJ and negative ψ, coupled with high forward sweep maximises the flutter speed. On the other hand, maximising positive ψ and aft sweep maximises divergence speed. However, it should be noted that GJ and ψ are inversely

proportional to each other, and also that the rigidities EI, GJ and K are not all independent. Therefore a delicate balance is needed to achieve the best possible aeroelastic stability.

5.7 The Importance of Torsional and Bending-Torsion Coupling Rigidities on the Aeroelastic Behaviour of Composite Wings

In section 5.6 the variation of flutter and divergence speeds with fibre orientation was demonstrated for both swept and unswept wings. Various laminate configurations were used, such as, an uncoupled laminate offering the maximum GJ, and a unidirectional laminate offering the maximum ψ. Although significant variation in flutter speed was observed as the plies of a unidirectional laminate were reoriented similar to Ref. [1.6], a laminate configuration with higher GJ may give much higher flutter speed in certain cases, see for example Figs 5.10 and 5.14.

The above observations partly motivated the present work as it does not appear to be clear yet whether, by incorporating the stiffness coupling in the analysis, higher aeroelastic stability can be achieved than by maximising GJ. Therefore, this study is focused on the aeroelastic stability improvements that can be achieved through the use of the elastic coupling between bending and torsional deformations and the torsional rigidity. Results obtained by laminates possessing various values of ψ are presented alongside those obtained by two uncoupled wings, one of which is the uncoupled laminate offering the maximum possible GJ and the other is a comparable metallic wing made of aluminium. The aim is to show in which cases the bending-torsion coupling can be beneficially used to raise and/or eliminate flutter and divergence and in which cases sticking to the classical theory of aeroelasticity and thus maximising GJ can be a better choice.

Five example wings are considered in this case, of which four have the same material and geometrical properties (but different ply orientations) as the 14 ply laminates used in section 5.6. The fifth is constructed from aluminium and has the same geometrical properties as the composite examples. The material and other properties for the graphite/epoxy wings are show in Table 5.2. The material properties

for the metallic wing were obtained from Ref. [2.21] and shown along with the calculated structural properties in Table 5.4.

In the first laminated wing (wing 1) all the plies in the laminate are oriented symmetrically at $\beta = \pm 45^0$ giving the maximum possible GJ but zero bending-torsion coupling (i.e., $\psi = 0$ in this case). In the other three laminated wings, a stiffness coupling is introduced progressively until the maximum coupling is achieved, that is, the laminate configuration $[\beta_{14}]$ (wing 4) which was also used in section 5.6. The two intermediate wings are $[\pm 45_2 / 45 / \beta_4 / -45 / \pm 45_2]$ (wing 2) and $[\pm 45 / 45 / \beta_8 / -45 / \pm 45]$ (wing 3).

Firstly the non-dimensionalised rigidity and coupling parameters are plotted against the fibre angle, β, for the five wings, see Figs 5.20-5.22. In these figures, EI_0 and GJ_0 are the bending and torsional rigidities corresponding to the fibre orientation of 0^0 for each of the plies in the laminate. The rigidity properties for the aluminium wing and laminated wing 1 are shown with horizontal lines since they are not affected by changes in the fibre angle, β. Figure 5.20 shows that the unidirectional laminate (wing 4) gives the highest bending rigidity at $\beta = 0^0$ whereas wing 1 ($[\pm 45^0_7]$) gives the lowest. It is interesting to note the very high bending rigidity offered by the aluminium wing.

Figure 5.21 shows the variation of ψ with fibre angle, β, for wings 2, 3 and 4. Results for the aluminium wing and laminated wing 1 are not shown in this case since no bending-torsion coupling is present (i.e., $\psi = 0$). The torsional rigidity GJ is shown against the fibre angle for the five wings in Fig. 5.22. The results in Figs 5.21 and 5.22 show that the unidirectional laminate (wing 4) gives the most pronounced variation of ψ and GJ. It gives the maximum ψ and the lowest GJ at any fibre angle β when compared to the other three laminated wings. The relatively low GJ given by the aluminium wing is worth noting.

Based on the rigidity variations, the ratio of the (uncoupled) fundamental torsional to fundamental bending natural frequencies (ω_α / ω_h) for the five wings is also plotted against the fibre angle in Fig. 5.23. In classical aeroelasticity, this frequency ratio is regarded as the single most important factor influencing the flutter speed of metallic wings (see Figs 9.7 and 9.8 of Ref. [5.1]). It was shown that as this

non-dimensional frequency ratio increases, the flutter speed increases as well [5.1, 5.12]. The same conclusion was also drawn by Banerjee [5.2] in his parametric investigation into the flutter characteristics of metallic wings. However, as can be seen from Fig. 5.23, in the case of composite materials the frequency ratio (ω_α / ω_h) can be very high when both EI and GJ decrease with the former falling off more rapidly (see Figs 5.20 and 5.22). With the laminated plate model used to calculate the rigidity properties, this occurs when $\beta>30^0$. Therefore from the flutter standpoint, the optimum value of the frequency ratio ω_α / ω_h is achieved when the GJ of the wing is a maximum whereas EI is relatively low (see, for example, Figs 5.20 and 5.22). These values are shown in Fig. 5.23 as D, C, B and A for the four laminated wings respectively. Thus, the optimum value of ω_α / ω_h is given by wing 1 which offers the maximum possible GJ and relatively low EI. In contrast, the frequency ratio ω_α / ω_h for the aluminium wing is very low which is detrimental from the flutter standpoint.

Based on rigidity variations, the non-dimensional flutter and divergence speeds are computed for the five wings and shown in Figs 5.24-5.28. Figure 5.24 shows the variation of flutter speed with fibre angle for the five wings. The flutter speed for wing 1 is shown with dotted line for clarity. In Fig. 5.24, although the variation of flutter speed is more pronounced when bending-torsion coupling is present, none of the three laminated wings gives higher flutter speed than wing 1 which offers the maximum GJ. This observation is in sharp contrast to the generally adopted views of many researchers that the bending-torsion coupling can always be turned to an advantage in increasing the flutter speed of a composite wing. Furthermore, the maximum flutter speed for wings 2, 3 and 4 are also obtained when their GJ is maximum, i.e., when ω_α / ω_h corresponds to points C, B and A of Fig. 5.23 respectively. As ψ is reduced and GJ is increased (i.e., wings 4, 3, and 2 respectively), the flutter speed tends towards the value given by wing 1. It is important to note the similarities that exist between the variations of GJ and flutter speed with fibre angle, see Figs 5.22 and 5.24. As for the aluminium wing, it gives very low flutter speed when compared to those given by the first three laminated composite wings but it gives higher flutter speed for a wide range of fibre angles than those given by wing 4.

In contrast, the divergence results in Fig. 5.25 show a completely different picture. For wing 4 the divergence speed is eliminated at any positive fibre angle. However, as ψ is reduced and GJ is increased (i.e., wings 3, 2 and 1 respectively), the

range of positive fibre angles that can eliminate divergence is reduced. It is important to note that even with a very low value of positive ψ (see, for example, wing 2 where ψ = 0.023), the divergence of the unswept composite wing can be eliminated. This is very important since in the design of a realistic composite wing, only a small percentage of plies in the laminate will be available for aeroelastic considerations. Thus, it is possible in practice to eliminate divergence of unswept wing by introducing only a small amount of positive bending-torsion coupling. These results are in accord with the two earlier investigations of sections 5.5 and 5.6.

Figure 5.26 shows the flutter speed against fibre orientation for the five wings when 30 degree forward sweep is present. (Note that, like the investigation reported in section 5.6, the wing is rotated about an axis at the root, perpendicular to the wing planform, to provide the required sweep angle.) In this case the flutter speed can be raised above the one given by wing 1 only when the maximum negative ψ is present, i.e., the case of wing 4 with the fibre angle of all plies in the laminate set to $\beta = -25^0$. It should be noted, however, that strength considerations would preclude the use of such a laminate in actual design and thus maximising GJ appears to offer a better prospect of maximising the flutter speed of swept-forward wings. Furthermore, this laminate configuration is accompanied by low divergence speed (see, for example, Figs 5.10 and 5.11).

In Fig. 5.27 where the divergence speed is plotted against the ply angle β for a 30 degree swept-forward wing, wing 1 gives a very low divergence speed which is even lower than the one given by the aluminium wing. This can be attributed to the fact that wing 1 gives the lowest bending rigidity (see Fig. 5.20) and since it is materially uncoupled, the wash-in exhibited by swept-forward wings is very effective in this case. On the other hand, the aluminium wing offers a very high bending rigidity and as result the wash-in effect is less effective, thus giving a higher divergence speed than wing 1. Very high divergence speeds can be obtained when ψ has significant positive values, as in the case of wing 4. Note that very high divergence speeds can be achieved by utilising laminates that exhibit only a small amount of positive bending-torsion coupling without significantly affecting the flutter speed (see wing 2 in Figs 5.26 and 5.27).

The results in Fig. 5.28 correspond to the 30 degree swept-back wing. In contrast to the swept-forward wing, the flutter speed can be significantly raised above that given by wing 1 if small amount of negative ψ is present. Results for divergence are not shown since the specific swept-back wing investigated is free from divergence instabilities.

5.8 Comparison of Flutter and Divergence Speeds Using Strip and Lifting Surface Theories

Since the Strip Theory (S-T) is based on two-dimensional (2D) incompressible flow, it should be less accurate than the Lifting Surface (L-S) theory which takes into account the effect of three-dimensional (3D) compressible flow. In order to compare the results obtained using the above two theories, the three laminated unswept wings of section 5.6 were taken as test examples. The calculated flutter and divergence speeds for the three unswept wings are shown in tabular form in Tables 5.5 and 5.6 and graphically in Figs 5.29-5.31. From Table 5.5 and Figs 5.29-5.31, it can be seen that the agreement between the two set of flutter results is generally quite satisfactory, (i.e., the disagreement is within 10%). However, the effect of compressibility and that of finite span become more apparent in the case of divergence where the disagreement between the two theories is generally within 25%, see Table 5.6 and Figs 5.29-5.31.

Generally, the Strip theory gives lower flutter and divergence speeds. This is in part, due to lower lift curve slopes in Lifting Surface theory as opposed to higher ones in Strip theory. However, the lower flutter and divergence speeds given by Strip theory would give a greater margin of safety compared with those given by the Lifting Surface theory. The behaviour of flutter and divergence speeds as a function of fibre angle is similar for both theories with the maximum instability speeds occurring at the same fibre angle in all three cases, see Figs 5.29-5.31. Hence for quick, adequate and preliminary results, aeroelastic analysis of high aspect ratio wings using Strip theory would seem to be justified.

5.9 Conclusions

One interesting aspect of aeroelastic tailoring studies presented in this chapter is the required compromise between flutter speed and divergence speed. One striking feature is that the ply orientations in a given laminate which result in the wash-in effect was shown to increase the flutter speed of composite wings, while decreasing the divergence speed. Conversely, the objective of an increased divergence speed invariably leads to a wash-out effect which is likely to be accompanied by a lower flutter speed. These results are in line with previous studies, such as, the ones carried out by Weisshaar [1.6, 1.12] and Lottati [2.69].

The use of aeroelastic tailoring to increase wing wash-out can achieve a compromise, or harmonious balance, between flutter and divergence speeds of a swept-forward wing whose divergence speed is usually lower than the flutter speed. Conversely, the increase in wing wash-in can achieve the same balance when the wing is swept-back where flutter speed is usually lower than divergence speed.

Perhaps the most intriguing feature of these investigations is that they have shown (in contrast to all previous investigations [1.6, 1.12, 2.69]) that the torsional rigidity GJ can be the most important parameter to be considered when the objective is that of increased flutter speed. The study showed that flutter speed is more sensitive to changes in the non-dimensional frequency ratio ω_α / ω_h rather than changes in the mode shapes by the use of bending-torsion stiffness coupling. This is especially true for the unswept and swept-forward wings. However, a negative bending-torsion coupling, which results into the wash-in effect, can be beneficial for the flutter of swept-back wings.

As for divergence, the results have shown that the divergence speed is solely dependent on wash-in and wash-out effects and, as a consequence, on ψ. The torsional rigidity GJ is the most important parameter to be considered when the object is that of maximising the divergence speed of unswept, symmetric and balanced laminated wings for which there is no coupling present.

TABLE 5.1

Structural and geometrical properties for the example wing of section 5.5

Parameter	Value / unit
EI	9.870×10^6 Nm^2
GJ	0.987×10^6 Nm^2
m/L	35.75 Kg/m
I_α	7.473 Kgm
x_α	0.0
L	6.096 m
semi-chord (b)	0.9144 m

TABLE 5.2

Material and other properties for Hercules ASI/3501-6 graphite/epoxy wings

Property	Value/Unit
E_1	98.0 GN/m^2
E_2	7.90 GN/m^2
ν_{12}	0.28
$G_{12} = G_{13} = G_{23}$	5.60 GN/m^2
Density	1520 Kg/m^3
m/L	0.2172 Kg/m
I_α	0.1052×10^{-3} m
Ply thickness	0.134×10^{-3} m
L	0.6 m
semi-chord (b)	0.0381 m
x_α	0.0
a	0.0

TABLE 5.3

Material and other properties for the graphite/epoxy example wing 4 of section 5.6 [1.7].

Property	Value/Unit
E_1	206.92 GN/m^2
E_2	5.17 GN/m^2
ν_{12}	0.25
$G_{12} = G_{13} = G_{23}$	3.10 GN/m^2
Density	1529.5 kg/m^3
m/L	8.8414 Kg/m
I_α	0.05993 Kgm
x_α	0.0
L	2.032 m

TABLE 5.4

Material and structural properties for the aluminium wing of section 5.6 [2.21].

Property	Value/Unit
E	73.11 GN/m^2
G	27.50 GN/m^2
γ	0.33
Density, ρ	2768 kg/m^3
EI	3.0648 Nm^2
GJ	1.3104 Nm^2
m/L	0.3955 Kg/m
I_α	1.9158×10^{-4} Kgm

TABLE 5.5

Comparison of flutter speeds (m/s) obtained using Strip theory and Lifting Surface theory for the three unswept laminated wings of section 5.6.

	WING 1 $[\beta]_{14}$			WING 2 $[0/\pm45/\beta/\beta/\beta/\beta]_s$			WING 3 $[\pm\beta]_7$		
β, degrees	**S-T**	**L-S**	**% difference**	**S-T**	**L-S**	**% difference**	**S-T**	**L-S**	**% difference**
-90	32.3	33.5	-3.79	51.5	52.3	-1.45	32.23	33.5	-3.79
-80	32.8	34.0	-3.50	52.6	53.2	-1.09	38.23	40	-4.43
-70	34.4	35.5	-3.04	54.1	55.1	-1.80	50.77	53.2	-4.57
-60	37.5	39.0	-3.97	55.5	57.6	-3.49	61.76	64.7	-4.54
-50	41.8	43.5	-3.89	56.7	58.2	-2.63	67.98	71.4	-4.79
-45	-----	-----	-----	-----	-----	-----	68.73	71.7	-4.14
-40	47.4	49.0	-3.35	56.9	58.9	-3.34	67.86	71.15	-4.62
-35	50.4	51.0	-1.25	56.6	58.1	-2.63	-----	-----	-----
-30	52.4	53.0	-1.08	55.6	57.4	-3.08	61.42	63.5	-3.28
-25	53.2	62.5	-14.82	54.4	55.8	-2.53	-----	-----	-----
-20	51.6	51.0	1.24	53.2	54.6	-2.66	52.64	49.5	6.34
-10	39.9	32.0	24.56	51.0	51.0	0.08	38.91	42.45	-8.34
-5	-----	-----	-----	-----	-----	-----	34	37.35	-8.97
0	32.4	35.3	-8.03	53.5	51.0	4.86	32.42	35.25	-8.03
5	-----	-----	-----	-----	-----	-----	34	37.35	-8.97
10	32.6	35.5	-8.14	53.1	52.7	0.70	38.91	42.45	-8.34
20	35.2	38.8	-9.16	54.4	55.2	-1.38	52.64	49.5	6.34
25	35.4	39.3	-9.81	55.6	56.8	-2.08	-----	-----	-----
30	35.0	39.2	-10.76	56.9	57.1	-0.37	61.42	63.5	-3.28
35	34.0	39.0	-12.82	56.6	57.4	-1.46	-----	-----	-----
40	33.8	38.7	-12.56	55.9	57.4	-2.70	67.86	71.15	-4.62
45	-----	-----	-----	-----	-----	-----	68.73	71.7	-4.14
50	33.0	38.6	-14.51	55.3	55.8	-0.84	67.98	71.4	-4.79
60	32.8	37.0	-11.35	54.7	54.0	1.20	61.76	64.7	-4.54
70	33.1	35.7	-7.28	52.9	53.0	-0.15	50.77	53.2	-4.57
80	32.7	34.2	-4.30	51.7	52.2	-0.90	38.23	40	-4.43
90	32.2	33.6	-3.93	51.6	52.7	-2.13	32.23	33.5	-3.79

TABLE 5.6

Comparison of divergence speeds (m/s) obtained using Strip theory and Lifting Surface theory for the three unswept laminated wings of section 5.6.

	WING 1 $[\beta]_{14}$			WING 2 $[0/\pm45/\beta/\beta/\beta/\beta]_s$			WING 3 $[\pm\beta]_7$		
β, degrees	**S-T**	**L-S**	**% difference**	**S-T**	**L-S**	**% difference**	**S-T**	**L-S**	**% difference**
-90	34.0	40.2	-15.47				34.0	40.2	-15.47
-80	19.8	23.2	-14.83				40.4	47.7	-15.32
-70	15.4	19.5	-21.08				53.4	62.6	-14.76
-60	13.1	17.0	-23.24				64.9	76.1	-14.69
-50	11.8	15.8	-25.32	58.2			71.5	83.5	-14.40
-45	-----	-----	-----	-----	-----	-----	72.4	84.5	-14.30
-40	11.2	14.5	-22.97	43.8	68.7	-36.20	71.5	83.5	-14.40
-35	11.2	13.7	-18.47	39.6	52.5	-24.55	-----	-----	-----
-30	11.3	13.5	-16.07	37.3	47.7	-21.87	64.9	76.1	-14.69
-25	11.8	13.7	-13.87	36.3	45.1	-19.45	-----	-----	-----
-20	12.6	14.4	-12.64	36.6	43.7	-16.16	53.4	62.4	-14.49
-10	15.9	19.4	-18.25	42.3	50.6	-16.46	40.4	47.6	-15.15
-5	-----	-----	-----	-----	-----	-----	35.7	42.1	-15.20
0	34.0	40.0	-15.05	66.5	76.4	-12.98	34.0	40.0	-15.05
5							35.7	42.1	-15.20
10							40.4	47.6	-15.15
20							53.4	62.4	-14.49
25							-----	-----	-----
30							64.9	76.1	-14.69
35							-----	-----	-----
40							71.5	83.5	-14.40
45							72.4	84.5	-14.30
50							71.5	83.5	-14.40
60							64.9	76.1	-14.69
70				68.1	78.4	-13.20	53.4	62.6	-14.76
80				60.2	70.6	-14.69	40.4	47.7	-15.32
90				45.5	51.0	-10.78	34.0	40.2	-15.47

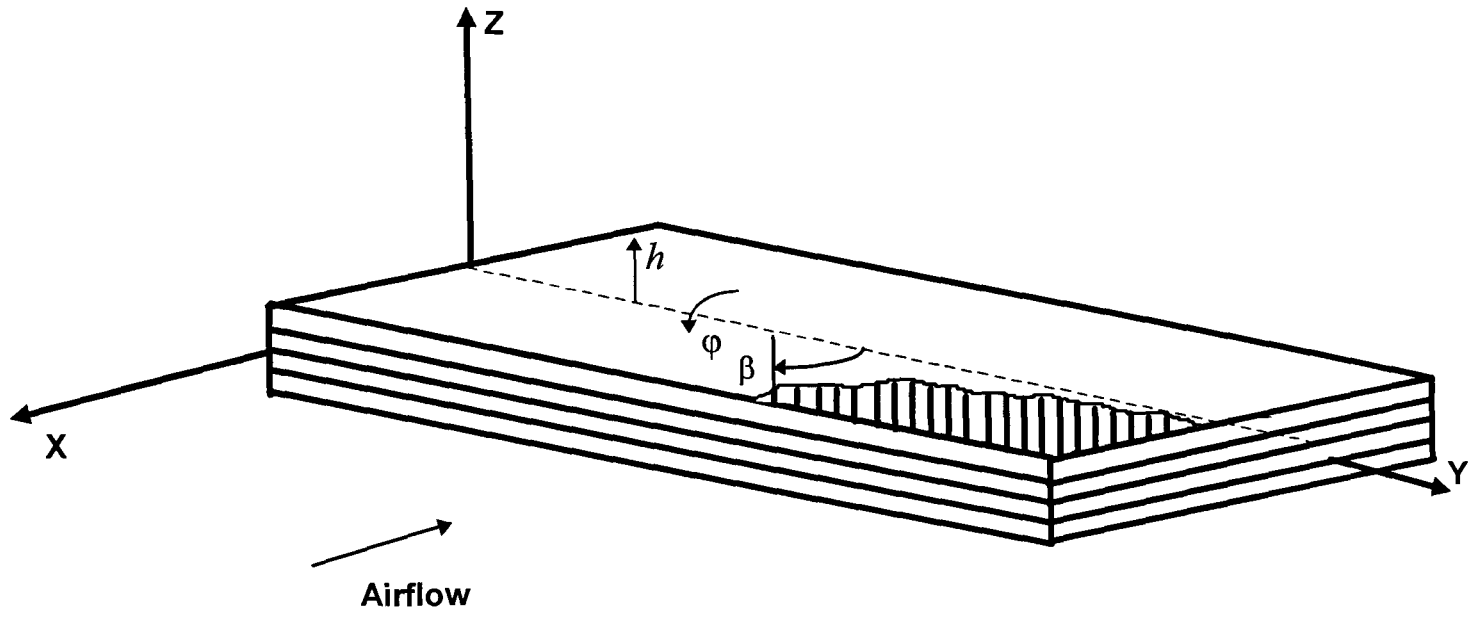

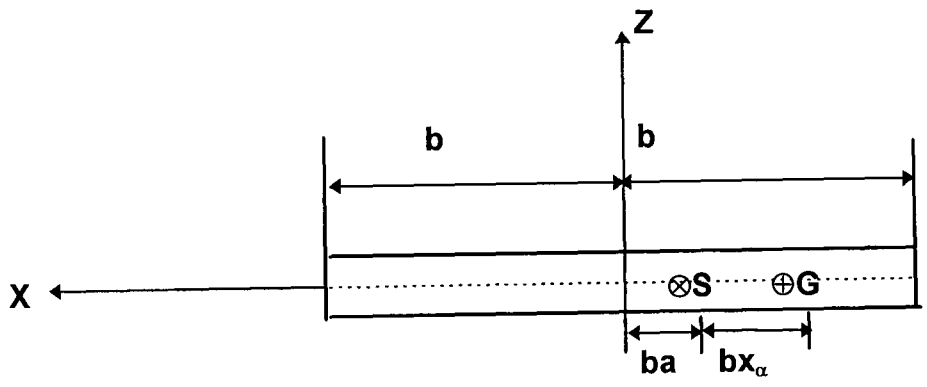

Fig. 5.1. Coordinate system and sign convention for a laminated composite beam;
(S : Shear centre ; G : Centroid).

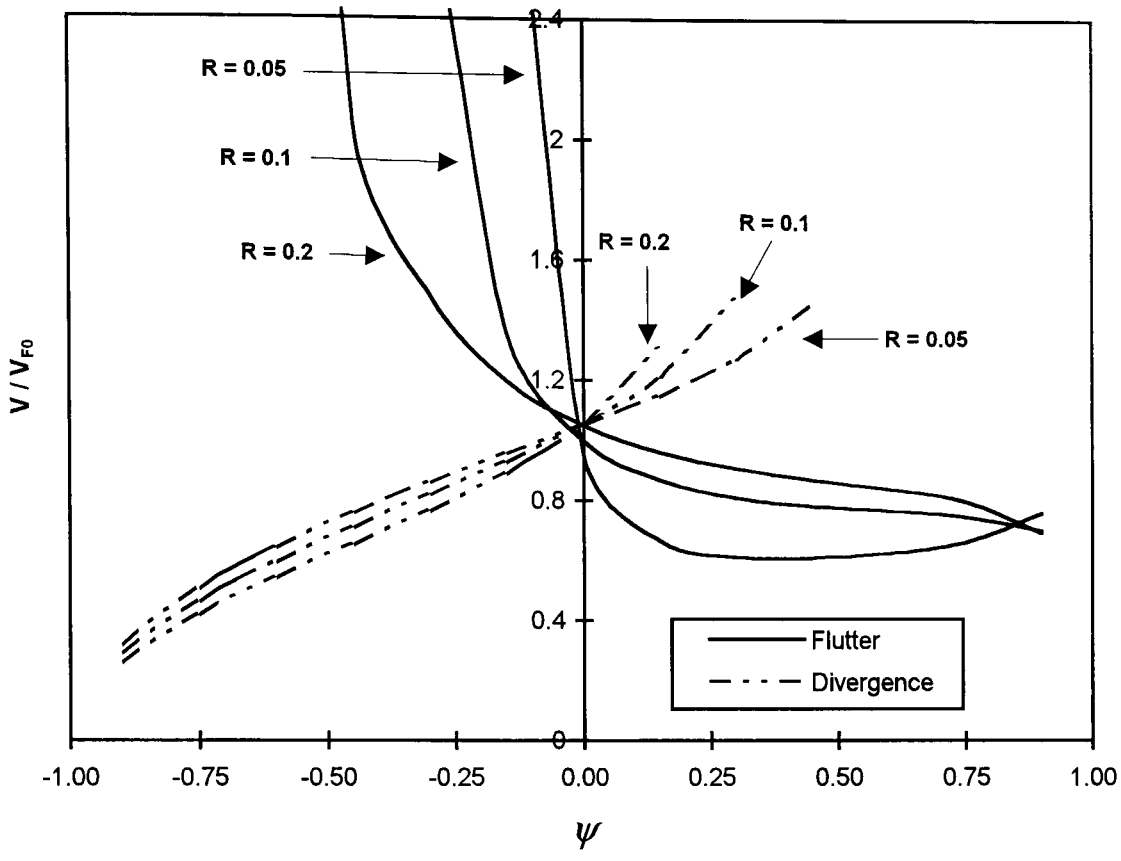

Fig. 5.2. Flutter and divergence speed boundaries as functions of ψ and R for an unswept wing.

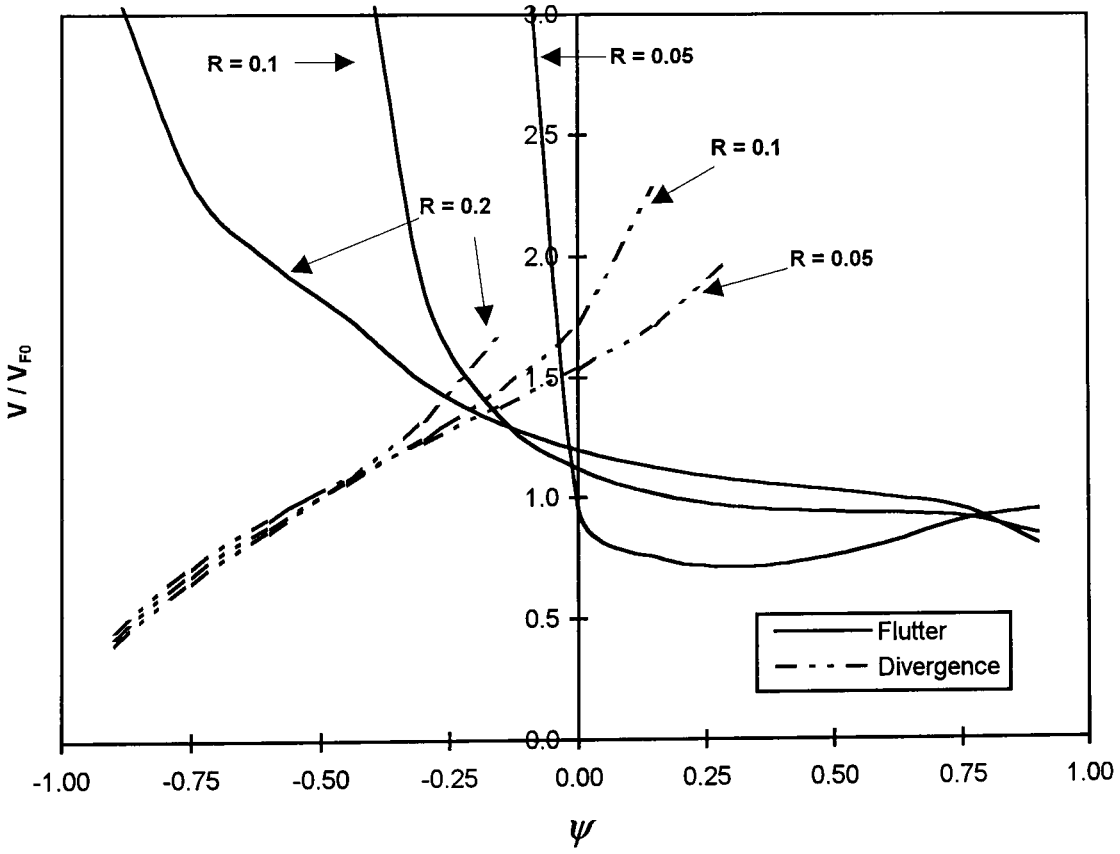

Fig. 5.3. Flutter and divergence speed boundaries as functions of ψ and R for a 30 degree swept-back wing.

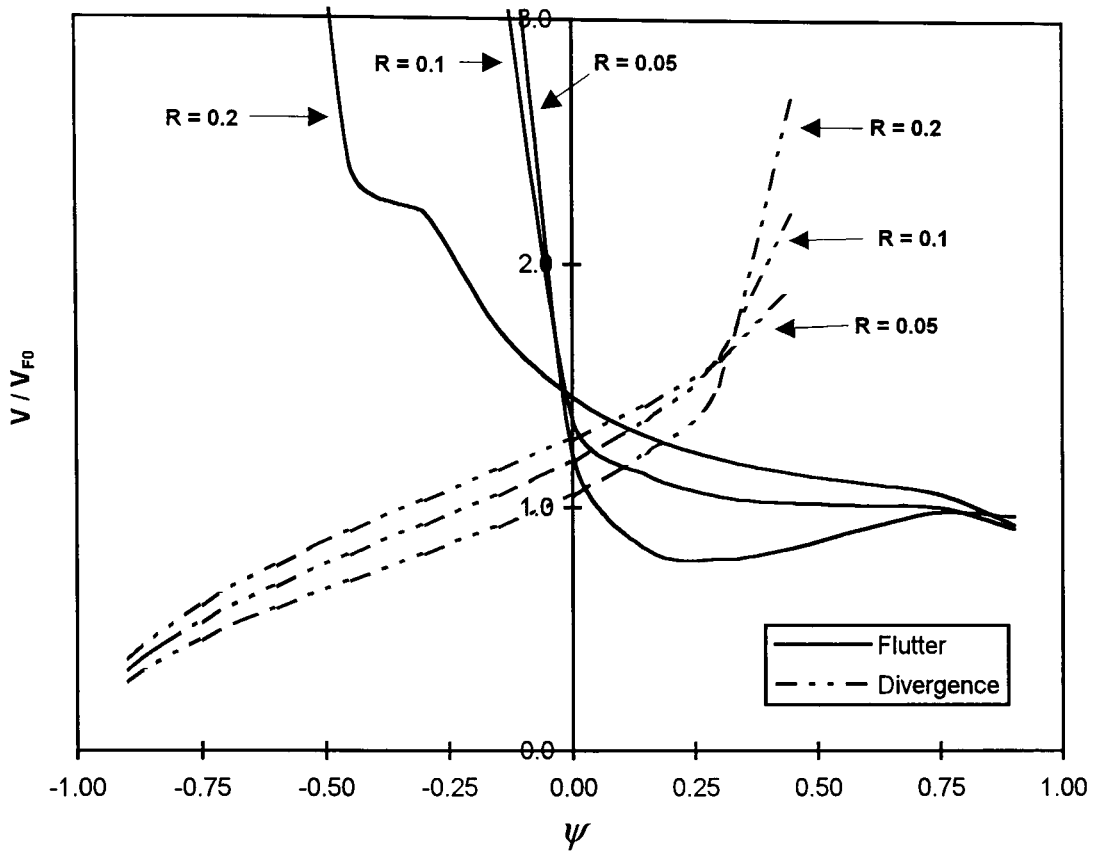

Fig. 5.4. Flutter and divergence speed boundaries as functions of ψ and R for a 30 degree swept-forward wing.

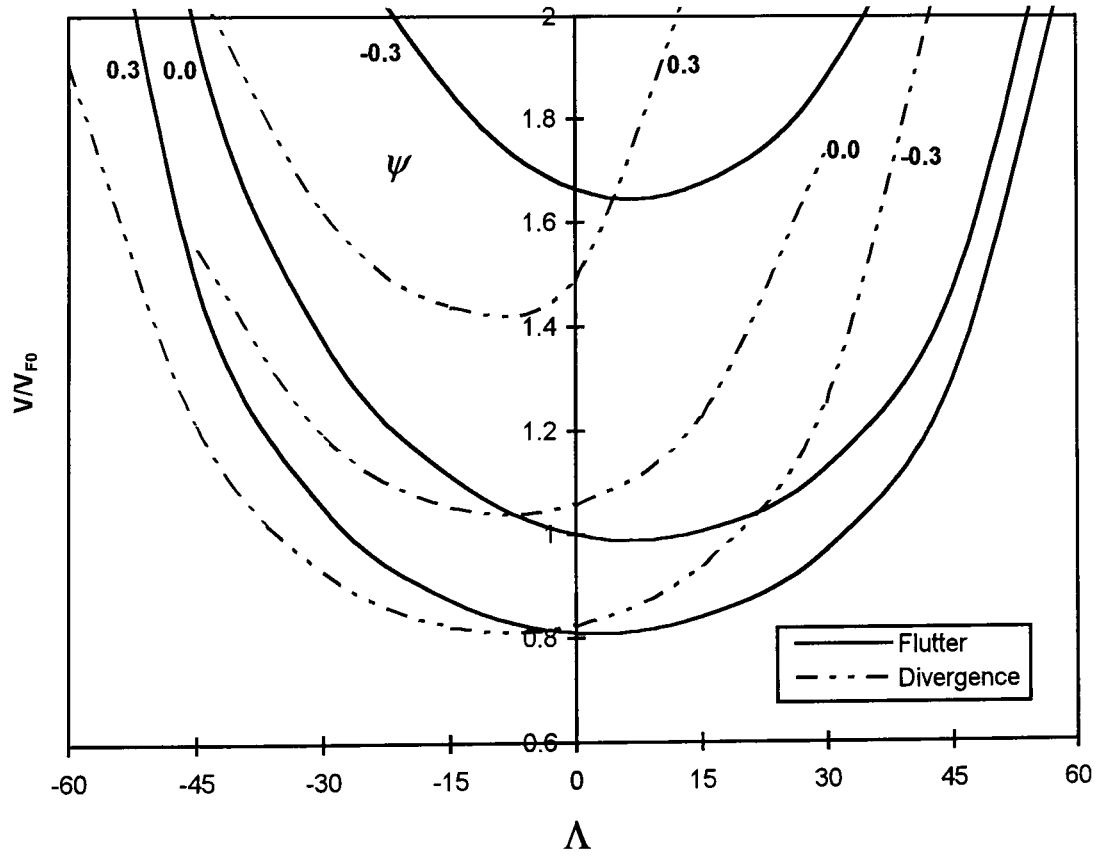

Fig. 5.5. Flutter and divergence speed boundaries as functions of Λ and ψ for an unswept wing, R = 0.1.

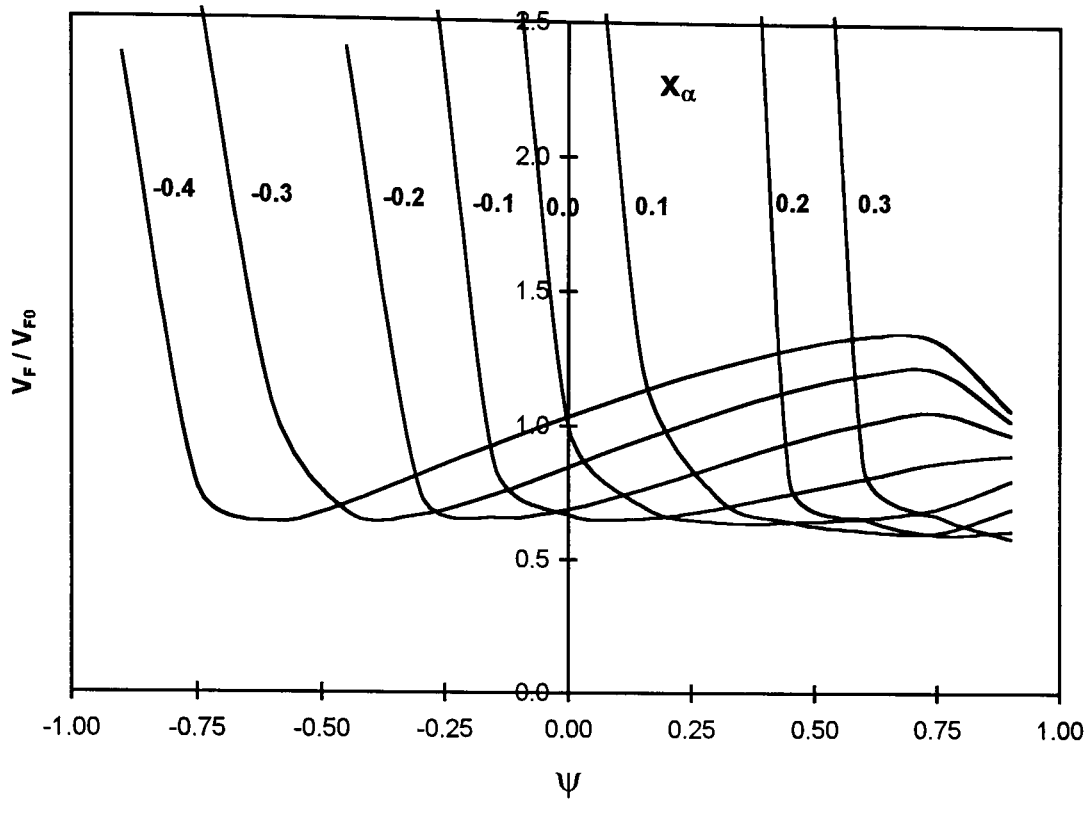

Fig. 5.6. The behaviour of flutter speed as a function of ψ and x_α for an unswept wing, R = 0.1.

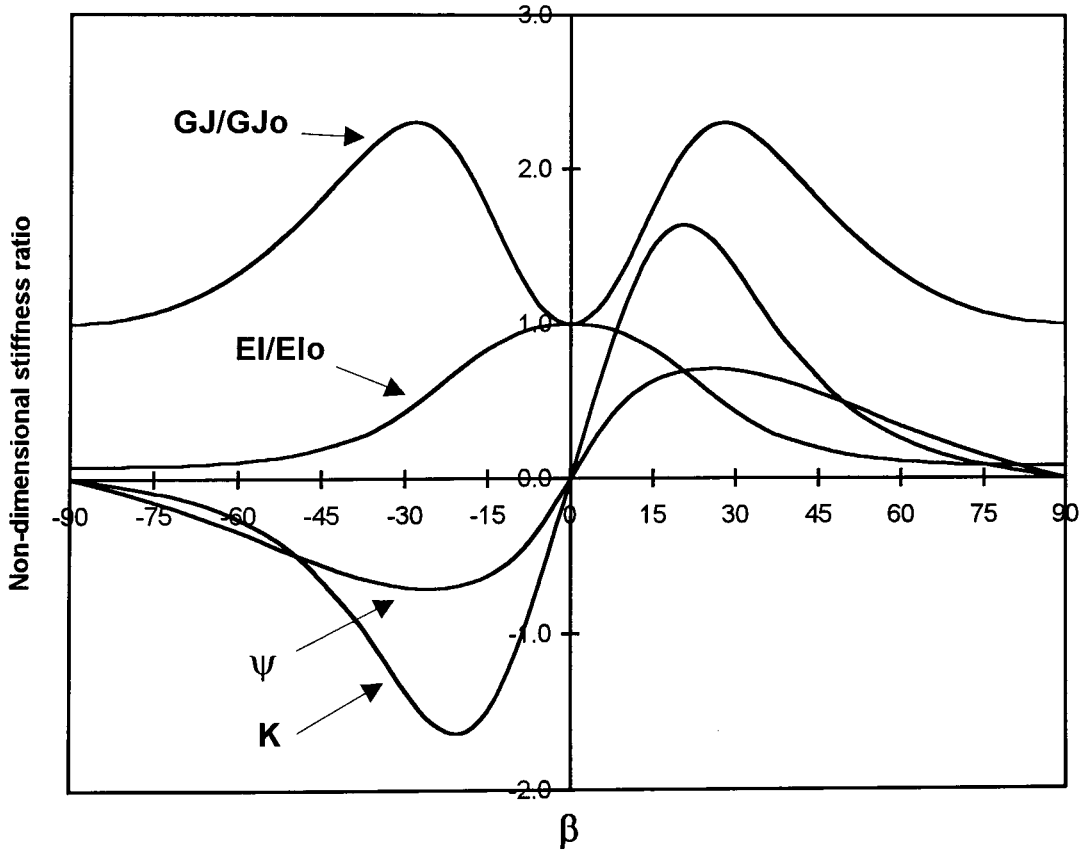

Fig. 5.7. Variation of rigidity and coupling parameters with fibre angle, β, for the example wing 1 $[\beta]_{14}$.

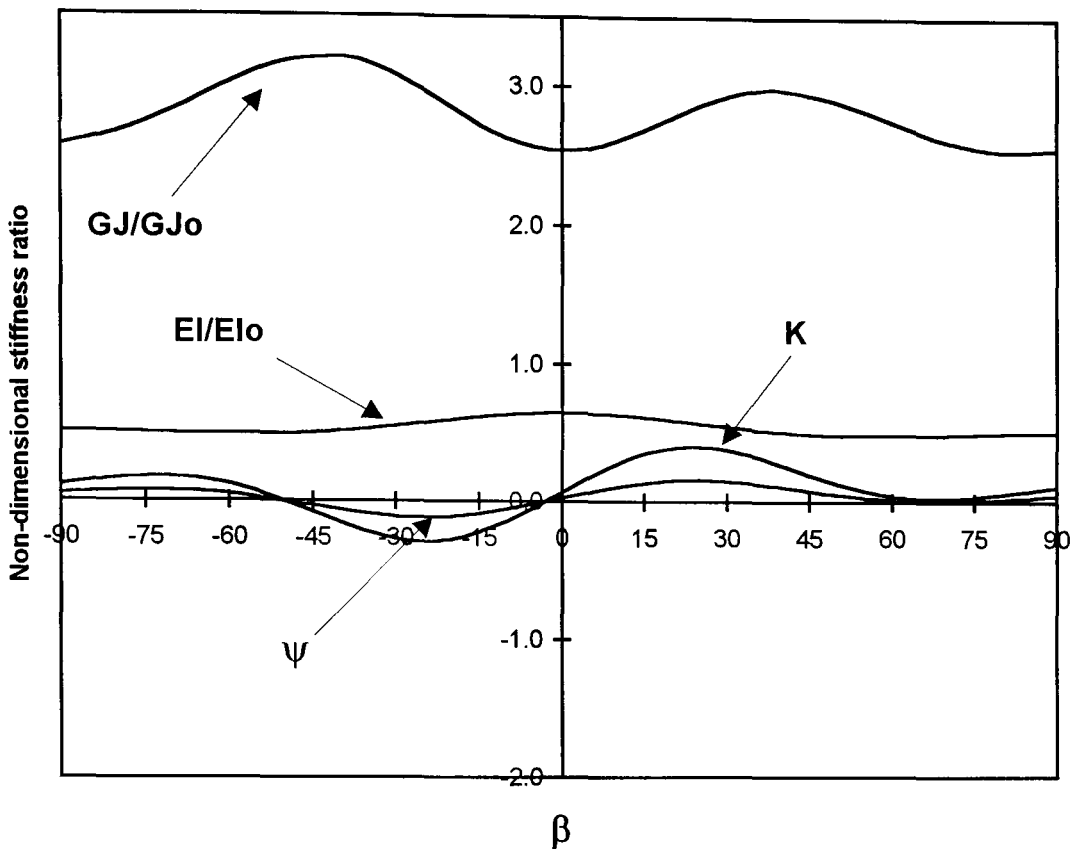

Fig. 5.8. Variation of rigidity and coupling parameters with fibre angle, β, for the example wing 2 $[0/\pm 45/\beta/\beta/\beta/\beta]_s$.

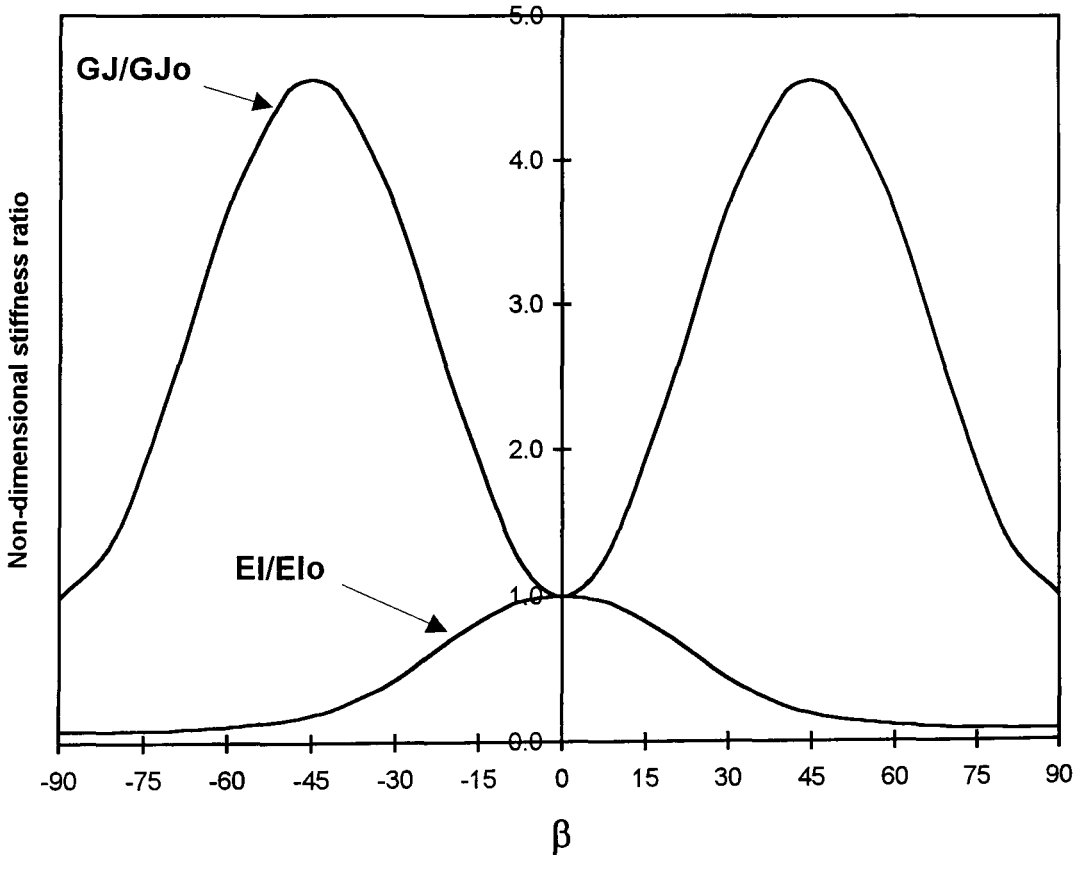

Fig. 5.9. Variation of rigidity and coupling parameters with fibre angle, β, for the example wing 3 $[\pm\beta]_7$.

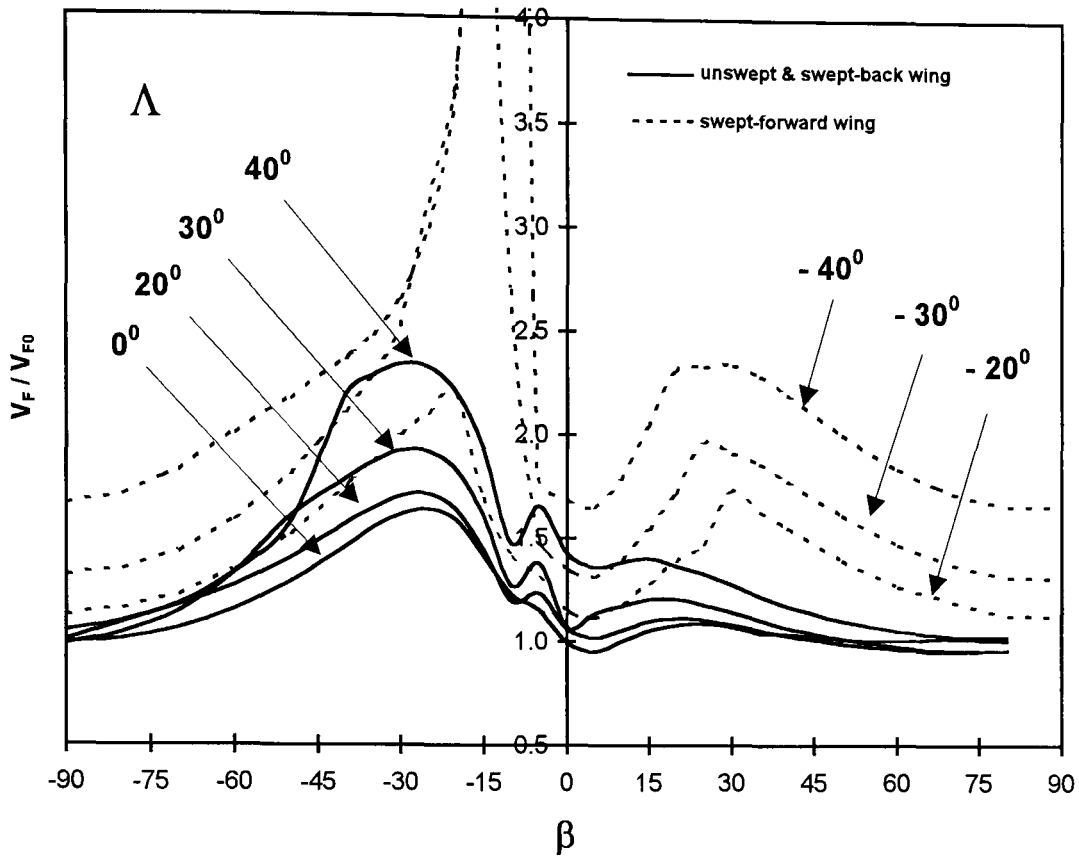

Fig. 5.10. The behaviour of flutter speed as a function of fibre angle β and sweep angle Λ, for the example wing 1 $[\beta]_{14}$.

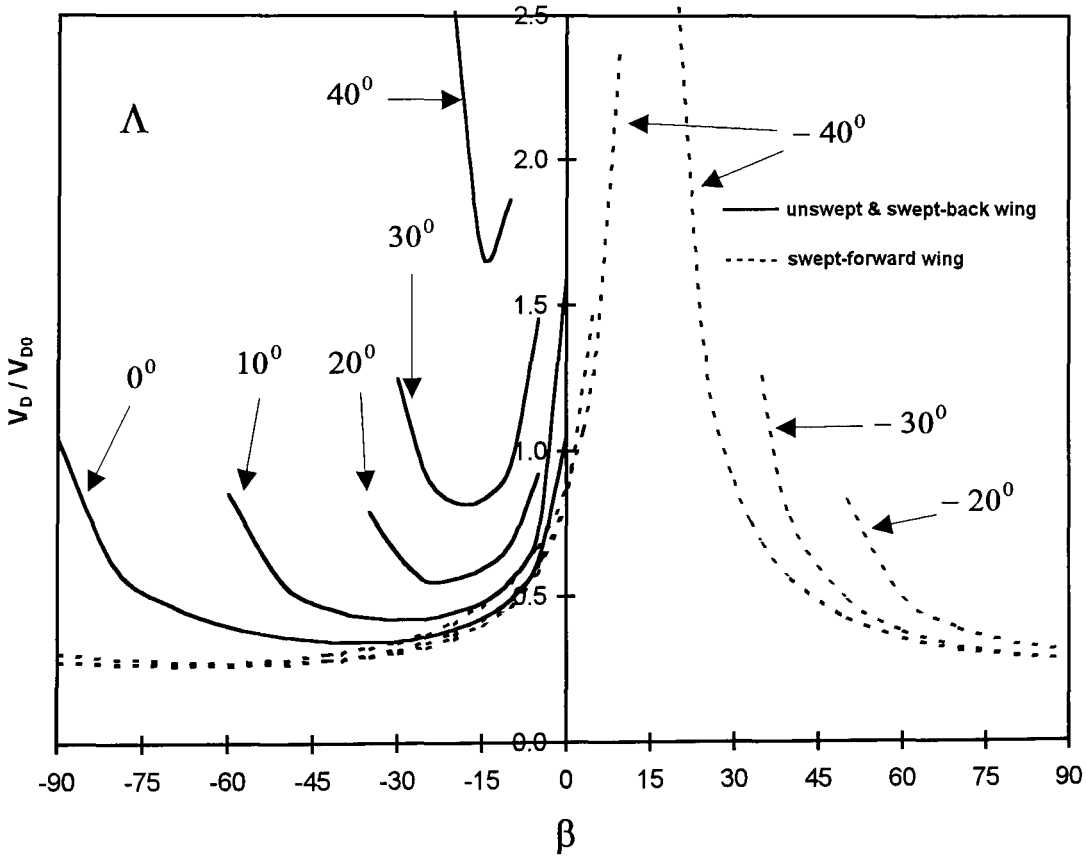

Fig. 5.11. The behaviour of divergence speed as a function of fibre angle β and sweep angle Λ, for the example wing 1 $[\beta]_{14}$.

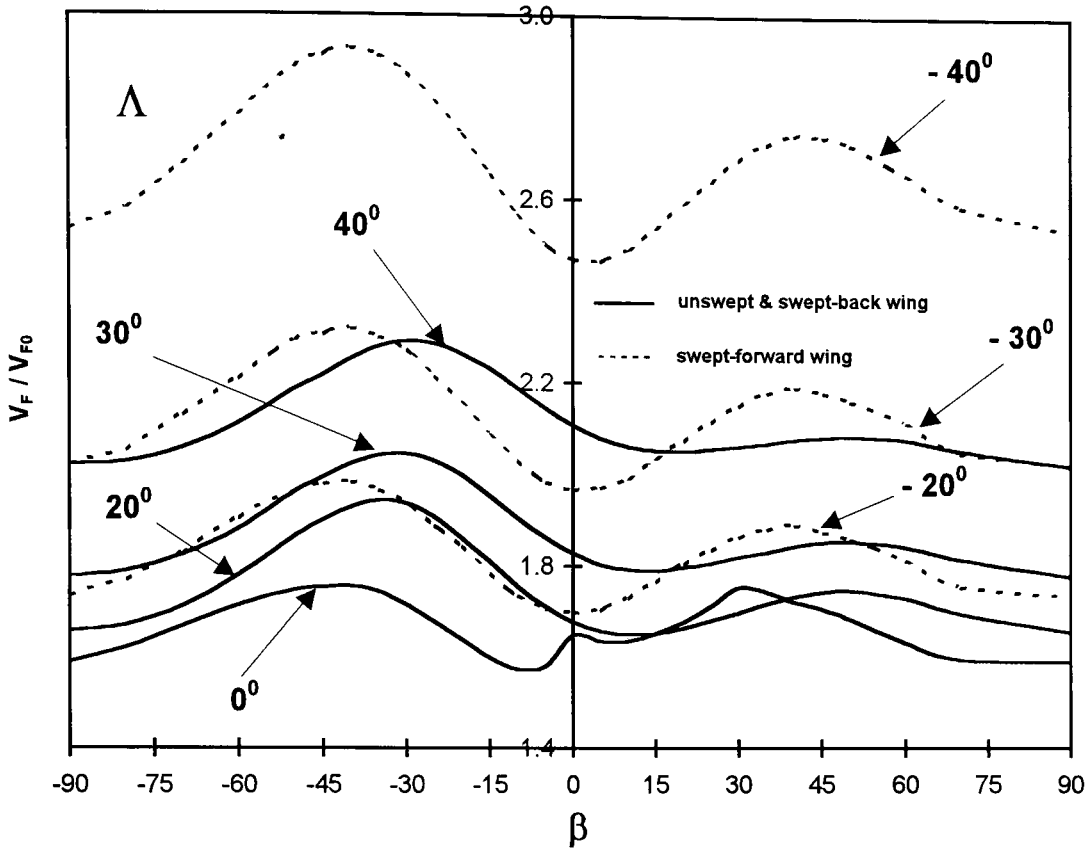

Fig. 5.12. The behaviour of flutter speed as a function of fibre angle β and sweep angle Λ, for the example wing 2 $[0/\pm45/\beta/\beta/\beta/\beta]_s$.

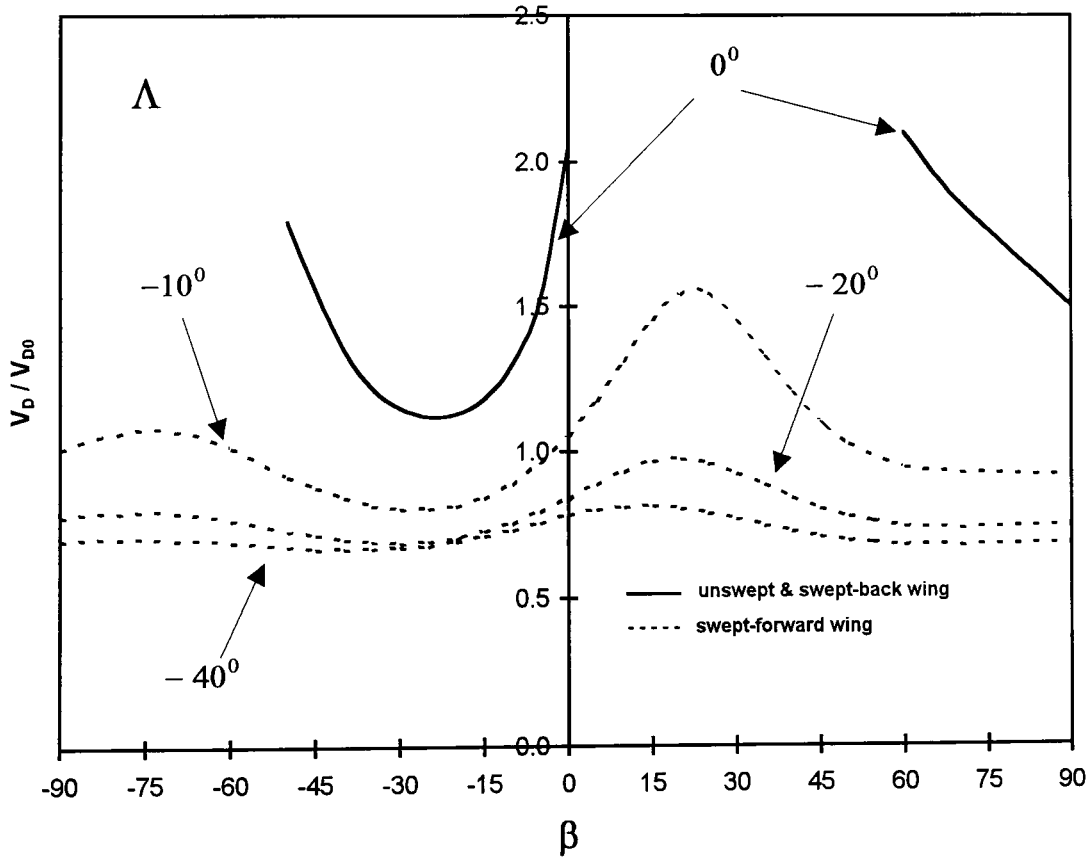

Fig. 5.13. The behaviour of divergence speed as a function of fibre angle β and sweep angle Λ, for the example wing 2 $[0/\pm45/\beta/\beta/\beta/\beta]_s$.

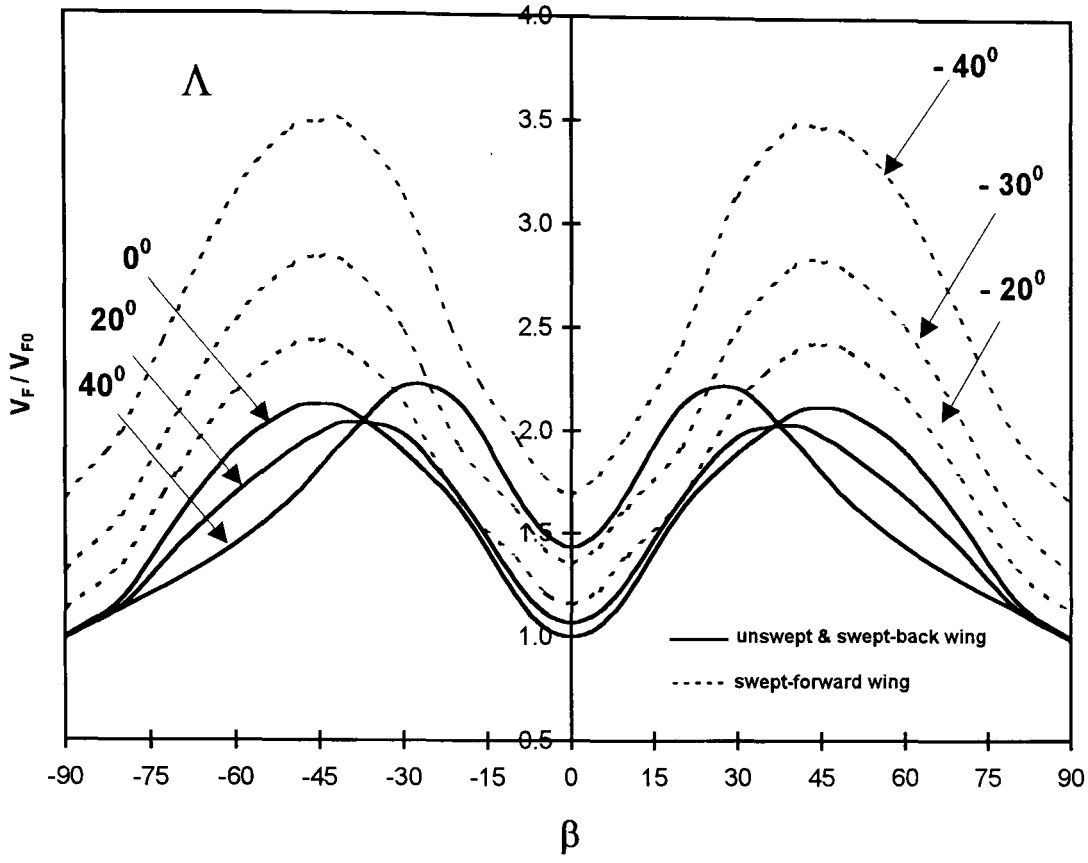

Fig. 5.14. The behaviour of flutter speed as a function of fibre angle β and sweep angle Λ, for the example wing 3 $[\pm\beta]_7$.

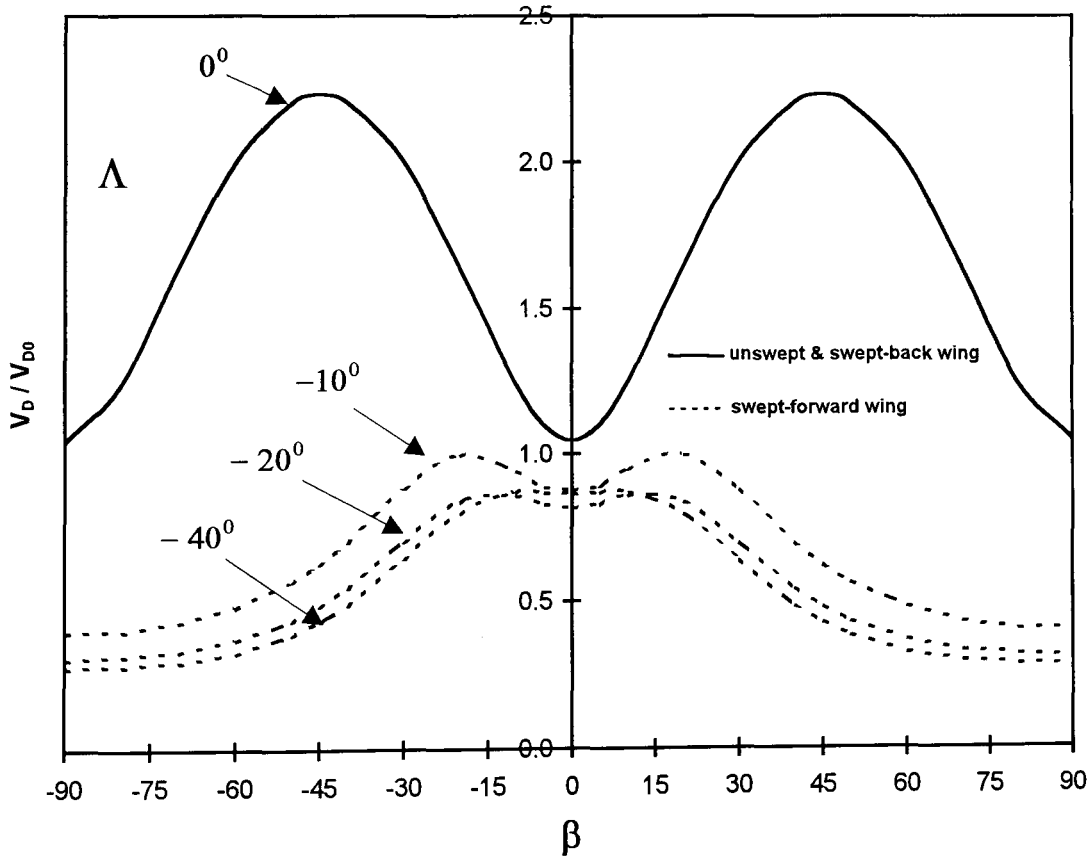

Fig. 5.15. The behaviour of divergence speed as a function of fibre angle β and sweep angle Λ, for the example wing 3 $[\pm\beta]_7$.

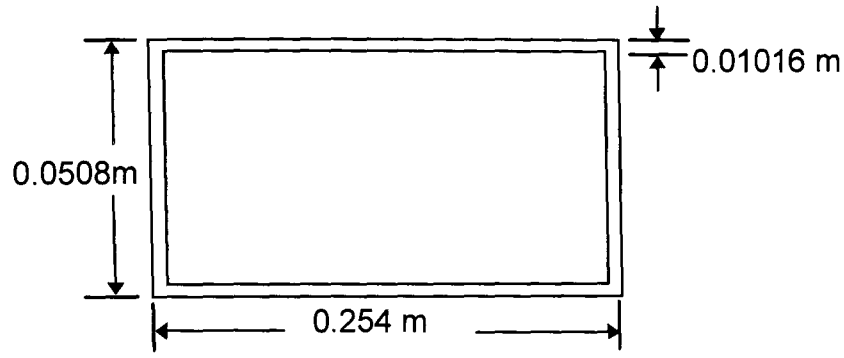

Fig. 5.16. CAS box-beam cross-section of Ref. [1.7]

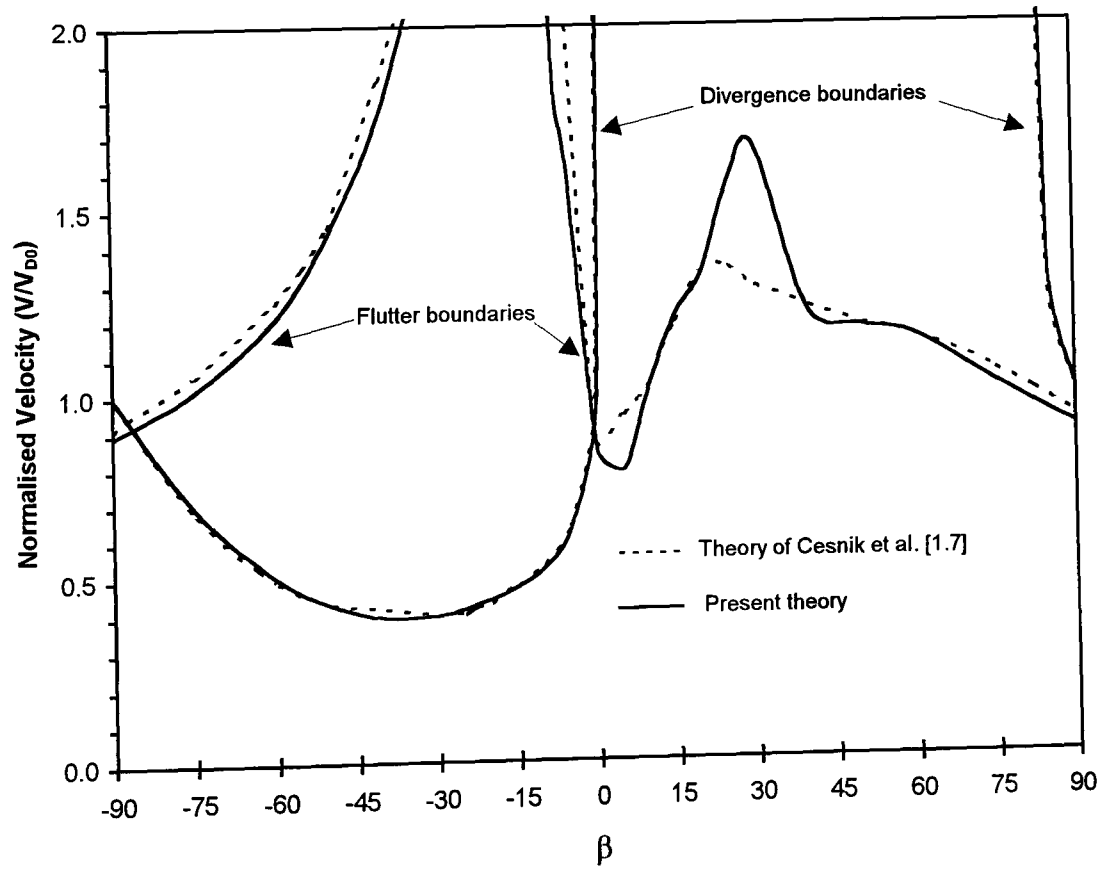

Fig. 5.17. The behaviour of flutter and divergence speeds as functions of fibre angle β, for the example wing 4 with lay-up : [β] in top wall, [-β] in bottom wall, and [β/-β] in vertical walls.

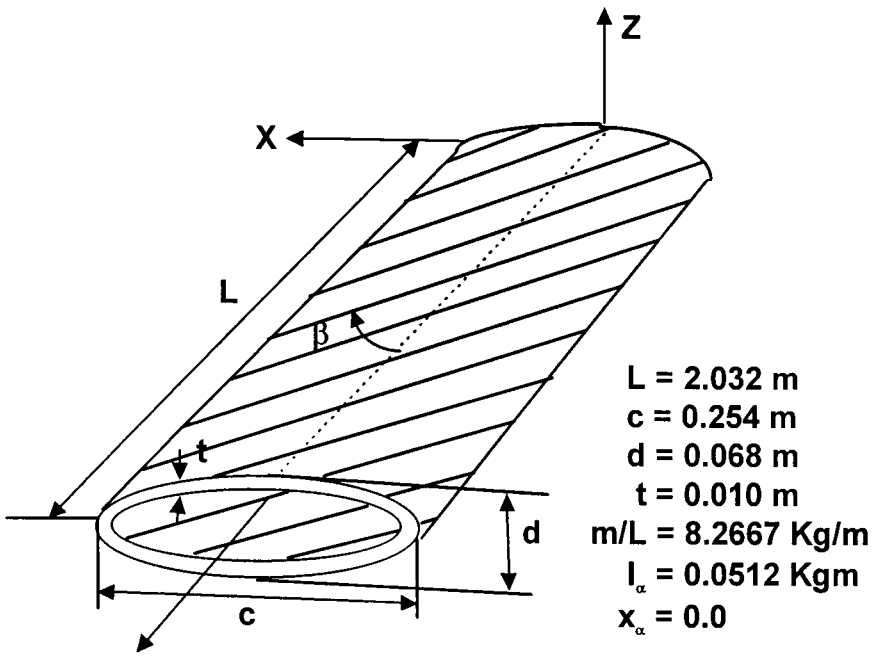

Fig. 5.18. Coordinates, dimensions and other properties for the thin-walled biconvex beam of Refs [5.10, 511].

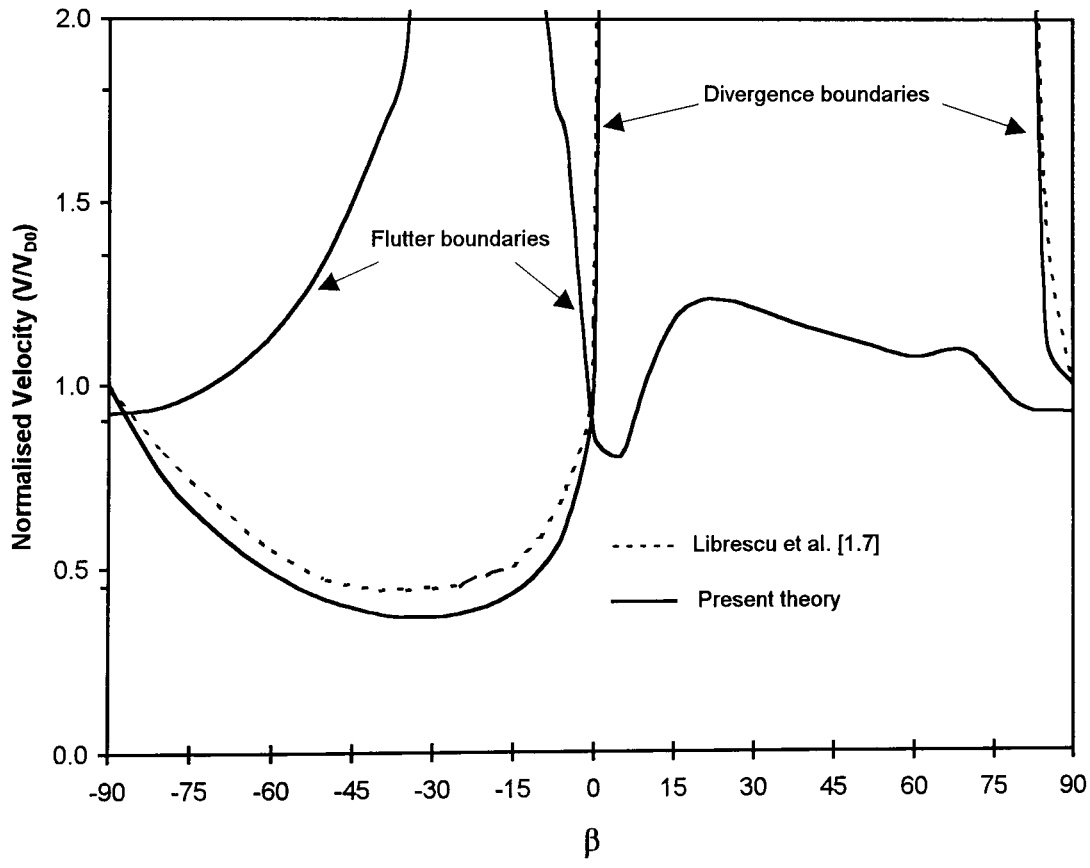

Fig. 5.19. The behaviour of flutter and divergence speeds as functions of fibre angle β, for the example wing 5. The fibres in upper and lower surfaces are in parallel direction.

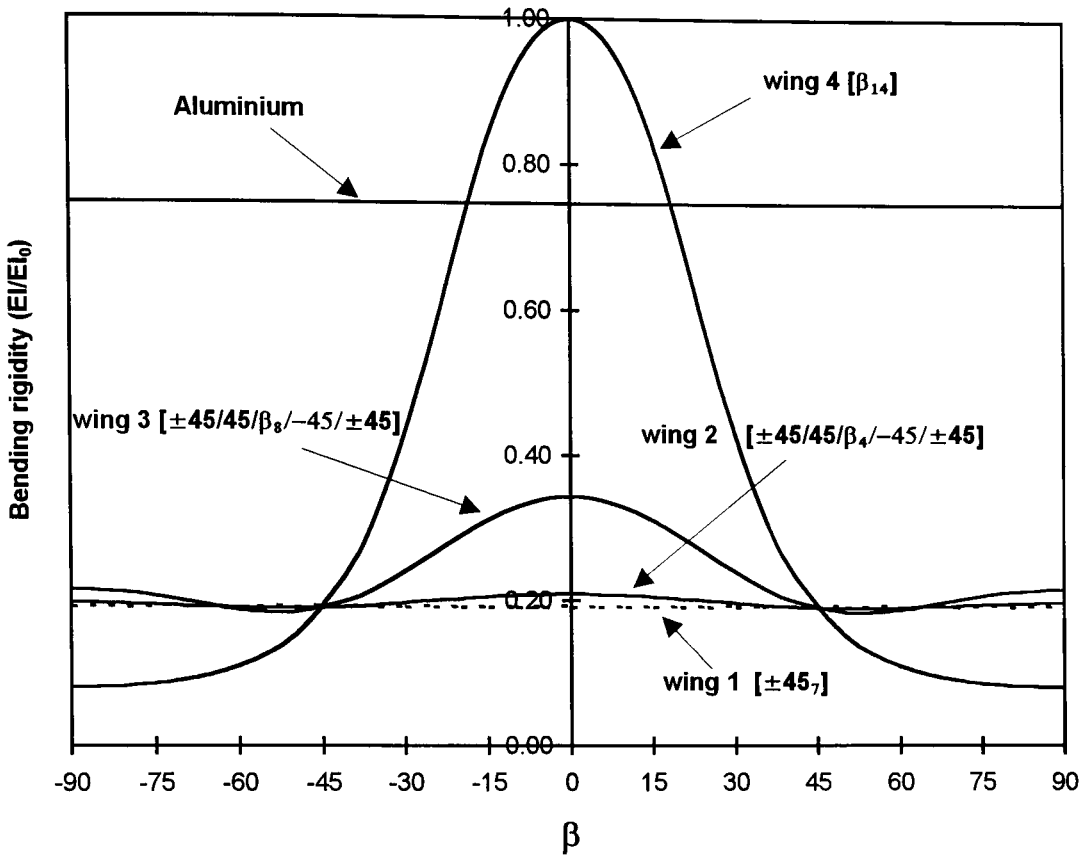

Fig. 5.20. Bending rigidity EI versus fibre angle, β, for the five example wings of section 5.7.

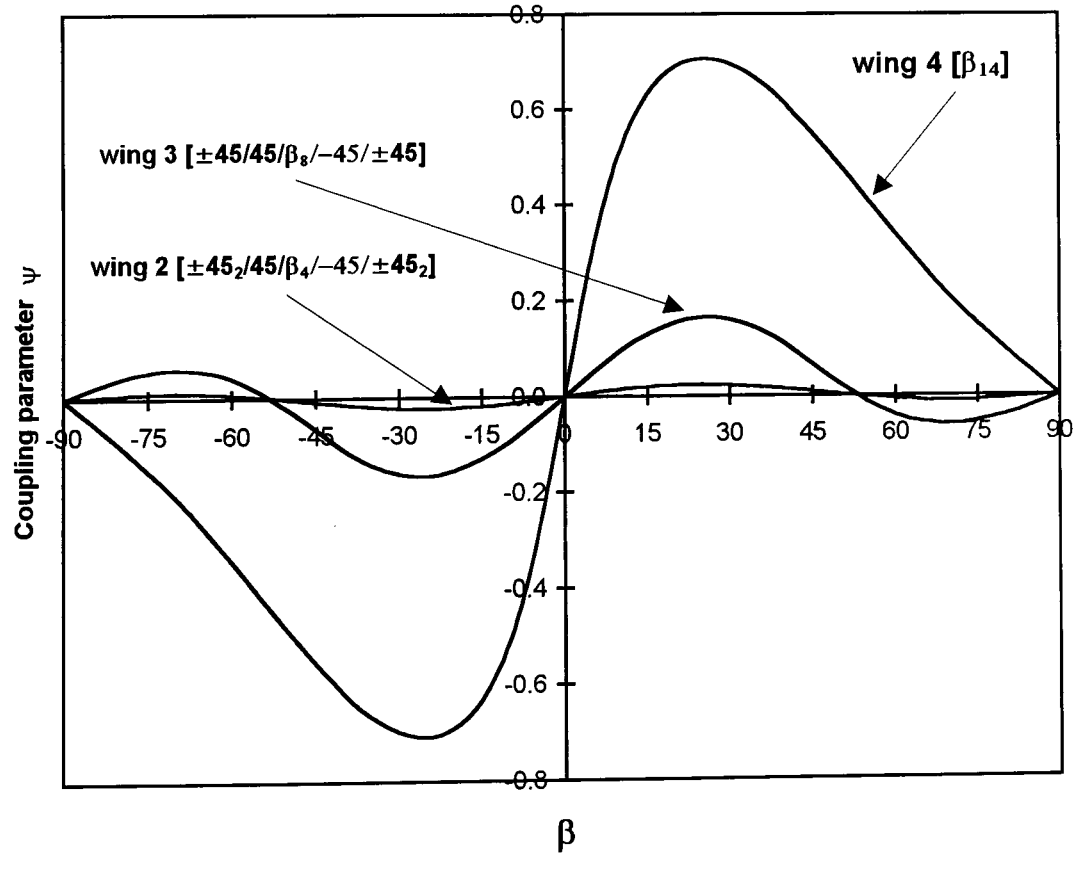

Fig. 5.21. Bending-torsion coupling parameter, ψ, versus fibre angle, β, for the three coupled example wings of section 5.7.

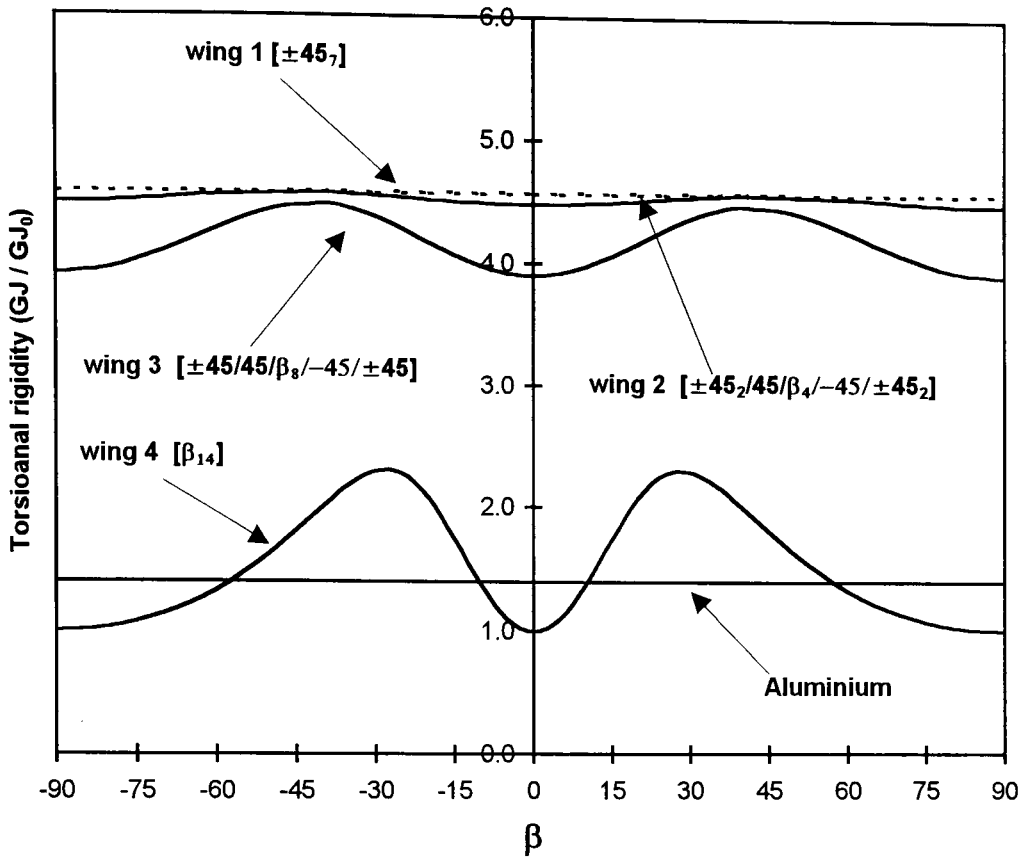

Fig. 5.22. Torsional rigidity GJ versus fibre angle, β, for the five example wings of section 5.7.

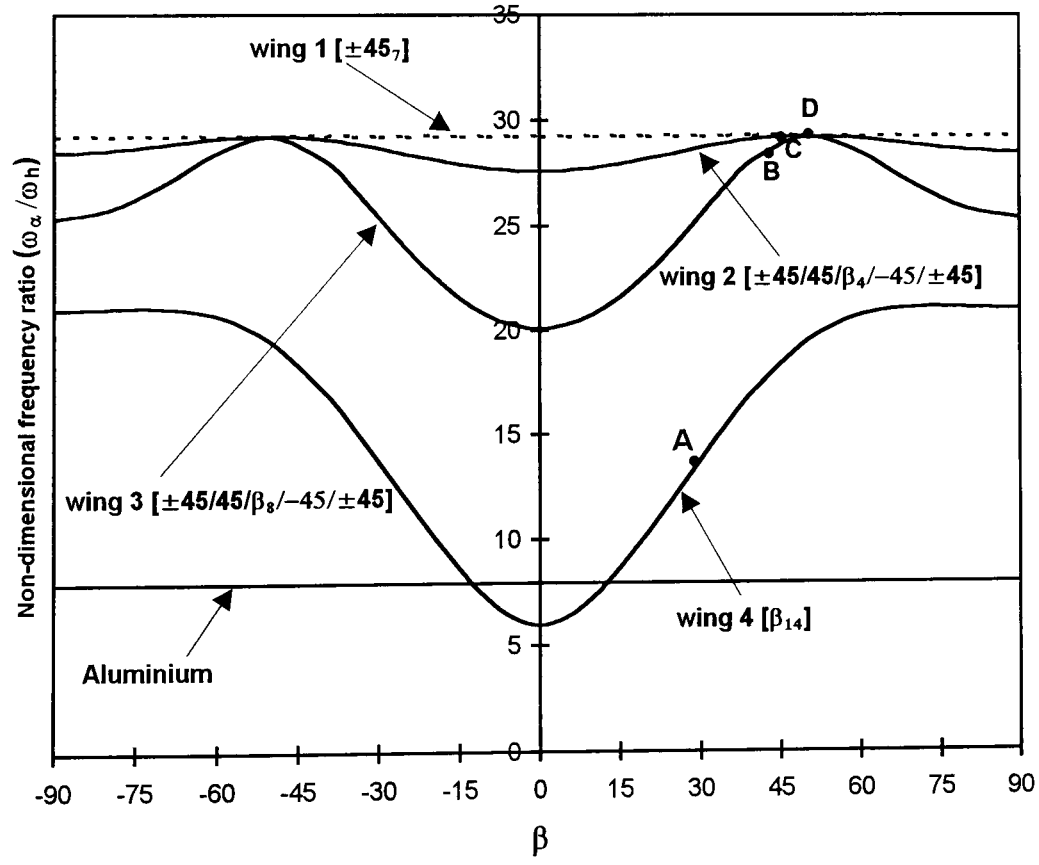

Fig. 5.23. The ratio of the uncoupled fundamental torsional to fundamental bending frequency, ω_α/ω_h, versus fibre angle, β, for the five example wings of section 5.7.

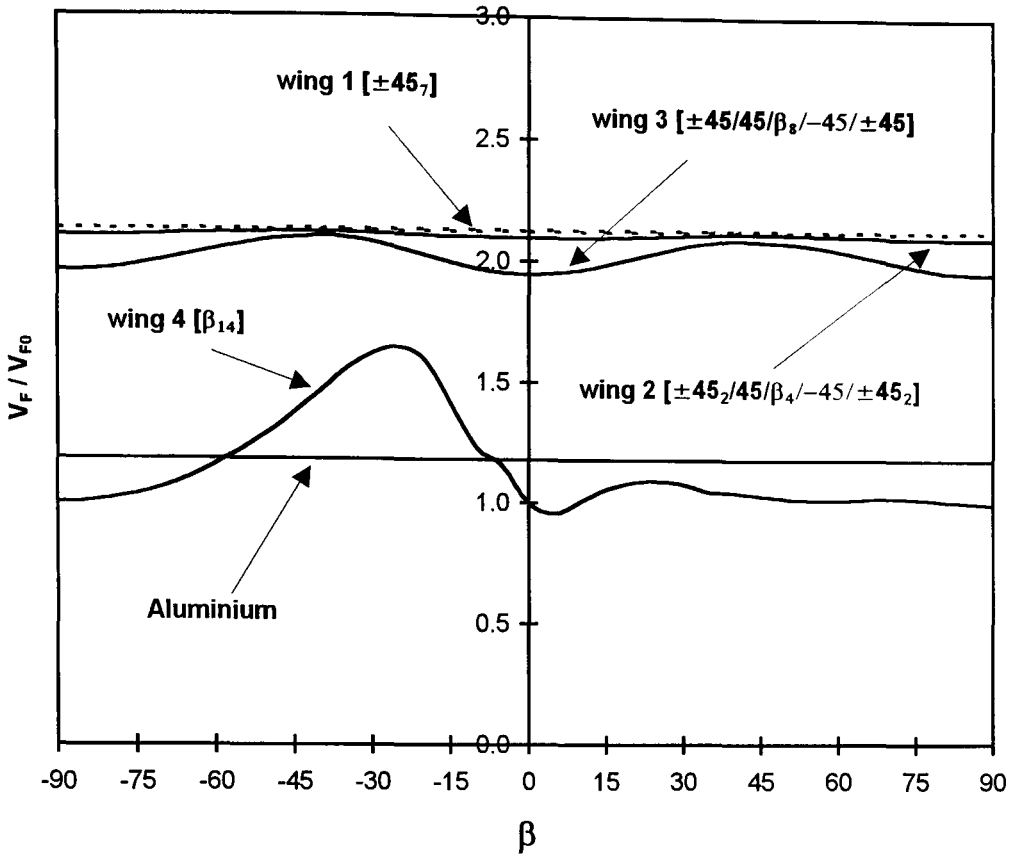

Fig. 5.24. Flutter speed as a function of fibre angle, β, for the five example wings of section 5.7, (0^0 sweep).

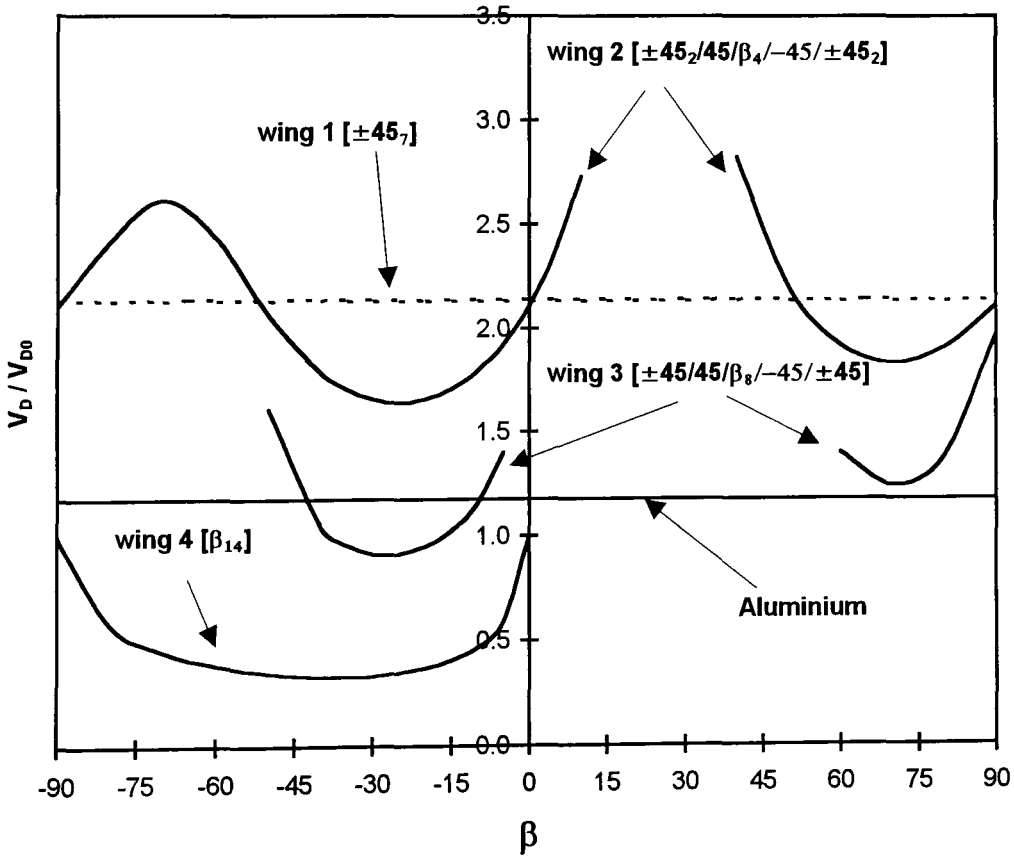

Fig. 5.25. Divergence speed as a function of fibre angle, β, for the five example wings of section 5.7, (0^0 sweep).

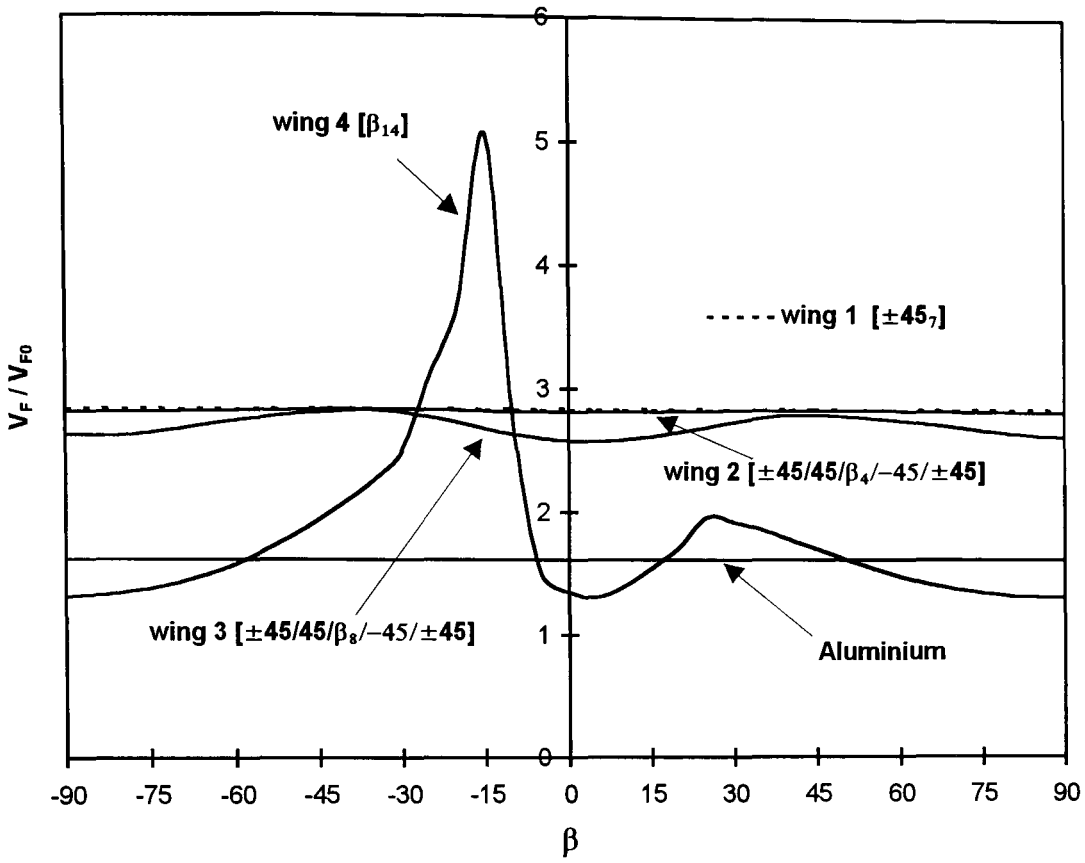

Fig. 5.26. Flutter speed as a function of fibre angle, β, for the five example wings of section 5.7, (30^0 forward sweep).

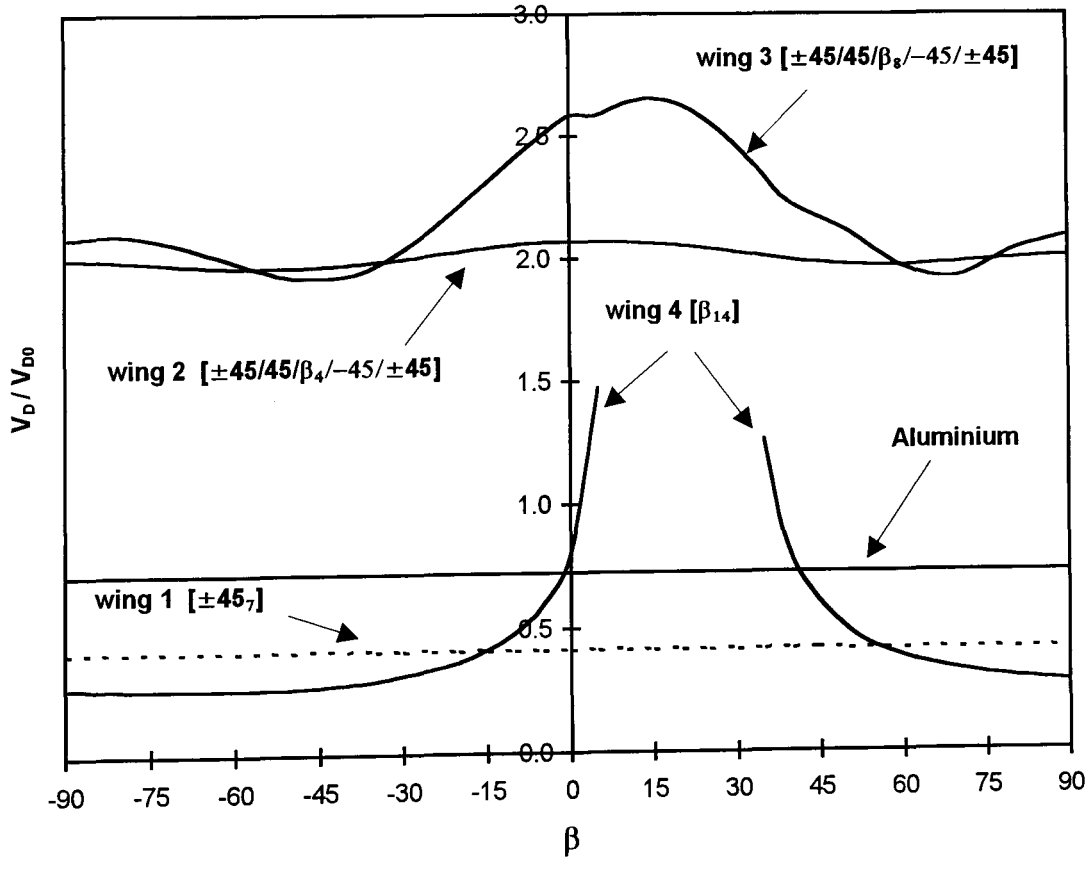

Fig. 5.27. Divergence speed as a function of fibre angle, β, for the five example wings of section 5.7, (30^0 forward sweep).

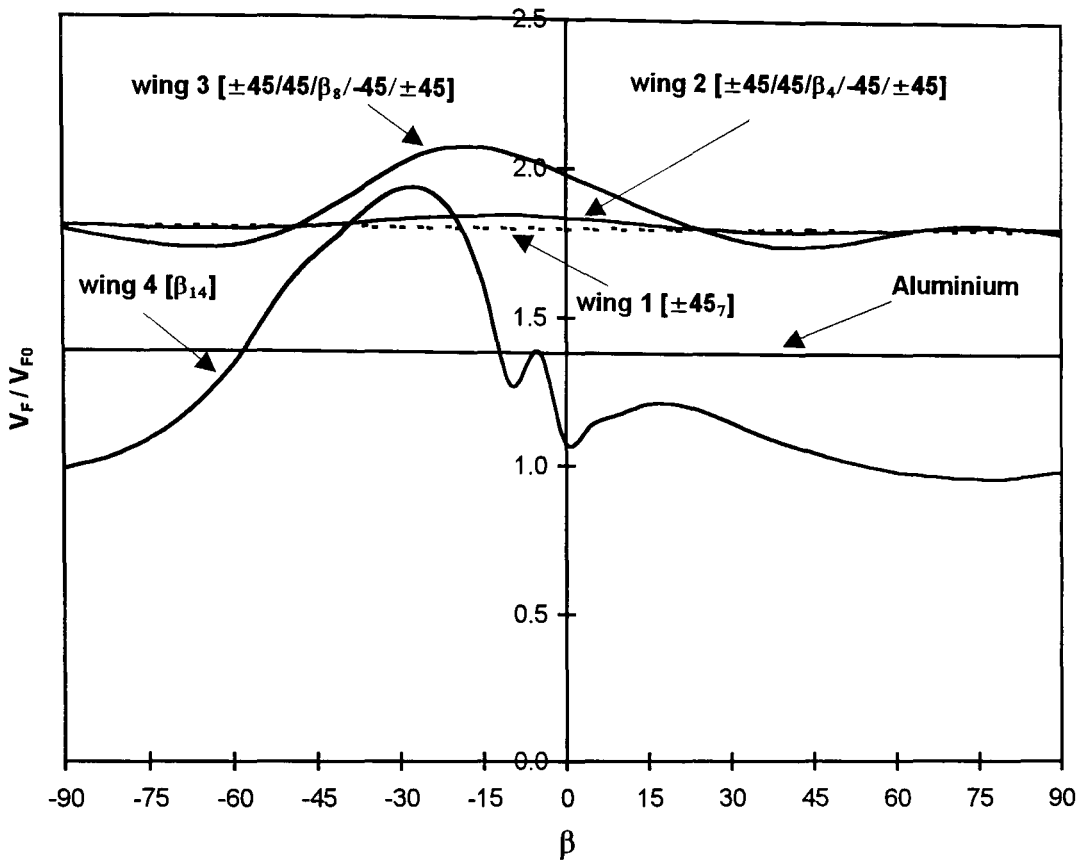

Fig. 5.28. Flutter speed as a function of fibre angle, β, for the five example wings of section 5.7, (30^0 back sweep).

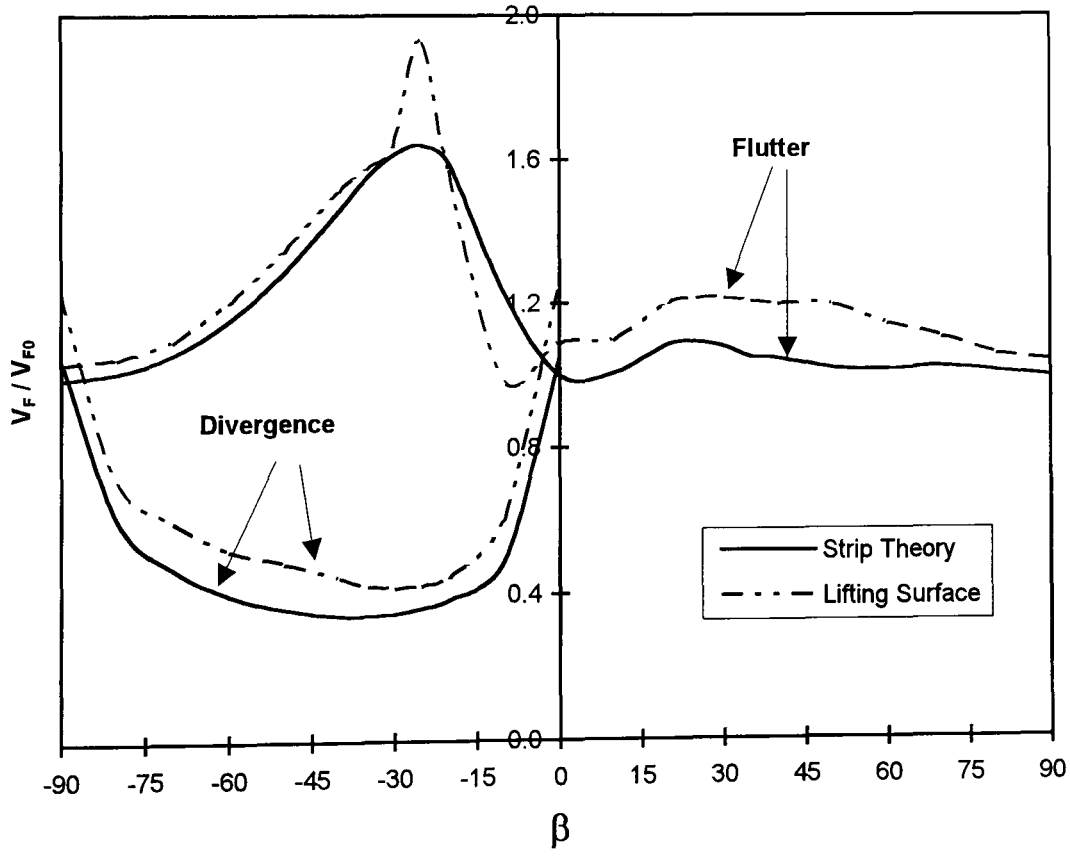

Fig. 5.29. Flutter and divergence speeds, obtained using Strip and Lifting Surface theories, versus fibre angle, β, for lay-up $[\beta]_{14}$.

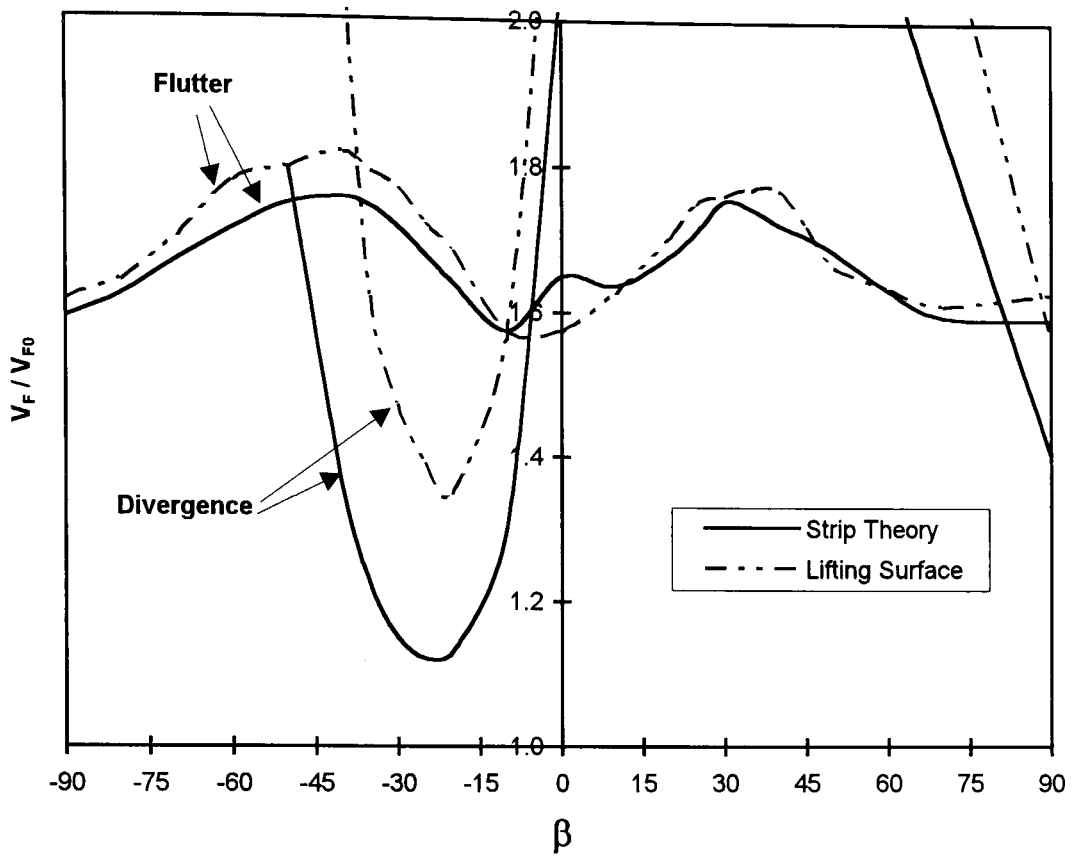

Fig. 5.30. Flutter and divergence speeds, obtained using Strip and Lifting Surface theories, versus fibre angle, β, for lay-up $[0/\pm45/\beta/\beta/\beta/\beta]_s$.

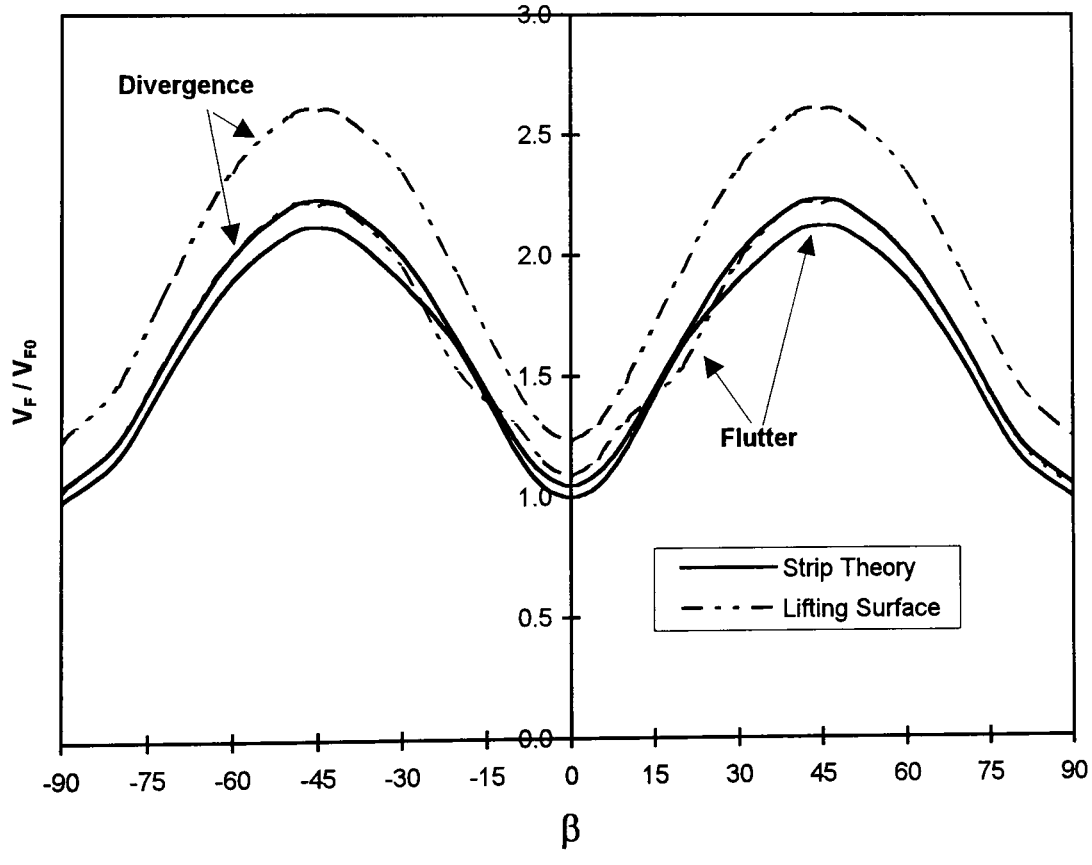

Fig. 5.31. Flutter and divergence speeds, obtained using Strip and Lifting Surface theories, versus fibre angle, β, for lay-up $[\pm\beta]_7$.

CHAPTER 6

FURTHER INVESTIGATIONS INTO THE FLUTTER CHARACTERISTICS OF COMPOSITE WINGS

6. FURTHER INVESTIGATIONS INTO THE FLUTTER CHARACTERISTICS OF COMPOSITE WINGS

6.1 Introduction

In the previous chapter, many important aspects of aeroelastic tailoring were demonstrated. A significant number of graphical results were presented which contribute towards a better insight into the problem of improving the flutter and divergence stabilities through the use of composite materials, and with the purpose of showing the strong interrelations that exist when attempting to treat separately only some of the aspects associated with the wider problem.

In general, the divergence speed was shown to have a predictable pattern and be very sensitive to changes in the bending-torsion coupling parameter. It was found that the higher the positive bending-torsion coupling parameter, the higher the divergence speed. In contrast, flutter admittedly is a more complicated phenomenon with very often an unpredictable behaviour and many uncharacteristic features. A careful review of the literature and the results and conclusions of chapter 5 led to the identification of the following areas that need further investigation:

- the non-dimensional presentation of flutter behaviour to enable its understanding and prediction.

For instance, in Ref. [1.12], flutter was shown to be eliminated at a relatively low value of negative bending-torsion coupling parameter ψ, which was confirmed by the present study in section 5.5. However, in section 5.6 of the present study, also see Ref. [1.6], (where a plate model based on lamination theory was used to predict the stiffness data), the maximum value of ψ did not eliminate flutter. An unexpected pattern in the flutter behaviour was also observed in Fig. 5.14 where the flutter speed of an uncoupled laminated wing was plotted against the fibre angle. Although in Figs 5.10 and 5.12 the flutter speeds of two coupled wings were shown to increase with the angle of sweep, in Fig. 5.14 no coherent pattern seemed to be apparent. Therefore, it is quite apparent that the matter needs further investigation.

- the significance of positive coupling on the flutter of composite wings which has been overshadowed by the beneficial effects of its negative counterpart.

It was previously shown that, although the negative coupling is generally beneficial for flutter, in some cases, and especially in the case of swept-forward wings, positive coupling may have to be used for aeroelastic tailoring considerations (i.e., taking both flutter and divergence into account). Therefore, an investigation into the effects of positive coupling on the flutter behaviour will reveal how it can be best exploited leading to aeroelastic tailoring of aircraft wings.

- the unexpected blips and/or sharp discontinuities in the flutter behaviour of composite wings occurring at certain fibre angles of the laminate (see, for example Fig. 5.10 around $\beta = -5^0$).

This uncharacteristic feature has also been reported in a number of cases in the literature [1.6-1.7, 1.9]. However, no one appears to have given any details or any convincing reasons as to the cause of their unusual occurrence.

- the reason why the wash-in behaviour, which usually increases the aerodynamic load on the wing, is more beneficial than the wash-out behaviour for the flutter of composite wings.

One striking feature of the three studies in chapter 5, and also of other earlier works, is that the ply orientation in a given laminate which results in the so-called wash-in effect is found to increase the flutter speed of composite wings, while decreasing the divergence speed [1.7, 1.11-1.12]. Surprisingly, the author's literature survey shows that no one seems to have given any detailed explanations or reasons for the effects of wash-in or wash-out on the flutter behaviour of composite wings. Thus this matter needs further investigation.

The material in this chapter is organised as follows. In section 6.2 flutter results are provided using suitable non-dimensional parameters for wings exhibiting wash-in behaviour (i.e., ψ is negative), while in section 6.3 the beneficial (or otherwise) effects of wings exhibiting wash-out on the flutter behaviour are examined. Then in section 6.4 the role of modal interchange on the flutter behaviour of composite wings is studied.

This investigation is focused on some of the unusual features of composite wings, such as, the unexpected blips in the flutter behaviour and the reasons why wash-in behaviour is beneficial for flutter as opposed to wash-out. Finally brief conclusions are drawn in section 6.5.

6.2 Flutter Analysis Using the Non-Dimensional Frequency Ratio ω_h / ω_α

The aim of this study is to investigate the flutter behaviour of composite wings exhibiting wash-in behaviour using suitable non-dimensional parameters. In this way, the flutter behaviour of realistic composite wings is approximated, thus making the understanding and prediction of such behaviour possible. This provides a clearer understanding of flutter and, in contrast to earlier investigations, shows whether or not bending-torsion coupling can be used beneficially to eliminate flutter throughout the flight envelope. This has been achieved by plotting the non-dimensional flutter speed $V_F / b\omega_\alpha$, where V_F is the actual flutter speed, b is the semi-chord and ω_α is the (uncoupled) fundamental torsional natural frequency, against the ratio of the fundamental bending to fundamental torsional natural frequency (ω_h / ω_α) for selected values of ψ and x_α. The investigation is carried out on both swept and unswept wings.

Several other investigators have studied the aeroelastic stability of laminated wings in recent years using ply orientation as the main design variable [1.6-1.9]. However, there are notable exceptions where rigidity properties have been directly used as design variables [1.10-1.12] instead of ply orientation. For instance Ref. [1.10] uses the ratio between the bending-torsion coupling rigidity and the bending rigidity (K / EI) as a variable, although it is difficult to put upper and lower limits on this ratio. On the other hand, Ref. [1.11] uses two non-dimensional ratios, one being the ratio between the bending and torsional flexibility while the other being the non-dimensional flexibility cross-coupling parameter. In contrast, Ref. [1.12] uses rigidity based non-dimensional parameters which are essentially the ratio between the torsional and bending rigidity (GJ / EI) and the non-dimensional bending-torsion coupling parameter (ψ). The results given in Ref. [1.12] are limited in the sense that they illustrate the variation of flutter and divergence speeds for only three values of the ratio of torsional

and bending rigidities. In this section, however, the ratio between the uncoupled bending and torsional natural frequencies in the fundamental mode is taken as the variable instead of the ratio of the corresponding rigidities. This gives much wider applicability of results because it involves more parameters such as mass, inertia and length of the wing, and thus covers a broad range of variables when presenting the results. However, the non-dimensional coupling parameter (ψ) of Ref. [1.12] has been retained in the analysis because it is dependent on the fibre orientation in a laminate and thus offers flexibility in design. (Note that the range for ψ is given by $-1 < \psi < 1$.)

The investigation has been carried out in the following stages. First the rigidity properties of a composite wing are established using classical lamination theory (see chapter 3). Next the free vibration characteristics are studied using the dynamic stiffness matrix method (see chapter 4). Finally the flutter speed is computed by varying significant structural parameters which include the bending-torsion coupling parameter (ψ), the ratio of the (uncoupled) fundamental bending and torsional natural frequencies (ω_h / ω_α) and the static unbalance (x_α). The computer program CALFUN (the details of which were provided in section 5.2) was run to obtain the results. The non-dimensional flutter speed $V_F / b\omega_\alpha$ is plotted against the above parameters. For a given range of input parameters, the maximum flutter speed obtained from the above analysis was further checked by the well known optimisation program ADS [1.40]. An outline of the program ADS and its options are given in Appendix 'E'. The results presented in this section are fairly general and apply to composite wings of any cross-section so long as the rigidity and other properties are known within reasonable accuracy.

6.2.1 Flutter Optimisation Using ADS

Complementary to the flutter results obtained by varying the non-dimensional frequency ratio ω_h / ω_α, an optimisation study of composite wings using the well known program ADS [1.40] has been taken up as illustrated in this section.

A task, such as, maximising the flutter speed by varying the fibre orientation can be described as an unconstrained optimisation problem. The problem is therefore described as,

$$\text{minimise} \quad f(\beta) \text{ with } \{\beta_l\} \le \{\beta\} \le \{\beta_u\}$$

where $f(\beta)$ represents a defined objective function related to flutter speed which is a function of the ply orientation (β), and $\{\beta_l\}$ and $\{\beta_u\}$ are the lower and upper bounds of the variable β.

The Sequential Unconstrained Minimisation process is used as strategy (see Table E.1 in Appendix 'E') while the Davidon-Fletcher-Powell (DFP) variable metric method [2.10, 6.1] is used as optimiser (see Table E.2). The Golden Section Method [6.2] followed by Polynomial Interpolation (see Table E.3) is used for the one-dimensional search. These methods are all part of the computer program ADS (see Appendix 'E').

The objective function chosen to optimise the flutter speed has the form

$$f(\beta) = \left[1 - \frac{V_F(\beta_T) - V_F(\beta_I)}{V_F(\beta_I)}\right]^2$$

where $V_F(\beta_I)$, $V_F(\beta_T)$ are the flutter speeds for the initial and tailored laminate configurations respectively. The above chosen objective function is based on experience gained from working with ADS which showed that the above function helps the optimisation program to converge closer to the final solution.

6.2.2 Discussion of Results

In the computation of numerical results, the procedure described in section 6.2 is initially applied to a laminated flat plate (beam) which is a stack of identical plies. Results are generalised from this elementary structure to any assembly of plies which is symmetric about the mid-thickness plane. In this way the flutter behaviour of realistic composite wings which exhibit (material) coupling between bending and torsional deformations is approximated.

Figure 6.1 shows the coordinate system and sign convention used in this investigation for a laminated composite beam (wing) together with the positive direction of the airflow. The results which follow apply to more general cross-sections but the rectangular cross-section is shown in the figure for convenience.

Figures 6.2-6.6 show the variation of the non-dimensional flutter speed $V_F / b\omega_\alpha$ against the non-dimensional uncoupled frequency ratio ω_h / ω_α for five different values of ψ, i.e., ψ = 0, +0.4, -0.4, +0.7, -0.7 respectively. The first six normal modes of the cantilever wing were used (which were subsequently found to be adequate) in the analysis which included both the fundamental bending and torsional natural frequencies. The density ratio $m / \pi\rho b^2$ and the non-dimensional radius of gyration $r_\alpha = \sqrt{I_\alpha / mb^2}$ were kept constant at 10 and 0.5 respectively for all cases. The elastic axis location was assumed to be 20% of the semi-chord forward of the mid-chord position (i.e., a = -0.2). Several representative values of x_α were used in obtaining the results as shown in each of the figures. The results of Fig. 6.2 correspond to the degenerate case of a metallic wing because ψ = 0 in this case. These results generally agree with the results given in the classical text of Bisplinghoff, Ashley and Halfman [5.1] for a representative section of a rigid aerofoil (see Fig. 9.5(A) Graph (o) on page 540 of Ref. [5.1]). The results of Figs 6.3-6.6, however, apply only to composite wings. (When the study was reanalysed with the density ratio and the non-dimensional radius of gyration changed, results similar to those of Figs 6.3-6.6 were observed.) It is easily seen that negative values of ψ give higher flutter boundaries (see Figs 6.4 and 6.6) as opposed to the cases with positive values (see Figs 6.3 and 6.5). This is in accord with observations made previously (see chapter 5) that the wash-in effect (negative ψ in this case) is generally beneficial from the flutter standpoint as it increases the flutter speed. The results of Figs 6.4 and

6.6, particularly for lower values of x_α are helpful because they can be exploited to achieve higher (or even eliminate) flutter speeds.

In further studies it is clear that, a representative value of x_α = -0.1 (which gave a suitable trend towards higher flutter speeds for composite wings as shown in Figs 6.3-6.6) may be chosen to define a base from which further results for the flutter speed may be obtained, when the non-dimensional frequency ratio is varied as ψ varies. Negative values of ψ were used because they induce the wash-in effect which is beneficial for flutter. Figures 6.7-6.9 show representative results for the unswept wing where the non-dimensional flutter speed $V_F / b\omega_\alpha$ has been plotted against the non-dimensional frequency ratio for three values of the density ratio $m / \pi\rho b^2$ which cover a wide range of practical cases. The variation of ψ is shown in each of the three figures. The following observations can be made from these figures.

First of all, when ψ = -0.7, the non-dimensional flutter speed increases rapidly for values of the non-dimensional frequency ratio greater than 0.15 whereas it is almost invariant when this ratio is less than 0.15. This behaviour is observed in all the three cases shown in Figs 6.7-6.9. It should be noted, however, that due to large torsional rigidity GJ usually associated with composite wings made of laminated plates or box-beams [1.24, 2.85, 3.11] the non-dimensional frequency ratio is quite often very small, i.e., below 0.15. In such cases any benefit that can be derived by changing ψ (which can be changed by altering the ply orientation) to increase the flutter speed is quite marginal. In contrast, if GJ is relatively low whereas the coupling rigidity K is much higher (i.e., ψ is high) the graphs shown in Figs 6.7-6.9 for values of the non-dimensional frequency ratio above 0.15, show that higher flutter speeds can be achieved. Thus for values of non-dimensional frequency ratio less than 0.15, maximising GJ offers a better prospect of maximising the flutter speed, as can be seen. Therefore, a laminate configuration that offers either the maximum GJ or maximum negative ψ (i.e., minimum ψ) gives the maximum flutter speed for an unswept wing. (Note that from a divergence point of view, the maximum negative ψ would be detrimental, see chapter 5).

Next sweep is introduced in the analysis. The results in Fig. 6.10 correspond to a 30 degree swept-forward wing. Representative values of $m / \pi\rho b^2$ = 40 and

x_α = -0.1 were chosen to obtain results for the flutter speed when ω_h / ω_α is varied for different values of ψ. In contrast to the unswept wing, Fig. 6.10 shows that a very high negative ψ can be more beneficial for flutter than high GJ. Thus, maximising the negative ψ offers a better prospect of maximising the flutter speed of swept-forward wings. It is important to note, however, that the maximum flutter speed in this case can be obtained when the negative ψ has a large value, i.e., $\psi \leq$ -0.6 (see Fig. 6.10), which may be difficult, if at all, possible to be attained in practice. For $\psi \geq$ -0.6 maximising GJ again appears to offer a better prospect of maximising the flutter speed. (Note that although the non-dimensional flutter speed ratio is seen to be increasing with ω_h / ω_α for ψ = -0.4 with a small gradient, the fundamental torsional frequency ω_α decreases more rapidly. As a consequence, the flutter speed decreases, even though the non-dimensional flutter speed increases in this case.)

Similarly, the results of Fig. 6.11 correspond to a 30 degree swept-back wing. In contrast to the unswept and swept-forward wings, very high flutter speeds can be achieved for low values of negative ψ when ω_h / ω_α is below 0.1. Maximising GJ appears not to be beneficial for flutter in this case, because of the dominant effect of ψ.

The three earlier investigations in chapter 5, i.e., sections 5.5, 5.6, and 5.7, and two significant pieces of work in the literature [1.6, 1.12] are to be interpreted in relation to the present study as follows.

In Ref. [1.12] and section 5.5 of the present study, flutter was eliminated at a relatively low value of ψ. This is because the EI and GJ used in the above two studies resulted in a high non-dimensional frequency ratio (ω_h / ω_α) which was well above 0.15 (see Figs 6.7-6.9), giving large variations in flutter speed with small changes in ψ. However, in Ref. [1.6] where a plate model based on lamination theory was used to predict the stiffness data, significant variation in flutter speed against the fibre orientation was observed but this variation being shown in non-dimensional form (i.e., it was shown relative to the flutter speed calculated when all the ply angles were set to zero) did not reveal the independent effect of the torsional rigidity (GJ) on the flutter speed. Clearly the maximum value of the negative ψ did not eliminate flutter in the above study [1.6]. This is because the ratio ω_h / ω_α was less than 0.15

(see Figs 6.7-6.9). In the present work, however, the relative importance of GJ and ψ in improving the flutter speed was investigated in sections 5.6 and 5.7. The results revealed quite convincingly that for the unswept wing, the laminate configuration with maximum GJ gave much higher flutter speed than the one obtained using the maximum value of the negative ψ for the particular laminate (see, for example, Fig. 5.22).

In Fig. 5.24 of chapter 5 where the non-dimensional flutter speed was plotted against the fibre angle β for a 30 degree swept-forward wing, higher flutter speed than the one obtained using the maximum GJ was obtained when the maximum negative ψ was present, i.e., ψ = -0.707. This is in accord with the conclusions drawn from Fig. 6.10 where for a value of the frequency ratio ω_h / ω_α below 0.15, higher flutter speeds than the one obtained using the maximum GJ are shown to be possible when $\psi \leq$ -0.6. In contrast, in Fig. 5.26 of chapter 5 where the flutter speed was plotted against the fibre angle β for a 30 degree swept-back wing, higher flutter speed than the one obtained by the maximum GJ obtained by using laminates offering a low value of negative ψ. This is clearly in accord with the results and conclusions drawn from Fig. 6.11, where for ω_h / ω_α < 0.1, small values of negative ψ could give higher flutter speed than the one obtained using the maximum GJ.

Before carrying out an optimisation study to validate the above conclusions, a parametric investigation is carried out in order to identify the values of ω_h / ω_α which are relevant to realistic wings. The frequency ratio ω_h / ω_α is dependent on the aspect ratio (AR), the stiffness ratio R = EI/GJ and the (rectangular) cross-section's depth-to-width ratio k= d/c. Figures 6.12-6.14 show ω_h / ω_α against R for various values of AR and k. As can be seen, the effect of AR on ω_h / ω_α is significant whereas the effects of k and R are rather marginal. For high aspect ratio wings, i.e., AR > 5, values of ω_h / ω_α <0.15 appear to be relevant while values of the frequency ratio higher than 0.15 apply only to low aspect ratio wings.

To confirm the above explanations, an optimisation study is carried out using the computer program ADS [1.40]. Five illustrative composite wings are investigated of which four are idealised as laminated flat beams and the remaining one as

thin-walled box-beam of rectangular cross-section. The material and other properties of the wings are shown in Tables 6.1 and 6.2.

The first two examples optimised are unswept laminated wings of lengths 0.6 m and 0.3 m respectively. For illustrative purpose, the non-dimensional flutter speed was computed first for a wing with the same density ratio, non-dimensional radius of gyration and static unbalance as given in Table 6.1. The results are shown in Fig. 6.15 for a wide range of non-dimensional frequency ratios. As the results of Fig. 6.15 are shown in non-dimensional form, they apply to both wings of the illustrative examples. It is quite clear from the figure that when the non-dimensional frequency ratio is below 0.15, the non-dimensional flutter speed is almost invariant and is independent of ψ. However, it should be noted that for the first example wing of length 0.6 m the non-dimensional frequency ratio is always less than 0.15, so variation of ψ will not significantly alter the flutter speed for this wing but the maximum value of GJ will give the maximum flutter speed instead. This is confirmed by the results of optimisation studies shown in Fig. 6.16 for this wing. The optimisation was carried out for a number of different starting points of laminate configurations. For illustrative purposes, the final computer run that gave the maximum flutter speed is shown in Fig. 6.16. The variation of EI, GJ, ψ and V_{F0}/V_F is plotted against the number of iterations. (V_F is the computed flutter speed for a given stacking sequence whereas V_{F0} is the flutter speed when all the plies are set to 0^0.) As can be seen the optimiser moves to maximum GJ which gives the maximum flutter speed. This was predicted earlier from the results shown in Figs 6.7-6.9 and 6.15.

In the case of the second example, i.e., the wing with length of 0.3 m, the optimisation results shown in Fig. 6.17 show a different picture for the following reasons. First of all the range of the non-dimensional frequency ratio for this wing exceeds 0.15 because of its shorter length, implying (see Fig. 6.15) that the effect of ψ on the flutter speed predominates. Thus the optimiser in this case (see Fig. 6.17) moves to the laminate configuration that gives the maximum negative ψ, which in effect gives maximum flutter speed. Figure 6.17 shows that the value of ψ to be about -0.7 when the flutter speed is optimised, i.e., as large a negative value as possible. This is in accord with the results shown in Figs 6.7-6.9 and 6.15.

The third example investigated is the unswept composite box-beam shown in Fig. 6.18 of which the material and other properties are shown in Table 6.2. Due to the relatively high torsional rigidity present in thin-walled box-beams, the non-dimensional frequency ratio ω_h / ω_α of this wing is well below 0.15. The optimisation results, which were similar to the ones shown in Fig. 6.16, showed that the laminate configuration with $[\pm 45]_3$ in each of the sides of the beam (i.e., the one which gives the maximum GJ) offers the maximum flutter speed. This is in accord with the results shown in Figs 6.7-6.9 and 6.15.

The fourth wing studied is the same wing as example wing 1 but swept 30 degrees forward. The optimisation results showed that the laminate configuration $[-23.0/89.0/-44.0]_s$ with ψ = -0.685 gave the highest flutter speed. Although this laminate configuration gives lower negative ψ than the maximum possible, i.e., ψ = -0.707, its non-dimensional frequency ratio ω_h / ω_α is higher giving higher flutter speed, see Fig. 6.10.

The final example is a the same wing as above but rotated 30 degrees backwards. The optimisation results showed that the laminate configuration $[-25_6]$ with ψ = -0.707 gave the highest flutter speed in this case as expected (see Fig. 6.11).

Because of the lack of correlative experimental evidence to confirm that a supposed optimum structure is indeed optimal, and to demonstrate that a design is not significantly degraded if there are errors in the assumed values of design parameters, a sensitivity analysis has been carried out. Errors may arise due to the unsuccessful predictions of bending and torsional rigidities which can sometimes differ by over 100% from experimental measurements [1.13, 3.17]. This is especially true in the case of torsional rigidity where certain effects, such as the torsional warping, which are omitted from most theories, can have significant effects. Other factors responsible for such deviation from test measurements were found to be the exceeded thickness tolerances along the span of a wing model and the modification of the flow over the wing by the support mechanisms [1.13].

For this reason, flutter speed sensitivities for the optimised wing 1 (i.e., the lay-up $[\pm 45]_3$ with L = 0.6 m and other properties given in Table 6.1) have been carried out. The bending (EI) and torsional (GJ) rigidities, the fibre angle (β) and the wall

thickness (t) were varied independently (i.e., one parameter at a time is changed while keeping the others constant) and their subsequent effect on the optimised flutter speed was investigated. The variations of the structural parameters against the percentage variations in the optimised flutter speed are shown in Table 6.3. The results indicate that variations in bending rigidity (EI) and fibre angle (β) have virtually no effect on the optimised flutter speed of the example wing 1. However, the effect of the torsional rigidity (GJ) and the wall thickness (t) on the optimised flutter speed are more pronounced. Although the effect of the wall thickness appears to be more pronounced than that of GJ, its deviation from the nominal value is usually small while that of GJ is usually very high. Thus, the accurate prediction of torsional rigidity ranks highest in importance since it can have significant effect on the flutter speed of an aircraft wing.

6.3 The Significance of Positive Coupling for the Flutter of Composite wings

The observation by a number of investigators [1.6-1.7, 1.11-1.12] - that when the wing is designed to exhibit wash-in behaviour is beneficial for flutter as opposed to wash-out (see, for example, Figs 5.2 and 5.10) - led most of them to concentrate on the potential of the former to enhance and/or eliminate flutter, putting aside the potential of the latter which is known to be only beneficial for divergence [1.7, 1.11-1.12]. In section 5.5 it was shown that to tailor aeroelastically a composite wing taking into account both flutter and divergence, a positive coupling (wash-out) may have to be used, as divergence is much more sensitive to changes in bending-torsion coupling as compared to flutter. This is usually the case with swept-forward wings where the divergence speed is lower than the flutter speed, see Fig. 5.4.

Therefore, this section investigates the aeroelastic characteristics of wings exhibiting wash-out behaviour. The method of analysis is essentially that of section 6.2. However, in this case the non-dimensional flutter speed ratio $V_F / b\omega_\alpha$ is plotted for a selected values of the non-dimensional frequency ratio (ω_h / ω_α) and coupling parameter (ψ) against the static unbalance (x_α).

Figures 6.19-6.22 show the variation of $V_F / b\omega_\alpha$ against x_α for four different positive values of ψ, i.e., ψ = 0, +0.2, +0.4, +0.6 respectively. Several representative

values of the frequency ratio ω_h / ω_α were used in obtaining the results as shown in each of the figures. For comparison purposes, results for negative values of ψ, i.e., for ψ = -0.2, -0.4, -0.6, are shown in Figs 6.23-6.25 respectively. (It should be noted that the values of x_α plotted in Figs 6.19-6.26 are all negative, i.e., the mass axis is behind the elastic axis, which is usually the case.) The density ratio $m / \pi\rho b^2$ and the radius of gyration defined as $r_\alpha = \sqrt{I_\alpha / mb^2}$ were kept constant at 20 and 0.5 respectively for all cases. The elastic axis location was assumed to be 20% of the semi-chord forward of the mid-chord position (i.e., a = -0.2). A modal elimination procedure has shown that in most cases the inclusion of the first two normal modes were adequate to calculate the flutter speed with satisfactory accuracy. However, three modes were used for better accuracy.

The results of Fig. 6.19 correspond to the degenerate case of a metallic wing since ψ = 0 in this case, whereas the results of Figs 6.20-6.25 apply to composite wings. One striking feature of the results shown in Figs 6.20-6.22 is that at certain combinations of positive ψ and negative x_α the flutter speed is unaffected by changes in the frequency ratio ω_h / ω_α. This phenomenon was first noticed in Fig. 5.6 of chapter 5.

The negative value of x_α, where the above phenomenon occurs, gets smaller with increase in the value of positive ψ as shown in Figs 6.20-6.22. A detailed investigation was carried out around these intersection points and the results confirmed the existence of such points. The results of this investigation are shown in Tables 6.4-6.7.

The cause of these intersection points was further investigated. They occur because at these particular values of ψ and x_α, an increase in the frequency ratio ω_h / ω_α is accompanied by an increase in the first bending and first torsional frequencies. The increase in value of these two frequencies is such that, although the flutter frequency increases as expected, the flutter speed remains constant, see for example Fig. 6.26 where the flutter speed is calculated for three values of ω_h / ω_α for ψ = 0.4 and x_α = -0.225 (see also Table 6.6).

Another important observation that can be made from Figs 6.19-6.22 is that for certain values of ω_h / ω_α, the flutter speed is unaffected from changes in x_α. In other words, the mass can be favourably distributed in a chordwise sense without adversely affecting the flutter speed. Furthermore, for high values of ω_h / ω_α, the flutter speed increases with increase in the negative value of x_α. This is in contrast with the results obtained using a negative ψ where the flutter speed decreases with increase in negative x_α as expected (see Figs 6.23-6.25). It is interesting to note that when high negative x_α is present, positive ψ gives higher flutter speeds than the negative ψ (see, for example, Figs 6.22 and 6.25).

The above observation can be tentatively attributed to the fact that when negative x_α is combined with positive ψ or vice-versa, frequency separation occurs between the fundamental bending and torsional modes when compared to the case of $x_\alpha = 0$. This is shown in Fig. 6.27 where the frequency of the first bending and torsional modes for $\psi = 0.4$ are plotted against negative x_α for a selected values of the frequency ratio ω_h / ω_α. From this figure, it can be seen that as the negative x_α increases, the frequency difference between the two vibrational modes increases as well.

In contrast, when negative ψ (ψ = -0.4 in this case) is present together with negative x_α (see Fig. 6.28), frequency convergence occurs between the two modes and as a result the flutter speed reduces. The above phenomenon was first noticed in chapter 4 (see Figs 4.9 and 4.10).

Thus it can be concluded that positive bending-torsion coupling or wash-out behaviour can be useful for flutter when the mass axis is well behind the shear centre of the cross-section giving higher flutter speeds than the negative one or wash-in behaviour. At certain combinations of positive ψ and negative x_α the flutter speed is unaffected by changes in the frequency ratio ω_h / ω_α.

6.4 The Role of Modal Interchange on the Flutter of Composite Wings

One striking feature of all previous investigations of chapters 5 and 6 is that the ply orientations in a given laminate which result into the wash-in effect is found to increase the flutter speed as opposed to wash-out which usually has an unwelcome effect on flutter. Surprisingly, the author's literature survey shows that no one seems to have given any detailed explanations or reasons for the beneficial or otherwise effects of wash-in or wash-out on the flutter behaviour of composite wings. Furthermore, several authors investigating the flutter behaviour of composite wings, have observed some unexpected blips or abrupt changes in the flutter behaviour occurring at certain fibre angles of the laminate (e.g., Figs 7 and 10 of Ref. [1.9], Figs 11 and 12 of Ref. [1.6]). No satisfactory explanation has been given of these observations which were confirmed by the present study in chapter 5, see Fig. 5.10. It was concluded in chapter 5 that the primary cause for these blips lies in the modal contributions at flutter, arising from ply orientations in the laminate. Therefore, the objective of this section is to further investigate the above unusual features of composite wings and to pin-point their underlying cause.

6.4.1 Method of Analysis

The method of analysis is essentially that of section 5.6. For illustrative purposes, one of the example wings of the above section which exhibited the above two uncharacteristic features is further studied. First, a modal elimination technique is used to establish the number of dominant normal modes which contributed to the flutter behaviour for different ply angles in the laminate. Next, the flutter mode is computed using selected normal modes which were found to be primarily responsible to cause flutter. Finally, the contribution from each normal mode to the flutter mode is isolated in each case and their relative individual contributions are presented. The results are discussed and some conclusions are drawn.

6.4.2 Calculation of Flutter Modes

The flutter speed (V_F) and flutter frequency (ω_F) are computed (by setting the determinant of the flutter matrix [QA] in Eqn. (5.1) to zero and seeking a non-trivial solution) for further investigation of the associated flutter mode. This flutter mode can be recovered by giving one of the generalised coordinates an arbitrary value and then determining the rest of the generalised coordinates by back-substitution. Thus, if 'n' is the number of normal modes used in the analysis, the flutter problem is formulated as,

$$[QA]\{q\} = 0 \tag{6.1}$$

where $[QA]$ is the nxn flutter matrix obtained by summing the generalised mass, stiffness and aerodynamic matrices, and $\{q\}$ is the vector of n generalised coordinates, q_i (i =1,2,...n). Note that $[QA]$ is a matrix whose elements are complex numbers dependent on airspeed (V) and frequency (ω). For each singular root of $[QA]$ the flutter speed V_F, and the flutter frequency ω_F are found, together with the associated vector q_1, q_2, q_3 ... and q_{n-1} whilst q_n being given the arbitrary value (1+i) where i = $\sqrt{-1}$.

The flutter mode for the vertical displacement (H) and the pitching rotation (Φ) at a spanwise station y can then be expressed as,

$$H(y) = q_1 h_1(y) + q_2 h_2(y) + \ldots + q_n h_n(y) = \sum_1^n q_i h_i(y) \tag{6.2}$$

$$\Phi(y) = q_1 \phi_1(y) + q_2 \phi_2(y) + \ldots + q_n \phi_n(y) = \sum_1^n q_i \phi_i(y) \tag{6.3}$$

where $h_i(y)$ and $\phi_i(y)$ are mode shapes in the i-th normal mode corresponding to the bending displacement and torsional rotation at a spanwise distance y from the root.

The terms $q_i h_i(y)$ and $q_i \phi_i(y)$ in Eqns (6.2) and (6.3) are respectively the contributions of the i-th normal mode to the bending displacement $H(y)$, and torsional rotation $\Phi(y)$ of the flutter mode. Since q_i is complex, both $q_i h_i(y)$ and $q_i \phi_i(y)$ are also complex, so that both $H(y)$ and $\Phi(y)$ will have an absolute value and a phase which can be plotted along the span to provide relative measures of the bending displacements, torsional rotations and their phase difference at flutter speed. Alternatively $q_i h_i(y)$ and $q_i \phi_i(y)$ at various spanwise stations may be plotted vectorially in an Argand diagram, showing magnitude, direction and phase of the contribution from the i-th normal mode to the flutter mode. This procedure has been followed in the example which follows.

6.4.3 Discussion of Results

First the unexpected blips or abrupt changes in the flutter behaviour occurring at certain fibre angles of the laminate are investigated. One of the illustrative examples given in section 5.6 of chapter 5 which is representative of the present analysis, is used here to obtain the results. The wing is modelled using a total of 14 plies of graphite/epoxy material with all fibres in the laminate oriented in the same direction, i.e., the stacking sequence used is $[\beta]_{14}$ where β is the fibre angle in degrees. The material and other properties of the wing are given in Table 5.2 of chapter 5. The specific case of the 20^0 swept-back wing is taken up for further studies. Negative ply angles are given precedence in obtaining the results because the unexpected blips in the flutter behaviour occurred mainly at negative ply angles.

Table 6.8 shows the rigidity properties of the wing used in this analysis for various (negative) ply angles. These data are given for interested readers who would like to investigate the problem further.

The flutter speed of the above wing for various negative ply angles is shown in Fig. 6.29, but to a much larger scale than the one shown in chapter 5. As shown in the figure, the maximum achievable flutter speed occurs when the fibre angle β is around -30^0 where the ratio V_F / V_{F0} is about 1.7. V_F is the actual flutter speed of the laminated wing and V_{F0} is the corresponding flutter speed when the sweep angle and fibre orientation in each of the plies in the laminate representing the wing are set to zero.

However, the flutter behaviour for the ply angles between -5^0 and -15^0 is somehow unusual showing a sudden jump, or blip, in the flutter speed around $\beta = -8^0$. The reasons for this unexpected behaviour in flutter speed are discussed next.

Although the first five normal modes of the wing were used in the flutter analysis reported earlier in section 5.6, it was later found that for most of the cases only the first three were necessary to compute the flutter speed with sufficient accuracy. These three modes with corresponding natural frequencies are shown in Fig. 6.30 for fibre angles -8^0, -10^0 and -25^0 respectively. (Note that these fibre angles were chosen because they correspond to points B, C and D of Fig. 6.29.) The first natural frequency has significantly altered only for $\beta = -25^0$ but the corresponding mode shapes for this frequency are virtually unaltered for the three cases. However, the first mode shows very strong coupling between the bending and torsional modes of deformation of the wing. The second natural frequency gets reduced like the first one, as β is reduced from -8^0 to -25^0 but more importantly, the mode shapes have changed significantly. (Investigations of vibration of composite beams in chapter 4 have shown that a very small change in natural frequency may result into quite dramatic change in the mode shape, e.g., see Figs 4.5 and 4.6.) It is evident from Fig. 6.30 that the third mode is more or less a pure torsional mode. One distinctive feature of the modes shown is that the torsional displacement in all of them is quite pronounced.

Next the flutter analysis was carried out using (i) all the three modes, (ii) modes 1 and 2 only, and (iii) modes 1 and 3 only. The fundamental (mode 1) is always included in the analysis to ensure the lowest boundary of flutter speeds. A modal elimination procedure is then adopted to determine the relative importance of modes 1, 2 and 3 when initiating flutter at various (negative) ply angles. Representative results are shown in Table 6.9.

It is clear from the results shown in Table 6.9 that for $\beta = -5^0$ and $\beta = -8^0$, the flutter speed can be predicted within reasonable accuracy using modes 1 and 3 only so that mode 2 becomes relatively unimportant in the flutter analysis. These two ply angles correspond to points A and B of Fig. 6.29. Table 6.9 also shows that for ply angles -10^0 (point C on Fig. 6.29) and -12^0, all the three modes are required in the analysis to achieve acceptable accuracy in flutter speed. However, when the ply angle

is -25^0 (point D on Fig. 6.29), once again modes 1 and 3 give sufficiently accurate results in flutter speeds. Thus, it appears that if mode 2 is completely omitted from the analysis, the points A, B and D can be joined to give a smooth curve without the dip at point C. This will naturally give considerable error in flutter speed in the region $-20^0 < \beta < -8^0$ where mode 2 plays a relatively important role in flutter prediction (see Table 6.9).

It will be seen later from further investigation of the flutter modes and their constituent components of normal modes that the results given in Table 6.9 are verified. First, however, the absolute values of the bending displacement and torsional rotation in the flutter mode (as given by Eqns (6.2) and (6.3)), together with their corresponding phase angles are computed using all the three modes. The results for ply angles -8^0, -10^0 and -25^0 are shown in Fig. 6.31. The flutter modes in all cases clearly show that the deformation of the wing is dominated by torsion as was the case with the normal modes of free vibration shown in Fig. 6.30. The plots of the phase difference between the bending displacements and torsional rotations show predictable pattern, particularly for $\beta = -8^0$ and $\beta = -25^0$ where torsional motion lags the bending motion as would normally be expected in a flutter situation. However, the results on phase difference for $\beta = -10^0$ case, show a somewhat unusual pattern. The torsional motion lags the bending motion from 35% to 100% of the span (i.e., the tip) whereas it leads the bending motion from root to 35% of the span in an unusual way. The investigation has shown that the presence of mode 2 is primarily responsible for this unusual behaviour.

To gain further insights into the flutter behaviour of the wing, each component of $q_i h_i(y)$ and $q_i \phi_i(y)$ is calculated to determine the relative measures of modal contributions to bending displacements and torsional rotations in the flutter mode (see Eqns (6.2) and (6.3)). Figure 6.32 shows the contribution of normal modes to the flutter mode for the case $\beta = -10^0$ in an Argand diagram for both bending displacement and torsional rotation at three spanwise stations of the wing. (Note that unlike Fig. 6.31 the (net) relative bending displacement (H) and torsional rotation (Φ) are not shown to scale, although the relative contributions of normal modes are accurately scaled.) The results are presented for this case because all three modes are involved (see Table 6.9). Similar analyses were carried out at various ply angles and the results confirmed the flutter predictions given by Table 6.9. As an illustration, when

the ply angles were -8^0 and -25^0, only modes 1 and 3 contributed significantly to flutter so that the vectorial representation of flutter modes H and Φ consisted of ($h_1 q_1$, $h_3 q_3$) and ($\phi_1 q_1$ and $\phi_3 q_3$) respectively. It can be thus concluded that modal interchanges can and will significantly alter the flutter speed and associated flutter mode of a composite wing in an unexpected way : one in which it is possible to observe sudden jumps or discontinuities in flutter speeds as a result of changing the ply orientations in a laminate.

A similar procedure to the one used in the above investigation is also used to investigate the wash-in and wash-out behaviour of laminated composite wings and their subsequent effects on flutter speed.

The previous example, i.e., $[\beta]_{14}$ which is representative of the present analysis as well, is used here to obtain the results. However, in this case the specific case of the unswept wing is taken up for further studies. This is so chosen to study the sole effect of ply orientation (and hence wash-in and wash-out) avoiding the coupling between the bending and torsional deformations exhibited by the swept wings.

The flutter speed for the above wing for ply angles $-90^0 < \beta < 90^0$ is shown in Fig. 6.33. As can be seen in the figure, the maximum achievable flutter speed occurs when the fibre angle β is around -25^0 where the ratio V_F / V_{F0} is about 1.65. At this fibre angle the wash-in behaviour of the wing is quite pronounced. On the other hand, when the fibre angle $\beta = 25^0$, the wing exhibits wash-out behaviour and there is not much improvement as evident from Fig. 6.33. The reasons for these phenomena for the above two ply angles, i.e., $\beta = 25^0$ and $\beta = -25^0$ are discussed below.

The bending, torsional and bending-torsion coupling rigidities were calculated using Eqns (3.24)-(3.26) of chapter 3 as EI = 2.313 Nm^2, GJ = 2.132 Nm^2 and K = $\pm$ 1.570 Nm^2 for the two laminate configurations respectively. These rigidities were subsequently used in the free vibration and flutter analysis of the cantilever composite wing. The associated values of ψ are $\pm$ 0.707.

Like previous examples, the first three normal modes were adequate to compute the flutter speed for most cases with sufficient accuracy. These three modes with corresponding natural frequencies are shown in Fig. 6.34 for fibre angles 25^0 and

-25^0 respectively. The first mode clearly shows very strong coupling between the bending and torsional modes of deformation whereas the second mode indicates relatively less coupling between the two. The third mode is more or less a pure torsional mode as evident from Fig. 6.34. It should be noted that the natural frequencies are unchanged for the two ply angles, i.e., $\beta = -25^0$ and $\beta = 25^0$ as expected, but the mode shapes have changed in the sense that the former gives the wash-in behaviour whereas the latter gives the wash-out behaviour of the wing (with the absolute values of the bending and torsional displacements remaining unchanged). Note that the torsional displacement of all the modes shown is quite pronounced.

As in the previous investigation, the flutter analysis was carried out using (i) all the three modes, i.e., modes 1, 2 and 3, (ii) modes 1 and 2, and (iii) modes 1 and 3. A modal elimination procedure is then adopted to determine the relative importance of modes 1, 2 and 3 when causing flutter of the wing for $\beta = -25^0$ and $\beta = 25^0$. The results are shown in Table 6.10.

It is quite clear from the results shown in Table 6.10 that for $\beta = -25^0$, the flutter speed can be predicted quite accurately using modes 1 and 3 only whereas for $\beta = 25^0$ all the three modes are needed to obtain acceptable accuracy. Clearly mode 2 influences the flutter speed for the latter case but is quite unimportant in the former case. Thus, if mode 2 is completely omitted from the analysis, the laminate with $\beta = 25^0$ gives deceptive results as shown in Table 6.10.

The absolute values of the flutter mode for its bending displacements (H) and torsional rotations (Φ) and their corresponding phase angles are computed using all the three modes. The results for ply angles -25^0 and 25^0 are respectively shown in Fig. 6.35. The flutter modes in all cases clearly show that the deformation of the wing is dominated by torsion. A similar pattern was observed with the normal modes of free vibration, see Fig. 6.34. The plots of the phase difference between the bending displacements and torsional rotations show a predictable pattern for $\beta = -25^0$, where the torsional motion lags the bending motion as expected. However, the results on phase difference for $\beta = 25^0$ case, show a somewhat unusual pattern. The torsional motion lags the bending motion only from 45% to 100% of the span whereas it leads the bending motion from root to about 45% of the span in an unusual way. The

investigation has shown that the presence of mode 2 is primarily responsible for this behaviour.

Figures 6.36 and 6.37 respectively show the contribution of normal modes to the flutter mode for $\beta = -25^0$ and $\beta = 25^0$ in an Argand diagram for both bending displacement and torsional rotation at three spanwise stations of the wing. (Note that unlike Fig. 6.35 the (net) relative bending displacement (H) and torsional rotation (Φ) are not shown to scale, although the relative contributions of normal modes are accurately scaled.) It is important to note that the mode 2 makes significant contribution to the flutter mode when $\beta = 25^0$ (see Fig. 6.37) whereas its contribution is relatively marginal when $\beta = -25^0$ (see Fig. 6.36). Analyses similar to the ones shown in Figs 6.35-6.37 were carried out at various positive and negative ply angles and the results confirm that modal interchanges in the free vibration behaviour of laminated composite wings are primarily responsible for the wash-in behaviour being more beneficial for flutter than wash-out behaviour.

6.5 Conclusions

Several issues related to the flutter characteristics of cantilever composite wings have been identified and illustrated in this chapter. The modal interchanges in the free vibration and flutter behaviour of laminated composite wings have been shown to be primarily responsible for many of their unusual characteristics, such as, the unexpected blips and/or abrupt changes in the flutter behaviour and the wash-in behaviour being more beneficial for the flutter than the wash-out one.

The most interesting feature of this part of the study, however, is the identification of two very important parameters which influence the flutter behaviour of composite wings. These are (i) the ratio of the (uncoupled) fundamental bending and torsional natural frequencies (ω_h / ω_α) and (ii) the bending-torsion coupling parameter ψ. The use of non-dimensional parameter combinations such as ψ and ω_h / ω_α for design trade-off studies are very useful since the laminate geometry and construction details need not be defined for such a study.

Generally, the results show that for an unswept wing when the ratio ω_h / ω_α is less than about 0.15, the maximum flutter speed can be achieved by maximising the torsional rigidity GJ, whereas for higher frequency ratios the maximum flutter speed can be achieved by obtaining the largest negative value of the bending-torsion coupling parameter ψ. Thus, the maximum flutter speed of an unswept wing can be achieved either by maximising GJ or negative ψ and therefore general optimisation studies using the fibre angle or other rigidity properties as design variables are not required in this case. In contrast, the maximum flutter speed of a swept-forward wing can be achieved generally by maximising the negative ψ for all values of ω_h / ω_α. However, to maximise GJ when ψ > -0.6 (which is usually the case) offers a better prospect of maximising the flutter speed of a swept-forward wing. Results for the swept-back wing show that very high flutter speeds can be achieved for relatively small values of negative ψ when ω_h / ω_α is below 0.1. Maximising GJ appears not to be that beneficial in this case. The above conclusions have been confirmed by independent optimisation studies. It is important to emphasise, however, that large negative values of ψ are accompanied by very low divergence speeds.

Another interesting aspect of this study shows that at certain combinations of positive values of ψ (wash-out) and negative values of x_α (the centroid of the cross-section situated behind the shear centre), the flutter speed is unaffected by changes in the frequency ratio ω_h / ω_α. Also interesting is the fact that at certain combinations of ω_h / ω_α and positive values of ψ, the flutter speed is shown to be unaffected or even raised when x_α increases backwards, (i.e., it becomes more negative) giving higher flutter speeds than the negative ψ (wash-in). Thus, the general statement that wash-in is always beneficial for flutter as opposed to wash-out is not always true.

Having established the ability to design a composite wing with an optimised flutter speed, attention now turns to gust alleviation of composite wings by the use of trailing edge active controls without compromising the already optimised flutter speed. This topic is discussed in the next chapter.

TABLE 6.1

Material and other properties for the Hercules ASI/3501-6 graphite/epoxy optimised wings 1,2,4 and 5

Property	Value/Unit
E_1	98.0 GN/m^2
E_2	7.90 GN/m^2
ν_{12}	0.28
$G_{12} = G_{13} = G_{23}$	5.60 GN/m^2
ρ	1520 kg/m^3
Ply thickness	0.134×10^{-3} m
Chord	0.0761 m
Number of Plies	6
Density ratio	16.67
r_α^2	0.3334
x_α	- 0.1
a	- 0.2

TABLE 6.2

Material and other properties for the graphite/epoxy (HTA-6376C) optimised wing 3

Property	Value/Unit
E_1	146. 86 GN/m^2
E_2	11.03 GN/m^2
ν_{12}	0.28
$G_{12} = G_{13}$	6.205 GN/m^2
G_{23}	4.826 GN/m^2
ρ	1604.1 kg/m^3
Ply thickness	0.1397×10^{-3} m
Number of Plies on each side	6
Density ratio	121
r_α^2	0.7
x_α	- 0.1
a	- 0.2

TABLE 6.3

Sensitivity analysis for the optimised flutter speed of the example wing 1

Change in EI versus $V_{F(max)}$		**Change in GJ versus $V_{F(max)}$**		**Change in β versus $V_{F(max)}$**		**Change in wall thickness t versus $V_{F(max)}$**	
EI (%)	**V_F (%)**	**GJ (%)**	**V_F (%)**	**β (deg.)**	**V_F (%)**	**t (%)**	**V_F (%)**
-5	-0.15	-5	-2.59	- 2	-0.30	-0.5	-0.92
-10	-0.19	-10	-5.20	- 1	-0.12	-1.0	-1.58
-15	-0.22	-25	-13.53	+ 1	-0.15	-2.0	-3.08
-20	-0.25	-40	-22.77	+ 2	-0.29	-5.0	-7.54

TABLE 6.4

Natural frequencies, flutter speed and flutter frequency for $\psi = 0.0$ and x_α = - 0.5

ω_h / ω_α	**MODE**	**NATURAL FREQUENCY (rad/s)**	**FLUTTER SPEED (m/s)**	**FLUTTER FREQUENCY (rad/s)**
0.1	1B	6.6	22.2	32.9
	2C	39.9		
	3T	67.8		
0.2	1B	13.0	21.3	34.4
	2T	61.3		
	3T	84.5		
0.3	1B	19.0	20.7	37.5
	2T	65.2		
	3T	109.6		
0.4	1T	24.5	20.3	41.4
	2T	68.0		
	3T	125.2		
0.5	1T	29.2	20.6	44.8
	2T	71.4		
	3T	133.7		
0.6	1T	33.0	21.7	48.6
	2T	75.6		
	3T	138.5		
0.7	1T	36.0	23.6	52.8
	2T	80.7		
	3T	141.6		

TABLE 6.5

Natural frequencies, flutter speed and flutter frequency for $\psi = 0.2$ and $x_\alpha = -0.3$

ω_h / ω_α	MODE	NATURAL FREQUENCY (rad/s)	FLUTTER SPEED (m/s)	FLUTTER FREQUENCY (rad/s)
0.1	1B	6.4	24.5	32.9
	2C	39.7		
	3T	67.0		
0.2	1B	12.6	23.4	36.5
	2T	66.3		
	3T	78.2		
0.3	1B	18.5	22.7	40.0
	2T	68.7		
	3T	107.7		
0.4	1T	24.0	22.1	44.0
	2T	70.6		
	3T	128.9		
0.5	1T	29.0	21.7	49.2
	2T	73.1		
	3T	141.9		
0.6	1T	33.5	21.7	53.9
	2T	76.2		
	3T	149.6		
0.7	1T	37.2	22.3	59.3
	2T	79.9		
	3T	154.3		

TABLE 6.6

Natural frequencies, flutter speed and flutter frequency for $\psi = 0.4$ and $x_\alpha = -0.225$

ω_h / ω_α	MODE	NATURAL FREQUENCY (rad//s)	FLUTTER SPEED (m/s)	FLUTTER FREQUENCY (rad/s)
0.1	1B	6.0	24.6	31.4
	2C	37.1		
	3T	67.0		
0.2	1B	11.7	23.8	36.6
	2T	68.4		
	3T	70.8		
0.3	1T	17.1	23.1	40.7
	2T	70.1		
	3T	98.8		
0.4	1T	22.1	22.7	45.1
	2T	72.2		
	3T	119.3		
0.5	1T	26.7	22.7	50.2
	2T	74.8		
	3T	132.9		
0.6	1T	30.7	22.8	55.5
	2T	77.9		
	3T	141.5		
0.7	1T	34.3	23.2	60.4
	2T	81.6		
	3T	147.1		

TABLE 6.7

Natural frequencies, flutter speed and flutter frequency for $\psi = 0.6$ and $x_\alpha = -0.15$

ω_h / ω_α	MODE	NATURAL FREQUENCY (rad/s)	FLUTTER SPEED (m/s)	FLUTTER FREQUENCY (rad/s)
0.1	1B	5.2	23.7	27.6
	2C	32.3		
	3T	67.1		
0.2	1B	10.2	23.4	35.9
	2T	60.0		
	3T	70.2		
0.3	1T	14.9	23.1	40.8
	2T	68.7		
	3T	87.8		
0.4	1T	19.2	22.8	45.3
	2T	71.3		
	3C	105.9		
0.5	1T	23.2	22.8	50.4
	2T	74.0		
	3C	118.6		
0.6	1T	26.7	22.9	55.7
	2T	77.1		
	3C	127.2		
0.7	1T	29.8	23.3	61.3
	2T	80.7		
	3C	133.1		

TABLE 6.8

Rigidity properties for negative ply angles of the example composite wing. Length = 0.6 m, mass per unit length (m) = 0.2172 Kg/m and mass moment of inertia (I_α) = 0.1052×10^{-3} Kgm.

Ply Angle (β) (degrees)	Bending rigidity (Nm^2)	Torsional rigidity (Nm^2)	Bending-torsion coupling rigidity (Nm^2)
- 5	4.039	1.034	-0.600
-8	3.926	1.174	-0.930
-10	3.818	1.294	-1.130
-12	3.683	1.428	-1.296
-25	2.313	2.132	-1.570

TABLE 6.9

Effects of the number of normal modes on flutter speeds at various ply angles for the laminated wing $[\beta]_{14}$.

	FLUTTER SPEED (m/s)		
Ply angle	**Normal modes used**		
β (degrees)	**(1,2,3)**	**(1, 2)**	**(1, 3)**
- 5	**40.0**	**71.4**	**45.5**
-8	**44.1**	**117.2**	**45.5**
-10	**37.5**	**108.5**	**48.1**
-12	**40.2**	**98.9**	**49.4**
-25	**64.7**	**--------**	**65.0**

TABLE 6.10

Effects of the number of normal modes on flutter speeds at two ply angles for the laminated wing $[\beta]_{14}$.

	FLUTTER SPEED (m/s)		
Ply angle	**Normal modes used**		
β (degrees)	**(1,2,3)**	**(1, 2)**	**(1, 3)**
-25	**63.9**	**-------**	**64.0**
25	**39.6**	**56.9**	**51.6**

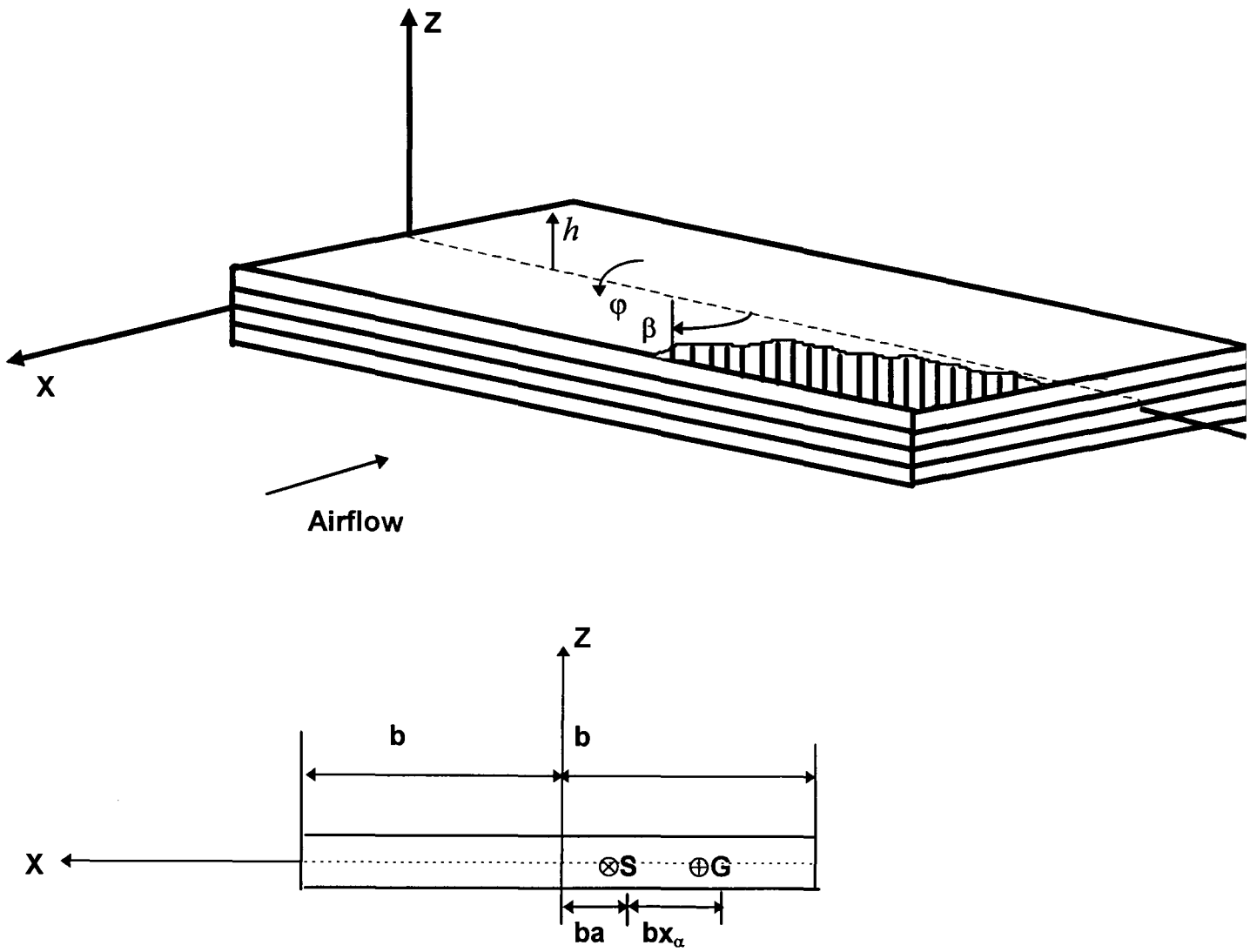

Fig. 6.1. Coordinate system and sign convention for a laminated composite beam; (S : Shear centre ; G : Centroid).

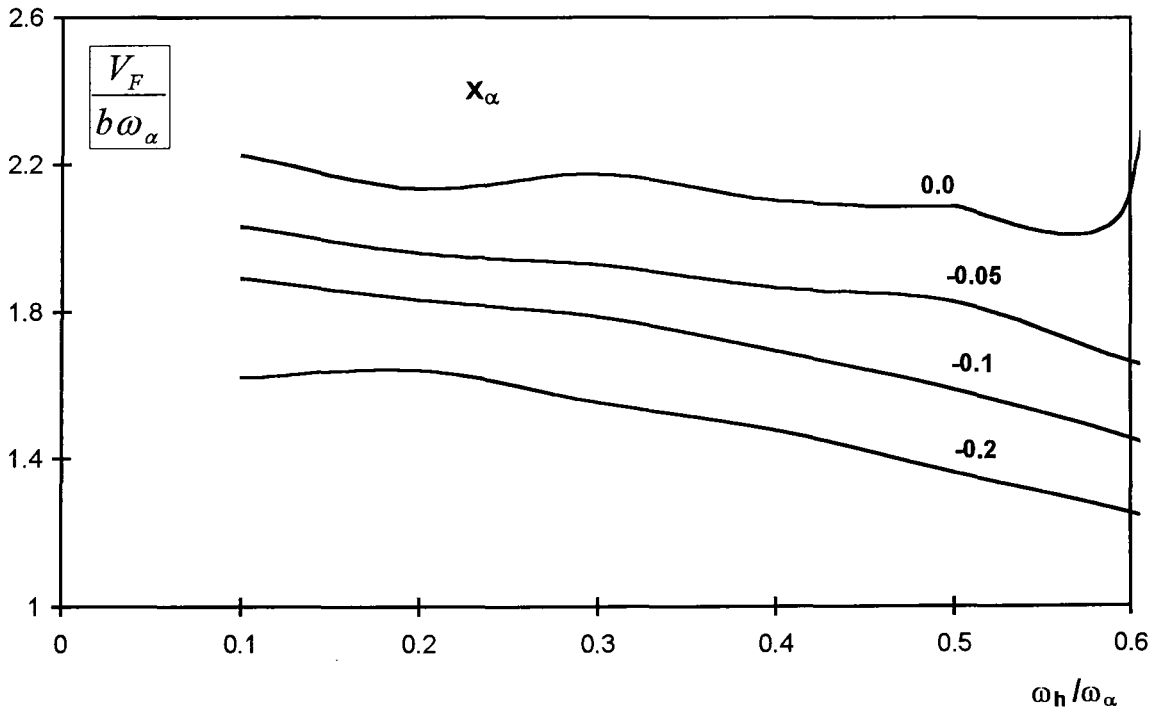

Fig. 6.2. Dimensionless flutter speed $V_F/b\omega_\alpha$ plotted against frequency ratio ω_h/ω_α for various values of dimensionless static unbalance x_α for ψ = 0; $m/\pi\rho b^2$ =10 , r_α = 0.5 , a = -0.2.

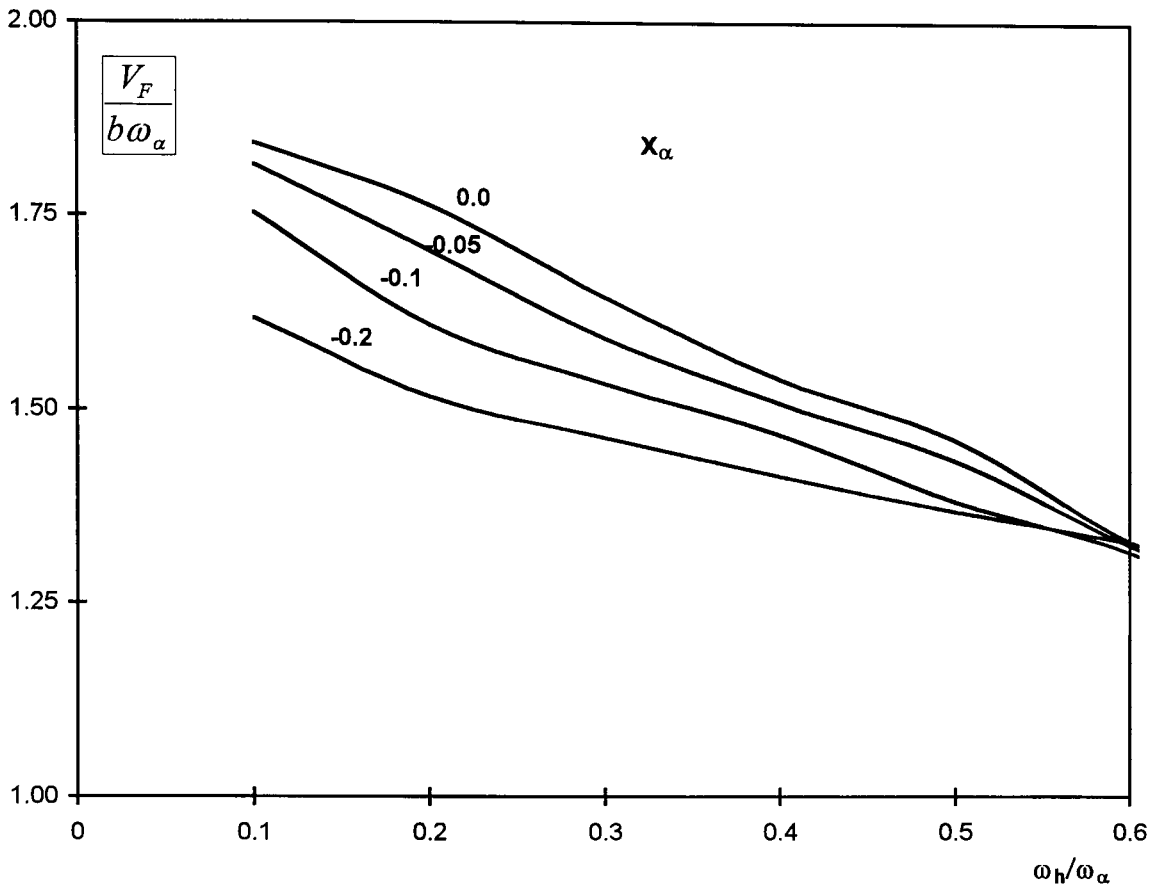

Fig. 6.3. Dimensionless flutter speed $V_F/b\omega_\alpha$ plotted against frequency ratio ω_h/ω_α for various values of dimensionless static unbalance x_α for ψ = 0.4; $m/\pi\rho b^2$ =10 , r_α = 0.5 , a = -0.2.

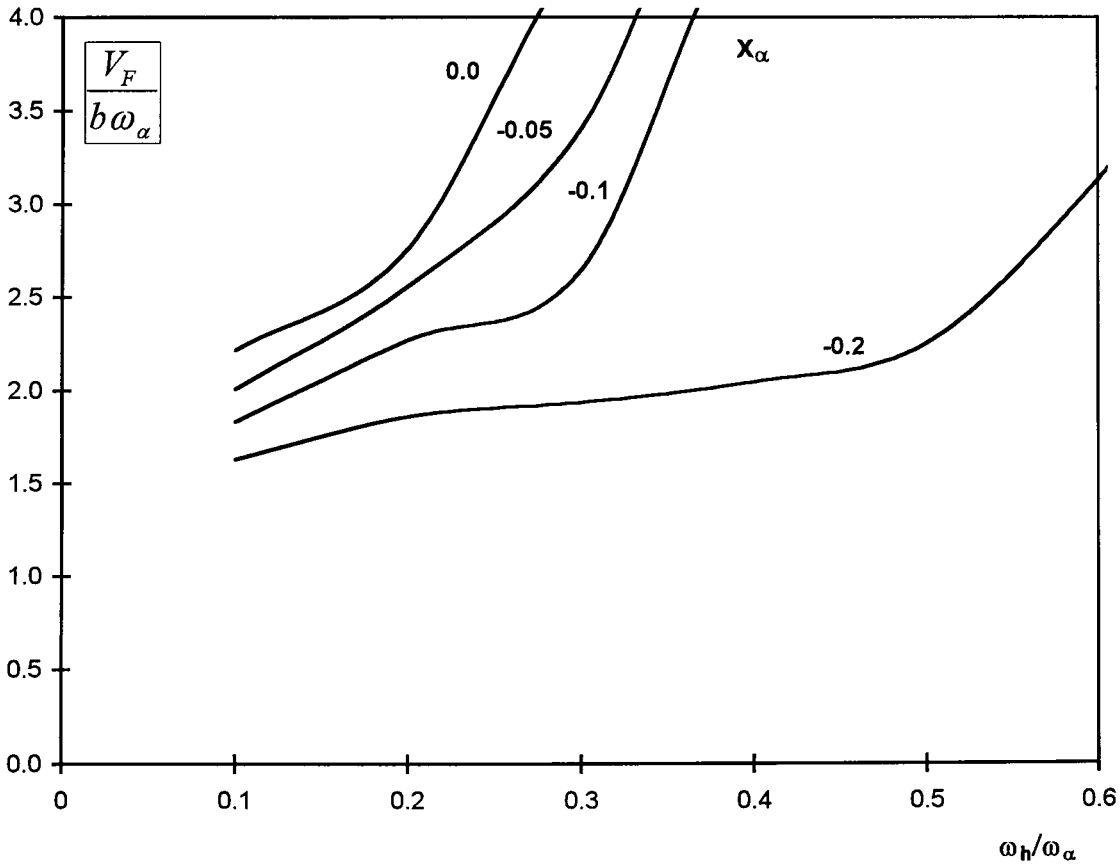

Fig. 6.4. Dimensionless flutter speed $V_F/b\omega_\alpha$ plotted against frequency ratio ω_h/ω_α for various values of dimensionless static unbalance x_α for ψ = - 0.4; $m/\pi\rho b^2$ =10 , r_α = 0.5 , a = -0.2.

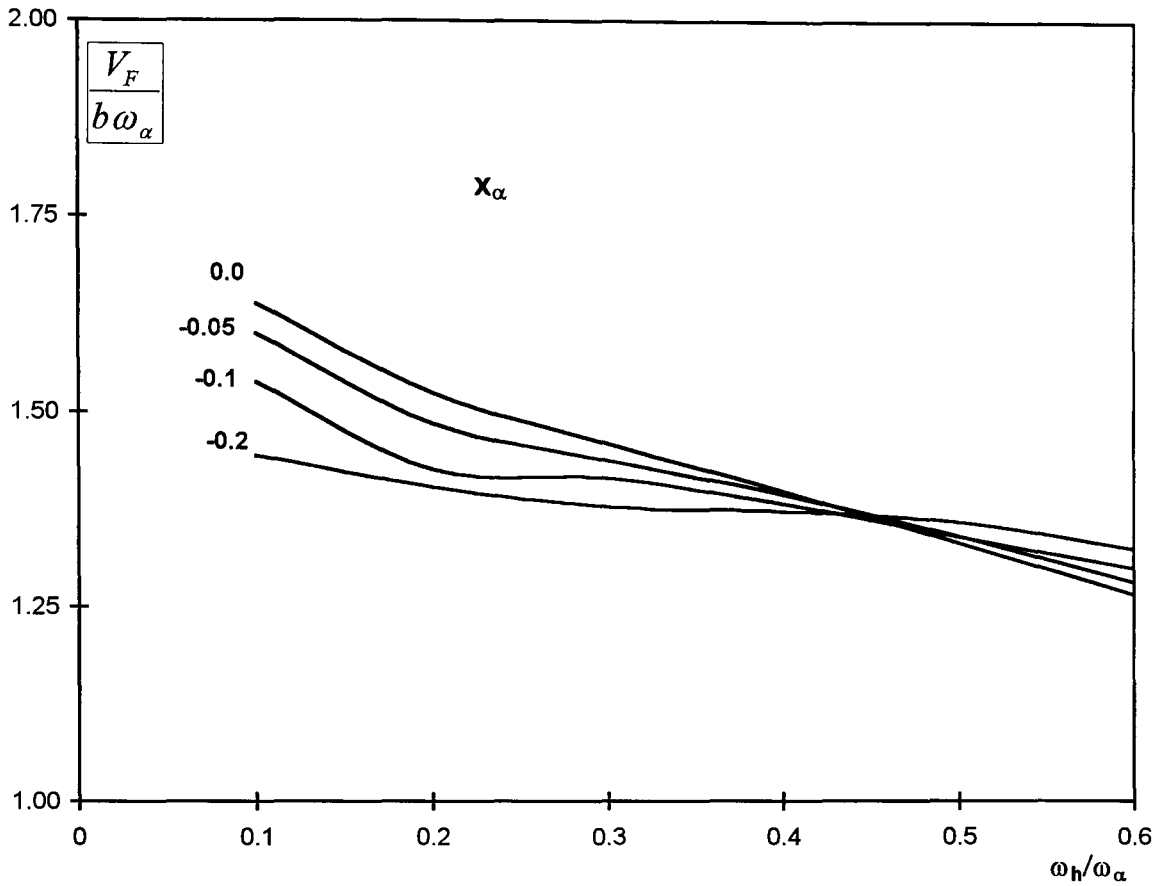

Fig. 6.5. Dimensionless flutter speed $V_F/b\omega_\alpha$ plotted against frequency ratio ω_h/ω_α for various values of dimensionless static unbalance x_α for ψ = 0.7; $m/\pi\rho b^2$ =10 , r_α = 0.5 , a = -0.2.

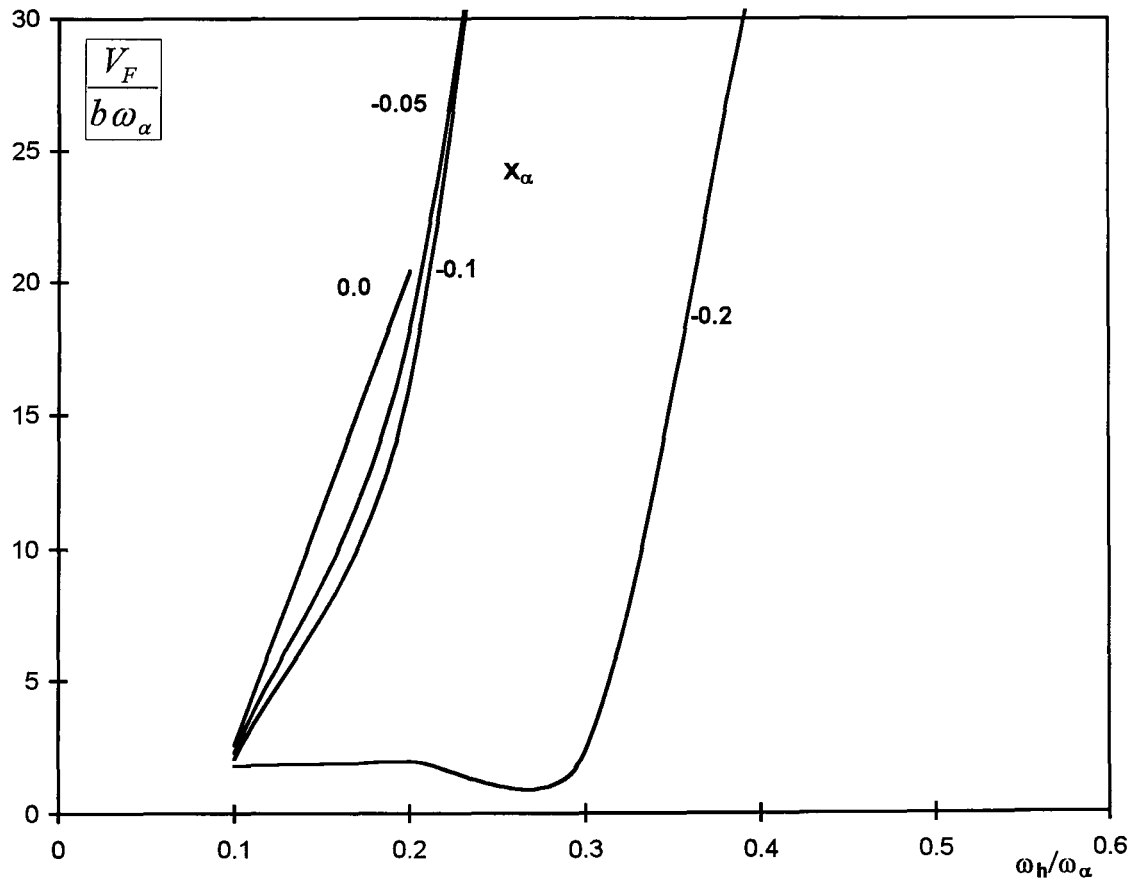

Fig. 6.6. Dimensionless flutter speed $V_F/b\omega_\alpha$ plotted against frequency ratio ω_h/ω_α for various values of dimensionless static unbalance x_α for ψ = -0.7; $m/\pi\rho b^2$ =10 , r_α = 0.5 , a = -0.2.

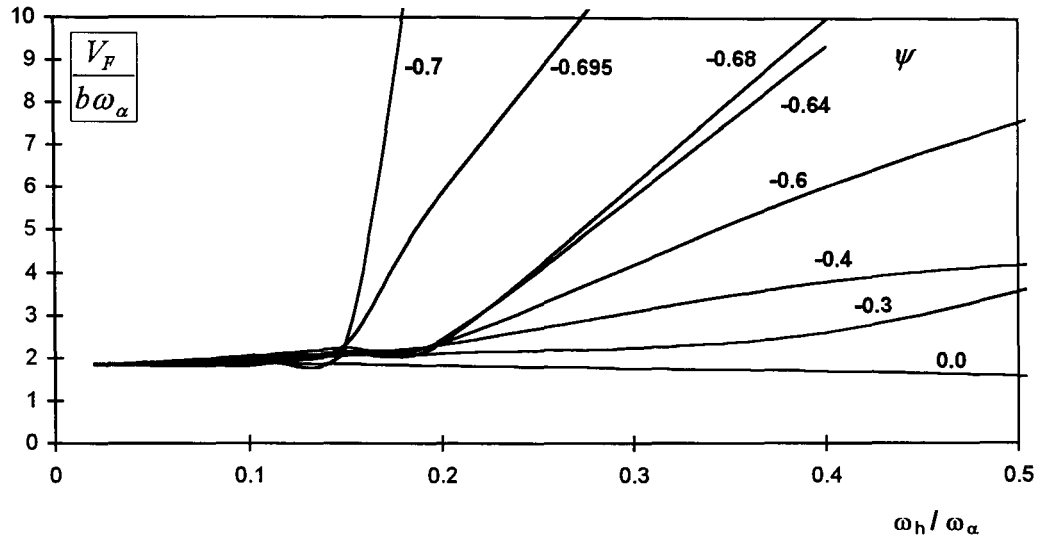

Fig. 6.7. Dimensionless flutter speed $V_F/ b\omega_\alpha$ against frequency ratio ω_h/ω_α for various values of coupling parameter ψ for density ratio $m/\pi\rho b^2 = 10$; $r_\alpha = 0.5$, $x_\alpha = -0.1$, $a = -0.2$.

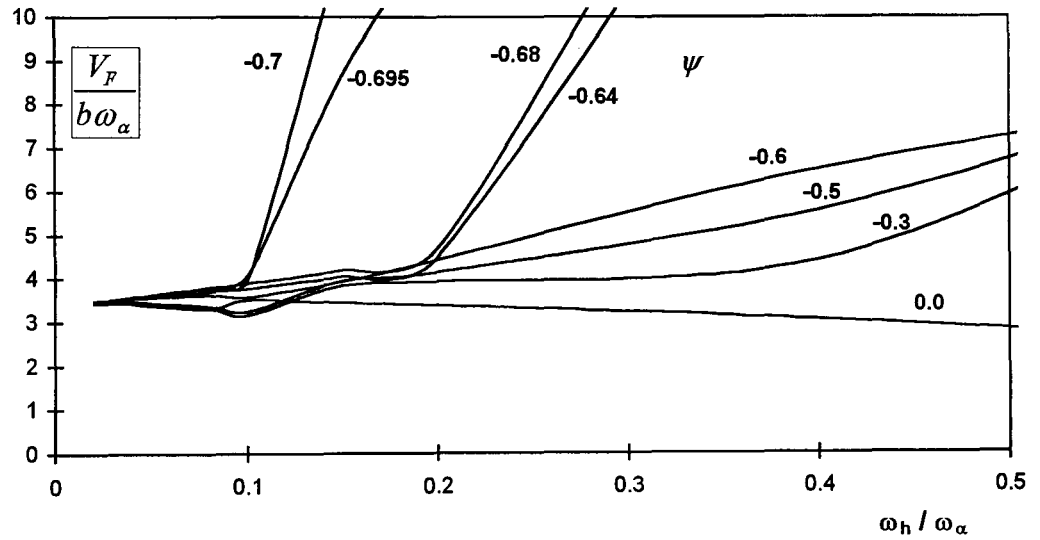

Fig. 6.8. Dimensionless flutter speed $V_F/ b\omega_\alpha$ against frequency ratio ω_h/ω_α for various values of coupling parameter ψ for density ratio $m/\pi\rho b^2 = 40$; $r_\alpha = 0.5$, $x_\alpha = -0.1$, $a = -0.2$.

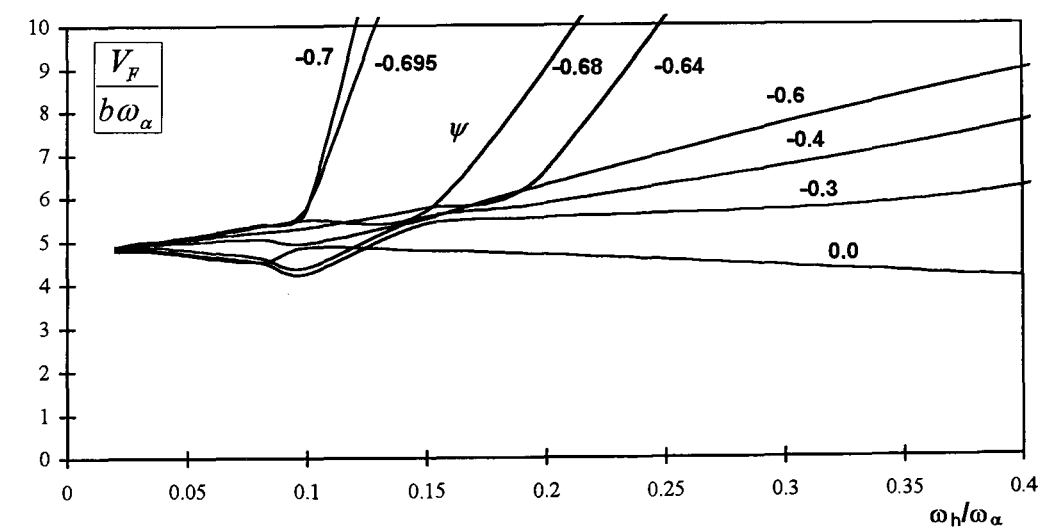

Fig. 6.9. Dimensionless flutter speed $V_F/ b\omega_\alpha$ against frequency ratio ω_h/ω_α for various values of coupling parameter ψ for density ratio $m/\pi\rho b^2 = 80$; $r_\alpha = 0.5$, $x_\alpha = -0.1$, $a = -0.2$.

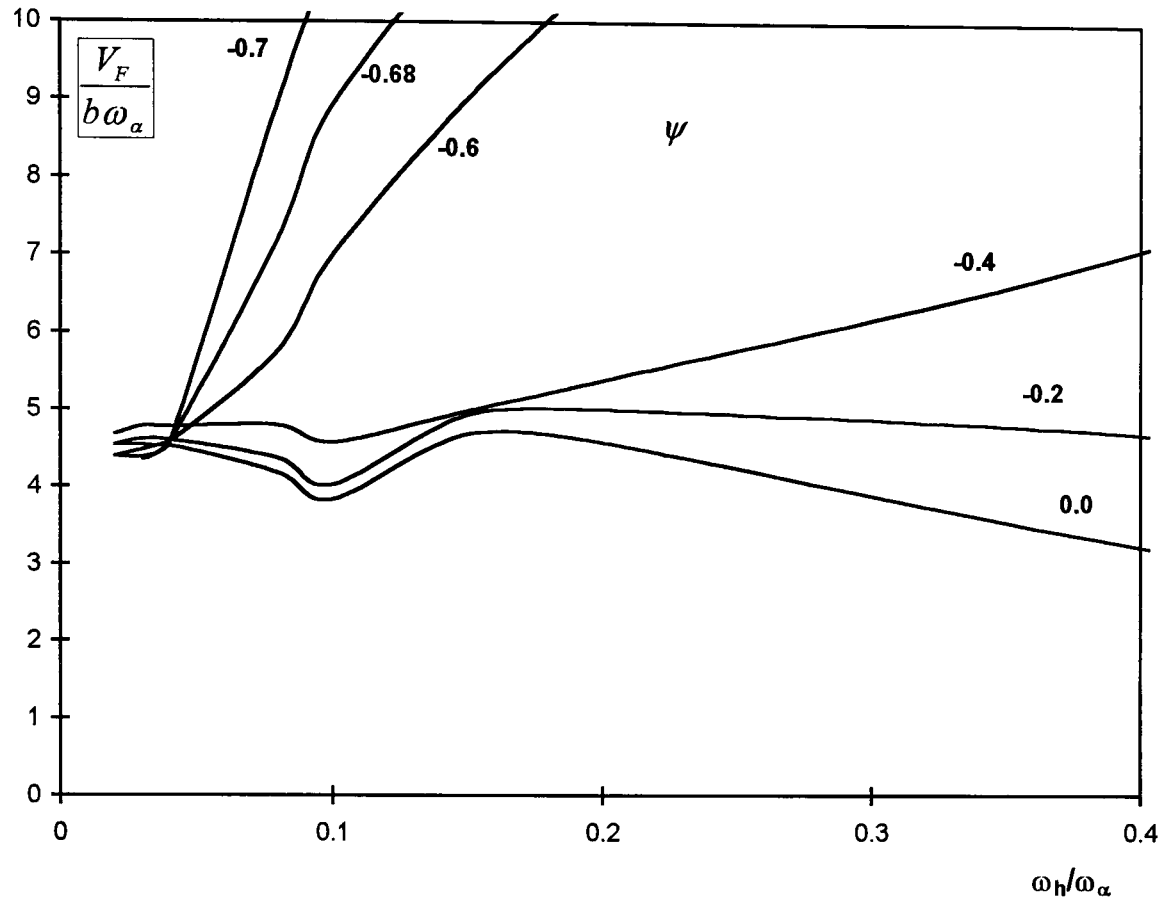

Fig. 6.10. Dimensionless flutter speed $V_F/ b\omega_\alpha$ against frequency ratio ω_h/ω_α for various values of coupling parameter ψ for a 30 degree swept-forward wing; $m/\pi\rho b^2 = 40$, $r_\alpha = 0.5$, $x_\alpha = -0.1$, $a = -0.2$.

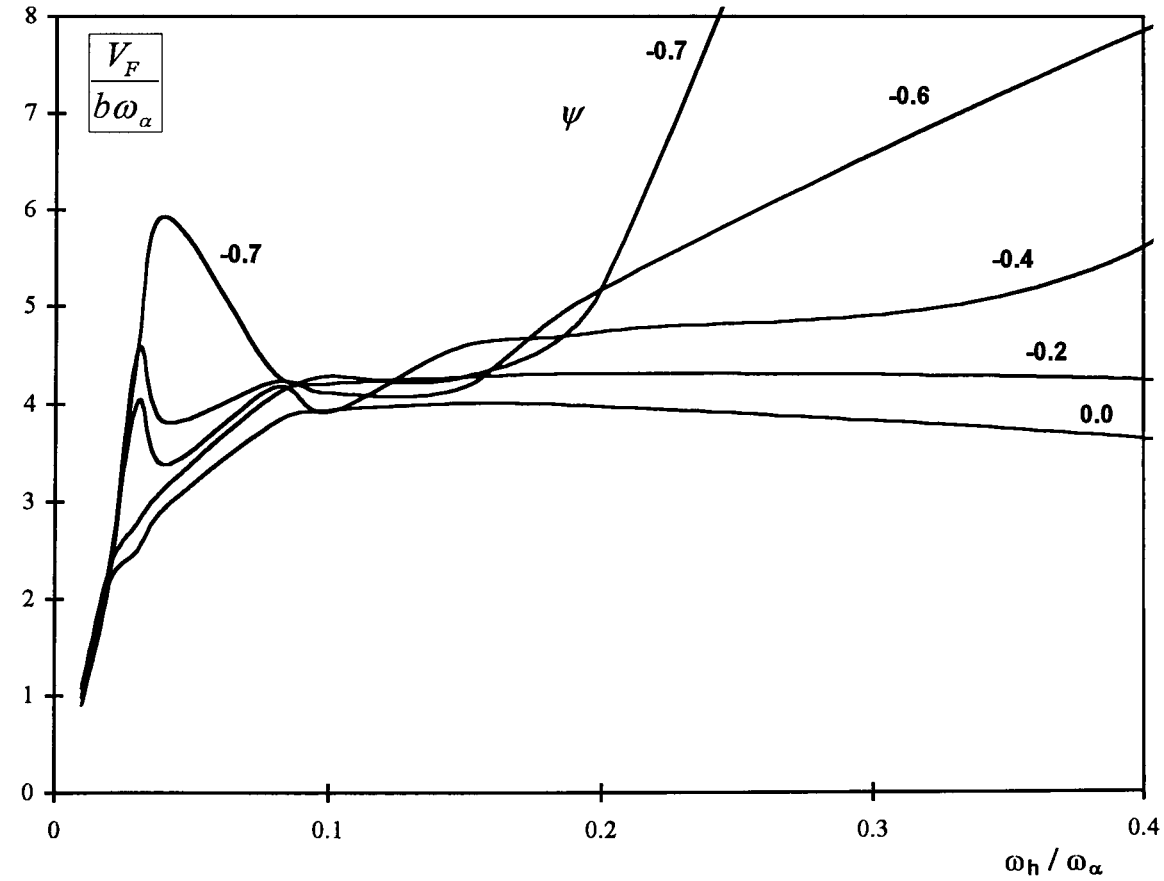

Fig. 6.11. Dimensionless flutter speed $V_F/ b\omega_\alpha$ against frequency ratio ω_h/ω_α for various values of coupling parameter ψ for a 30 degree swept-back wing; $m/\pi\rho b^2 = 40$, $r_\alpha = 0.5$, $x_\alpha = -0.1$, $a = -0.2$.

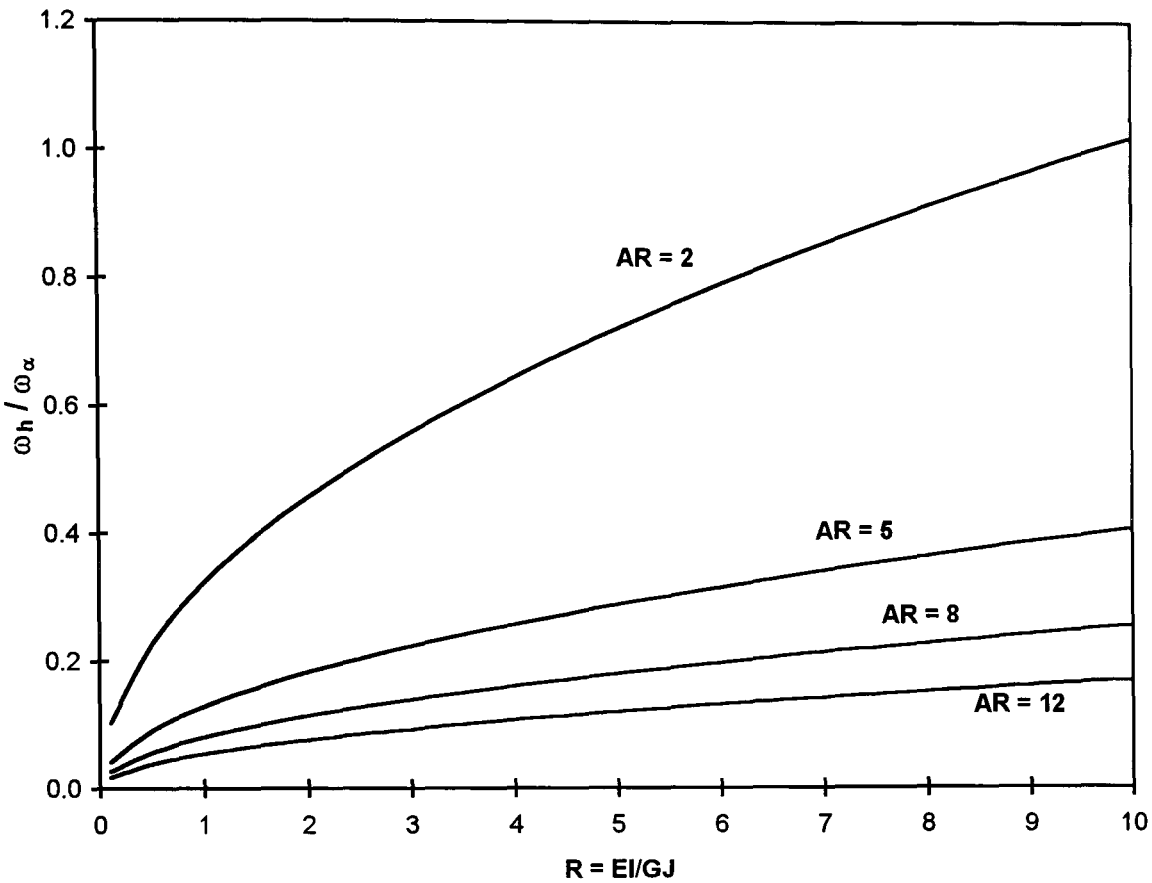

Fig. 6.12. Stifness Ratio R = EI/GJ plotted against frequency ratio ω_h / ω_α for various values of Aspect Ratio (AR), k = d/c = 0.01.

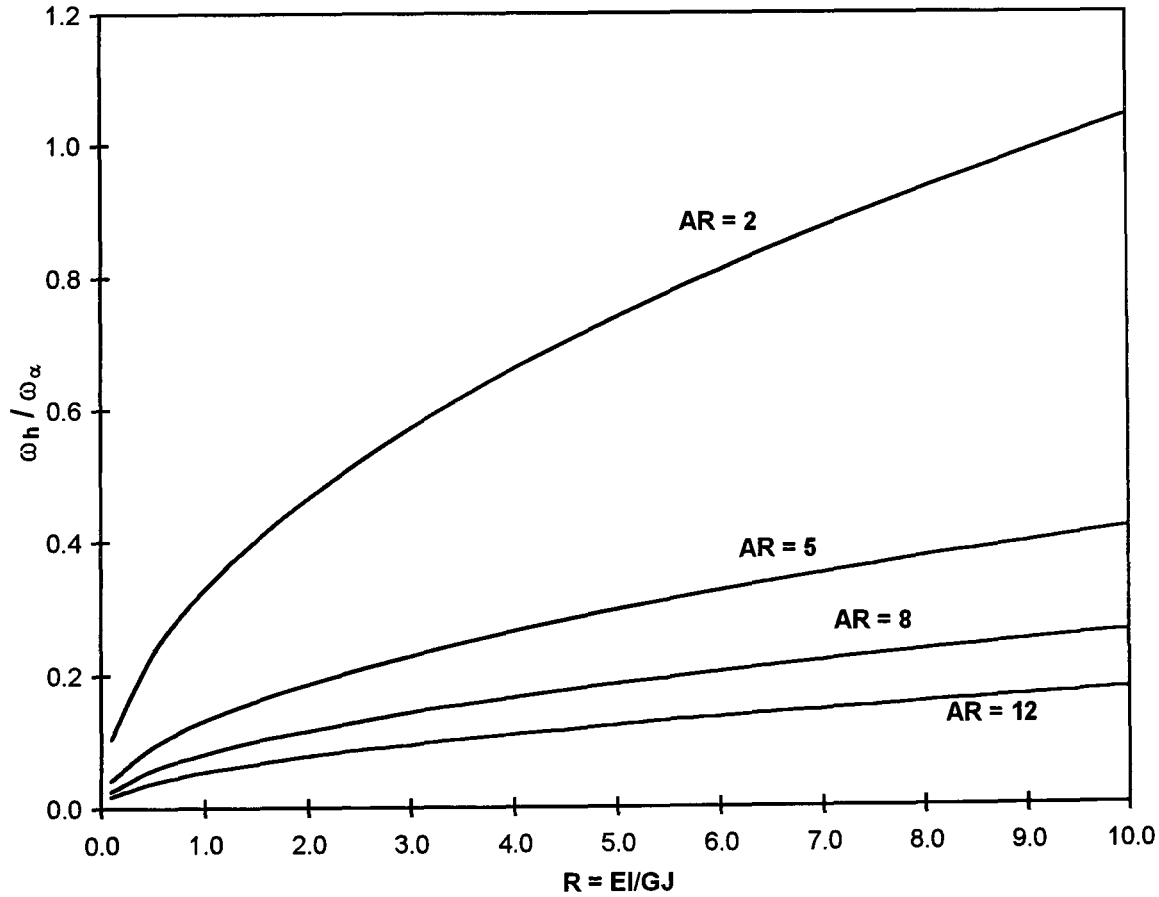

Fig. 6.13. Stifness Ratio R = EI/GJ plotted against frequency ratio ω_h / ω_α for various values of Aspect Ratio (AR), k = d/c = 0.2.

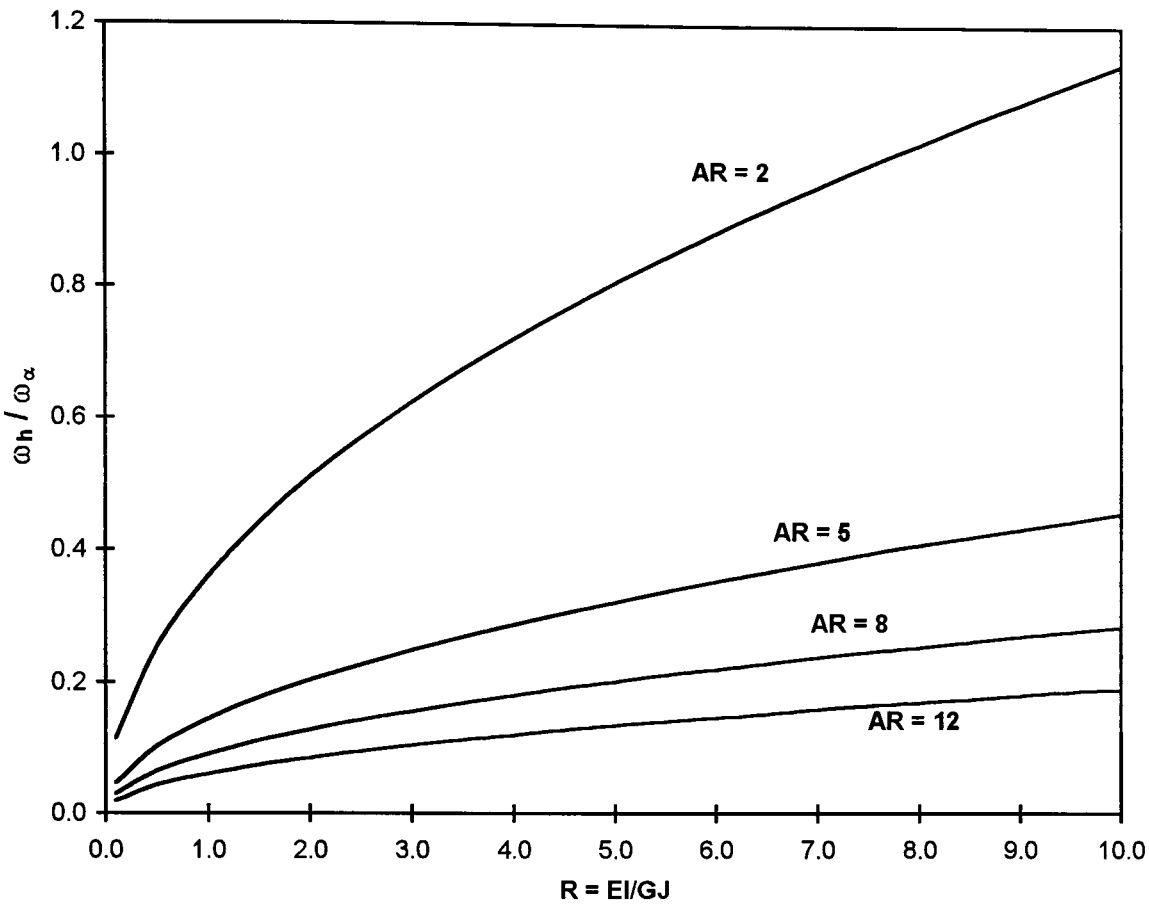

Fig. 6.14. Stifness Ratio R = EI/GJ plotted against frequency ratio ω_h / ω_α for various values of Aspect Ratio (AR), k = d/c = 0.5.

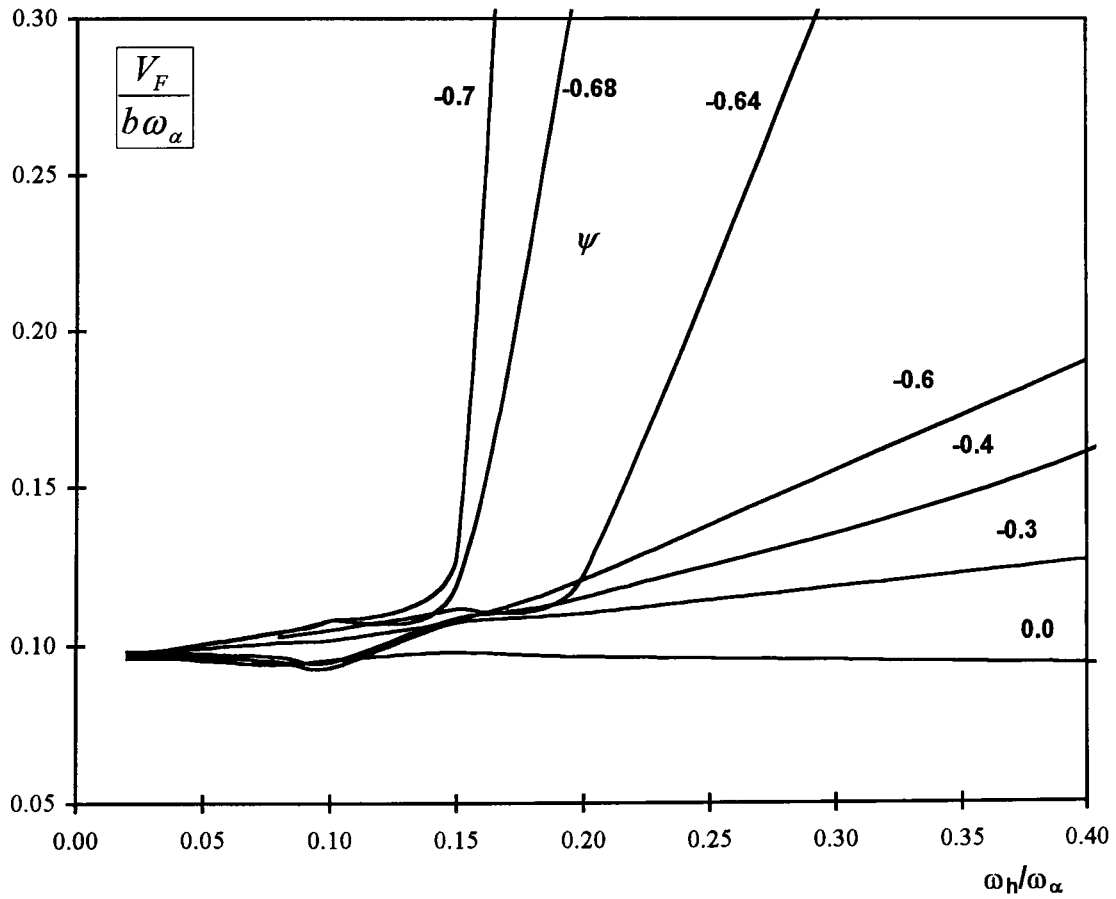

Fig. 6.15. Dimensionless flutter speed $V_F/b\omega_\alpha$ against frequency ratio ω_h/ω_α for various values of coupling parameter ψ for the example wings 1 and 2; $m/\pi\rho b^2$ = 16.67, r_α = 0.577, x_α = -0.1, a = -0.2.

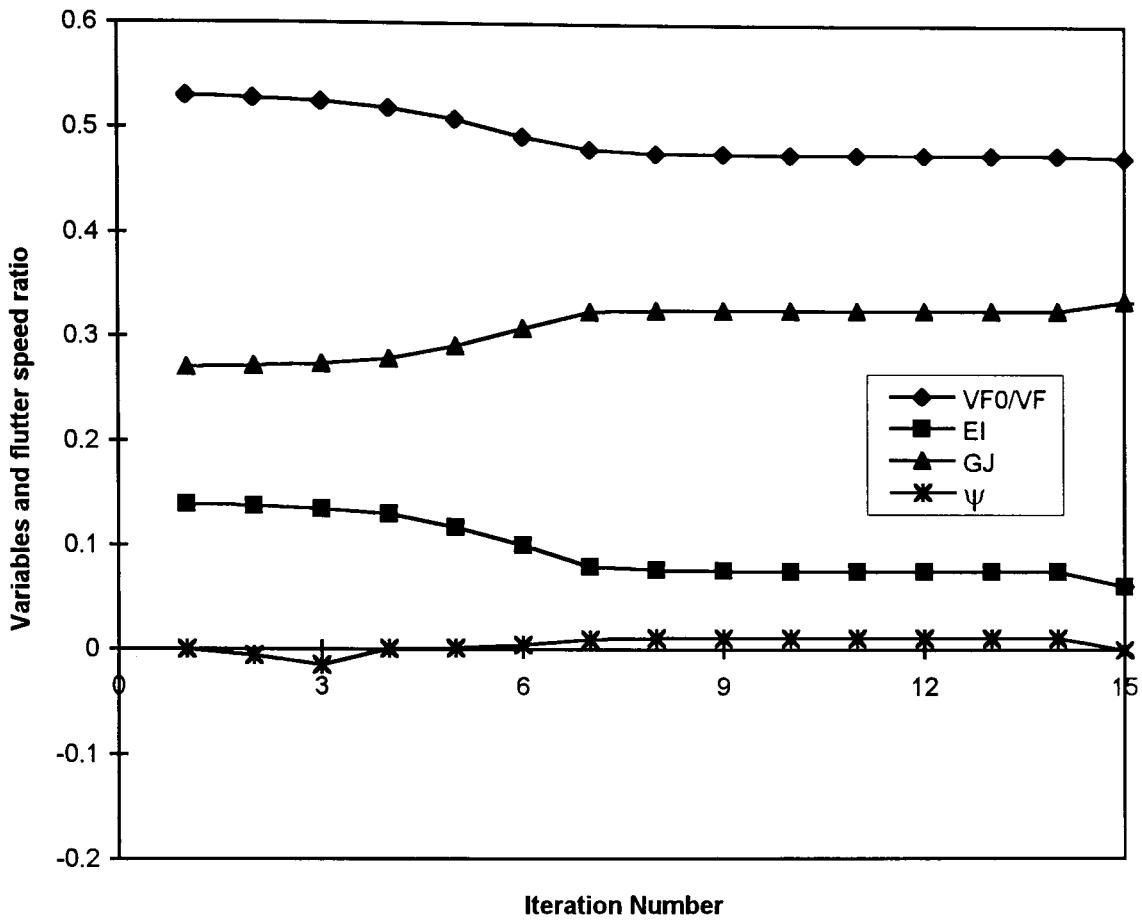

Fig. 6.16. Aeroelastic tailoring history of example wing 1.

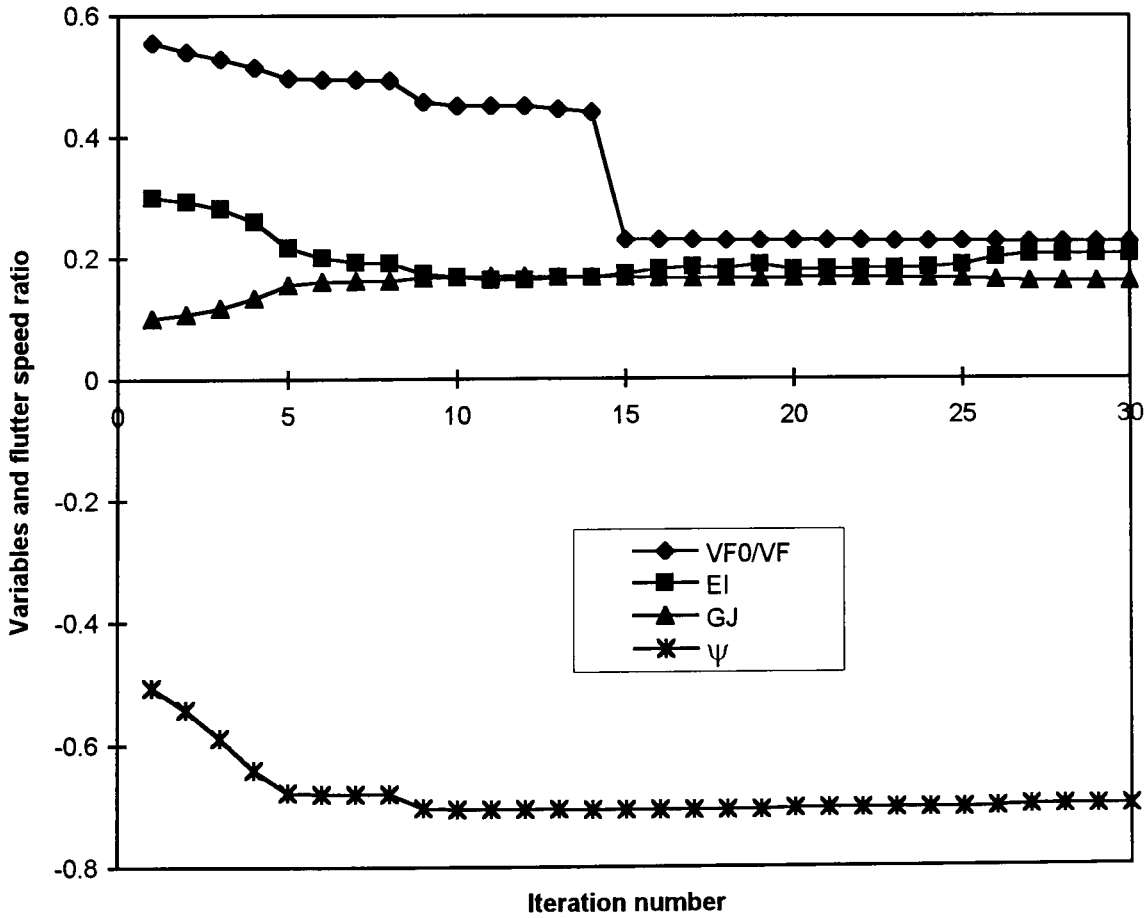

Fig. 6.17. Aeroelastic tailoring history of example wing 2.

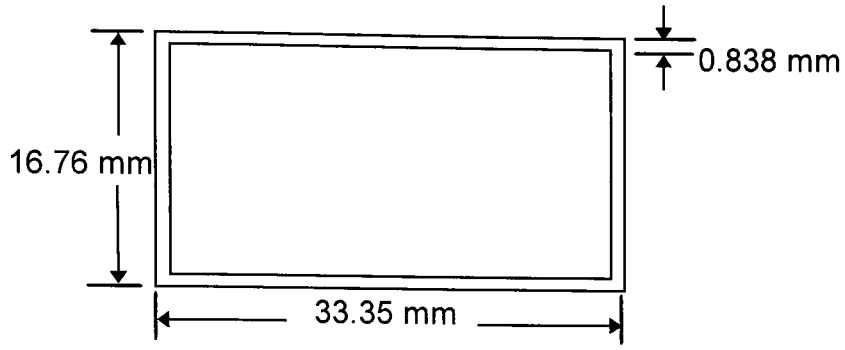

Fig. 6.18. Box-beam cross-section for the optimised wing 3.

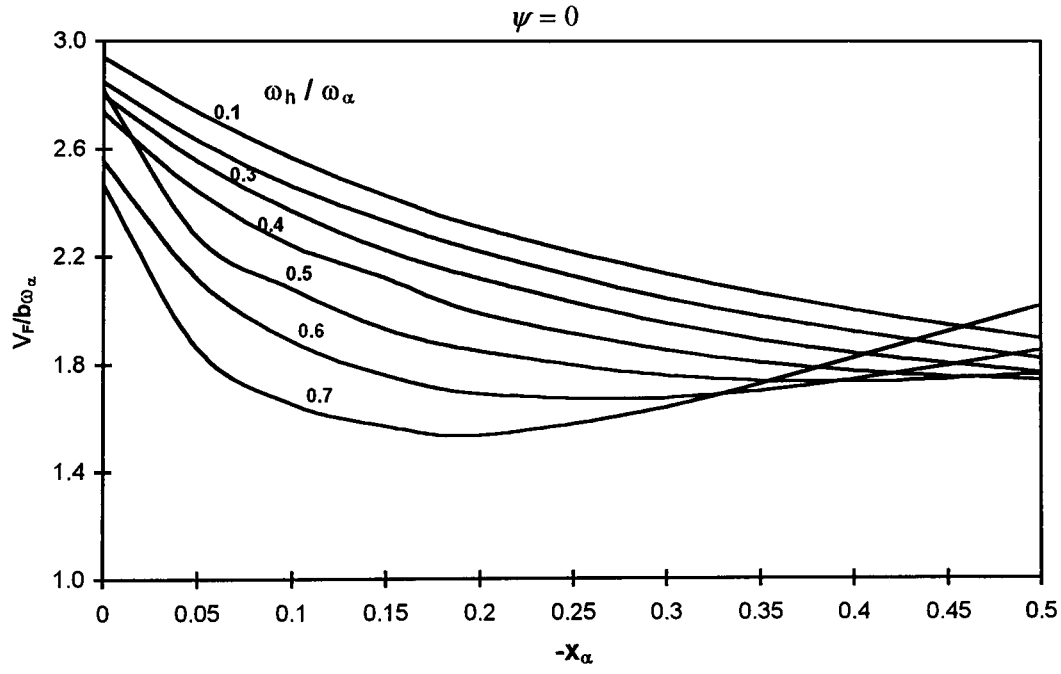

Fig. 6.19. Dimensionless flutter speed $V_F/ b\omega_\alpha$ against static unbalance x_α for various values of frequency ratio ω_h/ω_α, ψ = 0.0; $m/\pi\rho b^2$ = 20, r_α = 0.5, a = -0.2.

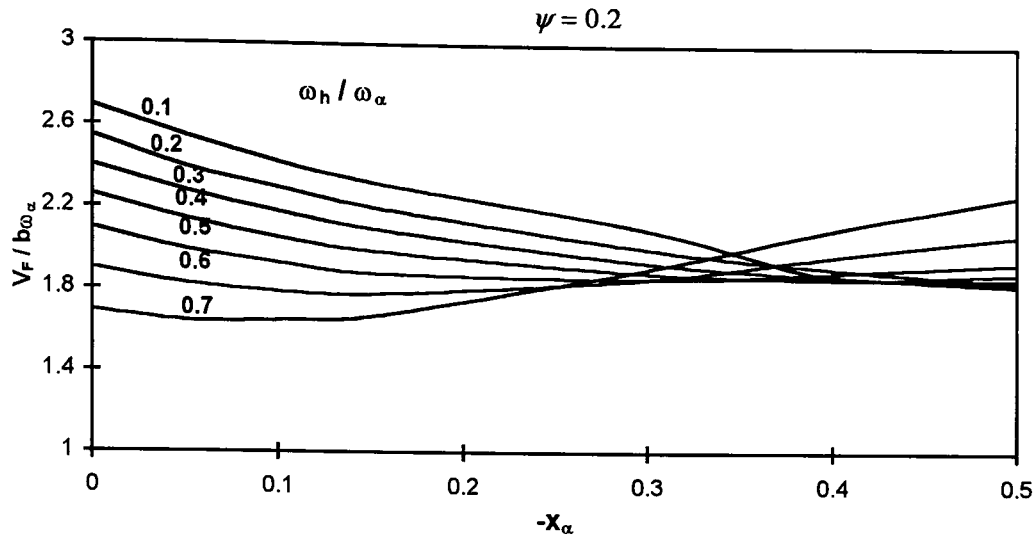

Fig. 6.20. Dimensionless flutter speed $V_F/ b\omega_\alpha$ against static unbalance x_α for various values of frequency ratio ω_h/ω_α, ψ = 0.2; $m/\pi\rho b^2 = 20$, $r_\alpha = 0.5$, a = -0.2.

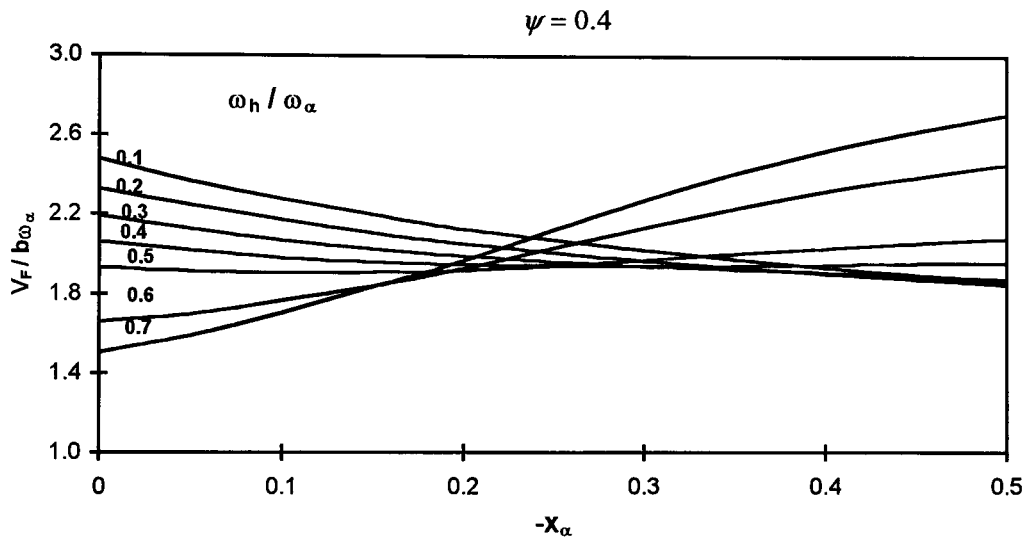

Fig. 6.21. Dimensionless flutter speed $V_F/ b\omega_\alpha$ against static unbalance x_α for various values of frequency ratio ω_h/ω_α, ψ = 0.4; $m/\pi\rho b^2 = 20$, $r_\alpha = 0.5$, a = -0.2.

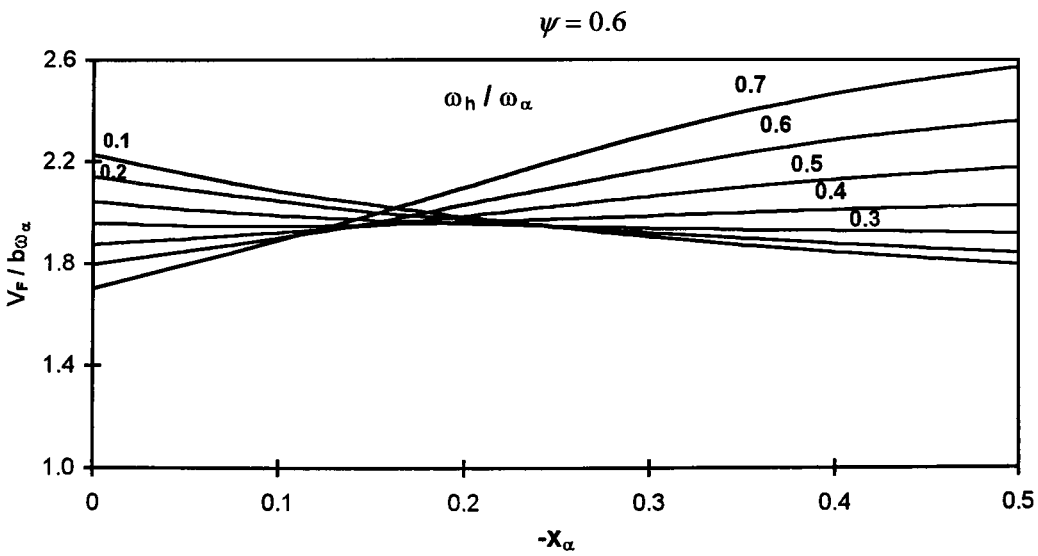

Fig. 6.22. Dimensionless flutter speed $V_F/ b\omega_\alpha$ against static unbalance x_α for various values of frequency ratio ω_h/ω_α, ψ = 0.6; $m/\pi\rho b^2 = 20$, $r_\alpha = 0.5$, a = -0.2.

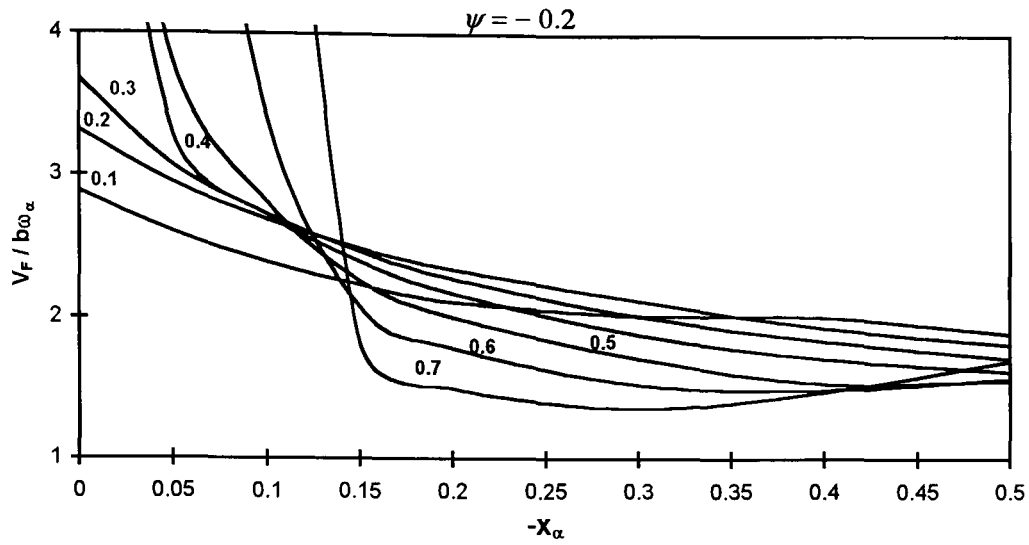

Fig. 6.23. Dimensionless flutter speed $V_F/ b\omega_\alpha$ against static unbalance x_α for various values of frequency ratio ω_h/ω_α, ψ = -0.2; $m/\pi\rho b^2 = 20$, $r_\alpha = 0.5$, a = -0.2.

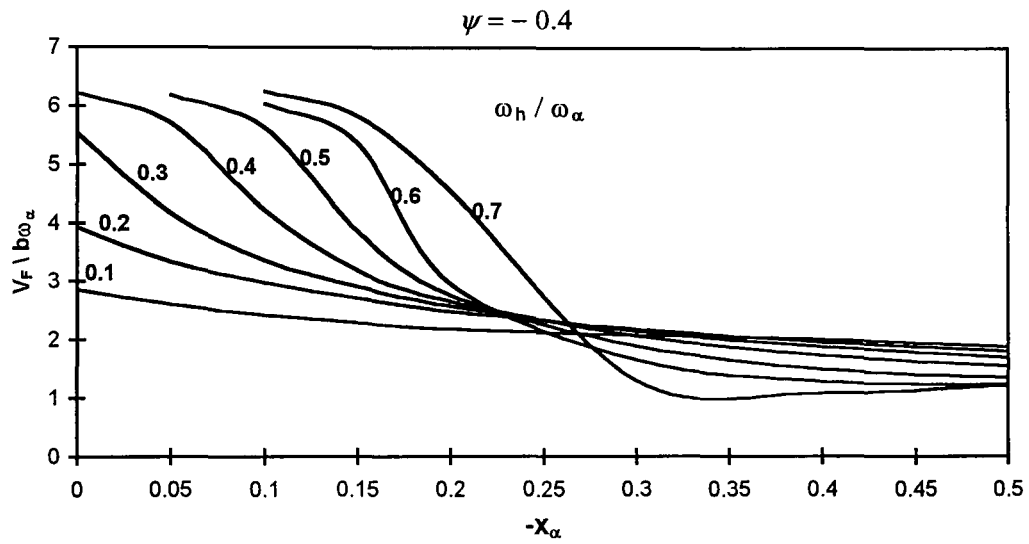

Fig. 6.24. Dimensionless flutter speed $V_F/ b\omega_\alpha$ against static unbalance x_α for various values of frequency ratio ω_h/ω_α, ψ = -0.4; $m/\pi\rho b^2 = 20$, $r_\alpha = 0.5$, a = -0.2.

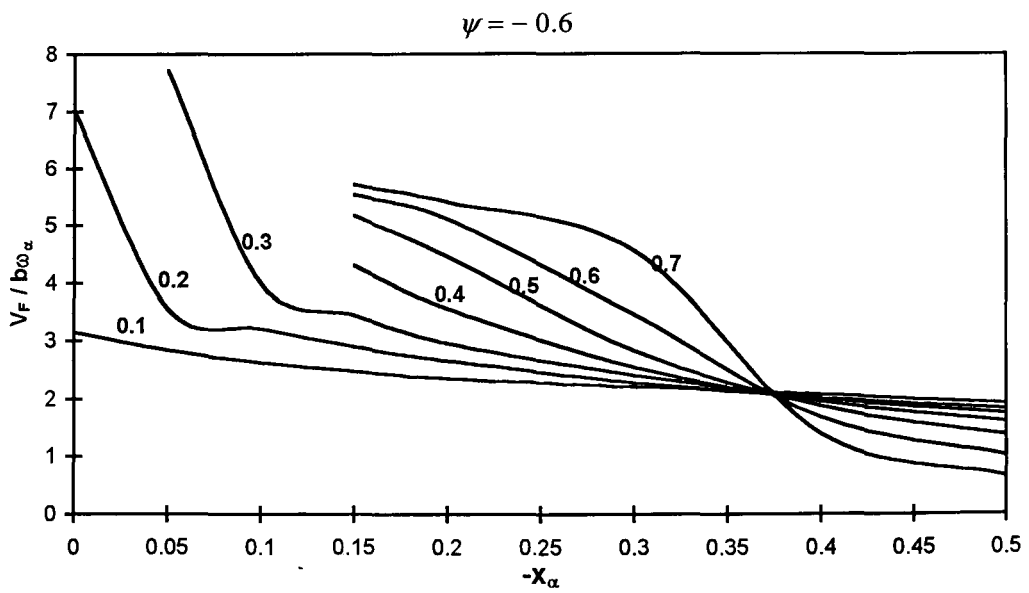

Fig. 6.25. Dimensionless flutter speed $V_F/ b\omega_\alpha$ against static unbalance x_α for various values of frequency ratio ω_h/ω_α, ψ = -0.6; $m/\pi\rho b^2 = 20$, $r_\alpha = 0.5$, a = -0.2.

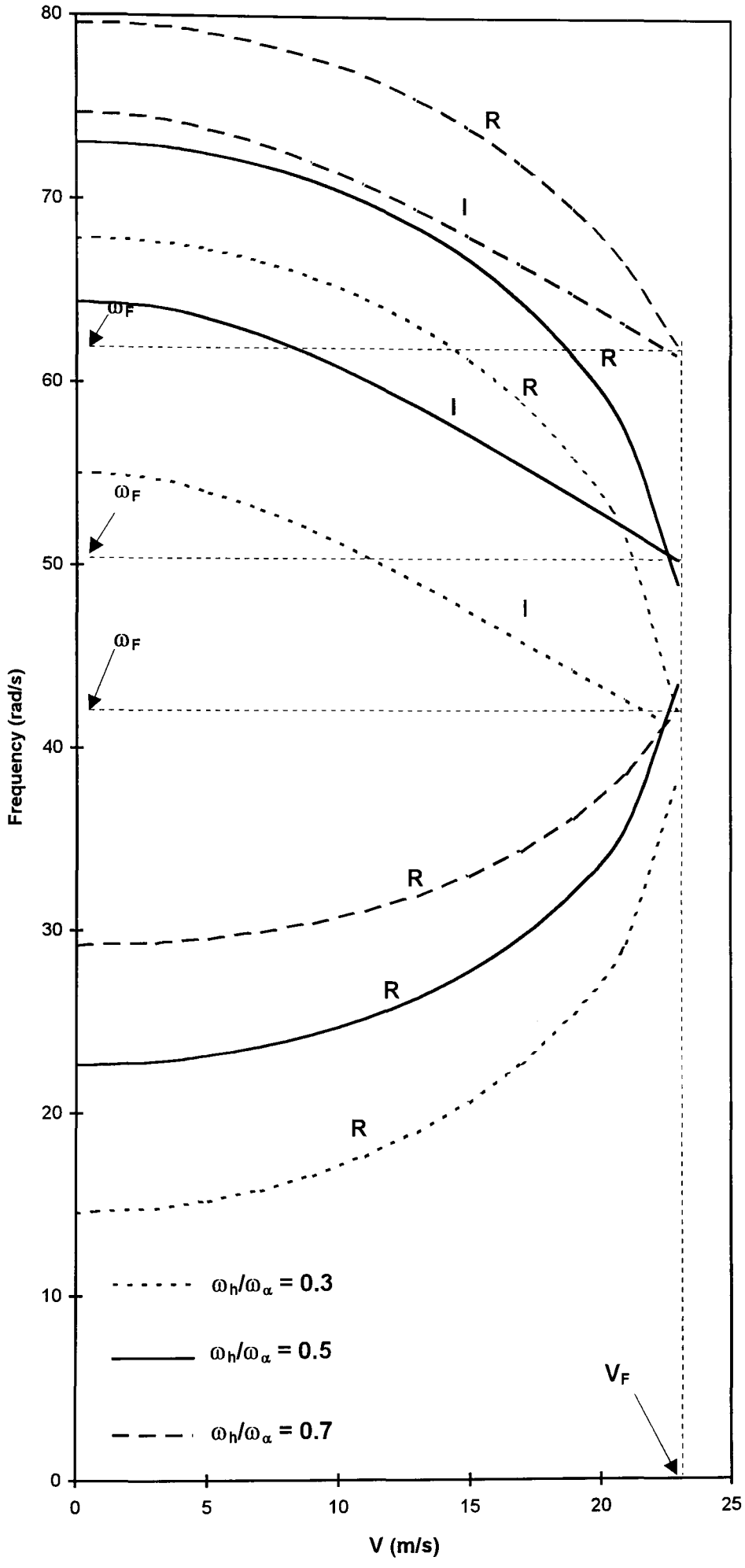

Fig. 6.26. Flutter speed prediction for three different values of the frequency ratio ω_h/ω_α using the Determinant method (i.e., $\Delta = 0$), $\psi = 0.4$.
I : locus of the roots of the imaginary part (i.e., $\Delta_I = 0$)
R : locus of the roots of the real part (i.e., $\Delta_R = 0$)

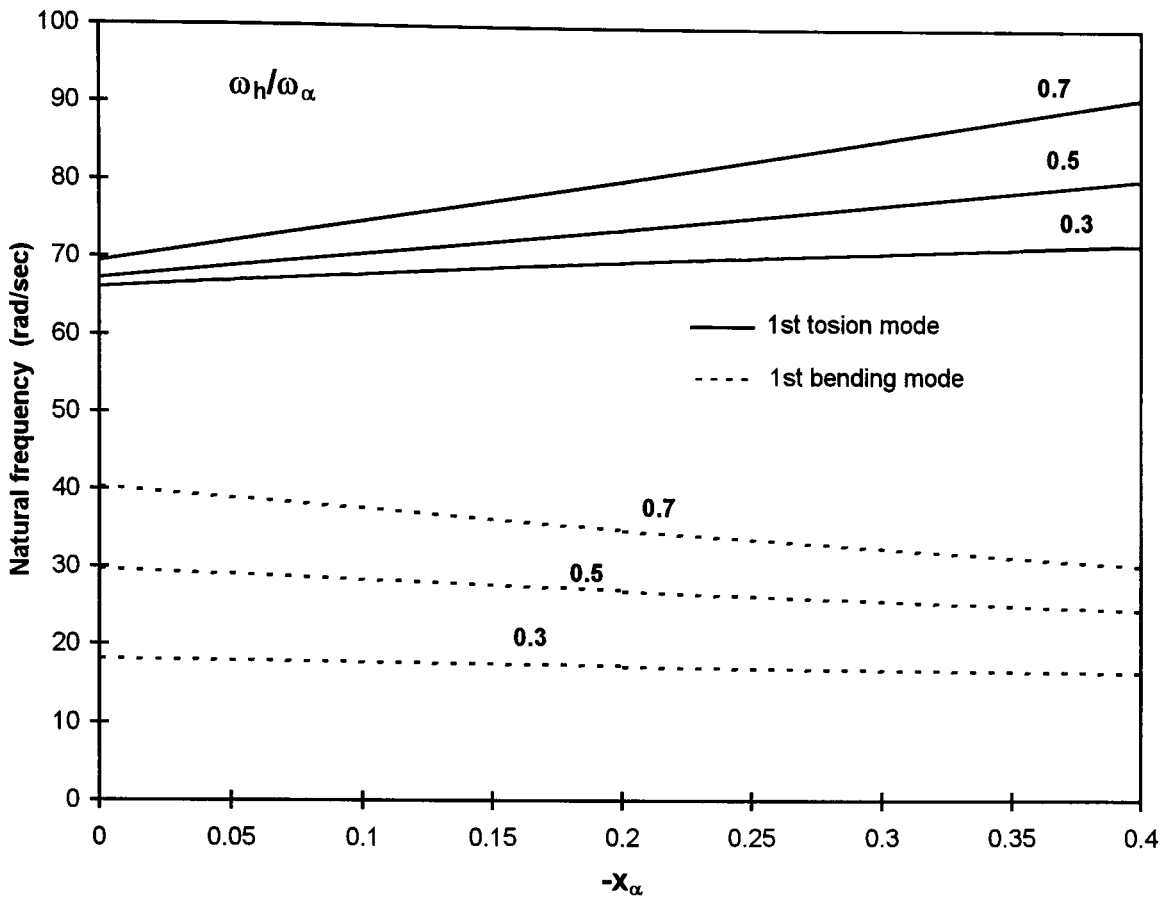

Fig. 6.27. Natural frequencies for the first bending and torsional modes against x_α for selected values of frequency ratio ω_h/ω_α, ψ = 0.4.

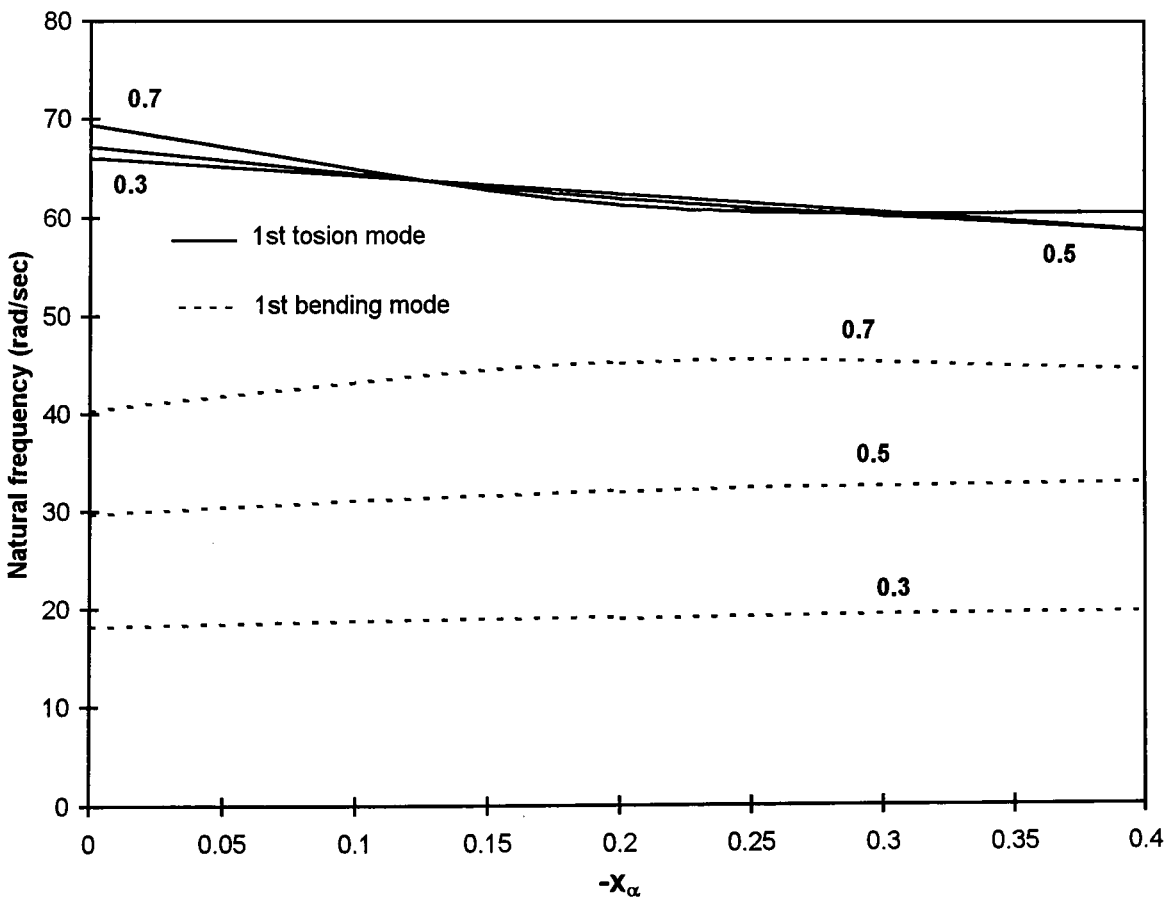

Fig. 6.28. Natural frequencies for the first bending and torsional modes against x_α for selected values of frequency ratio ω_h/ω_α, ψ = -0.4.

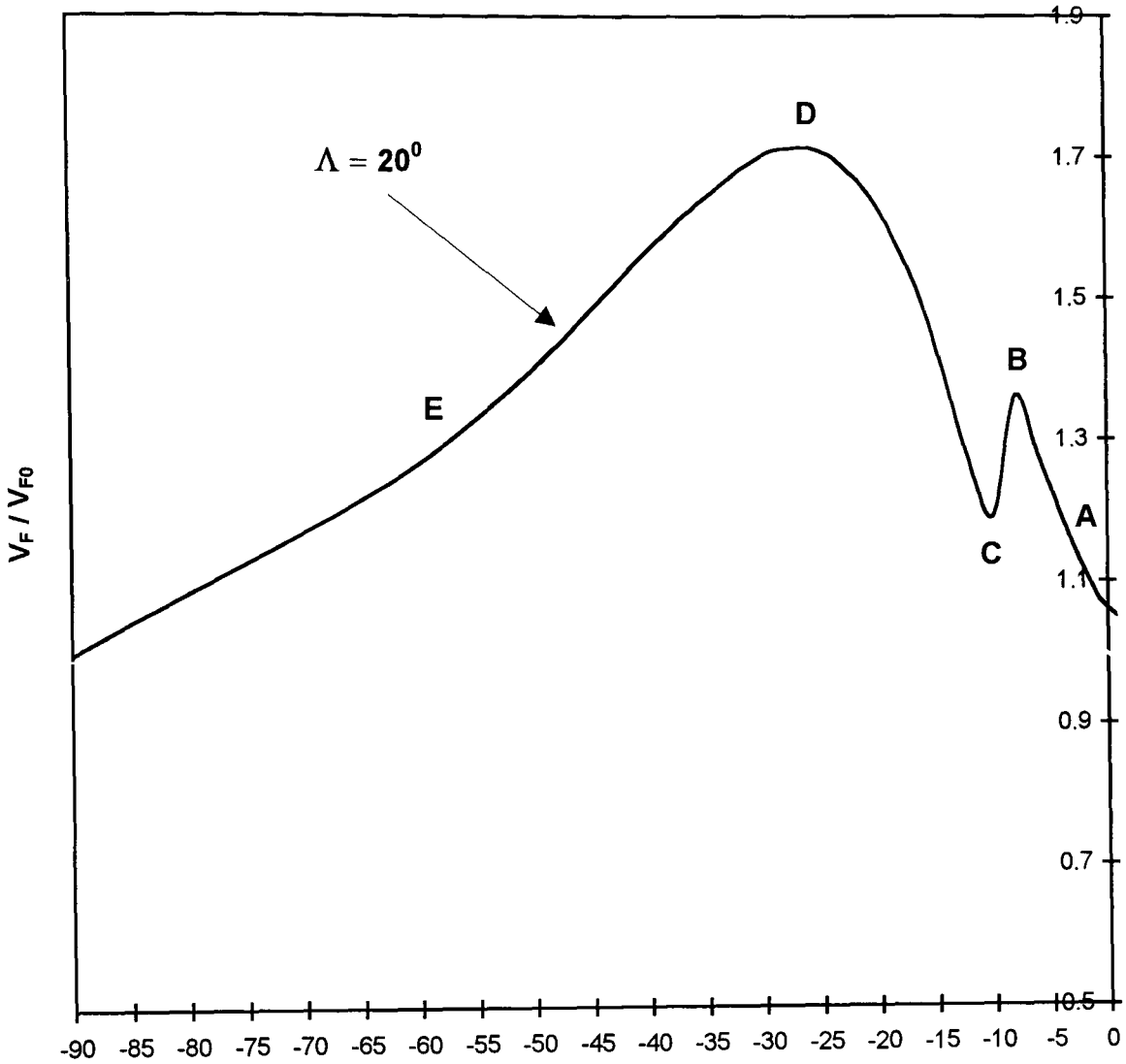

Fig. 6.29. Variation of flutter speed with fibre angle, β, for the example wing 1 of section 5.6 with stacking sequence $[\beta]_{14}$ and sweep angle $\Lambda = 20^0$.

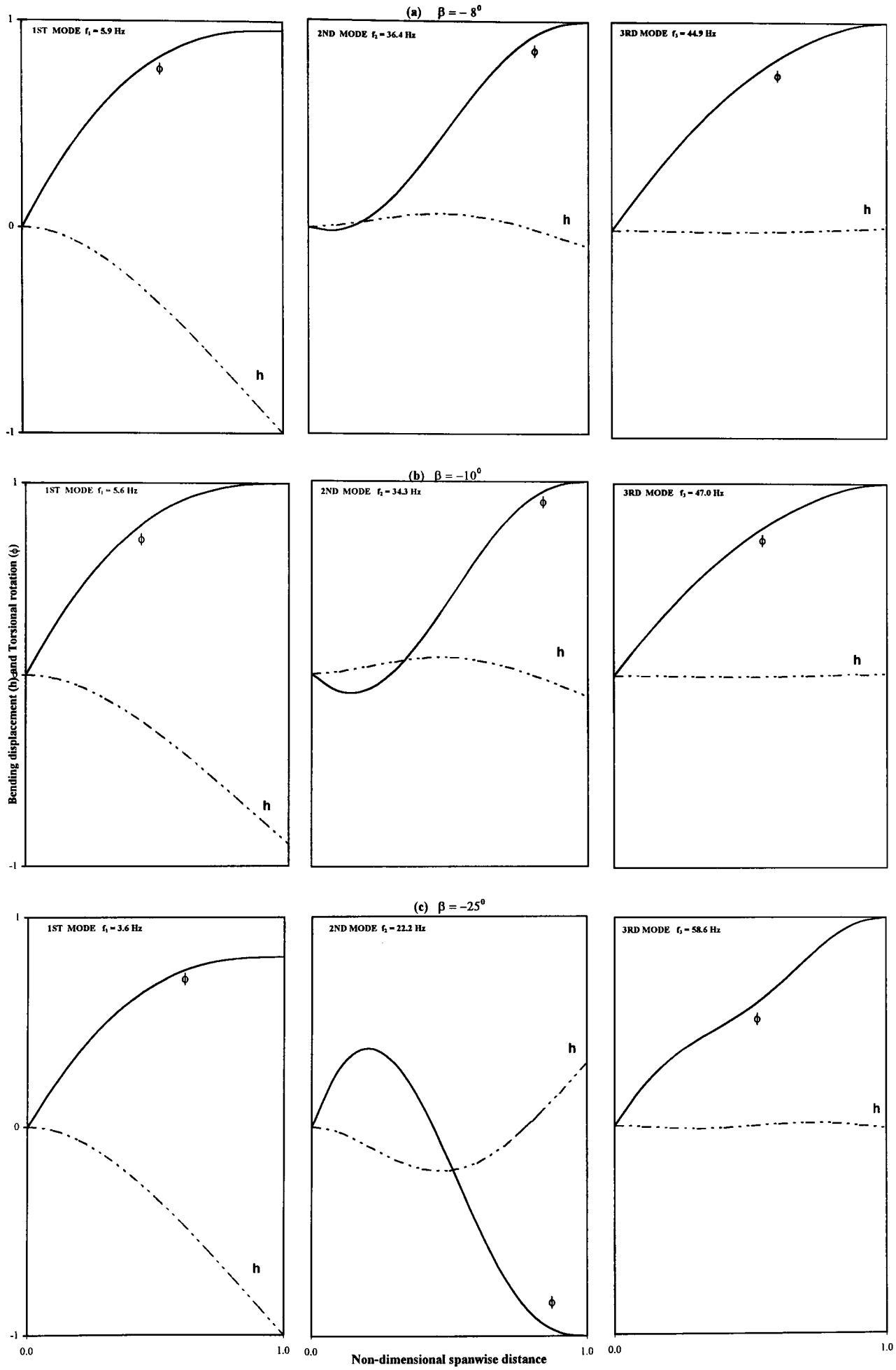

Fig. 6.30. Natural frequencies and mode shapes of laminated cantilever composite wings with stacking sequence $[\beta]_{14}$.

(a) $\beta = -8^0$

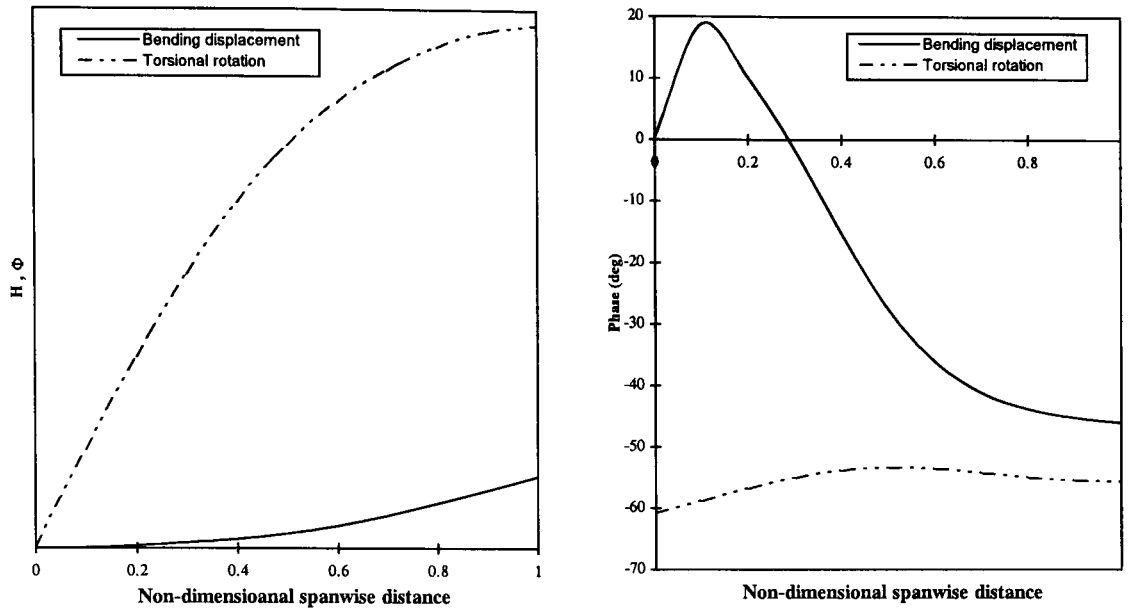

(b) $\beta = -10^0$

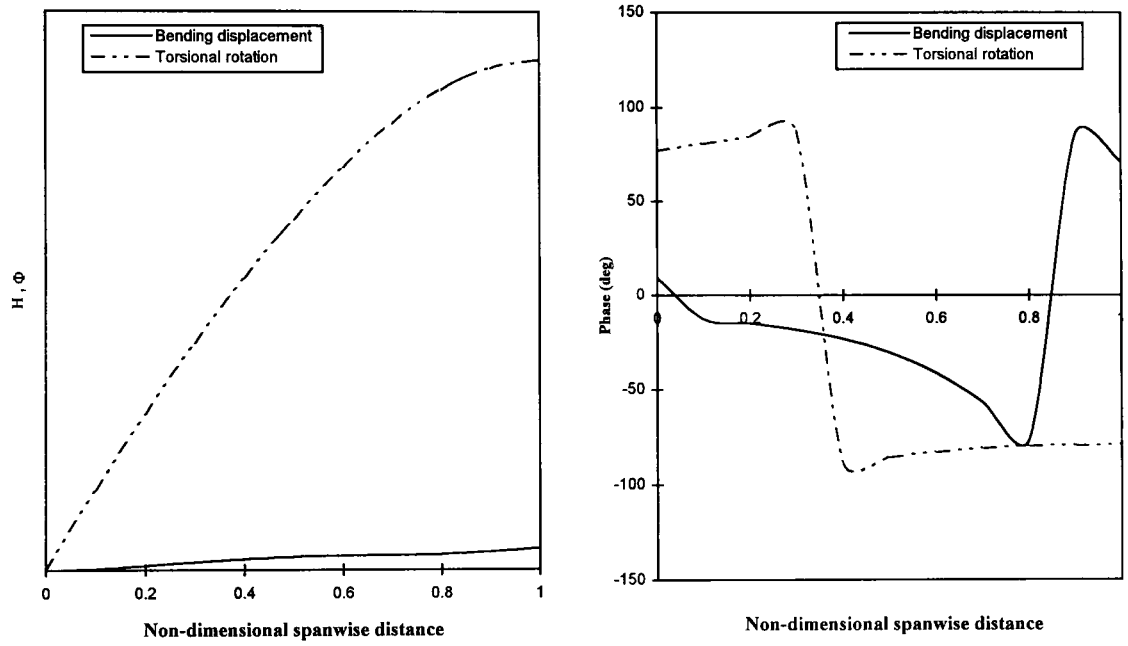

(c) $\beta = -25^0$

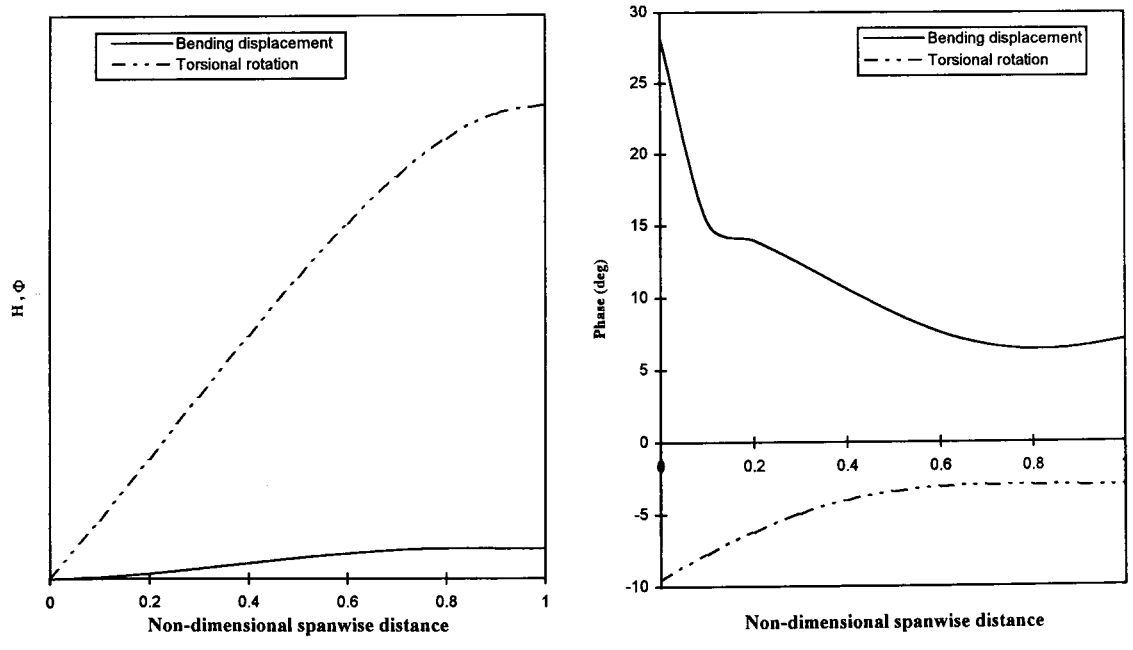

Fig. 6.31. Flutter modes showing the absolute values of the bending displacements (H) and torsional rotations (Φ) and the phase differences between the two for (a) $\beta = -8^0$, (b) $\beta = -10^0$, (c) $\beta = -25^0$.

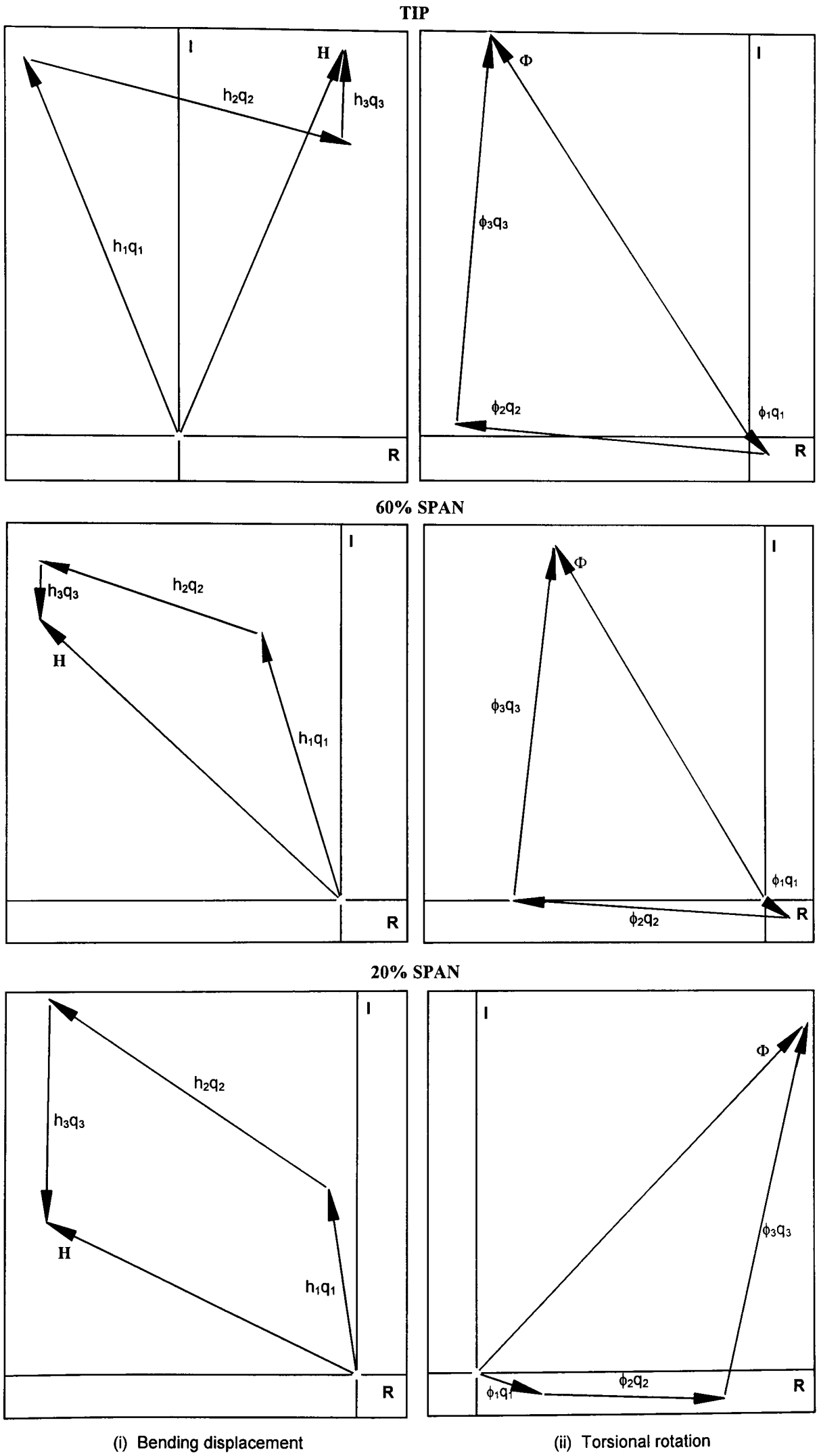

(i) Bending displacement (ii) Torsional rotation

Fig. 6.32. Contribution of normal modes to the flutter mode for the case with $\beta = -10^0$.

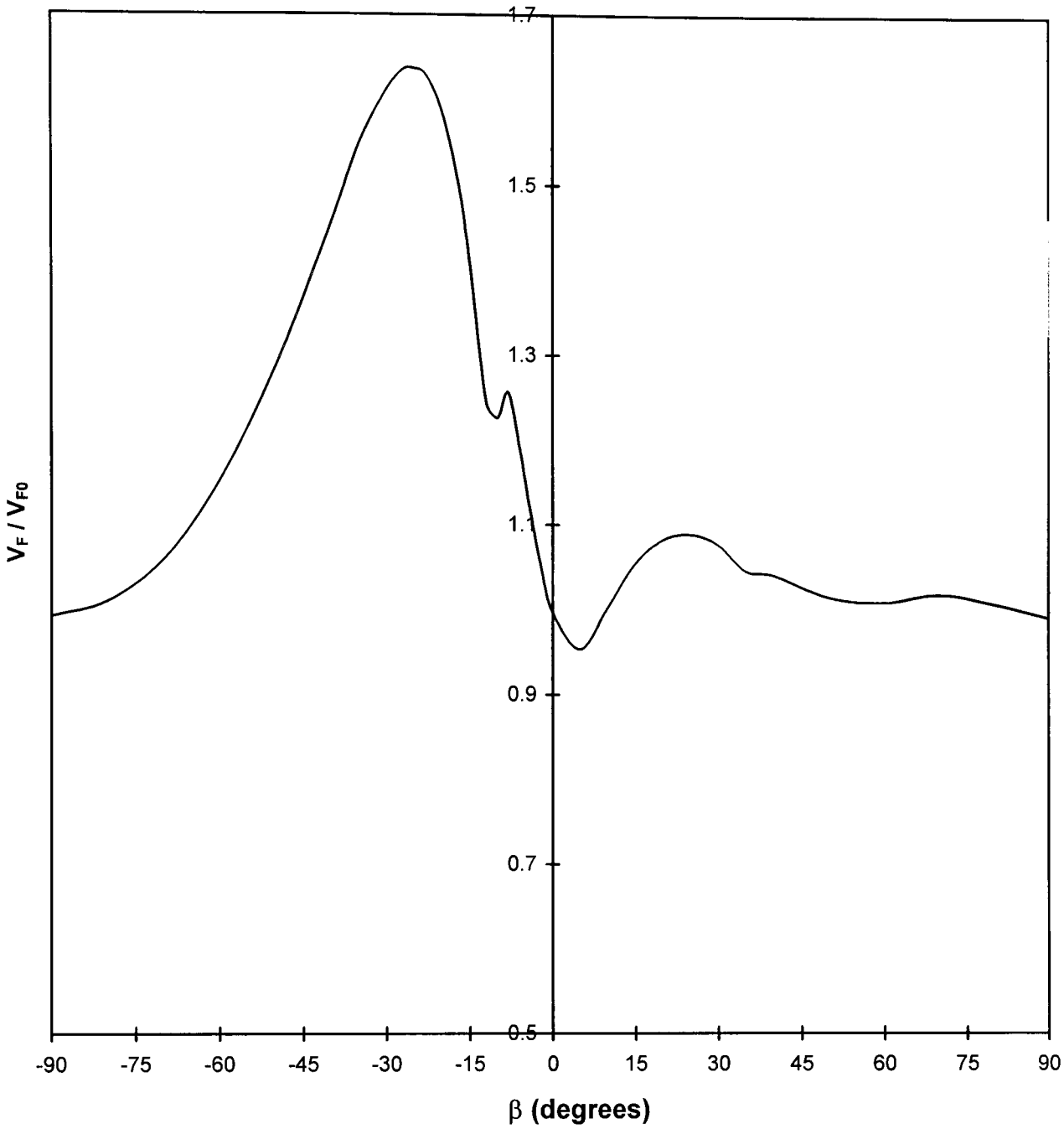

Fig. 6.33. Variation of flutter speed with fibre angle β for the unswept case of the example wing 1 of section 5.6 with stacking sequence $[\beta]_{14}$.

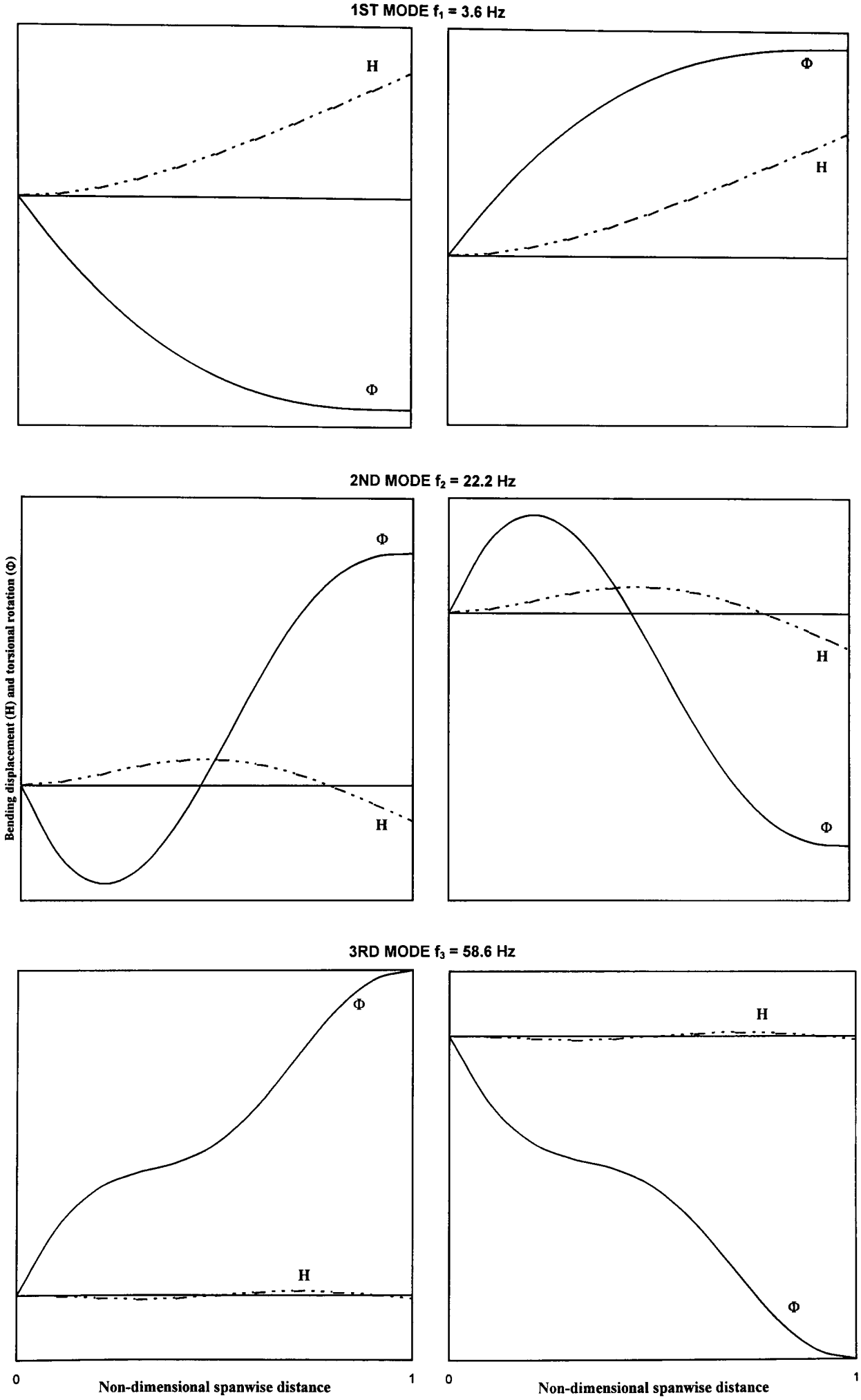

(i) $\beta = -25^0$ (ii) $\beta = 25^0$

Fig. 6.34. Natural frequencies and mode shapes of laminated composite wings with stacking sequence $[\beta]_{14}$.

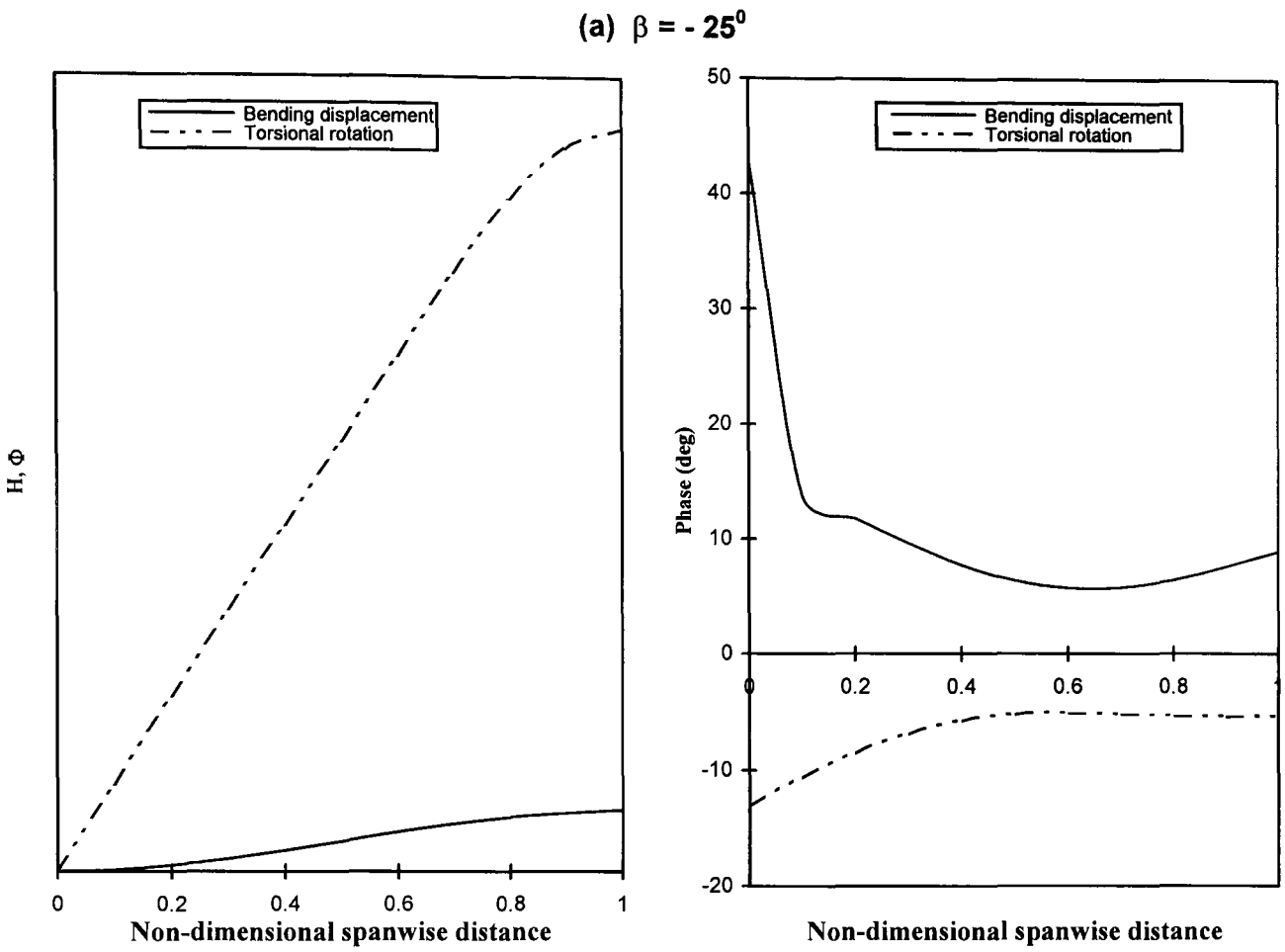

Fig. 6.35. Flutter modes showing the absolute values of the bending displacements (H) and torsional rotations (Φ) and the phase differences between the two for (a) $\beta = -25^0$, (b) $\beta = 25^0$.

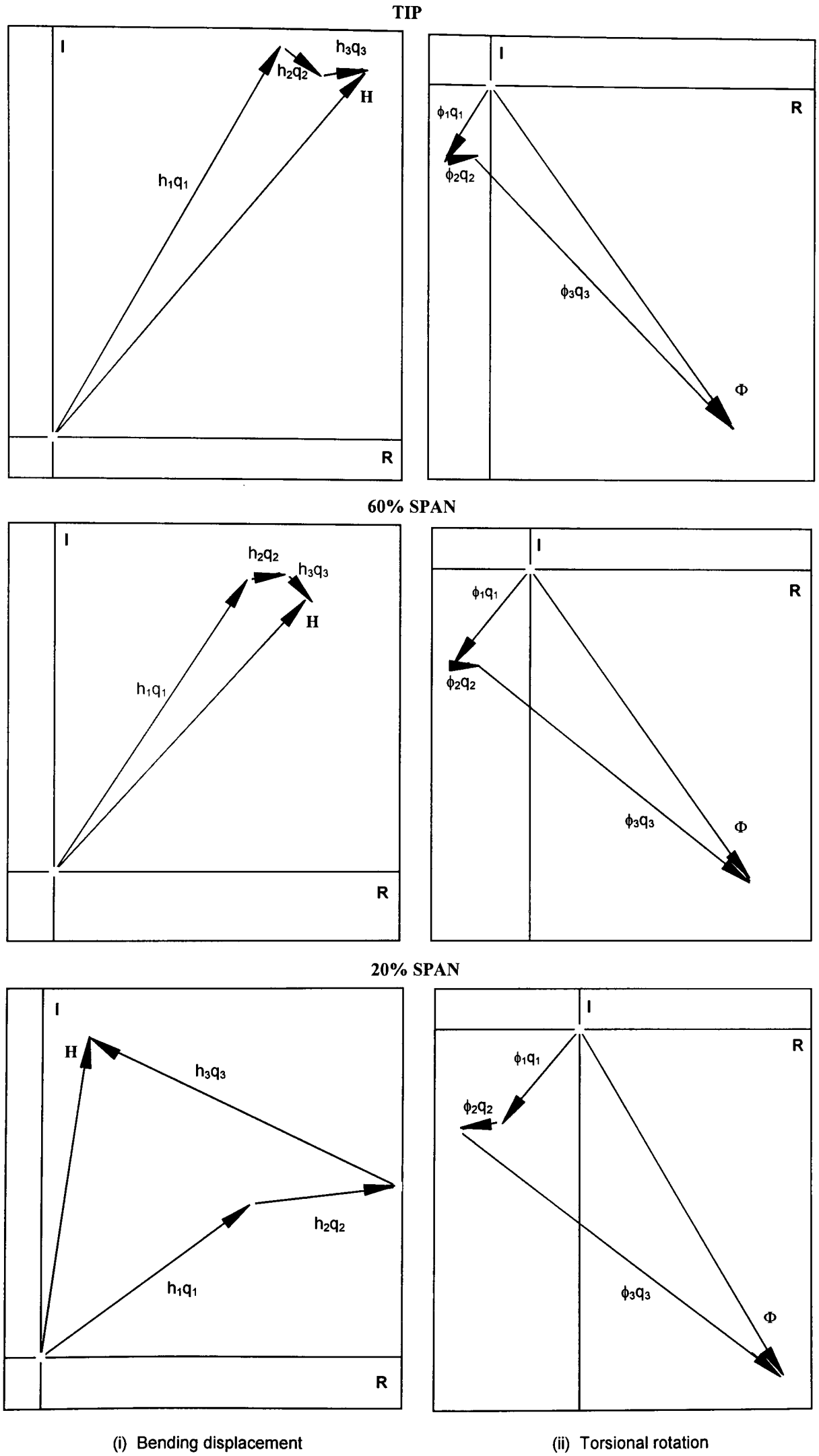

(i) Bending displacement

(ii) Torsional rotation

Fig. 6.36. Contribution of normal modes to the flutter mode for the case with $\beta = -25^0$.

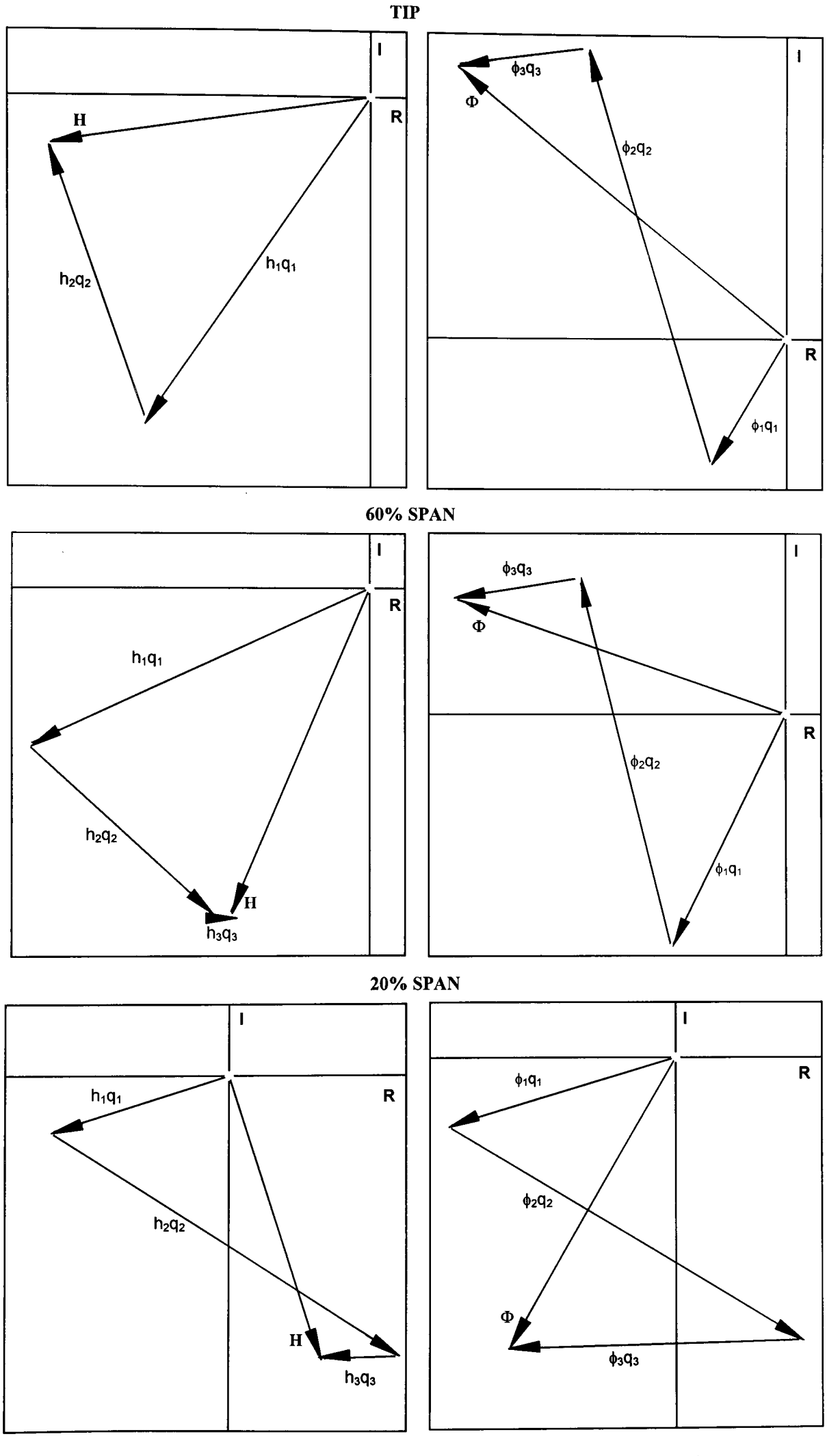

Fig. 6.37. Contribution of normal modes to the flutter mode for the case with $\beta = 25^0$.

CHAPTER 7

GUST ALLEVIATION AND FLUTTER SUPPRESSION OF AN OPTIMISED COMPOSITE WING USING ACTIVE CONTROLS

7. GUST ALLEVIATION AND FLUTTER SUPPRESSION OF AN OPTIMISED COMPOSITE WING USING ACTIVE CONTROLS

7.1 Introduction

In the previous chapters we have seen how passive control in the form of aeroelastic tailoring can be used to enhance aeroelastic stability. Although aeroelastic tailoring (passive in the sense that no external energy source is used directly) and active control methodology are not the same, similarities do, however, exist. For example, aeroelastic tailoring may use a form of pre-programmed control laws to modify the behaviour of a structural system. Thus an aeroelastically tailored structure may act both as a sensor and as an actuator; e.g., the control laws may be embedded within the structure in the form of material constitutive relations. On the other hand, with active control, the aeroelastic model may be modified to allow control surfaces and a system of sensors to control the dynamic response.

The technological advances made in recent years in the field of control systems have stimulated considerable interest in evaluating the advantages of incorporating active control systems in aircraft for gust alleviation and flutter suppression [7.1]. The potential of active controls for gust alleviation and mode stabilisation has been analysed for some specific aircraft such as the XB-70 [7.2- 7.3] and B-52 [7.4-7.5]. Within the last two decades, control systems that increase the damping of the lower frequency structural modes have evolved from analytical feasibility studies to production hardware. Such a system, which controls the response of the rigid-body mode and one elastic mode (first aft body bending) to gust inputs, has been successfully installed on the B-52H fleets. As a consequence, a reduction in gust loads and a considerable extension of the fatigue life of the aircraft [7.6] have resulted.

As for flutter, some developed hardware indicates that flutter suppression systems (controlling high frequency unstable modes) are now technologically feasible. Analytical studies have shown that in many instances, weight savings by as much as 4 percent of the total structural weight of large aircraft, such as, a supersonic transport or the Rockell International B-1 can be achieved by suppressing flutter by active

controls rather than by passive methods. This is a considerable weight saving when it is considered that the payload may be as small as 20 percent of the structural weight, i.e., an increase of payload of about 20 percent can be achieved [7.7-7.8].

Flutter suppression and gust alleviation problems, however, are closely interrelated and should be preferably treated in a combined manner. This is because flutter suppression considerations impose no limitations on the values of the control law parameters whereas gust response considerations yield an upper bound to the control law values [1.34]. This upper bound ensures reasonable control-surface rotations over the flight envelope of the aircraft. Furthermore, the effects of the flutter suppression system on the gust response characteristics of the aircraft need to be established.

The gust response of aircraft has been a topic of research for a number of years [7.9]. The goal of this research has been to reduce the Root Mean Square (RMS) values of the loads that an aircraft experiences due to gust. This leads to increased fatigue life, better design of the structure, an increased comfort to the passengers and crew, and a reduction in the effect of the gust on the cargo [1.35, 7.9]. Typically, research approaches to gust alleviation have been divided into two areas. The first is the passive approach, where an existing structure is re-sized to alleviate gust loads [7.10-7.12] while the second (where the work reported here falls), has been to include active control systems in the design [1.34-1.35, 7.13-7.22].

To complement the theoretical efforts, there have been flight and wind tunnel tests, and actual production systems, which have addressed the gust alleviation problem. The first flight test was on a B-52 in 1962 [7.9]. More recently, an active gust alleviation system has been installed on the B-1B to improve ride comfort for the crew [7.17]. This has been followed by several wind tunnel tests of a transport type wing by NASA [7.16]. The most recent effort has been the wind tunnel tests in Japan on a transport category wing which includes an active control system for gust load alleviation [7.14, 7.18].

A number of these efforts have used frequency domain techniques either to quantify the gust response or to design an active control system for gust load alleviation [1.34, 7.9, 7.13, 7.16-7.17, 7.20]. While the frequency domain approach

uses many powerful design tools, the development of modern control analysis tools has brought time domain techniques to a practical level [7.23].

Time domain analysis and the modelling of aeroelastic systems have been in use for a number of years [7.17]. Typically, the time domain models have been used for modern control system design, both for flutter suppression and gust load alleviation [1.35, 7.13-7.15, 7.18-7.21]. However, frequency domain techniques are used to determine the RMS behaviour of the model, primarily for closed-loop systems [7.13, 7.16, 7.20], and require large amounts of computer time [7.13].

There have been many research efforts into aeroservoelastic design for gust response. References [1.34, 7.10-7.11, 7.13, 7.15-7.20, 7.22, 7.24] have examined the design of a wing system for gust response and flutter suppression when a controller is included. A number of these efforts have focused primarily on the design of the control system. However, to the best of the author's knowledge, in none of the investigations referred to above a control law has been optimised for gust response with flutter speed as a constraint. Although several authors examined flutter suppression and gust alleviation by use of active controls, different control laws were used for these two phenomena. As stated earlier, the latter yields an upper bound to the control law values whereas the former does not.

One of the major difficulties which characterises the introduction of active control systems into elastic structures is the need to determine a large number of parameters associated with the control system. Another is the fact that an elastic structure, like an aircraft, cannot be considered as a fixed system since the properties of the system vary with the flight configuration, time of flight, etc. Hence, a proper optimisation process must take into account a very large number of parameters, including a large number of flight configurations. The determination of a satisfactory control law which copes with the variety of flight configurations has been found to be a difficult task which requires considerable ingenuity. As will be shown later, a change in the flight speed or control size has a large effect on the value of the optimised control law parameters. For this reason, the full potential of applying these techniques to aircraft design has yet to be realised, especially in the early stages of design.

This chapter presents an approach to aeroservoelastic tailoring for gust response using optimisation techniques, which seeks to minimise (optimise) the RMS

response of a cantilever unswept wing subject to a gust, while maintaining the initial optimised flutter speed. The variation of this measure of response with respect to various control trailing edge positions, control sizes and flight speeds will be examined to gain some insight into active control design for gust alleviation and flutter suppression. Optimisation of control laws will be carried out for both flutter suppression and gust alleviation for the specific wing model examined. This work differs from earlier investigations because the same control law is optimised for both flutter suppression and gust alleviation. In particular, attention is focused on achieving a maximum flutter speed of a cantilever composite wing, and at the same time alleviating its gust response by applying both the aeroelastic tailoring as well as active control technology. For simplicity, the wing is modelled as a laminated composite flat beam (plate), see Eqns (3.24) and (3.26) in chapter 3. The dynamic stiffness matrix method discussed in section 4.2 is used to investigate the free vibration characteristics of the wing. With regard to the unsteady aerodynamic idealisation, lifting surface theory developed by Davies [1.39] which accounts for air compressibility, is used to calculate the aerodynamic forces. The response to gusts and atmospheric turbulence is calculated in the frequency domain using the Power Spectra Density (PSD) method [7.25]. The well known Von Karman spectrum [7.25] is used to represent the atmospheric turbulence. Prior to the PSD analysis, a continuous sinusoidal gust model is considered as the input to calculate the frequency response function of the wing. The RMS value of the normal acceleration of the wing is taken as the objective function in the optimisation of active control laws.

The work in this chapter is basically carried out in two stages. In the first stage, aeroelastic tailoring is performed by optimising the stacking sequence of the composite wing for maximum flutter speed, but without taking the control surface into account. In the second stage, the control surface of the wing is taken into consideration, and an optimised control law to alleviate the gust response, is calculated. This is achieved without reducing the optimised flutter speed already determined in the first stage. Thus, the problem is essentially described as a constrained optimisation, one where the objective is to alleviate the gust response whilst maintaining a certain specified flutter speed. Results for all optimisation studies are obtained using the well established computer program ADS (Automatic Design Synthesis) [1.40].

The following sections briefly discuss the development of a continuous cantilever model including the gust modelling, followed by the control system design techniques. The procedure for computing the RMS response of the system is presented. Results of the optimisation are then presented for several different cases which are examined and compared. Finally, some conclusions drawn from the above optimisation studies are presented.

7.2 Aeroelastic Behaviour of an Actively Controlled Wing

Using the generalised coordinates and normal mode method of flutter and response analysis, the equations of motion for an oscillating wing can be expressed as follows:

$$\left[\left(\left[K_D(\omega)\right]+\left[QA\right]_R\right)+i\left(\omega[D]+\left[QA\right]_I\right)\right]\{q\}=\{QF\}_E \tag{7.1}$$

where $\left[K_D(\omega)\right]$ is the generalised dynamic stiffness matrix; $[D]$ is the generalised damping matrix; $\left[QA\right]_R$ and $\left[QA\right]_I$ are respectively the real and imaginary parts of the generalised unsteady aerodynamic matrix $\left[QF\right]$ resulting from the motion, $\{QF\}_E$ is the generalised aerodynamic force matrix resulting from external excitation and ω is the circular frequency of harmonic oscillation.

For flutter analysis, $\{QF\}_E$ in Eqn. (7.1) is set to zero whereas for response analysis, $\{QF\}_E$ is calculated from the input excitation, e.g., a gust or atmospheric model.

If *n* number of modes (including the control surface mode) are used in the analysis, the order of the above [ ] matrices will be *nxn* whereas that of { } matrices will be *nx1*.

In the current analysis, only one control mode which is designated as its rotational movement, is considered along with (*n* - 1) elastic modes of the wing. Thus

the relationship between the generalised aerodynamic matrix and generalised coordinates of the (*n* - 1) modes of the main wing and the single rotational mode of the control surface can be expressed by partitioning the matrix $[QF]$ given above in the following form

$$[QF]\{q\} = [QA_m \quad QA_\delta]\begin{Bmatrix} q_m \\ q_\delta \end{Bmatrix} \tag{7.2}$$

where $\{q_m\}$ represents the generalised coordinates corresponding to the (*n* - 1) modes of the main lifting surface (wing) whereas $\{q_\delta\}$ represents the generalised coordinate corresponding to the control surface movement.

For zero control movement, $\{q_\delta\}$ is zero and the only additional aerodynamic force is that due to the main surface movement. When the control surface is moved, the non-zero rotation $\{q_\delta\}$ of the control surface is linked to the movement of the main surface through a closed-loop active control system. In practice, the control surface is driven by an actuator according to a pre-set control law and also governed by the measured movements of the wing (bending displacement and torsional rotation) at specified points. In the numerical analysis, the control law which represents the control system behaviour needs to be optimised as in the present case, according to the control requirement. The desired control law in this section concerns flutter only so that it can get a compensation from $[QA_\delta]\{q_\delta\}$ for $[QF]$ to suppress flutter by driving the control surface. In the aerodynamic energy concept presented by Nissim [1.34], the right control should make the oscillating wing do positive work on the surrounding airstream. Hence one of the major tasks in the current work is to identify such a desirable control law.

7.3 Control System

The basic control system consists of a single trailing-edge control surface aligned in the streamwise direction which has a length of the order of one tenth (10%) of the wing semi-span and a width of 20% of the wing chord.

The aerodynamic forces acting on a wing section depend on the transverse displacement h_p and the pitching rotation φ_p at a specified point on the wing, see for example Fig. 7.1. Considering a simple constant gain and continuous control system, the relationship between $\{q_\delta\}$ (the generalised coordinate corresponding to the control surface movement), h_p and φ_p can be represented (see Fig. 7.1) by

$$\{q_\delta\} = [C]\begin{Bmatrix} h_p \\ \varphi_p \end{Bmatrix} \tag{7.3}$$

where $[C] = \begin{bmatrix} C_1 + iG_1 & C_2 + iG_2 \end{bmatrix}$ is the damping type control law in complex matrix form [7.26]. For a linear system, the h_p and φ_p can be represented by modal superposition of the wing modes as follows:

$$\begin{Bmatrix} h_P \\ \varphi_P \end{Bmatrix} = [\Phi_P]\{q_m\} \tag{7.4}$$

where $[\Phi_P]$ is the modal matrix of m = (n - 1) number of modes of the main surface at measurement point and $\{q_m\}$ are the (n - 1) generalised coordinates, i.e., q_1, $q_2 \cdots q_{n-1}$.

Substituting Eqns (7.3) and (7.4) into Eqn. (7.2), the generalised aerodynamic force can be represented in terms of $\{q_m\}$ as follows

$$[QF]\{q\} = \left([QA_m] + [AC_\delta][\Phi_P]\right)\{q_m\} \tag{7.5}$$

where

$$[AC_\delta] = [QA_\delta][C] \tag{7.6}$$

is a complex matrix.

Thus, the flutter equations of a wing with control surface can be represented in matrix form as below

$$\left[\left(\left[K_D(\omega)\right]+\left[QA_m\right]_R+\left[AC_\delta\right]_R\left[\Phi_P\right]\right)+i\left(\omega[D]+\left[QA_m\right]_I+\left[AC_\delta\right]_I\left[\Phi_P\right]\right)\right]\{q_m\}=0 \quad (7.7)$$

7.4 Gust Response with Control Surface

Unlike the unsteady aerodynamic forces at flutter condition induced by harmonic motion, the gust load on the wing needs to be treated separately as an additional external force. If the normal modes of the wing are taken into account to calculate the unsteady aerodynamic forces due to motion as well as external excitation, the governing equations of motion of the wing-control surface movement in the presence of a gust loading can be written in a similar form as Eqn. (7.7) except that the right-hand side representing the gust loading is now non-zero. Thus,

$$\left[\left(\left[K_D(\omega)\right]+\left[QA_m\right]_R+\left[AC_\delta\right]_R\left[\Phi_P\right]\right)+i\left(\omega[D]+\left[QA_m\right]_I+\left[AC_\delta\right]_I\left[\Phi_P\right]\right)\right]\{q_m\}=\{QG\} \quad (7.8)$$

where $\{QG\}=\left\{Q_{g1} \quad Q_{g2} \quad ..... \quad Q_{gm}\right\}$ is the generalised aerodynamic force due to the gust loading.

7.5 Methods of Gust Analysis

Two methods are common in gust analysis - the one which uses a discrete gust approach and the other which uses a continuous gust approach. There are some distinct advantages to the continuous gust approach. It is not biased towards a specific gust frequency or gust shape since it uses atmospheric turbulence information as input. Furthermore, oscillatory aerodynamic coefficients (including control-surface coefficients) are used, and these are readily available for both compressible and incompressible flows. Its main disadvantage lies, however, in the fact that statistical quantities are involved as response output, which do not lend

themselves readily to an understanding of the physics of the problem. The discrete gust approach is computationally more expensive but enables one to follow the response of the aircraft in the time domain and thus improves an understanding of the physical aspects of the problem. It has, however, its own disadvantages. It is over-dependent upon the gust input parameters, such as the gust frequency and gust velocity (often stipulated by the Airworthiness requirements), and the aerodynamic coefficients relating to control rotations or to unsteady compressible flow are not readily available. Therefore, the continuous gust approach has been adopted in this work since it is more widely accepted and it is not biased towards gust input parameters.

7.6 Gust Model

In order to calculate the frequency response function of the wing, a continuous sinusoidal vertical gust is considered as input excitation. The downwash of this gust loading is represented by [7.27],

$$W = \widetilde{W}_g e^{i\omega(t-x/V)} \tag{7.9}$$

where $\widetilde{W}_g$ is the amplitude of the gust velocity, x is the chordwise distance from the reference axis, V is the airspeed, ω is the frequency of the gust and t is time.

The relationship between the downwash and the displacement $Z(x,\omega)$ of the wing can be written as [7.27],

$$W(x,\omega,t) = \left(V\frac{\partial}{\partial x} + \frac{\partial}{\partial t}\right) Z(x,\omega) e^{i\omega t} \tag{7.10}$$

Conversely, the displacement which can generate the above type of downwash can be represented in the following form [7.28]

$$Z(x,\omega)e^{i\omega t} = \left(\frac{W_g}{V} x e^{-i\omega t/V}\right) e^{i\omega t} \tag{7.11}$$

Based on the above reasoning, the gust wave is represented by an equivalent wing oscillation given by Eqn. (7.11). Since the air pressure due to gust can be obtained from the air pressure due to the above motion, a similar procedure to that of the calculation of unsteady aerodynamic force due to the wing flexible modes, can be performed for gust loading.

Thus, from the dynamic equation of the wing under gust loading, the frequency response function at a specific point of the wing can be obtained as,

$$H_g(\omega) = \omega^2 \left[\Phi_1(x_P, y_P) \ldots \Phi_m(x_P, y_P)\right] \{q(\omega)\} \tag{7.12}$$

where Φ_1 , ... Φ_m are mode shapes corresponding to the point of x_P and y_P only. The aircraft frequency response function $H_g(\omega)$ represents the response function at a specific point of the wing to a unit sinusoidal gust velocity.

7.7 Determination of the System RMS

The response to gusts and atmospheric turbulence is calculated in the frequency domain using the Power Spectral Density (PSD) method. This method has been continuously applied to the aircraft turbulence response problem for more than 40 years [7.25]. The PSD method has become so widely accepted that the federal aviation regulations (specifically, FAR 25.305(d)) require that, unless a more rational method is used, an aircraft manufacturer must use it to establish the dynamic response of aircraft to atmospheric turbulence.

The core of the PSD method is the PSD function, or power spectrum. This contains all of the statistical information describing a random process, including the Root Mean Square (RMS) value. In the present application the relevant random processes are atmospheric turbulence (the input random process) and aircraft responses (the output random processes). The input is assumed Gaussian, and

because the system is assumed linear, the output is also Gaussian. It is assumed that the turbulence is one-dimensional, and so uniform across the span, homogeneous, isotropic, and "frozen" in space during the time it takes the aircraft to traverse its own length.

Once the frequency response function is known, the response to atmospheric turbulence can be calculated by relating the PSD of the output to the PSD of the input excitation using the frequency response function, as given by the following equation

$$\Phi_\alpha(\omega) = \left|H_g(\omega)\right|^2 \Phi_g(\omega) \tag{7.13}$$

Here $\Phi_\alpha(\omega)$ is the wing response power spectrum, $\Phi_g(\omega)$ is the atmospheric turbulence power spectrum and $H_g(\omega)$ is the transfer function or frequency response function of the wing defined by Eqn. (7.12).

For the present purposes, the Von Karman spectrum [7.25] was chosen to represent the atmospheric turbulence power spectrum, given as follows

$$\Phi_g(\omega) = \frac{\sigma_{\omega g}^2 L_g}{\pi V} \frac{1+(8/3)\left[1.339\left(L_g/V\right)\omega\right]^2}{\left\{1+\left[1.339\left(L_g/V\right)\omega\right]^2\right\}^{11/6}} \tag{7.14}$$

where $\sigma_{\omega g}$ is the mean square value of the gust velocity, L_g is the scale length of the turbulence depending upon the flight altitude and V is the flight speed.

The mean square value of the gust (wing) response to gust loading can then be obtained from

$$\sigma_g^2 = \int_0^\infty \Phi_\alpha(\omega) d\omega \tag{7.15}$$

However, the gust (wing) response will depend upon the control surface movement.

7.8 Wing Model

In the current analysis, only the wing is taken into account and not the whole aircraft as one dynamic system. The wing is assumed to be cantilevered at the root. Four elastic modes are used for the main wing surface along with one control mode which is designated as its rotational movement. It is assumed that there is only one control surface at a given spanwise location of the wing. However, four different spanwise locations of the control surface are included in the analysis. The results for each activated control surface provide information regarding gust alleviation achievable with flutter speed as a constraint. It is hoped that by analysing this simple wing, results can be applied to a wide variety of aircraft wings.

7.9 Optimisation of Control Parameters

As stated earlier, the objective is both gust alleviation and flutter suppression of an aeroelastically optimised wing using active control. In contrast to structural optimisation, this task is essentially a constrained optimisation problem in which the parameters in the control laws are taken as the design variables to minimise the following objective function

$$q(C) = 1 - \frac{\sigma_g^2(0) - \sigma_g^2(C)}{\sigma_g^2(0)} \tag{7.16}$$

with the following constraint conditions

$$h(C) = \frac{V_F(C) - V_{F\max}}{V_{F\max}} \geq 0, \tag{7.17}$$

$$\text{and} \quad \{C_l\} \leq \{C\} \leq \{C_u\}$$

$\sigma_g^2(C)$ and $\sigma_g^2(0)$ are respectively the mean square values of the gust response with and without the active control, while $\{C\}$ represents the control parameters when

active control is used. $V_{F\max}$ is the maximum flutter speed determined in the aeroelastic optimisation carried out using the fibre orientation as the design variable, that is, before incorporating the control surface. $V_F(C)$ represents the flutter speed with control, with $\{C_l\}$ and $\{C_u\}$ being the lower and upper bounds of the design variables $\{C\}$.

7.10 Discussion of Results

The geometric data of the fourteen layer unswept composite wing used in the present analysis is shown in Fig. 7.2. The mass per unit length of the wing is m = 0.2172 kg/m, the mass moment of inertia per unit length is $I_\alpha = 0.1052 \times 10^{-3}$ Kgm and the static unbalance is $x_\alpha = 0$. The chord centre and the shear centre coincide, i.e., a = 0.

As shown in chapters 5 and 6, the maximum flutter speed of the unswept wing is given by the laminate configuration that offers the maximum torsional rigidity, that is, when the fibre angles of all the plies in the laminate are set alternatively at angles $\beta = \pm 45^0$. Therefore, to optimise the flutter speed of the wing before using active control technology to reduce its gust response, the fibre angles of the laminate were set alternatively at $\beta = \pm 45^0$. The bending and torsional rigidities of the above laminate configuration were calculated using the HARP model (i.e., Eqns (3.24)-(3.26) of chapter 3) as EI = 0.7815 Nm^2 and GJ = 4.281 Nm^2 respectively. The bending-torsion coupling rigidity K is zero in this case.

Firstly the flutter speed of the wing was calculated without taking the control surface into account, and was found to be V_F = 75 m/s. Then the control surface of the wing was taken into consideration and an optimised control law to alleviate the gust response was identified. However, when actuating the control surface to alleviate the gust response of the wing, it is desirable to retain the aeroelastic features which gave the maximum flutter speed without using the active control. Thus the flutter speed estimated without using the active control, i.e., V_F = 75 m/s is set as a constraint. The procedure is demanding on computing time because flutter analysis is required at each step of the optimisation for the control law parameters.

Four different spanwise control locations are investigated as shown in Fig. 7.2. Each control surface planform is taken to be 10% of the semi-span and 20% of the semi-chord. The RMS values of the normal acceleration ($\sigma_{n\alpha}$) of the wing for all four control surface positions are calculated at the tip.

In order to simplify the problem, the stiffness and inertia coupling between the wing main surface and the control surface is ignored in the analysis.

The flight speed of the aircraft is assumed to be 40 m/s (as opposed to its flutter speed of 75 m/s when not using the active control).

Figures 7.3-7.6 show the optimisation histories of the control law parameters, flutter speed, and gust response respectively for the four spanwise locations of the control surface (see Fig. 7.2). The optimisation history of control law parameters $\{C\}$ for the control position 1 is shown in Fig. 7.3 (a). The corresponding optimisation history of the flutter speed is shown in Fig. 7.3 (b) whereas Fig. 7.3 (c) shows the optimisation history of the gust response (see Eqn. (7.15)). Similar plots are shown for the control positions 2, 3, 4 in Figs 7.4, 7.5 and 7.6 respectively. The respective optimised control laws $\begin{bmatrix} C_1 + iG_1 & C_2 + iG_2 \end{bmatrix}$ for the four control positions to alleviate the gust response without compromising the maximum flutter speed are shown in Table 7.1.

The results presented in Table 7.1 show that the control is more effective in alleviating the gust response of the specific wing investigated in position 3 with a reduction in gust response of about 31.2%. An explanation of this can be that the accelerations and therefore displacements of the wing at the tip can be more effectively controlled by controlling the same displacements at the middle of the wing, see, for example, the first four mode shapes in Fig. 7.7.

Even more significant reductions in gust response could be achieved using the control in position 3 if a flutter speed of 75 m/s had not been set as a constraint. This can be seen in Fig. 7.5 (c) where, in contrast to the other three control surface positions, the flutter speed is oscillating about the constraint value (see Fig. 7.5 (b)). In the other three spanwise control positions, however, flutter appears to be no obstacle

in reducing the gust response of the wing even further (see Figs 7.3 (b), 7.4 (b) and 7.6 (b)).

In order to investigate the effect of the control size on gust response alleviation, the size of the control at position 1 was increased from 10% to 20% of the wing span. The optimised control law was calculated to be $[-8.057 + 6.582i \quad -1.290 + 0.8951i]$ which alleviate the gust response by about 22% as opposed to the 19.71% obtained by the 10% span control.

In order to investigate the effect of flight speed on the gust response and the alleviation that can be achieved using the active control at position 1, the flight speed has been increased from 40 m/s to 70 m/s which is now about 93% of the flutter speed. The optimised control law was calculated to be $[-0.05769 + 0.2924i \quad -0.344 + 0.9448i]$ alleviating the gust response by only 13%. An explanation of this can be that at very low speeds the RMS for both bending and torsional displacement are small and thus their reduction using active control will be more effective. As the flutter (instability) speed is approached, however, it is expected that the RMS will increase because disturbing a system that is almost unstable will result in large responses. Note that at high flight speeds much smaller control rotations are needed when compared to those at low flight speeds because the control becomes more effective due to the higher dynamic pressure.

7.11 Conclusions

An analysis of active control has been carried out on a laminated composite wing. The effectiveness of activated trailing-edge control systems on flutter suppression and gust alleviation has been determined.

The results of optimisation of control parameters have revealed that the response of the wing to gusts and atmospheric turbulence can be reduced by 31% without making any compromise on the flutter speed. This can be achieved when the control surface is installed somewhere in the middle of the wing. However, the optimal position of the control surface to alleviate the gust response of the wing varies with the

type of the wing under investigation thus making it difficult to draw general conclusions.

A significant number of graphical results have been presented in the present work with the intention of contributing toward a better insight into the problem of flutter suppression and gust alleviation using active controls. The purpose has been to show the strong interrelations that exist when attempting to treat separately only some of the aspects associated with the wider problem. However, additional work is required where the control can move in any pattern and not simply sinusoidally, and it is also necessary to use more sophisticated wing models. Nevertheless, it is very encouraging to discover the considerable effectiveness of the activated control system in flutter suppression and gust alleviation.

TABLE 7.1

Optimised control laws and respective Root Mean Square (RMS) values for the four spanwise control positions.

Control Location	Optimised control law $[C_1 + iG_1 \quad C_2 + iG_2]$	Root Mean Square value $\sigma_{n\alpha}/\sigma_{wg}$ (s^{-1})	Gust response alleviation (%)	V_F (m/s)
1	$[-4.539+10i \quad -1.429-0.645i]$	**0.40×10^6**	**19.71**	**76.53**
2	$[-10.0+5.69i \quad -1.647+0.79i]$	**0.40×10^6**	**19.47**	**76.94**
3	$[-3.301+4.14i \quad -10.0+0.701i]$	**0.34×10^6**	**31.18**	**75.35**
4	$[-10.0+5.772i \quad -1.77+0.495i]$	**0.40×10^6**	**19.47**	**76.94**

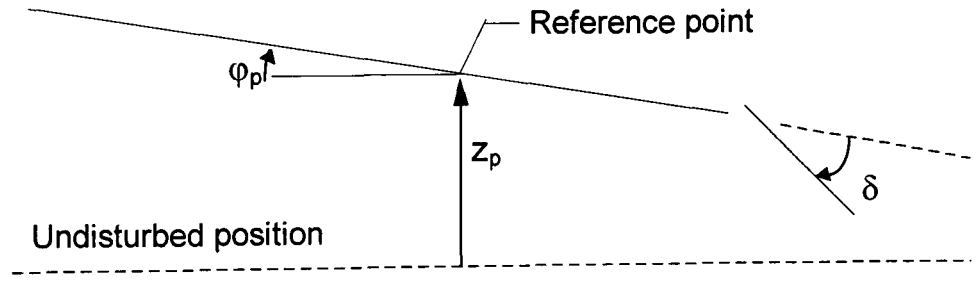

Fig. 7.1. Control system.

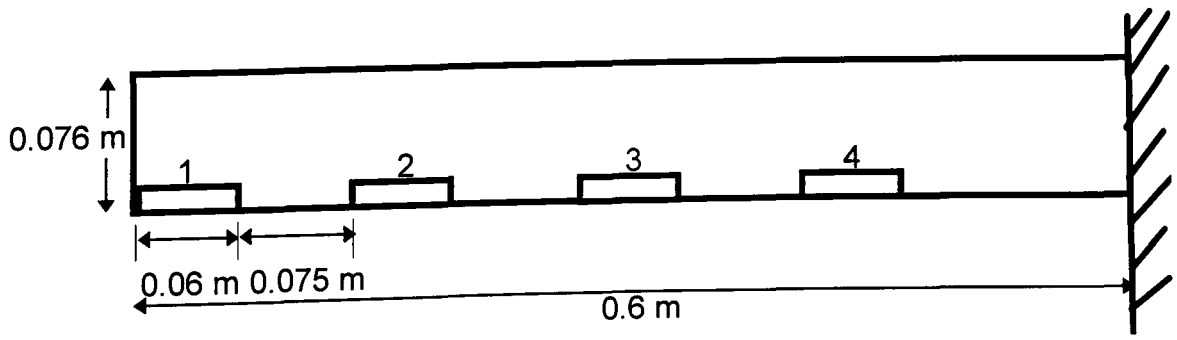

Fig. 7.2. Control allocations along the wing span.

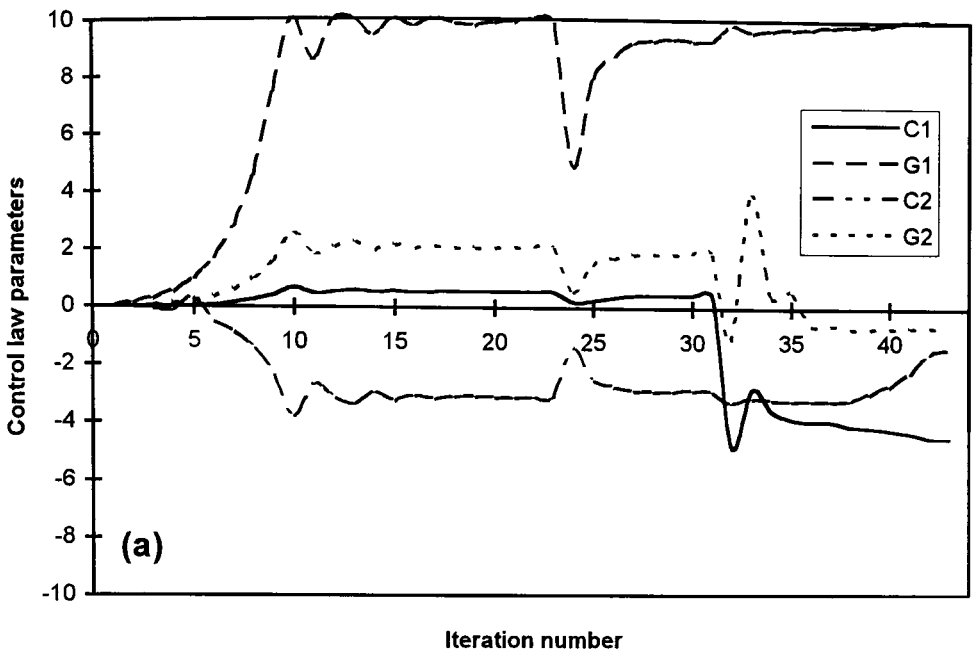

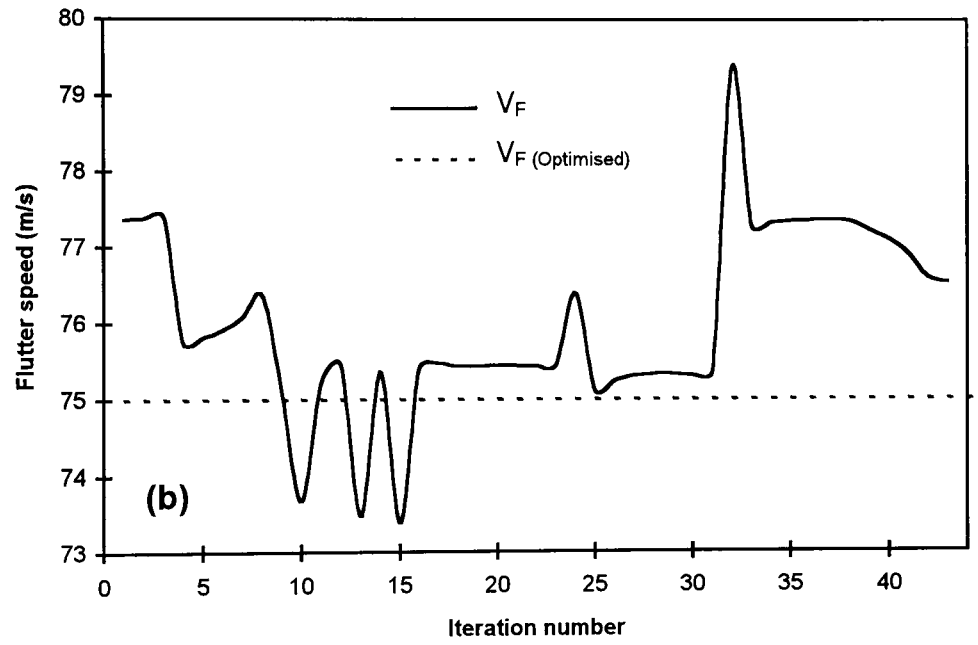

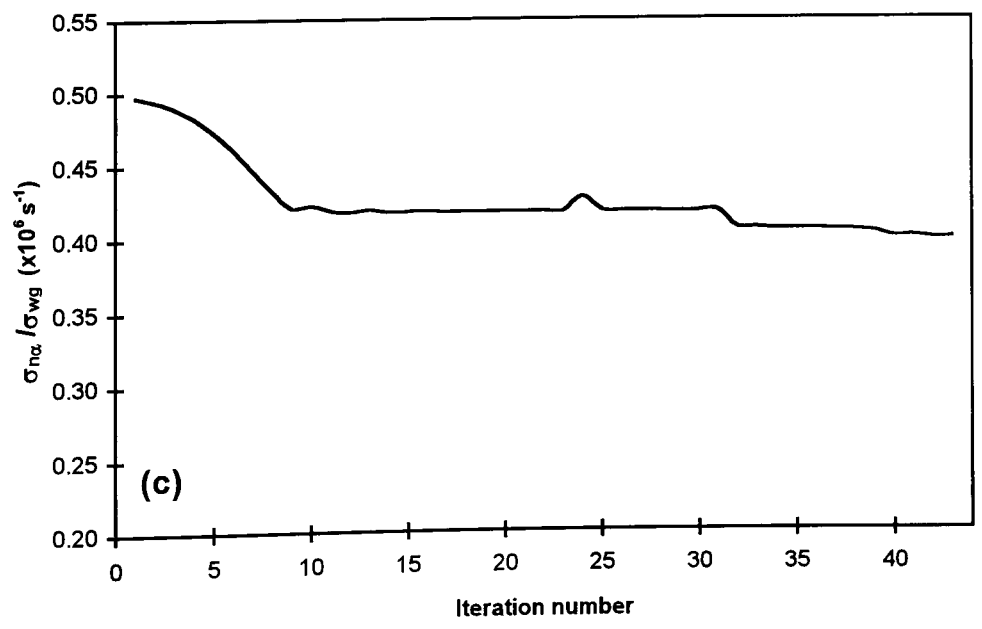

Fig. 7.3. Optimisation history of (a) control law parameters, (b) flutter speed and (c) gust response for control position 1.

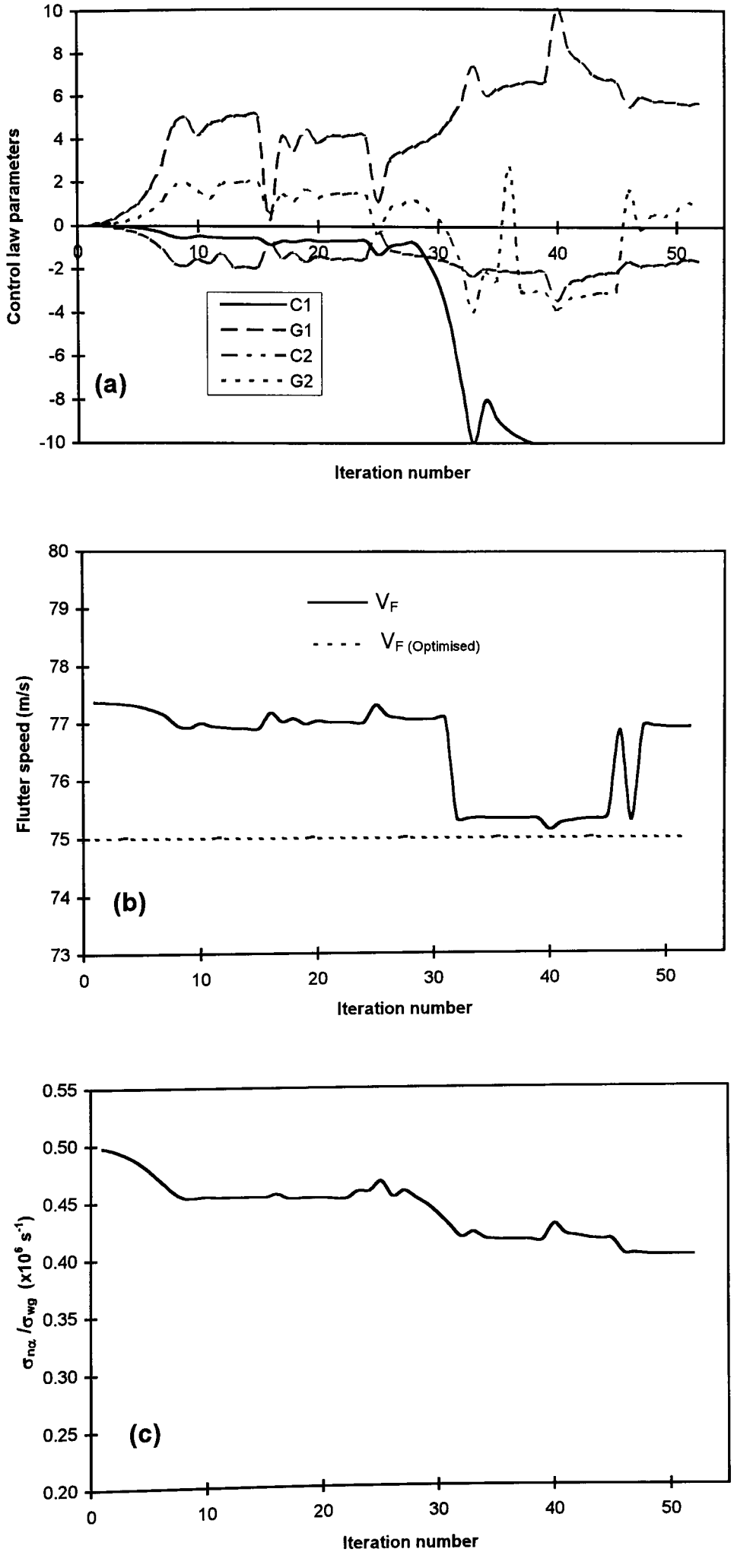

Fig. 7.4. Optimisation history of (a) control law parameters, (b) flutter speed, and (c) gust response for control position 2.

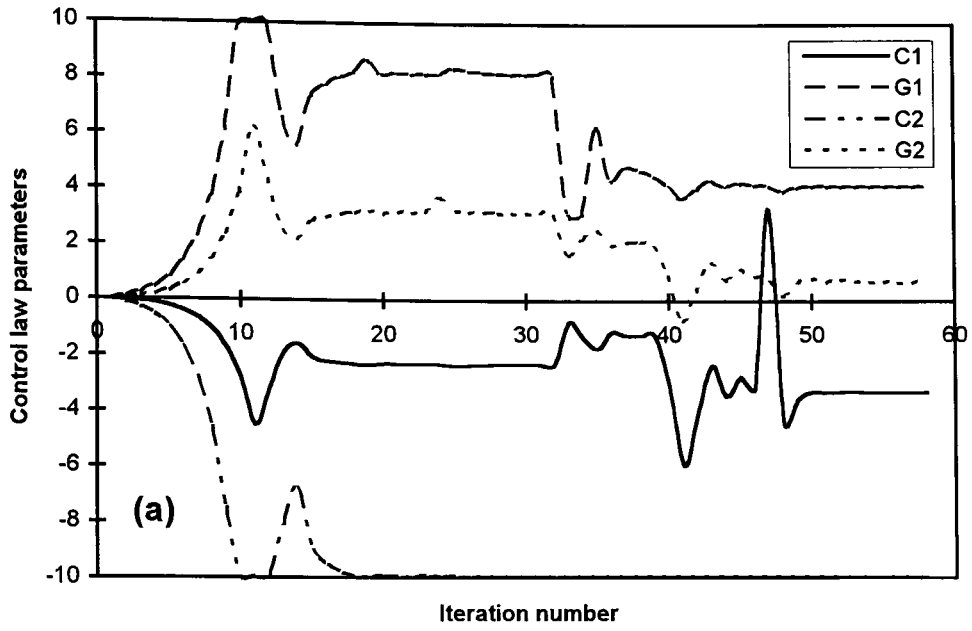

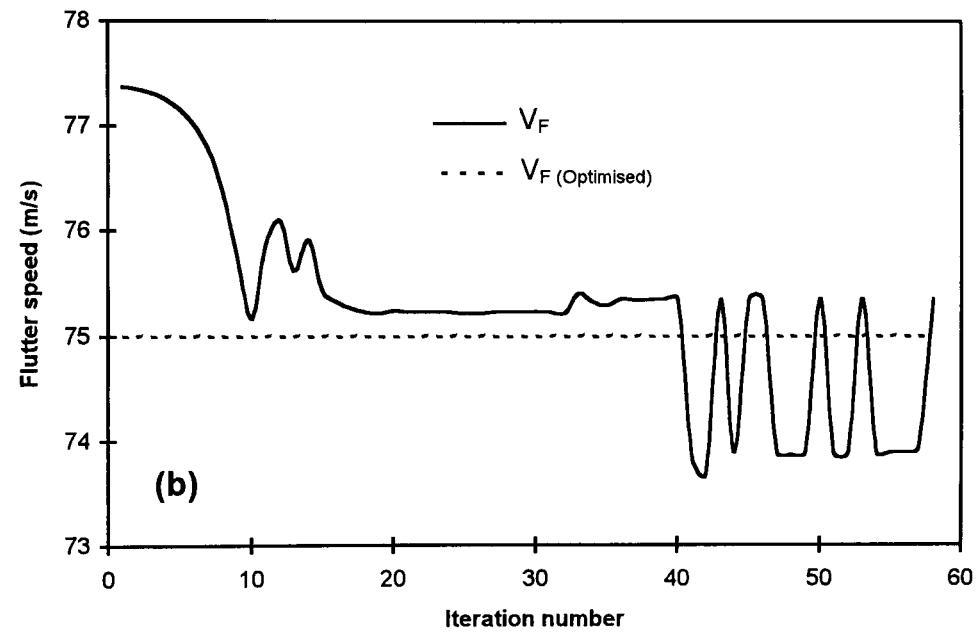

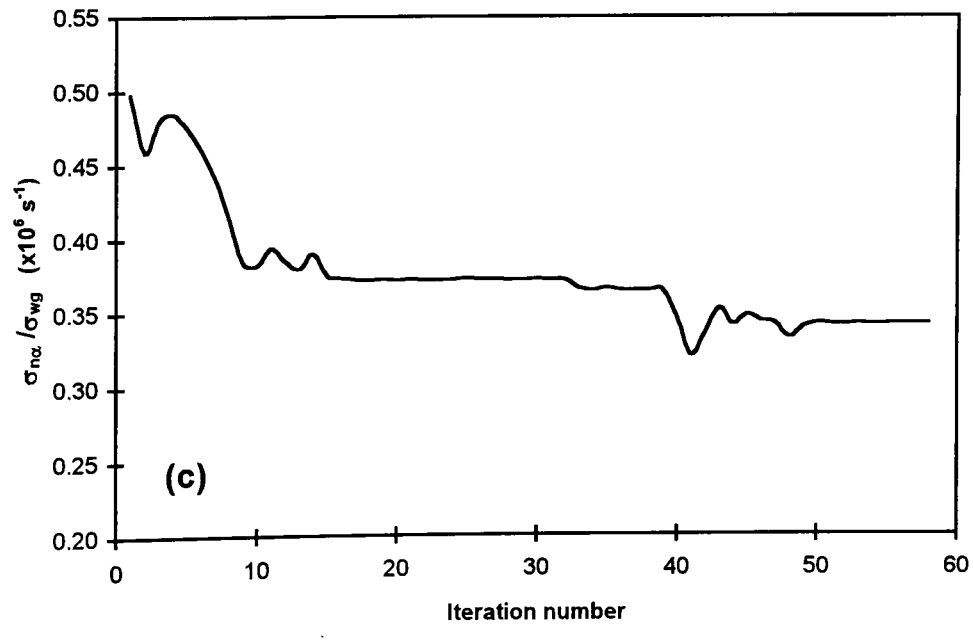

Fig. 7.5. Optimisation history of (a) control law parameters, (b) flutter speed, and (c) gust response for control position 3.

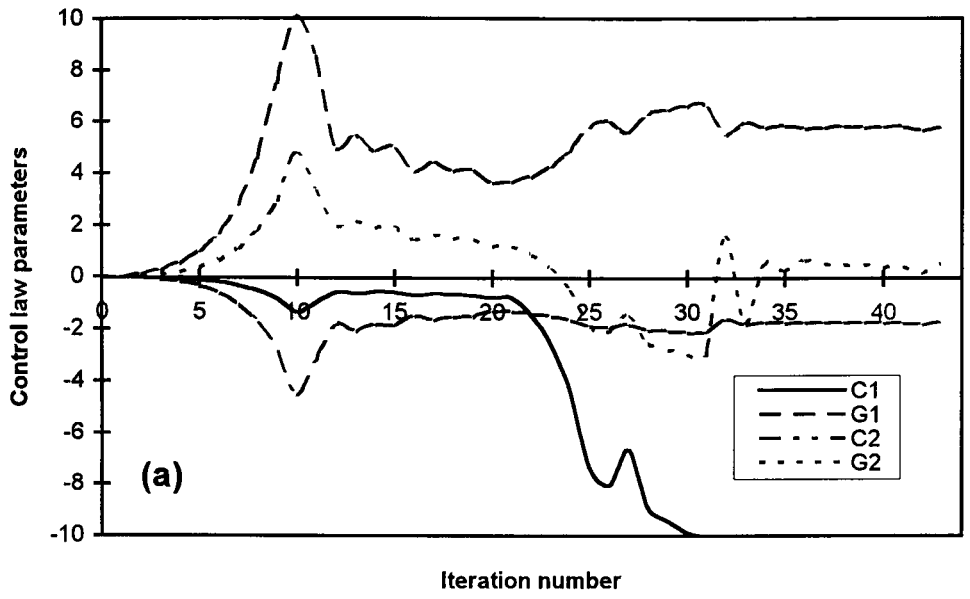

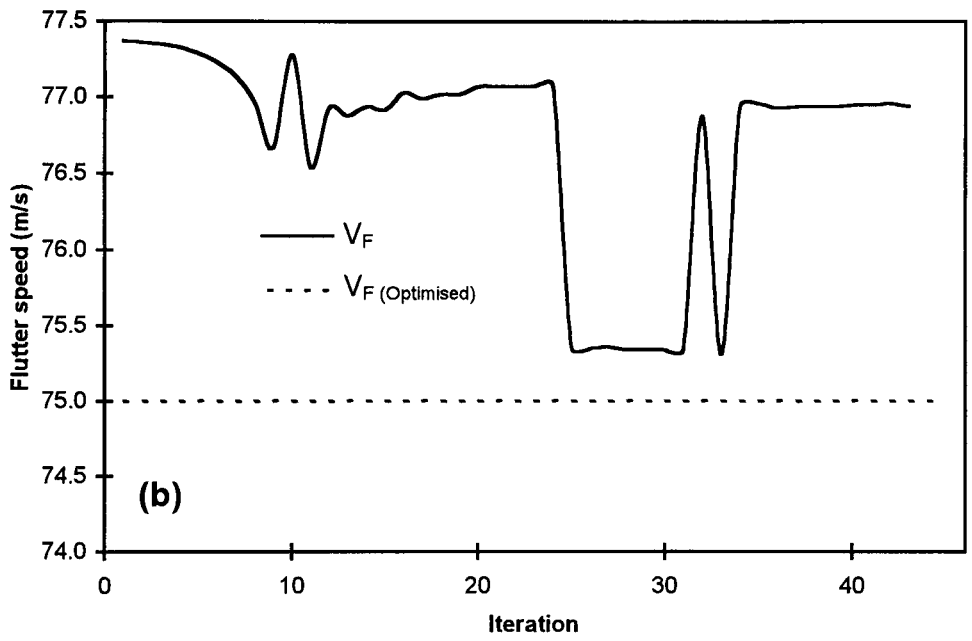

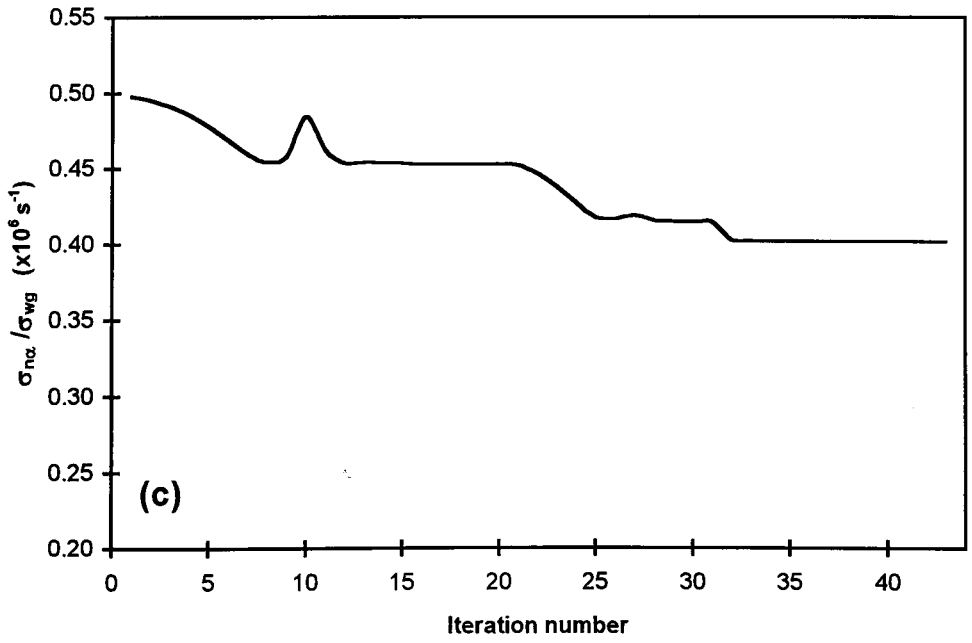

Fig. 7.6. Optimisation history of (a) control law parameters, (b) flutter speed, and (c) gust response for control position 4.

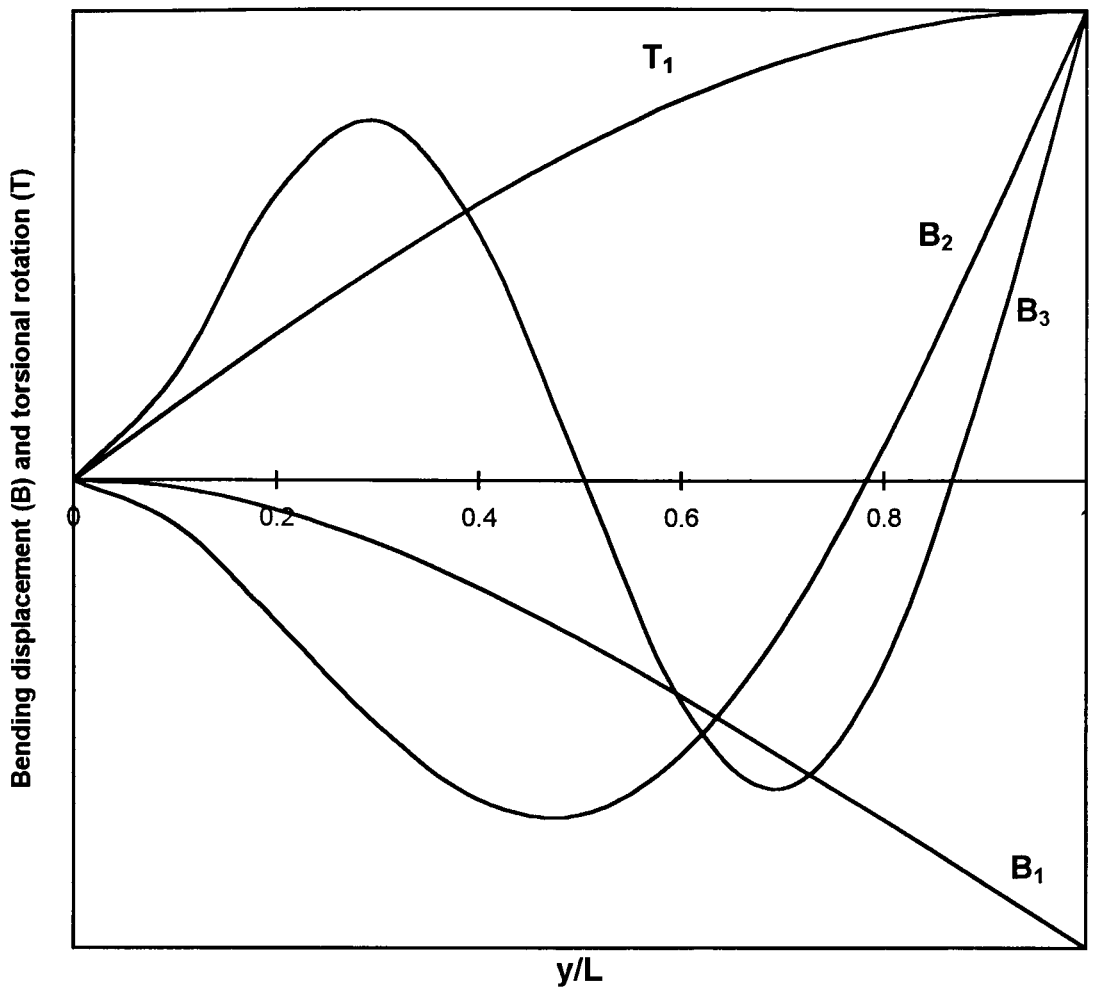

Fig. 7.7. Normalised modes for the actively controlled wing.

B_1 : First bending mode

B_2 : Second bending mode

B_3 : Third bending mode

T_1 : First torsion mode

CHAPTER 8

PRINCIPAL CONCLUSIONS

AND

RECOMMENDATION FOR FUTURE WORK

8. PRINCIPAL CONCLUSIONS AND RECOMMENDATION FOR FUTURE WORK

8.1 Principal Conclusions

The investigations and examples presented in this thesis have focused upon the potential of composite materials to enhance aeroelastic stability whilst saving or, at worst, preserving weight. In the course of these investigations two essential prerequisites of any aeroelastic analysis have been examined, namely the static and dynamic behaviour of composite wings. In addition, the possibility of alleviating the gust response of a wing by the use of active controls without reducing its already optimised flutter speed has been studied.

In investigating the static behaviour of composite wings, rather than developing a unified idealised model in which non-dimensional combinations of parameters appear as variables, illustrations have been drawn from physically realisable examples. The potential danger of this approach has been illustrated by the comparison of various methods of predicting rigidity parameters essential to the structural dynamic analysis. For flat beams (plates), chordwise stiffness has been shown to be an important parameter to be considered since it has a significant effect on the amount of bending-torsion coupling present in a structure and thus on the predicted value of torsional rigidity. The effects of assuming that this chordwise rigidity is present when, in fact, it is not, may be significant for plates with high bending-torsion stiffness coupling. When thin-walled beam cross-sections are considered, such as a torque box of relatively small width-to-depth ratio typically present in a wing, the effects of assuming an infinite shear stiffness for the vertical webs can give significant differences in the predicted bending, torsional and coupling stiffnesses though mainly in the torsional rigidity.

The free vibration characteristics of composite beams have been examined using the dynamic stiffness matrix method. The accuracy of the method in predicting the natural frequencies has been demonstrated by comparing with results for a range of composite beams with varying lay-ups and cross-sections that are available in the literature. The examples chosen have illustrated the effect of moderate values of bending-torsion stiffness coupling on natural frequencies, which

has been found to be generally small, while its effect on mode shapes has been shown to be substantial. The study has also shown that the anisotropic property of composite materials can be used as a modal coupler/decoupler, and can be applied to decouple modes which are geometrically (inertially) coupled in the same way as with mass balancing, but without a weight penalty. It can also be used to reverse completely the unfavourable coupling introduced by sweep angle.

Classical flutter and divergence of swept and unswept composite wings have been investigated using laminated flat beams (plates) and thin-walled (box) beams of rectangular and biconvex cross-sections. Results have been compared with published results for composite beams with varying lay-ups and cross-sections, and the agreement between the results has been shown to be very good. Various parameters, such as, the fibre angle, β, the bending-torsion coupling parameter, ψ, the angle of sweep, Λ, and the static unbalance, x_α, have been varied and their subsequent effects on the flutter and divergence speeds have been investigated. The results have shown that, using tailoring procedures (i.e., combinations of the above parameters), flutter and classical divergence can be controlled and, in certain cases, effectively eliminated from the flight envelope.

One interesting aspect of the above investigations is that they have shown (in contrast to all previous investigations) that the torsional rigidity GJ can be the most important parameter to be considered when the objective is that of increased flutter speed. The study has shown that flutter speed is more sensitive to changes in the non-dimensional ratio of the fundamental (uncoupled) bending to fundamental torsional frequency, ω_h / ω_α, rather than changes in the modes shapes by the use of bending-torsion stiffness coupling. This is especially true for the unswept and forward-swept wings. However, a negative bending-torsion coupling, which results in the wash-in effect, can be beneficial for the flutter of swept-back wings.

As for divergence, the results have shown the sole dependence of divergence speed on wash-in and wash-out effects and, as a consequence, on ψ. The torsional rigidity GJ is the most important parameter to be considered when the object is that of maximising the divergence speed of unswept and balanced laminated wings where no coupling is present.

Another interesting aspect of this study is that which shows that the modal interchanges in the free vibration and flutter behaviour of laminated composite wings are primarily responsible for many of their unusual characteristics, such as, the unexpected blips in the variation of flutter speed with fibre angle. They are also responsible for the wash-in behaviour, which usually causes the aerodynamic load on the wing to increase, being more beneficial for the flutter of composite wings than the wash-out one.

One of the most interesting features of this study is the identification of two very important parameters which are independent of laminate geometry and can represent the flutter behaviour of realistic composite wings, making the understanding and prediction of such behaviour possible. These are the non-dimensional frequency ratio, ω_h / ω_α, and the bending-torsion coupling parameter ψ. When the flutter speed is plotted against the above two non-dimensional parameters, several conclusions regarding flutter prediction and optimisation can be drawn which can be useful in any preliminary design. This has been confirmed by independent optimisation studies. The author feels that this is a significant contribution to the state-of-the-art.

The sensitivity of the optimised flutter speed to various parameters, such as, the bending and torsional rigidities, fibre angle and wall thickness, has also been demonstrated. The results have indicated that the sort of variations likely to be experienced in practice in bending rigidity (EI) and fibre angle (β) have virtually no effect on the optimised flutter speed while those of torsional rigidity (GJ) and wall thickness (t) are significant.

A preliminary investigation has been carried out into the flutter suppression and gust alleviation of a laminated composite wing by the use of active controls. Control laws have been optimised for various trailing edge control positions. The results have shown that by using an active control in an optimum trailing edge position, the gust response of a composite wing can be significantly alleviated without compromising the already optimised flutter speed by the use of aeroelastic tailoring.

Generally, this study has discussed aeroelastic tailoring in terms of laminated composite construction. Despite the extensive research that has been carried out in the field, formal strategies and design goals for efficient utilisation of advanced composite materials have yet to be fully developed. Such design strategies require consideration of issues such as durability and damage tolerance, automatic control and their interaction with structural response, and overall aircraft performance. The literature cited in this report, together with the examples presented, have shown that new approaches and new thought will be required for the new era of structural design.

8.2 Recommendation for Future Work

As with any study, a great number of new studies suggest themselves. In particular, the extension of the present studies to non-uniform variable chord wings should be done. At the same time experiments should be carried out using flat composite plates to validate the results and conclusions of the present study. Firstly simple flat plate models should be constructed in order to validate the theory presented in this study and then a more advanced experimental investigation should be carried out to confirm its results and conclusions. For this purpose the following experimental procedures are proposed to be followed in conjunction with the T3 low speed wind tunnel of Handley Page laboratory at City University.

Model design is driven by several constraints imposed by the study objectives and available facilities. Models would be required to

- demonstrate a wide range of bending-torsion coupling;

- be rectangular shaped constant thickness, flat plates, with varying sweep. Flat plates of various aspect ratio should be used in order to alter the value of the frequency ratio ω_h / ω_α which has been shown to be an important parameter influencing the flutter speed;

- be of relatively small size and exhibit flutter within the 55 m/s velocity limitation of the wind tunnel;

- be tough enough to withstand repeated large static and oscillatory loads.

The first constraint indicates that unbalanced laminated plates which are symmetric about the mid-plane are desirable while the third constraint imposes limitations on the thickness and size of the plates. Taking the above four constraints into account, a graphite/epoxy flat plates with lay-up $[\beta_2/0]_s$ and semi-span, chord and ply thickness of 0.6 m, 0.076 m and 0.134 mm respectively should be constructed and tested to validate the present theory. A theoretical investigation has shown that the variation of flutter speed with fibre angle for the proposed laminate configuration remains within the speed capability of the wind tunnel. Positive and negative fibre angles (β) should be used in order to investigate both the wash-in and wash-out behaviours. Five different laminated flat plates with fibre angle varied by increments of 15^0 are actually needed for this investigation as follows: $[0_3]_s$, $[+15_2/0]_s$, $[+30_2/0]_s$, $[+45_2/0]_s$ and $[\pm 45_2/0]_s$. The first laminated plate provides the highest bending rigidity while the next three provide various amounts of bending-torsion coupling. The fifth plate offers the highest torsional rigidity as expected. In order to investigate the aeroelastic behaviour of laminates with negative fibre angles the above specimens can be rotated by 180^0.

A bending and a torsion strain gauge should be attached to the base of both sides of each model, at the mid-chord. Prior to attaching the strain gauges, each model should be measured (thickness, width, and length), and weighed. These figures should be recorded and compared to nominal (theoretical) values.

To confirm some of the results and conclusions of this study, the theoretical investigation of section 5.6 of chapter 5 can be repeated experimentally using models of wings with various aspect ratios and sweep angles.

The analytical and experimental investigations using a cantilever wing should be extended to the whole aircraft configuration. A comparison between the cantilever flutter speed with that of the whole aircraft is important since rigid-body modes can play an important role on the flutter of composite wings. It would also be

interesting to show how the fibres of the tail can be oriented in order to assist in raising the flutter speed of the whole aircraft and also to eliminate wing-tail interference flutter.

Another important area than needs further investigation is the use of active control for flutter suppression and gust alleviation. It is understood that, different control laws are currently used to control each of the above two phenomena and therefore the present study appears to be the first to merge them into one control law. However, an extension of the present simplified study where the control moves sinusoidally to one that moves in any pattern, is required. The use of more sophisticated structural models than the flat constant chord beam used in the present study is also desirable.

Another aspect of aeroelastic tailoring which has rapidly attracted the attention of many researchers in the field, is the application of optimisation techniques. Aeroelastic tailoring is considered to be a particular application of the general field of structural optimisation under aeroelastic constraints. During the period of this investigation, the computer program developed for flutter optimisation can be modified for minimum weight optimisation of structures with static, dynamic and aeroelastic constraints.

Control effectiveness or degradation of such effectiveness due to adverse deformation is clearly an other potential area that needs investigation. Although only a small amount of tailoring work has been done in this area, some investigators regard this a very promising area for the use of aeroelastic tailoring.

Large space structures provide another potential area of aeroelastic tailoring research. The repetitive lattice arrangement of a number of space structures forms an anisotropic design. The active control system of these space structures can be enhanced by achieving passive modal control through tailoring the orientations of the structural members.

The examples presented in this thesis have shown the potential for aeroelastic tailoring for a simple structure, and provides a spur for further investigations of more advanced designs and applications.

APPENDIX 'A'

THE MACROMECHANICAL PROPERTIES OF COMPOSITE MATERIALS

A.1 Introduction

This appendix deals with the macromechanical properties of composites which is a very important topic in design analysis. In particular, section A.2 covers the stress-strain relations for isotropic, specially orthotropic and generally orthotropic plies. Formulas are derived for the engineering elastic constants in the x-y directions in terms of the elastic constants in material directions 1-2. Then section A.3 deals with the general laminate constitutive equations for load-deformation relationships. The modifications of the above equations due to ply orientation and stacking sequence are discussed. In section A.4 the effect of ply orientation on the extensional, coupling and bending stiffness terms, and laminate engineering elastic constants, is examined. Finally, some conclusions are drawn in section A.5.

A.2 Laminate Equivalent Elastic Constants

The stress-strain relations in principal material coordinates for an isotropic ply subjected to a combination of direct and shear stresses or strains are given in matrix form as [2.24],

$$\begin{Bmatrix} \sigma_1 \\ \sigma_2 \\ \tau_{12} \end{Bmatrix} = \begin{bmatrix} Q_{11} & Q_{12} & 0 \\ Q_{12} & Q_{22} & 0 \\ 0 & 0 & Q_{66} \end{bmatrix} \begin{Bmatrix} \varepsilon_1 \\ \varepsilon_2 \\ \gamma_{12} \end{Bmatrix} \tag{A.1}$$

where the suffixes 1 and 2 represent the material axes as shown in Fig. A.1. The Q_{ij} terms are the so-called reduced stiffnesses given in terms of the engineering (elastic) constants as [2.24],

$$Q_{11} = \frac{E_1}{1 - \nu_{12}\nu_{21}}$$

$$Q_{12} = \frac{\nu_{12}E_2}{1 - \nu_{12}\nu_{21}} = \frac{\nu_{21}E_1}{1 - \nu_{12}\nu_{21}} \qquad \text{(A.2)}$$

$$Q_{22} = \frac{E_2}{1 - \nu_{12}\nu_{21}}$$

$$Q_{66} = G_{12}$$

In composite materials, a specially orthotropic lamina is one whose principal material axes (1 and 2) are aligned with the reference axes, (x and y) and therefore,

$$\begin{Bmatrix} \sigma_x \\ \sigma_y \\ \tau_{xy} \end{Bmatrix} = \begin{Bmatrix} \sigma_1 \\ \sigma_2 \\ \tau_{12} \end{Bmatrix} = \begin{bmatrix} Q_{11} & Q_{12} & 0 \\ Q_{12} & Q_{22} & 0 \\ 0 & 0 & Q_{66} \end{bmatrix} \begin{Bmatrix} \varepsilon_1 \\ \varepsilon_2 \\ \gamma_{12} \end{Bmatrix} \qquad \text{(A.3)}$$

However, in order to exploit the unique characteristics of composite materials, so as to get the required stiffness and strength of an element in desired directions, orthotropic laminae are usually constructed in such a way that the principal material axes do not coincide with the material reference axes as shown in Fig. A.2. When the material axes do not coincide with the reference or loading axes, the ply is said to be generally orthotropic. In order to derive the stress-strain relations for a generally orthotropic ply the stresses and strains need to be transformed from one set of axes to another. This transformations are covered in standard text books [2.23-2.24], and, therefore only the results will be quoted here. Essentially, the transformations involve trigonometric functions of the ply angle, β.

The stress-strain relations of a generally orthotropic ply is given as [2.24],

$$\begin{Bmatrix} \sigma_x \\ \sigma_y \\ \tau_{xy} \end{Bmatrix} = \begin{bmatrix} \overline{Q}_{11} & \overline{Q}_{12} & \overline{Q}_{16} \\ \overline{Q}_{12} & \overline{Q}_{22} & \overline{Q}_{26} \\ \overline{Q}_{16} & \overline{Q}_{26} & \overline{Q}_{66} \end{bmatrix} \begin{Bmatrix} \varepsilon_x \\ \varepsilon_y \\ \gamma_{xy} \end{Bmatrix} \qquad \text{(A.4)}$$

The $\overline{Q}_{ij}$ terms are given in matrix form in terms of reduced stiffnesses Q_{ij} (given by Eqn. (A.2)) as [2.24],

$$\begin{Bmatrix} \overline{Q}_{11} \\ \overline{Q}_{22} \\ \overline{Q}_{66} \\ \overline{Q}_{12} \\ \overline{Q}_{16} \\ \overline{Q}_{26} \end{Bmatrix} = \begin{bmatrix} m^4 & n^4 & 2m^2n^2 & 4m^2n^2 \\ n^4 & m^4 & 2m^2n^2 & 4m^2n^2 \\ m^2n^2 & m^2n^2 & -2m^2n^2 & \left(m^2-n^2\right)^2 \\ m^2n^2 & m^2n^2 & m^4+n^4 & -4m^2n^2 \\ m^3n & -mn^3 & mn^3-m^3n & 2\left(mn^3-m^3n\right) \\ mn^3 & -m^3n & m^3n-mn^3 & 2\left(m^3n-mn^3\right) \end{bmatrix} \begin{Bmatrix} Q_{11} \\ Q_{22} \\ Q_{12} \\ Q_{66} \end{Bmatrix} \tag{A.5}$$

where $m = \cos\beta$ and $n = \sin\beta$.

By definition of an orthotropic material, a composite ply will have different properties in different directions at a point. Once the elastic constants in the material axes directions 1 and 2 are known the same elastic constants need to be established at a point in other directions. The compliance relationship of such a ply, i.e., the strain-stress relationship is given as [2.24],

$$\begin{Bmatrix} \varepsilon_x \\ \varepsilon_y \\ \gamma_{xy} \end{Bmatrix} = \begin{bmatrix} \overline{S}_{11} & \overline{S}_{12} & \overline{S}_{16} \\ \overline{S}_{12} & \overline{S}_{22} & \overline{S}_{26} \\ \overline{S}_{16} & \overline{S}_{26} & \overline{S}_{66} \end{bmatrix} \begin{Bmatrix} \sigma_x \\ \sigma_y \\ \tau_{xy} \end{Bmatrix} \tag{A.6}$$

According to Hooke's law, $E_x = \sigma_x/\varepsilon_x$ when the only nonzero stress applied is σ_x (in direction x) and E_x is the Young's modulus in the direction of x. Now, combining Eqn. (A.6) with Hooke's law given above and Poisson's ratio, $\nu_{xy} = -\varepsilon_y/\varepsilon_x$, and then substituting for the required $\overline{S}_{ij}$ expression in terms of the reduced compliance terms S_{ij} (which are dependent only on the four elastic constants E_1, E_2, G_{12} and ν_{12}) and ply angle β, we get the elastic constants in the x-y directions in terms of the elastic constants in the material directions 1-2. These are derived as follows:

$$\frac{1}{E_x} = \frac{m^4}{E_1} + \frac{n^4}{E_2} + m^2n^2\left(\frac{1}{G_{12}} - \frac{2\nu_{12}}{E_1}\right) \tag{A.7}$$

$$\frac{1}{E_y} = \frac{n^4}{E_1} + \frac{m^4}{E_2} + m^2 n^2 \left(\frac{1}{G_{12}} - \frac{2\nu_{12}}{E_1} \right) \tag{A.8}$$

$$\frac{1}{G_{xy}} = m^2 n^2 \left(\frac{4}{E_1} + \frac{4}{E_2} + \frac{8\nu_{12}}{E_1} \right) + \left(m^2 - n^2 \right)^2 \frac{1}{G_{12}} \tag{A.9}$$

$$\nu_{xy} = E_x \left[\left(m^4 + n^4 \right) \frac{\nu_{12}}{E_1} - m^2 n^2 \left(\frac{1}{E_1} + \frac{1}{E_2} - \frac{1}{G_{12}} \right) \right] \tag{A.10}$$

$$\nu_{yx} = E_y \left[\left(m^4 + n^4 \right) \frac{\nu_{12}}{E_1} - m^2 n^2 \left(\frac{1}{E_1} + \frac{1}{E_2} - \frac{1}{G_{12}} \right) \right] \tag{A.11}$$

In the case of a generally orthotropic ply, any application of a uniaxial direct stress results in direct and shear deformations due to shear coupling effects. Therefore, to account for these shear coupling effects, a new elastic constant called the shear coupling coefficient, S, is introduced [2.25]. As in the case of the other elastic constants, the shear coupling coefficient in the reference x-direction is S_x and in the y-direction is S_y. The shear coupling coefficient in both the x and y direction is defined as [2.25],

$$S_x = \frac{-\gamma_{xy}}{\varepsilon_x} \qquad S_y = \frac{-\gamma_{xy}}{\varepsilon_y} \tag{A.12}$$

which they give after substituting the $\bar{S}_{ij}$ in Eqn. (A.6) in terms of the four independent engineering elastic constants

$$S_x = E_x \left[m^3 n \left(\frac{1}{G_{12}} - \frac{2\nu_{12}}{E_1} - \frac{2}{E_1} \right) - mn^3 \left(\frac{1}{G_{12}} - \frac{2\nu_{12}}{E_1} - \frac{2}{E_2} \right) \right] \tag{A.13}$$

$$S_y = E_y \left[mn^3 \left(\frac{1}{G_{12}} - \frac{2\nu_{12}}{E_1} - \frac{2}{E_1} \right) - m^3 n \left(\frac{1}{G_{12}} - \frac{2\nu_{12}}{E_1} - \frac{2}{E_2} \right) \right] \tag{A.14}$$

The expressions in Eqns (A.7)-(A.11) therefore give the variation of the engineering elastic constants in the reference x and y directions for any ply angle β. Thus, given the four independent engineering elastic constants, E_1, E_2, G_{12} and ν_{12}, in the material axes 1 and 2, the variation of the properties in any direction other than 1 and 2 can be obtained.

A.3 Laminate Constitutive Equations

The general laminate constitutive equations for load-deformation relationships are as follows (see, for example, Ref. [2.24]):

$$\begin{Bmatrix} N_x \\ N_y \\ N_{xy} \end{Bmatrix} = \begin{bmatrix} A_{11} & A_{12} & A_{16} \\ A_{12} & A_{22} & A_{26} \\ A_{16} & A_{26} & A_{66} \end{bmatrix} \begin{Bmatrix} \varepsilon_x^\circ \\ \varepsilon_y^\circ \\ \gamma_{xy}^\circ \end{Bmatrix} + \begin{bmatrix} B_{11} & B_{12} & B_{16} \\ B_{12} & B_{22} & B_{26} \\ B_{16} & B_{26} & B_{66} \end{bmatrix} \begin{Bmatrix} k_x \\ k_y \\ k_{xy} \end{Bmatrix} \qquad \text{(A.15)}$$

and

$$\begin{Bmatrix} M_x \\ M_y \\ M_{xy} \end{Bmatrix} = \begin{bmatrix} B_{11} & B_{12} & B_{16} \\ B_{12} & B_{22} & B_{26} \\ B_{16} & B_{26} & B_{66} \end{bmatrix} \begin{Bmatrix} \varepsilon_x^\circ \\ \varepsilon_y^\circ \\ \gamma_{xy}^\circ \end{Bmatrix} + \begin{bmatrix} D_{11} & D_{12} & D_{16} \\ D_{12} & D_{22} & D_{26} \\ D_{16} & D_{26} & D_{66} \end{bmatrix} \begin{Bmatrix} k_x \\ k_y \\ k_{xy} \end{Bmatrix} \qquad \text{(A.16)}$$

where

N_x, N_y = normal forces per unit length in x and y directions respectively

N_{xy} = shear forces per unit length

ε_x°, ε_y° = normal strains in x and y directions

γ_{xy}° = shear strain

M_x, M_y, M_{xy} = moments per unit length

k_x, k_y, k_{xy} = twist curvatures of the middle surface

The matrices A_{ij}, B_{ij} and D_{ij} are the extensional, coupling and bending stiffnesses respectively given by [2.24],

$$A_{ij} = \sum_{p=1}^{N} \left(z_p - z_{p-1}\right)\left(\overline{Q}_{ij}\right)_p \tag{A.17}$$

$$B_{ij} = \sum_{p=1}^{N} -\frac{1}{2}\left(z_p^2 - z_{p-1}^2\right)\left(\overline{Q}_{ij}\right)_p \tag{A.18}$$

$$D_{ij} = \sum_{p=1}^{N} \frac{1}{3}\left(z_p^3 - z_{p-1}^3\right)\left(\overline{Q}_{ij}\right)_p \tag{A.19}$$

where z_p and z_{p-1} is the z-ordinate corresponding to the top and bottom surfaces respectively of ply p measured from the mid-plane.

The A_{ij} terms in Eqn. (A.17) are the extensional stiffness terms which relate the membrane (in-plane) forces to the laminate mid-plane membrane strains. The B_{ij} terms in Eqn. (A.18) are the coupling stiffness terms which relate the membrane forces to the out-of-plane curvature deformations. Thus, an extensional force on a laminate with non-zero B_{ij} term will result in not only extensional deformations, but also twisting and/or bending of the laminate. In addition, any applied moment in a laminate with coupling stiffness terms present, will unavoidably cause an extension of the middle surface. The D_{ij} terms in Eqn. (A.19) relate the moments to the bending curvatures. From Eqns (A.18) and (A.19), it can also be seen that the coupling and bending stiffness terms B_{ij} and D_{ij} respectively are dependent on the ply position relative to the laminate mid-plane. However, this is not the case for the extensional stiffness terms A_{ij} which are dependent on the ply thickness (see Eqn. (A.17)).

Depending on the way the fibre angle in the ply and the sequence in which the plies are stacked, some of the terms in Eqns (A.15) and (A.16) are zero. Some other terms may be eliminated or minimised. In the case of symmetric laminate with multiple generally orthotropic layers, the coupling stiffness matrix B will vanish and Eqns (A.15) and (A.16) will decouple to give the following load-deformation relationship for the force intensities,

$$\begin{Bmatrix} N_x \\ N_y \\ N_{xy} \end{Bmatrix} = \begin{bmatrix} A_{11} & A_{12} & A_{16} \\ A_{12} & A_{22} & A_{26} \\ A_{16} & A_{26} & A_{66} \end{bmatrix} \begin{Bmatrix} \varepsilon_x^\circ \\ \varepsilon_y^\circ \\ \gamma_{xy}^\circ \end{Bmatrix} \tag{A.20}$$

and

$$\begin{Bmatrix} M_x \\ M_y \\ M_{xy} \end{Bmatrix} = \begin{bmatrix} D_{11} & D_{12} & D_{16} \\ D_{12} & D_{22} & D_{26} \\ D_{16} & D_{26} & D_{66} \end{bmatrix} \begin{Bmatrix} k_x \\ k_y \\ k_{xy} \end{Bmatrix} \tag{A.21}$$

for the moments. Thus, a symmetric laminate of multiple generally orthotropic plies exhibits no coupling between bending and extension; in other words the B_{ij} are zero. Therefore, the force and moment resultants are represented by Eqns (A.20) and (A.21) in this case. In the above two equations all the A_{ij} and D_{ij} terms are required (i.e., they are non-zero) due to the coupling between normal forces and shearing strain, shearing force and normal strains, normal moments and twist, and twisting moment and normal curvatures. These coupling are given by the terms A_{16}, A_{26}, D_{16}, and D_{26} respectively.

Although symmetry of a laminate about the middle surface is often desirable, for example, to increase aeroelastic stability by selection of lamina thickness and fibre orientations, many physical applications of laminated composites require nonsymmetric laminates to achieve design objectives [1.2]. For example, coupling between extension and twist is a necessary feature to make jet turbine fan blades with pre-twist. Therefore, in these cases, symmetry about the middle surface is destroyed and as a result substantially different behavioural characteristics can be introduced. In antisymmetric laminates, the B_{ij} terms are not zero but certain stiffness simplifications are possible as the terms A_{16}, A_{26}, D_{16}, and D_{26} are zero. This means that the coupling between normal forces and shearing strain, shearing force and normal strains, normal moments and twist, and twisting moment and normal curvatures, present in symmetric laminates, is non-existent in antisymmetric laminates. Thus, the constitutive equations can be modified as,

$$\begin{Bmatrix} N_x \\ N_y \\ N_{xy} \end{Bmatrix} = \begin{bmatrix} A_{11} & A_{12} & 0 \\ A_{12} & A_{22} & 0 \\ 0 & 0 & A_{66} \end{bmatrix} \begin{Bmatrix} \varepsilon_x^\circ \\ \varepsilon_y^\circ \\ \gamma_{xy}^\circ \end{Bmatrix} + \begin{bmatrix} 0 & 0 & B_{16} \\ 0 & 0 & B_{26} \\ B_{16} & B_{26} & 0 \end{bmatrix} \begin{Bmatrix} k_x \\ k_y \\ k_{xy} \end{Bmatrix} \quad \text{(A.22)}$$

and

$$\begin{Bmatrix} M_x \\ M_y \\ M_{xy} \end{Bmatrix} = \begin{bmatrix} 0 & 0 & B_{16} \\ 0 & 0 & B_{26} \\ B_{16} & B_{26} & 0 \end{bmatrix} \begin{Bmatrix} \varepsilon_x^\circ \\ \varepsilon_y^\circ \\ \gamma_{xy}^\circ \end{Bmatrix} + \begin{bmatrix} D_{11} & D_{12} & 0 \\ D_{12} & D_{22} & 0 \\ 0 & 0 & D_{66} \end{bmatrix} \begin{Bmatrix} k_x \\ k_y \\ k_{xy} \end{Bmatrix} \quad \text{(A.23)}$$

Thus, an antisymmetric lay-up beam displays extension-torsion coupling and bending-shear coupling instead of bending-torsion coupling and extension-shear coupling.

A.4 Parametric Study on Ply Orientation of a Single Layer Laminate

A parametric study of the effect of ply orientation on the laminate engineering elastic constants, and the extensional, coupling and bending stiffness terms A_{ij}, B_{ij} and D_{ij} of a unidirectional laminate was conducted. In the coordinate system adopted, the y-axis lies along the spanwise direction whereas the x-axis lies along the chordwise direction (see for example Fig. A.3(a)). As shown earlier, when the y-axis is aligned with composite fibre direction then the material elastic constants in the x and y directions will be the same as the laminate equivalent elastic constants. However, when the fibres are oriented at an angle to the y-axis then the laminate equivalent elastic constants in the x and y directions will vary in their magnitude according to Eqns (A.7)-(A.11).

The laminate chosen to study the effect of fibre orientation on the laminate engineering elastic constants in the reference axes directions x and y is a unidirectional single layer Hercules ASI/3501-6 graphite/epoxy with E_1 = 98 GN/m^2, E_2 = 7.9 GN/m^2, ν_{12} = 0.28, $G_{12} = G_{13} = G_{23}$ = 5.6 GN/m^2, ρ=1520 kg/m^3 and ply thickness of 0.804x10^{-3} m.

The variation of the elastic constants with fibre angle is shown in Figs A.4-A.7. These trends of the variation of elastic properties with direction of ASI/3501-6 graphite/epoxy ply are typical, although the actual magnitudes of the elastic constants will depend on the material used. Some important comments on the general behaviour of graphite/epoxy plies can be made from Figs A.4-A.7.

In Fig. A.4, the variation of Young's modulus in both x and y directions is plotted against the fibre angle, β. When the fibre angle is set to 0^0, i.e., when the ply is a specially orthotropic with the fibre direction coinciding with the reference y direction, the Young's modulus in y direction is equal to the Young's modulus in the fibre direction and the same modulus in x direction is equal to the one in the orthogonal direction to the fibres, i.e., $E_y = E_1$ and $E_x = E_2$. With a small change in the fibre orientation the Young's modulus in the y direction decreases rapidly whereas in the x direction increases slightly up to $\beta = 45^0$. At this fibre angle the Young's modulus in the two directions are equal and the two curves are mirror image of each other. At $\beta = 90^0$ the $E_x = E_1$ and $E_y = E_2$ where the generally orthotropic ply transforms to a specially orthotropic one. Thus, the maximum membrane resistance can be obtained when the fibres are aligned in the direction of the applied membrane load falling off rapidly with a small change in the fibre orientation. On the other hand, the least membrane resistance is obtained in the transverse direction, i.e., when $\beta = 90^0$.

In Fig. A.5 the variation of shear modulus is plotted against the fibre angle, β. At $\beta = 0^0$ and 90^0, the shear modulus $G_{yx} = G_{12}$. The maximum in-plane shear modulus G_{yx} can be obtained when $\beta = 45^0$ and is symmetric about this fibre angle. Thus, the greatest resistance to shear can be achieved when $\beta = 45^0$. For fibre angles other than 0^0 and 90^0, shear coupling effects are induced as can be seen in Fig. A.6. These are maximum in the region of $\beta \approx 10^0$-15^0 where the resistance to shear is very small (Fig. A.5). Finally in Fig. A.7 the variation of the Poisson's ratio is plotted against the fibre angle. Its maximum value is offered when the fibre angle is set to $\beta = 0^0$.

In the laminate constitutive Eqns (A.15) and (A.16) the loads are expressed as force and moment intensities denoted by the suffixes N_x, N_y, N_{xy} and M_x, M_y, M_{xy} respectively. These forces and moments are per unit width of the laminate section as

described earlier. Thus, the stiffness terms A_{ij}, B_{ij} and D_{ij} in the laminate constitutive Eqns (A.15) and (A.16) are the stiffness per unit width of the appropriate laminate section in the y-z and x-z plane. In the next paragraphs the physical significance of these stiffness terms will be considered.

Figures A.8 and A.9 show the variation of the A_{ij} and D_{ij} stiffness terms against the fibre angle, β. Modifying Eqns (A.15) and (A.16) according to the coordinate system shown in Fig. A.3, the A_{11} and D_{11} stiffnesses relate the applied load N_y and the moment about the laminate x-axis, M_y, to the membrane strain ε_y° and bending curvature about the x-axis, k_y, respectively. Thus, A_{11} is the axial stiffness of the laminate in the direction of the applied load, the x-direction, and D_{11} is the bending stiffness when a bending moment about the x-axis is applied. From Figs A.8 and A.9, it can be seen that the maximum axial and bending stiffnesses A_{11} and D_{11} respectively are offered when the fibre angle is set to $\beta = 0^0$. They rapidly reduce with a small change in fibre angle with minimum value at $\beta = 90^0$. Due to the Poisson effect, as a result of the applied force N_y a lateral membrane stain ε_x° is induced on the laminate. The A_{12} is the stiffness term relating the applied force in the y-direction to the strain in the lateral x-direction. In the same way, the curvature k_y will cause an 'anticlastic' shape [A.1] (a saddle shaped surface) causing a curvature about the laminate y-axis, k_x, related by the stiffness term D_{12}. The same stiffness terms, A_{12} and D_{12}, give the Poisson effect contribution when the force and bending moment are applied in the x-direction and about the y-axis respectively. Both the A_{12} and D_{12} stiffness terms have maximum value at $\beta = 45^0$ and they are symmetric about this point.

In certain cases, depending on the ply angles and ply stacking sequence, such as unbalance laminates, a force in the y-direction can result in a membrane shearing deformation ε_{xy}°. The A_{16} is the stiffness term relating the applied force N_y to the shear strain ε_{xy}°. In the same way, an applied bending moment M_y can also cause a twisting curvature k_{xy} in addition to the bending curvatures k_y and k_x. It is the stiffness D_{16} which relates the M_y value to the twisting curvature k_{xy}. Usually the D_{16} (and D_{26}) term is defined as the bending-torsion coupling term as it relates the

bending moment M_y to a twisting deformation k_{xy}, or it relates a twisting moment M_{xy} to a bending deformation k_y. Unlike the stiffness terms A_{12} and D_{12}, the stiffness terms A_{16} and D_{16} are not symmetrical about $\beta = 45^0$ and their maximum value is offered around $\beta = 30^0$.

The A_{22} and D_{22} relate the membrane strain ε_x° and bending curvature about the y-axis, k_x, to the applied force N_x and bending moment M_x respectively. It is also possible to induce a shear strain ε_{xy}° as a result of the force in the x-direction N_x and this shear coupling is given by the stiffness A_{26}. Similarly, the D_{26} term is the bending-torsion contribution. The D_{66} term relates the twisting moment, M_{xy}, to the twisting curvature, k_{xy}, and therefore it is the torsional stiffness term. The maximum value of the torsional stiffness term, D_{66}, is offered at $\beta = 45^0$ and is symmetric about this fibre angle. The twisting moment M_{xy} will also cause the bending curvatures k_y and k_x related by the bending-torsion terms D_{16} and D_{26} respectively.

The magnitude and sense (i.e., sign) of D_{16} and D_{26} terms are very important from the aeroelasticity standpoint as they determine the direction and the extent of bending-torsion coupling present in a structure. A simple example of the deformation control possible through laminate design is presented in Fig. A.3. The thick arrow indicates the direction in which the highest percentage of the lamina is oriented for each example shown. A balanced symmetrical laminate such as the one shown in Fig. A.3 (a) will display orthotropic deflection with respect to a given set of axes, one of which is usually oriented along the elastic axis, i.e., a bending moment causes only bending curvature but no twisting of the surface in which case the terms D_{16}, and D_{26} are zero. An unbalanced symmetrical laminate such as the ones shown in Figs A.3 (b) and A.3 (c) will display nonorthotropic, or anisotropic, deflections about these axes. An applied bending moment will cause not only curvature of a wing surface, but twisting of the surface as well. In Fig. A.3 (b) a higher percentage of the lamina is oriented in the positive direction, i.e., more fibres are aligned with the direction of the airflow. In this case, an applied positive (upward) bending moment causes nose-down twist. This kind of deformation is usually defined as wash-out. The D_{16} and D_{26} terms are nonzero and of positive sign as shown in Fig. A.3 (b). On the other hand, in Fig. A.3 (c) a higher percentage of the lamina is oriented in the negative direction. In this case

an applied positive bending moment will cause a nose-up twist or wash-in. The D_{16} and D_{26} terms are nonzero and they are of negative sign as shown in Fig. A.3 (c).

The sign of D_{16} and D_{26} terms depends on the coordinate system adopted and also on the definition of positive fibre angle. Here a positive fibre angle results in positive reduced stiffness terms $\overline{Q}_{ij}$ and as a consequence in positive bending-torsion coupling stiffness K. This in turn gives a positive bending-torsion coupling parameter ψ, which is a measure of bending-torsion coupling present in a structure (see chapter 3).

As it was shown earlier the B_{ij} terms are the coupling stiffness terms which relate the membrane forces to the out-of-plane curvature deformations. Again by modifying Eqn. (A.15), according to the coordinate system shown in Fig. A.3 (i.e., the y-axis is aligned with the spanwise direction) the B_{11} term relates the membrane force N_y to the bending curvature k_y, the B_{12} relates the same force to the curvature k_x and the B_{13} excites the twisting curvature k_{xy}.

A.5 Conclusions

For a unidirectional ply laminate, the Young's modulus value is greatest in the fibre direction, that is when $\beta = 0^0$ and therefore, the maximum membrane resistance is offered when the fibres are aligned in the direction of the applied membrane load. This value falls off rapidly with a small change in the fibre orientation.

The in-plane shear modulus for a unidirectional ply laminate is largest when $\beta = 45^0$ and is symmetric about this fibre angle. Thus the greatest resistance to shear is offered by 45^0 plies. For fibre angles other than 0^0 or 90^0, shear coupling effects are induced.

The study has shown that a laminate can be designed to exhibit a desired set of deformations. Symmetric lay-up beams display bending-torsion coupling and

extension-shear coupling. Antisymmetric lay-up beams, on the other hand, display extension-torsion coupling and bending-shear coupling.

The physical significance of the stiffness terms A_{ij}, B_{ij} and D_{ij} in the laminate constitutive equations has also been discussed. The A_{11}, D_{11}, D_{16} and D_{66} terms represent the axial, bending, bending-torsion and torsional stiffnesses respectively. The maximum value of axial and bending stiffnesses, A_{11} and D_{11} respectively, is offered when the fibres are aligned in the spanwise direction, i.e., when $\beta = 0^0$. This value reduces with a change in the fibre orientation, as expected. The torsional stiffness term, D_{66}, is largest when $\beta = 45^0$ and is symmetric about this point. Finally the bending-torsion coupling stiffness term D_{16} is largest when $\beta = 30^0$.

For fixed wing aircraft the bending stiffness matrix D plays a vital role. The bending and torsional deformations are elastically uncoupled if the D_{16}, and D_{26} terms in the third row and column of the matrix are zero. However, if the D matrix is fully populated then a coupling between the bending and torsional deformations will exist. The magnitude and sense (i.e., sign) of D_{16} and D_{26} terms determine the direction and the extent of this coupling. For example, if a right handed coordinate system is adopted with the y-axis aligned in the spanwise direction as shown in Fig. A.3, a positive (upward) bending moment will cause a nose-down twist (wash-out) when the D_{16} and D_{26} terms are positive, and nose-up twist (wash-in) when they are negative.

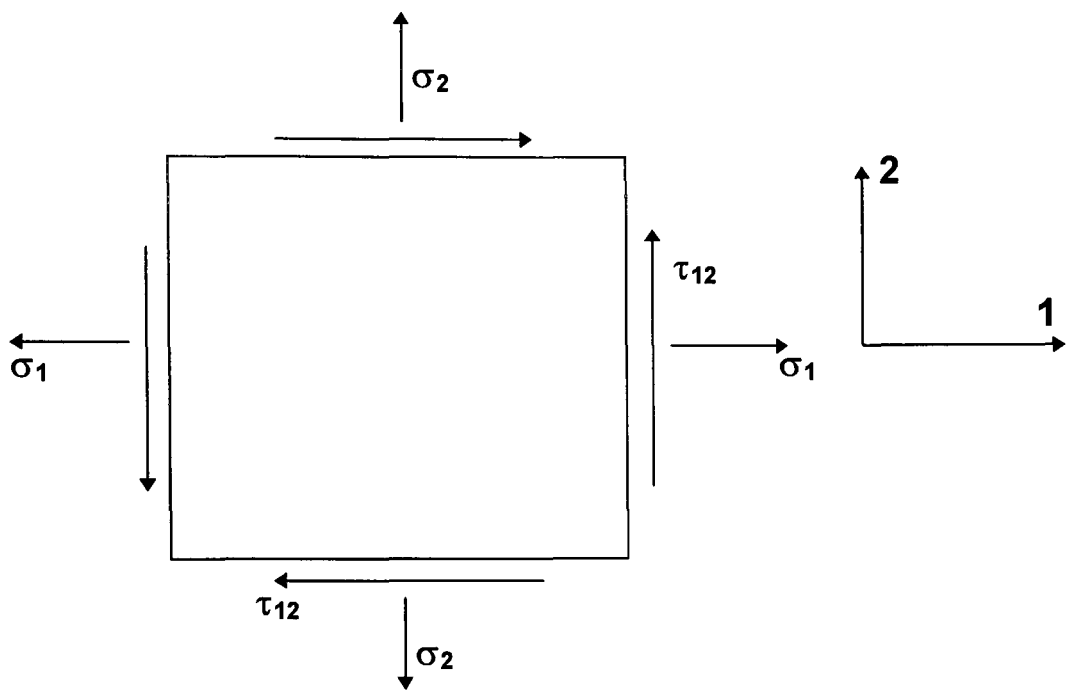

Fig. A.1. Positive stress system.

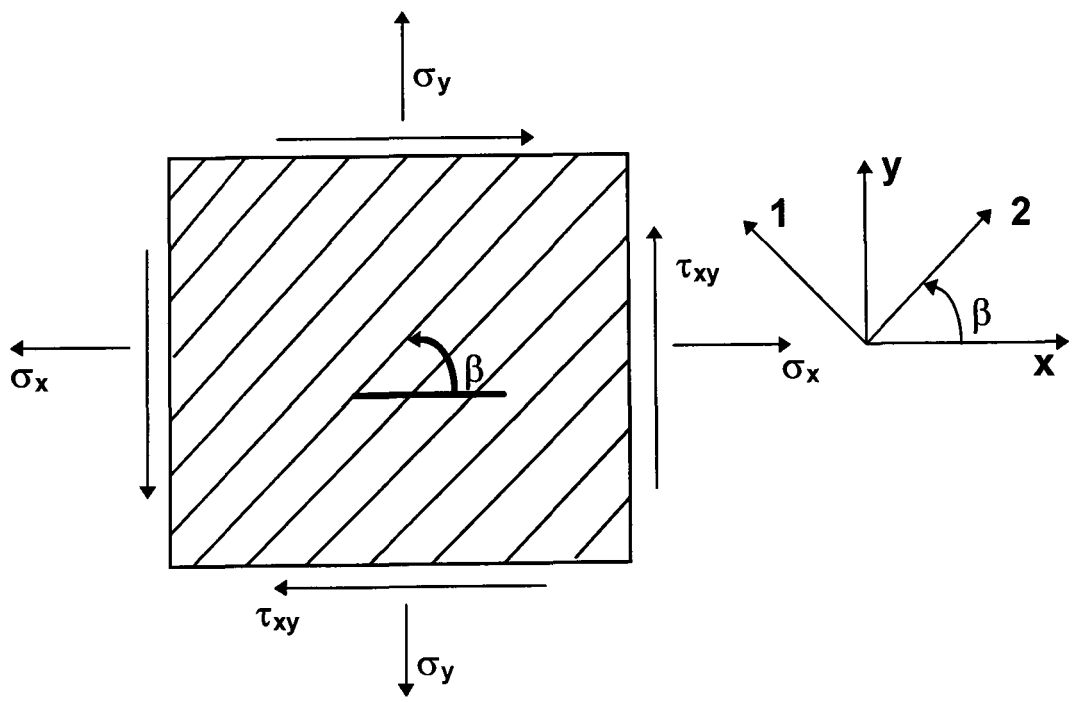

Fig. A.2. Positive stress system in x-y axes.

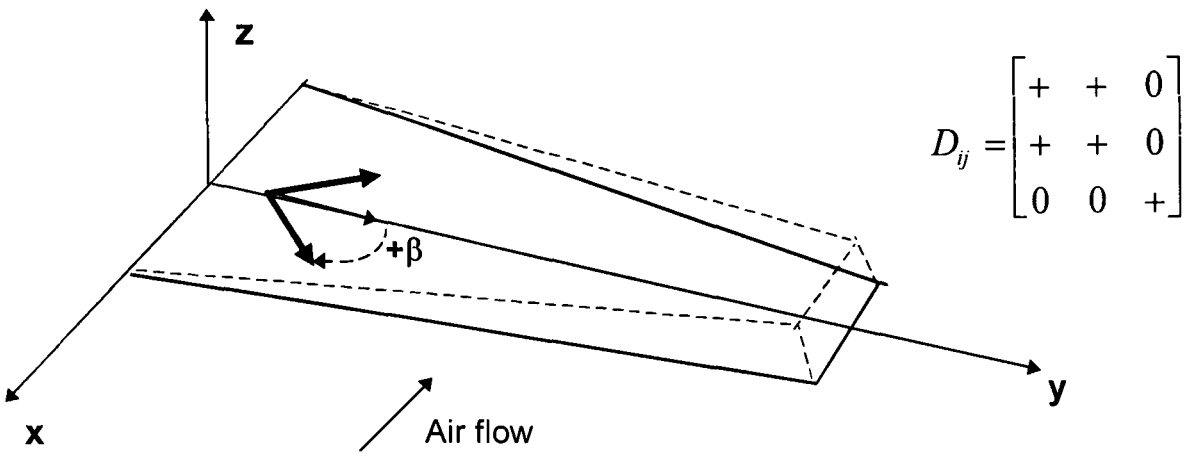

$$D_{ij} = \begin{bmatrix} + & + & 0 \\ + & + & 0 \\ 0 & 0 & + \end{bmatrix}$$

(a) Orthotropic bending (bending-torsion coupling is not present)

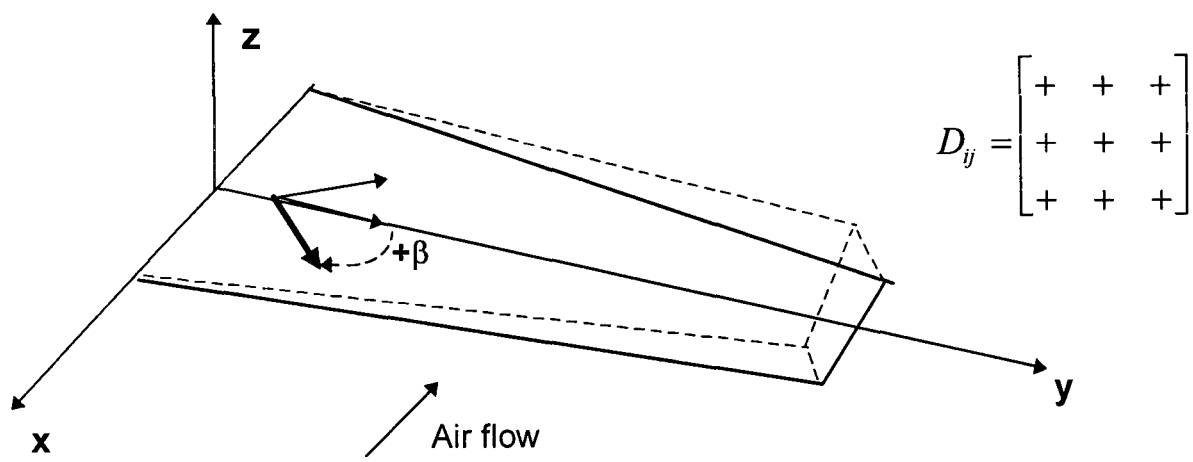

$$D_{ij} = \begin{bmatrix} + & + & + \\ + & + & + \\ + & + & + \end{bmatrix}$$

(b) Anisotropic positive bending-torsion coupling (wash-out)

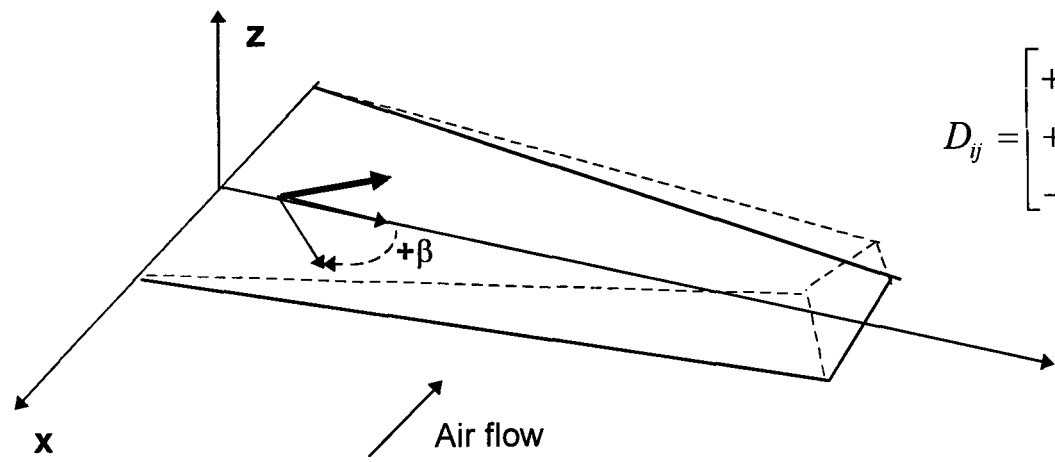

$$D_{ij} = \begin{bmatrix} + & + & - \\ + & + & - \\ - & - & + \end{bmatrix}$$

(c) Anisotropic negative bending-torsion coupling (wash-in)

Fig. A.3. Deformation shapes of composite wings.

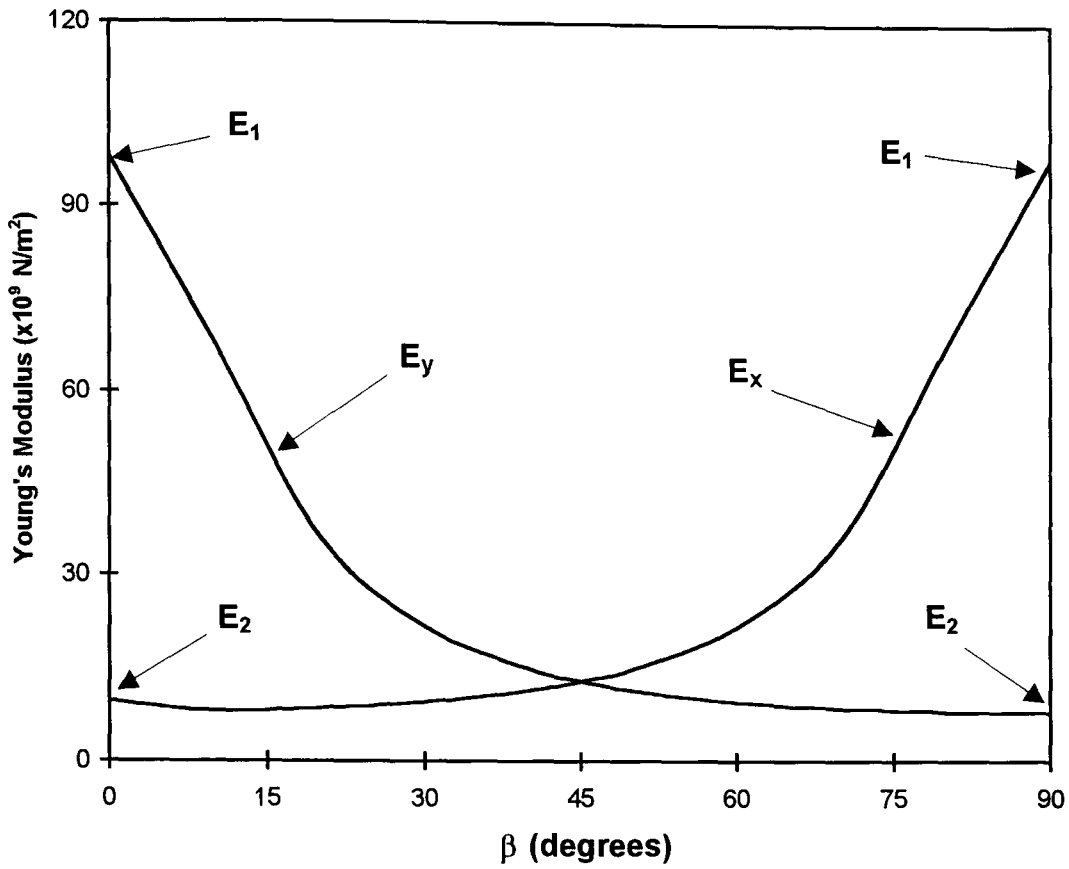

Fig. A.4. Young's modulus variation with ply angle for a uniderectional ply.

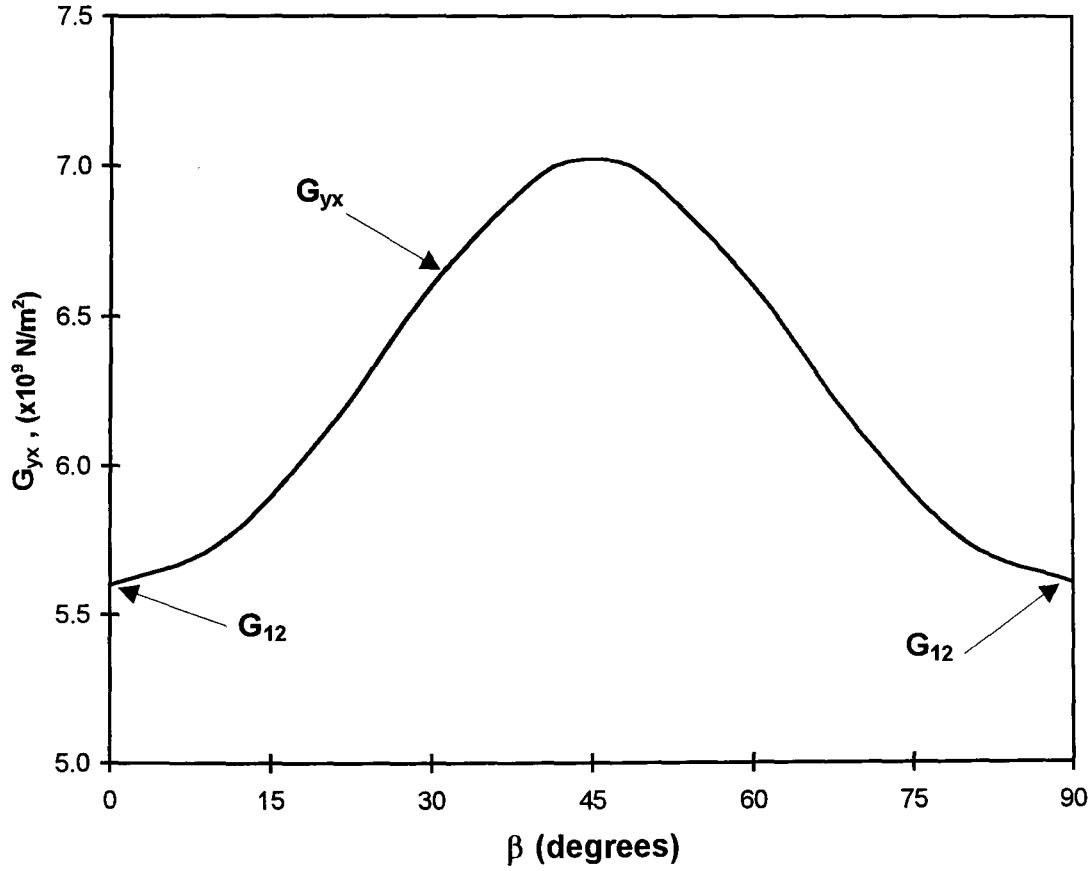

Fig. A.5. Shear modulus variation with ply angle for a uniderectional ply.

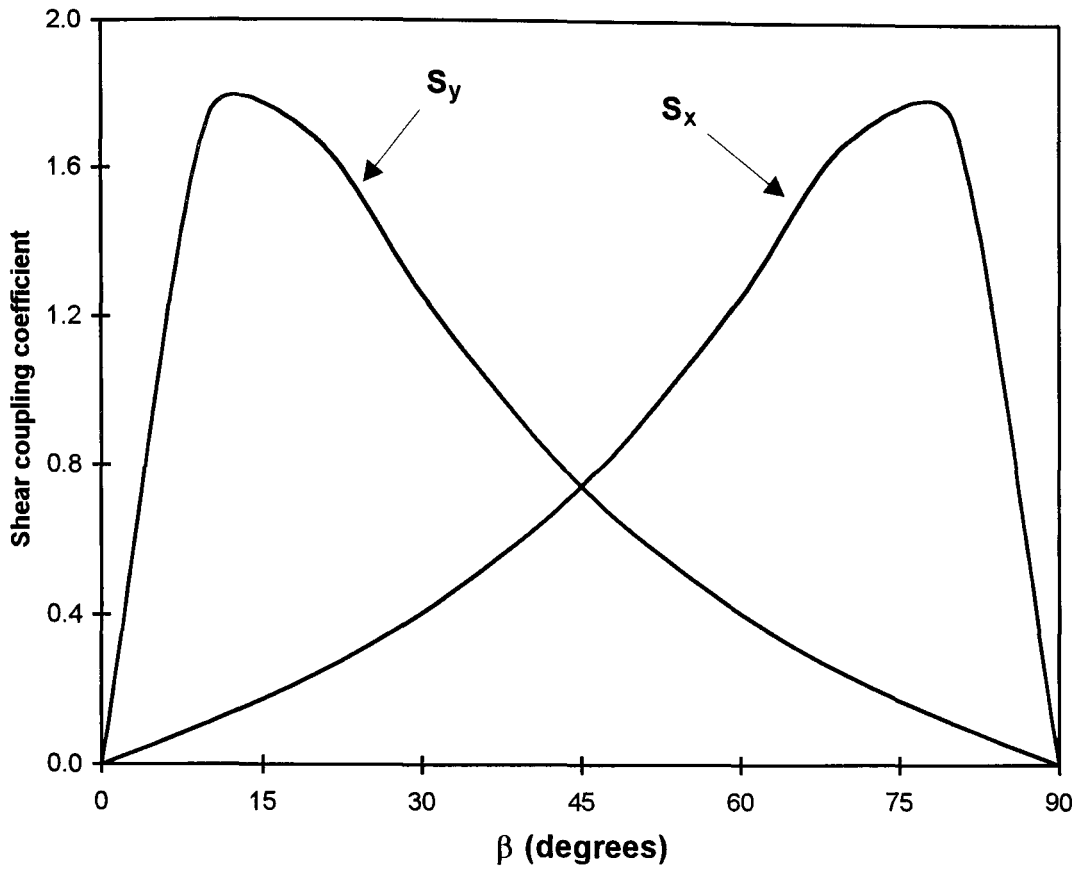

Fig. A.6. Shear coupling coefficient variation with ply angle for a unidirectional ply.

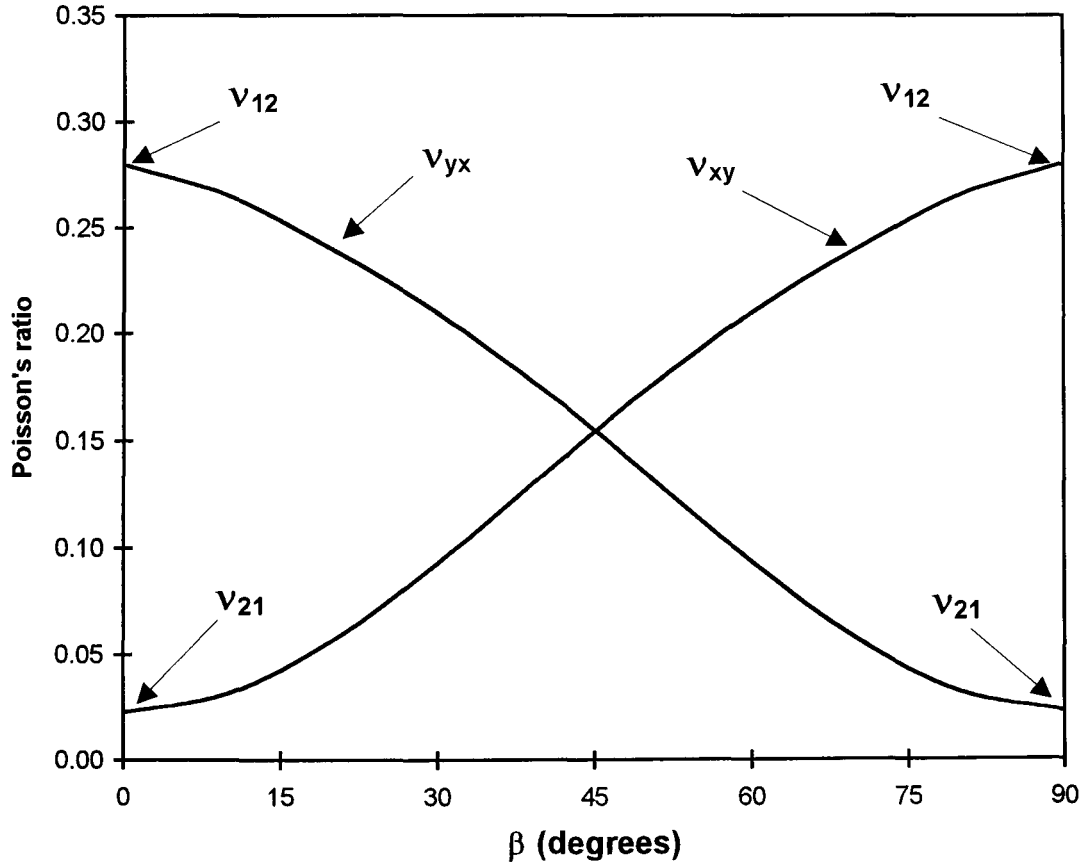

Fig. A.7. Poisson's ratio variation with ply angle for a uniderectional ply.

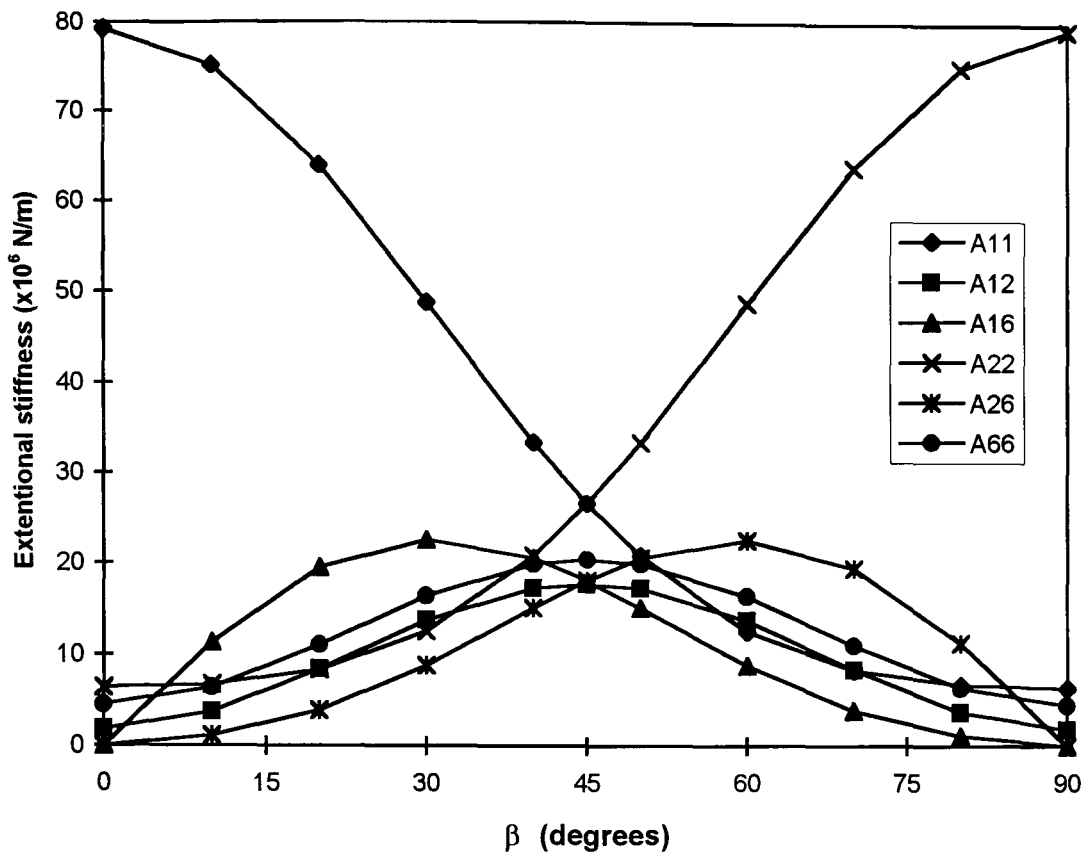

Fig. A.8. The variation of extentional stiffness (A-Matrix) terms with ply angle, β, for a unidirectional laminate.

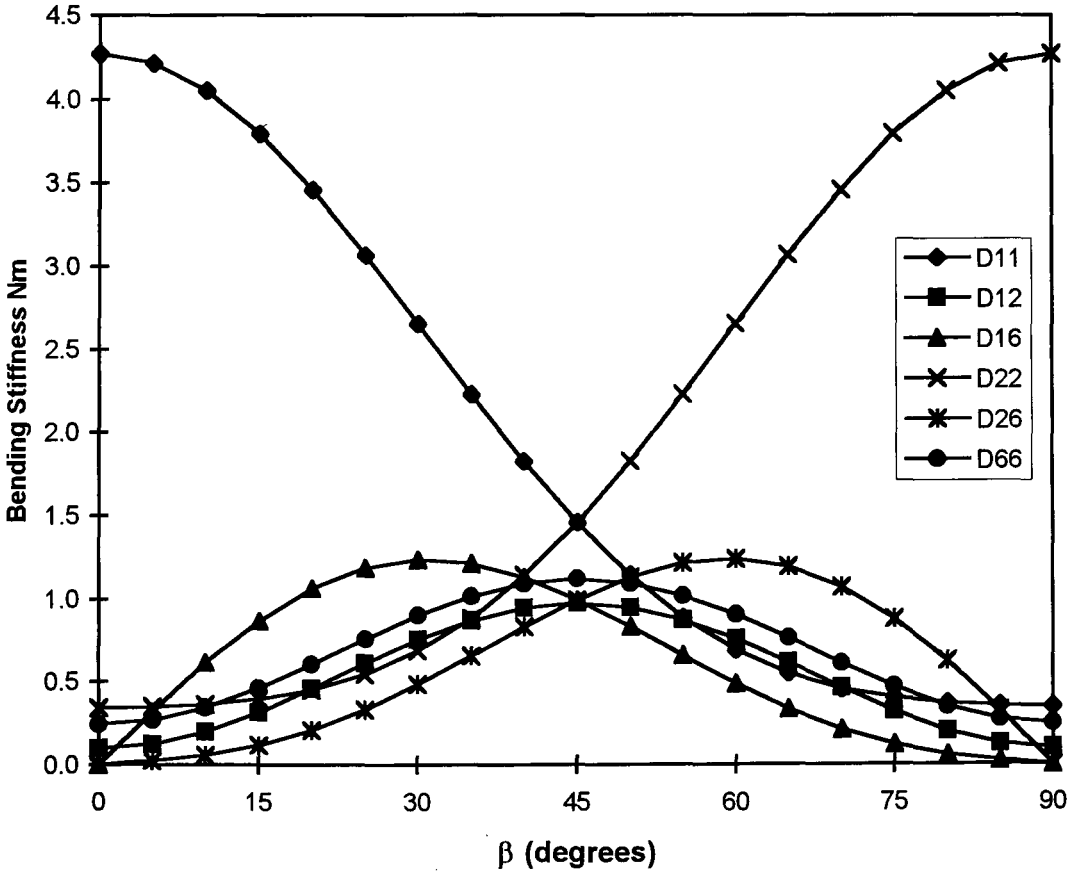

Fig. A.9. The variation of bending stiffness (D-Matrix) terms with ply angle, β, for a unidirectional laminate.

APPENDIX 'B'

STIFFNESS MODELS FOR THIN-WALLED COMPOSITE BEAMS

B.1 Mansfield and Sobey Stiffness Model [2.67]

In this contour analysis a cylindrical tube (Fig. B.1) subjected to torsion, bending and longitudinal tension is considered. Shear and hoop stresses are neglected and the shear flow is considered to be constant. The torsion-related warping and transverse shear deformation are also neglected. The displacement field in Cartesian coordinates and the notation of Berdichevsky et al. [23], is of the form

$$u_1 = U_1(x) - y(s)U_2'(x) - z(s)U_3'(x)$$

$$u_2 = U_2(x) - z(s)\varphi(x) \tag{B.1}$$

$$u_3 = U_3(x) + y(s)\varphi(x)$$

and the associated strain field is given by

$$\varepsilon_{xx} = U_1'(x) - y(s)U_2''(x) - z(s)U_3''(x)$$

(B.2)

$$\gamma_{xs} = 2A_e\varphi'$$

The constitutive relationships can be written in terms of stress resultants as follows:

$$T = \oint N_{xx}\,ds$$

$$M_x = \oint N_{xs} r_n(s)\,ds = 2A_e N_{xs} \tag{B.3}$$

$$M_y = -\oint N_{xx} z(s) ds$$

$$M_z = -\oint N_{xx} y(s) ds$$

where A_e is the enclosed area of the cross-section and r_n is the projection of the position vector r in the normal direction and expressed as,

$$r_n = y\frac{dz}{ds} - z\frac{dy}{ds} \qquad \text{or} \qquad \oint r_n ds = 2A_e \tag{B.4}$$

As the forces and moments are linearly related to the displacements, a symmetric 4x4 stiffness matrix, P, can then be defined such that,

$$F = Pu \tag{B.5}$$

or as,

$$\begin{Bmatrix} T \\ M_x \\ M_y \\ M_z \end{Bmatrix} = \begin{bmatrix} P_{11} & P_{12} & P_{13} & P_{14} \\ P_{12} & P_{22} & P_{23} & P_{24} \\ P_{13} & P_{23} & P_{33} & P_{34} \\ P_{14} & P_{24} & P_{34} & P_{44} \end{bmatrix} \begin{Bmatrix} U_1' \\ \varphi' \\ U_3'' \\ U_2'' \end{Bmatrix} \tag{B.6}$$

where T, M_x, M_y and M_z represent the tension, torsional moment and bending moments, respectively.

The following expressions for the bending, torsional and bending-torsion coupling stiffnesses are obtained from Eqn. (B.6):

$$EI = \oint z^2 H_{11} ds + \frac{\oint z H_{21} ds}{\oint H_{22} ds} \tag{B.7}$$

$$GJ = \frac{4A_e^{\,2}}{\oint H_{22}\,ds} \tag{B.8}$$

$$K = -\frac{2A_e}{\oint H_{22}\,ds} \tag{B.9}$$

where each of the above H_{ij} terms are combinations of element compliances and therefore stiffnesses (see Ref. [2.67]).

B.2 Rehfield [3.11] and Rehfield and Atilgan [3.18] Stiffness Models

This contour analysis is similar to that of Mansfield and Sobey [2.67] in which a general rotor-blade cross-section is idealised as a single-celled box-beam subjected to axial, bending, torsional, transverse shear, and warping loads. The torsional warping function and the transverse shear deformation were included. The displacement field, in Cartesian coordinates (see Fig. B.1) and the notation of Berdichevsky et al. [2.85], is of the form

$$\begin{aligned} u_1 &= U_1(x) - y(s)\left[U_2'(x) - 2\gamma_{xy}(x)\right] - z(s)\left[U_3'(x) - 2\gamma_{xz}(x)\right] + g(s,x) \\ u_2 &= U_2(x) - z(s)\varphi(x) \\ u_3 &= U_3(x) + y(s)\varphi(x) \end{aligned} \tag{B.10}$$

where γ_{xz} and γ_{xy} are the transverse shear strains, $\varphi(x)$ is an arbitrary function that represents the cross-sectional rotation about the x-axis, and $g(s,x)$ is the warping function given by

$$g(s,x) = \overline{G}(s)\varphi'(x) \tag{B.11}$$

where

$$\overline{G}(s) = 2A_e \frac{s}{l} - \int_o^s r_n(\tau) d\tau \tag{B.12}$$

and r_n is given in Eqn. (B.4).

The torsional warping function in Eqn. (B.12) was later modified by Rehfield and Atilgan [3.18] as,

$$\overline{G}(s) = \int_o^s \left[\frac{2A_e}{l\overline{c}_1} c_1 - r_n(\tau) \right] d\tau \tag{B.13}$$

where

$$c_1 = \frac{1}{C - \left(\left(B^2 \right) / A \right)} \tag{B.14}$$

A, *B* and *C* are the in-plane stiffnesses given by Eqns (3.38) - (3.40) of chapter 3.

As in usual theory of torsion for thin-walled beams made of isotropic materials, the shear strain is assumed to be independent of *s*. Therefore, let $\gamma_{xy} = \gamma_{xy}(x)$ and $\gamma_{xz} = \gamma_{xz}(x)$ be the transverse shear strains of any cross-section. They are assumed to be uniform for each cross-section so that there is no warping due to transverse shear; that is, a pure transverse shear strain results in a plane cross-section. Furthermore, let $\gamma = \gamma(x)$ be the shear strain due to twisting. Therefore, from the strain transformation law and elementary geometrical considerations, the membrane shear strain in the beam wall is given by

$$\gamma_{xs} = \gamma_{xy} \frac{dy}{ds} + \gamma_{xz} \frac{dz}{ds} + \gamma \tag{B.15}$$

The axial strain is obtained by differentiate the expression of axial displacement in Eqn. (B.10) as,

$$\varepsilon_{xx} = U_1'(x) - y(s)\left[U_2''(x) - 2\gamma_{xy}'(x) \right] - z(s)\left[U_3''(x) - 2\gamma_{xz}'(x) \right] + G(s)\varphi''(x) \tag{B.16}$$

and the shear strain is obtained from Eqn. (B.15) as,

$$\gamma_{xs} = \gamma_{xy}\frac{dy}{ds} + \gamma_{xz}\frac{dz}{ds} + \frac{2A_e}{c}\varphi'(x) \tag{B.17}$$

$U_1'(x)$ is the axial strain, while $\varphi'(x)$, $\left[U_2''(x) - 2\gamma'_{xy}(x)\right]$ and $\left[U_3''(x) - 2\gamma'_{xz}(x)\right]$ are the twisting and bending curvatures, respectively. $\varphi''(x)$ is the additional kinematic variable associated with torsional warping, A_e is the enclosed area of the cross-section, $c = \oint_\Gamma ds$ is the circumference, and Γ represents the cross-section shape.

Composite thin-walled construction is characterised by the membrane stiffness matrix which relates the non-zero stress resultants to the membrane strains. The constitutive relations in terms of stiffnesses *A*, *B* and *C* of Eqns (3.38) - (3.40) are given by (see also Ref. [2.83])

$$N_{xx} = A\varepsilon_{xx} + \frac{B}{2}\gamma_{xs} \tag{B.18}$$

$$N_{xs} = \frac{B}{2}\varepsilon_{xx} + \frac{C}{4}\gamma_{xs} \tag{B.19}$$

For thin-walled beams, local shell bending and twisting moment resultants can be ignored, and thus, the beam reacts to external forces by membrane action in the wall. By introducing axial and shear stress resultants, N_{xx} and N_{xs}, respectively, and assuming that there is no internal pressure so that the hoop stress resultant, N_{ss}, can be ignored, the generalised internal forces can be defined as,

$$\oint_\Gamma N_{xx}\left(1, \quad z, \quad -y, \quad \overline{G}\right)ds = \left(T, \quad M_y, \quad M_z, \quad Q_w\right) \tag{B.20}$$

$$\oint_\Gamma N_{xs}\left(\frac{dy}{ds}, \quad \frac{dz}{ds}, \quad \frac{2A_e}{c}\right)ds = \left(Q_y, \quad Q_z, \quad M_x\right) \tag{B.21}$$

where T is the tension, Q_y and Q_z are the shear forces, M_x is the torsional moment, M_y and M_z are the bending moments and Q_w is the generalised warping related force.

The deformational variables or generalised strains can easily be obtained from the strain expressions. In matrix form they are,

$$u = \left[U_1'(x) \quad \gamma_{xy} \quad \gamma_{xz} \quad \varphi'(x) \quad \left\{ U_2''(x) - 2\gamma_{xy}'(x) \right\} \quad \left\{ U_3''(x) - 2\gamma_{xz}'(x) \right\} \quad \varphi''(x) \right] \tag{B.22}$$

Similarly the generalised internal forces can be written in matrix form as,

$$F = \left[T \quad Q_y \quad Q_z \quad M_x \quad M_y \quad M_z \quad Q_w \right] \tag{B.23}$$

As the force and the deformation are linearly related, a symmetric 7x7 stiffness matrix, P, can then be defined such that

$$F = Pu \tag{B.24}$$

All the stiffness terms of matrix, P, are expressed in terms of Eqns (3.38)-(3.40) where the bending, torsional and bending-torsion coupling stiffnesses are given as,

$$EI = \oint_T Az^2 ds \tag{B.25}$$

$$GJ = \left(\frac{A_e}{c} \right)^2 \oint_T C ds \tag{B.26}$$

$$K = \frac{A_e}{c} \oint_T Bz ds \tag{B.27}$$

B.3 Chandra et al. Stiffness Model [3.17]

This is a simplified linear analysis for the extension, bending and torsion of thin-walled symmetric composite beams. The effects of cross-sectional warping due to torsion were included in an approximate manner and the effects of transverse shear were neglected. The four sides of the box-beam are modelled as general composite laminated plates (Fig. B.2).

The displacement field expressed in Cartesian coordinates (see Fig. B.2) and the notation of Berdichevsky et al. [2.85], is of the form

$$u_1 = U_1(x) - yU_2'(x) - zU_3'(x) - \lambda\varphi'(x)$$

$$u_2 = U_2(x) - z\varphi(x) \tag{B.28}$$

$$u_3 = U_3(x) + y\varphi(x)$$

where λ is the torsional warping function which is given in an approximate manner as,

$$\lambda = \frac{(c-d)}{(c+d)}yz \tag{B.29}$$

where c and d are the beam width and depth respectively.

The strains are determined by differentiating the displacement expressions of Eqn. (B.28). Since the walls of the box-beam are assumed to be relatively thin, only axial and in-plane shear strains are considered non-negligible. The resulting strains are,

$$\varepsilon_{xx} = U_1'(x) - yU_2'' - zU_3''' - \lambda\varphi''(x)$$

$$\varepsilon_{xz} = \left[y - \frac{\partial\lambda}{\partial z}\right]\varphi' \tag{B.30}$$

in the vertical walls, and

$$\varepsilon_{xx} = U_1'(x) - yU_2'' - zU_3''' - \lambda\varphi''(x)$$

$$\varepsilon_{xy} = \left[z - \frac{\partial\lambda}{\partial y}\right]\varphi' \tag{B.31}$$

in the horizontal walls.

The stress-strain relationship for the vertical (right and left) flanges of the box-beam shown in Fig. B.2 is given by the following expression:

$$\begin{Bmatrix}\sigma_{xx}\\ \sigma_{zz}\\ \tau_{xz}\end{Bmatrix} = \begin{bmatrix}\overline{Q}_{11} & \overline{Q}_{12} & \overline{Q}_{16}\\ \overline{Q}_{12} & \overline{Q}_{22} & \overline{Q}_{26}\\ \overline{Q}_{16} & \overline{Q}_{26} & \overline{Q}_{66}\end{bmatrix}\begin{Bmatrix}\varepsilon_{xx}\\ \varepsilon_{zz}\\ \gamma_{xz}\end{Bmatrix} \tag{B.32}$$

where $\overline{Q}$ is the stiffness matrix of *k*th lamina in *x-y* or *x-z* plane.

Assuming each lamina of the laminates is orthotropic and there is no shear stress through the thickness direction, i.e., $\sigma_{zz} = 0$, Eqn. (B.32) can be simplified by solving for ε_{zz} as follows:

$$\begin{Bmatrix}\sigma_{xx}\\ \tau_{xz}\end{Bmatrix} = \begin{bmatrix}\overline{C}_{11} & \overline{C}_{16}\\ \overline{C}_{16} & \overline{C}_{66}\end{bmatrix}\begin{Bmatrix}\varepsilon_{xx}\\ \gamma_{xz}\end{Bmatrix} \tag{B.33}$$

where

$$\overline{C}_{11} = \overline{Q}_{11} - \frac{\overline{Q}_{12}^2}{\overline{Q}_{22}} \tag{B.34}$$

$$\overline{C}_{16} = \overline{Q}_{16} - \frac{\overline{Q}_{12}\overline{Q}_{26}}{\overline{Q}_{22}} \tag{B.35}$$

$$\overline{C}_{66} = \overline{Q}_{66} - \frac{\overline{Q}_{26}^2}{\overline{Q}_{22}} \tag{B.36}$$

Similarly for horizontal (top and bottom) flanges with $\sigma_{yy} = 0$, the following relationship can be obtained:

$$\begin{Bmatrix} \sigma_{zz} \\ \tau_{xy} \end{Bmatrix} = \begin{bmatrix} \overline{C}_{11} & \overline{C}_{16} \\ \overline{C}_{16} & \overline{C}_{66} \end{bmatrix} \begin{Bmatrix} \varepsilon_{zz} \\ \gamma_{xy} \end{Bmatrix} \tag{B.37}$$

The relation between moments and curvatures is given as [3.17],

$$\begin{Bmatrix} M_y \\ M_x \end{Bmatrix} = \begin{bmatrix} EI & K \\ K & GJ \end{bmatrix} \begin{Bmatrix} U_2'' \\ \varphi' \end{Bmatrix} \tag{B.38}$$

where M_y and M_x are the bending and torsional moments, EI is the effective flap bending stiffness, GJ is the effective torsional stiffness, K is the bending-torsion coupling stiffness, U_2'' is the bending curvature, and φ' is the twist derivative.

Substituting the stresses, known in terms of displacements, into the equations of net forces and moments, the bending, torsional and bending-torsion coupling stiffnesses are obtained as,

$$EI = \sum_{K=1}^{N} \iint_{h,h} \overline{C}_{11}^{(K)} z^2 dydz + \sum_{l=1}^{M} \iint_{\upsilon,\upsilon} \overline{C}_{11}^{(K)} z^2 dydz \tag{B.39}$$

$$GJ = \sum_{K=1}^{N} \iint_{h,h} \overline{C}_{66}^{(K)} z^2 dydz + \sum_{l=1}^{M} \iint_{\upsilon,\upsilon} \overline{C}_{66}^{(K)} \hat{y}^2 dydz \tag{B.40}$$

$$K = \sum_{K=1}^{N} \iint_{h,h} \overline{C}_{16}^{(K)} \hat{z} z dydz \tag{B.41}$$

where

$$\hat{y} = y - \lambda, z \tag{B.42}$$
$$\hat{z} = z + \lambda, y$$

Subscript h represents the horizontal (top and bottom) flanges of the laminated box-beam and υ represents the vertical (the left and right). N and M are numbers of layers in the horizontal and vertical laminates respectively.

B.4 Smith and Chopra Stiffness Model [2.84]

This analysis is an extension of that of Chandra et al. [3.17]. Each beam wall is considered to be a single laminated plate as shown in Fig. B.2. Only when the warping function is considered are the cross-sections treated using the contour level of thin-walled beams, and this is then transformed from contour form to two-dimensional cross-sectional form. The warping function is then carried through the entire analysis, from the initial kinematic relations to the effective stiffnesses of the beam cross-section. In addition, the transverse shear deformation is also included.

The displacement field is of the form

$$u_1 = U_1(x) - y\left[U_2'(x) - \gamma_{xy}(x)\right] - z\left[U_3'(x) - \gamma_{xz}(x)\right] - \lambda\varphi'(x)$$

$$u_2 = U_2(x) - z\varphi(x) \qquad \text{(B.43)}$$

$$u_3 = U_3(x) + y\varphi(x)$$

The term $\lambda\varphi'(x)$ represents the warping of the cross-section, namely the torsion-related warping. In this analysis, the thin-walled beam theory approach described in Megson [3.20] is modified to determine the shape of the warping deflections for a composite box-beam. The warping function is defined along the contour as,

$$\lambda(s) = 2A_e\left(\frac{\delta_{os}}{\delta} - \frac{A_{os}}{A_e}\right) \qquad \text{(B.44)}$$

For the rectangular box-beam under consideration, the enclosed area of the cross-section is $A_e = cd$. A_{os} is the area swept out by a generator, with origin at the box-beam centre, from $s = 0$ to $s = s$ on the contour. Other contour parameters in Eqn. (B.44) are defined as,

$$\delta = \int_s \frac{ds}{G(s)t(s)} \quad \text{and} \quad \delta_{os}(s) = \int_0^s \frac{ds}{G(s)t(s)} \qquad \text{(B.45)}$$

For relatively thin-walled beams, the contour warping function $\lambda(s)$, can be simply transformed into the two-dimensional cross-sectional form

$$\lambda(y,z) = \beta yz \tag{B.46}$$

with β and α given by

$$\beta = -\frac{(1-\alpha)}{(1+\alpha)} \qquad \text{and} \qquad \alpha = \left(\frac{c}{d}\right)\left(\frac{t_\upsilon}{t_h}\right)\left(\frac{G_\upsilon}{G_h}\right) \tag{B.47}$$

where G_υ and G_h are the effective in-plane shear stiffness of the vertical and horizontal walls respectively.

The strains are determined by differentiating the displacement expressions of Eqn. (B.43). Since the walls of the box-beam are assumed to be relatively thin, only axial and in-plane shear strains are considered non-negligible. The resulting strains are

$$\varepsilon_{xx} = U_1'(x) - y\left[U_2''(x) - \gamma'_{xy}(x)\right] - z\left[U_3''(x) - \gamma'_{xz}(x)\right] - \lambda\varphi''(x)$$

$$\varepsilon_{xz} = \left[y - \frac{\partial\lambda}{\partial z}\right]\varphi' + \gamma_{xz} \tag{B.48}$$

in the vertical walls, and

$$\varepsilon_{xx} = U_1'(x) - y\left[U_2''(x) - \gamma'_{xy}(x)\right] - z\left[U_3''(x) - \gamma'_{xz}(x)\right] - \lambda\varphi''(x)$$

$$\varepsilon_{xy} = \left[z - \frac{\partial\lambda}{\partial y}\right]\varphi' + \gamma_{xy} \tag{B.49}$$

in the horizontal walls.

The stress-strain relationship (for example, for the vertical wall) can be expressed as,

$$\begin{Bmatrix} \sigma_{xx} \\ \sigma_{zz} \\ \tau_{xz} \end{Bmatrix} = \begin{bmatrix} \overline{Q}_{11} & \overline{Q}_{12} & \overline{Q}_{16} \\ \overline{Q}_{12} & \overline{Q}_{22} & \overline{Q}_{26} \\ \overline{Q}_{16} & \overline{Q}_{26} & \overline{Q}_{66} \end{bmatrix} \begin{Bmatrix} \varepsilon_{xx} \\ \varepsilon_{zz} \\ \gamma_{xz} \end{Bmatrix} \tag{B.50}$$

where

$$\varepsilon_{zz} = \alpha U_1' + b\left(U_2'' - \gamma_{xy}'\right) + c\left(U_3'' - \gamma_{xz}'\right) + d\varphi' + e\varphi'' + f\gamma_{xy} + g\gamma_{xz} \tag{B.51}$$

The coefficient of the deformation are linear functions within the cross-section. For example,

$$\alpha = \alpha_0 + \alpha_1 y + \alpha_2 z \tag{B.52}$$

where the constants are determined from the three conditions on the in-plane stresses.

The net forces and moments acting over the cross-section can be related to the stresses in the beam walls by equilibrium as follows:

$$\begin{aligned} T &= \iint \sigma_{xx} dA \\ Q_y &= \iint \sigma_{xy} dA \qquad Q_z = \iint \sigma_{xz} dA \\ M_x &= \iint \left[\left(y - \frac{\partial \lambda}{\partial z} \right) \sigma_{xz} - \left(z + \frac{\partial \lambda}{\partial y} \right) \sigma_{xy} \right] dA + \frac{\partial}{\partial x} \left[\iint \lambda \sigma_{xx} dA \right] \\ M_y &= -\iint \sigma_{xx} z dA \qquad M_z = -\iint \sigma_{xx} y dA \end{aligned} \tag{B.53}$$

where T is the tension, Q_y and Q_z are the shear forces, M_x is the torsional moment, and M_y and M_z are the bending moments.

The deformational variables or generalised strains can easily be obtained from the strain expressions. In matrix form these can be written as,

$$u = \left[U_1'(x) \quad \gamma_{xy} \quad \gamma_{xz} \quad \varphi'(x) \quad \left\{ U_2''(x) - 2\gamma_{xy}'(x) \right\} \quad \left\{ U_3''(x) - 2\gamma_{xz}'(x) \right\} \right] \quad \text{(B.54)}$$

Similarly the generalised internal forces can be written in matrix form as,

$$F = \left[T \quad Q_y \quad Q_z \quad M_x \quad M_y \quad M_z \right] \quad \text{(B.55)}$$

As the forces and moments are linearly related to the displacements, a symmetric 6x6 stiffness matrix, P, can then be defined such that

$$F = Pu \quad \text{(B.56)}$$

where the stiffness parameters are given as,

$$EI = \iint_{h,\upsilon} \overline{Q}_{11} z^2 dA - c_2 \iint_{h,\upsilon} \overline{Q}_{12} z^2 dA \quad \text{(B.57)}$$

$$\begin{aligned} GJ = &\left(1+\beta\right)^2 \iint_h \overline{Q}_{66} z^2 dA + \left(1-\beta\right)^2 \iint_\upsilon \overline{Q}_{66} y^2 dA \\ &+ d_0 \left[\left(1-\beta\right) \iint_\upsilon \overline{Q}_{26} y dA - \left(1+\beta\right) \iint_h \overline{Q}_{26} z dA \right] \\ &+ d_1 \left(1-\beta\right) \iint_\upsilon \overline{Q}_{26} y^2 dA - d_2 \left(1+\beta\right) \iint_h \overline{Q}_{26} z^2 dA \end{aligned} \quad \text{(B.58)}$$

$$K = \left(1+\beta\right) \iint_\upsilon \overline{Q}_{16} z^2 dA - d_2 \iint_{h,\upsilon} \overline{Q}_{12} z^2 dA \quad \text{(B.59)}$$

where β is the non-dimensional warping function.

The above stiffness parameters contain a number of constants such as c_2, d_0, d_1 and d_2. These constants arise from the refined treatment of the two-dimensional in-plane elastic behaviour. The constants are defined by the expressions given below

$$c_2 = \iint_{h,\upsilon} \overline{Q}_{12} z^2 dA \Big/ \iint_{h,\upsilon} \overline{Q}_{22} z^2 dA$$

$$d_0 = \left[(1+\beta)\iint_h \overline{Q}_{26} z dA - (1-\beta)\iint_\upsilon \overline{Q}_{26} y dA\right] \Big/ \iint_{h,\upsilon} \overline{Q}_{22} dA \qquad \text{(B.60)}$$

$$d_1 = -(1-\beta)\iint_\upsilon \overline{Q}_{26} y^2 dA \Big/ \iint_{h,\upsilon} \overline{Q}_{22} y^2 dA$$

$$d_2 = (1+\beta)\iint_h \overline{Q}_{26} z^2 dA \Big/ \iint_{h,\upsilon} \overline{Q}_{22} z^2 dA$$

B.5 Berdichevsky et al. Stiffness Model [2.85]

This analysis is based on a variationally and asymptotically consistent theory applicable to any single-cell cross-section and laminate configuration. The theory is based on an asymptotic analysis of two-dimensional shell theory.

A displacement field consistent with a hypothesis of in-plane nondeformability of the cross-section, but allowing for out-of-plane warping is derived using an asymptotic variational method.

The development of this analysis encompasses mainly five equations. The first is the displacement field in curvilinear coordinates (see Fig. B.3) given as,

$$\upsilon_1 = U_1(x) - y(s)U_2'(x) - z(s)U_3'(x) + g(s,x)$$

$$\upsilon_2 = U_2(x)\frac{dy}{ds} + U_3(x)\frac{dz}{ds} + \varphi(x)r_n \qquad \text{(B.61)}$$

$$\upsilon = U_2(x)\frac{dz}{ds} - U_3(x)\frac{dy}{ds} - \varphi(x)r_t$$

where r_n is given by Eqn. (B.4) and $g(s,x)$ is the warping function given as,

$$g(s,x) = G(s)\varphi'(x) + g_1(s)U_1'(x) + g_2(s)U_2''(x) + g_3(s)U_3''(x) \tag{B.62}$$

where

$$g_1(s) = \int_0^s \left[b(\tau) - \frac{\bar{b}}{\bar{c}} c(\tau) \right] d\tau$$

$$g_2(s) = -\int_0^s \left[b(\tau) y(\tau) - \frac{by}{\bar{c}} c(\tau) \right] d\tau \tag{B.63}$$

$$g_3(s) = -\int_0^s \left[b(\tau) z(\tau) - \frac{bz}{\bar{c}} c(\tau) \right] d\tau$$

and

$$b(s) = -\frac{2B(s)}{C(s)} \qquad c(s) = \frac{1}{C(s)} \tag{B.64}$$

The expressions for the displacements υ_2 , υ and the first three terms in υ_1 (Eqn. (B.61)) and the first term in Eqn. (B.62) are analogous to the classical theory of extension, bending and torsion of beams. The additional terms $g_1(s)U_1'$, $g_2(s)U_2''$ and $g_3(s)U_3''$ in the expression for υ_1 (see Eqns (B.61) and (B.62)) represent warping due to axial strain and bending. These new terms emerge naturally in addition to the classical torsion-related warping $G(s)\varphi'$. They are strongly influenced by the material's anisotropy, and vanish for materials that are either orthotropic or whose properties are antisymmetric relative to the shell middle surface.

The expressions of Eqn. (B.61) are related to the displacement components in Cartesian coordinates (see Fig. B.2) by

$$\upsilon_1 = u_1$$

$$\upsilon_2 = u_2 \frac{dy}{ds} + u_3 \frac{dz}{ds} \tag{B.65}$$

$$\upsilon = u_2 \frac{dz}{ds} - u_3 \frac{dy}{ds}$$

Thus in Cartesian coordinates the displacement field is given by

$$u_1 = U_1(x) - y(s)U_2'(x) - z(s)U_3'(x) + G(s)\varphi'(x)$$
$$+g_1(s)U_1'(x) + g_2(s)U_2''(x) + g_3(s)U_3''(x)$$

$$u_2 = U_2(x) - z(s)\varphi(x) \tag{B.66}$$

$$u_3 = U_3(x) + y(s)\varphi(x)$$

The second set of equations is the associated strain field given by

$$\varepsilon_{xx} = U_1'(x) - y(s)U_2''(x) - z(s)U_3''(x)$$

$$2\gamma_{xs} = \frac{2A_e}{l\bar{c}}c(s)\varphi' + \left[b(s) - \frac{\bar{b}}{\bar{c}}c(s)\right]U_1'$$
$$-\left[b(s)y(s) - \frac{by}{\bar{c}}c(s)\right]U_2'' - \left[b(s)z(s) - \frac{bz}{\bar{c}}c(s)\right]U_3'' \tag{B.67}$$

$$\varepsilon_{ss} = 0$$

In Eqn. (B.67) the terms of smaller order in the shell energy were neglected. Its also worth noting in Eqn. (B.67) the vanishing of hoop strain.

The stress resultants are given by

$$N_{xx} = A(s)\varepsilon_{xx} + B(s)\gamma_{xs}$$

$$N_{xs} = \frac{1}{2}\left(B(s)\varepsilon_{xx} + C(s)\gamma_{xs}\right) = constant \tag{B.68}$$

$$N_{ss} = 0$$

The constitutive relationships can be written in terms of stress resultants as given by Eqn. (B.3). The relationship between forces, moments and displacements

can then be written in matrix form as in Eqn. (B.6) where T, M_x, M_y and M_z represent the tension, torsional moment and bending moments, respectively. The cross-sectional stiffness coefficients, denoted by P_{ij} in Eqn. (B.6), are formulated in terms of closed form integrals of the material constants and geometry. The bending, torsional and bending-torsion coupling stiffnesses are therefore given as [2.85],

$$EI = \oint \left(A - \frac{B^2}{C} \right) z^2 ds + \frac{\left[\oint (B/C) z ds \right]^2}{\oint (1/C) ds} \tag{B.69}$$

$$GJ = \frac{1}{\oint (1/C) ds} A_e^2 \tag{B.70}$$

$$K = -\frac{\oint (B/C) z ds}{\oint (1/C) ds} A_e \tag{B.71}$$

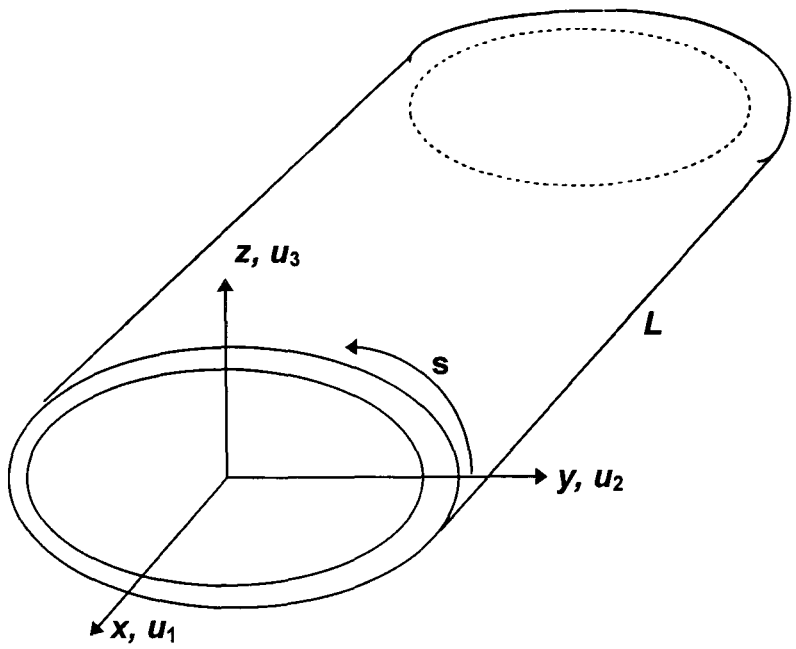

Fig. B.1. Cartesian coordinate system

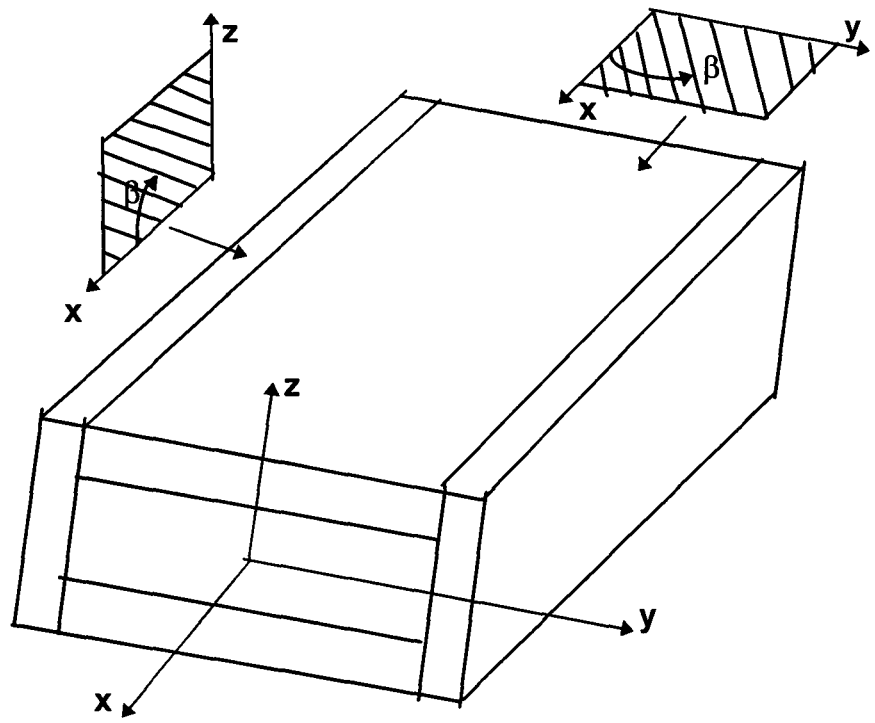

Fig. B.2. Box-beam configuration and coordinates for Refs [2.84, 3.17].

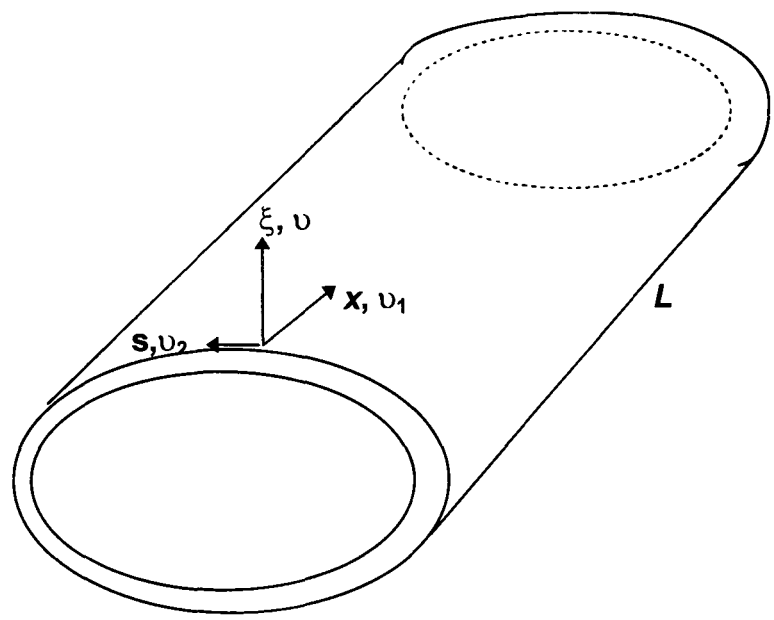

Fig. B.3. Curvilinear coordinate system for Ref. [2.85].

APPENDIX 'C'

DYNAMIC STIFFNESS MATRIX OF A BENDING-TORSION COUPLED COMPOSITE BEAM

Figure C.1 shows a composite beam with a solid rectangular cross-section and with a symmetric but unbalanced lay-up. Bending-torsion coupling occurs for such configurations. The beam is assumed to be uniform and straight with length L. In the right-handed axis system shown, the Y axis coincides with the elastic axis, with associated bending displacement $h(y,t)$ and torsional rotation $\varphi(y,t)$ as indicated, where y is measured from the origin shown and t is time. Using the coupled bending-torsional beam theory for thin-walled composites with shear deformation, rotary inertia and warping stiffness neglected, the governing differential equations of motion of the beam in free vibration are given by [2.69]

$$EIh''''' + K\varphi''' + m\ddot{h} = 0 \tag{C.1}$$

$$GJ\varphi'' + Kh''' - I_\alpha \ddot{\varphi} = 0 \tag{C.2}$$

where m is the mass per unit length, I_α is the polar mass moment of inertia per unit length about the Y-axis, and primes and dots denote differentiation with respect to position y and time t, respectively.

If a sinusoidal variation of h and φ, with circular frequency ω, is assumed, then

$$\left.\begin{aligned} h(y,t) &= H(y)\sin\omega t \\ \varphi(y,t) &= \Phi(y)\sin\omega t \end{aligned}\right\} \tag{C.3}$$

where $H(y)$ and $\Phi(y)$ are the amplitudes of the sinusoidally varying bending displacement and torsional rotation respectively.

Substituting Eqns (C.3) into Eqns (C.1) and (C.2) gives

$$EIH''' + K\Phi'' - m\omega^2 H = 0 \tag{C.4}$$

$$GJ\Phi'' + KH'' + I_\alpha \omega^2 \Phi = 0 \tag{C.5}$$

Equations (C.4) and (C.5) can be combined into one equation by eliminating either H or Φ to give

$$\left(D^6 + aD^4 - bD^2 - abc\right)W = 0 \tag{C.6}$$

where

$$W = H \text{ or } \Phi \tag{C.7}$$

$$D = \frac{d}{d\xi}$$
$$\xi = \frac{y}{L} \tag{C.8}$$

$$a = \bar{a} / c$$
$$b = \bar{b} / c \tag{C.9}$$
$$c = 1 - K^2 / EIGJ$$

with

$$\bar{a} = I_\alpha \omega^2 L^2 / GJ$$
$$\bar{b} = m\omega^2 L^4 / EI \tag{C.10}$$

In Eqn. (C.6) a, b, and c are non-dimensional quantities and are all positive because it is known that [1.12, 1.24]

$$0 < c < 1 \tag{C.11}$$

The solution of the differential Eqn. (C.6) shows that both $H(\xi)$ and $\Phi(\xi)$ have the form

$$W(\xi) = C_1 \cosh\alpha\xi + C_2 \sinh\alpha\xi + C_3 \cos\beta\xi + C_4 \sin\beta\xi + C_5 \cos\gamma\xi + C_6 \sin\gamma\xi \quad \text{(C.12)}$$

where $W(\xi) = H(\xi)$ or $\Phi(\xi)$, $C_1 - C_6$ are constants, and

$$\alpha = \left[2(q/3)^{1/2} \cos(\phi/3) - \alpha/3\right]^{1/2}$$
$$\beta = \left[2(q/3)^{1/2} \cos\{(\pi - \phi)/3\} + \alpha/3\right]^{1/2} \quad \text{(C.13)}$$
$$\gamma = \left[2(q/3)^{1/2} \cos\{(\pi + \phi)/3\} + \alpha/3\right]^{1/2}$$

with

$$q = b + a^2/3$$
$$\phi = \cos^{-1}\left[(27abc - 9ab - 2a^3) / \{2(a^2 + 3b)^{3/2}\}\right] \quad \text{(C.14)}$$

Hence,

$$H(\xi) = A_1 \cosh\alpha\xi + A_2 \sinh\alpha\xi + A_3 \cos\beta\xi + A_4 \sin\beta\xi + A_5 \cos\gamma\xi + A_6 \sin\gamma\xi \quad \text{(C.15)}$$

$$\Phi(\xi) = B_1 \cosh\alpha\xi + B_2 \sinh\alpha\xi + B_3 \cos\beta\xi + B_4 \sin\beta\xi + B_5 \cos\gamma\xi + B_6 \sin\gamma\xi \quad \text{(C.16)}$$

where $A_1 - A_6$ and $B_1 - B_6$ are two different sets of constants.

Substituting Eqns (C.15) and (C.16) into Eqn. (C.4) shows that the constants $A_1 - A_6$ are related to the constants $B_1 - B_6$ by the following relationships:

$$B_1 = (k_\alpha / L)A_2, \quad B_2 = (k_\alpha / L)A_1$$
$$B_3 = (k_\beta / L)A_4, \quad B_4 = -(k_\beta / L)A_3 \quad \text{(C.17)}$$
$$B_5 = (k_\gamma / L)A_6, \quad B_6 = -(k_\gamma / L)A_5$$

where

$$k_\alpha = \left(\bar{b} - \alpha^4\right) / \bar{k}\alpha^3, \quad k_\beta = \left(\bar{b} - \beta^4\right) / \bar{k}\beta^3$$
$$k_\gamma = \left(\bar{b} - \gamma^4\right) / \bar{k}\gamma^3 \tag{C.18}$$

with

$$\bar{k} = K / EI \tag{C.19}$$

Following the sign convention given in Fig. C.2, the anticlockwise rotation $\theta(\xi)$, the bending moment $M(\xi)$, the transverse force $S(\xi)$ and the torque $T(\xi)$ can be obtained from Eqns (C.15) and (C.16) as follows [2.69] (prime now denotes differentiation with respect to ξ):

$$\begin{aligned}\theta(\xi) = H'\left(\xi\right) / L = (1/L)\{&A_1\alpha\sinh\alpha\xi + A_2\alpha\cosh\alpha\xi \\ &- A_3\beta\sin\beta\xi + A_4\beta\cos\beta\xi - A_5\gamma\sin\gamma\xi + A_6\gamma\cos\gamma\xi\}\end{aligned} \tag{C.20}$$

$$\begin{aligned}M\left(\xi\right) &= -\left(EI / L^2\right)H''\left(\xi\right) - (K/L)\Phi'\left(\xi\right) \\ &= -\left(EI / L^2\right)\left\{H''\left(\xi\right) + \bar{k}L\Phi'\left(\xi\right)\right\} \\ &= -\left(EI / L^2\right)\{A_1\bar{\alpha}\cosh\alpha\xi + A_2\bar{\alpha}\sinh\alpha\xi \\ &\quad - A_3\bar{\beta}\cos\beta\xi - A_4\bar{\beta}\sin\beta\xi - A_5\bar{\gamma}\cos\gamma\xi \\ &\quad - A_6\bar{\gamma}\sin\gamma\xi\}\end{aligned} \tag{C.21}$$

$$\begin{aligned}S\left(\xi\right) &= \left(EI / L^3\right)H'''\left(\xi\right) + \left(K / L^2\right)\Phi''\left(\xi\right) \\ &= \left(EI / L^3\right)\left\{H'''\left(\xi\right) + \bar{k}L\Phi''\left(\xi\right)\right\} \\ &= \left(EI / L^3\right)\{A_1\alpha\bar{\alpha}\sinh\alpha\xi + A_2\alpha\bar{\alpha}\cosh\alpha\xi \\ &\quad + A_3\beta\bar{\beta}\sin\beta\xi - A_4\beta\bar{\beta}\cos\beta\xi + A_5\gamma\bar{\gamma}\sin\gamma\xi \\ &\quad - A_6\gamma\bar{\gamma}\cos\gamma\xi\}\end{aligned} \tag{C.22}$$

$$\begin{aligned} T(\xi) &= (GJ/L)\Phi'(\xi) + (K/L^2)H''(\xi) \\ &= (GJ/L)\{\Phi'(\xi) + (K/GJL)H''(\xi)\} \\ &= (GJ/L^2)\{A_1 g_\alpha \cosh\alpha\xi + A_2 g_\alpha \sinh\alpha\xi \\ &\quad - A_3 g_\beta \cos\beta\xi - A_4 g_\beta \sin\beta\xi - A_5 g_\gamma \cos\gamma\xi \\ &\quad - A_6 g_\gamma \sin\gamma\xi\} \end{aligned} \tag{C.23}$$

where

$$\bar{\alpha} = \bar{b}/\alpha^2, \quad \bar{\beta} = \bar{b}/\beta^2, \quad \bar{\gamma} = \bar{b}/\gamma^2 \tag{C.24}$$

$$g_\alpha = (\bar{b} - c\alpha^4)/\bar{k}\alpha^2, \quad g_\beta = (\bar{b} - c\beta^4)/\bar{k}\beta^2, \quad g_\gamma = (\bar{b} - c\gamma^4)/\bar{k}\gamma^2 \tag{C.25}$$

The end conditions for displacements and forces (see Fig. C.3) are respectively,

at end 1 (i.e., $\xi = 0$)

$$H = H_1, \quad \theta = \theta_1 \quad \text{and} \quad \Phi = \Phi_1 \tag{C.26a}$$

at end 2 (i.e., $\xi = 1$)

$$H = H_2, \quad \theta = \theta_2 \quad \text{and} \quad \Phi = \Phi_2 \tag{C.26b}$$

at end 1 (i.e., $\xi = 0$)

$$S = S_1, \quad M = M_1 \quad \text{and} \quad T = -T_1 \tag{C.27a}$$

at end 2 (i.e., $\xi = 1$)

$$S = -S_2, \quad M = -M_2 \quad \text{and} \quad T = T_2 \tag{C.27b}$$

The dynamic stiffness matrix that relates the amplitudes of the sinusoidally varying forces to the corresponding displacement amplitudes can now be derived with the help of Eqns (C.15-C.27) as follows.

Substituting Eqns (C.26) into Eqns (C.15), (C.20), and (C.16) and using the relationships given by Eqns (C.17) gives

$$\begin{bmatrix} H_1 \\ \theta_1 \\ \Phi_1 \\ H_2 \\ \theta_2 \\ \Phi_2 \end{bmatrix} = \begin{bmatrix} 1 & 0 & 1 & 0 & 1 & 0 \\ 0 & \alpha/L & 0 & \beta/L & 0 & \gamma/L \\ 0 & k_\alpha/L & 0 & k_\beta/L & 0 & k_\gamma/L \\ C_{h\alpha} & S_{h\alpha} & C_\beta & S_\beta & C_\gamma & S_\gamma \\ \alpha S_{h\alpha}/L & \alpha C_{h\alpha}/L & -\beta S_\beta/L & \beta C_\beta/L & -\gamma S_\gamma/L & \gamma C_\gamma/L \\ k_\alpha S_{h\alpha}/L & k_\alpha C_{h\alpha}/L & -k_\beta S_\beta/L & k_\beta C_\beta/L & -k_\gamma S_\gamma/L & k_\gamma C_\gamma/L \end{bmatrix} \begin{bmatrix} A_1 \\ A_2 \\ A_3 \\ A_4 \\ A_5 \\ A_6 \end{bmatrix} \quad \text{(C.28)}$$

i.e.,

$$U = BA \quad \text{(C.29)}$$

where

$$C_{h\alpha} = \cosh\alpha, \quad C_\beta = \cos\beta, \quad C_\gamma = \cos\gamma$$
$$S_{h\alpha} = \sinh\alpha, \quad S_\beta = \sin\beta, \quad S_\gamma = \sin\gamma \quad \text{(C.30)}$$

Substituting Eqns (C.27) into Eqns (C.22), (C.21), and (C.23) gives

$$\begin{bmatrix} S_1 \\ M_1 \\ T_1 \\ S_2 \\ M_2 \\ T_2 \end{bmatrix} = \begin{bmatrix} 0 & W_3\alpha\bar{\alpha} & 0 & -W_3\beta\bar{\beta} & 0 & -W_3\gamma\bar{\gamma} \\ -W_2\bar{\alpha} & 0 & W_2\bar{\beta} & 0 & W_2\bar{\gamma} & 0 \\ -W_1 g_\alpha/L & 0 & W_1 g_\beta/L & 0 & W_1 g_\gamma/L & 0 \\ -W_3\alpha\bar{\alpha}S_{h\alpha} & -W_3\alpha\bar{\alpha}C_{h\alpha} & -W_3\beta\bar{\beta}S_\beta & W_3\beta\bar{\beta}C_\beta & -W_3\gamma\bar{\gamma}S_\gamma & W_3\gamma\bar{\gamma}C_\gamma \\ W_2\bar{\alpha}C_{h\alpha} & W_2\bar{\alpha}S_{h\alpha} & -W_2\bar{\beta}C_\beta & -W_2\bar{\beta}S_\beta & -W_2\bar{\gamma}C_\gamma & -W_2\bar{\gamma}S_\gamma \\ W_1 g_\alpha C_{h\alpha}/L & W_1 g_\alpha S_{h\alpha}/L & -W_1 g_\beta C_\beta/L & -W_1 g_\beta S_\beta/L & -W_1 g_\gamma C_\gamma/L & -W_1 g_\gamma S_\gamma/L \end{bmatrix} \begin{bmatrix} A_1 \\ A_2 \\ A_3 \\ A_4 \\ A_5 \\ A_6 \end{bmatrix} \quad \text{(C.31)}$$

i.e.,

$$F = DA \quad \text{(C.32)}$$

where

$$W_1 = GJ/L, \quad W_2 = EI/L^2, \quad W_3 = EI/L^3 \quad \text{(C.33)}$$

Equations (C.32) and (C.29) give

$$F = KU \tag{C.34}$$

$$\begin{bmatrix} S_1 \\ M_1 \\ T_1 \\ S_2 \\ M_2 \\ T_2 \end{bmatrix} = \begin{bmatrix} K_{1,1} & K_{1,2} & K_{1,3} & K_{1,4} & K_{1,5} & K_{1,6} \\ & K_{2,2} & K_{2,3} & K_{2,4} & K_{2,5} & K_{2,6} \\ & & K_{3,3} & K_{3,4} & K_{3,5} & K_{3,6} \\ & SYM & & K_{4,4} & K_{4,5} & K_{4,6} \\ & & & & K_{5,5} & K_{5,6} \\ & & & & & K_{6,6} \end{bmatrix} \begin{bmatrix} H_1 \\ \theta_1 \\ \Phi_1 \\ H_2 \\ \theta_2 \\ \Phi_2 \end{bmatrix} \tag{C.35}$$

where

$$K = DB^{-1} \tag{C.36}$$

is the required stiffness matrix. Expressions for the K_{ij} stiffness terms are given in Ref. [1.37].

Equation (C.36) can be solved algebraically with the help of the symbolic computing package Reduce [C.1, C.2], i.e., the B matrix of Eqns (C.28) and (C.29) is inverted algebraically and then premultiplied by the D matrix of Eqns (C.31) and (C.32), again algebraically.

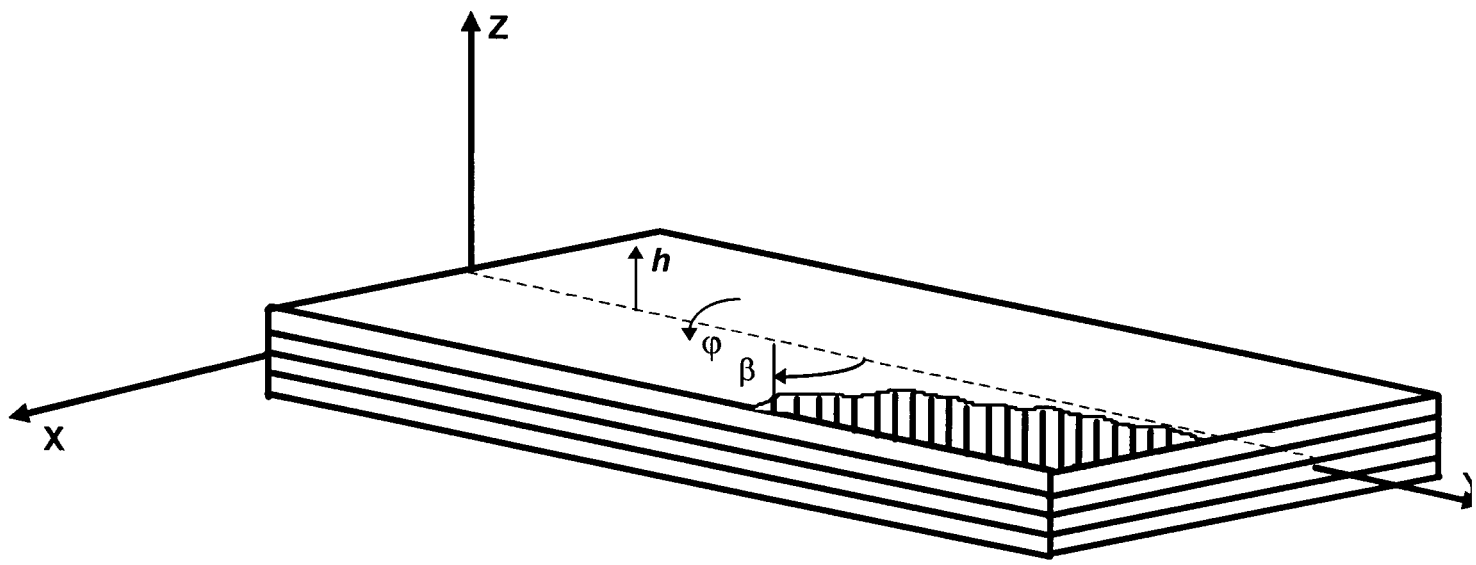

Fig. C.1. Coordinate system and sign convention for positive ply angle of a laminated composite beam.

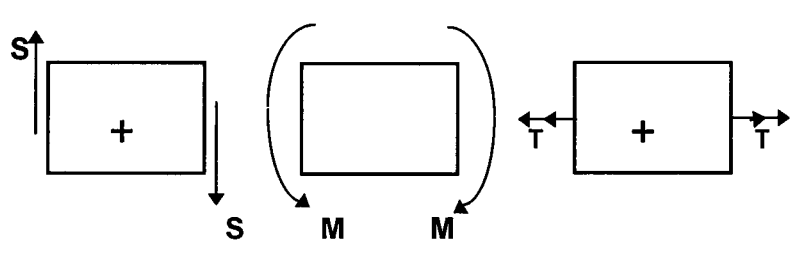

Fig. C.2. Sign convention for positive transverse force *S*, bending moment *M*, and torque *T*.

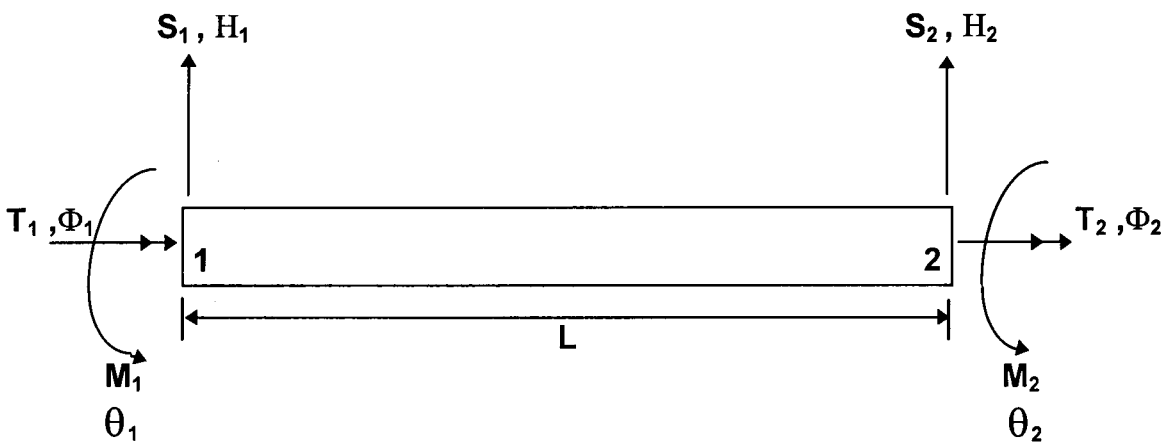

Fig. C.3. End conditions for forces and displacements of a bending-torsion coupled composite beam.

APPENDIX 'D'

FLUTTER ANALYSIS USING GENERALISED COORDINATES AND NORMAL MODES

D.1 Summary of the Method

The normal mode method of flutter analysis is well established and has been reported in a number of papers [5.4-5.6]. Basically the method relies on the fact that the mass, stiffness and aerodynamic properties of an aircraft can be expressed in terms of the generalised coordinates. The steps required when using this method for flutter analysis are summarised as follows:

1. Determination of natural frequencies and mode shapes.

2. Selection of normal modes for flutter analysis.

3. Reduction of mass and stiffness matrices to diagonal form to give generalised mass and stiffness matrices respectively.

4. Expression of aerodynamic matrix in modal coordinates to give generalised aerodynamic matrix.

5. Formation of flutter matrix by algebraically summing generalised mass, stiffness and aerodynamic matrices.

6. Solution of flutter determinant (formed from the flutter matrix) for flutter speed and flutter frequency.

D.2 Determination of Natural Frequencies and Mode Shapes

The equation for free vibratory motion of an aircraft wing can be expressed in terms of mass and stiffness matrices as follows:

$$[M]\{\ddot{u}\} + [K]\{u\} = 0$$

or

$$[K_D]\{u\} = 0 \tag{D.1}$$

where $[K_D]$ is the generalised dynamic stiffness matrix and u are the time dependent set of generalised coordinates representing the system.

In order to solve this equation efficiently it has to be rendered more manageable. To do this the normal modes of the continuous system are incorporated and the principal of orthogonality applied.

To obtain the natural frequencies and normal modes of free vibration, motion of the form $u = \phi e^{i\omega t}$ is assumed. The resulting dynamic stiffness is solved for

$$(K - \omega^2 M)\phi = 0 \tag{D.2}$$

where ω is the natural frequency and ϕ is the corresponding mode shape.

D.3 Generalised Mass and Stiffness Matrices in Modal Coordinates

For modes with distinct frequencies, i.e., $\omega_i \neq \omega_j$, it follows that

$$\phi_i^T M \phi_j = 0 \qquad (\omega_i \neq \omega_j) \tag{D.3}$$

The ith and jth modes are orthogonal with respect to the mass matrix. The same principle can be applied to the stiffness matrix in which case the ith mode and jth mode are also orthogonal with respect to the stiffness matrix, that is,

$$\phi_i^T K \phi_j = 0 \qquad (\omega_i \neq \omega_j) \tag{D.4}$$

Once the frequencies ω and mode shapes Φ where $\Phi = [\phi_1, \phi_2, \ldots \phi_n]$ have been established the following coordinate transformation $u(t) = \Phi q(t)$ is introduced, where $q(t)$ are referred to as normal coordinates. Therefore the equation of forced motion can be expressed as,

$$[M_G]\{q\} + [K_G]\{q\} = [F]\{q\}$$

or

$$[K_D]\{q\} = [F]\{q\} \tag{D.5}$$

where

$[M_G]$ = generalised mass matrix

$= [\phi]^T [M][\phi]$

$[K_G]$ = generalised stiffness matrix

$= [\phi]^T [K][\phi]$

$[F]$ = generalised force matrix

$= [\phi]^T [F][\phi]$

$[\phi]^T$ = transpose of $[\phi]$

This transformation has the effect of uncoupling the equations of motion. This leads to N separate single degree of freedom equations. This significantly reduces the computational time for solving the equations. This technique is known as the mode-superposition method [D.1].

D.4 Generalised Aerodynamic Matrix Using Strip Theory

To create the necessary displacement dependent forces of lift L and pitching moment M, Theodorsen's explicit terms for these forces [5.8] are applied. It is assumed that Lift and Moments are linear functions of the bending displacement (h) and torsional rotation (φ) and the airflow is two-dimensional, i.e., the wing has an infinite aspect ratio. The aerodynamic coefficients are calculated for a flat plate aerofoil at zero mean angle of attack. Neglecting flap terms the lift L and pitching moment M can be expressed as,

$$\frac{L}{\rho\pi b U^2} = -k^2\left(\frac{h}{b} - \mathrm{a}\,\varphi\right) + ik\varphi + 2C(k)\left[\varphi + \frac{ihk}{b} + \left(\frac{1}{2} - \mathrm{a}\right)ik\varphi\right]$$

$$\frac{M}{\rho\pi b^2 U^2} = \left(\frac{1}{2} + \mathrm{a}\right)2C(k)\left[\varphi + \frac{ihk}{b} + \left(\frac{1}{2} - \mathrm{a}\right)ik\varphi\right] - k^2\,\mathrm{a}\left(\frac{h}{b} - \mathrm{a}\,\varphi\right) - \left(\frac{1}{2} + \mathrm{a}\right)ik\varphi + \frac{k^2}{8}\varphi \qquad \text{(D.6)}$$

where $k = \dfrac{\omega b}{U}$ = *reduced frequency parameter*

L = *lift (positive upward)*

M = *moment (positive leading edge up)*

h = *bending displacement (positive upward)*

φ = *torsional rotation (positive leading edge up)*

a = *elastic axis location from mid-chord*

C(k) = *Theodorsen function*

The Theodorsen function *C(k)* is expressed as,

$$C(k) = \frac{H_1^{(2)}(k)}{H_1^{(2)}(k) + iH_0^{(2)}(k)} = F(k) + iG(k) \qquad \text{(D.7)}$$

where $H_1^{(2)}(k)$ and $H_0^{(2)}(k)$ are the Hankel functions.

The Theodorsen function *C(k)* has the effect of modifying the phase between the forcing and damping components of the oscillatory aerodynamic forces. The values of *C(k)* may be readily calculated within a subroutine of a main program.

Equations (D.6) can be written in matrix form as,

$$\begin{Bmatrix} L \\ M \end{Bmatrix} = \begin{bmatrix} A_{11} & A_{12} \\ A_{12} & A_{22} \end{bmatrix} \begin{Bmatrix} h \\ \varphi \end{Bmatrix} \tag{D.8}$$

where

$$\begin{aligned} A_{11} &= -\pi\rho U^2 \{-k^2 + 2C(k)ik\} \\ A_{12} &= -\pi\rho U^2 b \left\{ (\mathrm{a} + ik) + 2C(k)\left[1 - ik\left(\frac{1}{2} - \mathrm{a}\right)\right]\right\} \\ A_{21} &= \pi\rho U^2 b \left\{ 2C(k)ik\left(\frac{1}{2} + \mathrm{a}\right) - k^2\,\mathrm{a}\right\} \\ A_{22} &= \pi\rho U^2 b^2 \left\{ 2\left(\frac{1}{2} + \mathrm{a}\right)C(k)\left[1 + ik\left(\frac{1}{2} - \mathrm{a}\right)\right] + \frac{k^2}{8} + k^2\,\mathrm{a}^2 + \left(\mathrm{a} - \frac{1}{2}\right)ki\right\} \end{aligned} \tag{D.9}$$

The signs of A_{11} and A_{12} have been reversed in order to make lift positive downwards, in order to be consistent with the coordinate system and in the structural idealisation.

In order to apply the transformation into normal coordinates, uncoupled or coupled normal modes are chosen to represent heave (h) and rotation (φ) about the elastic axis. Assuming only three modes for simplicity, the aerodynamic matrix in terms of generalised coordinates (q_1, q_2, q_3) can then be derived as follows:

$$\begin{Bmatrix} h(y,t) \\ \varphi(y,t) \end{Bmatrix} = \begin{bmatrix} h_1(y) & h_2(y) & h_3(y) \\ \varphi_1(y) & \varphi_2(y) & \varphi_3(y) \end{bmatrix} \begin{Bmatrix} q_1(t) \\ q_2(t) \\ q_3(t) \end{Bmatrix} \tag{D.10}$$

or expressed in summation signs

$$\left.\begin{aligned} h(y,t) &= \sum_{i=1}^{3} h_i(y) q_i(t) \\ \varphi(y,t) &= \sum_{i=1}^{3} \varphi_i(t) q_i(t) \end{aligned}\right\} \tag{D.11}$$

where $h_i(y)$ is the vertical displacement (bending mode) at section y for the ith node and $\varphi_i(y)$ is the torsional rotation (torsional mode) about the reference axis (shear centre) at station y for the ith mode.

The generalised force Q_i corresponding to the generalised coordinates q_i are found by calculating the work done δW by the airforces in varying q_i to $q_i + \delta q_i$

$$\delta W_i = \delta q_i \int_0^{\ell} \{L(y)h_i(y) + M(y)\varphi_i(y)\}dy \tag{D.12}$$

In matrix form

$$\begin{bmatrix} \frac{\delta W_1}{\delta q_1} \\ \frac{\delta W_2}{\delta q_2} \\ \frac{\delta W_3}{\delta q_3} \end{bmatrix} = \int_0^{\ell} \begin{bmatrix} h_1 & \varphi_1 \\ h_2 & \varphi_2 \\ h_3 & \varphi_3 \end{bmatrix} \begin{bmatrix} L \\ M \end{bmatrix} dy \tag{D.13}$$

Combining Eqns (D.8), (D.10) and (D.13) gives

$$\begin{bmatrix} \frac{\delta W_1}{\delta q_1} \\ \frac{\delta W_2}{\delta q_2} \\ \frac{\delta W_3}{\delta q_3} \end{bmatrix} = \int_0^{\ell} \begin{bmatrix} h_1 & \varphi_1 \\ h_2 & \varphi_2 \\ h_3 & \varphi_3 \end{bmatrix} \begin{bmatrix} A_{11} & A_{12} \\ A_{12} & A_{22} \end{bmatrix} \begin{bmatrix} h \\ \varphi \end{bmatrix} dy$$

$$= \int_0^{\ell} \begin{bmatrix} h_1 & \varphi_1 \\ h_2 & \varphi_2 \\ h_3 & \varphi_3 \end{bmatrix} \begin{bmatrix} A_{11} & A_{12} \\ A_{12} & A_{22} \end{bmatrix} \begin{bmatrix} h_1(y) & h_2(y) & h_3(y) \\ \varphi_1(y) & \varphi_2(y) & \varphi_3(y) \end{bmatrix} \begin{Bmatrix} q_1(t) \\ q_2(t) \\ q_3(t) \end{Bmatrix}$$

$$= \begin{bmatrix} QF_{11} & QF_{12} & QF_{13} \\ QF_{21} & QF_{22} & QF_{23} \\ QF_{31} & QF_{32} & QF_{33} \end{bmatrix} \begin{bmatrix} q_1 \\ q_2 \\ q_3 \end{bmatrix} \tag{D.14}$$

where

$$QF_{ij} = \int_0 \left(A_{11} h_i h_j + A_{21} h_j \varphi_i + A_{12} h_i \varphi_j + A_{22} \varphi_i \varphi_j \right) dy \tag{D.15}$$

$[QF]$ is the generalised aerodynamic matrix.

D.5 Generalised Aerodynamic Matrix Using Lifting Surface Theory

Methods for calculating generalised airforce coefficients on a harmonically oscillating flat plate wing in subsonic flow based on linearised theory [5.1] have been in the course of development for many years. The linearised theory is used to set up an integral equation relating the unknown loading distribution to the known upwash distribution of the wing.

$$w_\alpha(x,y) = \frac{1}{4\pi\rho} \iint_S L(\varsigma,\eta) Ker(x-\varsigma, y-\eta) d\varsigma d\eta \tag{D.16}$$

where $L(\varsigma,\eta)$ is the loading to be determined over the planform S, $w_\alpha(x,y)e^{i\omega t}$ is the harmonic downwash and Ker, the known Kernel of this integral, is like an aerodynamic influence function giving the induced normal velocity at the surface field point x, y due to isolated unit loading at ζ, η. Ker contains the frequency and Mach number as parameters and has been expressed in various explicit forms for different speed regimes. There are various methods for solving the integral equation numerically. In one the loading distribution is replaced by a distribution of concentrated loads on certain lines and is known as the doublet lattice method, whereas in another the loading distribution is replaced by an approximation which is continuous over the wing except in the neighbourhood of its leading edge is known as the lifting surface method. There are also methods which are not based on the above mention integral equation, for example, the vortex lattice method. This section is

concerned exclusively with the lifting surface method as presented by Davies [2.52, D.2, D.3]. This uses the method of solution as presented in the steady flow lifting surface of Multhopp type extended to general-frequency harmonic oscillations.

The coordinate system is as shown in Fig. D.1 where a flat plate wing with an axis of symmetry is situated in the space with all its points fixed relative to the coordinate system 0XYZ. The wing axis of symmetry passes through the origin 0, the axis 0X is along the wing axis of symmetry, the axis 0Y lies in the plane of the wing and the axis 0Z is perpendicular to the plane of the wing.

The flat plate wing is immersed in a uniform airstream having speed V in the direction of the positive X-axis. It is made to oscillate with circular frequency ω about its mean position in the Z = 0 plane in one of a number of modes of oscillation. In the mode of oscillation K, the displacement $Z_k\,(x, y, t)$ in the direction of the positive X-axis at time t of a point on the wing from the point $(x, y, 0)$ is given by

$$Z_k(x,y,t) = l\varsigma_k(x,y)e^{i\omega t} \tag{D.17}$$

The modal function $\varsigma_k(x,y)$ in Eqn. (D.17) is non-dimensional.

At the point on the oscillating wing displaced along the Z direction from the point $(x,y,0)$ there is a pressure $p_k^+(x,y,t)$ acting on the upper surface of the wing and a pressure $p_k^-(x,y,t)$ acting on the lower surface of the wing in the mode K of oscillation the corresponding aerodynamic loading $L_k(x,y,t)$ acting on the wing in the mode K of oscillation is given by

$$L_k(x,y,t) = p_k^-(x,y,t) - p_k^+(x,y,t) \tag{D.18}$$

and is the aerodynamic force per unit area acting on the wing in the direction of the positive Z-axis at time t.

We may write

$$L_k(x,y,t) = \rho V^2 l_k(x,y;\nu,M)e^{i\omega t} \tag{D.19}$$

where ρ is the air density and M is the Mach number.

$$\nu = \frac{\omega l}{V} \tag{D.20}$$

is the frequency parameter based on the typical length l and $l_k(x,y;\nu,M)$ is a non-dimensional complex loading function which depends directly on the upwash function

$$w_\alpha(x,y;\nu) = l\frac{\partial \varsigma_k}{\partial x}(x,y) + l\nu\varsigma_k(x,y) \tag{D.21}$$

The dependence is expressed in the integral relationship

$$w_\alpha(x,y;\nu) = \frac{1}{l^2}\iint_S l_k(x_0,y_0;\nu,M)Ker(\frac{x-x_0}{l},\frac{y-y_0}{l};\nu,M)dxdy \tag{D.22}$$

where *S* is the planform of the complete wing and $Ker(\frac{x}{l},\frac{y}{l};\nu,M)$ is a Kernel function whose form is known.

The generalised airforce coefficient $Q_{jk}(\nu,M)$ for the wing, corresponding to the loading in the mode K and displacement in the mode *j*, is the non-dimensional quantity given by the formula

$$Q_{jk}(\nu,M) = \frac{1}{l^2}\iint_S \varsigma_j(x,y)l_k(x,y;\nu,M)dxdy \tag{D.23}$$

It is convenient to write

$$Q_{jk}(\nu,M) = Q'_{jk}(\nu,M) + iQ''_{jk}(\nu,M) \tag{D.24}$$

where $Q'_{jk}(\nu,M)$ and $Q''_{jk}(\nu,M)$ are real quantities.

The modal functions $\varsigma_k(x,y)$ for all the modes K of oscillation are taken to be known and then the upwash functions $w_\alpha(x,y,\nu)$ are determined from Eqn. (D.21). The loading functions $l_k(x,y;\nu,M)$ are then determined from the integral Eqn. (D.22) and finally the generalised airforce coefficients $Q_{jk}(\nu,M)$ are determined from Eqn. (D.23) on substituting for the known functions $\varsigma_j(x,y)$ and the already determined functions $l_k(x,y;\nu,M)$.

The loading function $l_k(x,y;\nu,M)$ is determined by solving the integral Eqn. (D.22) numerically. To do this, an approximation $\hat{l}_k(x,y)$ to the loading function $l_k(x,y;\nu,M)$ must first be specified, involving a finite number parameters whose values are initially unknown. These parameters can be taken to be the approximate values of $l_k(x,y;\nu,M)$ at a finite number of separate points on the wing, which we shall call the loading points the approximation $\hat{l}_k(x,y)$ to the loading function $l_k(x,y;\nu,M)$ is the expressed as an interpolation function on the approximations to $l_k(x,y;\nu,M)$ at the loading points, which properly takes into account the edge behaviour of the loading in the peripheral regions of the wings as a result of the condition that the loading at the trailing edge of *S* vanishes. The approximations to $l_k(x,y;\nu,M)$ at the loading points occur in the expression for the approximation $\hat{l}_k(x,y)$, as a linear combination. Hence using this approximation $\hat{l}_k(x,y)$ an approximation to the generalised force may be obtained $\hat{Q}_{ij}$ using Eqn. (D.23).

D.6 Formation of Flutter Matrix and Flutter Determinant

The flutter matrix is formed by summing the generalised mass, stiffness and aerodynamic matrices as follows:

$$[QA]\{q\} = \left[-\omega^2[M_G] + [K_G] - [QF]\right]\{q\}$$

or

$$[QA]\{q\} = \left[[K_D(\omega)] - [QF]\right]\{q\} \qquad \text{(D.25)}$$

where

$[QA]$ = flutter matrix

$[QF]$ = generalised aerodynamic matrix which is complex

The flutter determinant is formed from the flutter matrix and for flutter condition, this determinant must be zero, i.e.,

$$\left|-\omega^2[M_G]+[K_G]-[QF]\right|=0$$

or

$$\left|[K_D(\omega)]-[QF]\right|=0 \tag{D.26}$$

D.7 Solution of Flutter Determinant Using the Determinant and V-g Methods

D.7.1 Determinant Method

The complex flutter determinant given in Eqn. (D.26) is a function of airspeed and frequency. At the flutter speed both the real and imaginary parts of the determinant must vanish. A range of frequency values are assumed and for each airspeed real and imaginary parts of the flutter determinant are calculated. Real and imaginary parts of the flutter determinant are plotted against frequency and airspeed. Flutter condition is reached when both curves intersect, see, for example, Fig. D.2 where the flutter speed (87 m/s) and flutter frequency (58.3 rad/s) of the Loring wing [5.6] are calculated using the Determinant method. This method is often referred to as Theodorsen's method [5.8].

D.7.2 V-g Method

In this method, the damping coefficient g, introduced into the equations of motion, is plotted against velocity for each normal mode. Since solutions to the equations of motion represent conditions for neutral stability, the value of g obtained in this manner represents the amount of damping that must be added to the structure to

attain neutral stability (flutter) at the given velocity. Thus, negative values of damping indicate that the structure is stable. Flutter occurs when the damping is equal to zero. This is illustrated in Figs D.3 and D.4 where the flutter speed and flutter frequency of the Loring wing [5.6] are calculated using the V-g method.

D.8 Aeroelastic Analysis of Metallic Wings Using CALFUN

The flutter speed, flutter frequency and divergence speed of two metallic wings, namely that of Loring [5.6] and Goland [D.4], have been calculated using the Strip and Lifting Surface theories. For illustrative purposes, the flutter speed and flutter frequency of the Loring wing [5.6] have been calculated using the two methods described in section D.7, that is, the Determinant and V-g methods (see Figs D.2-D.4). The calculated speed and frequency parameters are given together with the structural and geometrical properties of the above wings in the following sections.

D.8.1 Loring Wing [5.6]

$EI = 677.6\ Nm^2$ $\quad$ $c = 0.3048\ m$

$GJ = 1019\ Nm^2$ $\quad$ $b = 0.1524\ m$

$m = 8.06\ Kg/m$ $\quad$ $a = -0.4$

$I_\alpha = 0.0585\ Kgm$ $\quad$ $r_\alpha = 0.559$

$x_\alpha = -0.038\ m$ $\quad$ $m/\pi\rho b^2 = 90.2$

$L = 2.06\ m$

	Strip theory		Lifting Surface
	Determinant	**V-g**	
V_F (m/s)	87.0	87.0	92.0
ω_F (rad/s)	58.3	58.3	64.0
V_D (m/s)	181.8		188.5

D.8.2 Goland Wing [D.4]

$EI = 9.7567 \times 10^6\ Nm^2$ $\quad c = 1.8288\ m$

$GJ = 9.88 \times 10^5\ Nm^2$ $\quad b = 0.9144\ m$

$m = 35.75\ Kg/m$ $\quad a = -0.34$

$I_\alpha = 8.65\ Kgm$ $\quad r_\alpha = 0.538$

$x_\alpha = -0.183\ m$ $\quad m/\pi\rho b^2 = 11.16$

$L = 6.096\ m$

	Strip theory	Lifting Surface theory
V_F (m/s)	136.9	158
ω_F (rad/s)	70.0	65.5
V_D (m/s)	252.1	257.5

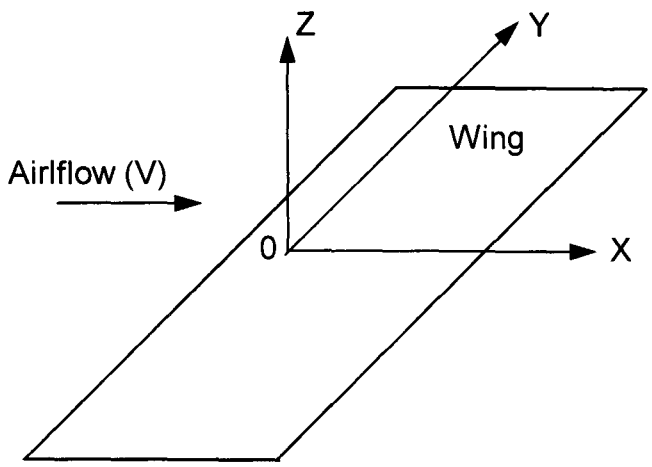

Fig. D.1 Coordinate system for Davies Lifting Surface theory.

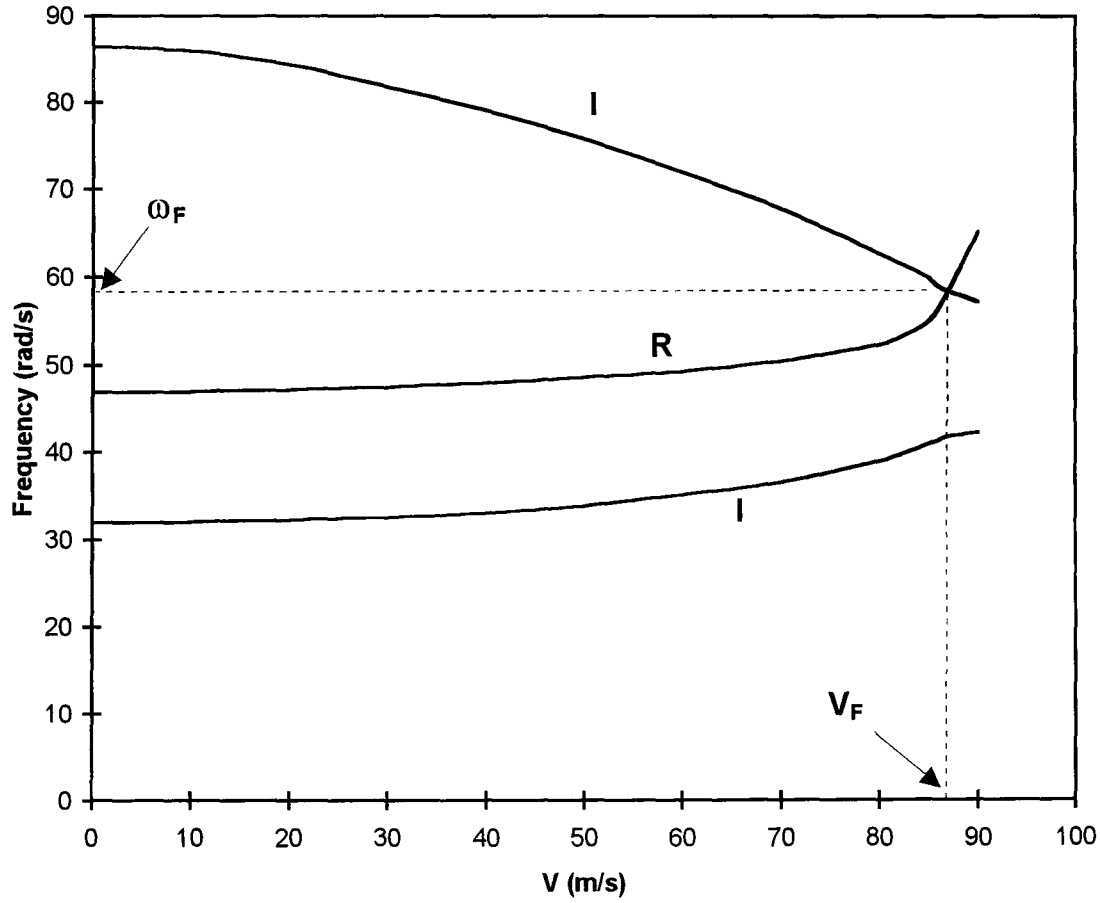

Fig. D.2. Flutter speed prediction for Loring wing using the Determinant method (i.e., $\Delta = 0$). I : locus of the roots of the imaginary part (i.e., $\Delta_I = 0$), R : locus of the roots of the real part (i.e., $\Delta_R = 0$).

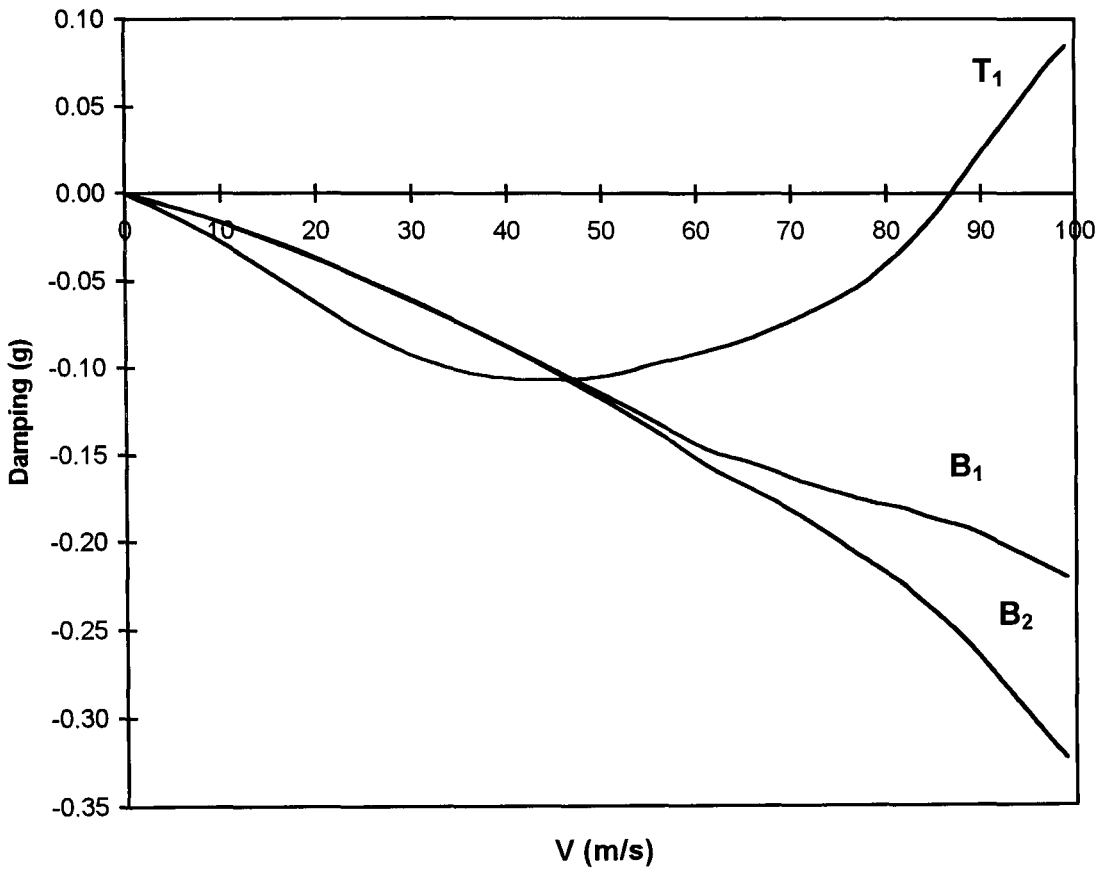

Fig. D.3. V-g plot for Loring wing.

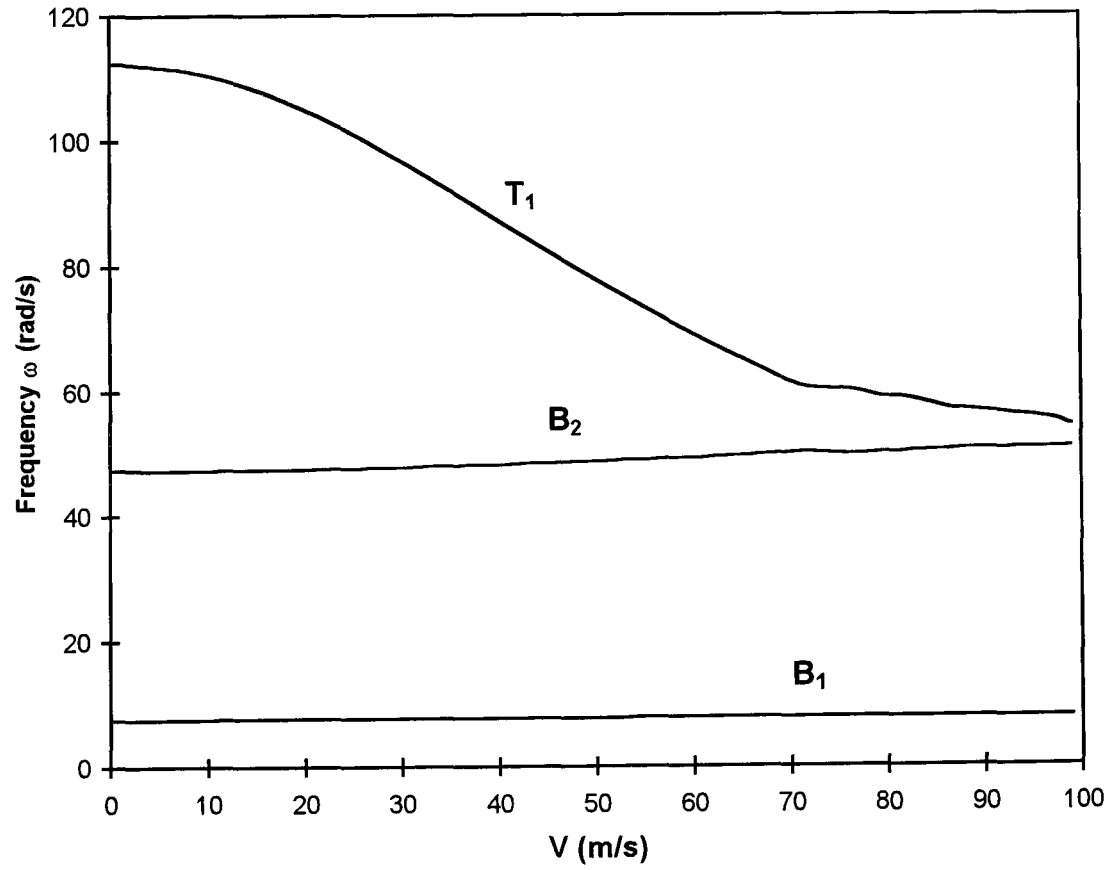

Fig. D.4. V-ω plot for Loring wing.

APPENDIX 'E'

ADS (AUTOMATED DESIGN SYNTHESIS) - PROGRAM OPTIONS

E.1 Introduction

ADS (Automated Design Synthesis) is a FORTRAN program for solution of non-linear constrained optimisation problems. The program is segmented into three levels which are (i) strategy, (ii) optimiser and (iii) one-dimensional search. At each level, several options are available so that a total of over 100 possible combinations can be created (see Tables E.1-E.3)

ADS is a general purpose numerical optimisation program containing a wide variety of optimisation algorithm. The problem solved is

$$\begin{aligned} &\text{Minimise} && F(x) && \\ &\text{subject to} && G_j(x) \le 0 && j = 1, m \\ & && H_k(x) = 0 && k = 1,1 \\ & && XL_i \le X_i \le XU_i && i = 1, n \end{aligned}$$

The solution of this general problem is separated into three basic levels:

1. **Strategy** - For example, Sequential Unconstrained Minimisation or Sequential Linear Programming.

2. **Optimiser** - For example, Variable Metric methods for unconstrained minimisation or the Method of Feasible Directions for constrained minimisation.

3. **One-Dimensional Search** - For example, Golden Section or Polynomial Interpolation.

By choosing the strategy, Optimiser and One-Dimensional Search, the user is given a considerable flexibility in creating an optimisation program which work well for a given class of design problems.

E.2. Program Options

In this section, the option available in the ADS program are discussed. At each of the three solution levels, several options are available for the user.

E.2.1 Strategy

Table E.1 lists the strategies available. The parameter ISTRAT would be sent to the ADS program to identify the strategy the user wants. The ISTRAT= 0 option would indicate that control should transfer directly to the optimiser.

TABLE E.1

Strategy options

ISTRAT	STRATEGY TO BE USED
0	None. Go directly to the optimiser.
1	Sequential unconstrained minimisation using the exterior penalty function method.
2	Sequential unconstrained minimisation using the linear extended interior penalty function method.
3	Sequential unconstrained minimisation using the quadratic extended interior penalty function method.
4	Sequential unconstrained minimisation using the cubic extended interior penalty function method.
5	Augmented Lagrange Multiplier method.
6	Sequential Linear Programming.
7	Method of Centres (method of inscribed hyperspheres)
8	Sequential Quadratic Programming.
9	Sequential Convex Programming

This would be the case, for example, when using the Method of Feasible Directions to solve constrained optimisation problems because the optimiser works directly with the constrained problem. On the other hand, if the constrained optimisation problem is to be solved by creating a sequence of unconstrained minimisations, with penalty functions to deal with constraints, one of the appropriate strategies would be used.

E.2.2 Optimiser

Table E.2 lists the optimisers available. IOPT is the parameter used to indicate the optimiser desired. In choosing the optimiser (as well as strategy and one-dimensional search) it is assumed that the user is knowledgeable enough to choose an algorithm consistent with the problem at hand. For example, a variable metric optimiser would not be used to solve constrained problems unless a strategy is used to create the equivalent unconstrained minimisation task via some form of penalty function.

TABLE E.2

Optimiser options

IOPT	OPTIMISER TO BE USED
0	None. Go directly to the one-dimensional search. This option should be used only for program development.
1	Fletcher-Reeves algorithm for unconstrained minimisation .
2	Davidon-Fletcher-Powell (DFP) variable metric method for unconstrained minimisation
3	Broydon-Fletcher-Goldfarb-Shanno (BFGS) variable metric method for unconstrained minimisation
4	Method of Feasible Directions (MFD) for constrained minimisation.
5	Modified Method of Feasible Directions for constrained minimisation

E.2.3 One-Dimensional Search

Table E.3 lists the one-dimensional search options available for unconstrained and constrained problems. The parameter IONED is used to identify the algorithm to be used.

TABLE E.3

One-dimensional search options

IONED	ONE-DIMENSIONAL SEARCH OPTION
1	Find the minimum of an unconstrained function using the Golden Section method.
2	Find the minimum of an unconstrained function using the Golden Section method followed by polynomial interpolation.
3	Find the minimum of an unconstrained function by first finding bounds and then using polynomial interpolation.
4	Find the minimum of an unconstrained function by polynomial interpolation/extrapolation without first finding bounds on the solution.
5	Find the minimum of an constrained function using the Golden Section method.
6	Find the minimum of an constrained function using the Golden Section method followed by polynomial interpolation.
7	Find the minimum of an constrained function by first finding bounds and then using polynomial interpolation.
8	Find the minimum of an constrained function by polynomial interpolation/extrapolation without first finding bounds on the solution.

REFERENCES

CHAPTER 1

1.1 Shanley, F. R., Weight-Strength Analysis of Aircraft Structures, Dover Publications, 1960, p. 8.

1.2 Shirk, H. M., Hertz, J. T., and Weisshaar, T. A., "Aeroelastic Tailoring-Theory, Practice, and Promise," *Journal of Aircraft*, Vol. 23, 1986, pp. 6-18.

1.3 McCullers, L. A., and Lynch, R. W., "Dynamic Characteristics of Advanced Filamentary Composite Structures, Volume II - Aeroelastic Synthesis Procedure Development," AFFDL-TR-73-111, Sept. 1974.

1.4 Wilkinson, K., Markowitz, J., Lerner, E., George, D., and Batill, S. M., "FASTOP: A Flutter and Strength Optimisation Program for Lifting Surface Structures," *Journal of Aircraft,* Vol. 14, 1977, pp. 581-587.

1.5 Krone, N. J. Jr., "Divergence Elimination with Advanced Composites," Ph.D. Thesis, University of Maryland, College Park, MD, Dec. 1974.

1.6 Weisshaar, T. A., and Foist, B. L., "Vibration and Flutter of Advanced Composite Lifting Surfaces," *Proceedings of the 24th AIAA/ASME/ ASCE/AHS Structures, Structural Dynamics and Materials Conference,* AIAA Paper 84-0961, 1983, pp. 498-508.

1.7 Cesnik, E. S. C, Hodges, D. H., and Patil, J. M., "Aeroelastic Analysis of Composite Wings," *Proceedings of the 37th AIAA/ASME/ASCE/AHS Structures, Structural Dynamics and Materials Conference,* AIAA Paper 96-1444, 1996, pp. 1113-1123.

1.8 Weisshaar, T. A., "Divergence of Forward Swept Composite Wings," *Journal of Aircraft,* Vol. 17, 1980, pp. 442-448.

1.9 Housner, J. M., and Stein, M., "Flutter Analysis of Swept-Wing Subsonic Aircraft with Parameter Studies of Composite Wings," NASA TN-D7539, Sept. 1974.

1.10 Austin, F., Hadcock, R., Hutchings, D., Sharp, D., Tang, S., and Waters, C., "Aeroelastic Tailoring of Advanced Composite Lifting Surfaces in Preliminary Design," *Proceedings of the 17th AIAA/ASME/SAE Structures, Structural Dynamics and Materials Conference*, 1976, pp. 69-79.

1.11 Niblett, L. T., "Divergence and Flutter of Swept-Forward Wings with Cross-Flexibilities," Royal Aircraft Establishment TR 80047, April 1980.

1.12 Weisshaar, T. A., and Ryan, J. R., "Control of Aeroelastic Instabilities Through Stiffness Cross-Coupling," *Journal of Aircraft*, Vol. 23, 1986, pp. 148-155.

1.13 Blair, M., and Weisshaar, T. A., "Swept Composite Wing Aeroelastic Divergence Experiments," *Journal of Aircraft*, Vol. 19, 1982, pp. 1019-1024.

1.14 Hollowell, S. J., and Dugundji, J., "Aeroelastic Flutter and Divergence of Stiffness Coupled, Graphite/Epoxy, Cantilevered Plates," *Proceedings of the 23rd AIAA/ASME/ASCE/AHS Structures, Structural Dynamics and Materials Conference*, AIAA Paper 82-0722, 1982, pp. 416-426.

1.15 Landsberger, B. J., and Dugundji, J., "Experimental Aeroelastic Behaviour of Unswept and Forward-Swept Cantilever Graphite/Epoxy Wings," *Journal of Aircraft*, Vol. 22, 1985, pp. 679-686.

1.16 Weisshaar, T. A., and Foist, B. L., "Aeroelastic Tailoring of Aircraft Subject to Body Freedom Flutter," AFWAL-TR-83-3137, Nov. 1983.

1.17 Chen, G. S., and Dugundji, J., "Experimental Aeroelastic Behaviour of Forward-Swept Graphite/Epoxy Wings with Rigid-Body Freedom," *Journal of Aircraft*, Vol. 24, 1987, pp. 454-462.

1.18 Lynch, R. W., Rogers, W. A., and Braymen, W. W., "Aeroelastic Tailoring of Advanced Composite Structures for Military Aircraft, Volume I-General Study," AFFDL-TR-76-100, April 1977.

1.19 Weisshaar, T. A., "Aeroelastic Tailoring of Forward Swept Composite Wings," *Journal of Aircraft,* Vol. 18, 1981, pp. 669-676.

1.20 Shirk, M. H., and Griffin, K. E., "The Role of Aeroelasticity in Aircraft Design with Advanced Filamentary Composite Materials," *Proceedings of the 2nd Conference on Fibrous Composites in Flight Vehicle Design*, AFFDL-TR-74-103, May 1974, pp. 405-438.

1.21 Weisshaar, T. A., "Structural Dynamic Tailoring of Advanced Composite Lifting Surfaces," Purdue University, West Lafayette, IN, AAE-82-1, June 1982.

1.22 Crawley, E. F., and Dugundji, J., "Frequency Determination and Non-dimensionalization for Composite Cantilever Plates," *Journal of Sound and Vibration,* Vol. 72, 1980, pp. 1-10.

1.23 Jensen, D. W., Crawley, E. F., and Dugundji, J., "Vibration of Cantilevered Graphite/Epoxy Plates with Bending-Torsion Coupling," *Journal of Reinforced Plastics and Composites,* Vol. 1, 1982, pp. 254-269.

1.24 Weisshaar, T. A. and Foist, B. F., "Vibration Tailoring of Advanced Composite Lifting Surfaces," *Journal of Aircraft,* Vol. 22, 1985, pp. 141-147.

1.25 Clary, R. R., "Vibration Characteristics of Unidirectional Filamentary Composite Material Panels." *Composite Materials : Testing and Design (Second Conference),* ASTM STP 497, American Society for Testing and Materials, 1972, pp. 415-438.

1.26 Rithcie, I. G., and Rosinger, H. E., "Torsion-Flexural Coupling in a Composite Material," *Journal of Physics (D) : Applied Physics*, Vol. 7, 1974, pp. 94-98.

1.27 Rithcie, I. G., Rosinger, H. E., Shillinglaw, A. J., and Fleury, W. H., "The Dynamic Elastic Behaviour of a Fibre-Reinforced Composite Sheet : I. The Precise Experimental Determination of the Principal Elastic Moduli," *Journal of Physics (D) : Applied Physics*, Vol. 8, 1975, pp. 1733-1749.

1.28 Rithcie, I. G., Rosinger, H. E., and Fleury, W. H., "The Dynamic Elastic Behaviour of a Fibre-Reinforced Composite Sheet : II. The Transfer Matrix Calculation of the Resonant Frequencies and Vibration Shapes," *Journal of Physics (D) : Applied Physics*, Vol. 8, 1975, pp. 1750-1768.

1.29 Wallace, M. M., and Bert, C. W., "Transfer Matrix Analysis of Dynamic Response of Composite-Material Structural Elements with Material Damping," *Shock and Vibration Bulletin 50*, Part 3, Sept. 1980.

1.30 Hodges, D. H., and Dowell, E. H., "Nonlinear Equations of Motion for the Elastic Bending and Torsion of Twisted Nonuniform Blades," NASA TN D-7818, 1974.

1.31 Panda, B., and Chopra, I., "Dynamics of Composite Rotor Blades in Forward Flight," *Vertica,* Vol. 11, (1/2), 1987.

1.32 Banerjee, J. R., and Williams, F. W., "Coupled Bending-Torsional Dynamic Stiffness Matrix of an Axially Loaded Timoshenko Beam Element," *International Journal of Solids and Structures,* Vol. 31, 1994, pp. 749-762.

1.33 Nissim, E., "Flutter Suppression Using Active Controls Based on the Concept of Aerodynamic Energy," NASA TN D-6199, Sept. 1971.

1.34 Nissim, E., Caspi, A., and Lottati, I., "Application of the Aerodynamic Energy Concept to Flutter Suppression and Gust Alleviation by Use of Active Controls, NASA TN D8212, June 1976.

1.35 Suzuki, S., and Yonezawa, S., "Simultaneous Structure/Control Design Optimization of a Wing Structure with a Gust Alleviation System," *Journal of Aircraft,* Vol. 30, 1993, pp. 268-274.

1.36 Layton, J. B., "Aeroservoelastic Tailoring for Gust Response of a Typical Section Aeroelastic Model," *Proceedings of the 36th AIAA/ SME/ ASEC/ AHS / ASC Structures, Structural Dynamics, and Materials Conference,* AIAA Paper 95-1192, 1995, pp. 306-313.

1.37 Banerjee, J. R., and William, F. W., "Vibration of Composite Beams - An Exact Method Using Symbolic Computation," *Journal of Aircraft,* Vol. 32., 1995, pp. 636-642.

1.38 Wittrick, W. H., and Williams, F. W., "A General Algorithm for Computing Natural Frequencies of Elastic Structures," *Quarterly Journal of Mechanics and Applied Mathematics,* Vol. 24, 1971, pp. 263-284.

1.39 Davies, D. E., "Theoretical Determination of Subsonic Oscillatory Airforce Coefficients," ARC R and M 3804, May 1976.

1.40 Vanderplaats, G. N., "ADS-A Fortran Program for Automated Design Synthesis," NASA CP-177985, Sept. 1985.

1.41 Weisshaar, T. A., "Flutter and Divergence of Airfoils with Stiffness Cross-Coupling," Purdue University, West Lafayette, IN, AAE-84-15, Aug. 1984, p. 36.

CHAPTER 2

2.1 Voigt, W., "Lehrbuch der Kristallphysik," Teuber, 1928.

2.2 Brown, W. F. J., "Interpretation of Torsional Frequencies of Crystal Specimens," *Physical Review*, Vol. 58, 1940, pp. 998-1001.

2.3 Hearmon, R. F. S., "The Significance of Coupling Between Shear and Extension in the Elastic Behaviour of Wood and Plywood," *Proceedings of the Physical Society*, Vol. 55, 1943, pp. 67-80.

2.4 Munk, M. M., "Propeller Containing Diagonally Disposed Fibrous Material," U.S. Patent 2,484,308,1111, Oct. 1949.

2.5 "Sherpa Takes the Air," *Flight and Aircraft Engineer*, No. 2334, Vol. LXIV, 1953, pp. 535.

2.6 "Pterodactyl to Sherpa," *Flight and Aircraft Engineer*, No. 2339, Vol. LXIV, 1953, pp. 680-681.

2.7 Waddoups, M. E., Smith, C. B., and McMickle, R. W., "Composite Wing for Transonic Improvement, Composite Wing Aeroelastic Response Study," AFFDL-TR-71-24, Vol. I, Dec. 1972.

2.8 Shirk, M. H., Hertz, T. J., and Weisshaar, T. A., "Aeroelastic Tailoring - Theory, Practice, and Promise," *Journal of Aircraft*, Vol. 23, 1986. (Waddoups, M. E., private communication, General Dynamics, Ft. Worth Div., Ft. Worth, TX, July 14, 1983.)

2.9 "Dynamic Characteristics of Advanced Filamentary Composite Structures," USAF Contract F33615-70-C-1837, Sept. 1970.

2.10 Fletcher, R., and Powell, M. J. D., "A Rapidly Convergent Descent Method for Minimisation," *The Comp. Journal*, Vol. 6, 1963, pp. 163-168.

2.11 Dong, S. B., Matthiesen, R. B., Pister, K. S., and Taylor, R. L., "Analysis of Structural Laminates," Aeronautical Research Laboratory, University of California, Los Angeles, Rept. 76, 1961.

2.12 Young, D., "Vibration of Rectangular Plates by the Ritz Method," *Journal of Applied Mechanics,* Vol. 17, 1950, pp. 448-453.

2.13 Barton, M. V., "Vibration of Rectangular and Skew Cantilever Plates Representing Idealised Missile Fins," Defence Research Laboratory, University of Texas, Austin, Rept. 222, Dec. 1949.

2.14 Waddoups, M. E., "The Vibration Response of Laminated Orthotropic Plates," M.S. Thesis, Dept. of Mechanical Engineering, Brigham Young University, Provo, UT, Aug. 1965.

2.15 Waddoups, M. E., and McCullers, L. A., "Structural Synthesis of Anisotropic Plates," *presented at the AIAA/ASME Structures, Structural Dynamics and Materials Conference,* April 1970.

2.16 Ashton, J. E., and Waddoups, M. E., "Analysis of Anisotropic Plates," *Journal of Composite Materials,* Vol. 3, 1969, pp. 148-165.

2.17 Ashton, J. E., "Analysis of Anisotropic Plates II," *Journal of Composite Materials,* Vol. 3, 1969, pp. 470-479.

2.18 Price, M. A., "HiMAT Structural Development Design Methodology," NASA CR-144886, Oct. 1979.

2.19 Busemann, A., 5th Volta Congress on High Speeds in Aviation, Compedoglio, Italy, Oct. 1935.

2.20 Krone, N. J. Jr., "Divergence Elimination with Advanced Composites," Ph.D. Thesis, University of Maryland, College Park, MD, Dec. 1974.

2.21 Krone, N. J. Jr., "Divergence Elimination with Advanced Composites," AIAA Paper 75-39511, 1975.

2.22 Krone, N. J. Jr., "Forward Swept Wing Flight Demonstrator," AIAA Paper 80-1882, 1980.

2.23 Tsai, S. W., and Hahn, H. T., Introduction to Composite Materials, Technomic, Westport, CT, 1980.

2.24 Jones, R. M., Mechanics of Composite Materials, Scripta Book Company, Washington, D.C., 1975.

2.25 Datoo, H. M., Mechanics of Fibrous Composites, Elsevier Applied Science, England, 1991.

2.26 Shirk, M. H., and Griffin, K. E., "The Role of Aeroelasticity in Aircraft Design with Advanced Filamentary Composite Materials," *Proceedings of the 2nd Conference on Fibrous Composites in Flight Vehicle Design*, AFFDL-TR-74-103, 1974, pp. 405-438.

2.27 McCullers, L. A., "Automated Design of Advanced Composite Structures," *Proceedings of the ASME Structural Optimisation Symposium*, Vol. 7, 1974, pp. 119-133.

2.28 Schmit, L. A., "Structural Synthesis-Its Genesis and Development," *AIAA Journal,* Vol. 19, 1981, pp. 1249-1263.

2.29 Ashley, H., "On Making Things the Best-Aeronautical Uses of Optimisation," *Journal of Aircraft,* Vol. 19, 1982, pp. 5-28.

2.30 Lansing, W., Lerner, E., and Taylor, R. F., "Applications of Structural Optimisation for Strength and Aeroelastic Design Requirements," AGARD-R-664, Sept. 1977.

2.31 Waddoups, M. E., Smith, C. B., and McMickle, R. W., "Composite Wing Aeroelastic Response Study," AFFDL-TR-71-24, Dec. 1972.

2.32 Waddoups, M. E., McCullers, L. A., and Naberhaus, J. D., "Composite Wing for Transonic Improvement, Vol. II, Advanced Analysis Evaluation," AFFDL-TR-71-24, Nov. 1971.

2.33 Forsch, H., "Advanced Design Composite Aircraft (ADCA) Study," AFFDL-TR-76-97, Vol. I, Nov. 1976.

2.34 Naberhaus, J. D., and Waddoups, M. E., "Dynamic Characteristics of Advanced Filamentary Composite Structures, Vol. III - Demonstration Component Program," AFFDL-TR-73-111, Sept. 1974.

2.35 Lynch, R. W., Rogers, W. A., and Braymen, W. W., "Aeroelastic Tailoring of Advanced Composite Structures for Military Aircraft, Volume I-General Study," AFFDL-TR-76-100, April 1977.

2.36 Rogers, W. A., Braymen, W. W., Murphy, A. C., Graham, D. H., and Love, M. H., "Validation of Aeroelastic Tailoring by Static Aeroelastic and Flutter Tests," AFWAL-TR-81-3160, Sept. 1982.

2.37 Rogers, W. A., Braymen, W. W., and Shirk, M. H., "Design, Analysis and Model Tests of an Aeroelastically Tailored Lifting Surface," AIAA Paper 81-1673, 1981.

2.38 Braymen, W. W., Rogers, W. A., and Shirk, M. H., "Wind Tunnel Test and Aerodynamic Analysis of Three Aeroelastically Tailored Wings," *presented at the 13th Congress of the International Council of the Aeronautical Sciences and AIAA Aircraft Systems and Technology Conference*, ICAS-82-5.7.3, Aug. 1982.

2.39 Maske, E. B., "Wing/Inlet Composite Advanced Development," AFFDL-TR-76-88, Sept. 1976.

2.40 Lockenhauer, J. L., and Layton, G. P., "RPRV Research Focus on HiMAT," *Astronautics & Aeronautics*, Vol. 14, 1976, pp. 36-41.

2.41 Price, M. A., "HiMAT Structural Development Design Methodology," NASA CR-144886, Oct. 1979.

2.42 Brown, L. E. Jr., Price, M A., and Genyrich, P. B., "Aeroelastically Tailored Wing Design," *Proceedings of Evolution of Aircraft Wing Design Symposium,* Dayton, Ohio, 1980, pp. 141-146.

2.43 Lokos, W., "HiMAT Aeroelastic Analysis," Research and Technology Annual Report 1983, NASA TM-85865, Nov. 1983.

2.44 Hertz, T. J., Shirk, M. H., Ricketts, R. H., and Weisshaar, T. A., "On the Track of Practical Forward-Swept Wings," *Astronautics & Aeronautics*, Vol. 20, 1982, pp. 40-52.

2.45 Wilkinson, K., and Rauch, F., "Predicted and Measured Divergence Speeds of an Advanced Composite Forward Swept Wing Model," AFWAL-TR-80-3059, July 1980.

2.46 Ellis, J. W., Dobbs, S. K., and Miller, G. D., "Structural Design and Wind Tunnel Testing of a Forward Swept Fighter Wing," AFWAL-TR-80-3073, July 1980.

2.47 Gimmestad, D., "An Aeroelastic Optimisation Procedure for Composite High Aspect Ratio Wings," AIAA Paper 79-0726, 1979.

2.48 Gimmestad, D., "Aeroelastic Tailoring of a Composite Winglet for KC-135," *Proceedings of the 22nd Structures, Structural Dynamics and Materials Conference*, 1981, pp. 373-376.

2.49 Triplett, W. E., "Aeroelastic Tailoring Studies in Fighter Aircraft Design," *Proceedings of the 20th Structures, Structural Dynamics and Materials Conference*, 1979, pp. 72-78.

2.50 Triplett, W. E., "Aeroelastic Tailoring of a Forward Swept Wing and Comparisons with Three Equivalent Aft Swept Wings," *Proceedings of the 21st AIAA/ASME/ASCE/AHS Structures, Structural Dynamics and Materials Conference*, 1980, pp. 754-760.

2.51 Sensburg, O., Becker, J., Lusebrink, H., and Weiss, F. "Gust Load Alleviation on Airbus A-300," *presented at 13th Congress of the Aeronautical Sciences*, 1982.

2.52 Schweiger, J., Sensburg, O., and Berns, H. J., "Aeroelastic Problems and Structural Design of a Tailless CFC-Sailplane," *presented at the Second International Symposium of Aeroelasticity and Structural Dynamics*, Aachen, FRG, 1985.

2.53 Shirk, M. H., Hertz, T. J., and Weisshaar, T. A., "Aeroelastic Tailoring - Theory, Practice, and Promise," *Journal of Aircraft*, Vol. 23, 1986. (Reply by Lerner, E. in response to AFWAL/FIBR survey letter, March 8, 1983.)

2.54 Austin, F., Hadcock, R., Hutchings, D., Sharp, D., Tang, S., and Waters, C., "Aeroelastic Tailoring of Advanced Composite Lifting Surfaces in Preliminary Design," *Proceedings of the AIAA/ASME/SAE 17th Structures, Structural Dynamics and Materials Conference*, 1976, pp. 69-79.

2.55 Asceni, L., and et al., "A Structural Weight Estimation Programme (SWEEP) for Aircraft," ASD/XR 74-10, June 1974.

2.56 Dodd, A. J., and et al., "Aeroelastic Design Optimisation Program," *Journal of Aircraft*, Vol. 27, 1990, pp. 1028-1036.

2.57 Herendeen, D. L., Hoesly, R. L., Johnson, E. H., and Venkayya, V. B., "ASTROS - An Advanced Software Environment for Automated Design," AIAA Paper 86-0856, 1986.

2.58 Lillico, M., Butler, R., Banerjee, J. R., and Guo, S., "Aeroelastic Optimization of High Aspect Ratio Wings Using an Exact Dynamic Stiffness Matrix Method," *Proceedings of the 5th AIAA/USAF/NASA/ISSMO Symposium on Multidisciplinary Analysis and Optimization*, AIAA Paper 94-4401, 1994 pp. 1301-1309.

2.59 Butler, R., Lillico, M., Banerjee, J. R., and Guo, S., "Optimum Design of High Aspect Ratio Wings Subject to Aeroelastic Constraints," *Proceedings of the 36th AIAA/ASME/ASCE/AHS/ASC Structures, Structural Dynamics and Materials Conference*, AIAA Paper 95-1223, 1995, pp. 558-566.

2.60 Butler, R., and Banerjee, J. R., "Optimum Design of Bending-Torsion Coupled Beams with Frequency or Aeroelastic Constraints," *Computers and Structures*, Vol. 60, 1996, pp. 715-724.

2.61 Weisshaar, T. A., "Forward Swept Wing Static Aeroelasticity," AFFDL-TR-79-3087, June 1979.

2.62 Weisshaar, T. A., "The Influence of Aeroelasticity on Swept Composite Wings," AFWAL-TR-80-3137, Nov. 1980.

2.63 Lerner, E., and Markowitz, J., "An Efficient Structural Resizing Procedure for Meeting Static Aeroelastic Design Objectives," *Journal of Aircraft,* Vol. 16, 1979, pp. 65-71.

2.64 Sherrer, V. C., Hertz, T. J., and Shirk, M. H., "Wind Tunnel Demonstration of Aeroelastic Tailoring Applied to Forward Swept Wings," *Journal of Aircraft,* Vol. 18, 1981, pp. 976-983.

2.65 Schneider, G., Godel, H., and Sensburg, O., "Structural Optimisation of Advanced Aircraft Structures," *presented at the 12th Congress of the International Council of the Aeronautical Sciences*, 1980.

2.66 Weisshaar, T. A., "Aeroelastic Stability and Performance Characteristics on Aircraft with Advanced Composite Swept-forward Wing Structures," Air Force Flight Dynamics Laboratory, AFFDL-TR-78-116, Wright-Patterson AFB, Ohio, Sept. 1978.

2.67 Mansfield, E. H., and Sobey, A. J., "The Fibre Composite Helicopter Blade," *Aeronautical Quarterly,* Vol. 30, 1979, pp. 413-449.

2.68 Weisshaar, T. A., and Ryan, J. R., "Control of Aeroelastic Instabilities Through Stiffness Cross-Coupling," *Journal of Aircraft*, Vol. 23, 1986, pp. 148-155.

2.69 Lottati, I., "Flutter and Divergence Aeroelastic Characteristics for Composite Forward Swept Cantilevered Wing," *Journal of Aircraft*, Vol. 22, 1985, pp. 1001-1007.

2.70 Stukel, S. P., "Aeroelastic Tailoring for Passive Flutter Suppression," M.S. Thesis, School of Aeronautics and Astronautics, Purdue University, West Lafayette, IN, Dec. 1982.

2.71 Ryan, R. J., "The Effect of Aeroelastic Tailoring in the Passive Control of Flutter and Divergence of Aircraft Wings," M.S. Thesis, School of Aeronautics and Astronautics, Purdue University, West Lafayette, IN, Dec. 1983.

2.72 Bakthavatsalam, T. N., "Suppression of Interference Flutter by Composite Tailoring," Ph.D. Thesis, University of Texas, Austin, May 1983.

2.73 Cwach, E. E., and Stearman, R. O., "Suppression of Flutter on Interfering Lifting Surfaces by the Use of Active Controls," AFOSR Interim Report, Jan. 1974.

2.74 Foist, B. L., "Aeroelastic Stability of Aircraft with Advanced Composite Wings," M.S. Thesis, School of Aeronautics and Astronautics, Purdue University, West Lafayette, IN, Aug. 1982.

2.75 Weisshaar, T. A., and Foist, B. L., "Aeroelastic Tailoring of Aircraft Subject to Body Freedom Flutter," AFWAL-TR-83-3137, Nov. 1983.

2.76 Chen, G. S., and Dugundji, J., "Experimental Aeroelastic Behaviour of Forward-Swept Graphite/Epoxy Wings with Rigid-Body Freedom," *Journal of Aircraft*, Vol. 24, 1987, pp. 454-462.

2.77 Niblett, L. T., "Aileron Reversal of Swept Wings with Cross-Flexibilities," RAE-TR 83023, Feb. 1983.

2.78 McCullers, L. A., Naberhaus, J. D., and Bensinger, C. T., "Dynamic Characteristics of Advanced Filamentary Composite Structures, Volume I-Test Specimen Program," AFFDL-TR-73-111, Sept. 1974.

2.79 Dwyer, W. J., and Rogers, J. B., "Aeroelastically Tailored Propellers," SAE Paper 770455, March 1977.

2.80 Rogers, J. B., "Aeroelastically Tailored Propellers," M.S. Thesis, University of Texas, Austin, May 1976.

2.81 Williams, J. G., "Analysis / Theory of Controlled Configurated Structures," AFFDL-TR-74-137, 1974.

2.82 Gratke, S. D., and Williams, J. G., "Analysis / Theory of Controlled Configured Structures (CCS)," AIAA Paper 77-1212, 1977.

2.83 Rehfield, L. W., Atilgan, A. R., and Hodges, D. H., "Nonclassical Behaviour of Thin-Walled Composite Beams with Closed Cross Sections," *Journal of the American Helicopter Society,* Vol. 35, 1988, pp. 42-50,.

2.84 Smith, E. C., and Chopra, I., "Formulation and Evaluation of an Analytical Model for Composite Box-Beams," *Journal of the American Helicopter Society,* Vol. 36, 1991, pp. 23-35.

2.85 Berdichevsky, V., Armanios, E. A., and Badir, A. M., "Theory of Anisotropic Thin-Walled Closed-Cross-Section Beams," *Composite Engineering,* Vol. 2, 1992, pp. 411-43.

2.86 Song, O., and Librescu, L., "Free Vibration and Aeroelastic Divergence of Aircraft Wings Modelled as Composite Thin-Walled Beams," *Proceedings of the 32nd AIAA/ASME/ASCE/AHS/ASC Structures, Structural Dynamics and Materials Conference*, AIAA Paper 91-1187, 1991, pp. 2128-2136.

2.87 Librescu, L., and Simovich, J., "General Formulation for the Aeroelastic Divergence of Composite Swept-Forward Wing Structures," *Journal of Aircraft,* Vol. 25, 1988, pp. 364-371.

2.88 Librescu, L., and Khdeir, A. A., "Aeroelastic Divergence of Swept-Forward Composite Wings Including Warping Restraint Effect," *AIAA Journal*, Vol. 26, 1988, pp. 1373-1377.

2.89 Librescu, L., and Thangjitham, S, "Analytical Studies on Static Aeroelastic Behaviour of Forward-Swept Composite Wing Structures," *Journal of Aircraft*, Vol. 28, 1991, pp. 151-157.

2.90 Librescu, L., and Song, O., "On the Static Aeroelastic Tailoring of Composite Aircraft Swept Wings Modelled as Thin-Walled Beam Structures," *Composite Engineering*, Vol. 2, 1992, pp. 497-512.

2.91 Cesnik, C. E. S., Hodges, D. H., and Patil, M. J., "Aeroelastic Analysis of Composite Wings," *Proceedings of the 37th AIAA/ASME/ASCE/AHS /ASC Structures, Structural Dynamics and Materials Conference*, AIAA Paper 96-1444, 1996, pp. 1113-1123.

2.92 Chattopadhyay, A, Zhang, S., and Ratneshwar, J., "Structural and Aeroelastic Analysis of Composite Wing Box Sections Using a Higher-Order Laminate Theory," *Proceedings of the 37th AIAA/ASME/ASCE/AHS/ASC Structures, Structural Dynamics and Materials Conference*, AIAA Paper 96-1567, 1996, pp. 2185-2198.

CHAPTER 3

3.1 Worndle, R., "Calculation of the Cross Section Properties and the Shear Stresses of Composite Rotor Blades," *Vertica,* 1982, Vol. 6, pp. 111-129.

3.2 Bauchau, O. A., "A Beam Theory for Anisotropic Materials," *Journal of Applied Mechanics*, Vol. 52, 1985, pp. 416-422.

3.3 Kosmatka, J. B., "Structural Dynamic Modelling of Advanced Composite Propellers by the Finite Element Method," Ph.D. Dissertation, University of California, Los Angeles, 1986.

3.4 Giavotto, V., Borri, M., Mantegazza, P., Ghiringhelli, G., Carmaschi, V., Maffioli, G. C., and Mussi, F., "Anisotropic Beam Theory and Applications," *Computers and Structures,* Vol. 16, 1983, pp. 403-413.

3.5 Borri, M., and Mantegazza, P., "Some Contributions on Structural and Dynamic Modelling of Rotor Blades," *I' Aerotecnica Missilie Spazio,* Vol. 64, 1985, pp. 143-154.

3.6 Borri, M., and Merlini, T., "A Large Displacement Formulation for Anisotropic Beam Analysis," *Meccanica,* Vol. 21, 1986, pp. 30-37.

3.7 Lee, S. W., and Stemple, A. D., "A Finite Element Model for Composite Beams with Arbitrary Cross-Sectional Warping," *AIAA Journal,* Vol. 26, 1988, pp. 1512-1520.

3.8 Stemple, A. D., and Lee, S. W. "A Finite Element Modelling for Composite Beams Undergoing Large Deflections with Arbitrary Cross Sectional Warping," *International Journal of Numerical Methods in Engineering,* Vol. 28, 1989, pp. 2143-2163.

3.9 Libove, C., "Stresses and Rate of Twist in Single-Cell Thin-Walled Beams with Anisotropic Walls," *AIAA Journal,* Vol. 26, 1988, pp. 1107-1118.

3.10 Mansfield, E. H., "The Stiffness of a Two-Cell Anisotropic Tube," *Aeronautical Quarterly,* Vol. 32, 1981, pp. 338-353.

3.11 Rehfield, L. W., "Design Analysis Methodology for Composite Rotor Blades," AFWAL-TR-85-3094, June 1985, pp. (V(a)-1)-(V(a)-15).

3.12 Nixon, M. W., "Extension-Twist Coupling of Composite Circular Tubes and Application to Tilt Rotor Blade Design," *Proceedings of the 28th Structures, Structural Dynamics and Materials Conference,* AIAA Paper 87-0772, 1987, pp. 295-303.

3.13 Hodges, D. H., Nixon, M. W., and Rehfield, L. W., "Comparison of Composite Rotor Blade Models: A Coupled-Beam Analysis and an MSC/NASTRAN Finite-Element Model, " NASA TM 89024, 1987.

3.14 Hong, C. H., and Chopra, I., "Aeroelastic Stability of a Composite Blade," *Journal of the American Helicopter Society*, Vol. 30, 1985, pp. 57-67.

3.15 Hong, C. H., and Chopra, I., "Aeroelastic Stability Analysis of a Composite Bearingless Rotor Blade," *Journal of the American Helicopter Society,* Vol. 31, 1986 , pp. 29-35.

3.16 Hodges, D. H., and Dowell, E. H., "Nonlinear Equations of Motions for the Elastic Bending and Torsion of Twisted Nonuniform Blades," NASA TN D-7818, Dec. 1974.

3.17 Chandra, R., Stemple, A. D., and Chopra, I., "Thin-Walled Composite Beams Under Bending, Torsional, and Extensional Loads," *Journal of Aircraft,* Vol. 27, July 1990, pp. 619-626.

3.18 Rehfield, L. W., and Atilgan, A. R., "Shear Centre and Elastic Axis and their Usefulness for Composite Thin-Walled Beams," *Proceedings of the American Society for Composites, Fourth Technical Conference,* 1989, pp. 179-188.

3.19 Hodges, D. H., Atilgan, A. R., Fulton, M. V., and Rehfield, L. W., "Dynamic Characteristics of Composite Beam Structures," *Proceedings of the AHS National Specialists' Meeting on Rotorcraft Dynamics,* Fort Worth, Texas, 1989.

3.20 Megson, T. H. G., Linear Analysis of Thin-Walled Elastic Structures, John Wiley & Sons, New York, 1974.

3.21 Timoshenko, S., and Goodier, J. N., Theory of Elasticity, McGraw-Hill, New York, 1951.

3.22 Sokolnikoff, I. S., Mathematical Theory of Elasticity, McGraw-Hill, New York, 1956.

3.23 Washizu, K., Variational Methods in Elasticity and Plasticity, Pergamon, New York, 1968.

3.24 Crandall, S. H., Dahl, N. C., and Lardner, T. J., An Introduction to the Mechanics of Solids, McGraw-Hill, Scarborough, CA, 1978.

3.25 Wempner, G., Mechanics of Solids with Applications to Thin Bodies, Sijthoff & Noordhoff, Leyden, 1981.

3.26 Gjelsvik, A., The Theory of Thin Walled Bars, John Wiley, New York, 1981.

3.27 Libai, A., and Simmonds, J. G., The Nonlinear Theory of Elastic Shells: One Spatial Dimension, Academic Press, New York, 1988.

3.28 Reissner, E., and Tsai, W. T., "Pure Bending, Stretching, and Twisting of Anisotropic Cylindrical Shells," *Journal of Applied Mechanics,* Vol. 39, 1972, pp. 148-154.

3.29 Jensen, D. W., and Crawley, E. F., "Frequency Determination Techniques for Cantilevered Plates with Bending-Torsion Coupling," *AIAA Journal,* Vol. 22, 1984, pp. 415-420.

CHAPTER 4

4.1 Abarcar, R. B., and Cunniff, P. F., "The Vibration of Cantilever Beams of Fibre Reinforced Material", *Journal of Composite Materials,* Vol. 6, 1972, pp. 504 - 517.

4.2 Teoh, L. S., and Huang, C. C., "The Vibration of Beams of Fibre Reinforced Material", *Journal of Sound and Vibration,* Vol. 51, 1977, pp. 467-473.

4.3 Teh, K. K., and Huang, C. C., "The Vibrations of Generally Orthotropic Beams, a Finite Element Approach", *Journal of Sound and Vibration,* Vol. 62, 1979, pp. 195 - 206.

4.4 Crawley, E. F., "The Natural Modes of Graphite/Epoxy Cantilever Plates and Shells", *Journal of Composite Material*, Vol. 13, 1979, pp. 195-205.

4.5 Green, J. A., "Aeroelastic Tailoring of Aft-Swept High-Aspect-Ratio Composite Wings," *Journal of Aircraft*, Vol. 24, 1987, pp. 812-819.

4.6 Bank, L. C., "Modifications to Beam Theory for Bending and Twisting of Open-Section Composite Beams," *Composite Structures*, Vol. 15, 1990, pp. 93-114.

4.7 Suresh, J. K., Venkatesan, C., and Ramamurti, V., "Structural Dynamic Analysis of Composite Beams," *Journal of Sound and Vibration*, Vol. 143, 1990, pp. 503-519.

4.8 Minguet, P., and Dugundji, J., "Experiments and Analysis for Composite Blades under Large Deflections," Part I : Static Behaviour, Part II : Dynamic Behavior, *AIAA Journal,* Vol. 28, 1990, pp. 1573-1588.

4.9 Hodges, D. H., Atilgan A. R., Fulton, M. V., and Rehfield L. W., "Free vibration Analysis of Composite Beams," *Journal of the American Helicopter Society,* Vol. 36, 1991, pp. 36-47.

4.10 Wu, X. X., and Sun, C. T., "Vibration Analysis of Laminated Composite Thin-Walled Beams Using Finite Elements," *AIAA Journal*, Vol. 29, 1991, pp. 736-742.

4.11 Thangjitham, S., and Librescu, L, "Vibration Characteristics of Anisotropic Composite Wing Structures," *Proceedings of the 32nd AIAA/ASME/ASCE/ AHS/ASC Structures, Structural Dynamics and Materials Conference*, AIAA Paper 91-1185, 1991, pp. 2115-2122.

4.12 Kosmatka, J. B., "Extension-Bend-Twist Coupling Behaviour of Thin-Walled Advanced Composite Beams with Initial Twist," *Proceedings of the 32nd AIAA/ASME/ASCE/AHS/ASC Structures, Structural Dynamics and Materials Conference*, AIAA Paper 91-1023, 1991, pp. 1037-1049.

4.13 Wu, X. X., and Sun, C. T., "Simplified Theory for Composite Thin-Walled Beams," *AIAA Journal*, Vol. 32, 1992, pp. 2945-2951.

4.14 Chandrashekhara, K., and Bangera, K. M., "Free Vibration of Composite Beams Using a Refined Shear Flexible Beam Element," *Computers and Structures*, Vol. 43, 1992, pp. 719-727.

4.15 Bank, L. C., and Cofie, E., "Coupled Deflection and Rotation of Open-Section Composite Stiffeners," *Journal of Aircraft*, Vol. 30, 1993, pp. 139-141.

4.16 Banerjee, J. R., and Butler, R., "Coupled Extensional -Torsional Vibration of Composite Beams - an Exact Method," *Proceedings of the 35th AIAA/ ASME/ ASCE/AHS/ASC Structures, Structural Dynamics and Materials Conference*, AIAA Paper 94-1325, 1994, pp. 147-154.

4.17 Teboub, Y., and Hajela, P., "Free Vibration of Generally Layered Composite Beams Using Symbolic Computations," *Composite Structures*, Vol. 33, 1995, pp. 123-134.

4.18 Armanios, E. A., and Badir, A. M., "Free Vibration Analysis of Anisotropic Thin-Walled Closed-Section Beams," *AIAA Journal*, Vol. 33, 1995, pp. 1905-1910.

4.19 Rodden, W. R., and Johnson, E. H., MSC/NASTRAN Aeroelastic Analysis, User's Guide, The Macneal-Schwendler Corporation, California, U.S.A., 1994.

4.20 Dancila, D. S., and Armanios, E. A., "The Influence of Coupling on the Free Vibration of Anisotropic Thin-Walled Closed-Section Beams," *Proceedings of the 36th AIAA/ASME/ASCE/AHS/ASC Structures, Structural Dynamics and Materials Conference*, AIAA Paper 95-141, 1995, pp. 2106-2115.

4.21 Williams, F. W., and Wittrick, W. H., "Exact Buckling and Frequency Calculations Surveyed," *Journal of Structural Engineering*, Vol. 109, 1983, pp. 169-187.

4.22 Williams, F. W., Howson, W. P., and Banerjee, J. R., "Natural Frequencies of Members with Coupled Extensional-Torsional Motion : A Physical Approach," *Journal of Sound and Vibration*, Vol. 165, 1993, pp. 373-375.

CHAPTER 5

5.1 Bisplinghoff, R. L., Ashley, H., and Halfman, R. L., Aeroelasticity, Addison-Wesley Publishing Co., Reading, Mass., 1955.

5.2 Banerjee, J. R., "Flutter Sensitivity Studies for High Aspect Ratio Aircraft Wings," *Proceedings of the 3rd International Conference on Computer Aided Optimum Design of Structures*, 1993, pp. 373-387.

5.3 Banerjee, J. R., "Use and Capability of CALFUN - A Program for Calculation of Flutter Speed Using Normal Modes," *Proceedings of the International AMSE Conference. on Modelling & Simulation,* Vol. 27-29, 1984, pp. 121-131.

5.4 Banerjee, J. R., "Flutter Characteristics of High Aspect Ratio Tailless Aircraft," *Journal of Aircraft*, Vol. 21, 1984, pp. 733-736.

5.5 Banerjee, J. R., "Flutter Modes of High Aspect Ratio Tailless Aircraft," *Journal of Aircraft*, Vol. 25, 1988, pp. 473-476.

5.6 Loring, S. J., "Use of Generalised Co-ordinates in Flutter Analysis," *SAE Journal*, Vol. 52, April 1944, pp. 113-132.

5.7 Williams, W. F., "Review of Exact Buckling and Frequency Calculations with Optional Multi-Level Substructuring," *Journal of Computers and Structures*, Vol. 48, 1993, pp. 547-552.

5.8 Theodorsen, T., "General Theory of Aerodynamic Instability and the Mechanism of Flutter," NACA Rept. 496, 1934.

5.9 Dowell, E. H., Curtiss, Jr., H. C., Scanlan, R. H., and Sisto, F., A Modern Course in Aeroelasticity, Kluwer Academic Publishers, 2nd Edition, 1989.

5.10 Librescu, L., Meirovitch, L., and Song, O., "Refined Structural Modelling for Enhancing Vibrational and Aeroelastic Characteristics of Composite Aircraft Wings," *La Recherche Aerospatiale*, No. 1, 1996, pp. 23-35.

5.11 Librescu, L., Meirovitch, L., and Song, O., "Integrated Structural Tailoring and Control Using Adaptive Materials for Advanced Aircraft Wings," *Journal of Aircraft*, Vol. 33, 1996, pp. 203-213.

5.12 Fung, Y. C., An Introduction to the Theory of Aeroelasticity, John Wiley and Sons, New York, 1955.

CHAPTER 6

6.1 Davidon, C. W., " Variable Metric Method for Minimization," Argone National Laboratory, ANL-5990 Rev., University of Chicago, 1959.

6.2 Fox, L. R., Optimization Methods for Engineering Design, Addison-Wesley, 1971.

CHAPTER 7

7.1 Davis, H. M., and Swaim, R. L., "Controlling Dynamic Response in Rough Air," AIAA Paper 66-997, 1966.

7.2 Wykes, J. H., and Mori, A. S., "Techniques and Results of an Analytical Investigation Into Controlling the Structural Modes of Flexible Aircraft," *AIAA Symposium on Structural Dynamics and Aeroelasticity*, 1965, pp. 419-433.

7.3 Wykes, J. H., and Mori, A. S., "An Analysis of Flexible Aircraft Structural Mode Control," AFFDL-TR-65-190, Pt. I, U.S. Air Force, June 1996.

7.4 Dempster, J. B., and Roger, K. L., "Evaluation of B-52 Structural Response to Random Turbulence With Stability Augmentation Systems," *Journal of Aircraft*, Vol. 4, 1967, pp. 507-512.

7.5 Rohling, W. J., "Flying Qualities: An Integral Part of a Stability Augmentation System, *Journal of Aircraft*, Vol. 6, 1969, pp. 510-515.

7.6 Dempster, J. B., and Arnold, J. I., "Flight Test Evaluation of an Advanced Stability Augmentation System for the B-52 Aircraft," AIAA Paper 68-1068, 1968.

7.7 Thompson, G. O., and Kass, G. J., "Active Flutter Suppression - An Emerging Technology," *Journal of Aircraft*, Vol. 9, 1972, pp. 230-235.

7.8 Topp, L. J., "Potential Performance Gains by Use of a Flutter Suppression System," *Joint Automatic Control Conference*, Paper 7-B3,1971.

7.9 Wykes, J. H., "Structural Dynamic Stability Augmentation and Gust Alleviation of Flexible Aircraft," *Presented at the AIAA 5th Annual Meeting and Technical Display*, AIAA Paper 68-1067, 1968.

7.10 Haftka, R. T., "Structural Optimization with Aeroelastic Constraints : A Survey of US Applications," *International Journal of Vehicle Design*, Vol. 7, 1986, pp. 381-392.

7.11 Rao, S. S., "Automated Optimum Design of Wing Structures : A Probabilistic Approach," *Computers and Structures*, Vol. 24, 1986, pp. 799-808.

7.12 Hajela, P., and Bach, C. T., "Optimum Structural Sizing for Gust Induced Response," *Journal of Aircraft*, Vol. 26, 1989, pp. 395-397.

7.13 Kerpel, M., "Design for Active and Passive Flutter Suppression and Gust Alleviation" NASA CR-3482, 1981.

7.14 Ohta, H., and Fujimori, A., "A Synthesis of Robust Optimal Regulators Using Singular Value with Application to Gust Load Alleviation," *Proceedings of the 29th AIAA/ASME/ASCE/AHS/ASC Structures, Structural Dynamics and Materials Conference*, AIAA Paper 88-4114, 1988, pp. 519-528.

7.15 Liebst, B. S., Garrard, W. L., and Farm, J. A., "Design of a Multivariable Flutter Suppression/Gust Load Alleviation System," *Journal of Guidance, Control and Dynamics*, Vol. 11, 1988, pp. 220-229.

7.16 Perry, B., "Qualitative Comparison of Calculated Turbulence Responses with Wind-Tunnel Measurements for a DC-10 Derivative Wing with an Active Control System," *Proceedings of the Dynamic Specialists Conference*, AIAA Paper 81-0567, 1981, pp. 633-643.

7.17 Wykes, J. H., and Borland, C. J., "B-1 Ride Control," AGARD No. 234, Active Controls in Aircraft Design, 1978.

7.18 Ueda, T., Matsushita, H., Suzuki, S., and Miyazawa, Y., "ACT Wing-Tunnel Experiments of a Transport-Type Wing," *Journal of Aircraft*, Vol. 28, 1992, pp. 139-145.

7.19 Livne, E., Schmit, L. A., and Friedmann, P. P., "Exploratory Design Studies Using an Integrated Multidisciplinary Synthesis," *AIAA Journal*, Vol. 30, 1992, pp. 1171-1179.

7.20 Gangsaas, D., Ly, U., and Norman, D. C., "Practical Gust Load Alleviation and Flutter Suppression Control Laws Based on a LQG Methodology," *Presented at the AIAA 19th Aerospace Sciences Meeting,* Jan. 12-15, 1981.

7.21 Zeiler, T. A., and Weisshaar, T. A., "Integrated Aeroservoelastic Tailoring of Lifting Surfaces," *Journal of Aircraft*, Vol. 25, 1988, pp. 76-83.

7.22 Suzuki, S., and Matsuda, S., "Structure/Control Design Synthesis of Active Flutter Suppression System by Goal Programming," *Journal of Guidance, Control, and Dynamics*, Vol. 14, 1991, pp. 1260-1266.

7.23 Skelton, R. E., Dynamic Systems Control : Linear Systems Analysis and Synthesis, John Wiley & Sons, New York, 1988.

7.24 Ohta, H., Fujimori, A., Nikiforuk, P. N., and Gupta, M. M., "Active Flutter Suppression for Two-Dimensional Airfoils," *Journal of Guidance, Control, and Dynamics*, Vol. 12, 1989, pp. 188-194.

7.25 Perry, B., Pototzky, S. A., and Woods, A. J., "NASA Investigation of a Claimed Overlap Between Two Gust Response Analysis Methods," *Journal of Aircraft,* Vol. 27, 1990, pp. 605-612.

7.26 Layton, J. B., "Aeroservoelastic Tailoring for Gust Response of a Typical Section Aeroelastic Model," *Proceedings of the 36th AIAA/SME/ASEC/ AHS/ASC Structures, Structural Dynamics, and Materials Conference,* AIAA Paper 95-1192, 1995, pp. 306-313.

7.27 Pratt, G. K., "Response of Flexible Airplanes to Atmospheric Turbulence," NASA SP-258, 1971.

7.28 Guo, S., Cheung, W. C., Banerjee, J. R., and Butler, R., "Gust Alleviation and Flutter Suppression of an Optimized Composite Wing With Active Control," *Proceedings of the International Forum on Aeroelasticity and Structural Dynamics*, 1995, pp. 41.1-41.9.

APPENDIX 'A'

A.1 Timoshenko, S. P., and Woinowsky-Kreiger, S., Theory of Plates and Shells, McGraw-Hill, New York, 1959.

APPENDIX 'C'

C.1 Fitch, J., "Solving Algebraic Problems with REDUCE," *Journal of Symbolic Computing*, Vol. 1, 1985, pp. 211-227.

C.2 Rayna, G., REDUCE Software for Algebraic Computation, Springer-Verlag, New York, 1986.

APPENDIX 'D'

D.1 Craig, R. R., Structural Dynamics an Introduction to Computer Methods, John Wiley & Sons, 1981.

D.2 Rodden, W. P., "The Role of Structural Aerodynamic Damping on the Aeroelastic Behaviour of Wings," *Journal of Aircraft*, Vol. 25, 1988, pp. 286-288.

D.3 Davies, D. E., "On the Use of Fortran Programs for Evaluating the Generalised and Aerodynamic Loading on a Flat Plate Wing Oscillating Harmonically in Subsonic Flow," R.A.E. Technical Memo Structures 881, Jan. 1988.

D.4 Goland, M., "The Flutter of a Uniform Cantilever Wing," *Journal of Applied Mechanics*, Vol. 12, 1945, pp. A.197 - A.208.